2016

Seismic Response Analysis of Structures with Nonlinear Mechanisms Using a Modal Approach

Tugce Akbas
Lehigh University

Seismic Response Analysis of Structures with Nonlinear Mechanisms Using a Modal Approach

by

Tugce Akbas

Presented to the Graduate and Research Committee
of Lehigh University
in Candidacy for the Degree of
Doctor of Philosophy

in

Structural Engineering

Lehigh University

May 2016

Approved and recommended for acceptance as a dissertation in partial fulfillment of the requirements for the degree of Doctor of Philosophy.

_____
Date

_____
Dr. Richard Sause
Dissertation Co-advisor

_____
Dr. James M. Ricles
Dissertation Co-advisor

_____
Accepted Date
Committee Members:

_____
Dr. John L. Wilson
Committee Chair

_____
Dr. Shamim N. Pakzad
Member

_____
Dr. Maria Garlock
External Member

To the women of Anatolia

ACKNOWLEDGEMENTS

The research in this document was conducted Center for Advanced Technology for Large Structural Systems (ATLSS), Department of Civil and Environmental Engineering, Lehigh University, Bethlehem, Pennsylvania.

I would like to express my sincere gratitude to my dissertation advisors, Dr. Richard Sause and Dr. James M. Ricles for their support, guidance, direction, patience, and advice throughout the doctoral studies. I would like to thank to Dr. Sause for his patience and endless support to put together a high quality document. Their efforts were invaluable towards my academic progress and becoming a skillful engineer.

I would like to thank to the committee chairperson and my academic advisor, Dr. John Wilson, for his mentorship, guidance, and advice during my studies at Lehigh University. I greatly appreciate his role in my academic progress.

I would like to express my special thanks to my committee member Dr. Shamim Pakzad for his sincere support and important role in my decision to do a PhD at Lehigh University. I am also thankful to my other committee member, Dr. Maria Garlock, whose studies and career are very inspirational for me.

I would like to thank to Dr. Ben Yen for his generosity in funding Yen Fellowship which I received for the two academic years.

The part of research presented in this document is supported by National Science Foundation. I would like to thank to the team for this project: Dr. Shiling Pei of the

Colorado School of Mines; Dr. Dan Dolan of Washington State University; Dr. Jeffrey Berman from University of Washington, Dr. John van de Lindt of Colorado State University; Marjan Popovski of FP Innovations; Hans-Erik Blomgren of Arup; Douglas Rammer of US Forest Service; and my fellow graduate students Ryan Ganey and Sara Loftus for running the experiments at Washington State University.

I would also like to thank to professors: Dr. Sibel Pamukcu, Dr. Clay Naito, Dr. Mesut Previzpour, Dr. David Roke, Dr. Matthew R. Eatherton.

I appreciate the help and assistance of the ATLSS center and laboratory support staff especially Peter Bryan, Prisca Vidanage, Doris Oravic, Leila Mazarul.

My heartfelt thanks goes to Prof. Donna McHugh and Dr. Anthony McHugh for making me feel at home in Bethlehem, for the lovely piano recitals and dinners at their house.

My sincere thanks also goes to Dale Falcinelli who inspired me with his lectures, experience, and gave me the encouragement for my professional career.

Another special thanks to my undergraduate professors Dr. Cetin Yilmaz, Dr. Guney Ozcebe, Dr. Erhan Karaesmen, Dr. Polat Gulkan, and Dr. Cem Topkaya for their guidance, support, and time for writing me letters of recommendation during my application procedure for the graduate school.

I am grateful to Dr. Brent Chancellor and Dr. Ebrahim Tahmasebi, my fellow research mates, for their invaluable help and support during my research studies. Thanks are extended to my fellow graduate students, Samantha Sabatino, Sila Gulgec, Ecem Bas, Aman Karamlou, Duygu Saydam, Georgios Tsampras, Moises Rivera, Leary Pakiding, Chinmoy Kolay, Xin Chu, Golnaz Shahidi, Tom Matarazzo, Patrick Trasborg, Sonam

Srivastava, Christina Cercone, Jeng Joo Kim and to my dear colleagues in Leslie E. Robertson Associates during my internship.

I would like to thank all my friends, especially to Meltem Ozmadenci, Bora Baloglu, Cem Alper Ozen, Gizem Bozkurt, Okan Ilhan, Idil Baykam, Emir Sadi Cansu, and Mehmet Can Mailmail for their company which made me feel at home, here in the US.

I wish to extend a *heartfelt thank you* with abundant appreciation to my family for their endless support and patience. I would like to thank to my mother, Gulsun Akbas, for always being very caring, supportive, and gracious, and always taking time to deal with the concerns of each one of us despite her busy work schedule. I owe a debt of gratitude to my father, Halit Levent Akbas, as he is the person who inspired me with all his life and the reason why I was willing to become a Structural Engineer since the age of 10. He is my biggest supporter as an entrepreneur, engineer, and a dreamer. I am grateful to him for his patience, respect, and faith to all my decisions and steps. I am extremely thankful to my sister, Gulce Akbas, whom I followed as a lodestar from kindergarten to the graduate school and who generously shared all her belongings, friends, schools, classmates, apartment, and experience with me. I am inpatient for the future accomplishments that we will achieve together as a team, shoulder to shoulder, in our professional career.

Most of all, thanks to the glorious people of Anatolia, I have been able to become an educated lady. This dissertation is dedicated to the women of Anatolia, who have suffered much but have never given up.

TABLE OF CONTENTS

LIST OF TABLES

LIST OF FIGURES

ABSTRACT

This research investigates the seismic response of nonlinear (NL) structures with yielding or rocking mechanisms using a modal approach. The focus is on quantifying the 1st and higher (i.e., the nth) mode responses, after the yielding or rocking mechanism forms. The static lateral load responses and the dynamic seismic responses of NL wall and frame structures are studied.

To accurately quantify the nth mode seismic response of a NL structure, two time-varying modal response variables are introduced, namely the *nth mode effective pseudo-acceleration* and the *nth mode effective deformation*. These modal response variables are obtained by decomposing the total seismic response of a NL multi-degree of freedom (MDF) structure. The nth mode effective pseudo-acceleration and effective deformation variables provide unambiguous and accurate quantification of the modal response of a NL structure, which can be used to achieve better understanding of the NL response in terms of the 1st and higher modes and as benchmarks for analytical methods intended to predict this NL response using modal responses (e.g., conventional modal response spectrum analysis for NL structures). The nth mode responses of NL wall and frame structures are examined and compared with predictions from existing analytical methods.

In addition, this research investigates a consistent approach to quantify the n^{th} mode response of NL structures with clearly defined yielding or rocking mechanisms. In this approach, a set of mode shapes, which are called *mechanism mode shapes*, are used to decompose the seismic response of a NL structure instead of mode shapes that are based on the initial, linear-elastic state of the NL structure. Using mechanism mode shapes, the n^{th} mode responses of NL wall and frame structures are examined. The results show that mechanism mode shapes can be used to accurately quantify and to create better understanding of the 1^{st} mode and higher mode responses of a NL structure with a clearly-defined yielding or rocking mechanism.

In addition to accurately and more consistently quantifying the 1^{st} and higher mode seismic responses of NL structures with clearly-defined yielding or rocking mechanisms, this research also investigates methods of controlling the 2^{nd} mode response of such NL structures by introducing an additional (second) yielding or rocking mechanism. An approach for locating and determining the strength of the second mechanism is established based on the modal properties of the NL structure. This approach is applied to NL wall and frame structures and the effect of the second mechanism in controlling the 2^{nd} mode response is demonstrated using nonlinear time history analysis (NLTHA) results.

As an application of the work on the n^{th} mode seismic responses of NL MDF structures, this research investigates the seismic response of buildings which use the Self-Centering Cross Laminated Timber (SC-CLT) wall system as the primary lateral-load resisting

system. SC-CLT walls are constructed by post-tensioning (PT) CLT wall panels to the foundation using vertical PT bars. A design-oriented analytical model based on simple closed-form equations (CFE) is introduced to estimate the lateral load response of SC-CLT walls. Numerical models of SC-CLT walls are developed using fiber elements. The analytical results (from both the CFE and fiber-based models) are compared with experimental results. The seismic response of SC-CLT wall buildings is investigated. A performance-based seismic design approach is proposed for SC-CLT wall buildings. The design approach is evaluated using NLTHA results for 6- and 11-story prototype SC-CLT wall buildings under a suite of ground motion records.

CHAPTER 1

INTRODUCTION

1.1. Overview

Structures designed to resist earthquakes are usually given a distribution of internal member strength to promote the development of a selected yielding mechanism. For example, slender reinforced concrete walls are proportioned to promote a flexural yielding hinge near the base of the wall and to avoid a shear yielding mechanism. The intended yielding mechanism is often assumed to reduce or limit the force demands on the structure. This assumption is evident in conventional modal response spectrum analysis (MRSA) procedure included in current design provisions (e.g., ASCE, 2010) where the elastic design response spectrum is reduced uniformly by a response modification coefficient, which is applied to the response of all relevant modes of vibration.

Research has shown that the formation of the intended yielding mechanism may not reduce the response of all modes (e.g. Blakely et al., 1975). Often the force response of the higher modes (i.e., higher than the 1st mode) of a nonlinear (NL) structure will reach or exceed the linear-elastic level of response after the intended yielding mechanism has formed. Methods have been proposed to quantify this higher mode response, especially for design calculations (e.g. Paulay and Priestley, 1992; Eberhard and Sozen, 1993). Many studies

(e.g. Eibl and Keinzel, 1988; Rodriguez et al., 2001; Priestley and Amaris, 2002; Chancellor, 2014) have suggested using a modified MRSA procedure, where the first mode response is reduced by a response modification factor but the higher mode response is not reduced. Priestley (2003) suggests, however, that assuming the higher mode response to be linear-elastic (un-reduced) may be conservative for frame structures.

This research investigates methods to accurately quantify the 1st and higher mode seismic response of NL structures. To accurately quantify the nth mode seismic response of a NL structure, two time-varying modal response variables are introduced, namely the *nth mode effective pseudo-acceleration* and the *nth mode effective deformation*. These modal response variables are obtained by decomposing the total seismic response of a NL multi-degree of freedom (MDF) structure. The nth mode effective pseudo-acceleration and effective deformation variables provide unambiguous and accurate quantification of the modal response of a NL structure, which can be used to achieve better understanding of the NL response in terms of the 1st and higher modes and as benchmarks for analytical methods intended to predict this NL response using modal responses (e.g., conventional modal response spectrum analysis for NL structures). The nth mode responses of NL wall and frame structures are examined and compared with predictions from existing analytical methods.

A conventional MRSA procedure and many alternative design methods use modal properties based on the initial, linear-elastic matrix of a NL structure to quantify the 1st and higher mode force response. Some research has shown that this approach may not be appropriate and may lead to unconservative design force estimates (e.g., Villaverde, 1991; 1997; Chao et al., 2007). Alternate approaches based on the tangent or secant stiffness matrix of a NL structure have been proposed. For example, Sullivan et al. (2008) proposed design force estimates based on the tangent stiffness after the yielding mechanism forms using *transitory inelastic modes* (TIMS). This study investigates an alternate approach for quantifying the n^{th} mode seismic response of NL structures with clearly defined yielding or rocking mechanisms, similar to the use of TIMS (Sullivan et al., 2008). An alternate set of displaced shapes which can consistently represent the n^{th} mode response of the structure after the yielding mechanism forms is investigated.

In addition to accurately and more consistently quantifying the 1st and higher mode of such NL structures, this research also investigates the methods of controlling the 2nd mode response of NL structures with clearly-defined yielding or rocking mechanisms by introducing an additional (second) yielding or rocking mechanism. Some previous research has investigated methods of reducing the higher mode response of such NL structures by adding a second yielding mechanism to the structure. Panagiotou and Restrepo (2009) developed a dual-plastic hinge (DPH) design approach for reinforced concrete shear walls in which the shear wall is designed to form two yielding hinges, one at the base of the wall and one at the mid-height of the wall. Wiebe et al. (2008, 2013) investigated methods for controlling the higher mode response in controlled rocking walls and rocking

concentrically braced frames by adding a second rocking mechanism in the structure. This research proposes an approach for locating and determining the strength of the second yielding (or rocking) mechanism based on the modal properties of the NL structure. This approach is applied to NL wall and frame structures and the effect of the second mechanism in controlling the 2^{nd} mode response is demonstrated using nonlinear time history analysis (NLTHA) results.

In addition, it was observed during preliminary NLTHA as part of the above studies that the using conventional stiffness proportional linear viscous damping models to model the inherent damping of NL building structures may lead to artificially large local damping forces. A study was conducted to develop a consistent model for the inherent damping of such NL structures.

As an application of the work on the n^{th} mode seismic responses of NL MDF structures, this research investigates the seismic response of Self-Centering Cross-Laminated Timber (i.e., SC-CLT) walls. A cross-laminated timber (CLT) panel is a heavy timber structural component fabricated by laminating layers of timber boards in an orthogonal pattern. SC-CLT walls are constructed by post-tensioning CLT wall panels to the foundation with vertical post-tensioning steel bars. Recent experimental studies on the lateral load response of SC-CLT walls under cyclic loading (Ganey, 2015) showed that SC-CLT walls have large deformation capacity, which suggests SC-CLT walls can be used as the primary lateral-load resisting system for buildings located in regions of high seismicity. This

research introduces a design-oriented analytical model based on simple closed-form equations (CFE) to estimate the lateral load response of SC-CLT walls. Numerical models of SC-CLT walls are developed using fiber elements. The analytical results (from both CFE and fiber-based numerical models) are compared with experimental results. This research also investigates the seismic response and performance of SC-CLT wall buildings which are designed based on a performance-based seismic design approach.

1.2. Research Objectives

The overall objective of this research is to investigate the seismic response of nonlinear (NL) structures with yielding or rocking mechanisms using a modal approach, with a focus on quantifying the 1st and higher (i.e., the nth) mode responses. More specific objectives were identified for the work presented in each of the chapters of this dissertation, as follows:

Chapter 2. The work presented in Chapter 2 has the following objectives:

- To develop an approach to accurately quantify the nth (i.e., 1st and higher) mode responses of NL wall and frame structures.
- To achieve better understanding of the NL response in terms of the nth mode response.
- To provide benchmarks for analytical methods developed by others that are intended to predict the NL response using modal responses.

Chapter 3. The work presented in Chapter 3 has the following objectives:

- To develop a consistent approach for quantifying the n^{th} mode response of NL structures with clearly defined yielding or rocking mechanisms.
- To find an alternate set of modes shapes, instead of mode shapes that are based on the initial, linear-elastic state of the NL structure, to consistently quantify and to create better understanding of n^{th} mode response of a NL structure with a clearly-defined yielding or rocking mechanism.

Chapter 4. The work presented in Chapter 4 has the following objectives:

- To investigate problems observed when conventional stiffness proportional linear viscous damping models are used to model the inherent damping of NL building structures.
- To develop a consistent model for the inherent damping of such NL structures.

Chapter 5. The work presented in Chapter 5 has the following objectives:

- To investigate a method of controlling the 2^{nd} mode response of NL structures with clearly-defined yielding or rocking mechanisms by adding a second mechanism.
- To establish an approach for locating and determining the strength of the second mechanism based on modal properties of the NL structure.

Chapters 6 and 7. The work presented in Chapters 6 and 7 has the following objectives:

- To investigate the seismic response of buildings which use the Self-Centering Cross Laminated Timber (SC-CLT) wall system as the primary lateral-load resisting

system as an application to the work on n^{th} mode seismic responses of NL MDF structures

- To develop analytical models (a design-oriented analytical model based on simple closed-form equations and numerical models based on fiber elements) that provide an accurate estimate of the lateral load response of SC-CLT walls.
- To propose a seismic design approach for SC-CLT walls buildings.

1.3. Research Approach

To achieve the research objectives, research tasks were performed as follows, organized according to the chapters of the dissertation:

Chapter 2. The research tasks associated with the work presented in Chapter 2 are as follows:

- Study previous research related to the 1^{st} and higher mode responses of NL structures and methods used to quantify the 1^{st} and higher mode seismic responses of a NL structure.
- Introduce two time-varying modal response variables, namely the *n^{th} mode effective pseudo-acceleration* and the *n^{th} mode effective deformation*, to accurately quantify the 1^{st} and higher (i.e., the n^{th}) mode seismic responses of a NL structure.
- Examine the n^{th} mode responses of NL wall and frame structures based on NLTHA results for a suite of ground motion records.

- Quantify the n^{th} mode responses of NL wall and frame structures using *n^{th} mode effective pseudo-acceleration* and the *n^{th} mode effective deformation*.
- Compare these n^{th} mode responses with results from existing analytical methods.

Chapter 3. The research tasks associated with the work presented in Chapter 3 are as follows:

- Study previous research related to modal properties that can be used to quantify the n^{th} mode seismic responses of NL structures with clearly defined yielding or rocking mechanisms.
- Introduce *mechanism mode shapes* which are based on the state of a NL structure after the yielding mechanism forms.
- Using both mechanism mode shapes and elastic mode shapes (based on the initial, linear-elastic state of the NL structure), decompose the seismic response of NL wall and frame structures obtained from NLTHA results for a suite of ground motion records, and compare the results with results from existing analytical methods.

Chapter 4. The research tasks associated with the work presented in Chapter 4 are as follows:

- Study previous research related to the modeling of the inherent damping of NL building structures and the problems from using conventional stiffness proportional linear viscous damping to model the inherent damping of NL structures.
- Examine the n^{th} mode response of NL frame building structures with conventional stiffness proportional linear viscous damping

- Propose a model for the inherent damping of NL frame building structures using a *damping substructure* and establish the *damping substructure concept* (DSC).
- Compare the n^{th} mode response of NL frame building structures with an inherent damping model based on DSC and stiffness proportional linear viscous damping models.
- Extend DSC to model the inherent damping of a building using NL viscous damping.

Chapter 5. The research tasks associated with the work presented in Chapter 5 are as follows:

- Study previous research on controlling the higher mode response of NL structures with clearly-defined yielding or rocking mechanisms.
- Establish an approach for locating and determining the strength of a second mechanism for controlling the 2^{nd} mode response, based on modal properties of the NL structure.
- Evaluate the effect of the second yielding mechanism on controlling the 2^{nd} mode response of NL wall and frame structures.

Chapters 6 and 7. The research tasks associated with the work presented in Chapters 6 and 7 are as follows:

- Study previous research on the material properties and response of CLT under compression loading and previous research on the design and response of post-tensioned self-centering (SC) shear walls under lateral and earthquake loading.

- Develop analytical models (i.e., the CFE and fiber-based models) to estimate the lateral load response of SC-CLT walls.
- Compare the analytical and experimental lateral load response of SC-CLT walls.
- Propose a seismic design approach for SC-CLT wall buildings.
- Validate the design approach using NLTHA results for 6- and 11-story prototype SC-CLT wall buildings under a suite of ground motion records.

1.4. Organization of Dissertation

The dissertation is organized into six main chapters (i.e., Chapter 2- 7) and a final chapter (i.e., Chapter 8) which presents a summary of the research. Each main chapter is presented in the form of a paper with an abstract, introduction, main sections, and summary and conclusions. The remaining chapters of the dissertation are organized as follows:

- Chapter 2 presents a study of methods to accurately quantify the 1st and higher (i.e., nth) mode responses of NL wall and frame structures. Two time-varying modal response variables, namely the *nth mode effective pseudo-acceleration* and the *nth mode effective deformation,* are introduced. The nth mode responses of NL wall and frame structures are examined and compared with predictions from existing analytical methods.
- Chapter 3 presents a study of a consistent approach to quantify the nth mode response of NL structures with clearly defined yielding or rocking mechanisms. A set of mode shapes, which are called *mechanism mode shapes*, are used to

decompose the seismic response of a NL structure, instead of mode shapes that are based on the initial, linear-elastic state of the NL structure. Using mechanism mode shapes, the n^{th} mode responses of NL wall and frame structures are examined.

- Chapter 4 presents a study of a consistent model for the inherent damping of such NL building structures, based on a certain, specific understanding of the energy dissipation that is expected from inherent damping. The problems from using conventional stiffness proportional linear viscous damping models are investigated. The *damping substructure concep*t (DSC) is introduced to model the inherent damping of NL building structures. The n^{th} mode responses of NL frame structures with inherent damping modeled using DSC and with inherent damping modeled using conventional stiffness proportional linear viscous damping are compared.
- Chapter 5 presents a study of methods for controlling the 2^{nd} mode response of NL structures with clearly-defined yielding (or rocking) mechanisms. An approach for locating and determining the strength of a second mechanism for controlling the 2^{nd} mode response, based on modal properties of the NL structure, is presented. The n^{th} mode responses of NL wall and frame structures with two yielding (or rocking) mechanisms are examined and quantified.
- Chapter 6 presents a study of the lateral load response of SC-CLT walls under quasi-static cyclic loading. Analytical models (a design-oriented analytical model based on simple closed-form equations (CFE) and numerical models based on fiber elements) that provide an accurate estimate of the lateral load response of SC-CLT walls are presented. Analytical results (from both the CFE and fiber-based models) are compared with experimental results.

- Chapter 7 presents a study of the seismic response of SC-CLT wall buildings. A seismic design approach is proposed for SC-CLT wall buildings. The design approach is evaluated using NLTHA results for 6- and 11-story prototype SC-CLT wall buildings under a suite of ground motion records.
- Chapter 8 presents a summary and the conclusions of this research and make suggestions for future research.

CHAPTER 2

QUANTIFYING MODAL RESPONSE OF NONLINEAR STRUCTURES UNDER SEISMIC LOADING

Overview

The importance of higher mode contributions to the total seismic response of nonlinear (NL) structures has been widely recognized. Past research has investigated the higher mode seismic response of NL structures with a focus on predicting the higher mode response amplitudes, for example, by using modal response spectrum analysis with a reduced pseudo-acceleration response spectrum to account for NL response. The accuracy of these higher mode response amplitude predictions is often unclear, because comparisons are made using peak total response amplitudes (e.g., peak total base shear) obtained using approximate modal combination methods. This paper focuses on accurately quantifying the first and higher mode (i..e, the n^{th} mode) seismic response of NL structures to establish the actual n^{th} mode response that the predictive methods are seeking. Time-varying response variables to quantify the n^{th} mode response, which are obtained from the total NL seismic response of a multi-degree of freedom (MDF) structure, are introduced. The n^{th} mode responses of NL cantilever wall structures and a frame structure are examined using nonlinear time history analysis results. A parametric study is performed. Comparisons with

results from existing methods for predicting the n^{th} mode seismic response of NL structures are made.

2.1. Introduction

The contributions of higher mode response to the total seismic response of multi-degree-of-freedom (MDF) structures has been of interest since the study by Clough (1954). Blakely et al. (1975) showed that the higher mode response is significant when structures respond in the nonlinear (NL) range. Many subsequent studies (e.g., Derecho et al., 1978; Kabeyasawa and Ogata, 1984; Eibl and Keintzel, 1988; Paulay and Priestley, 1992; Eberhard and Sozen, 1993) have shown the importance of higher mode contributions for both linear-elastic and NL structures.

Methods have been proposed to predict higher mode seismic response of NL structures, especially for design purposes. The conventional modal response spectrum analysis (MRSA) procedure is widely utilized for estimating the first mode and higher mode responses, and is included in current design provisions (e.g., ASCE, 2010). In a conventional MRSA, the mode shapes and periods, and corresponding modal properties (e.g., equivalent static forces) are calculated from eigen analysis results for a linear-elastic model of the structure. The peak dynamic response of each participating mode is determined from a design pseudo-acceleration response spectrum using the corresponding modal period. For the conventional MRSA included in current design provisions (e.g.,

ASCE, 2010), the design pseudo-acceleration response spectrum is scaled down by a single response modification factor (R) in the process of determining the response for each mode. This use of a single R value assumes that the force response for each mode is equally reduced by NL response, which is questionable. The peak total response of the structure is usually obtained by combining the modal response using a modal combination rule (e.g., square root of the sum of the squares (SRSS) or complete quadratic combination (CQC)).

Modifications to the conventional MRSA and other methods to better predict the higher mode response have been proposed. Many studies (e.g., Eibl and Keintzel, 1988; Rodriguez et al., 2002; Priestley and Amaris, 2003; Roke et al. 2010; Calaguru and Panagiotou, 2010), have suggested using a modified pseudo-acceleration response in a MRSA, where the first mode response is reduced by a response modification factor but the higher mode response is not reduced. Priestley (2003) suggests, however, that assuming the higher mode response to be linear-elastic (un-reduced) may be conservative for frame structures. In addition, multi modal pushover analysis procedures have been developed (e.g., Bracci et al., 1997; Chopra and Goel, 2001; Gupta and Kunnath, 2000) to predict the higher mode response for design purposes.

The goal of this chapter is to develop and apply response variables to accurately quantify that higher mode response of NL MDF structures. Two time-varying modal response variables, the modal effective pseudo-acceleration response ($A_{eff_n}(t)$) and the modal effective deformation response ($D_{eff_n}(t)$), are developed. $A_{eff_n}(t)$ and $D_{eff_n}(t)$, are derived

from modal decomposition of the total NL response using a set of mass orthogonal deformation shapes, such as the mode shapes from the eigen analysis of a linear-elastic model of the structure. $A_{eff_n}(t)$ and $D_{eff_n}(t)$ are analogous to the modal pseudo-acceleration ($A_n(t)$) and deformation ($D_n(t)$) used in linear modal response history analysis.

The higher mode responses of both wall and frame structures are investigated. Nonlinear time history analysis (NLTHA) results for 4-, 9-, and 12-story cantilever walls as well as a 9-story, 4-bay steel special moment-resisting frame (SMRF) are used. Parameters of the wall structures, such as the shear stiffness, number of stories, fundamental period, and ductility demand are varied. The contributions of higher mode responses are quantified using $A_{eff_n}(t)$ and $D_{eff_n}(t)$, as well as conventional MRSA approaches. The contributions of higher modes to various seismic response quantities are investigated. Higher mode responses quantified using different approaches are compared**.**

2.2. Theory

2.2.1. Modal Pseudo-Acceleration Response for a Linear Structure

For a linear MDF structure, a total response to a given earthquake ground motion, r, can be expressed as a sum of the modal responses, r_n, which equal the modal static responses, r_n^{st}, under the modal external force distribution, $\mathbf{s}_n$, multiplied by modal pseudo-accelerations, $A_n(t)$, as follows (Chopra, 2012):

$$r(t) = \sum_{n=1}^{N} r_n(t) = \sum_{n=1}^{N} r_n^{st} A_n(t) \tag{2.1}$$

where r_n^{st} = nth mode static response to $\mathbf{s}_n$; $\mathbf{s}_n$= nth mode external forces. Note that bold font is used represents vector and matrix quantities.

Using Eq. (2.1), the total restoring force vector (equivalent static forces) for a linear MDF structure, $\boldsymbol{f}_r(t)$, can be expressed as follows (Chopra 2007):

$$\boldsymbol{f}_r(t) = \sum_1^N \boldsymbol{f}_{r,n}(t) = \sum_1^N \boldsymbol{s}_n A_n(t) = \sum_1^N (\Gamma_n \boldsymbol{m} \boldsymbol{\phi}_n) A_n(t) \quad (2.2)$$

where $\boldsymbol{f}_{r,n}(t)$ = nth mode restoring force vector (equivalent static forces); $\Gamma_n = \frac{\boldsymbol{\phi}_n^T \boldsymbol{m} i}{M_n}$ = nth mode participation factor; $\boldsymbol{\phi}_n$ = nth mode shape vector which is mass-orthogonal to the other mode shape vectors (Chopra, 2012); $M_n = \boldsymbol{\phi}_n^T \boldsymbol{m} \boldsymbol{\phi}_n$ = nth mode mass; $\boldsymbol{m}$ = mass matrix for the MDF; i = influence vector for the structure.

When the linear MDF structure has "classical" damping (Chopra 2007), the modal responses are uncoupled and $A_n(t)$ can be calculated from the response history analysis of a single degree of freedom (SDF) system corresponding to nth mode for the given ground motion. The nth mode pseudo-acceleration response from this SDF analysis is denoted as $A_n^{SDF}(t)$.

If $\boldsymbol{f}_r(t)$ is known from time history analysis of the linear MDF structure for the given ground motion, $A_n(t)$ can be calculated from $\boldsymbol{f}_r(t)$ using the mass orthogonality of the mode shapes as follows:

$$A_n^{MDF}(t) = \frac{\boldsymbol{\phi}_n^T \boldsymbol{f}_r(t)}{\Gamma_n M_n} \tag{2.3}$$

where $A_n^{MDF}(t) = A_n(t)$ determined from $\boldsymbol{f}_r(t)$ of the linear MDF structure for the given ground motion.

Figure 2.1 shows that for a linear MDF structure with classical damping, $A_n^{MDF}(t)$ and $A_n^{SDF}(t)$ are, as expected, identical. The results in Figure 2.1 are from time history analysis of a linear-elastic 4-story cantilever wall structure subjected to the CHY015W ground motion record (described later, see Table 2.1).

2.2.2. Modal Deformation Response for a Linear Structure

The total deformation response, $\mathbf{u}(t)$, of a linear MDF structure can be expressed as a sum of modal response as follows (Chopra, 2012):

$$\mathbf{u}(t) = \sum_{n=1}^{N} \boldsymbol{\phi}_n \, q_n(t) \tag{2.4}$$

where $q_n(t)$ = n^{th} mode deformation response.

When the modal responses are uncoupled, $q_n(t)$ is related to the nth mode deformation response of the SDF system corresponding to mode n, $D_n^{SDF}(t)$, which is related to $A_n^{SDF}(t)$ as follows:

$$D_n^{SDF}(t) = \frac{q_n(t)}{\Gamma_n} \tag{2.5}$$

$$D_n^{SDF}(t) = \frac{A_n^{SDF}(t)}{\omega_n^2} \tag{2.6}$$

where ω_n = nth mode natural frequency

If $\mathbf{u}(t)$ is known from time history analysis of the linear MDF structure for the given ground motion, $D_n(t)$ can be calculated from $\mathbf{u}(t)$ using the mass orthogonality of the mode shapes, as follows:

$$D_n^{MDF}(t) = \frac{\boldsymbol{\phi}_n^{\boldsymbol{T}}\, \boldsymbol{m}\, \mathbf{u}(t)}{\Gamma_n M_n} \tag{2.7}$$

Figure 2.2 shows that for the linear-elastic 4-story cantilever wall structure subjected to the CHY015W ground motion record, as expected, $D_n^{MDF}(t)$ and $D_n^{SDF}(t)$ are identical.

2.2.3. nth Mode Effective Pseudo-Acceleration Response for a Nonlinear Structure

For a NL MDF structure, $A_n^{SDF}(t)$ is not useful for quantifying the nth mode contribution to the response for a given ground motion. However, Roke et al. (2010) extended the application of Eq. (2.3) to NL MDF structures, noting that it requires only mass

orthogonality of the mode shapes. The result is the "effective" modal pseudo-acceleration, $A_{eff_n}(t)$ for a NL structure as follows:

$$A_{eff_n}(t) = \frac{\boldsymbol{\phi}_n^T \boldsymbol{f}_r^{NL}(t)}{\Gamma_n M_n} \tag{2.8}$$

where $\boldsymbol{f}_r^{NL}(t)$ = total restoring force vector from NLTHA of the NL MDF structure for the given ground motion.

Similar to $A_n^{MDF}(t)$ for a linear MDF structure, $A_{eff_n}(t)$ quantifies the nth mode contribution to the total force response of the NL MDF structure.

Calculating $A_{eff_n}(t)$ using Eq. (2.8) depends only on the linear independence of the vectors $\mathbf{s}_n$, since any arbitrary time varying vector with N components (e.g., $\boldsymbol{f}_r^{NL}(t)$) can be expressed as a sum of N linearly-independent vectors (e.g., $\mathbf{s}_n$) multiplied by time varying scale factors (e.g., $A_{eff_n}(t)$), as follows:

$$\boldsymbol{f}_r^{NL}(t) = \sum_1^N \boldsymbol{f}_{r,n}^{NL}(t) = \sum_1^N \boldsymbol{s}_n A_{eff_n}(t) \tag{2.9}$$

Using Eq. (2.9), $\boldsymbol{f}_r^{NL}(t)$ can be regenerated from its modal components. Figure 2.3(a) shows the roof level component of $\boldsymbol{f}_r^{NL}(t)$ of a NL 4-story cantilever wall structure subjected to the CHY015W ground motion record, regenerated from its modal components

$\boldsymbol{f}_{r,n}^{NL}(t)$ using Eq. (2.8) and Eq. (2.9). In Figure 2.3(a), the roof level component of $\boldsymbol{f}_{r,n}^{NL}(t)$ is normalized by its peak value which is denoted as, $\boldsymbol{f}_{r,n}^{NL}$. These results show that $A_{eff_n}(t)$ can be used to accurately quantify the force response of a NL MDF structure using a set of mass orthogonal deformation shape vectors, such as $\boldsymbol{\phi}_n$.

2.2.4. nth Mode Modal Deformation Response for a Nonlinear Structure

Similar to $A_{eff_n}(t)$, an "effective" modal deformation for a NL MDF structure, $D_{eff_n}(t)$ can be obtained from the total deformation vector, $\boldsymbol{u}^{NL}(t)$, for a given ground motion determined from NLTHA, as follows:

$$D_{eff_n}(t) = \frac{\boldsymbol{\phi}_n^T \mathbf{m}\, \boldsymbol{u}^{NL}(t)}{\Gamma_n M_n} \tag{2.10}$$

$D_{eff_n}(t)$ quantifies the nth mode contribution to the total deformation response of the NL MDF structure and depends only on the mass orthogonality of mode shapes.

$\boldsymbol{u}^{NL}(t)$ can be regenerated from $D_{eff_n}(t)$, as follows:

$$\boldsymbol{u}^{NL}(t) = \sum_1^N \boldsymbol{u}_n^{NL}(t) = \sum_{n=1}^N \boldsymbol{\phi}_n \Gamma_n D_{eff_n}(t) \tag{2.11}$$

Figure 2.3(b) shows the roof level component of $\boldsymbol{u}^{NL}(t)$ of the NL 4-story cantilever wall structure, denoted as $\boldsymbol{u}_r^{NL}(t)$, subjected to the CHY015W ground motion record,

regenerated from its modal components $\boldsymbol{u}_n^{NL}(t)$ using Eq. (2.10) and Eq. (2.11). These results show that D_{eff_n} can be used to accurately quantify the deformation response of a NL structure using a set of mass orthogonal deformation shape vectors, such as $\boldsymbol{\phi}_n$.

2.2.5. Uncoupled Modal Response History Analysis for Nonlinear Structure

Uncoupled modal response history analysis (UMRHA) for a NL MDF building structure is similar to modal response history analysis for a linear MDF structure. UMRHA calculates the total response of a NL MDF structure from estimated modal responses, assuming that the modal responses are weakly coupled, and treating them as uncoupled (Chopra and Goel, 2002). Although this assumption may be questionable, UMRHA determines the nth mode response from the following equation of motion for the corresponding uncoupled nth mode SDF system (Chopra and Goel, 2002):

$$\ddot{D}_{um_n}(t) + 2\zeta_n\omega_n\dot{D}_{um_n}(t) + \frac{F_{sn}(t)}{L_n} = -\ddot{u}_g(t) \tag{2.12}$$

where $D_{um_n}(t)$ = nth mode deformation response for the nth mode SDF system; ζ_n = nth mode damping ratio; $L_n = \Gamma_n M_n$; $F_{sn}(t) = F_{sn}(D_{um_n}(t))$ = nth mode nonlinear spring force which depends on $D_{um_n}(t)$.

A modal pushover analysis (MPA) procedure is used to determine the normalized envelope nth mode NL spring force, (F_{s_n}/L_n), versus (vs.) deformation, D_{um_n}, relationship as follows. A static pushover analysis of the NL MDF structure, under the external lateral force

distribution $\mathbf{s}_n^* = \boldsymbol{m}\,\boldsymbol{\phi}_n$, provides the base shear, V_{bn}, vs. roof level deformation, u_{rn}, relationship, which is transformed into the (F_{s_n}/L_n) vs. D_{um_n} relationship, as follows:

$$\frac{F_{sn}}{L_n} = \frac{V_{bn}}{M_n^*} \tag{2.13a}$$

$$D_{um_n} = \frac{u_{r_n}}{\Gamma_n \phi_{rn}} \tag{2.13b}$$

where $M_n^* = \Gamma_n L_n$

The modified MPA (mMPA) procedure (Chopra et al., 2004) assumes that the higher mode (n > 1) responses are linear elastic, with the linear F_{s_n}/L_n vs. D_{um_n} relationship as follows:

$$\frac{F_{sn}(t)}{L_n} = \omega_n^2\, D_{um_n}(t) \tag{2.14}$$

For the mMPA procedure, the 1st mode envelope F_{s_1}/L_1 vs. D_{um_1} relationship is determined using the transformations of Eq. (2.13) from the V_{b1} vs. u_{r1} response obtained from a static pushover analysis of the NL structure under $\mathbf{s}_1^* = \boldsymbol{m}\,\boldsymbol{\phi}_1$.

In the present study, the nth mode force response, $F_{s_n}(t)/L_n$, and nth mode deformation response, $D_{um_n}(t)$, from solving Eq. (2.12) (i.e., from UMRHA), are compared to the actual nth mode responses, $A_{eff_n}(t)$ and $D_{eff_n}(t)$, calculated from NLTHA results using Eq. (2.8) and Eq. (2.10). For this comparison, the result $F_{s_n}(t)/L_n$ is denoted as $A_{um_n}(t)$. It can be

shown that, if $A_{um_n}(t)$ and $D_{um_n}(t)$, accurately quantify the n[th] mode NL response, then they would equal $A_{eff_n}(t)$ and $D_{eff_n}(t)$, respectively, so in this comparison, $A_{eff_n}(t)$ and $D_{eff_n}(t)$ are used to assess the accuracy of $A_{um_n}(t)$ and $D_{um_n}(t)$.

2.3. MDF Structures and Nonlinear Models

2.3.1. Cantilever Wall Structures

Seven example cantilever wall structures (MB1 to MB7) are studied. The properties of these wall structures are summarized in Table 2.2. Each wall structure has a constant story height, h_s, of 13 ft. and is idealized as a lumped-mass system with a unit mass, m, at each floor. Each story has the same stiffness, and this story stiffness is selected so the structure has the first mode period values, T_1, given in Table 2.2. The flexure-to-shear stiffness ratio, ρ, is used to quantify the deformation response of the example wall structures. The walls with ρ = 0 are flexure dominated (i.e., rigid in shear with purely flexural response). The wall (MB2) with the non-zero ρ value is shear deformation dominated. The nonlinearity of each wall structure is concentrated in a flexural yielding rotational spring at the base of the wall. The rest of the wall is assumed to be linear elastic. The base flexural yielding spring has an assumed elastic-perfectly plastic (EPP) response. The initial stiffness of the base flexural yielding spring, k_{spg}, is ten times the flexural stiffness of the first story.

The yield strength of the base flexural yielding spring, M_b^h, is established as follows. For MB1 to MB6 (as shown in Table 2.2), M_b^h is established uniquely for each ground motion (GM) in the GM set as follows:

$$M_b^h = M_{b1}^{st} \frac{SA_{GM}(T_1)}{R} \tag{2.15}$$

where M_{b1}^{st} = 1st mode static base overturning moment, determined from $\mathbf{s}_1$; $SA_{GM}(T_1)$ = 1st mode pseudo-acceleration for the GM; T_1 = 1st mode period; R = response modification factor.

M_b^h for MB7 (as shown in Table 2.2) is established from the *design* response spectrum from ASCE (2010), to enable investigation of the effect of increasing GM intensity on the response, as follows:

$$M_b^{h,DS} = M_{b1}^{st} \frac{SA_{DS}(T_1)}{6} \tag{2.16}$$

where $M_b^{h,DS}$ = yield strength of the base flexural yielding spring based on the *design* response spectrum; $SA_{DS}(T_1)$ = 1st mode pseudo-acceleration from the design response spectrum; R = 6.

To investigate the effect of shear deformation on the response, a 9-story wall structure that is rigid in shear (i.e., with purely flexural response denoted MB1) and a 9-story wall structure with significant shear flexibility (denoted MB2, respectively, as shown in Table 2.2) are included in the study. MB1 and MB2 have moderate ductility demand (i.e., R = 6).

To investigate the effect of the number of stories on the response, 4-story and 12-story wall structures with purely flexural response and moderate ductility demand (i.e., R = 6) (denoted as MB3 and MB4 in Table 2.2) are included in the study.

To investigate the effect of ductility demand on the response, two 9-story wall structures with purely flexural response, and with R = 2 to produce low ductility demand, or R = 10 to produce high ductility demand (denoted as MB5 and MB6 in Table 2.2) are included in the study.

Two dimensional numerical models of the cantilever wall structures were created in OpenSees (Mazzoni et al., 2009). Schematics of the wall structure models are shown in Figure 2.4. Force-based beam-column elements with linear-elastic material definitions were used to model the walls. The base flexural yielding spring was modeled by using a zero length element (Mazzoni et al., 2009). A lean-on-column with linear-elastic beam-column members was included to model the second-order effects of vertical loads. A unit seismic mass was assigned to the horizontal degree-of-freedom of each node of the lean-on-column at each floor level. The horizontal displacements of the wall and lean-on-column were constrained to each other with rigid links at each floor level. The corotational coordinate transformation was used for the elements. Caughey damping with a 5% damping ratio for each mode was used. Newmark constant average acceleration integration and the nonlinear Newton-Krylov solution algorithms were used in the NLTHA.

2.3.2. Special Moment-Resisting Frame Structure

An example 9-story, 4-bay steel special moment resisting frame (SMRF) structure is studied. Schematics of the floor plan and elevation of the example SMRF building are shown in Figure 2.5. A single SMRF from the building, with the associated seismic mass and gravity loads (within the seismic tributary area), constitute the SMRF structure.

The SMRF building is assumed to be an office-type building on a site in Southern California with NEHRP Site Class D conditions. Dead and live gravity loads for the SMRF building are given in Table 2.3 and Table 2.4. Gravity and seismic loads were considered in the design of a typical SMRF from the building. The SMRF was designed in accordance with ASCE (2010) criteria. For design, the short period spectral acceleration (S_s) was taken as 1.5g and the 1 s period spectral acceleration (S_1) was taken as 0.6g. Conventional MRSA was used for seismic design of the SMRF. The member sizes were governed by the drift control criteria of ASCE (2010), in which the story drift limit is limited to 2%. Reduced beam section (RBS) beam-to-column connections were used and the strong column-weak beam design criterion of AISC (2010) was applied. The panel zones of the beam-column connection region were designed in accordance with FEMA (2000). All members of the SMRF were ASTM A992 wide-flange shapes with a nominal steel yield strength of 50 ksi, meeting the seismic compactness requirements of AISC (2010).

A two dimensional numerical model of the SMRF was developed in OpenSees (Mazzoni et al., 2009). Each beam and column of the SMRF was modeled by five force-based beam-

column elements with fiber sections. Five integration points were used along the length of each force-based beam-column element. Gauss-Lobatto numerical integration was used. A bi-linear material model (with the Steel02 material definition in OpenSees (Mazzoni et al., 2009)) was used for the steel material of the SMRF. The SMRF columns were fixed at the base. Panel zones of the SMRF were modeled using the panel zone element developed by Seo et al. (2012). A lean-on-column with elastic beam-column elements was used to model the second-order effects of the gravity loads within the seismic tributary area of the SMRF. Seismic mass was assigned to the horizontal degree-of-freedom of the lean-on-column at each floor level. The horizontal displacements of the SMRF and lean-on-column were constrained to each other with rigid links at each floor level. The vertical and horizontal displacements at the base of the lean-on-column were restrained. The corotational coordinate transformation was used for the elements. Caughey damping with a 5% damping ratio for each mode was used. Newmark constant average acceleration integration and the nonlinear Newton-Krylov solution algorithms were used in the NLTHA.

2.4. Ground Motion Set

A ground motion (GM) set composed of 18 GM pairs listed in Table 2.1 was used in the NLTHA. The GM records were selected from the NGA (PEER, 2011) database for the site of the SMRF building (Chancellor, 2014). The site has a short period spectral acceleration (S_s) of 1.5g and 1 s period spectral acceleration (S_1) of 0.6g.

Each GM pair was scaled so that the geometric mean of the pseudo-acceleration response for the GM pair matches the design basis earthquake (DBE) design spectrum (ASCE, 2010) over a period range of 0.1-7.0 s. The DBE has a 10% probability of exceedance (POE) in 50 years corresponding to a return period of 475 years (BSSC, 2003). The scale factors were calculated using the average scaling method described in Baker (2011). The pseudo-acceleration response spectra of the scaled 18 pairs of GMs and the median spectrum are shown in Figure 2.6.

2.5. Response of NL Wall Structures

2.5.1. nth Mode Contribution to Static Response

To quantify the contribution of each mode to the total static base shear response (V_b^{st}) and the total static base overturning moment response (M_b^{st}), nth mode contribution factors (Chopra, 2012) for V_b^{st} and M_b^{st}, denoted $\bar{V}_{bn}$ and $\bar{M}_{bn}$, respectively, are calculated as follows:

$$\bar{V}_{bn} = \frac{V_{bn}^{st}}{V_b^{st}} \tag{2.17a}$$

$$\bar{M}_{bn} = \frac{M_{bn}^{st}}{M_b^{st}} \tag{2.17b}$$

where V_{bn}^{st} = nth mode contribution to V_b^{st}; $V_b^{st} = \sum_{i=1}^{N} V_{bn}^{st}$; M_{bn}^{st}= nth mode contribution to M_b^{st}; $M_b^{st} = \sum_{i=1}^{N} M_{bn}^{st}$

Table 2.5 shows $\bar{M}_{bn}$ and $\bar{V}_{bn}$ calculated for each wall structure. As seen in Table 2.5, the $\bar{M}_{b1}$ for MB1, MB5, and MB6 is 89.3%. The cumulative $\bar{M}_{bn}$ of the higher modes for MB1, MB5, and MB6 is less than 11%. $\bar{M}_{b1}$ for MB2 is approximately 100% and the higher mode $\bar{M}_{bn}$ for MB2 is negligibly small. The results show that as the shear flexibility of the wall structures increases, the higher mode $\bar{M}_{bn}$ decreases. Table 2.5 shows that the higher mode $\bar{M}_{bn}$ slightly increases as the number of stories in the wall structures increases. For example (Table 2.5), the cumulative higher mode $\bar{M}_{bn}$ is 9.8% for MB3, while it is 10.1% for MB4.

Table 2.5 shows that the higher mode $\bar{V}_{bn}$ is larger than the higher mode $\bar{M}_{bn}$ for all of the wall structures. Table 2.5 shows that $\bar{V}_{b1}$ is larger for MB2 than for MB1, which shows that as the shear flexibility of the wall structures increases, the higher mode $\bar{V}_{bn}$ decreases. Table 2.5 shows that the higher mode $\bar{V}_{bn}$ is larger for MB4 than for MB3, which shows that the higher mode $\bar{V}_{bn}$ increases with an increasing number of stories.

2.5.2. nth Mode Contribution to Dynamic Response

The nth mode peak effective pseudo spectral accelerations, A_{eff_n}, were calculated from the NLTHA results for each wall structure for each GM in the GM set, and the median value of A_{eff_n} for the GM set, $A_{eff_n,m}$ was calculated. These results are compared with the nth mode pseudo-accelerations from the *median* linear-elastic and *median* reduced (by *R*) pseudo-acceleration response spectra (i.e, at T_n) for the GM set, which are denoted $SA_{GM,m}(T)$ and

$SA_{GM,m}(T)/R$, respectively. The estimated 1st mode dynamic response based on UMRHA (from solving Eq. (2.12)), A_{um_1}, is also compared with $A_{eff_1,m}$.

2.5.2.1. Comparison of nth Mode Response from MRSA with A_{eff}

Figure 2.7 shows the 5% damped median linear-elastic and median reduced (by R = 6) pseudo-acceleration response spectra for the GM set. The peak effective pseudo-accelerations, A_{eff_n}, for the first three modes from the NLTHA results for MB1 for each GM are indicated on the plot. The median effective pseudo-accelerations, $A_{eff_n,m}$, are also shown for the first three modes of vibration. Figure 2.7 shows that, $A_{eff_1,m}$ (i.e., for the 1st mode) is close to the median *reduced* pseudo-acceleration spectrum. On the contrary, $A_{eff_2,m}$ and $A_{eff_3,m}$ (i.e., for the 2nd and 3rd modes) are close to the median linear-elastic (*un-reduced*) pseudo-acceleration response spectrum. Table 2.6 shows $A_{eff_n,m}$ and $SA_{GM,m}(T_n)$ for the first three modes of vibration. The ratio of $SA_{GM,m}(T_n)$ to $A_{eff_n,m}$ which is denoted as R_{act_n}, and the R values used to design the wall structures are given in Table 2.7. Table 2.7 shows that the 1st mode R_{act} (i.e, R_{act_1}, the ratio of $SA_{GM,m}(T_1)$ to $A_{eff_1,m}$) is 3.66, while the 2nd and 3rd mode R_{act_n} (i.e., the ratio of $SA_{GM,m}(T_2)$ to $A_{eff_2,m}$ and the ratio of $SA_{GM,m}(T_3)$ to $A_{eff_3,m}$, respectively) are 1.23 and 0.72, respectively. These results show that the 2nd and 3rd mode responses are close to the linear-elastic response and are not strongly affected by the formation of the base flexural yielding mechanism. There is considerable scatter in the A_{eff_2} and A_{eff_3} values for the different GM compared to the median values, $A_{eff_2,m}$ and $A_{eff_3,m}$. This observation is consistent with previous studies (e.g., Priestley, 2003). Since

the higher mode responses are not strongly affected by the formation of the base flexural yielding mechanism, the higher mode responses are sensitive to the characteristics of the GM record. The scatter in A_{eff_1} is much smaller than the scatter in A_{eff_2} and A_{eff_3} because the 1st mode response is strongly affected ("controlled") by the formation of the base flexural yielding mechanism. The results show that the 1st mode response is not *accurately* "controlled", since R_{act_1} = 3.66 is much smaller than R = 6 used to establish the base flexural yielding strength, and scatter in A_{eff_1} is observed. Overall, however, Figure 2.7 shows that the assumption of a conventional MRSA, that the higher mode responses and 1st mode response are equally reduced by yielding, which results in the use of a single R factor, is not valid for these wall structures.

Figure 2.8(a) shows $A_{eff_n}(t)$ normalized by the peak response amplitude, A_{eff_n}, for the first three modes of MB1 subjected to the ILA013W ground motion record (Table 2.1). The peak $A_{eff_n}(t)$, and the times of the peak base overturning moment response ($M_b(t)$) and the peak base shear response ($V_b(t)$) are indicated on the plot. At the time of the peak $M_b(t)$, the amplitude of $A_{eff_1}(t)$ is 85% of A_{eff_1}, while the amplitudes of $A_{eff_2}(t)$ and $A_{eff_3}(t)$ are much smaller (approximately 5% of A_{eff_2} and A_{eff_3}, respectively) with a sign opposite to $A_{eff_1}(t)$. At the time of peak the $V_b(t)$, $A_{eff_3}(t)$ is at its peak value while $A_{eff_1}(t)$ and $A_{eff_2}(t)$ have amplitudes equal to 54% of A_{eff_1} and 55% of A_{eff_2}, respectively, with the same sign as $A_{eff_3}(t)$.

Figure 2.8(b) shows the $M_b(t)$ and the nth mode base overturning moment response, $M_{bn}(t)$, for MB1 subjected to the ILA013W GM record. $M_b(t)$ is obtained from the NLTHA results and $M_{bn}(t)$ is the product of M_{bn}^{st} and $A_{eff_n}(t)$. The contributions of $M_{b2}(t)$ and $M_{b3}(t)$ to $M_b(t)$ are considerably smaller than the contribution of $M_{b1}(t)$. $M_{b1}(t)$ and $M_b(t)$ are similar to each other illustrating the dominance of 1st mode response on $M_b(t)$. Figures 2.7 and 2.8 illustrate the usefulness of $A_{eff_n}(t)$ for accurately quantifying the contribution of each mode to the total $M_b(t)$ and $V_b(t)$ response of a NL MDF structure.

Effect of Shear Flexibility

Figure 2.9 compares $A_{eff_n,m}$ for the first three modes of MB1 (purely flexural response) and MB2 (with significant shear flexibility) along with the 5% damped median linear-elastic and median reduced pseudo-acceleration response spectra for the GM set. Figure 2.9 shows that for both MB1 and MB2, $A_{eff_1,m}$ is close to the median reduced pseudo-acceleration spectrum. R_{act_1} is 3.66 for MB1 and 4.17 for MB2 (Table 2.7), indicating that the 1st mode response is effectively but not accurately "controlled" by the base flexural yielding mechanism. On the contrary**,** for both MB1 and MB2, $A_{eff_2,m}$ and $A_{eff_3,m}$ are close to the median linear-elastic pseudo-acceleration spectrum. R_{act_2} is 1.23 for MB1 and 0.90 for MB2, and R_{act_3} is 0.72 for MB1 and 0.98 for MB2. Table 2.5 shows that for MB2 $\bar{M}_{b1}$ is nearly 100%, while $\bar{M}_{b2}$ is about 4%. These results show that as the higher mode $\bar{M}_{bn}$ decrease, the higher mode responses of MB2 are less affected significantly by the base flexural yielding mechanism. Figure 2.9(b) shows that the 2nd mode response is slightly amplified after the formation of the base flexural yielding mechanism, where $A_{eff_2,m}$ of

MB2 is larger than $SA_{GM,m}(T)$. A similar observation regarding the amplification of higher mode responses with the formation of a yielding mechanism was made by Rodriguez et al. (2002) for a 12-story reinforced concrete wall structure

Figure 2.10 shows $A_{eff_n}(t)$ normalized by A_{eff_n} for the first three modes of MB2 subjected to the ILA013W GM record. At the time of peak $M_b(t)$, the amplitude of $A_{eff_1}(t)$ is 82% of A_{eff_1}, while the amplitude of $A_{eff_2}(t)$ is 9% of A_{eff_2} with the same sign as $A_{eff_1}(t)$ and and the amplitude of $A_{eff_3}(t)$ is close to zero. At the time of peak $V_b(t)$, the amplitude of $A_{eff_1}(t)$ is the peak value (i.e., A_{eff_1}) while the amplitudes of $A_{eff_2}(t)$ and $A_{eff_3}(t)$ are 65% of $A_{eff_2}$and 20% of A_{eff_3}, respectively, with the same sign as $A_{eff_1}(t)$.

Effect of Number of Stories

Figure 2.11 compares $A_{eff_n,m}$ for the first three modes of MB3 (4 stories) and MB4 (12 stories) along with the 5% damped median linear-elastic and median reduced pseudo-acceleration response spectra for the GM set. Figure 2.11 shows that the effect of the base flexural yielding mechanism is sensitive to the number of stories in the wall structure. Table 2.7 shows that R_{act_1} is 4.64 for MB3 and 3.53 for MB4, indicating the reduction in response (represented by the response modification factor *R*) is smaller for the structure with more stories. The higher mode responses are more affected by the base flexural yielding mechanism as the number of stories increases. R_{act_2} is 0.79 for MB3 and 1.28 for MB4. Table 2.5 shows that the higher mode $\bar{M}_{bn}$ increases slightly with an increasing number of

stories for the wall structures. As a result, the effect of the base flexural yielding mechanism on the higher mode responses increases slightly as the number of stories increases.

Effect of Anticipated Ductility Demand Level (R)

Figure 2.12 compares $A_{eff_n,m}$ for the first three modes of MB5 (R = 2) and MB6 (R = 10) along with the 5% damped median linear-elastic and median reduced pseudo-acceleration response spectra for the GM set. Figure 2.12 shows that regardless of the R value and resulting level of ductility demand, the 1st mode response is effectively "controlled" by the base flexural yielding mechanism, and $A_{eff_1,m}$ is significantly less than $SA_{GM,m}(T_1)$. Table 2.7 shows that R_{act_1} is 1.68 for MB5 (R = 2) and 4.93 for MB6 (R = 10), indicating the 1st mode response reduction follows the expected trend (R_{act_1} is larger for the wall structure with the larger R value), but the 1st mode response is not accurately "controlled" by the base flexural yielding mechanism. The higher mode responses are sensitive to the ductility demand. While $A_{eff_2,m}$ is essentially the same as $SA_{GM,m}(T_2)$ for MB5, $A_{eff_2,m}$ is less than $SA_{GM,m}(T_2)$ for MB6. Table 2.7 shows R_{act_2} is 1.07 for MB5 and 1.33 for MB6, and R_{act_3} is 0.78 for MB5 and 0.77 for MB6.

Figure 2.13 shows $A_{eff_n}(t)$ normalized by A_{eff_n} for the first three modes of MB5 and MB6 subjected to the ILA013W GM record. For both MB5 and MB6, at the time of peak $M_b(t)$ the amplitude of $A_{eff_1}(t)$ is nearly 80% of A_{eff_1}, while the amplitude of the higher modes is much smaller. However, at the time of the peak $V_b(t)$, the 1st mode response is much smaller

for MB6 than for MB5, where the amplitude of $A_{eff_1}(t)$ is about 75% of A_{eff_1} for MB5, but it is only 25% of A_{eff_1} for MB6. At the time of peak V_b, for both MB5 and MB6, the sign of $A_{eff_2}(t)$ and $A_{eff_3}(t)$ is the same as $A_{eff_1}(t)$ and the amplitudes of $A_{eff_2}(t)$ and $A_{eff_3}(t)$ are about 85% of A_{eff_2} and 75% of A_{eff_3}, respectively.

Figure 2.14 shows $M_b(t)$ and $M_{bn}(t)$ for MB5 and MB6 subjected to the ILA013W GM record. For MB5, $M_{b1}(t)$ and $M_b(t)$ are very similar, because the higher mode contributions to $M_b(t)$ are quite small. However, for MB6, $M_b(t)$ has significant higher mode contributions, so the differences between $M_{b1}(t)$ and $M_b(t)$ are larger. The increase in higher mode contributions to $M_b(t)$ as R increases can be understood by examining the components of $M_{bn}(t)$, which is a product of M_{bn}^{st} and $A_{eff_n}(t)$. Table 2.5 show that $\bar{M}_{b1}$ is about 12 times larger than $\bar{M}_{b2}$ for both MB5 and MB6. However, Table 2.6 shows that $A_{eff_2,m}$ is 3 times larger than $A_{eff_1,m}$ for MB5, but $A_{eff_2,m}$ is 11 times larger than $A_{eff_1,m}$ for MB6. So, although M_{b2}^{st} is much smaller than M_{b1}^{st}, when it is multiplied by a large effective pseudo-acceleration, as represented by $A_{eff_2,m}$, the 2nd mode contribution to M_{bn} becomes comparable to 1st mode contribution. The results in Figure 2.14 show the usefulness of A_{eff_n} for understanding the effect of ductility demand on the modal contribution to $M_b(t)$.

Effect of Ground Motion

To demonstrate the sensitivity of the higher mode response to the GM, NLTHA results for MB7 under the CHY047W and ILA013W GM records are presented. Note that the

strength of the base flexural yielding spring, M_b^h, for MB1 to MB6 was established uniquely for each GM, as shown by Eq. (2.15), resulting in the same *R* value (relative to the 1st mode base moment demand) for each GM; while, M_b^h for MB7 was established from the design response spectrum as shown by Eq. (2.16), resulting in a variation of the *R* value as the GM varies. Figure 2.15 shows the 5% damped linear-elastic pseudo-acceleration response spectra for the CHY047W and ILA013W GM records, and the respective values of A_{eff_n}, denoted as $A_{eff_n}^{CHY}$ and $A_{eff_n}^{ILA}$, where the superscripts distinguish the results for the two ground motions. Figure 2.15 shows that $A_{eff_2}^{CHY}$ and $A_{eff_2}^{ILA}$ as well as $A_{eff_3}^{CHY}$ and $A_{eff_3}^{ILA}$ are considerably different than each other and are close to the respective $SA_{GM,m}(T_n)$. On the contrary, $A_{eff_1}^{CHY}$ and $A_{eff_1}^{ILA}$ are quite close to each other, since the 1st mode response is effectively "controlled" by the base flexural yielding mechanism; A_{eff_1} is not sensitive to variations in the GM intensity near T_1. However, since the higher mode responses are not strongly affected by the base flexural yielding mechanism, they are sensitive to the characteristics of the GM record.

Effect of Deformation Shapes on A_{eff_n}

Table 2.7 shows that the R_{act_1} values are always less than the anticipated *R* values (used to establish M_b^h). The following discussion shows that the difference between *R* and R_{act_1} is related to the set of deformation shapes used in the calculation of $A_{eff_n}(t)$ using Eq. (2.8). The development of Eq. (2.8) shows that any mass-orthogonal set of deformation shapes can be used to calculate $A_{eff_1}(t)$. Up to this point in this chapter, the linear-elastic mode shapes, which are obtained from eigen analysis of linear-elastic models of the cantilever

wall structures, have been used as the deformation shapes. These deformation shape vectors are orthogonal with respect to the mass and linear-elastic stiffness matrices, but are coupled to each other through the base flexural yielding mechanism. This coupling can be observed from the M_b^{st} contribution factors given in Table 2.5, where each of the first four modes has a non-zero contribution. As a result, the base flexural yielding mechanism cannot *accurately* "control" the response in any particular mode, since all modes contribute to the base overturning moment, although as noted above, the base flexural yielding mechanism effectively controls the 1st mode response.

An alternate set of mass-orthogonal deformation mode shapes can be developed to uncouple the modes from the base flexural yielding mechanism. The basis for the alternate set of deformation mode shapes is to make the 1st mode deformation mode shape equal to the shape of the structure after the yielding mechanism forms (e.g., the deformed shape of the NL cantilever wall structures after the formation of base flexural yielding mechanism). Chapter 3 presents approaches for developing these deformation mode shapes. Sullivan et al. (2008) use a set of mode shapes, denoted as *TIMS* derived from the inelastic state of NL structure, similarly to quantify the modal response of a NL structure. The alternate set of deformation shapes mode shapes used here are from eigen analysis using the stiffness matrix of the structure after the base flexural yielding mechanism has formed (see Chapter 3).

Using these alternate deformation mode shapes, $A_{eff_n}(t)$, and A_{eff_n} were re-calculated from the NLTHA results for MB1 for each GM. Figure 2.16 shows the results for A_{eff_n} and A_{eff_n},m from using the alternate deformation shapes together with the 5% damped median linear-elastic and median reduced (by R = 6) pseudo-acceleration response spectra. Using these alternate results, R_{act_1} is 6.0 indicating that the 1st mode response (based on the alternate deformation mode shapes) is accurately "controlled" by the base flexural yielding mechanism. R_{act_2} is 1.05 and R_{act_3} is 0.67, which are similar to the previous results and indicate that the higher modes are not strongly affected by the flexural base yielding mechanism.

These results show that alternate deformation mode shapes can be used to quantify and understand the 1st mode and higher mode response of a NL structure using A_{eff}. The only requirement for this analysis is a set of mass-orthogonal deformation mode shapes.

2.5.2.2. Comparison of nth Mode Response from UMRHA and A_{eff}

The properties of the equivalent nth mode SDF systems for UMRHA of MB1 are shown in Table 2.8. Figure 2.17(a) shows $A_{um_n}(t)$ and $A_{eff_n}(t)$ and Figure 2.17(b) shows $D_{um_n}(t)$ and $D_{eff_n}(t)$ for the first three modes of MB1 subjected to the ILA013W GM record. $A_{um_n}(t)$ and $D_{um_n}(t)$ are from solving Eq. (2.12). $A_{eff_n}(t)$ and $D_{eff_n}(t)$ are from Eq. (2.8) and Eq. (2.10), applied to results from NLTHA of the NL MDF structure (MB1). Note that the results for $A_{eff_n}(t)$ and $D_{eff_n}(t)$ presented here and in the remainder of the paper are based

on mode shapes from eigen analysis of a linear-elastic model of the structure, not from the alternate deformation mode shapes described above. Figure 2.17(a) shows significant differences between $A_{um_1}(t)$ and $A_{eff_1}(t)$, which are expected. Particularly noteworthy in Figure 2.17(a) is the flat-topped $A_{um_1}(t)$ response, when the 1st mode SDF system yields in the UMRHA, which occurs because the 1st mode force response in the UMRHA is fully uncoupled from the higher mode responses. On the contrary, the actual 1st mode response, represented by $A_{eff_1}(t)$, is coupled to the higher mode response through the base flexural yielding mechanism. This coupling occurs because each mode contributes to M_b as shown in Table 2.5. As a result, the base flexural yielding mechanism does not fully control the 1st mode response, as the UMRHA result, $A_{um_1}(t)$, suggests. For the higher modes, $A_{um_2}(t)$ and $A_{eff_2}(t)$ as well as $A_{um_3}(t)$ and $A_{eff_3}(t)$ are similar, indicating that these higher modes of the wall structures respond almost linear elastically, which is consistent with the assumption of the mMPA (Chopra et al., 2004).

The differences between $D_{um_1}(t)$ and $D_{eff_1}(t)$ are smaller than the differences between $A_{um_1}(t)$ and $A_{eff_1}(t)$. However, the $D_{um_2}(t)$ and $D_{um_3}(t)$ are considerably different than $D_{eff_2}(t)$ and $D_{eff_3}(t)$, respectively. The results for $D_{eff_2}(t)$ and $D_{eff_3}(t)$ show considerable contributions of the higher modes to the total deformation response. Figure 2.17 illustrates the usefulness of $A_{eff_n}(t)$ and $D_{eff_n}(t)$ for quantifying the actual modal response results that NL modal analysis methods, such as UMRHA intended to predict.

2.6. Response of NL SMRF Structure

2.6.1. nth Mode Contribution to Static Response

$\bar{M}_{bn}$ and $\bar{V}_{bn}$ for the SMRF are given in Table 2.9. As seen in Table 2.9, $\bar{V}_{b1}$ is 77% and the cumulative higher mode $\bar{V}_{bn}$ is 23%, while $\bar{M}_{b1}$ is 97% and the cumulative higher mode $\bar{M}_{bn}$ is less than 3%. These results show that the contribution of higher modes to M_b is small.

Figure 2.18 shows the intended beam-sway yielding mechanism of the SMRF under seismic loading. As shown in Figure 2.18, in the beam-sway mechanism, plastic hinges form at the ends of the beams and the base of the first story column.

2.6.2. nth Mode Contribution to Dynamic Response

Figure 2.19 compares $A_{eff_{n,m}}$ for the first three modes of the SMRF along with the 5% damped median linear-elastic and median reduced (by R = 8) pseudo-acceleration response spectra for the GM set along with the *design* response spectrum based on ASCE (2010) and the reduced R = 8 *design* spectrum. R_{act_n} for the first three modes are 1.66, 1.22, and 1.08, respectively. These results show that R_{act_n} is much less than R = 8, used in design. Since the seismic design of the SMRF is governed by the drift limit in ASCE (2010) rather than the strength demand, having R_{act_n} less than 8 is expected.

Effect of GM intensity

To study the effect of GM intensity on the higher mode response, the SMRF was subjected to the GM set scaled to two times the Maximum Considered Earthquake (MCE) intensity level. The MCE is the GM intensity level with a 2% probability of exceedance in 50 years. The yielding mechanism that forms under the GM set scaled to two times the MCE level, shown in Figure 2.20(a) is more complex than the intended yielding mechanism, shown in Figure 2. 18(a). As seen in Figure 2.20(a), the yielding mechanism includes plastic hinges in the columns in many stories of the SMRF, when the GM intensity level is increased to two times the MCE level. The formation of further hinges in the columns over the height of the structure "controls" the higher mode responses and prevents the higher mode response from increasing with the increasing GM intensity (unlike to MB7 wall structure, as shown in Figure 2.15).

Figure 2.20(b) compares $A_{eff_n,m}$ for the first three modes of SMRF with the 5% damped median linear-elastic pseudo-acceleration response spectrum for the GM set scaled to two times the MCE. Figure 2.20(b) shows that A_{eff_n} for the first three modes of vibration are effectively "controlled" by the formation of plastic hinges in the columns over the height of the SMRF in addition to the plastic hinges formed in the beams and the base of the first story columns in accordance with the intended beam-sway mechanism.

Figure 2.21 shows $A_{eff_n}(t)$ normalized by A_{eff_n} for the first three modes of the SMRF subjected to ILA013W GM record. At the time of the peak $M_b(t)$, the amplitude of $A_{eff_1}(t)$ is at its peak value (100% of A_{eff_1}), while the amplitudes of $A_{eff_2}(t)$ and $A_{eff_3}(t)$ are 7% of A_{eff_2} and 4% of A_{eff_3}, respectively, with the same sign as $A_{eff_1}(t)$. At the time of the peak $V_b(t)$, the amplitude of $A_{eff_2}(t)$ is 81% of A_{eff_2}, while the amplitudes of $A_{eff_1}(t)$ and $A_{eff_3}(t)$ are 21% of A_{eff_1} and 63% of A_{eff_3}, respectively. These results show that the contributions of the 2nd and 3rd modes are much smaller than the contribution of the 1st mode response to the peak $M_b(t)$. However, the contributions of the 2nd and 3rd modes to the peak $V_b(t)$ are large compared to the contribution of the 1st mode response.

Figure 2.22 shows $V_b(t)$ and the roof level component of $\boldsymbol{u}(t)$, $u_r(t)$ and $V_b(t)$, for the SMRF subjected to ILA013W GM record. $V_b(t)$ is obtained from the NLTHA results and the modal components $V_{bn}(t)$ are the product of $V_{bn}^{st}(t)$ and $A_{eff_n}(t)$. Similarly, $u_r(t)$ is obtained from the NLTHA results and $u_{r_n}(t)$ are a product of $\phi_n \Gamma_n$ and $D_{eff_n}(t)$ (see Eq. (2.11)). As seen in Figure 2.22(a), $u_{r_1}(t)$ dominates $u_r(t)$ and the higher mode contributions to $u_r(t)$ are negligibly small. The contributions of $V_{b_2}(t)$ and $V_{b_3}(t)$ to, however, $V_b(t)$ are comparable to the contribution of $V_{b_1}(t)$ to $V_b(t)$. Figure 2.22(b) shows between 35-45 s of response history, $V_{b_2}(t)$ is as large as $V_{b_1}(t)$. However, after the 50 s of the response history, the contribution of $V_{b_1}(t)$ is dominant. These results show how the nth mode contributions to a total response quantity (e.g., $V_b(t)$ and $u_r^{NL}(t)$) are change during NLTHA.

2.7. Summary and Conclusions

This paper presents two time varying response variables $A_{eff_n}(t)$ and $D_{eff_n}(t)$ to quantify the nth mode response of NL MDF structures. $A_{eff_n}(t)$ and $D_{eff_n}(t)$ have been derived from the total NL response using a set of mass-orthogonal deformation shape vectors. $A_{eff_n}(t)$ and $D_{eff_n}(t)$ were used to investigate the modal responses of NL cantilever wall structures and a special moment resisting frame (SMRF). The NL response of 4-, 9-, and 12-story wall structures and a 9-story, 4-bay SMRF structure under a set of ground motions was studied. Parameters of the wall structures, shear stiffness, number of stories, fundamental period, and ductility demand were varied. Two time varying response variables, $A_{eff_n}(t)$ and $D_{eff_n}(t)$, are derived to quantify the nth mode response of NL MDF structures. In addition, $A_{eff_n}(t)$ and $D_{eff_n}(t)$ were compared with the nth mode response estimates using modal response spectrum analysis (MRSA) and uncoupled modal response history analysis (UMRHA).

The main findings are:

- For the wall structures, when a mode has a large $\bar{M}_{bn}$, the corresponding nth mode response is more effectively "controlled" by the formation of the base flexural yielding mechanism of the wall structure. In particular, the 1st mode has a large $\bar{M}_{b1}$, and is effectively "controlled" by the base flexural yielding mechanism.
- The higher mode responses of the wall structures, which are not strongly affected by the formation of the base flexural yielding mechanism, are sensitive to the characteristics of the GM record.

- The higher mode responses of the SMRF are not highly sensitive to the GM intensity due to the formation of additional plastic hinges over the height of the structure in addition to intended beam-sway mechanism considered in the design of the SMRF.
- The assumption of a conventional MRSA, that the higher mode responses and 1st mode response are equally reduced by yielding, which results in the use of a single *R* factor, is not valid for the wall structures, as noted in some prior studies (e.g., Eibl and Keintzel, 1988; Rodriguez et al., 2002).
- The results for the wall structures and the SMRF show that the 1st mode response is not accurately "controlled" when the linear-elastic mode shapes are used in calculation of $A_{eff_1}(t)$. The linear-elastic mode shapes are orthogonal with respect to the mass and linear elastic stiffness matrices, but they are coupled through the base flexural yielding mechanism. Therefore, the response of a particular mode such as the 1st mode cannot be accurately controlled (i.e., be restricted to a specific level of response) by the base flexural yielding mechanism.
- To uncouple the modes from the base flexural yielding mechanism, an alternate set of mode shapes can be developed by making the 1st mode deformation mode shape equal to the shape of the structure after the yielding mechanism forms.

In conclusion, this study shows that the time varying response variables, $A_{eff_n}(t)$ and $D_{eff_n}(t)$, which were presented for the purpose of accurately quantifying the nth mode response of a NL structure, are useful for understanding and comparing the nth mode response. Numerous comparisons of the example structure responses illustrate the accuracy of the assumptions made in conventional MRSA and UMRHA. The effects of wall

structure deformation type (shear-dominated, flexural-dominated), number of stories in the wall structure, level of ductility demand, and wall structure compared with SMRF have been shown.

2.8. References

AISC (2010). "Seismic Provisions for Structural Steel Buildings," *American Institute of Steel Construction*, Chicago, IL, USA.

ASCE (2010). "Minimum Design Loads for Buildings and Other Structures," *ASCE7-10*, Reston, VA, USA.

Baker, J.W. (2011). "Conditional Mean Spectrum: Tool for Ground-Motion Selection," *Journal of Structural Engrg.*, 137(3), pp 322-331.

Blakeley, R. W. G., Cooney, R. C., and Megget, L. M. (1975). "Seismic shear loading at flexural capacity in cantilever wall structures," *Bulletin of the New Zealand National Society for Earthquake Engrg.*, 8(4), pp. 278-290.

Bracci, J. M., Kunnath, S. K. and Reinhorn, A. M. (1997). "Seismic Performance and Retrofit Evaluation for Reinforced Concrete Structures," *Journal of Structural Engrg.*, 123(1), pp. 3-10.

BSSC (2003). "NEHRP Recommended Provisions for Seismic Regulations for New Buildings and Other Structures," *Building Seismic Safety Council, National Institute of Building Sciences, FEMA-450,* Washington, DC, USA.

Calugaru, V. and Panagiotou, M. (2010). "Seismic Isolation Using Single and Dual Shear Hinging of Tall Cantilever Wall Buildings Subjected to Near Fault Ground Motions," *Proc. of the 9th US National and 10th Canadian Conference on Earthquake Engrg.*, Toronto, Canada. July 25-29.

Chancellor, N.B. (2014). "Seismic Design and Performance of Self-Centering Concentrically-Braced Frames", Ph.D. Dissertation, Dept. of Civil and Env. Engrg., Lehigh Univ., Bethlehem, PA, USA.

Chopra, A. K. (2012). *Dynamics of structures*. (4th ed.). Prentice Hall, New Jersey, NJ.

Chopra, A. K. and Goel, R. K. (2002). "A modal pushover analysis procedure for estimating seismic demands for buildings," *Earthquake Engrg. and Structural Dynamics*, 31(3), pp. 561-582.

Chopra, A. K., Goel, R. K., and Chintanapakdee, C. (2004). "Evaluation of a modified MPA procedure assuming higher modes as elastic to estimate seismic demands," *Earthquake Spectra*, 20(3), pp. 757-778.

Clough, Ray W. "On the importance of higher modes of vibration in the earthquake response of a tall building." *Bulletin of the Seismological Society of America* 45 (1955), pp. 289-301.

Derecho, A. T., Ghosh, S. K., Iqbal, M., Freskakis, G. N., and Fintel, M. (1978). "Structural walls in earthquake-resistant buildings–analytical investigations, dynamic analysis of isolated structural walls–parametric studies," Final Report to the National Science Foundation, Portland Cement Association, Skokie, IL, USA.

Eberhard, M. O. and Sozen, M. A. (1993). "Behavior-based method to determine design shear in earthquake-resistant walls," *Journal of Structural Engrg.*, 119(2), pp. 619-640.

Eibl, J. and Keintzel, E. (1988). "Seismic shear forces in RC cantilever shear walls," *Proc. of the 9th World Conference on Earthquake Engrg. (vol. VI)*, Tokyo-Kyoto, Japan, August 2-9.

FEMA (2000). "Recommended Seismic Design Criteria for New Steel Moment Frame Buildings," *Prepared for the Federal Emergency Management Agency for FEMA, FEMA-350*, Washington, DC, USA.

Gupta, B. and Kunnath, S. K. (2000). "Adaptive spectra-based pushover procedure for seismic evaluation of structures," *Earthquake Spectra*, 16(2), pp. 367-392.

Kabeyasawa, T. and Ogata, K. (1984). "Ultimate-state design of RC wall-frame structures," *Transaction of the Japan Concrete Institute*, 6, pp. 629- 636.

Kurama, Y., Pessiki, S., Sause, R. and Lui, L. W. (1999). "Seismic behavior and design of unbonded posttensioned precast concrete walls," *PCI Journal*, 44(3), pp.72-89.

Mazzoni, S., McKenna, F., Scott, M.H., Fenves, G.L., et al. (2009). "Open System for Earthquake Engrg. Simulation (OpenSEES) User Command-Language Manual*,"* *Pacific Earthquake Engrg. Research Center*, Univ. of California, Berkeley, CA, USA.

Pacific Earthquake Engrg. Research Center (PEER) (2011). "Ground motion database flatfile," Retrieved from http://peer.berkeley.edu/nga/flatfile.html on December 12, 2013.

Paulay, T. and Priestley, M.J.N. (1992). *Seismic design of reinforced concrete and masonry buildings*. Wiley, New York, NY, USA.

Priestley, M.J.N. (2003). "Does capacity design do the job? An investigation of higher modes effects in cantilever walls," *Bulletin of the New Zealand Society for Earthquake Engrg.*, 36(4), pp. 276-292.

Priestley, M.J.N. and Amaris, A. (2003). "Dynamic amplification of seismic moments and shear forces in cantilever walls," *Proc. of the fib symposium on concrete structures in seismic regions,* Athens, Greece, May 6-8.

Rodriguez, M. E., Restrepo, J. I., and Carr, A. J. (2002). "Earthquake-induced floor horizontal accelerations in buildings," *Earthquake Engrg. and Structural Dynamics*, 31(3), pp. 693-718.

Roke, D., Sause, R., Ricles, J. M., and Chancellor, N.B. (2010). "Damage- Free Seismic-Resistant Self-Centering Concentrically-Braced Frames." ATLSS Report 10-09, ATLSS Engrg. Research Center, Lehigh Univ., Bethlehem, PA, USA..

Seo, C.-Y., Lin, Y.C., Sause, R., and Ricles, J.M., (2012), "Development of Analytical Models and Performance Evaluation for 0.6 Scale Self-Centering MRF with 355 Web Friction Devices," ATLSS Engrg. Research Center, Lehigh Univ., Bethlehem, PA, USA.

Sullivan, T. J., Priestley, M. J. N., and Calvi, G. M. (2008). "Estimating the higher-mode response of ductile structures," *Journal of Earthquake Engrg., ASCE,* 12(3), pp. 456-472.

Table 2.1 Ground motion set (Chancellor, 2014)

PEER-NGA Record Seq. #	Year	Event	Station	Component	Scale Factor
165	1979	Imperial Valley-06	Chihuahua	012, 282	2.17
169	1979	Imperial Valley-06	Delta	262, 352	1.63
728	1987	Superst. Hills-02	Westmorland	090, 180	2.01
778	1989	Loma Prieta	Hollister	165, 255	1.61
949	1994	Northridge-01	Arleta	090, 360	1.92
1100	1995	Kobe, Japan	Abeno (ABN)	000, 090	2.89
1101	1995	Kobe, Japan	Amagasaki	000, 090	1.20
1110	1995	Kobe, Japan	Morigawachi	000, 090	2.23
1187	1999	Chi-Chi, Taiwan	CHY015	N, W	2.31
1203	1999	Chi-Chi, Taiwan	CHY036	E, N	1.41
1204	1999	Chi-Chi, Taiwan	CHY039	E, N	2.62
1209	1999	Chi-Chi, Taiwan	CHY047	N, W	2.37
1236	1999	Chi-Chi, Taiwan	CHY088	E, N	2.56
1269	1999	Chi-Chi, Taiwan	HWA019	E, N	2.85
1294	1999	Chi-Chi, Taiwan	HWA048	N, W	2.84
1317	1999	Chi-Chi, Taiwan	ILA013	N, W	2.17
1484	1999	Chi-Chi, Taiwan	TCU042	E, N	1.75

Table 2.2 Properties of cantilever wall structures

Identifier (Id)	Stories	T_1 (s)	Dominant Behavior	$\rho = \frac{EI}{(5/6)L^2GA}$	R	M_b^h-Eqn.
MB1	9	1.5	*Flexural*	0	6	(2.15)
MB2	9	1.5	*Shear*	169	6	(2.15)
MB3	4	0.5	*Flexural*	0	6	(2.15)
MB4	12	2.0	*Flexural*	0	6	(2.15)
MB5	9	1.5	*Flexural*	0	2	(2.15)
MB6	9	1.5	*Flexural*	0	10	(2.15)
MB7	9	1.5	*Flexural*	0	6	(2.16)

Table 2.3 Dead loads for SMRF

Item	Dead Load for Floor 1 (psf)	Dead Load for Middle Floors (psf)	Dead Load for Roof (psf)
Floor/Roof Deck	3	3	3
Floor/Roof Slab	43	43	0
Roofing Material	0	0	10
Mechanical Weight	10	10	25
Ceiling Material	5	5	5
Floor Finish	2	2	0
Structural Steel	15	15	10
Steel Fireproofing	2	2	2
Building Envelope	8	7	5
Total	88	87	60

Table 2.4 Live loads for SMRF

Item	Live Load for Floors (psf)	Live Load for Roof (psf)
Office	50	0
Partitions (included in seismic mass)	15	0
Roof	0	20
Total	65	20

Table 2.5 $\bar{M}_{bn}$ and $\bar{V}_{bn}$ for MB1 to MB6

	$\bar{M}_{bn}$				$\bar{V}_{bn}$			
Mode	MB1, MB5, MB6	MB2	MB3	MB4	MB1, MB5, MB6	MB2	MB3	MB4
1	0.8931	1.0314	0.9012	0.8921	0.6485	0.8517	0.6963	0.6394
2	0.0786	-0.0371	0.0782	0.0787	0.1986	0.0912	0.2103	0.1961
3	0.0164	0.0076	0.0162	0.0165	0.0682	0.0304	0.0694	0.0674
4	0.0060	-0.0025	0.0044	0.0060	0.0347	0.0137	0.0240	0.0344

Table 2.6 Comparison of $A_{eff_{nm}}$ with SA_{GM,m_1}

Id	$A_{eff_{1,m}}$ (inch/s^2)	SA_{GM,m_1} (inch/s^2)	$A_{eff_{2,m}}$ (inch/s^2)	SA_{GM,m_2} (inch/s^2)	$A_{eff_{3,m}}$ (inch/s^2)	SA_{GM,m_3} (inch/s^2)
MB1	0.11	0.42	0.73	0.90	0.72	0.52
MB2	0.10	0.42	1.09	0.98	0.96	0.94
MB3	0.21	0.98	0.64	0.51	0.54	0.43
MB4	0.09	0.32	0.74	0.95	0.78	0.63
MB5	0.25	0.42	0.84	0.90	0.67	0.52
MB6	0.09	0.42	0.68	0.90	0.68	0.52

Table 2.7 Comparison of R with R_{act_n}

Id	R	R_{act_1}	R	R_{act_2}	$A_{eff_{3,m}}$ (inch/s^2)	R_{act_3}
MB1	6	3.66	6	1.23	0.72	0.72
MB2	6	4.17	6	0.90	0.96	0.98
MB3	6	4.64	6	0.79	0.54	0.79
MB4	6	3.53	6	1.28	0.78	0.81
MB5	2	1.68	2	1.07	0.67	0.78
MB6	10	4.93	10	1.33	0.68	0.77

Table 2.8 Modal properties of equivalent SDF systems for UMRHA of MB1

Mode/ Modal Property	Γ_n	M_n (kips/g)	F_{sny}/L_n (inch/s^2)	D_{ny} (inch)	T_n (s)
1	2.416	1.0	25.912	1.496	1.50
2*	1.337	1.0	-	-	0.24
3*	0.784	1.0	-	-	0.08
4*	-0.559	1.0	-	-	0.04

*Elastic response assumed

Table 2.9 $\bar{M}_{bn}$ and $\bar{V}_{bn}$ for SMRF

Mode	$\bar{M}_{bn}$	$\bar{V}_{bn}$
1	0.9822	0.7717
2	0.0061	0.1330
3	0.0122	0.0543
4	0.0003	0.0242

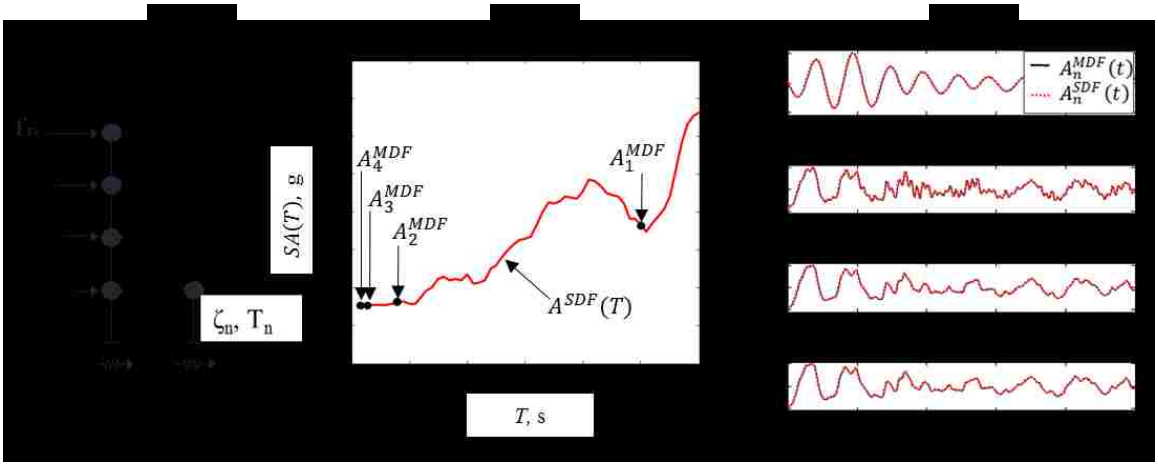

Figure 2.1 (a) 4-story cantilever wall structure and n[th] mode SDF structure; (b) A_n^{MDF} compared with pseudo-acceleration response spectrum; (c) comparison of $A_n^{MDF}(t)$ with $A_n^{SDF}(t)$ for linear-elastic 4-story cantilever wall structure subjected to CHY015W ground motion record

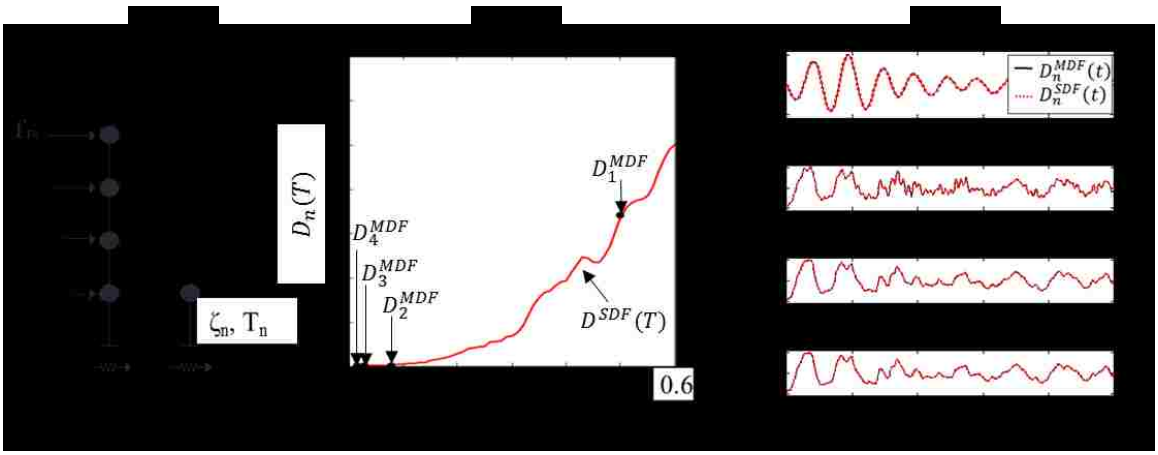

Figure 2.2 (a) 4-story cantilever wall structure and n[th] mode SDF structure; (b) D_n^{MDF} compared with deformation response spectrum; (c) comparison of $D_n^{MDF}(t)$ with $D_n^{SDF}(t)$ for linear-elastic 4-story cantilever wall structure subjected to CHY015W ground motion record

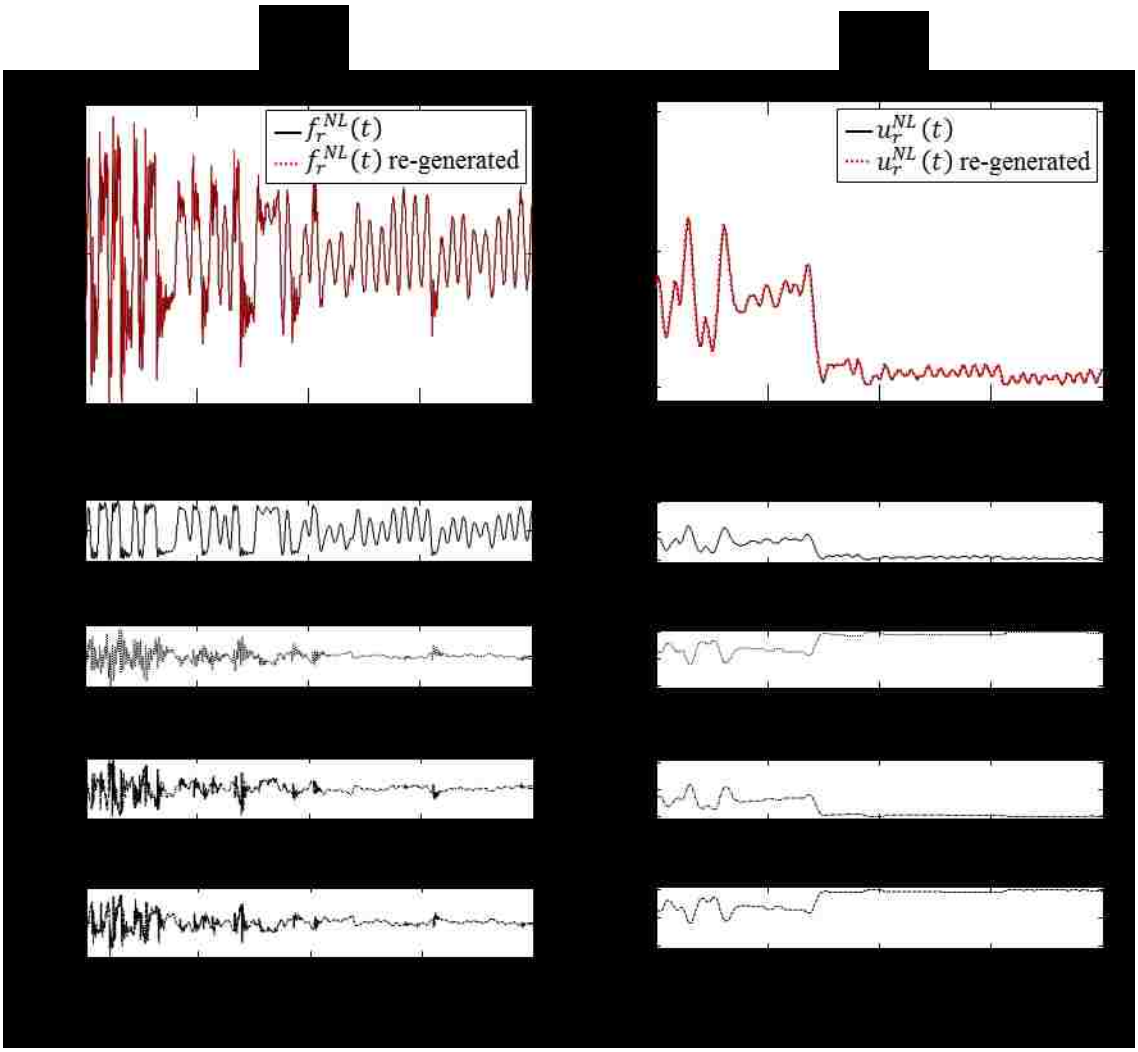

Figure 2.3 Regeneration of: (a) $f_r^{NL}(t)$ a from $f_{r_n}^{NL}(t)$ using $A_{eff_n}(t)$; (b) $u_r^{NL}(t)$ from $u_{r_n}^{NL}(t)$ using $D_{eff_n}(t)$ for NL 4-story cantilever wall structure subjected to CHY015W ground motion record

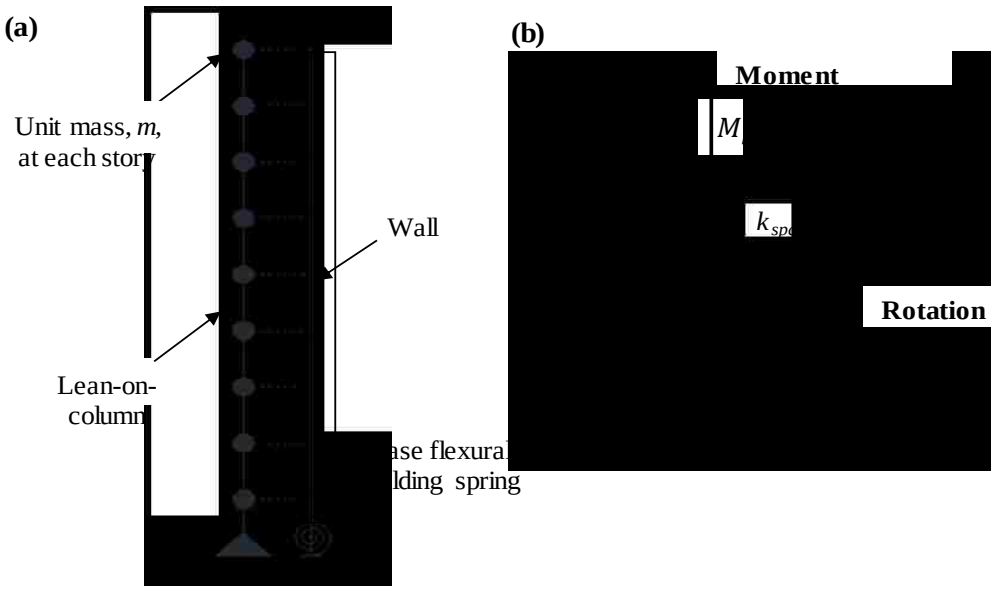

Figure 2.4 (a) NL 9-story cantilever wall structure model; (b) elastic-perfectly plastic hysteresis of base flexural hinge

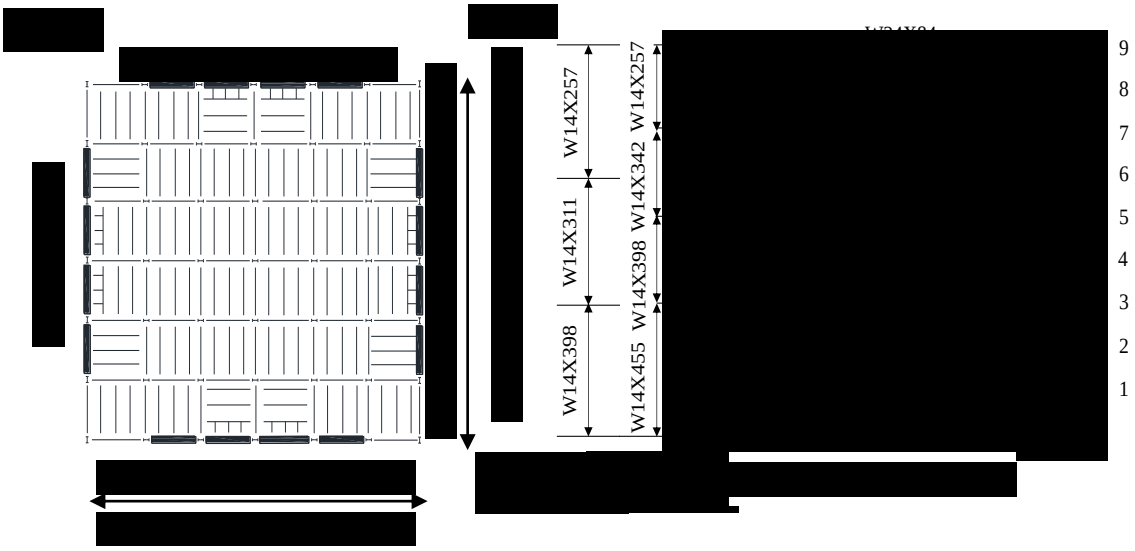

Figure 2.5 (a) Example SMRF building floor plan; (b) elevation of 9-story, 4-bay steel SMRF

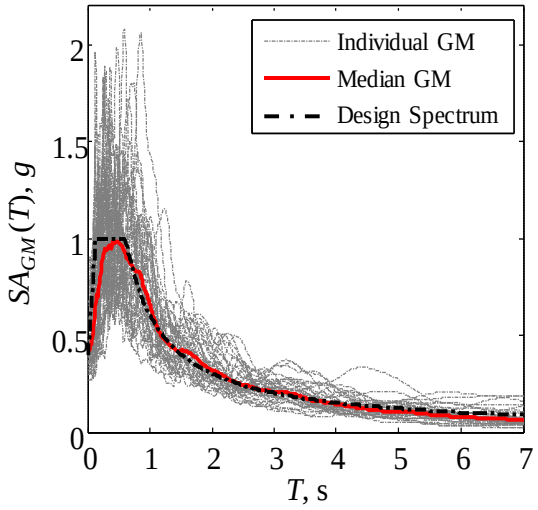

Figure 2.6 Pseudo-acceleration response spectra for ground motion set

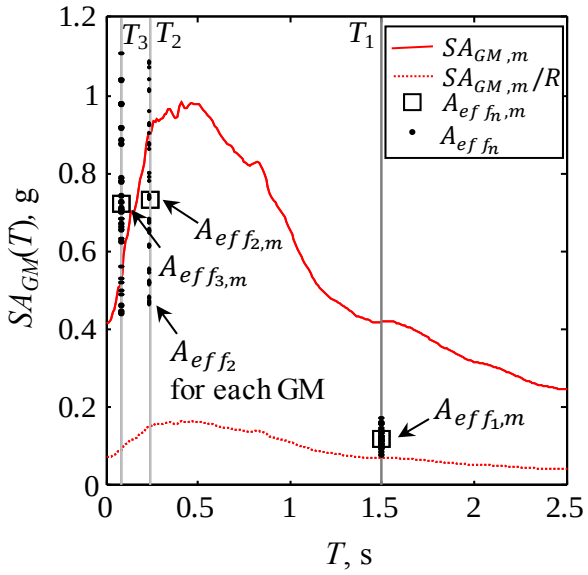

Figure 2.7 Median linear-elastic and median reduced 5% damped pseudo-acceleration spectra with A_{eff_n} and $A_{eff_{n,m}}$ identified for first three modes of MB1

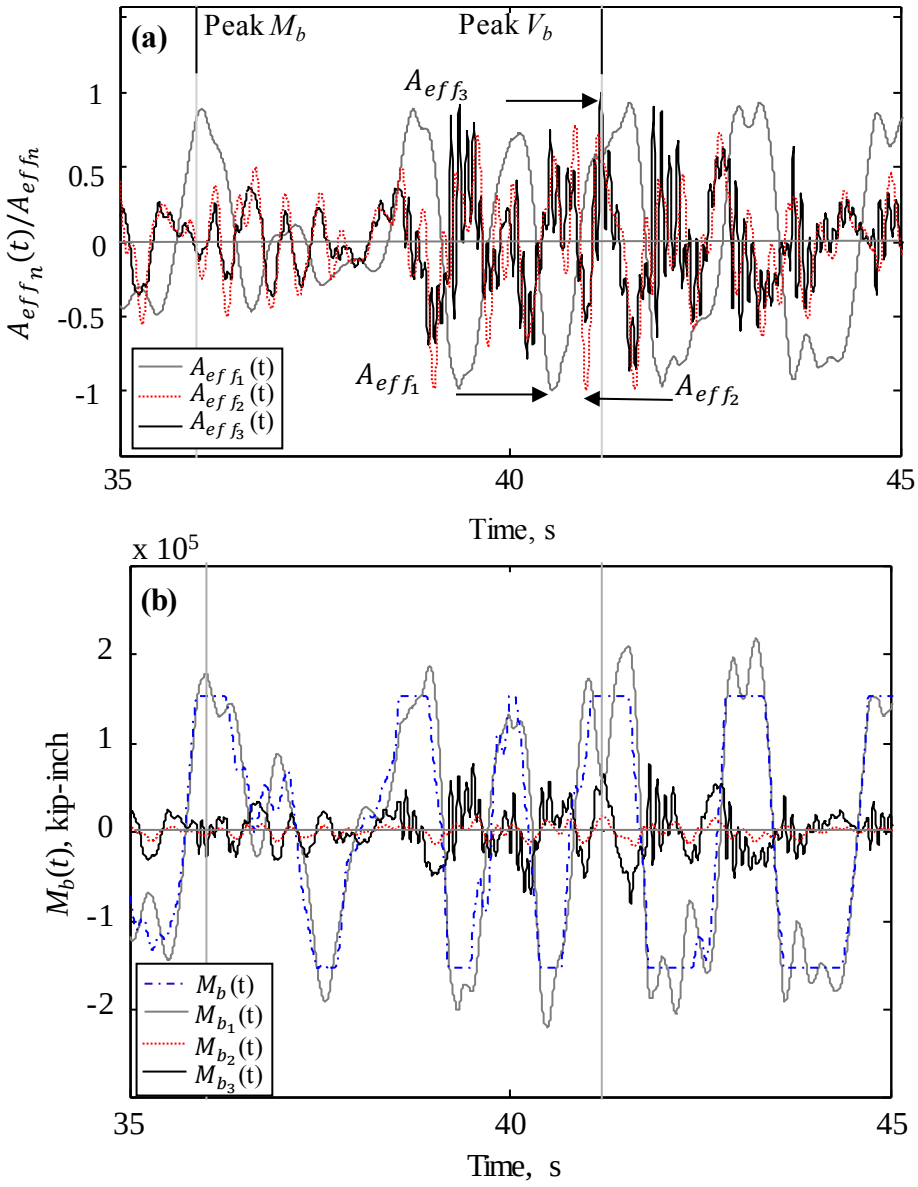

Figure 2.8 (a) $A_{eff_n}(t)$ normalized by A_{eff_n}; (b) $M_b(t)$ and $M_{bn}(t)$ for first three modes of MB1 under ILA013W ground motion record

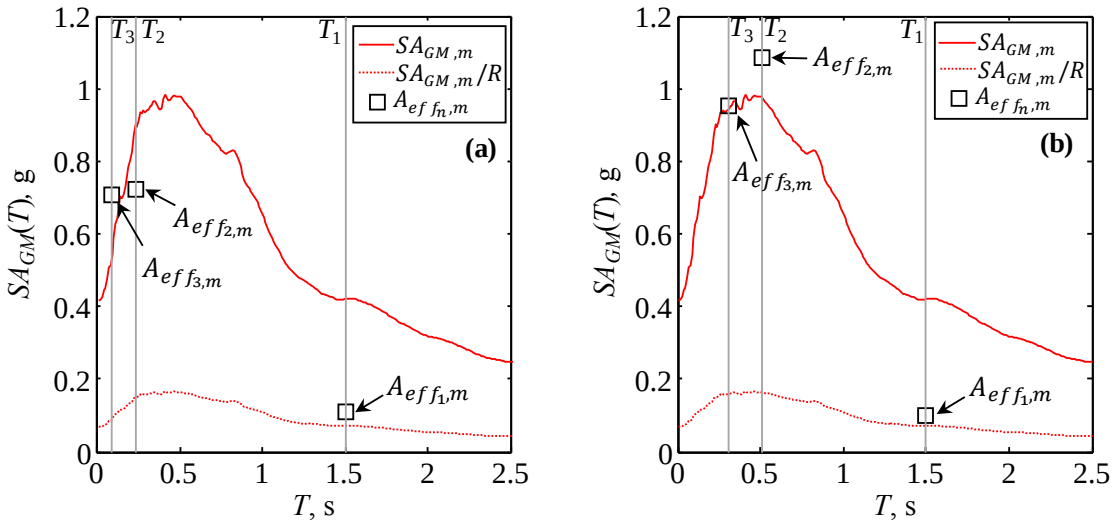

Figure 2.9 Median linear elastic and median reduced 5% damped pseudo-acceleration spectra with A_{eff_n} and $A_{eff_{n,m}}$ identified for first three modes: (a) MB1; (b) MB2

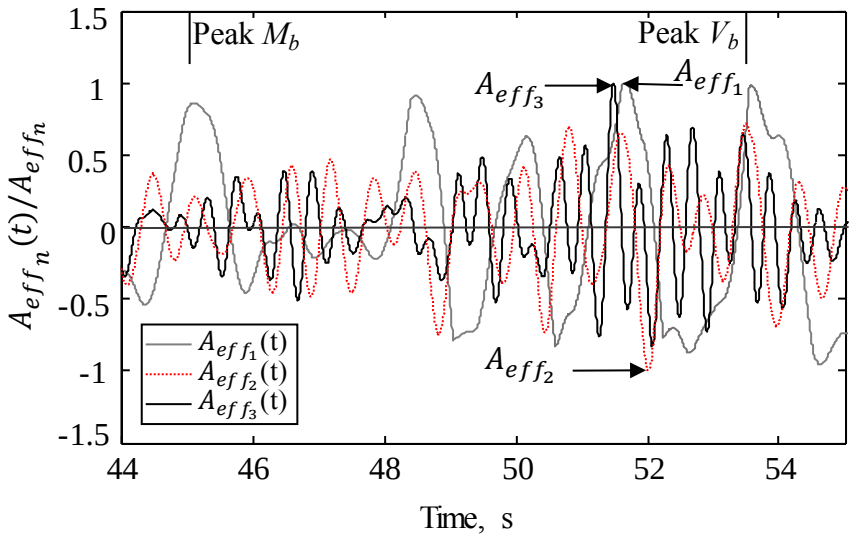

Figure 2.10 $A_{eff_n}(t)$ normalized by A_{eff_n} for first three modes of MB2 under ILA013W ground motion record

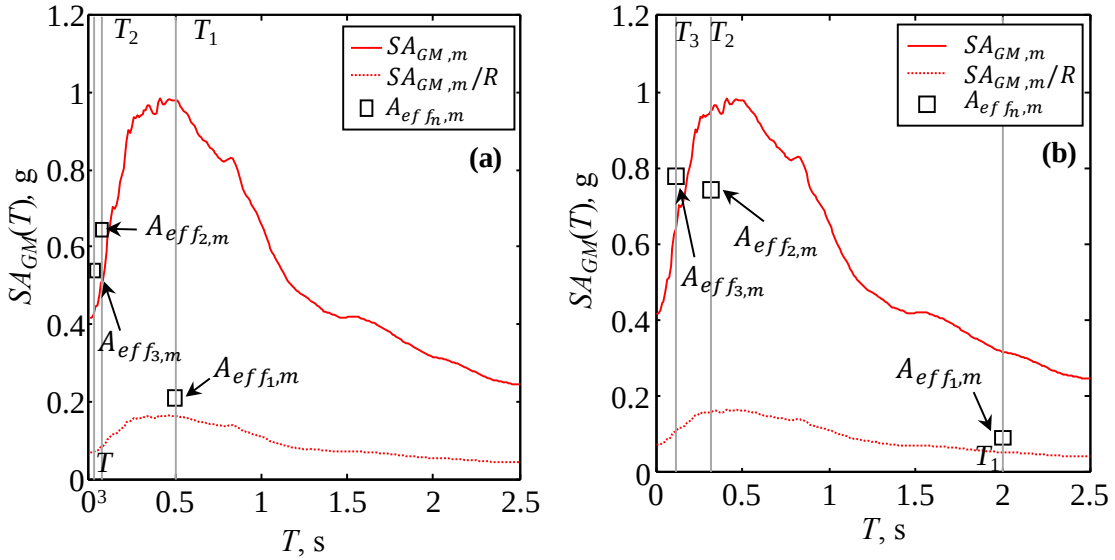

Figure 2.11 Median linear elastic and Median reduced 5% damped pseudo-acceleration spectra with A_{eff_n} and $A_{eff_{n,m}}$ identified for first three modes: (a) MB3; (b) MB4

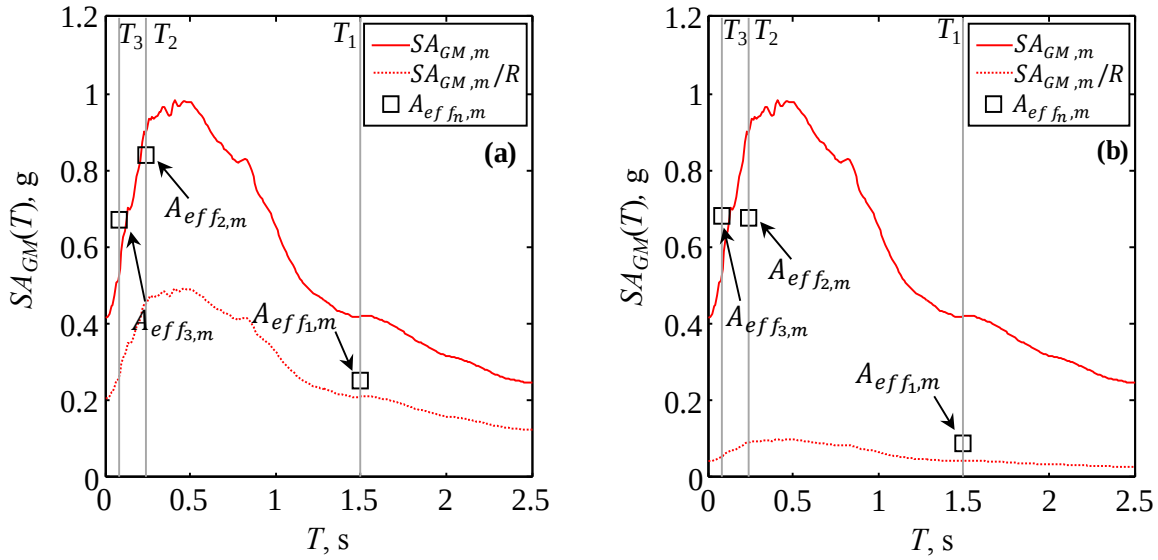

Figure 2.12 Median linear elastic and median reduced 5% damped pseudo-acceleration spectra with A_{eff_n} and $A_{eff_{n,m}}$ identified for first three modes: (a) MB5 (R =2); (b) MB6 (R =10)

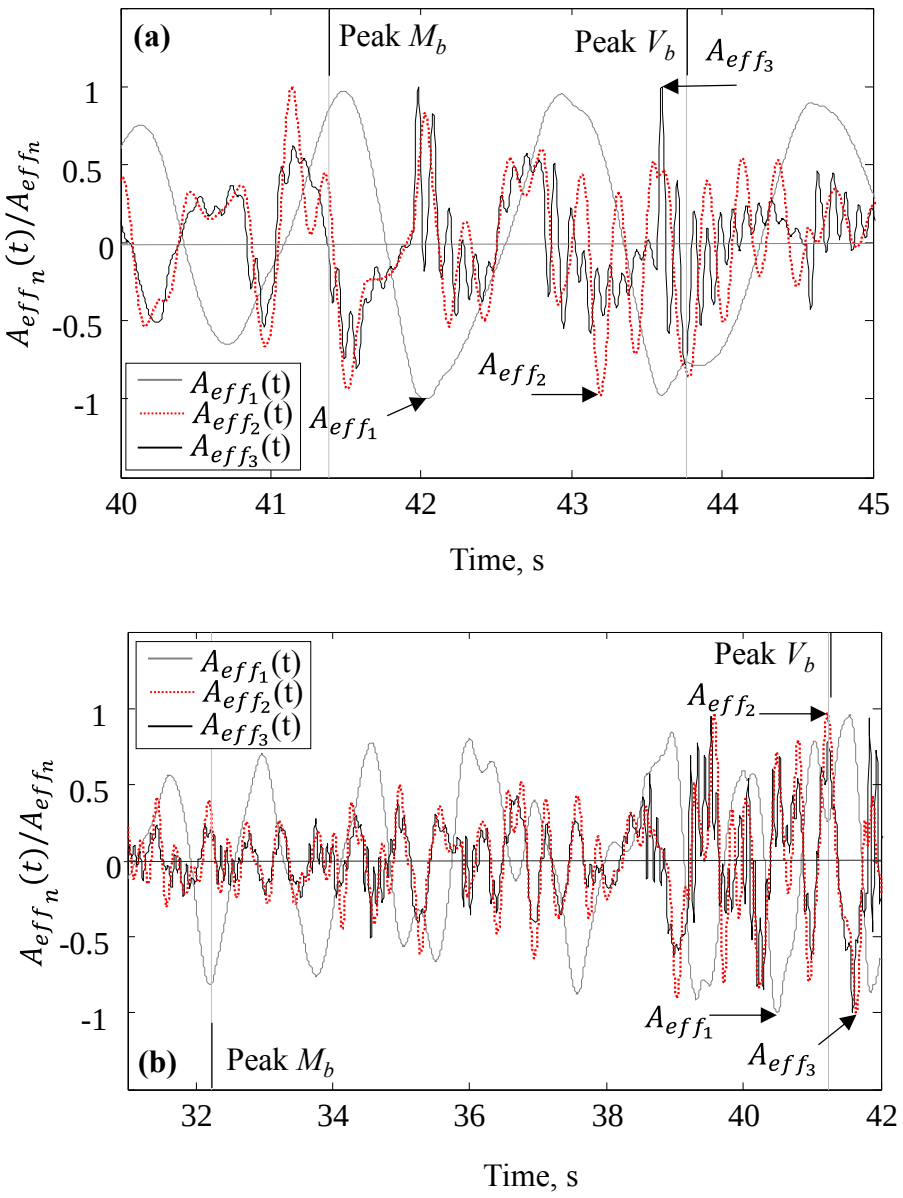

Figure 2.13 $A_{eff_n}(t)$ normalized by A_{eff_n} for first three modes of: (a) MB5; (b) MB6 under ILA013W ground motion record

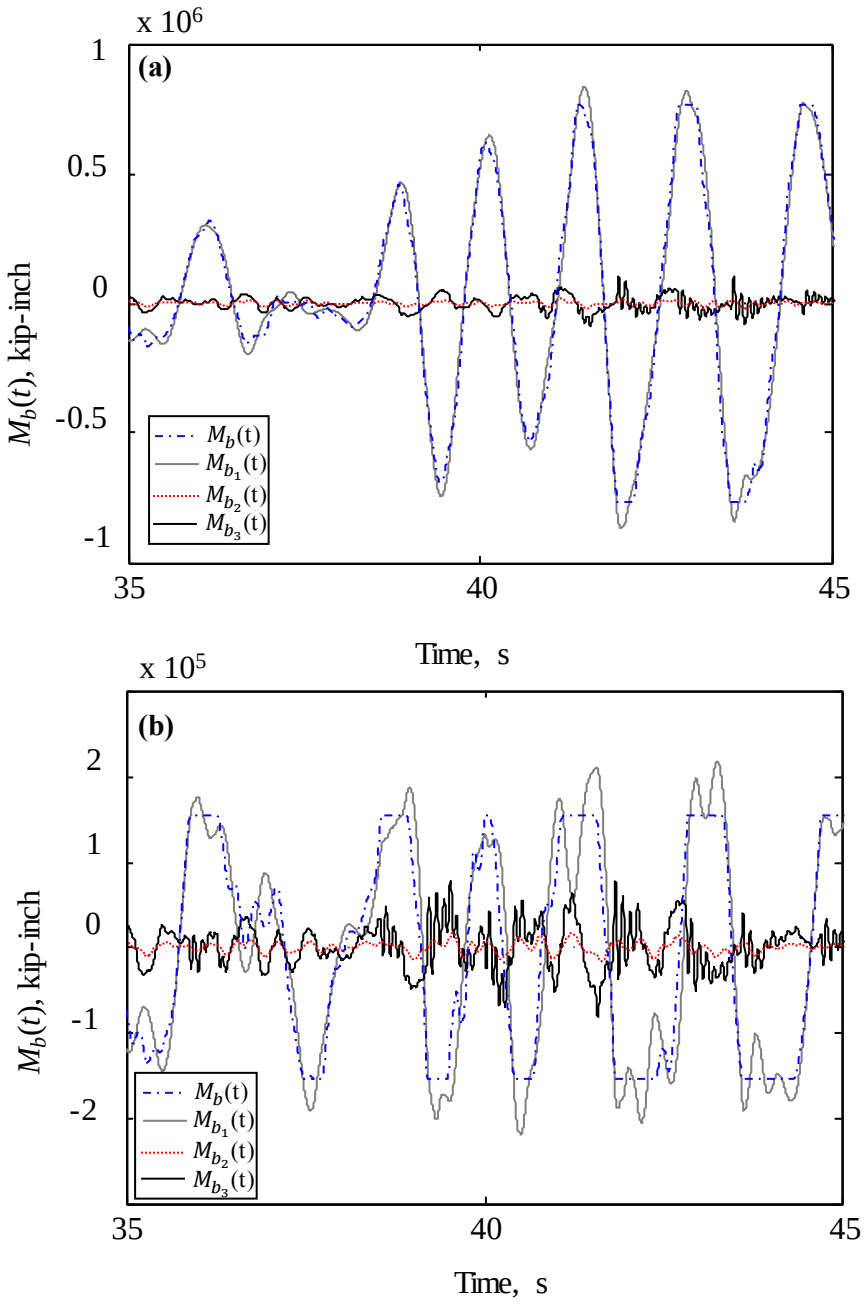

Figure 2.14 $M_b(t)$ and $M_{bn}(t)$ for first three modes of: (a) MB5 ; MB6 under ILA013W ground motion record

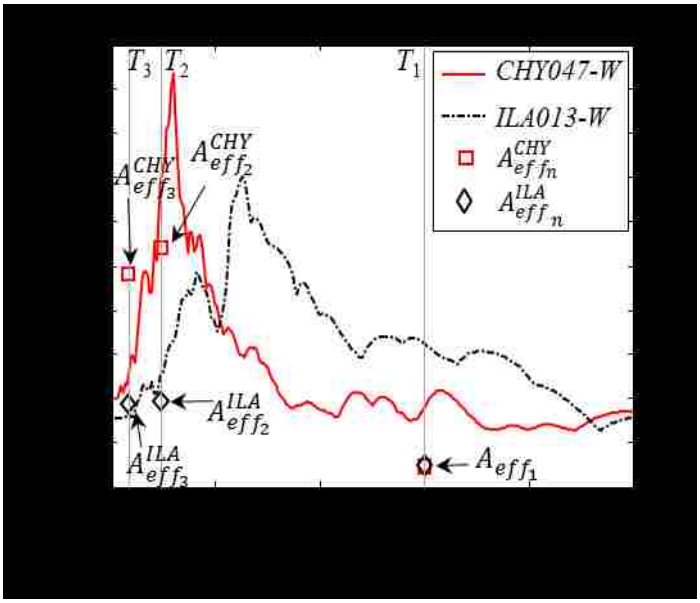

Figure 2.15 Median linear-elastic and median reduced 5% damped pseudo-acceleration spectra with A_{eff_n} and $A_{eff_{n,m}}$ identified for first three modes of MB7 (R =6)

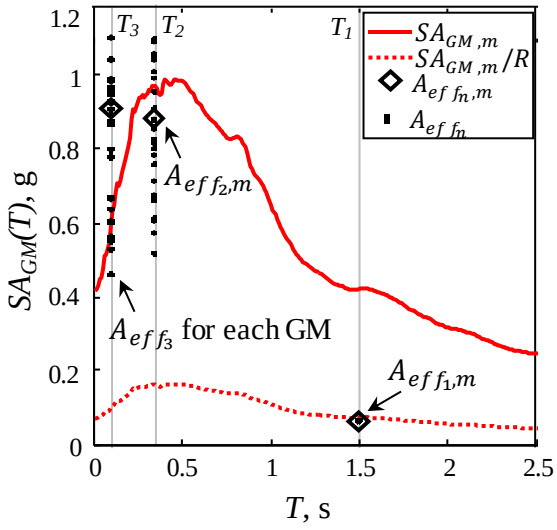

Figure 2.16 Median linear elastic and median reduced 5% damped pseudo-acceleration spectra with A_{eff_n} and $A_{eff_{n,m}}$ from alternate deformation mode shapes for first three modes of MB1

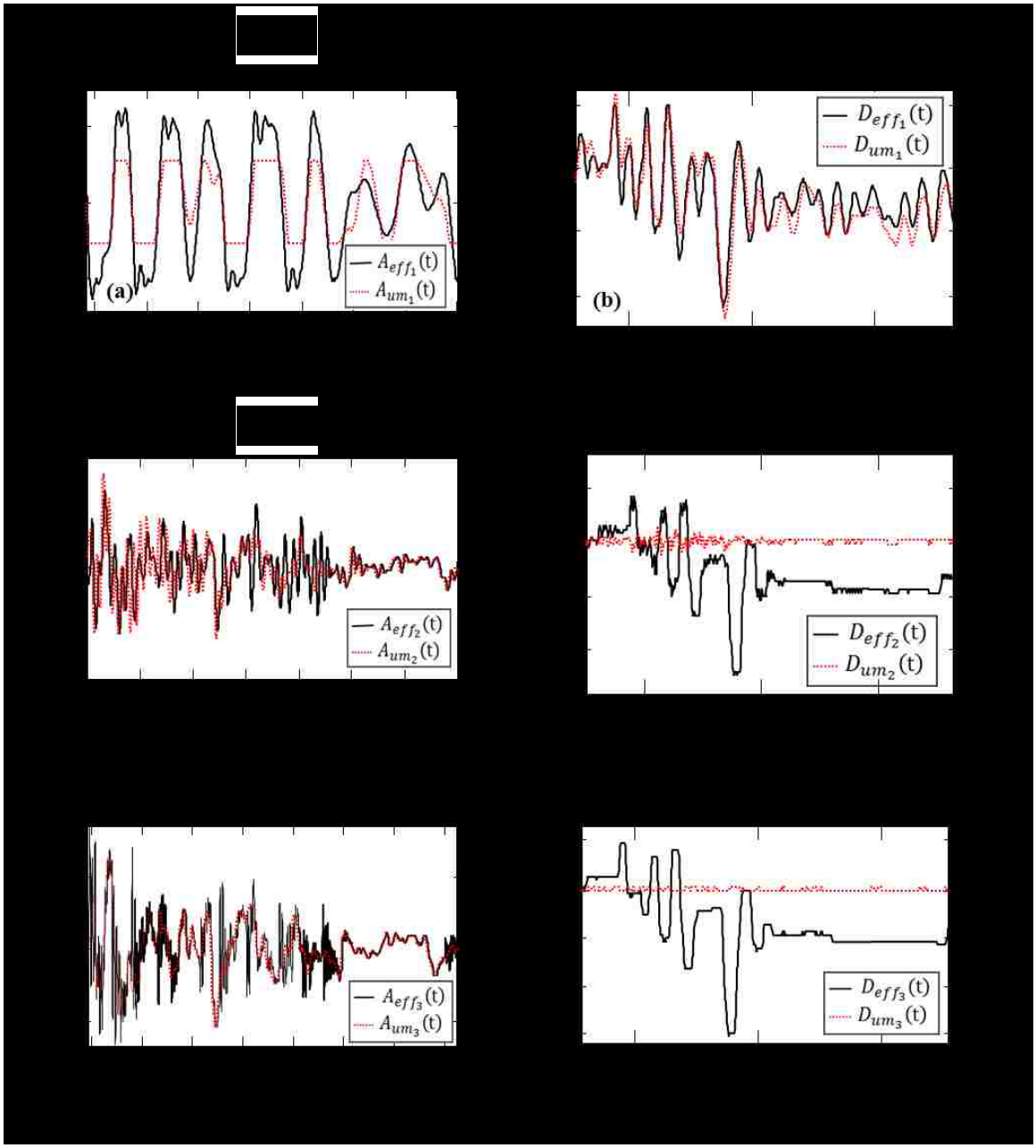

Figure 2.17 Comparison of response histories for first three modes of MB1 under ILA013W ground motion record: (a); (c); (f) $A_{eff_n}(t)$ and $A_{um_n}(t)$; (b); (d); (e) $D_{eff_n}(t)$ and $D_{um_n}(t)$,

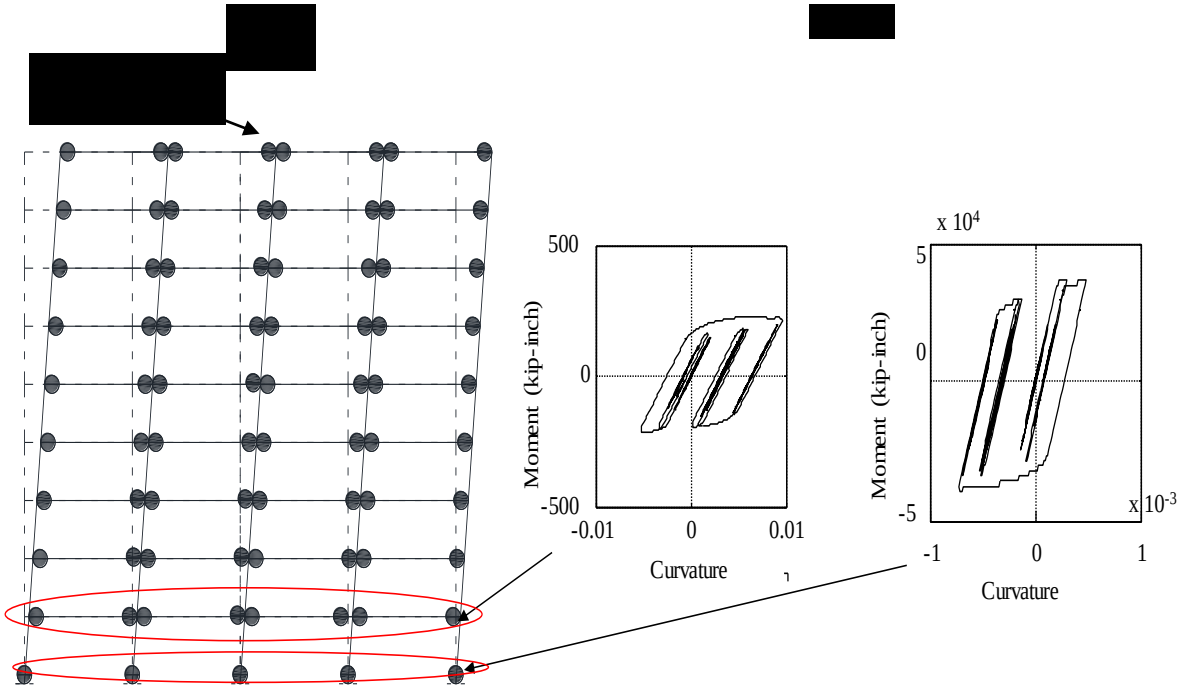

Figure 2.18 (a) Intended beam-sway yielding mechanism of SMRF; (b) moment vs. curvature response for plastic hinges in exterior bay first floor beam and a first story column end

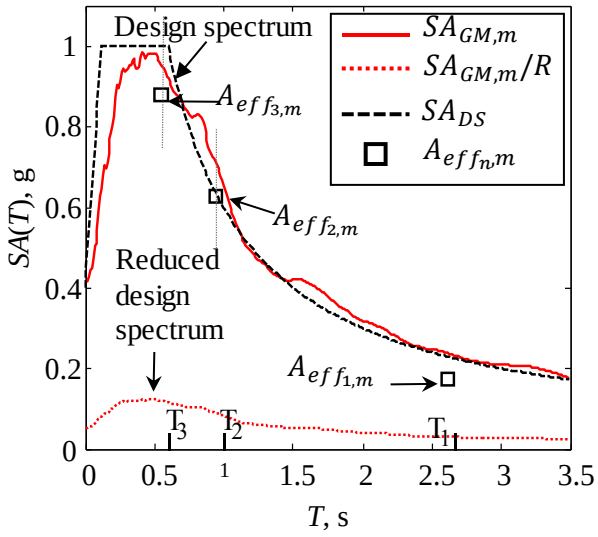

Figure 2.19 Design, median linear-elastic and median reduced 5% damped pseudo-acceleration spectra and $A_{eff_{n,m}}$ for first three modes of SMRF

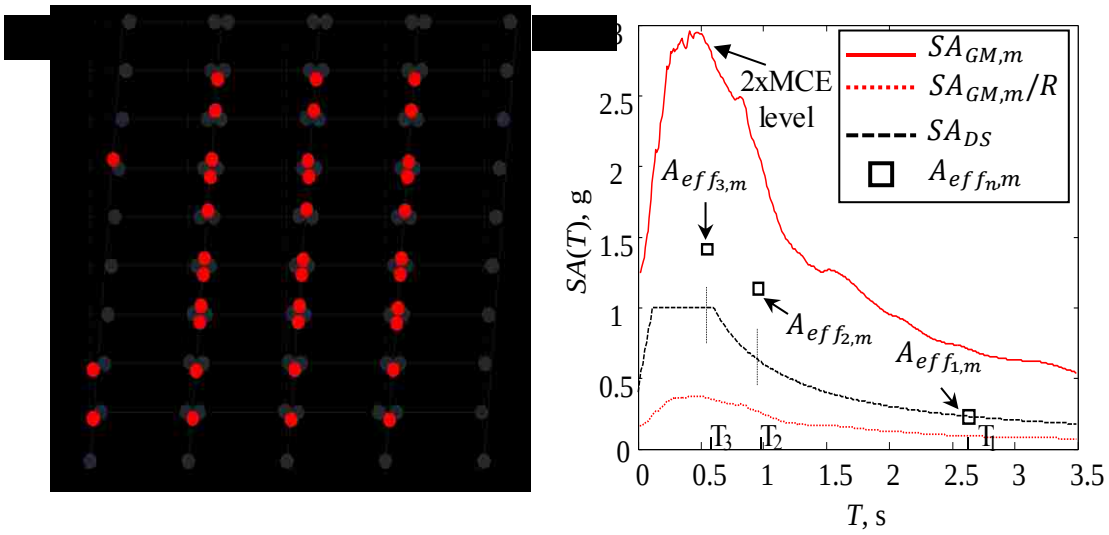

Figure 2.20 SMRF: (a) Complex yielding mechanism under GM set scaled to two times the MCE (2xMCE) level; (b) design, median 2xMCE level and design, median reduced 5% damped pseudo-acceleration spectra and $A_{eff_{n,m}}$ for first three modes

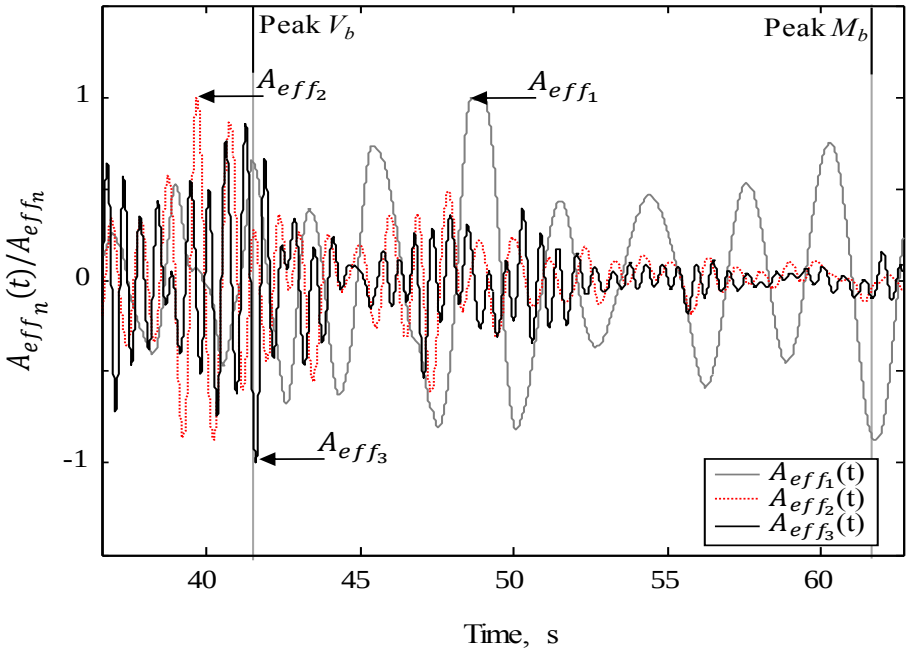

Figure 2.21 $A_{eff_n}(t)$ normalized by A_{eff_n} for first three modes of SMRF under ILA013W ground motion record

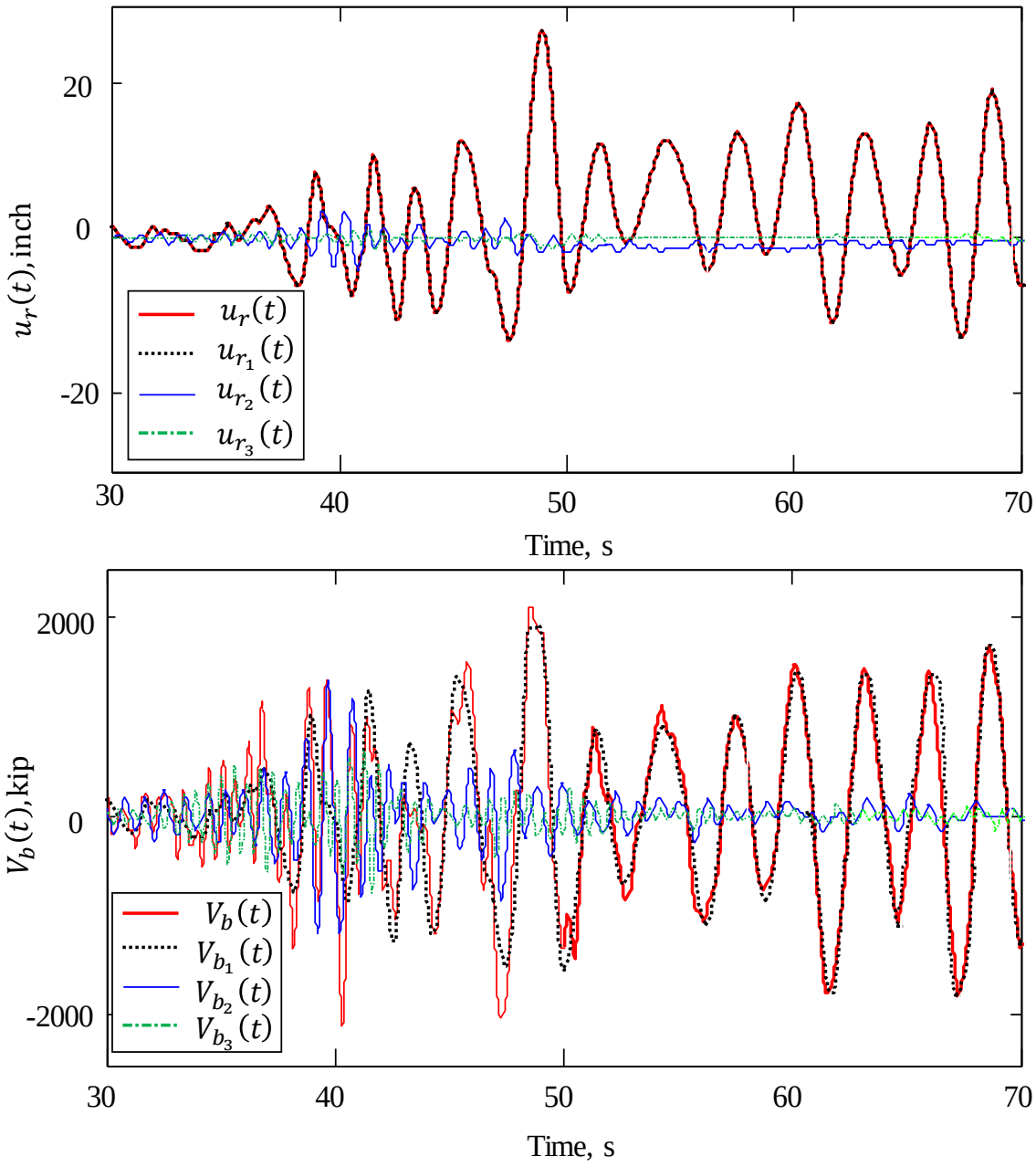

Figure 2.22 (a) $u_r(t)$ and $u_{r_n}(t)$; (b) $V_b(t)$ and $V_{b_n}(t)$ for first three modes of SMRF under ILA013W ground motion record

CHAPTER 3

MECHANISM MODE SHAPES

Overview

The importance of higher mode contributions to the total seismic response of nonlinear (NL) structures has been widely recognized. Many methods have been proposed to quantify the n^{th} mode seismic response of NL multi-degree-of-freedom (MDF) structures. Conventional modal response spectrum analysis (MRSA) and many alternative analysis methods for design purposes use modal properties based on the initial, linear-elastic stiffness matrix of a NL structure to quantify the n^{th} mode force response. The effect of NL response is not reflected in these modal properties, and therefore, using these modal properties may lead to inconsistent results. This research investigates a different approach for quantifying the n^{th} mode seismic response of NL structures with clearly defined yielding mechanisms. In this approach, a set of mode shapes, which are called *mechanism mode shapes*, determined after the yielding mechanism forms, are used to quantify the NL seismic response of the structure. Using NL time history analysis (NLTHA) results, the paper shows that these *mechanism mode shapes* can provide a better representation of the n^{th} mode response of a NL structure after the yielding mechanism forms, compared to mode shapes based on a linear-elastic model of the structure.

3.1. Introduction

The contributions of higher mode response to the total seismic response of multi-degree-of-freedom (MDF) structures have been of interest since the study by Clough (1954). Blakely et al. (1975) showed that the higher mode response is significant when structures respond in the nonlinear (NL) range. A conventional response spectrum analysis (MRSA) of a NL structure assumes that all modes are equally affected by NL response of the structure. Accordingly, the linear-elastic force response of each mode is reduced by a single response modification factor, R (e.g., as in ASCE, 2010). Alternate methods which combine the reduced first mode force response with linear-elastic higher mode force responses to estimate design force demands have been suggested (e.g., Eibl and Keintzel, 1988; Rodriguez et al., 2002; Priestley and Amaris, 2003; Calugaru and Panagiotou, 2010).

Conventional MRSA and many alternative design methods use modal properties based on the initial, linear-elastic stiffness matrix of a NL structure to quantify the n^{th} mode force response. Some research has shown that this approach may not be appropriate and may lead to unconservative design force estimates (e.g., Villaverde, 1991; 1997; Chao et al., 2007). Alternate approaches based on the tangent or secant stiffness matrix of a NL structure have been proposed. For example, Eberhard and Sozen (1993) proposed calculating the incremental restoring force vector of a NL frame-wall structure by multiplying a relative deformation increment with the tangent stiffness matrix of the structure, which is derived from analysis of the structure after the assumed yielding mechanism has formed.

Methods of adaptive pushover analyses have been developed (e.g., Bracci et al., 1997; Gupta and Kunnath, 2000; Elnashai A.S., 2000; Antoniou and Pinho, 2004; Kalkan and Kunnath, 2006) in which the n^{th} mode lateral force distribution and corresponding n^{th} mode dynamic response amplitude are recalculated at each step of the pushover analysis using instantaneous modal properties based on the tangent stiffness matrix of the NL structure. The changes in higher mode properties during the seismic response of NL frame-wall structures were considered by Sullivan et al. (2008). Assuming a structure is controlled by the first mode response, and with the aim of decoupling the first mode response from the higher mode response, Sullivan et al. (2008) developed a *transitory inelastic modes concept* (*TIMS*), in which modal properties (including the n^{th} mode periods and shapes) of the NL structure are derived from eigen analysis of the NL structure using the tangent stiffness. Sullivan et al. (2008) proposed design force estimates based on the tangent stiffness after the yielding mechanism has formed using *TIMS* for the n^{th} mode static response quantities (such as the static base shear response) and the n^{th} mode pseudo-spectral acceleration responses.

This study investigates an alternate approach for quantifying the n^{th} mode seismic response of NL structures with clearly defined yielding mechanisms, similar to the use of TIMS (Sullivan et al., 2008). An alternate set of displaced shapes which can consistently represent the n^{th} mode response of the structure after yielding is investigated. A set of *mechanism mode shapes*, $\boldsymbol{\phi}_n^m$, which are based on the stiffness matrix of the NL structure after the yielding mechanism has formed, is used as an alternate to the set of linear-elastic mode shapes, $\boldsymbol{\phi}_n^e$. The n^{th} mode responses quantified of example structures using $\boldsymbol{\phi}_n^e$ and $\boldsymbol{\phi}_n^m$ are

compared with each other. The advantages and limitations of $\boldsymbol{\phi}_n^m$ are shown using nonlinear time history analysis (NLTHA) results. Throughout this paper, ***bold italic font*** is used to represent vector and matrix variables, and conventional *italic font* is used to represent scalar variables.

3.2. Theory

3.2.1. Mechanism Mode Shapes

To derive $\boldsymbol{\phi}_n^m$, the initial linear-elastic numerical model of a NL structure is modified by adding hinges with negligible rotational stiffness at the expected yielding (i.e., plastic) hinge locations of the intended yielding mechanism. An eigen analysis of the modified model (with hinges at the location of the yielding hinges) is carried out to determine $\boldsymbol{\phi}_n^m$.

Alternatively, $\boldsymbol{\phi}_n^m$ can be derived without eigen analysis of the modified model using the initial, linear-elastic structural stiffness matrix of the structure, $\boldsymbol{k}$, and a pre-defined first mode mechanism shape (i.e., $\boldsymbol{\phi}_1^m$) as shown in Appendix A.

$\boldsymbol{\phi}_n^m$ are orthogonal with respect to the total mass matrix, $\boldsymbol{m}$, and stiffness matrix of the structure after the yielding mechanism has formed, $\boldsymbol{k}_m$:

$$(\boldsymbol{\phi}_i^m)^T \boldsymbol{m} \boldsymbol{\phi}_n^m = 0 \quad (i \neq n) \tag{3.1}$$

$$(\boldsymbol{\phi}_n^m)^T \boldsymbol{k}_m \boldsymbol{\phi}_i^m = 0 \quad (i \neq n) \tag{3.2}$$

It is also important to note that $\boldsymbol{\phi}_n^m$ are not orthogonal with respect to the linear-elastic stiffness matrix of the structure, $\boldsymbol{k}$:

$$(\boldsymbol{\phi}_n^m)^T \boldsymbol{k} \boldsymbol{\phi}_i^m \neq 0 \tag{3.3}$$

3.2.2. Elastic and Mechanism Modal Properties

nth mode static lateral force distributions (Chopra, 2012) and corresponding static story base moment and story shear profiles can be calculated using $\boldsymbol{\phi}_n^e$ or $\boldsymbol{\phi}_n^m$ as follows:

$$\boldsymbol{s}_n^e = \Gamma_n^e \boldsymbol{m} \boldsymbol{\phi}_n^e \text{ or } \boldsymbol{s}_n^m = \Gamma_n^m \boldsymbol{m} \boldsymbol{\phi}_n^m \tag{3.4}$$

$$M_{in}^{st,e} = \sum_{j=i+1}^{N} (h_j - h_i) \boldsymbol{s}_{jn}^e \text{ or } M_{in}^{st,m} = \sum_{j=i+1}^{N} (h_j - h_i) \boldsymbol{s}_{jn}^m \tag{3.5}$$

$$V_{in}^{st,e} = \sum_{j=i}^{N} \boldsymbol{s}_{jn}^e \text{ or } V_{in}^{st,m} = \sum_{j=i}^{N} \boldsymbol{s}_{jn}^m \tag{3.6}$$

where $\boldsymbol{s}_n^e$ = nth elastic mode static lateral force distribution; $\boldsymbol{s}_n^m$ = nth mechanism mode static lateral force distribution; $M_{in}^{st,e}$ = nth elastic mode static story base moment response at floor level i; $M_{in}^{st,m}$ = nth mechanism mode static story base moment response at floor level i; $V_{in}^{st,e}$ = nth elastic mode static story shear response at story level i; $V_{in}^{st,m}$ = nth mechanism mode static story shear response at story level i; N = number of floors.

The contributions of the nth elastic mode or mechanism modes to the total static base overturning moment response, M_b^{st}, and total static base shear response, V_b^{st}, are calculated, respectively, as follows:

$$\overline{M}_{bn}^{e} = \frac{M_{bn}^{st,e}}{M_b^{st}} \text{ or } \overline{M}_{bn}^{m} = \frac{M_{bn}^{st,m}}{M_b^{st}} \tag{3.7}$$

$$\overline{V}_{bn}^{e} = \frac{V_{bn}^{st,e}}{V_b^{st}} \text{ or } \overline{V}_{bn}^{m} = \frac{V_{bn}^{st,m}}{V_b^{st}} \tag{3.8}$$

where $\overline{M}_{bn}^{e}$= nth elastic mode contribution to M_b^{st}; $\overline{M}_{bn}^{m}$= nth mechanism mode contribution to M_b^{st}; $M_{bn}^{st,e} = M_{0n}^{st,e}$ = nth elastic mode static base overturning moment response; $M_{bn}^{st,m} = M_{0n}^{st,m}$ = nth mechanism mode static base overturning moment response; $M_b^{st} = \sum_{n=1}^{N} M_{bn}^{st,e} = \sum_{n=1}^{N} M_{bn}^{st,m}$; $\overline{V}_{bn}^{e}$= nth elastic mode contribution to V_b^{st}; $\overline{V}_{bn}^{m}$= nth mechanism mode contribution to V_b^{st}; $V_{bn}^{st,e} = V_{0n}^{st,e}$ = nth elastic mode static base shear response; $V_{bn}^{st,m} = V_{0n}^{st,m}$ = nth mechanism mode static base shear response; $V_b^{st} = \sum_{n=1}^{N} V_{bn}^{st,e} = \sum_{n=1}^{N} V_{bn}^{st,m}$; N= number of modes.

3.2.3. Virtual Work by nth Elastic and Mechanism Mode Static Force Profiles

The lateral force required to form the intended yielding mechanism of a structure can be calculated using virtual work:

$$W_{int} = W_{ext} \tag{3.9}$$

where $W_{int,}$= internal work; W_{ext} = external work.

If the virtual displacement vector is $\boldsymbol{u}$, and the virtual relative rotation at the location of each yielding hinge (where the moment is M_{p_k}) is θ_k, then W_{int} done at the yielding hinge locations equals W_{ext} done by lateral forces proportional to $\mathbf{s}_n^e$ or $\mathbf{s}_n^m$:

$$\sum_{k=1}^{N_h} M_{p_k}\theta_k = \sum_{n=1}^{N_m} \alpha_n (\boldsymbol{s}_n^e)^T \boldsymbol{u} \quad \text{or} \quad \sum_{k=1}^{N_h} M_{p_k}\theta_k = \sum_{n=1}^{N_m} \alpha_n (\boldsymbol{s}_n^m)^T \boldsymbol{u} \tag{3.10}$$

where N_m = number of modes considered ≤ N; M_{p_k}= moment capacity of the yielding hinges; N_h=number of hinges; α_n = scale factor.

If $\boldsymbol{u}$ is proportional to $\boldsymbol{\phi}_i^e$ or $\boldsymbol{\phi}_i^m$ (i.e., $\boldsymbol{u} = c_i^e \boldsymbol{\phi}_i^e$ or $\boldsymbol{u} = c_i^m \boldsymbol{\phi}_i^m$), the contribution to W_{ext} done by other modes ($n \neq i$) is zero, since:

$$(\boldsymbol{s}_n^e)^T c_i^e \boldsymbol{\phi}_i^e = 0 \qquad (n \neq i) \tag{3.11a}$$

$$(\boldsymbol{s}_n^m)^T c_i^m \boldsymbol{\phi}_i^m = 0 \quad (n \neq i) \tag{3.11b}$$

due to the orthogonality of the modes with respect to mass. In particular, if $\boldsymbol{u}$ is proportional to $\boldsymbol{\phi}_1^e$ or $\boldsymbol{\phi}_1^m$, the contribution of the higher modes is zero.

If $\boldsymbol{u}$ is proportional to the yielding mechanism of the NL structure, written as $c_i^m \boldsymbol{\phi}_1^m$, then the contribution to W_{ext} done by all elastic modes (i.e., $\boldsymbol{\phi}_i^e$) is non-zero, as $\boldsymbol{\phi}_i^e$ are not mass-orthogonal to $\boldsymbol{\phi}_1^m$.

$$(\boldsymbol{s}_n^e)^T c_i^e \boldsymbol{\phi}_1^m \neq 0 \tag{3.12}$$

3.2.4. Quantification of nth Mode Contribution to Total Seismic Response

This study quantifies the nth mode contribution to the total seismic response of a structure using the conventional nth mode pseudo-acceleration response, the nth mode effective pseudo-acceleration (see Chapter 2 and Roke et al., 2010), the nth mode effective deformation (see Chapter 2), and results from an uncoupled modal response history analysis (UMRHA) based on the approach of Chopra and Goel (2002). This section briefly explains how the nth mode contribution is quantified.

3.2.4.1. nth Mode Effective Pseudo-Acceleration Concept

When the total NL restoring force vector, $\boldsymbol{f}_r^{NL}(t)$, is known from NLTHA of an MDF structure for a given ground motion, the nth mode effective pseudo-acceleration response, $A_{eff_n}(t)$, is calculated from , $\boldsymbol{f}_r^{NL}(t)$, as follows:

$$A_{eff_n}(t) = \frac{\boldsymbol{\phi}_n^T \boldsymbol{f}_r^{NL}(t)}{\Gamma_n M_n} \tag{3.13}$$

where $\boldsymbol{f}_r^{NL}(t)$, = total restoring force vector from NLTHA; $A_{eff_n}(t)$ = nth mode effective pseudo-acceleration; Γ_n = modal participation factor = $\frac{\boldsymbol{\phi}_n^T \boldsymbol{m}\{i\}}{M_n}$; $\boldsymbol{\phi}_n^T$ = transpose of the nth mass-orthogonal mode shape; $M_n = \boldsymbol{\phi}_n^T \boldsymbol{m}\, \boldsymbol{\phi}_n$ = nth mode mass; $\{i\}$ = influence vector.

$\boldsymbol{\phi}_n^e$ or $\boldsymbol{\phi}_n^m$ can be used to calculate the nth mode effective pseudo-acceleration response, which are denoted as $A_{eff_n}^e(t)$ or $A_{eff_n}^m(t)$, respectively.

3.2.4.2. nth Mode Effective Deformation Concept

The nth mode contribution to the total deformation response of a NL MDF structure, $D_{eff_n}(t)$, can be obtained from the total deformation vector from NLTHA, $\boldsymbol{u}^{NL}(t)$, as follows:

$$D_{eff_n}(t) = \frac{\boldsymbol{\phi}_n^T \boldsymbol{m}\, \boldsymbol{u}^{NL}(t)}{\Gamma_n M_n} \tag{3.14}$$

$\boldsymbol{\phi}_n^e$ or $\boldsymbol{\phi}_n^m$ can be used to calculate the nth mode effective deformation response, which is denoted as $D_{eff_n}^e(t)$ or $D_{eff_n}^m(t)$, respectively.

3.2.4.3. Uncoupled Modal Response History Analysis (UMRHA)

Uncoupled modal response history analysis (UMRHA) for a NL MDF building structure is similar to modal response history analysis for a linear system. UMRHA calculates the total response of a NL MDF structure from estimated modal responses, assuming that the modal responses are weakly coupled, and treating them as uncoupled (Chopra and Goel, 2002). Although the assumption of uncoupled modes may be questionable, UMRHA determines the nth mode response from the following equation of motion for the corresponding uncoupled nth mode SDF system (Chopra and Goel, 2002):

$$\ddot{D}_{um_n}(t) + 2\zeta_n \omega_n \dot{D}_{um_n}(t) + \frac{F_{sn}(t)}{L_n} = -\ddot{u}_g(t) \tag{3.15}$$

where $D_{um_n}(t)$ = n[th] mode deformation response for the n[th] mode SDF system; ζ_n = n[th] mode damping ratio; $L_n = \Gamma_n M_n$; $F_{sn}(t) = F_{sn}\left(D_{um_n}(t)\right)$ = n[th] mode nonlinear spring force which depends on $D_{um_n}(t)$.

A modal pushover analysis (MPA) procedure is used to determine the normalized envelope n[th] mode NL spring force, (F_{s_n} / L_n), versus (vs.) deformation, D_{um_n}, relationship as follows (Chopra, 2012). A static pushover analysis of the NL MDF structure, under the external lateral force distribution, $\boldsymbol{s}_n^* = \boldsymbol{m}\,\boldsymbol{\phi}_n$, provides the base shear, V_{bn}, vs. roof level deformation, u_{rn}, relationship, which is transformed into the (F_{s_n} / L_n) vs. D_{um_n} relationship, as follows:

$$\frac{F_{sn}}{L_n} = \frac{V_{bn}}{\Gamma_n L_n} \tag{3.16a}$$

$$D_{um_n} = \frac{u_{r_n}}{\Gamma_n \phi_{rn}} \tag{3.16b}$$

The modified MPA (mMPA) procedure (Chopra et al., 2004) assumes that the higher mode (n > 1) responses are linear-elastic, with the linear F_{s_n} / L_n vs. D_{um_n} relationship as follows:

$$\frac{F_{sn}(t)}{L_n} = \omega_n^2 D_{um_n}(t) \tag{3.17}$$

For the mMPA procedure, the 1st mode envelope F_{s_1} / L_1 vs. D_{um1} relationship is determined using the transformations of Eq. (3.16) from the V_{b1} vs. u_{r1} response obtained from a static pushover analysis of the NL structure under $\boldsymbol{s}_1^* = \boldsymbol{m}\,\boldsymbol{\phi}_1$.

$\boldsymbol{\phi}_n^e$ or $\boldsymbol{\phi}_n^m$ can be used to quantify the nth mode force response, $F_{s_n} / L_n(t)$, which is denoted as $A_{um_n}^e(t)$ or $A_{um_n}^m(t)$, respectively, and the nth mode deformation response, which is denoted as $D_{um_n}^e(t)$ or $D_{um_n}^m(t)$, respectively. These results are determined by solving Eq. (3.15). $A_{um_n}^e(t)$ and $A_{um_n}^m(t)$ can be compared to the actual nth mode force responses, $A_{um_n}^e(t)$ and $A_{um_n}^m(t)$, calculated from NLTHA results using Eq. (3.13). Similarly, $D_{um_n}^e(t)$ and $D_{um_n}^m(t)$ can be compared to the actual nth mode force responses, $D_{eff_n}^e(t)$ and $D_{eff_n}^m(t)$, calculated from NLTHA results using Eq. (3.14).

3.3. Introductory Example

To illustrate how the formation of the intended yielding mechanism changes the modal properties of a NL structure and the resulting nth mode seismic response, the results for a 9-story cantilever wall structure are examined.

3.3.1. Description of Example Structure

The example 9-story wall structure is rigid in shear (i.e., has purely flexural response). The nonlinearity of the wall structure is concentrated in a flexural yielding rotational spring at

the base of the wall. The rest of the wall is assumed to be linear-elastic. The base flexural yielding spring has an assumed elastic-perfectly plastic (EPP) response. The initial stiffness of the base flexural yielding spring, k_{spg}, is set to 10 times the flexural stiffness of the first story. The yield strength of the base flexural yielding spring, M_b^h, is established uniquely for each ground motion (GM) in the GM set as follows:

$$M_b^h = M_{b1}^{st} \frac{SA_{GM}(T_1^e)}{R} \tag{3.18}$$

where $SA_{GM}(T_1^e)$ = 1st mode pseudo-acceleration for the GM; T_1^e = 1st elastic-mode period based on the initial linear-elastic model of the structure; R = response modification factor, assumed to be 6.

Figure 3.1 shows a schematic of the numerical model of the example wall structure and the EPP response of the flexural yielding rotational spring at the base. The details of the numerical model of the wall structure are explained later in this chapter.

3.3.2. nth Mode Response of Example Structure

The yielding mechanism of the example cantilever wall is yielding of the base flexural yielding spring, which is dictated by the base overturning moment (M_b) response of the NL structure. To investigate the contribution of each $\boldsymbol{\phi}_n^e$ to M_b^{st}, $\overline{M}_{bn}^e$, is calculated for the example wall structure. Table 3.1 shows the $\overline{M}_{bn}^e$ for the first three elastic modes. As seen in Table 3.1, $\overline{M}_{b1}^e$ is 89.3% and the cumulative $\overline{M}_{bn}^e$ of the higher modes is less than 11%.

These results show that the first mode is dominant, but the higher elastic modes also contribute to the M_b^{st}. Therefore, while $\boldsymbol{\phi}_n^e$ are orthogonal with respect to the mass and linear-elastic stiffness matrices, they are coupled through the base flexural yielding mechanism.

The alternate approach of quantifying the nth mode base overturning moment response using mechanism modes, $\boldsymbol{\phi}_n^m$, is applied to the example wall structure. $\boldsymbol{\phi}_n^m$ for the wall structure are derived after the base flexural yielding mechanism forms, and used to calculate the nth mode contribution to M_b^{st}. Table 3.1 shows that when $\overline{M}_{bn}^m$ is calculated using $\boldsymbol{\phi}_n^m$, only $\overline{M}_{b1}^m$ is non-zero. The higher mode contribution to M_b^{st} is eliminated by using $\boldsymbol{\phi}_n^m$ and the modes are not coupled through the base flexural yielding mechanism.

To further investigate the nth mode response of the example wall structure, results from NLTHA of the wall structure under a set of ground motion (GM) records (see Table 3.2) are presented. Figure 3.2 shows the 5% damped median linear-elastic and median reduced (by R = 6) pseudo-acceleration response spectra for the GM set. For the first three modes, the peak values of the nth elastic and mechanism mode effective pseudo-accelerations $A_{eff_n}^e(t)$ and $A_{eff_n}^m(t)$ from the NLTHA results for each GM, denoted $A_{eff_n}^e$ and $A_{eff_n}^m$, respectively, are indicated on the plot. The median effective pseudo-accelerations for the GM set, $A_{eff_n,m}^e$ and $A_{eff_n,m}^m$, are also shown. $A_{eff_n,m}^e$ and $A_{eff_n,m}^m$ are compared with the nth mode

pseudo-accelerations from the median elastic and reduced pseudo-acceleration response spectra $SA_{GM,m}(T)$ and $SA_{GM,m}(T)/R$, respectively, at the elastic mode periods, T_n^e.

Figure 3.2(a) shows that, $A^e_{eff_1,m}$ (i.e., for the 1st elastic mode) is close to the median *reduced* pseudo-acceleration spectrum. On the contrary, $A^e_{eff_2,m}$ and $A^m_{eff_3,m}$ (i.e., for the 2nd and 3rd elastic modes) are close to the median linear-elastic pseudo-acceleration response spectrum. The ratio of $SA_{GM,m}(T^e_n)$ to $A^e_{eff_2,m}$ is denoted as $R^e_{act_n}$. Based on Figure 3.2(a), the 1st mode R^e_{act} (i.e, $R^e_{act_1}$, the ratio of $SA_{GM,m}(T_1^e)$ to $A^e_{eff_1,m}$) is 3.66, while the $R^e_{act_2}$ and $R^e_{act_3}$ (i.e., the ratio of $SA_{GM,m}(T_2^e)$ to $A^e_{eff_2,m}$ and the ratio of $SA_{GM,m}(T_3^e)$ to $A^m_{eff_3,m}$, respectively) are 1.23 and 0.72, respectively. These results show that the 2nd and 3rd mode responses are close to the linear-elastic response and are not strongly affected by the formation of the base flexural yielding mechanism. Figure 3.2(a) further shows that there is a considerable scatter in the $A^e_{eff_2}$ and $A^e_{eff_3}$ values, and less scatter in the $A^e_{eff_1}$ values. These observations are consistent with previous studies (e.g., Priestley, 2003). The results show that the 1st mode response is *not accurately* controlled by the formation of the yielding mechanism, since $R_{act_1} = 3.66$ is much smaller than $R = 6$ used to establish the base flexural yielding strength, and scatter in $A^e_{eff_1}$ is observed.

Figure 3.2(b) shows $A^m_{eff_n}$ and $A^m_{eff_n,m}$ together with the 5% damped median linear-elastic and median reduced (by R = 6) pseudo-acceleration response spectra. The ratio of $SA_{GM,m}(T^e_n)$ to $A^m_{eff_n,m}$ is denoted as $R^m_{act_n}$. Based on the *mechanism mode shapes*, $R^m_{act_1}$ is

6.0 and there is no scatter in the $A^m_{eff_1}$ results indicating that the 1st mode response (based on the *mechanism mode shapes*) is *accurately* controlled by the base flexural yielding mechanism. In addition, there is no scatter in the $A^m_{eff_1}$ results. $R^m_{act_2}$ is 1.05 and $R^m_{act_3}$ is 0.67, which are similar to the previous results and indicate that the higher modes are not strongly affected by the base flexural yielding mechanism. These results show that *mechanism mode shapes* (ϕ^m_n) can be used to accurately quantify the 1st mode and higher mode response of a NL structure, thus motivating further study of ϕ^m_n.

3.4. Description of Example Structures

3.4.1. 9-story Cantilever Wall Structures

A 9-story wall structure that is rigid in shear (i.e., has purely flexural response) and a 9-story wall structure with shear flexibility are the primary example structures. The wall structures have a constant story height of 13 ft., and are idealized as a lumped-mass MDF system with a unit mass at each floor level. Each story has the same stiffness, and this stiffness is selected so that the first mode period of the linear-elastic model (T^e_1) is 1.5 s. The properties of these wall structures are summarized in Table 3.3.

Two dimensional numerical models of the cantilever wall structures were created in OpenSees (Mazzoni et al., 2009). Schematics of the wall structure models are shown in Figure 3.1. Force-based beam-column elements with linear-elastic material definitions were used to model the walls. The base flexural yielding spring was modeled by using a

zero length element (Mazzoni et al., 2009). A lean-on-column with linear-elastic beam-column members was included to model the second-order effects of vertical loads. A unit seismic mass was assigned to the horizontal degree-of-freedom of each node of the lean-on-column at each floor level. The horizontal displacements of the wall and lean-on-column were constrained to each other with rigid links at each floor level. The corotational coordinate transformation was used for the elements. Caughey damping with a 5% damping ratio for each mode was used. Newmark constant average acceleration integration and the Newton-Krylov solution algorithms were used in the NLTHA.

3.4.2. Frame Structures

3.4.2.1. Self-Centering Concentrically Braced Frame Structure

A 9-story self-centering concentrically braced frame (SC-CBF) structure designed by Chancellor (2014) and denoted as 9EO-GL, is used in this study. An SC-CBF (Sause et al., 2006; Roke, 2009; Chancellor, 2014) is a concentrically braced frame (CBF) with special column base details. Unlike a conventional CBF, the columns of an SC-CBF are not fully attached to the foundation and the special column base details permit the CBF to "rock" on the foundation. During this controlled rocking, the column under incremental tension from overturning moment uplifts from the foundation. As a result, the lateral drift capacity of the system prior to the initiation of structural damage is increased considerably. The resistance to rocking is provided by vertically-oriented post tensioning (PT) bars located within the CBF, which enable the system to self-center during the earthquake. Under the design basis earthquake (DBE), yielding of the CBF members is precluded by a

performance-based design procedure for SC-CBFs; however, a 50% probability of PT bar yielding under the DBE is considered acceptable (Chancellor, 2014).

Figure 3.3 shows the floor plan of the example SC-CBF building and the elevation of the SC-CBF. The braces of the example SC-CBF are arranged in an X-configuration (Figure 3.3(b)). To transfer the base shear from the uplifted column to the column in contact with foundation, a horizontal brace strut is located at the bottom of the SC-CBF. The SC-CBF building is assumed to be an office-type building on a site in Southern California with NEHRP Site Class D conditions. Dead and live loads used in design are given in Table 3.4 and Table 3.5. All members of the SC-CBF are ASTM A992 wide-flange shapes with a nominal steel yield strength of 50 ksi, meeting the seismic compactness requirements of AISC (2010). The total area of the PT bars, A_{PT}, located in the center of the SC-CBF is 3.4 in^2. The design yield strength for the PT steel, f_{py}, was 120 ksi. An initial prestressing force of $0.50f_{py}$ is assigned to the PT bars. A vertically-oriented energy dissipation device (EDP), which is assumed to be a constant-force energy dissipation device (e.g., a friction device), is attached to the foundation and to the base of each SC-CBF column. The force developed in each EDP, denoted V_{ED}, is 50 kip. The EDP dissipates energy when the SC-CBF column uplifts from the foundation.

A two dimensional numerical model of the SC-CBF was developed (Chancellor, 2014) in OpenSees (Mazzoni et al., 2009). Each beam, column, and brace of the SC-CBF was modeled by five force-based beam-column elements with fiber sections. Five integration

points were used along the length of each force-based beam-column element. Gauss-Lobatto numerical integration was used. A bi-linear material model (using the Steel02 material definition in OpenSees (Mazzoni et al., 2009)) was used for the steel material of the SC-CBF. A force-based beam-column element was used to the model the steel post tensioning (PT) bars. The PT bar steel was modeled with a bilinear-elastic-plastic material model with 2% post-yield slope. The potential for slack in the PT bars, that is, a gap occurring between the PT anchorage nut and the anchorage block after significant yielding and permanent deformation of the PT bar, was modeled using a zero-length element (Mazzoni et al., 2009) with a compressive stiffness equal to the 30000 kips/inch. Figure 3.3(c) shows the column base detail and a schematic of the boundary conditions of numerical model. Two zero-length elements were used to model the vertical and horizontal gap conditions at the base of each SC-CBF column. The vertical zero length elements at the SC-CBF column base have a linear-elastic gap behavior, which has a large stiffness when the column base moves towards the foundation while the stiffness in the other direction is very small. The horizontal gap elements have a large stiffness when the column base moves outward. To permit only axial deformation, the element that connects the zero-length element at the base of the PT bars to the foundation is restrained. Each EDP was modeled using a truss element with a bi-linear material model (using the Steel02 material definition in OpenSees (Mazzoni et al., 2009)). Each EDP truss element is attached to the SC-CBF column at the first floor column node and to a fixed node at the foundation level.

A lean-on-column with elastic beam-column elements was used to model the second-order effects of the gravity loads within the seismic tributary area of the SC-CBF. Seismic mass

was assigned to the horizontal degree-of-freedom of the lean-on-column at each floor level. The horizontal displacements of the SC-CBF and lean-on-column were constrained to each other with rigid links at each floor level. The vertical and horizontal displacements at the base of the lean-on-column were restrained. The corotational coordinate transformation was used for the elements. Rayleigh damping with a 2.6% damping ratio for first mode and 6.1% damping ratio for third mode was assigned using a damping substructure (Roke, 2010). Newmark constant average acceleration integration and the Newton-Krylov solution algorithms were used in the NLTHA.

3.4.2.2. Special Moment Resisting Frame Structure

An example 9-story, 4-bay steel special moment resisting frame (SMRF) structure was also studied. Schematics of the floor plan and elevation of the example SMRF building are shown in Figure 3.4. A single SMRF from the building, with the associated seismic mass and gravity loads (within the seismic tributary area), constitute the SMRF structure.

The SMRF building is assumed to be an office-type building on a site in Southern California with NEHRP Site Class D conditions. Dead and live gravity loads for the SMRF building are given in Table 3.4 and Table 3.5. Gravity and seismic loads were considered in the design of a typical SMRF from the building. The SMRF was designed in accordance with ASCE (2010) requirements. For design, the short period spectral acceleration (S_s) was taken as 1.5g and the 1 s period spectral acceleration (S_1) was taken as 0.6g. Conventional MRSA was used for seismic design of the SMRF. The member sizes were governed by the

drift control criteria of ASCE (2010). Reduced beam section (RBS) beam-to-column connections were used and the strong column-weak beam design criterion of AISC (2010) was taken into account. The panel zones of the beam-column connection region were designed in accordance with FEMA (2000). All members of the SMRF were ASTM A992 wide-flange shapes with a nominal steel yield strength of 50 ksi, meeting the seismic compactness requirements of AISC (2010).

A two dimensional numerical model of the SMRF was developed in OpenSees (Mazzoni et al., 2009). Each beam and column of the SMRF was modeled by five force-based beam-column elements with fiber sections. Five integration points were used along the length of each force-based beam-column element. Gauss-Lobatto numerical integration was used. A bi-linear material model (using the Steel02 material definition in OpenSees (Mazzoni et al., 2009)) was used for the steel material of the SMRF. The SMRF columns were fixed at the base. Panel zones of the SMRF were modeled using the panel zone element developed by Seo et al. (2012). A lean-on-column with elastic beam-column elements was used to model the second-order effects of the gravity loads within the seismic tributary area of the SMRF. Seismic mass was assigned to the horizontal degree-of-freedom of the lean-on-column at each floor level. The horizontal displacements of the SMRF and lean-on-column were constrained to each other with rigid links at each floor level. The vertical and horizontal displacements at the base of the lean-on-column were restrained. The corotational coordinate transformation was used for the elements. Caughey damping with a 5% damping ratio for each mode was used. Newmark constant average acceleration integration and the Newton-Krylov solution algorithms were used in the NLTHA.

3.5. Ground Motion Set Used in NLTHA

A ground motion (GM) set composed of 18 GM pairs listed in Table 3.2 was used in the NLTHA of the example structures. The GM records were selected from the NGA (PEER, 2011) database for the site of the SC-CBF and SMRF example buildings (Chancellor, 2014). The site has a short period spectral acceleration (S_s) of 1.5g and 1 s period spectral acceleration (S_1) of 0.6g based on ASCE (2010) definitions (ASCE, 2010).

Each GM pair was initially scaled so that the geometric mean of the pseudo-acceleration response for the GM pair matched the design basis earthquake (DBE) spectrum (ASCE, 2010) over a period range of 0.1-7.0 s. The DBE has a 10% probability of exceedance (POE) in 50 years (BSSC, 2003). For the SC-CBF, the GMs were scaled to both the DBE and to the maximum considered earthquake (MCE) spectrum. The MCE has a 2% POE in 50 years (BSSC, 2003). For the SMRF, the GMs were scaled to both the DBE and two times the MCE spectrum. The scale factors were calculated using the average scaling method described in Baker (2011). The pseudo-acceleration response spectra of GMs scaled to the DBE and the median spectrum for the GM set are shown in Figure 3.5.

3.6. Elastic and Mechanism Modal Properties for Example Structures

To derive $\boldsymbol{\phi}_n^m$, the numerical models of the example structures are modified by placing hinges with negligible rotational stiffness at the yielding hinge locations of the intended yielding mechanism. The yielding mechanism of the NL wall structures is a single yielding hinge at the base of the wall. To derive $\boldsymbol{\phi}_n^m$ for the NL wall structures, a rotational spring

with negligible stiffness is placed at the base of the NL wall structures to represent the intended base flexural yielding mechanism. The "yielding" mechanism for the SC-CBF is rocking of the base of the CBF on the foundation followed by yielding of the PT bars during the base rocking response of the SC-CBF. The SC-CBF model is pushed statically until the PT bars yield to reach a "yielding" mechanism. The base rocking response of the SC-CBF, however, occurs at a lower level of force and deformation than that corresponding to yielding of the PT bars. The yielding mechanism of the SMRF is the beam-sway yielding mechanism at which yielding hinges form at all the beam ends and at the base of first story columns. To derive $\boldsymbol{\phi}_n^m$ for the SMRF, rotational springs with negligible stiffness are placed at the beam ends and at the base of first story columns to represent the intended beam-sway yielding mechanism.

An eigen analysis of each modified model (with hinges at the location of the yielding hinges) is carried out to determine $\boldsymbol{\phi}_n^m$ and T_n^m. Figure 3.6 shows the assumed yielding mechanism for each example structure together with the first, second, and third mode static lateral force distributions ($\boldsymbol{s}_n^e$ and $\boldsymbol{s}_n^m$) and the corresponding static overturning moment profiles ($\boldsymbol{M}_n^{st,e}$ and $\boldsymbol{M}_n^{st,m}$).

Table 3.6 shows $\overline{M}_{bn}^{e}$ and $\overline{M}_{bn}^{m}$ for the example structures. Figure 3.6 and Table 3.6 shows that since the yielding mechanisms for all example structures are base moment mechanisms (i.e., it can be shown that they limit the base overturning moment, M_b, that can develop), $\overline{M}_{bn}^{m}$ for the 2nd and 3rd mechanism modes are zero for all example structures, while $\overline{M}_{bn}^{e}$

for the 2nd and 3rd elastic modes are non-zero. For the wall structure with shear flexibility and the SMRF; however, $\overline{M}_{bn}^{e}$ for the 2nd and 3rd elastic modes are quite small. The differences between $\overline{M}_{bn}^{e}$ and $\overline{M}_{bn}^{m}$ are greater for the wall structure with purely flexural response and for the SC-CBF.

Table 3.7 shows $\overline{V}_{bn}^{e}$ and $\overline{V}_{bn}^{m}$ for the example structures. $\overline{V}_{b1}^{e}$ and $\overline{V}_{b1}^{m}$ are greater than 60% and the cumulative higher mode $\overline{V}_{bn}^{e}$ and $\overline{V}_{bn}^{m}$ are less than 40% for all example structures. Since the yielding mechanisms for all example structures are not base shear mechanisms, the higher mode $\overline{V}_{bn}^{m}$ are non-zero unlike the higher mode $\overline{M}_{bn}^{m}$. As shown in Table 3.7, $\overline{V}_{b2}^{m}$ is smaller than $\overline{V}_{b2}^{e}$ for wall structure with purely flexural response and for the SC-CBF. For the wall structure with shear flexibility and for the SMRF, however, $\overline{V}_{b2}^{m}$ is greater than $\overline{V}_{b2}^{e}$. $\overline{V}_{b3}^{m}$ is smaller than $\overline{V}_{b3}^{e}$ for all example structures.

Table 3.8 shows the nth elastic and mechanism mode periods, T_n^e and T_n^m, for the example structures. As seen in Table 3.8, there is an elongation in the nth mode period, after the intended yielding mechanism forms. In theory, T_1^m is infinite, while the values in the table reflect the small stiffness assigned to the "hinges" in the modified models of the example structures. T_2^e elongates by 30% for the NL wall structure with purely flexural response, 5% for the NL wall structure with significant shear flexibility, 14% for the SC-CBF, and almost 400% for the SMRF after the intended yielding mechanism forms. T_3^e elongates by 1.3% for the cantilever walls, 5.5% for the SC-CBF, and almost 170% for the SMRF after the intended yielding mechanism forms. These results show that the formation of the

intended yielding mechanism causes a substantial decrease in the stiffness of the SMRF which results in significant period elongation for the higher modes.

The n[th] mode dynamic response amplitudes can be estimated from the design or median ground motion (GM) response spectrum at T_n^e and T_n^m, that is, $SA_{DS}(T_n^e)$ and $SA_{DS}(T_n^m)$ or $SA_{GM,m}(T_n^e)$ and $SA_{GM,m}(T_n^m)$, respectively. Depending on the shape of the pseudo-acceleration response spectrum and the extent of the period elongation after the formation of the intended yielding mechanism, $SA_{DS}(T_n^e)$ and $SA_{DS}(T_n^m)$ or $SA_{GM}(T_n^e)$ and $SA_{GM}(T_n^m)$ can be significantly different from each other.

Figure 3.7 shows the design spectrum for the example structures of this study. Table 3.8 shows that T_2^m is about 4.7 times greater than T_2^e for the SMRF. Therefore, as shown in Figure 3.7, while T_2^e lies near the beginning of the constant pseudo-velocity zone of the design spectrum (i.e., descending branch), T_2^m lies in the latter part of this descending branch of the design spectrum and $SA_{DS}(T_2^m)$ is much less than $SA_{DS}(T_2^e)$. This result suggests that the 2[nd] mode dynamic force response amplitude quantified using T_2^m will lead to an unconservative design force estimate, as $SA_{DS}(T_2^m)$ is much smaller than $SA_{DS}(T_2^e)$. On the contrary, Table 3.8 shows that T_2^m is 30% greater than T_2^e for the NL wall structure with purely flexural response and only 5% for the NL wall structure with significant shear flexibility. Therefore, T_2^e and T_2^m for the NL wall structures both lie on the constant pseudo-acceleration zone of the design spectrum. This result suggests that period elongation after the yielding mechanism forms does not change significantly the 2[nd] mode dynamic force

response amplitude for the NL wall structures. Overall, these results suggest that quantifying the nth mode dynamic force response amplitude from the design (or median GM) spectrum at T_n^m could lead to unconservative design force estimates for NL structures with significant period elongation after the intended yielding mechanism forms.

3.7. Response of NL Example Structures

3.7.1. Response of NL Wall Structure with Purely Flexural Response

This section examines the nth mode seismic response of the wall structure with purely flexural response quantified by using ϕ_n^e and ϕ_n^m.

nth Mode Contribution to Dynamic Response

Figure 3.8 shows $A_{eff_n}^e(t)$ and $A_{eff_n}^m(t)$ normalized by their peak values $A_{eff_n}^e$ and $A_{eff_n}^m$, respectively, for the first three modes of the wall structure with purely flexural response subjected to the ILA013W GM record. The peak $A_{eff_n}(t)$ (denoted A_{eff_n}) and the times of peak values of the base overturning moment response ($M_b(t)$), and peak base shear response ($V_b(t)$) are indicated on the plot. As seen in Figure 3.8(b), $A_{eff_1}^m(t)$ has flat-topped response with constant amplitude for extended durations of time due to formation of the base flexural yielding mechanism. This result shows that the nonlinearity due to the base flexural yielding mechanism influences only the 1st mode response. On the contrary, Figure 3.8(a) shows that $A_{eff_1}^e(t)$ has fluctuations during its entire response history, even during the times

when the flexural base yielding mechanism forms. The fluctuations in the $A^e_{eff_1}(t)$ response indicate that by using $\boldsymbol{\phi}^e_n$ to quantify the modal response, $A^e_{eff_1}(t)$ and $A^e_{eff_2}(t)$ are coupled through the yielding mechanism because of the non-zero 2nd mode contribution to M^{st}_b (as shown in Table 3.6). When $\boldsymbol{\phi}^m_n$ are used to quantify the modal response, the coupling vanishes. Figure 3.8 further shows that the time of the peak value of $A^m_{eff_1}(t)$, denoted $A^m_{eff_1}$, is coincident with the time of peak $M_b(t)$, but the time of the peak value of $A^e_{eff_1}(t)$, denoted $A^e_{eff_1}$ is different (earlier) than the time of peak $M_b(t)$.

At the time of the peak M_b(t), the amplitude of $A^e_{eff_1}(t)$ is 85% of $A^e_{eff_1}$, while the amplitudes of $A^e_{eff_2}(t)$ and $A^e_{eff_3}(t)$ are much smaller (approximately 5% of $A^e_{eff_2}$ and $A^e_{eff_3}$, respectively) with a sign opposite to $A^e_{eff_1}(t)$. At the time of the peak $V_b(t)$, $A^e_{eff_3}(t)$ is at its peak value, while $A^e_{eff_1}(t)$ and $A^e_{eff_2}(t)$ have amplitudes equal to 54% of $A^e_{eff_1}$ and 55% of $A^e_{eff_2}$, respectively, with the same sign as $A^e_{eff_3}(t)$. On the contrary, at the time of the peak $M_b(t)$, the amplitude of $A^m_{eff_1}(t)$ is at its peak value (i.e., equal to $A^m_{eff_1}$), while the amplitudes of $A^m_{eff_2}(t)$ and $A^m_{eff_3}(t)$ are around 5% of $A^m_{eff_2}$ and $A^m_{eff_3}$, respectively, with a sign opposite to $A^m_{eff_1}(t)$. At the time of the peak $V_b(t)$, $A^m_{eff_1}(t)$ is at its peak value while $A^m_{eff_2}(t)$ and $A^m_{eff_3}(t)$ have amplitudes equal to 80% of $A^m_{eff_2}$ and 61% of $A^m_{eff_3}$, respectively, with the same sign as $A^m_{eff_1}(t)$.

Comparison of nth Mode Response from UMRHA and A_{eff}

Figure 3.9 compares $A^e_{um_n}(t)$ and $A^m_{um_n}(t)$ with $A^e_{eff_n}(t)$ and $A^m_{eff_n}(t)$, respectively, for the first three modes of the wall structure with purely flexural response subjected to the ILA013W GM record. $A^e_{um_n}(t)$ and $A^m_{um_n}(t)$ are from solving Eq. (3.15). $A^e_{eff_n}(t)$ and $A^m_{eff_n}(t)$ are from Eq. (3.13), applied to NLTHA results for the wall structure. Figure 3.9(a) shows significant differences between $A^e_{um_1}(t)$ and $A^e_{eff_1}(t)$, while $A^m_{um_1}(t)$ and $A^m_{eff_1}(t)$ are quite similar. For the higher modes, $A^e_{um_n}(t)$ and $A^e_{eff_n}(t)$ as well as $A^m_{um_n}(t)$ and $A^m_{eff_n}(t)$ are both in good agreement with each other, indicating that these higher modes of the wall structure respond almost linear-elastically, which is consistent with the assumption of the mMPA procedure (Chopra et al., 2004).

Figure 3.10 compares $D^e_{um_n}(t)$ and $D^m_{um_n}(t)$ with $D^e_{eff_n}(t)$ and $D^m_{eff_n}(t)$, respectively, for the first three modes of the wall structure subjected to the ILA013W GM record. $D^e_{um_n}(t)$ and $D^m_{um_n}(t)$ are from solving Eq. (3.15). $D^e_{eff_n}(t)$ and $D^m_{eff_n}(t)$ are from Eq. (3.14), applied to results from NLTHA of the wall structure. Figure 3.10 shows that $D^e_{eff_1}(t)$ and $D^e_{um_1}(t)$ are similar, but $D^m_{eff_1}(t)$ and $D^m_{um_1}(t)$ are not as close. However, Figure 3.10 shows significant differences between the $D^e_{eff_2}(t)$ and $D^e_{um_2}(t)$ as well as between $D^e_{eff_3}(t)$ and $D^e_{um_3}(t)$. The differences between $D^m_{eff_2}(t)$ and $D^m_{um_2}(t)$ as well as between $D^m_{eff_3}(t)$ and $D^m_{um_3}(t)$. are also significant.

nth Mode NL Response

Figure 3.11 shows the roof level component of $\boldsymbol{u}(t)$**,** denoted $u_r(t)$**,** as well as $V_b(t)$ and $M_b(t)$ for the wall structure with purely flexural response subjected to the ILA013W GM record. $u_r(t)$ is obtained from the NLTHA results and $u^e_{r_n}(t)$ and $u^m_{r_n}(t)$ are the product of $\boldsymbol{\phi}^e_{rn}\Gamma^e_n$ and $D^e_{eff_n}(t)$, and of $\boldsymbol{\phi}^m_{rn}\Gamma^m_n$ and $D^m_{eff_n}(t)$, respectively. $V_b(t)$ and $M_b(t)$ are obtained from the NLTHA results. $V^e_{bn}(t)$ and $V^m_{bn}(t)$ are the product of $V^{st,e}_{bn}$ and $A^e_{eff_n}(t)$ and of $V^{st,m}_{bn}$ and $A^m_{eff_n}(t)$, respectively. $M^e_{bn}(t)$ and $M^m_{bn}(t)$ are the product of $M^{st,e}_{bn}$ and $A^e_{eff_n}(t)$ and of $M^{st,m}_{bn}$ and $A^m_{eff_n}(t)$, respectively. $u_r(t)$ is a first mode dominant response when either $\boldsymbol{\phi}^e_n$ or $\boldsymbol{\phi}^m_n$ are used to quantify the nth mode contributions. Figure 3.11 shows that $u_r(t)$ closely matches both $u^e_{r1}(t)$ and $u^m_{r1}(t)$. Figure 3.11 shows that in addition to the first mode contribution, the contributions of $V^e_{b2}(t)$ and $V^m_{b2}(t)$ to $V_b(t)$ are also considerable, especially between 30 s and 50 s of the response. The difference between using $\boldsymbol{\phi}^e_n$ or $\boldsymbol{\phi}^m_n$ is more obvious for $M_b(t)$. As seen from the M_b response histories in Figure 3.11(c), the higher mode contribution to $M_b(t)$ is eliminated by using $\boldsymbol{\phi}^m_n$; $M_b(t)$ is identical to $M^m_{b1}(t)$, while $M^m_{b2}(t)$ and $M^m_{b3}(t)$ are zero.

3.7.2. Response of NL Wall Structure with Shear Flexibility

This section examines the nth mode seismic response of the wall structure with shear flexibility quantified by using $\boldsymbol{\phi}^e_n$ and $\boldsymbol{\phi}^m_n$.

nth Mode Contribution to Static Response

$\overline{M}^{e}_{bn}$ and $\overline{M}^{m}_{bn}$ for the wall structure with shear flexibility are given in Table 3.6. As seen in Table 3.6, $\overline{M}^{e}_{b1}$ is nearly 100% and the $\overline{M}^{e}_{bn}$ of the higher modes is approximately 3%. As expected, $\overline{M}^{m}_{b1}$ is 100% and the mechanism modes, $\boldsymbol{\phi}^{m}_{n}$, are not coupled through the base flexural yielding mechanism.

nth Mode Contribution to Dynamic Response

Figure 3.12 shows $A^{e}_{eff_n}(t)$ and $A^{m}_{eff_n}(t)$ normalized by $A^{e}_{eff_n}$ and $A^{m}_{eff_n}$, respectively, for the first three modes of the wall structure with shear flexibility subjected to the ILA013W GM record. The peak $A_{eff_n}(t)$, and the times of the peak values of $M_b(t)$ and $V_b(t)$ are indicated on the plot. Figure 3.12(a) shows that the fluctuations in $A^{e}_{eff_1}(t)$ during the times when the base flexural yielding mechanism forms are smaller compared to the wall structure with purely flexural response (shown in Figure 3.8(a)). These results suggest that the higher mode contribution to $M_b(t)$ is smaller for the wall structure with shear flexibility compared to the wall structure with purely flexural response. This finding is consistent with the differences between $\overline{M}^{e}_{bn}$ for the two wall structures shown in Table 3.6, that is, $\overline{M}^{e}_{b1}$ is closer to 100% for the wall structure with shear flexibility. The decoupling of the higher modes from the yielding mechanism from using $\boldsymbol{\phi}^{m}_{n}$ to quantify the response is obvious in $A^{m}_{eff_1}(t)$ (shown in Figure 3.12(b)) which has flat-topped response during the times when the base flexural yielding mechanism forms.

At the time of the peak $M_b(t)$, the amplitude of $A^e_{eff_1}(t)$ is 82% of $A^e_{eff_1}$, while the amplitude of $A^e_{eff_2}(t)$ is 9% of $A^e_{eff_2}$ with the same sign as $A^e_{eff_1}(t)$ and the amplitude of $A^e_{eff_3}(t)$ is close to zero. At the time of the peak $V_b(t)$, the amplitude of $A^e_{eff_1}(t)$ is the peak value (i.e., $A^e_{eff_1}$) while the amplitudes of $A^e_{eff_2}(t)$ and $A^e_{eff_3}(t)$ are 65% of $A^e_{eff_2}$ and 20% of $A^e_{eff_3}$, respectively, with the same sign as $A^e_{eff_1}(t)$. On the contrary, at the time of the peak $M_b(t)$ the amplitude of $A^m_{eff_1}(t)$ is at its peak value (i.e., $A^m_{eff_1}$), while the amplitudes of $A^m_{eff_2}(t)$ and $A^m_{eff_3}(t)$ are around 30% and 20% of $A^m_{eff_2}$ and $A^m_{eff_3}$, respectively, with a sign opposite to $A^m_{eff_1}(t)$. At the time of the peak $V_b(t)$, $A^m_{eff_1}(t)$ and $A^m_{eff_3}(t)$ are at their peak value while $A^m_{eff_2}(t)$ has an amplitude equal to 85% of $A^m_{eff_2}$, with the same sign as $A^m_{eff_1}(t)$ and $A^m_{eff_3}(t)$.

nth Mode NL Response

Figure 3.13 shows $u_r(t)$, $V_b(t)$, and $M_b(t)$, as well as their modal components, for the wall structure with shear flexibility subjected to the ILA013W GM record. These results are obtained from the NLTHA results as described previously for the wall structure with purely flexural response. Similar to the wall structure with purely flexural response, $u_r(t)$ closely matches both $u^e_{r1}(t)$ and $u^m_{r1}(t)$. These results suggest that $u_r(t)$ is a first mode dominant response when either $\boldsymbol{\phi}^e_n$ or $\boldsymbol{\phi}^m_n$ are used to quantify the nth mode contributions. $V^e_{b2}(t)$ and $V^e_{b3}(t)$ are comparable in amplitude with $V^e_{b1}(t)$, and $V^m_{b2}(t)$ and $V^m_{b3}(t)$ are comparable in amplitude with $V^m_{b1}(t)$. Figure 3.13(c) shows the contributions of $M^e_{b2}(t)$ and $M^e_{b3}(t)$ to $M_b(t)$ are smaller for the wall structure with shear flexibility compared to the wall structure with purely flexural response shown in Figure 3.11(c). The higher mode contribution to $M_b(t)$

is again fully eliminated by using $\boldsymbol{\phi}_n^m$. Thus, $M_b(t)$ is identical to $M_{b1}^m(t)$, while $M_{b2}^m(t)$ and $M_{b3}^m(t)$ are zero.

3.7.3. Response of NL SC-CBF

This section examines the nth mode seismic response of the SC-CBF quantified by using $\boldsymbol{\phi}_n^e$ and $\boldsymbol{\phi}_n^m$.

Comparison of nth Mode Response from MRSA with $\boldsymbol{A_{eff}}$

Figure 3.14 shows the 5% damped median linear-elastic and median reduced (by R = 6) pseudo-acceleration response spectra for the GM set scaled to the DBE. For the first three modes, the peak nth elastic and mechanism mode effective pseudo-accelerations, $A_{eff_n}^e$ and $A_{eff_n}^m$, respectively, from the NLTHA results for the SC-CBF for each GM are indicated on the plot. The median effective modal pseudo-accelerations, $A_{eff_n,m}^e$ and $A_{eff_n,m}^m$, are also shown. $A_{eff_n,m}^e$ and $A_{eff_n,m}^m$ are compared with the nth mode pseudo-accelerations from the median elastic and reduced pseudo-acceleration response spectra $SA_{GM,m}(T)$ and $SA_{GM,m}(T)/(R{=}6)$, respectively, at the elastic mode periods, T_n^e.

Several different response modification factors are used in the design procedure for SC-CBFs proposed by Chancellor (2016). The response modification factor based on ASCE (2010), denoted R, equals to 6.0 for concentrically braced frames. R_A is the response

modification factor calculated as a ratio of the base overturning moment demand from the equivalent lateral forces (ASCE, 2010), denoted $OM_{elastic}$ in Chancellor (2014), to the base overturning moment resistance of the SC-CBF at the time of column decompression (i.e., when rocking of the CBF on the foundation initiates), denoted OM_D in Chancellor (2014). $R_{A,D}$ is the response modification factor calculated as a ratio of $OM_{elastic}$ modified to consider only the first mode mass, denoted $OM_{elastic,1}$ in Chancellor (2014), to OM_D. R_{yield} is the response modification factor which is calculated as the ratio of $OM_{elastic,1}$ to the base overturning moment resistance of the SC-CBF when the PT bars yield, denoted OM_Y in Chancellor (2014). $R_{A,}$ $R_{A,D}$, and R_{yield} for the 9-story SC-CBF are 6.97, 6.0, and 6.40, respectively. Note that these R values are with respect to the smooth DBE design spectrum. This study uses $R_{A,D}$ and R_{yield} as the expected response modification factors for the SC-CBF when rocking motion initiates and the when PT bars yield, respectively.

Figure 3.14(a) shows that, $A^e_{eff_1,m}$ (i.e., for the 1st elastic mode) is close to the median *reduced* pseudo-acceleration spectrum. On the contrary, $A^e_{eff_2,m}$ and $A^e_{eff_3,m}$ (i.e., for the 2nd and 3rd elastic modes) are close to the median linear-elastic pseudo-acceleration response spectrum. Based on Figure 3.14(a), the 1st mode R^e_{act} (i.e, $R^e_{act_1}$, the ratio of $SA_{GM,m}(T^e_1)$ to $A^e_{eff_1,m}$) is 4.01, while $R^e_{act_2}$ and $R^e_{act_3}$ (i.e., the ratio of $SA_{GM,m}(T^e_2)$ to $A^e_{eff_2,m}$ and the ratio of $SA_{GM,m}(T^e_3)$ to $A^e_{eff_3,m}$, respectively) are 0.98 and 1.14, respectively. These results show that the 2nd and 3rd mode responses are close to the linear-elastic response and are not strongly affected by the base rocking response. Figure 3.14(a) further shows that there is a considerable scatter in the $A^e_{eff_2}$ and $A^e_{eff_3}$ values, and smaller scatter in the $A^e_{eff_1}$ values.

Despite the smaller scatter in the $A^e_{eff_1}$ values, the 1st mode response is not accurately controlled by the formation of yielding mechanism (i.e., base rocking response followed by PT bar yielding) as $R^e_{act_1}$ is considerably smaller than $R_{A,D}$ and R_{yield}.

Figure 3.14(b) shows the $A^m_{eff_n}$ and $A^m_{eff_n,m}$ together with the 5% damped median linear-elastic and median reduced (by R = 6) pseudo-acceleration response spectra. There is much less scatter in the $A^m_{eff_1}$ results. Based on $\boldsymbol{\phi}^m_n$, $R^m_{act_1}$ is 7.31, $R^m_{act_2}$ is 0.87 and $R^m_{act_3}$ is 0.88, which are similar to the previous results and indicate that the higher modes are not strongly affected by the flexural yielding mechanism. $R^m_{act_2}$ is smaller than $R^e_{act_2}$ since $A^m_{eff_2,m}$ is about 1.4 times $A^e_{eff_2,m}$. Compared to $R^e_{act_1}$, $R^m_{act_1}$ is quite close to $R_{A,D}$ (= 6.97) and R_{yield} (= 6.40), keeping in mind that $R_{A,D}$ and R_{yield} are with respect to the smooth DBE design spectrum, and $R^m_{act_1}$ is with respect to the median linear-elastic pseudo-acceleration spectrum for the GM set which does not precisely match the smooth DBE spectrum. GM spectrum is greater than the design spectrum at T^e_1. This is the reason that $R^m_{act_1}$ is not bounded by $R_{A,D}$ and R_{yield} as might be expected. It is important to note that the DBE design spectrum and median GM spectrum are constructed for a 5% damping ratio. On the other hand, the actual 1st, 2nd, and 3rd mode damping ratios used for the SC-CBF in the NLTHA are 2.6%, 3.7%, and 6.1%, respectively. These results show that by using $\boldsymbol{\phi}^m_n$ the 1st mode response is shown to be accurately controlled by the yielding mechanism of the SC-CBF (despite the discrepancy in the damping ratio for the 1st mode). On the other hand, for the 2nd mode, which is not controlled by the yielding mechanism, $A^m_{eff_2,m}$ is much greater than of $SA_{GM,m}(T^e_2)$, and is, surprisingly, much greater than any point on $SA_{GM,m}(T)$, which is a

result of the difference in damping (i.e., 3.7% for the NLTHA which provides $A^m_{eff_2,m}$ and 5% for $SA_{GM,m}(T)$).

nth Mode Contribution to Dynamic Response

Figure 3.15 shows $M_b(t)$ normalized by the resistance to overturning moment when the PT bars yield, which is denoted as OM_y in Chancellor (2014), and the PT force response, F_{PT} (t), normalized by the PT force when PT bars yield, $F_{PT,y}$, for the SC-CBF subjected to ILA013W GM record scaled to the DBE (Figure 3.15(a)) and MCE (Figure 3.15(b)), respectively. As seen in Figure 3.15(a), the PT bars do not yield for the SC-CBF subjected to ILA013W GM record scaled to the DBE, the peak value of $F_{PT}(t)$, denoted F_{PT}, is 90% of $F_{PT,y}$. On the other hand, Figure 3.15(b) shows that the PT bars yield during the MCE level response of the SC-CBF.

Figure 3.16 shows $A^e_{eff_n}(t)$ and $A^m_{eff_n}(t)$ normalized by $A^e_{eff_n}$ and $A^m_{eff_n}$, respectively, for the first three modes of the SC-CBF subjected to the ILA013W GM record scaled to the DBE. The peak $A_{eff_n}(t)$, and the times of peak base overturning moment response ($M_b(t)$), and peak base shear response ($V_b(t)$) are indicated on the plot. Although the PT bars have not yielded under ILA013W GM record scaled to the DBE, the difference between $A^e_{eff_1}(t)$ and $A^m_{eff_1}(t)$ is still observable due to the rocking response of the SC-CBF. $A^e_{eff_1}(t)$ has fluctuations during its entire response history. These fluctuations indicate the coupling between ϕ^e_1 and the higher modes (ϕ^e_n for n > 1) through the yielding mechanism because

of the non-zero higher mode contributions to M_b^{st}. For example, the time of the peak value of $A_{eff_1}^e(t)$ (i.e., $A_{eff_1}^e$) is not coincident with the time of the peak $M_b(t)$. $A_{eff_1}^e$ is reached almost 8 s before the time of the peak $M_b(t)$. On the contrary, the high frequency fluctuations in $A_{eff_1}^m(t)$ are small but can be observed during the time period of base rocking response due to variations in the PT bar force as the SC-CBF rocks (before PT bar yielding).

Figure 3.16 shows that at the time of the peak $M_b(t)$, the amplitude of $A_{eff_1}^e(t)$ is 65% of $A_{eff_1}^e$, while the amplitudes of $A_{eff_2}^e(t)$ and $A_{eff_3}^e(t)$ are close to zero. At the time of the peak $V_b(t)$, the amplitudes of $A_{eff_2}^e(t)$ and $A_{eff_3}^e(t)$ are 100% of $A_{eff_2}^e$ and 85% of $A_{eff_3}^e$, respectively, while the amplitude of $A_{eff_1}^e(t)$ is 5% of $A_{eff_1}^e$, with the same sign as $A_{eff_2}^e(t)$ and $A_{eff_3}^e(t)$. At the time of the peak $M_b(t)$, on the other hand, the amplitude of $A_{eff_1}^m(t)$ is at its peak value, while the amplitudes of $A_{eff_2}^m(t)$ and $A_{eff_3}^m(t)$ are close to zero. At the time of the peak $V_b(t)$, $A_{eff_1}^m(t)$ is 97% of $A_{eff_1}^m$, while the amplitudes of $A_{eff_2}^m(t)$ and $A_{eff_3}^m(t)$ are 90% of $A_{eff_2}^m$ and 60% of $A_{eff_3}^m$, with the same sign as $A_{eff_1}^m(t)$.

Figure 3.17 shows $A_{eff_n}^e(t)$ and $A_{eff_n}^m(t)$ normalized by $A_{eff_n}^e$ and $A_{eff_n}^m$, respectively, for the first three modes of the SC-CBF subjected to the ILA013W GM record scaled to MCE. Similar to the DBE level response,$A_{eff_1}^e(t)$ has fluctuations during its entire response history, even during the times when PT bars are yielding. On the contrary, the high frequency fluctuations in $A_{eff_1}^m(t)$ are smaller and $A_{eff_1}^m(t)$ has a nearly flat-topped response

when the PT bars yield at around 48 s. The peak $A^m_{eff_1}(t)$ occurs at the time when the PT bars yield.

Figure 3.17 shows that at the time of the peak $M_b(t)$, the amplitudes of $A^e_{eff_1}(t)$ and $A^e_{eff_2}(t)$ are 55% of $A^e_{eff_1}$ and 11% of $A^e_{eff_2}$, while the amplitude of $A^e_{eff_3}(t)$ is close to zero. At the time of the peak $V_b(t)$, the amplitudes of $A^e_{eff_2}(t)$ and $A^e_{eff_3}(t)$ are 100% of $A^e_{eff_2}$ and 88% of $A^e_{eff_3}$, respectively, while the amplitude of $A^e_{eff_1}(t)$ is 60% of $A^e_{eff_1}$, with the opposite sign to $A^e_{eff_2}(t)$ and $A^e_{eff_3}(t)$. At the time of the peak $M_b(t)$, on the other hand, the amplitude of $A^m_{eff_1}(t)$ is at its peak value, while the amplitudes of $A^m_{eff_2}(t)$ and $A^m_{eff_3}(t)$ are close to zero. At the time of the peak $V_b(t)$, $A^m_{eff_2}(t)$ is at its peak value, while the amplitudes of $A^m_{eff_1}(t)$ and $A^m_{eff_3}(t)$ are 51% of $A^m_{eff_1}$ and 53% of $A^m_{eff_3}$, with the same sign as $A^m_{eff_2}(t)$.

Figure 3.18 shows $M_b(t)$ normalized by OM_y (Chancellor, 2014) and $F_{PT}(t)$ normalized by $F_{PT,y}$ for the SC-CBF subjected to the HWA019N GM record scaled to the MCE. As seen in Figure 3.18, the PT bars yield twice so $M_{b,y}$ is reached twice during the response history.

Figure 3.19 shows $A^e_{eff_n}(t)$ and $A^m_{eff_n}(t)$ normalized by $A^e_{eff_n}$ and $A^m_{eff_n}$, respectively, for the first three modes of the SC-CBF subjected to the HWA019N GM record scaled to the MCE. $A^e_{eff_1}(t)$ has fluctuations during its entire response history, even during the times when PT bars are yielding due to base rocking. The time of $A^e_{eff_1}$ is not coincident with the

time of the peak $M_b(t)$, because the higher elastic modes (ϕ_n^e for n > 1) have non-zero contribution to M_b^{st}. $A_{eff_1}^e$ is reached about 2 s after the PT bars yield. On the contrary, the high frequency fluctuations in $A_{eff_1}^m(t)$ are smaller but are observed during the time of base rocking response due to variations in the PT bar force as the SC-CBF rocks. As shown in Figure 3.18, the PT bars yield instantaneously at 41 s and unload immediately after yielding which causes the high frequency fluctuations in $A_{eff_1}^m(t)$. The peak $A_{eff_1}^m(t)$ occurs at the time when the PT bars are yielding.

Figure 3.19 shows that at the time of the peak $M_b(t)$, the amplitude of $A_{eff_1}^e(t)$ is 75% of $A_{eff_1}^e$, while the amplitudes of $A_{eff_2}^e(t)$ and $A_{eff_3}^e(t)$ are 13% of $A_{eff_2}^e$ and 27% of $A_{eff_3}^e$, respectively, with the opposite sign to $A_{eff_1}^e(t)$. At the time of the peak $V_b(t)$, the amplitudes of $A_{eff_2}^e(t)$ and $A_{eff_3}^e(t)$ are 95% of $A_{eff_2}^e$ and 58% of $A_{eff_3}^e$, respectively, while the amplitude of $A_{eff_1}^e(t)$ is 75% of $A_{eff_1}^e$, with the opposite sign to $A_{eff_2}^e(t)$ and $A_{eff_3}^e(t)$. At the time of the peak $M_b(t)$, on the other hand, the amplitude of $A_{eff_1}^m(t)$ is at its peak value, $A_{eff_2}^m(t)$ is close to zero and the amplitude of $A_{eff_3}^m(t)$ is 45% of $A_{eff_3}^m$ with the opposite sign to $A_{eff_1}^m(t)$. At the time of the peak $V_b(t)$, $A_{eff_2}^m(t)$ is nearly at its peak value, while the amplitudes of $A_{eff_1}^m(t)$ and $A_{eff_3}^m(t)$ are 33% of $A_{eff_1}^m$ and 20% of $A_{eff_3}^m$, respectively, with the same sign as $A_{eff_2}^m(t)$.

n^{th} Mode NL Response

Figure 3.20 shows $u_r(t)$, $V_b(t)$, and $M_b(t)$ for the SC-CBF subjected to ILA013W GM record scaled to the MCE. These results are obtained from the NLTHA results as described previously for the wall structure with purely flexural response (Figure 3.11). Similar to the observations from NLTHA results for the NL wall structures, $u_r(t)$ is a first mode dominant response, when either $\boldsymbol{\phi}_n^e$ or $\boldsymbol{\phi}_n^m$ are used. Therefore, it closely matches both $u_{r1}^e(t)$ and $u_{r1}^m(t)$. $V_{b2}^e(t)$ and $V_{b2}^m(t)$ contribute to $V_b(t)$ more than $V_{b1}^e(t)$ and $V_{b1}^m(t)$. As shown in Figure 3.20(a), $M_{b2}^e(t)$ contributes to $M_b(t)$. On the other hand, only $M_{b1}^m(t)$ contributes to significantly $M_b(t)$.

Figure 3.21 shows $u_r(t)$, $V_b(t)$, and $M_b(t)$ for the SC-CBF subjected to HWA019W GM record scaled to the MCE. $u_r(t)$ is again a first mode dominant response, when either $\boldsymbol{\phi}_n^e$ or $\boldsymbol{\phi}_n^m$ are used. Contributions of $V_{b2}^e(t)$ and $V_{b2}^m(t)$ to $V_b(t)$ are larger than the contributions of $V_{b1}^e(t)$ and $V_{b1}^m(t)$ to $V_b(t)$. As shown in Figure 3.21(a), $M_{b2}^e(t)$ contributes significantly to $M_b(t)$. On the other hand, the contribution of $M_{b2}^m(t)$ to $M_b(t)$ is small and essentially zero when $M_b(t)$ is large and the SC-CBF is rocking and especially at 41 s, when the PT bars yield. The elimination of the higher mode contribution to $M_b(t)$ by using $\boldsymbol{\phi}_n^m$ to quantify the response increases the potential for predicting the first mode contribution, $M_{b1}^m(t)$, which is clearly controlled by the yielding mechanism (i.e. rocking of the SC-CBF followed by yielding of the PT bars).

3.7.4. Response of NL SMRF

Static Response of NL SMRF

Figure 3.22 shows the V_b vs. roof drift (Θ_r) response of the SMRF from monotonic static pushover analysis under the lateral load profile s_1^e. The expected V_b and Θ_r demands under DBE (denoted as $V_{b,DBE}$ and $\Theta_{r,DBE}$), MCE (denoted as $V_{b,MCE}$ and $\Theta_{r,MCE}$), one and a half times the MCE (denoted as $V_{b,1.5xMCE}$ and $\Theta_{r,1.5xMCE}$), and two times the MCE (denoted as $V_{b,2xMCE}$ and $\Theta_{r,2xMCE}$) are indicated in Figure 3.22. $V_{b,DBE}$ is the product of $V_{b1}^{st,e}$ and $SA_{DS}(T_1^e)$, $V_{b,MCE}$ is the product of $V_{b1}^{st,e}$ and $1.5(SA_{DS}(T_1^e))$, $V_{b,1.5xMCE}$ is the product of $V_{b1}^{st,e}$ and $2.25(SA_{DS}(T_1^e))$, and $V_{b,2xMCE}$ is the product of $V_{b1}^{st,e}$ and $3.0(SA_{DS}(T_1^e))$ As seen in Figure 3.22, the SMRF has a significant over-strength. Two important sources of the over-strength are the application of the drift control criteria from ASCE (2010) in design of the SMRF, and strain hardening of the steel material model used in the OpenSees model of the SMRF.

As seen in Figure 3.22, at ($\Theta_{r,DBE}$, $V_{b,DBE}$), the global response of the SMRF is linear-elastic. At ($\Theta_{r,MCE}$, $V_{b,MCE}$), yielding initiates at the expected location of the yielding hinges , which initiates NL response of the SMRF. While $V_{b,MCE}$ is 1.5 times $V_{b,DBE}$, $\Theta_{r,MCE}$ is two times $\Theta_{r,DBE}$. At ($\Theta_{r,1.5xMCE}$, $V_{b,1.5xMCE}$), the NL response increases, and $\Theta_{r,1.5xMCE}$ is 9 times $\Theta_{r,DBE}$. At ($\Theta_{r,2xMCE}$, $V_{b,2xMCE}$), $V_{b,2xMCE}$ is 3 times $V_{b,DBE}$, while $\Theta_{r,2xMCE}$ is nearly 20 times $\Theta_{r,DBE}$.

Figure 3.23 shows the moment vs. curvature response for a yielding hinge of the SMRF from the monotonic static pushover analysis under the lateral load profile s_1^e. The yield moment capacity of each beam or column section, M_y, is assumed to be equal to the nominal yield stress of steel, F_y, multiplied by the elastic section modulus, S. The plastic moment capacity of each beam section, M_p, is assumed to be equal to F_y multiplied by the plastic section modulus, Z. M_y and M_p are indicated on the plot. The curvature at M_y and M_p, φ_y and φ_p, respectively, are also indicated on the plot. M_p is approximately 1.15 times M_y for wide flange sections and φ_p is 3.8 times φ_y (from Figure 3.23). As shown in Figure 3.23, at M_p, the hinge has already formed and accumulated some inelastic deformation. Therefore, yielding of yielding hinge is assumed to initiate at $1.1M_y$ and $1.7\varphi_y$ when significant nonlinearity in the moment vs. curvature response is apparent. Therefore, the intended beam-sway yielding mechanism of the SMRF shown in Figure 3.6, forms after the yielding hinges at the left and right ends of each beam, as well as at the base of first story columns reach $1.1M_y$. The total number of potential yielding hinges in the beam-way yielding mechanism is 77.

Using the results from Figure 3.23 (i.e., the yielding hinge forms at $1.1M_y$), the number of hinges forming at $V_{b,DBE}$, $V_{b,MCE}$, $V_{b,1.5xMCE}$, and $V_{b,2.0xMCE}$ is shown in Figure 3.22. At ($\Theta_{r,DBE}$, $V_{b,DBE}$), no hinge yielding hinges have formed as the SMRF responds linear-elastically. At ($\Theta_{r,MCE}$, $V_{b,MCE}$), 27 yielding hinges have formed, including at the left ends of the beams up to the 6th floor level as well as the hinges at the base of the first story interior columns. At ($\Theta_{r,1.5xMCE}$, $V_{b,1.5xMCE}$), 61 yielding hinges have formed, including all hinges in the beam-sway mechanism except for the hinges at the right ends of 6th, 7th, 8th,

and 9th floors. At ($\Theta_{r,2xMCE}$, $V_{b,2xMCE}$), 69 yielding hinges have formed, including all hinges in the beam-sway mechanism except for the hinges at the right ends of the 8th and 9th floors. In addition to these 69 hinges which are part of the beam-sway yielding mechanism, the yielding hinges at the tops of 6th, 7th, and 8th story columns have formed at ($\Theta_{r,2xMCE}$, $V_{b,2xMCE}$). These results suggest that the intended beam-sway yielding mechanism of the SMRF may never fully form. The NL dynamic responses of the SMRF subjected to GM scaled to two times the MCE (as well as GM scaled to the DBE) are investigated to understand the NL response when the intended beam-sway yielding mechanism is nearly formed.

nth Mode Contribution to Dynamic Response

Figure 3.24 shows the beam-sway yielding mechanism of the SMRF and the moment vs. curvature response histories for the yielding hinges at the left ends of first floor beams, at the right ends of ninth floor beams, and the base of the first story columns of the SMRF subjected to the HWA019N GM record scaled to two times the MCE. Except for the hinges at the right ends of ninth floor beams (as seen in Figure 3.24(b)), all hinges comprising the beam-sway yielding mechanism of the SMRF have formed. Figure 3.24(c) and Figure 3.24(d) show that yielding hinges have formed at the left and right ends of each beam and at the base of the first story columns.

Figure 3.25 compares the beam bending moment history, $M_{beam}(t)$, normalized by the peak bending moment capacity, M_{beam}, for beams at the right ends of the 1st story, 1st bay and

the 8th story, 4th bay beams of the SMRF subjected to the HWA019N GM record scaled to two times the MCE. Although the times of peak $M_{beam}(t)$ for the two beam ends are very close to each other for the two beam ends, the yielding hinges form at different times in the response history. There are times, such as between 47 s and 48 s of response, when the hinge at the right end of the 1st story, 1st bay beam is loading, while the hinge at the right end of the 8th story, 4th bay beam is unloading. These results show, that although Figure 3.24 shows many yielding hinges have formed during the SMRF response, the yielding hinges do not always occur simultaneously, so the intended beam-sway mechanism does not form.

Figure 3.26 shows $A^e_{eff_n}(t)$ and $A^m_{eff_n}(t)$ normalized by $A^e_{eff_n}$ and $A^m_{eff_n}$, respectively, for the first three modes of the SMRF subjected to the HWA019N GM record scaled to the DBE. The figure shows that $A^e_{eff_1}(t)$ and $A^m_{eff_1}(t)$ are similar. Using the results from Figure 3.23, the yielding hinges that formed in the SMRF subjected to the HWA019N GM record scaled to DBE were identified. Yielding hinges at the left ends of all beams and at the base of the first story columns (i.e., 41 hinges out of 77 hinges in the beam-sway mechanism) formed at various times during the response. It is notable that from the monotonic static pushover analysis under 1st mode forces (i.e., under $\boldsymbol{s}^e_1$) it was observed that no yielding hinges formed at the DBE level response, however, when the SMRF was subjected to the HWA019N GM record scaled to DBE, numerous yielding hinges formed due to higher mode response, although the beam-sway yielding mechanism did not form. Since the beam-sway yielding mechanism does not form at a specific point in time, neither $\boldsymbol{\phi}^e_1$ nor

$\boldsymbol{\phi}_1^m$ appears to provide an accurate representation of the SMRF response to a DBE-level GM. $A_{eff_2}^e(t)$ and $A_{eff_2}^m(t)$ as well as $A_{eff_3}^e(t)$ and $A_{eff_3}^m(t)$ are also similar.

Figure 3.26 shows that at the time of the peak $M_b(t)$, $A_{eff_1}^e(t)$ is at its peak value, while the $A_{eff_2}^e(t)$ is close to zero and the amplitude of $A_{eff_3}^e(t)$ is 65% of $A_{eff_3}^e$. At the time of the peak $V_b(t)$, the amplitude of $A_{eff_1}^e(t)$ is at 80% of $A_{eff_1}^e$, while the amplitudes of $A_{eff_2}^e(t)$ and $A_{eff_3}^e(t)$ are 40% of $A_{eff_2}^e$ and 40% of $A_{eff_3}^e$, respectively.

Figure 3.27 shows $A_{eff_n}^e(t)$ and $A_{eff_n}^m(t)$ normalized by $A_{eff_n}^e$ and $A_{eff_n}^m$, respectively, for the first three modes of the SMRF subjected to the HWA019N GM record scaled to two times the MCE. Yielding hinges at the left ends of all beams, at the right ends of all the beams up to 7th floor, and at the base of the first story columns (i.e., 65 hinges out of 77 hinges in the beam-sway mechanism) formed at various times during the response. Figure 3.18 shows, however, that $A_{eff_1}^e(t)$ and $A_{eff_1}^m(t)$ are similar. As shown in Table 3.6, $\bar{M}_{bn}^e$ for the 2nd and 3rd elastic modes are quite small, while $\bar{M}_{bn}^m$ for the 2nd and 3rd mechanism modes are zero. As a result, the model responses quantified using $\boldsymbol{\phi}_1^e$ and $\boldsymbol{\phi}_1^m$ are similar. Compared to the DBE-level response of the SMRF (Figure 3.25), $A_{eff_1}^e(t)$ and $A_{eff_1}^m(t)$ have a more flat-topped response during the times when many yielding hinges have formed and complete beam-sway yielding mechanism is nearly formed, such as at 48 s. Although the SMRF is intended to form the beam-sway yielding mechanism, the deformation shape of the SMRF changes during the NLTHA, as some of the yielding hinges are loading, and

other yielding hinges are unloading as shown in Figure 3.24 and Figure 3.25. Therefore, $\boldsymbol{\phi}_n^m$ is not consistent with the actual deformed shape of the SMRF during the NL seismic response.

Figure 3.27 shows that at the time of the peak $M_b(t)$, $A_{eff_1}^e(t)$ is at its peak value, while the amplitudes of $A_{eff_2}^e(t)$ and $A_{eff_3}^e(t)$ are 10% of $A_{eff_2}^e$ and 25% of $A_{eff_3}^e$, respectively. At the time of the peak $V_b(t)$, the amplitude of $A_{eff_1}^e(t)$ is at 80% of $A_{eff_1}^e$, while the amplitude of $A_{eff_2}^e(t)$ is at 10% of $A_{eff_2}^e$, and $A_{eff_3}^e(t)$ is nearly zero.

nth Mode NL Displacement Response

Figure 3.28 shows the profile of $\boldsymbol{u}(t)$ over the height of the SMRF subjected to the ILA013W GM record scaled to the MCE at time of the peak M_b (t) and 10 s after the time of the peak M_b (t). The values of $\boldsymbol{u}(t)$ are directly from the NLTHA results, while $\boldsymbol{u}_n^e(t)$ and $\boldsymbol{u}_n^m(t)$, denoted as $\boldsymbol{u}_n^e$ and $\boldsymbol{u}_n^m$ in Figure 3.27, are a product of $\boldsymbol{\phi}_n^e \Gamma_n^e$ and $D_{eff_n}^e(t)$ and $\boldsymbol{\phi}_n^m \Gamma_n^m$ and $D_{eff_n}^m(t)$, respectively. As seen in Figure 3.28(a), when the SMRF is closest to forming the beam-sway yielding mechanism, that is, at the time of the peak M_b (t), $\boldsymbol{u}_1^e(t)$ and $\boldsymbol{u}_1^m(t)$ dominate the $\boldsymbol{u}(t)$ resposne. However, at times away from the time of the peak M_b (t), some of the yielding hinges start unloading, the contributions of $\boldsymbol{u}_2^e(t)$ and $\boldsymbol{u}_2^m(t)$ to the $\boldsymbol{u}(t)$ increase.

3.8. Summary and Conclusions

This paper has presented an alternate approach for quantifying the nth mode seismic response of a nonlinear (NL) structure with a clearly defined yielding mechanism, based on a set of mode shapes, which are called *mechanism mode shapes*, $\boldsymbol{\phi}_n^m$. $\boldsymbol{\phi}_n^m$ are determined from eigen analysis of the structure after the yielding mechanism forms. The responses of several example NL wall structures and NL frame structures were studied. Based on based on NL time history analysis (NLTHA) results for the example structures, it is shown that $\boldsymbol{\phi}_n^m$ can provide a better representation of the nth mode response of a NL structure after the yielding mechanism forms, compared to mode shapes based on a linear-elastic model of the structure, $\boldsymbol{\phi}_n^e$.

The main findings of the study are:

- When $\boldsymbol{\phi}_n^e$ is used to quantify the nth mode responses, the 1st mode response, $A_{eff_1}^e(t)$, has fluctuations during its entire response history, even during times when the yielding mechanism forms. The fluctuations in $A_{eff_1}^e(t)$ indicate that the 1st mode response and the response of higher modes (i.e., for n > 1) are coupled through the yielding mechanism.
- The higher mode responses can be decoupled from the 1st mode response using $\boldsymbol{\phi}_n^m$. When $\boldsymbol{\phi}_n^m$ is used to quantify the nth mode responses, the time of the peak 1st mode response (i.e., the peak $A_{eff_1}^m(t)$) is coincident with the time of the peak base overturning moment response $M_b(t)$ and the times when the yielding mechanism forms can be clearly identified by a flat-topped $A_{eff_1}^m(t)$ history.

- $A^{m}_{eff_{n,m}}$ can be used to *accurately* quantify the 1st mode and higher mode response of a NL structure.
- The 2nd and 3rd mode responses, $A^{e}_{eff_2}(t)$ and $A^{m}_{eff_2}(t)$ and $A^{e}_{eff_3}(t)$ and $A^{m}_{eff_3}(t)$, were similar to each other (i.e., regardless of whether $\boldsymbol{\phi}^{m}_{n}$ or $\boldsymbol{\phi}^{e}_{n}$ are used) for all example structures indicating that the higher modes are not strongly affected by the formation of the yielding mechanism in the structure.
- The differences between $A^{e}_{eff_1}(t)$ and $A^{m}_{eff_1}(t)$ are apparent for the NL wall structures. Since the formation of the yielding mechanism is clearly identifiable and $A^{m}_{eff_1}(t)$ has an elongated flat-topped peak response history. When multiple ground motions (GM) are used in the NLTHA, there is no scatter in the peak 1st mode response $A^{m}_{eff_1}$ for the NL wall structures under the various GM, which exactly equals to $SA_{GM}(T^{e}_{n})/R$. On the other hand there is significant scatter in the peak 1st mode response $A^{e}_{eff_1}$ for the NL wall structures under the various GM.
- For the SC-CBF example structure, differences between $A^{e}_{eff_n}(t)$ and $A^{m}_{eff_n}(t)$ are significant due to the base rocking response of the SC-CBF. However, due to variations in the PT bar force as the SC-CBF rocks, $A^{m}_{eff_1}(t)$ does not have a smooth flat-topped response. When various GM are considered, there is much less scatter in the $A^{m}_{eff_1}$ values compared to the $A^{e}_{eff_1}$values showing that the 1st mode response is accurately controlled by the formation of yielding mechanism of the SC-CBF (i.e., base rocking motion followed by PT bar yielding).
- The NLTHA results for the SMRF example structure show that, even under intense seismic response, an SMRF with numerous stories and bays is unlikely to have all

the yielding hinges that compose the intended beam-sway mechanism form simultaneously. Therefore, the SMRF example structure is categorized as a structure which may not develop a clearly defined yielding mechanism for a significant duration of the NLTHA, although significant yielding occurs, and the use of ϕ_1^m appears to be inappropriate for quantifying the NL response.

In conclusion, the results of this study show that ϕ_n^m can be used to accurately quantify and understand the 1st mode and higher mode responses of a NL structure with a clearly-defined yielding mechanism.

3.9. References

AISC (2010). "Seismic Provisions for Structural Steel Buildings," American Institute of Steel Construction, Chicago, IL, USA.

Antoniou, S. and Pinho, R. (2004) "Advantages and limitations of adaptive and non-adaptive force-based pushover procedures," *Journal of Earthquake Engrg.*, 8(4), pp. 497–522.

ASCE (2010). "Minimum Design Loads for Buildings and Other Structures," ASCE7-10, Reston, VA, USA.

Baker, J.W. (2011). "Conditional Mean Spectrum: Tool for Ground-Motion Selection," *Journal of Structural Engrg.*, 137(3), pp. 322-331.

Blakeley, R. W. G., Cooney, R. C., and Megget, L. M. (1975). "Seismic Shear Loading at Flexural Capacity in Cantilever Wall Structures," *Bulletin of the New Zealand National Society for Earthquake Engrg.*, 8 (4), pp. 278-290.

Bracci, J. M., Kunnath, S. K., and Reinhorn, A. M. (1997). "Seismic performance and retrofit evaluation of reinforced concrete structures," *Journal of Structural Engrg.*, 123(1), pp. 3-10.

BSSC (2003). NEHRP Recommended Provisions for Seismic Regulations for New Buildings and Other Structures. FEMA 450. Building Seismic Safety Council, National Institute of Building Sciences, Washington, D.C., USA.

Calugaru, V. and Panagiotou, M. (2010). "Seismic Isolation Using Single and Dual Shear Hinging of Tall Cantilever Wall Buildings Subjected to Near Fault Ground Motions," *Proc. of the 9th US National and 10th Canadian Conference on Earthquake Engrg.*, Toronto, Canada. July 25-29.

Chancellor, N.B. (2014). "Seismic Design and Performance of Self-Centering Concentrically-Braced Frames," Ph.D. Dissertation, Department of Civil and Environmental Engrg., Lehigh Univ., Bethlehem, PA, USA.

Chao, S. H., Goel, S. C., and Lee, S. S. (2007). "A seismic design lateral force distribution based on inelastic state of structures," *Earthquake Spectra*, 23(3), pp. 547-569.

Chopra, A. K., and Goel, R. K. (2002). "A modal pushover analysis procedure for estimating seismic demands for buildings," *Earthquake Engrg. and Structural Dynamics*, 31(3), pp. 561-582.

Chopra, A. K., Goel, R. K., and Chintanapakdee, C. (2004). "Evaluation of a modified MPA procedure assuming higher modes as elastic to estimate seismic demands," *Earthquake Spectra*, 20(3), pp. 757-778.

Chopra, A. K. (2012). *Dynamics of structures*. (4th ed.). Prentice Hall, New Jersey, NJ.

Clough, R. W. "On the importance of higher modes of vibration in the earthquake response of a tall building," *Bulletin of the Seismological Society of America*, 45.4 (1955), pp. 289-301.

Eberhard, M.O. and Sozen, M.A. (1993). "Behavior-based Method to Determine Design Shear in Earthquake-Resistant Walls," *Journal of Structural Engrg.*, 119(2), pp. 619-640.

Eibl, J. and Keintzel, E. (1988). "Seismic Shear Forces in RC Cantilever Shear Ealls," *Proc. of the 9th World Conference on Earthquake Engrg. (vol. VI)*, Tokyo-Kyoto, Japan, August 2-9.

Elnashai, A. S. (2000). "Advanced Static Inelastic (pushover) Analysis for Seismic Design and Assessment," *Proc. of the George Penelis Symposium on Concrete and Masonry Structures*, Aristotle Univ. of Thessaloniki, Thessaloniki, Greece, October, pp. 23-34.

Federal Emergency Management Agency (FEMA) (2000). "Recommended Seismic Design Criteria for New Steel Moment Frame Buildings," FEMA 350. *SAC Joint Venture*, Washington, DC, USA.

Gupta, B. and Kunnath, S. K. (2000). "Adaptive Spectra-based Pushover Procedure for Seismic Evaluation of Structures," *Earthquake Spectra*, 16(2), pp. 367-392.

Kalkan, E. and Kunnath, S.K. (2006). "Adaptive Modal Combination Procedure for Nonlinear Static Analysis of Building Structures," *Journal of Structural Engrg.*, 132(11), pp. 1721-1732.

Mazzoni, S., McKenna, F., Scott, M.H., Fenves, G.L., et al. (2009). "Open System for Earthquake Engineering Simulation (OpenSEES) User Command-Language Manual*," Pacific Earthquake Engrg. Research Center*, Univ. of California, Berkeley, CA, USA.

Pacific Earthquake Engrg. Research Center (PEER) (2011). "Ground Motion Database Flatfile," http://peer.berkeley.edu/nga/flatfile.html on December 12, 2013.

Priestley, M.J.N. (2003). "Does Capacity Design Do The Job? An Investigation of Higher Modes Effects in Cantilever Walls," *Bulletin New Zealand Society for Earthquake Engrg.*, 36(4), pp. 276-292.

Priestley, M.J.N. and Amaris, A. (2003). "Dynamic Amplification of Seismic Moments and Shear Forces in Cantilever Walls," *Proc. of the Fib Symposium Concrete Structures in Seismic Regions*, Athens, Greece, May 6-8.

Rodriguez, M. E., Restrepo, J. I., and Carr, A. J. (2002). "Earthquake-induced Floor Horizontal Accelerations in Buildings," *Earthquake Engrg. and Structural Dynamics*, 31(3), pp. 693-718.

Roke, D., Sause, R., Ricles, J. M., and Chancellor, N.B. (2010). "Damage- Free Seismic-Resistant Self-Centering Concentrically-Braced Frames," ATLSS Report 10-09, ATLSS Engrg. Research Center, Lehigh Univ., Bethlehem, PA, USA.

Seo, C.-Y., Lin, Y.C., Sause, R., and Ricles, J.M., (2012), "Development of Analytical Models and Performance Evaluation for 0.6 Scale Self-Centering MRF with 355 Web Friction Devices," ATLSS Engrg. Research Center, Lehigh Univ., Bethlehem, PA, USA.

Sullivan, T. J., Priestley, M. J. N., and Calvi, G. M. (2008). "Estimating the Higher-Mode Response of Ductile Structures," *Journal of Earthquake Engrg.*, 12(3), pp. 456-472.

Villaverde, R. (1991). "Explanation for the Numerous Upper Floor Collapses During the 1985 Mexico City Earthquake," *Earthquake Engrg. and Structural Dyn*amics, 20, pp. 223–241.

Table 3.1 $\overline{M}_{bn}^{e}$ and $\overline{M}_{bn}^{m}$ for wall with purely flexural response

$\overline{M}_{b1}^{e}$	$\overline{M}_{b1}^{m}$	$\overline{M}_{b2}^{e}$	$\overline{M}_{b2}^{m}$	$\overline{M}_{b3}^{e}$	$\overline{M}_{b3}^{m}$
0.8931	1.0000	0.0786	0.0000	0.0164	0.0000

Table 3.2 Ground motion set (Chancellor, 2014)

PEER-NGA Record Seq. #	Year	Event	Station	Component	Scale Factor	
					DBE	MCE
165	1979	Imperial Valley-06	Chihuahua	012, 282	2.17	3.26
169	1979	Imperial Valley-06	Delta	262, 352	1.63	2.45
728	1987	Superst. Hills-02	Westmorland	090, 180	2.01	3.02
778	1989	Loma Prieta	Hollister (HDA)	165, 255	1.61	2.42
949	1994	Northridge-01	Arleta	090, 360	1.92	2.88
1100	1995	Kobe, Japan	Abeno (ABN)	000, 090	2.89	4.34
1101	1995	Kobe, Japan	Amagasaki	000, 090	1.20	1.80
1110	1995	Kobe, Japan	Morigawachi	000, 090	2.23	3.35
1187	1999	Chi-Chi, Taiwan	CHY015	N, W	2.31	3.47
1203	1999	Chi-Chi, Taiwan	CHY036	E, N	1.41	2.12
1204	1999	Chi-Chi, Taiwan	CHY039	E, N	2.62	3.93
1209	1999	Chi-Chi, Taiwan	CHY047	N, W	2.37	3.56
1236	1999	Chi-Chi, Taiwan	CHY088	E, N	2.56	3.84
1269	1999	Chi-Chi, Taiwan	HWA019	E, N	2.85	4.28
1294	1999	Chi-Chi, Taiwan	HWA048	N, W	2.84	4.26
1317	1999	Chi-Chi, Taiwan	ILA013	N, W	2.17	3.26
1484	1999	Chi-Chi, Taiwan	TCU042	E, N	1.75	2.63

Table 3.3 Properties of wall structures

	T_1^e (s)	$\rho = \frac{EI}{(5/6)L^2GA}$	R
Wall with purely flexural response	1.5	0	6
Wall with significant shear flexibility	1.5	169	6

where L = story height; (GA) = story shear stiffness; (EI) = story flexural stiffness

Table 3.4 Summary of dead loads for SC-CBF and SMRF

Item	Dead Load for Floor 1 (psf)	Dead Load for Middle Floors (psf)	Dead Load for Roof (psf)
Floor/Roof Deck	3	3	3
Floor/Roof Slab	43	43	0
Roofing Material	0	0	10
Mechanical Weight	10	10	25
Ceiling Material	5	5	5
Floor Finish	2	2	0
Structural Steel	15	15	10
Steel Fireproofing	2	2	2
Building Envelope	8	7	5
Total	88	87	60

Table 3.5 Summary of live loads for SC-CBF and SMRF

Item	Live Load for Floors (psf)	Live Load for Roof (psf)
Office	50	0
Partitions (included in seismic mass)	15	0
Roof	0	20
Total	65	20

Table 3.6 $\overline{M}_{bn}^{e}$ and $\overline{M}_{bn}^{m}$ for example structures

Structure	$\overline{M}_{b1}^{e}$	$\overline{M}_{b1}^{m}$	$\overline{M}_{b2}^{e}$	$\overline{M}_{b2}^{m}$	$\overline{M}_{b3}^{e}$	$\overline{M}_{b3}^{m}$
Wall with purely flexural response	0.8931	1.0000	0.0786	0.0000	0.0164	0.0000
Wall with shear flexibility	1.0314	1.0000	-0.0371	0.0000	0.0076	0.0000
SC-CBF	0.9097	1.0000	0.0670	0.0000	0.0152	0.0000
SMRF	0.9824	1.0000	0.0023	0.0000	0.0121	0.0000

Table 3.7 $\overline{V}_{bn}^{e}$ and $\overline{V}_{bn}^{m}$ for example structures

Structure	$\overline{V}_{b1}^{e}$	$\overline{V}_{b1}^{m}$	$\overline{V}_{b2}^{e}$	$\overline{V}_{b2}^{m}$	$\overline{V}_{b3}^{e}$	$\overline{V}_{b3}^{m}$
Wall with purely flexural response	0.6485	0.7895	0.1986	0.1407	0.0682	0.0383
Wall with shear flexibility	0.8517	0.7895	0.0912	0.1569	0.0304	0.0241
SC-CBF	0.6759	0.8082	0.1997	0.1294	0.0633	0.0330
SMRF	0.7686	0.7900	0.1277	0.1344	0.0492	0.0394

Table 3.8 T_n^e and T_n^m for example structures

Structure	T_1^e (s)	T_1^m (s)	T_2^e (s)	T_2^m (s)	T_3^e (s)	T_3^m (s)
Wall with purely flexural response	1.501	3.7E+05	0.238	0.341	0.085	0.105
Wall with shear flexibility	1.501	1.3E+05	0.505	0.528	0.309	0.313
SC-CBF	1.131	8.2	0.315	0.360	0.181	0.190
SMRF	2.804	3.5E+05	1.014	4.741	0.592	1.592

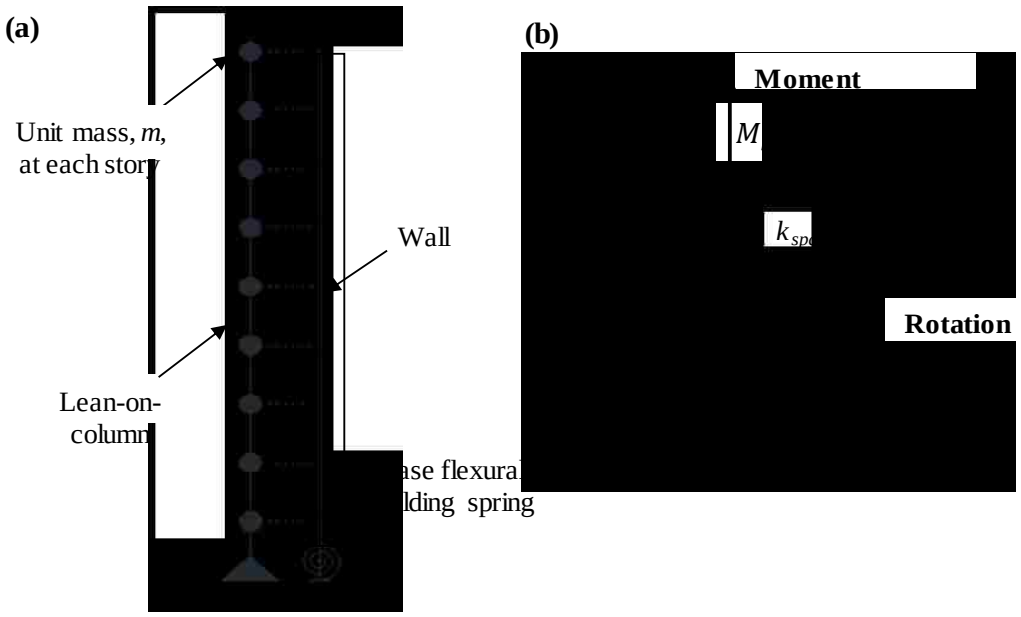

Figure 3.1 (a) 9-story cantilever wall structure model; (b) elastic-perfectly plastic hysteresis of base flexural yielding spring

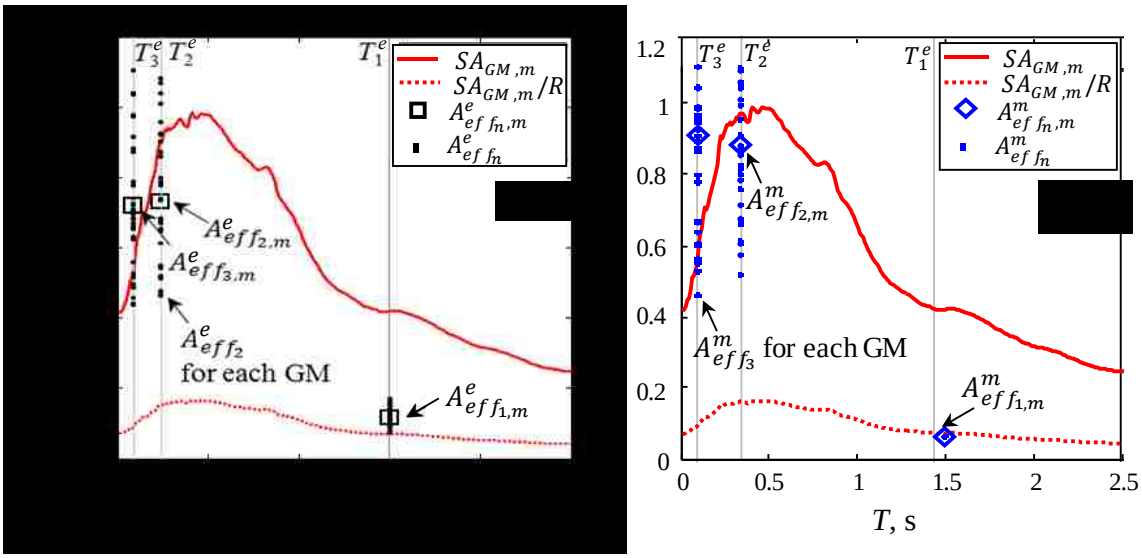

Figure 3.2 Median linear-elastic and median reduced 5% damped pseudo-acceleration spectra with A_{eff_n} and $A_{eff_{n,m}}$ for first three modes of wall structure with purely flexural response: (a) elastic modes; (b) mechanism modes

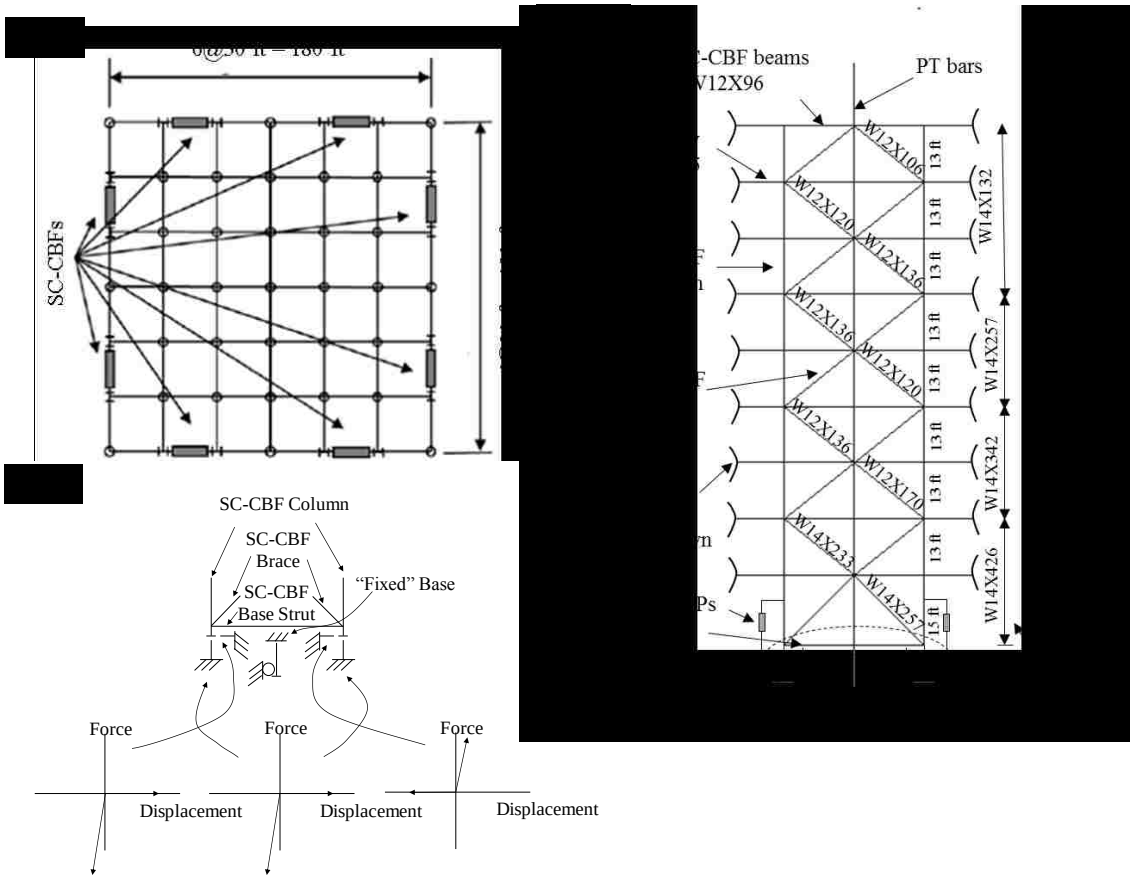

Figure 3.3 (a) Example SC-CBF building floor plan; (b) elevation of 9-story SC-CBF; (c) column base detail for numerical modeling (Chancellor, 2014)

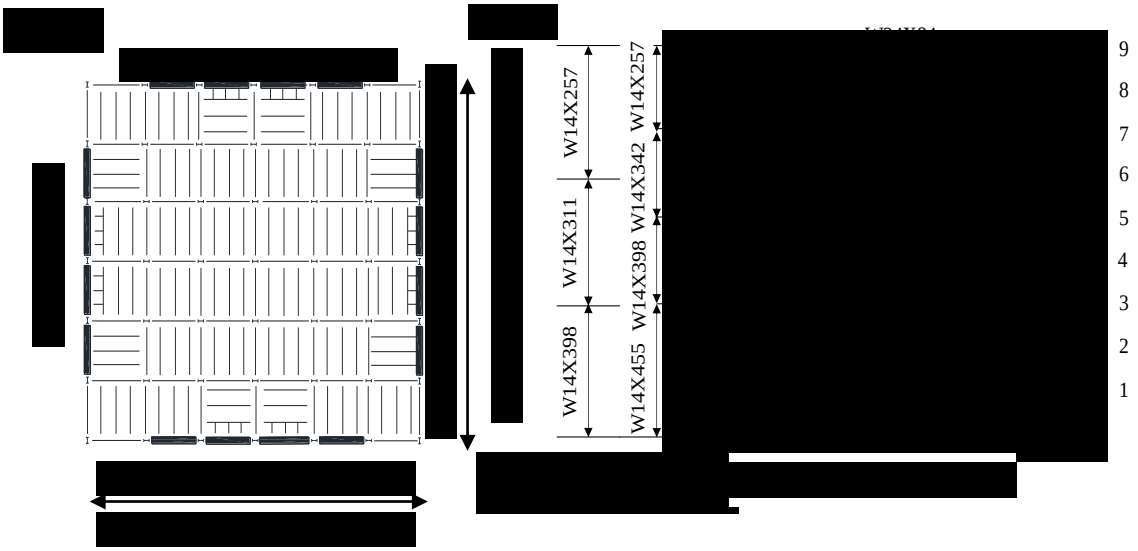

Figure 3.4 (a) Example SMRF building floor plan; (b) elevation of 9-story, 4-bay steel SMRF

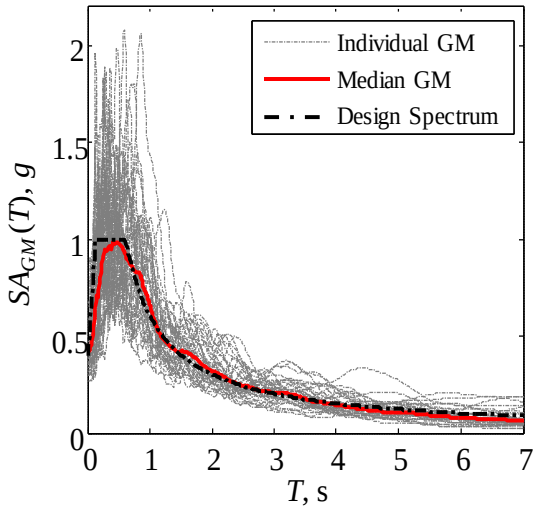

Figure 3.5 Pseudo-acceleration response spectra for ground motion set

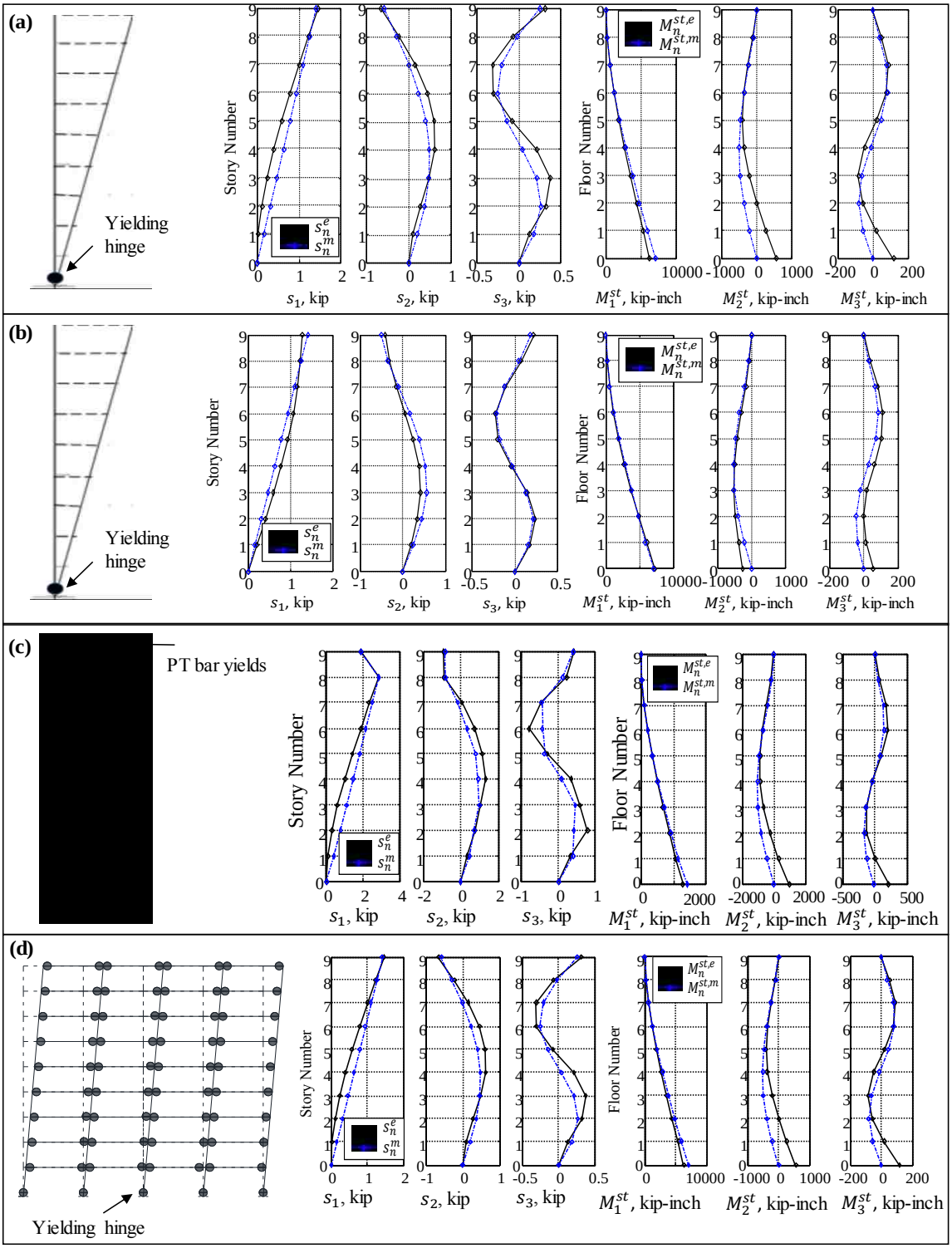

Figure 3.6 Intended yielding mechanism, $\boldsymbol{s}_n^e$ and $\boldsymbol{s}_n^m$, $M_n^{st,e}$ and $M_n^{st,m}$: (a) wall structure with purely flexural response; (b) wall structure with shear flexibility; (c) SC-CBF; (d) SMRF

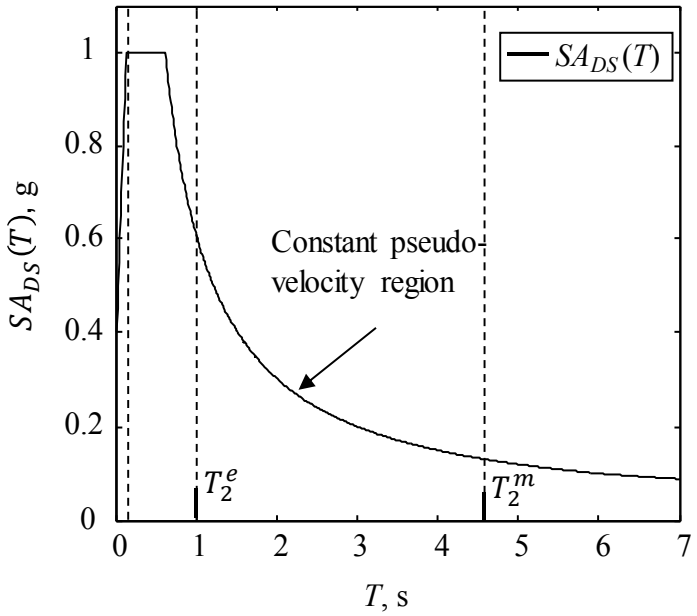

Figure 3.7 Design pseudo-acceleration spectrum and T_2^e and T_2^m for SMRF

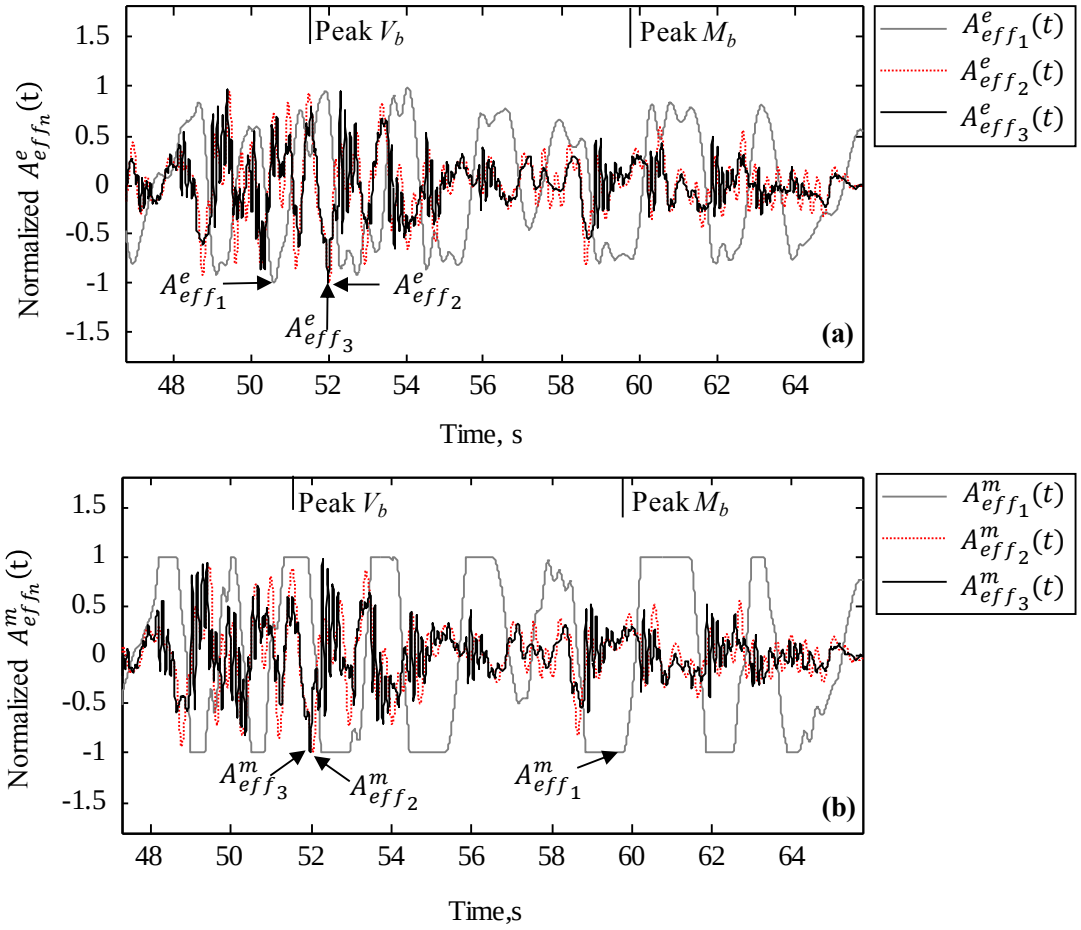

Figure 3.8 (a) $A^e_{eff_n}(t)$ normalized by $A^e_{eff_n}$; (b) $A^m_{eff_n}(t)$ normalized by $A^m_{eff_n}$ for first three modes of wall structure with purely flexural response under ILA013W ground motion

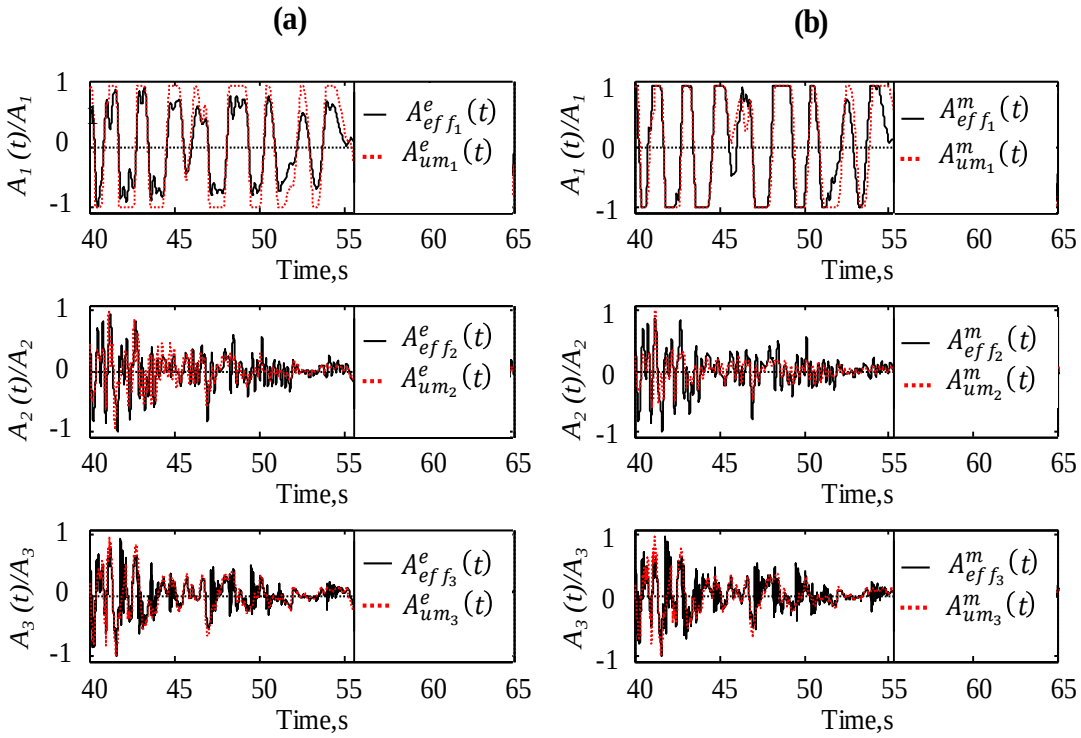

Figure 3.9 Comparison of normalized: (a) $A^e_{um_n}(t)$ and $A^e_{eff_n}(t)$; (b) $A^m_{um_n}(t)$ and $A^m_{eff_n}(t)$ response histories for first three modes of wall structure with purely flexural response under ILA013W ground motion

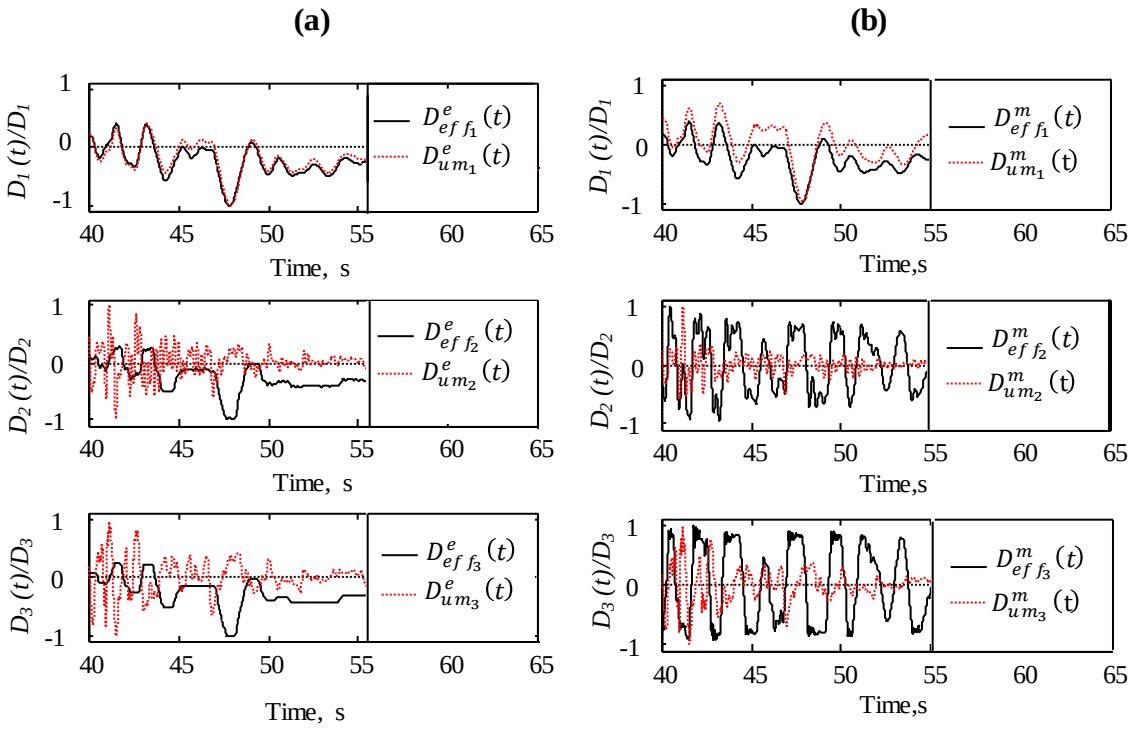

Figure 3.10 Comparison of normalized: (a) $D^e_{um_n}(t)$ and $D^e_{eff_n}(t)$; (b) $D^m_{um_n}(t)$ and $D^m_{eff_n}(t)$ response histories for first three modes of wall structure with purely flexural response under ILA013W ground motion

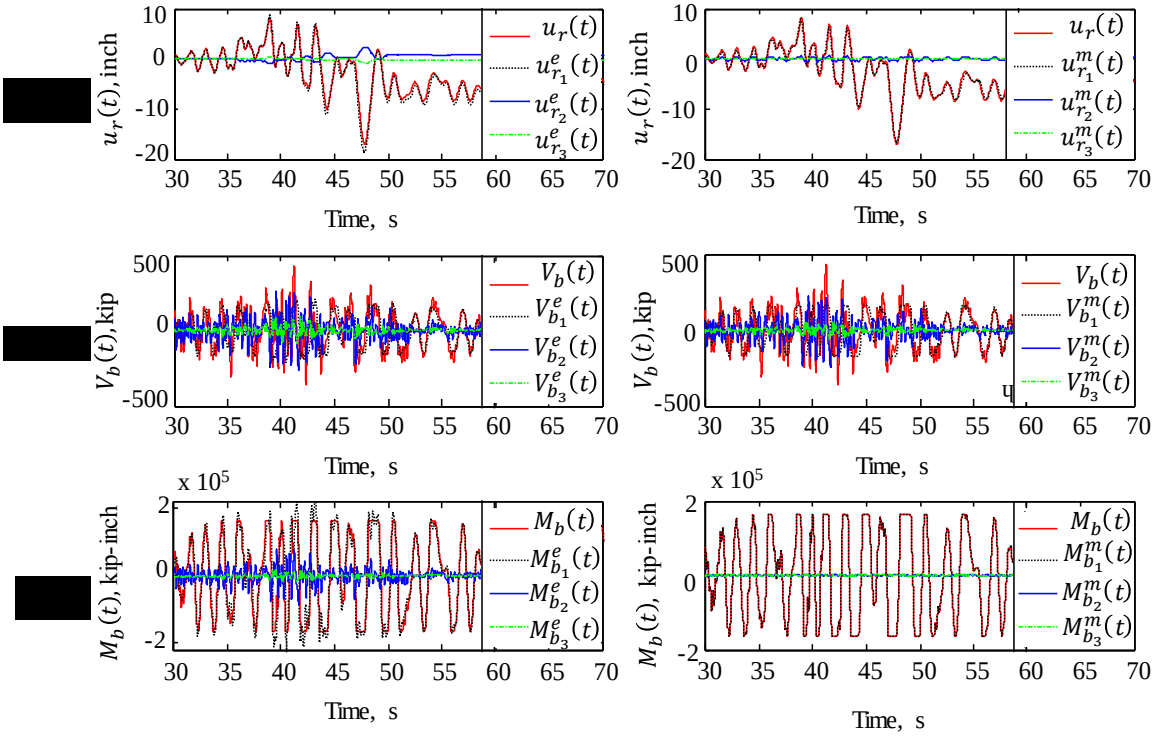

Figure 3.11 (a) $u_r(t)$ and $u_{rn}(t)$; (b) $V_b(t)$ and $V_{bn}(t)$; (c) $M_b(t)$ and $M_{bn}(t)$ for first three modes of wall structure with purely flexural response under ILA013W ground motion

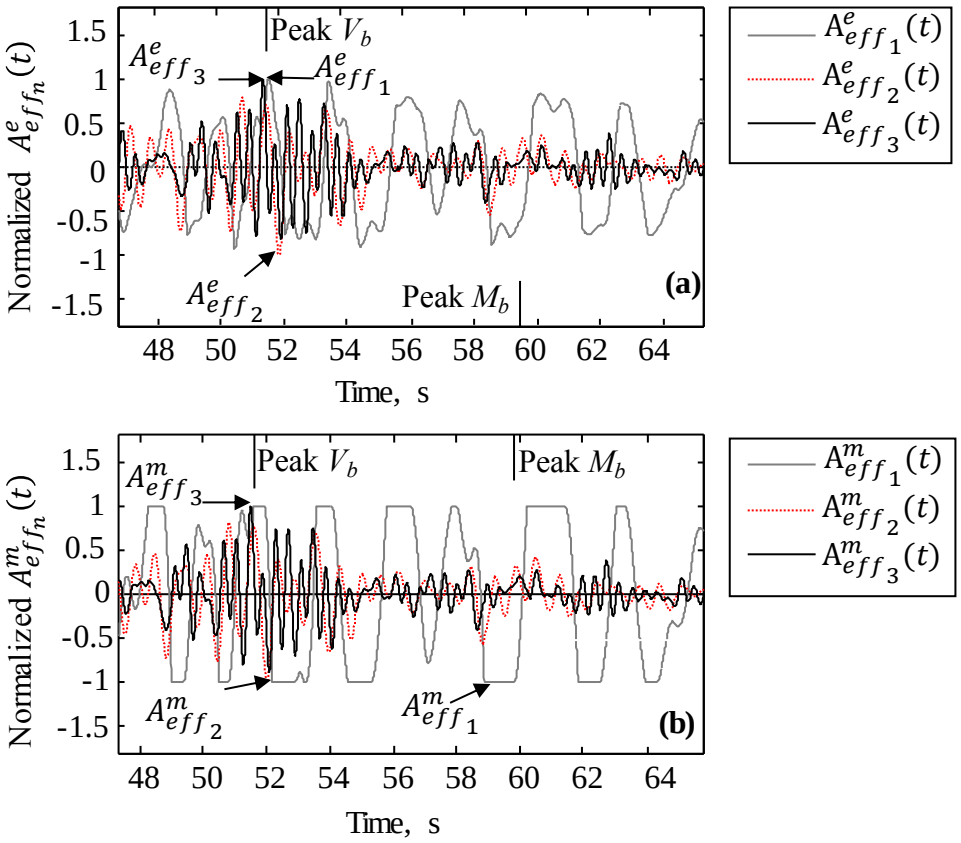

Figure 3.12 (a) $A^e_{eff_n}(t)$ normalized by $A^e_{eff_n}$; (b) $A^m_{eff_n}(t)$ normalized by $A^m_{eff_n}$ for first three modes of wall structure with significant shear flexibility under ILA013W ground motion

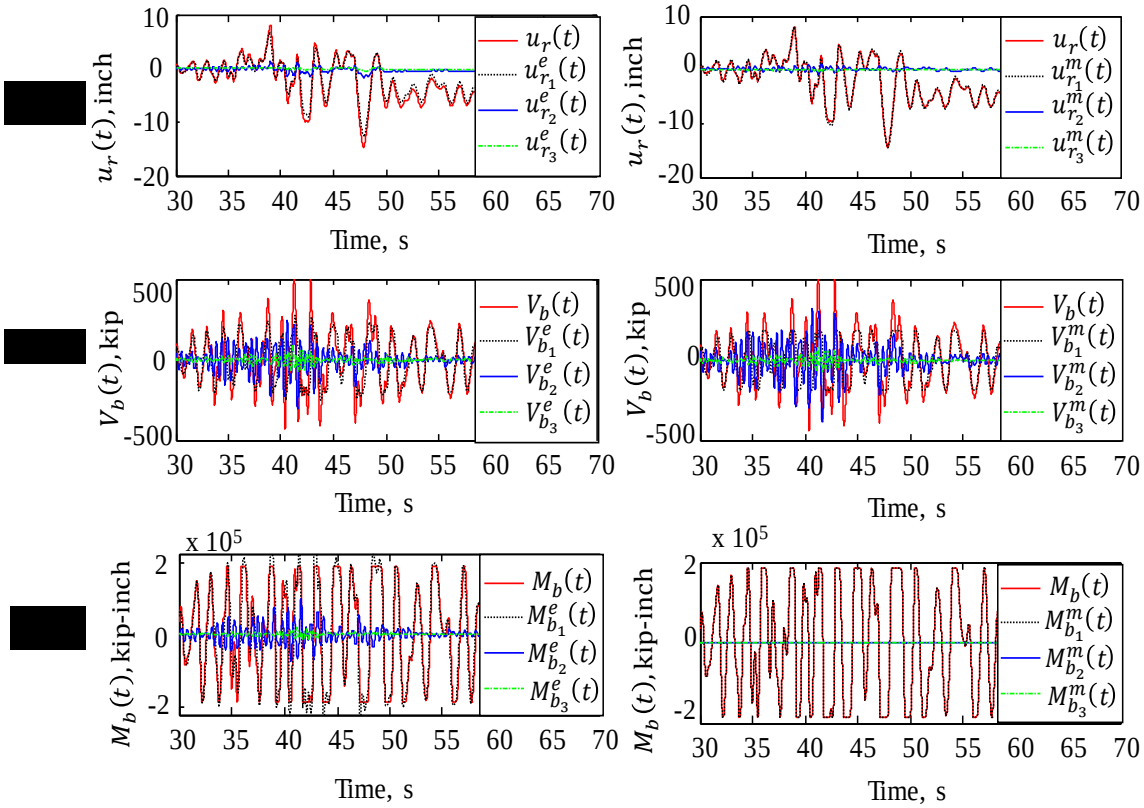

Figure 3.13 (a) $u_r(t)$ and $u_{rn}(t)$; (b) $V_b(t)$ and $V_{bn}(t)$; (c) $M_b(t)$ and $M_{bn}(t)$ for first three modes of wall structure with shear flexibility under ILA013W ground motion

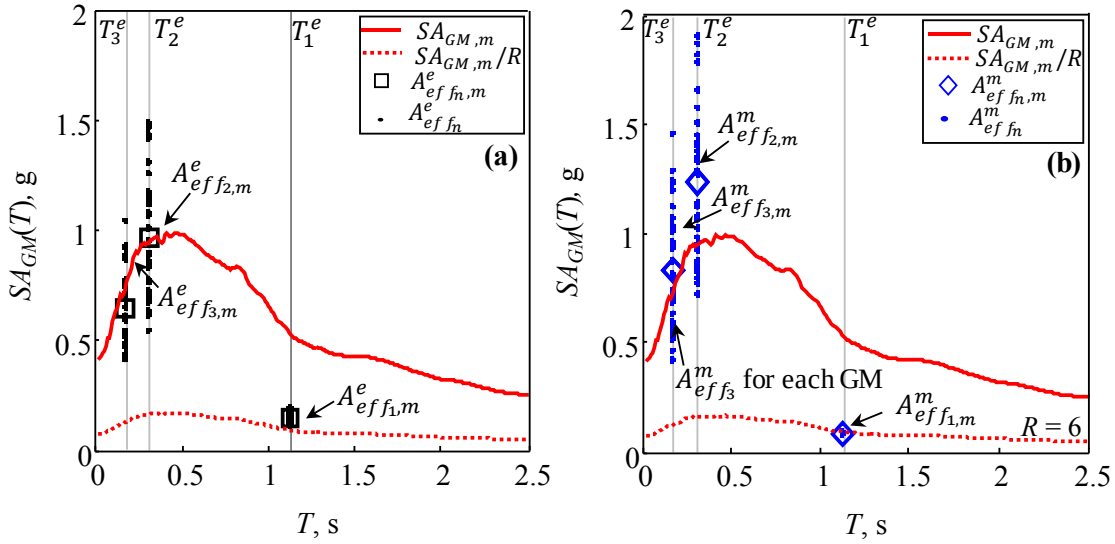

Figure 3.14 Median linear-elastic and median reduced 5% damped pseudo-acceleration spectra with A_{eff_n} and $A_{eff_{n,m}}$ for first three modes of SC-CBF response: (a) elastic modes; (b) mechanism modes

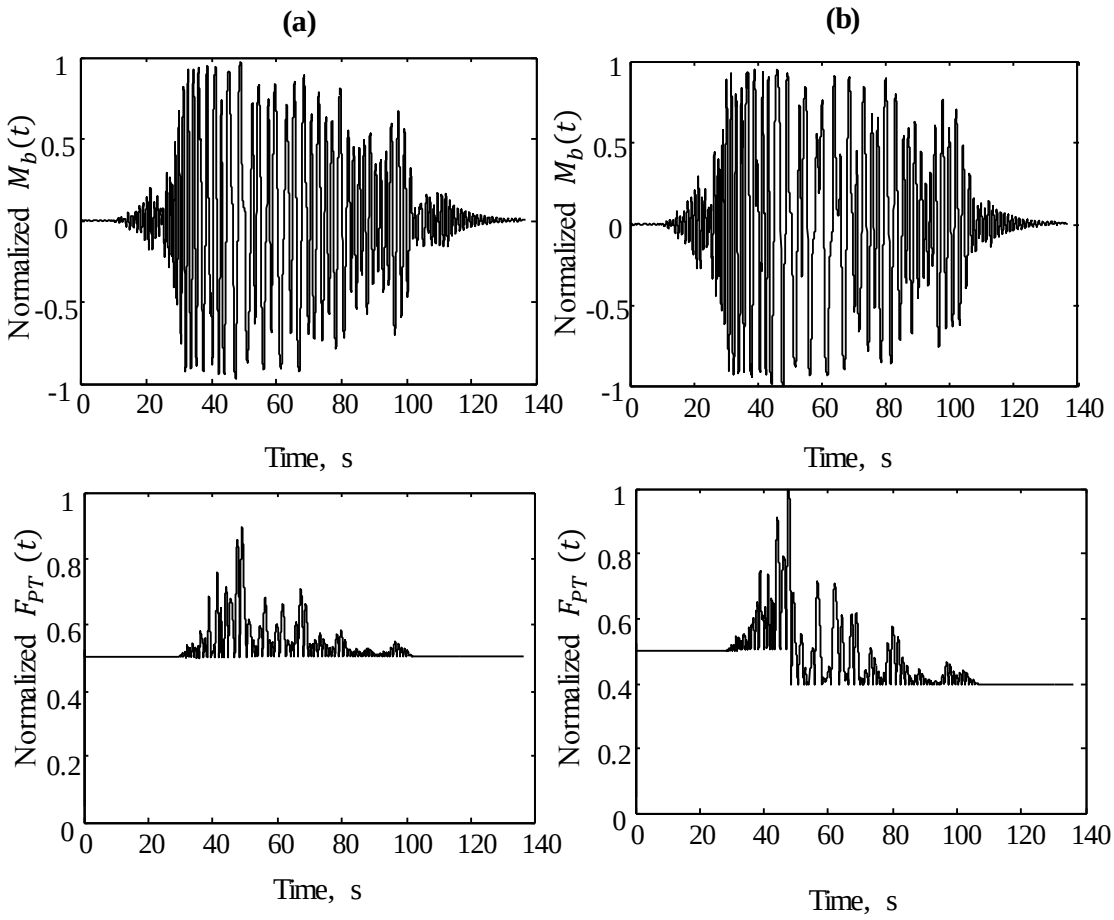

Figure 3.15 Normalized $M_b(t)$ and $F_{PT}(t)$ response history for SC-CBF under ILA013W ground motion scaled to: (a) DBE; (b) MCE

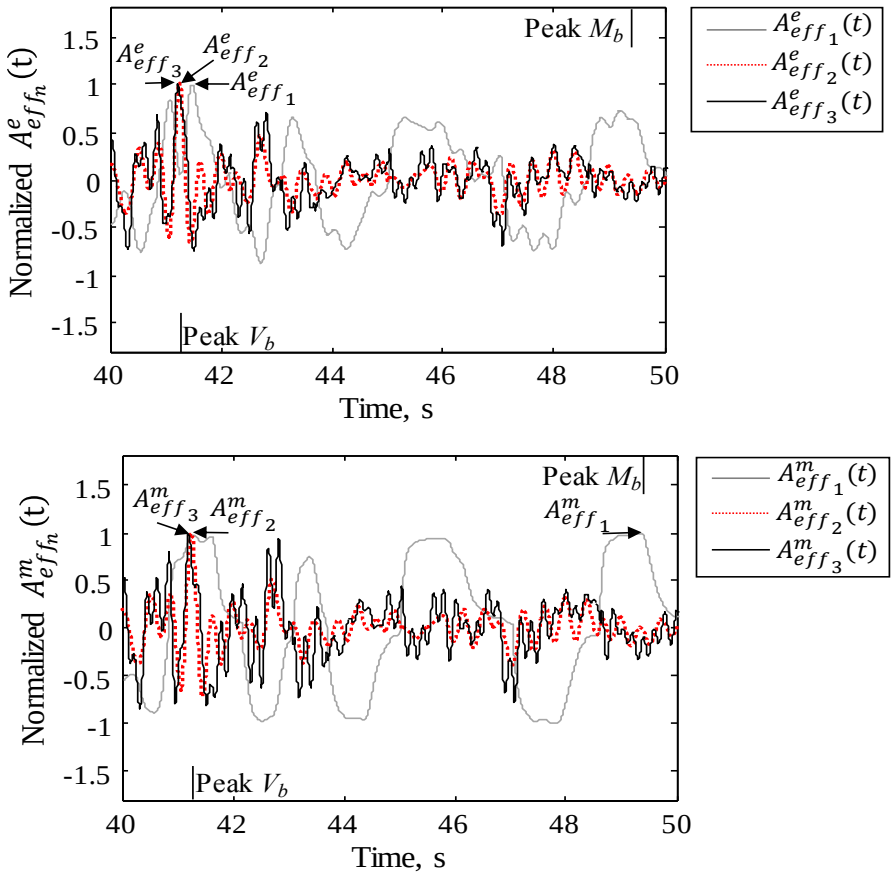

Figure 3.16 (a) $A^e_{eff_n}(t)$ normalized by $A^e_{eff_n}$; (b) $A^m_{eff_n}(t)$ normalized by $A^m_{eff_n}$ for first three modes of SC-CBF under ILA013W ground motion scaled to DBE

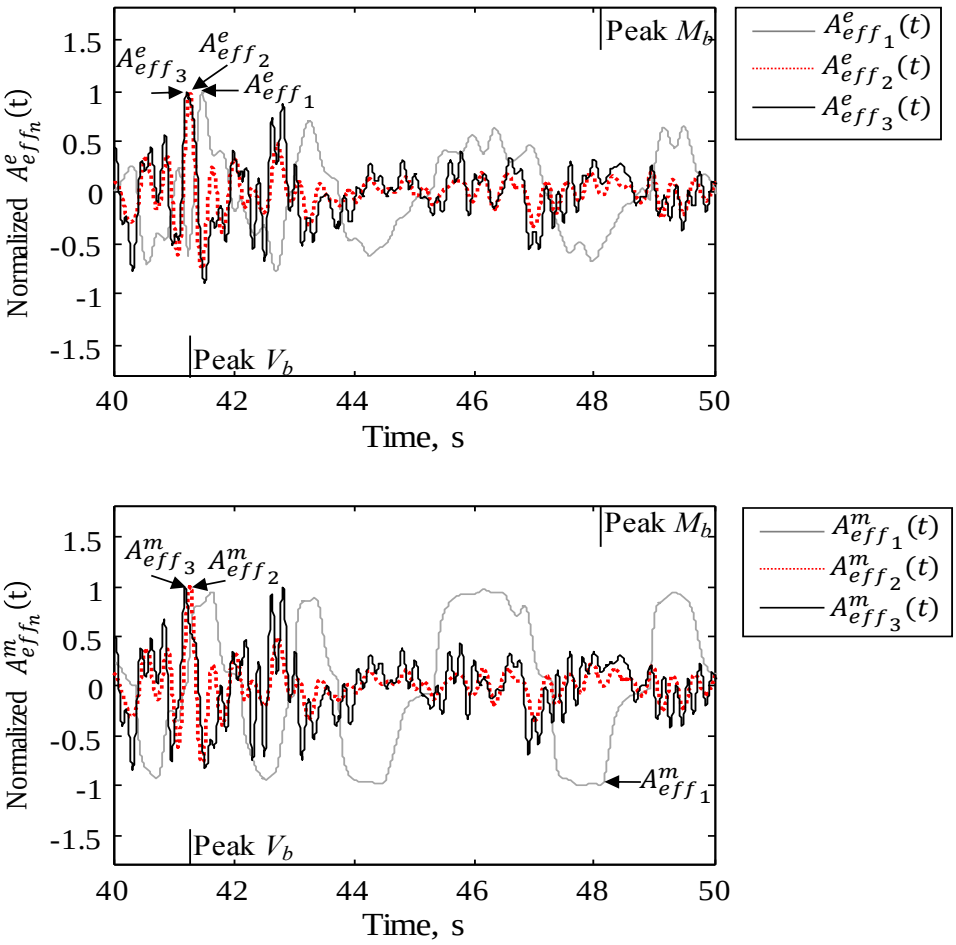

Figure 3.17 (a) $A^e_{eff_n}(t)$ normalized by $A^e_{eff_n}$; (b) $A^m_{eff_n}(t)$ normalized by $A^m_{eff_n}$ for first three modes of SC-CBF under ILA013W ground motion scaled to MCE

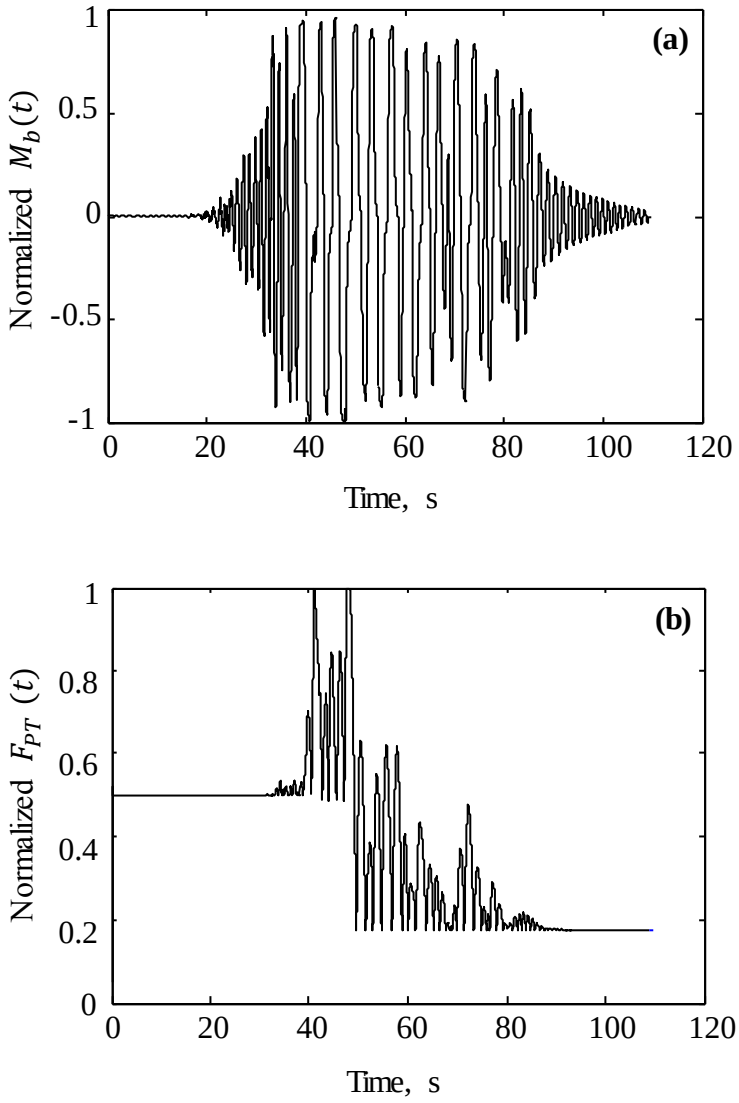

Figure 3.18 Normalized (a) M_b (t); (b) F_{PT} (t) response history for SC-CBF under HWA019N ground motion scaled to MCE

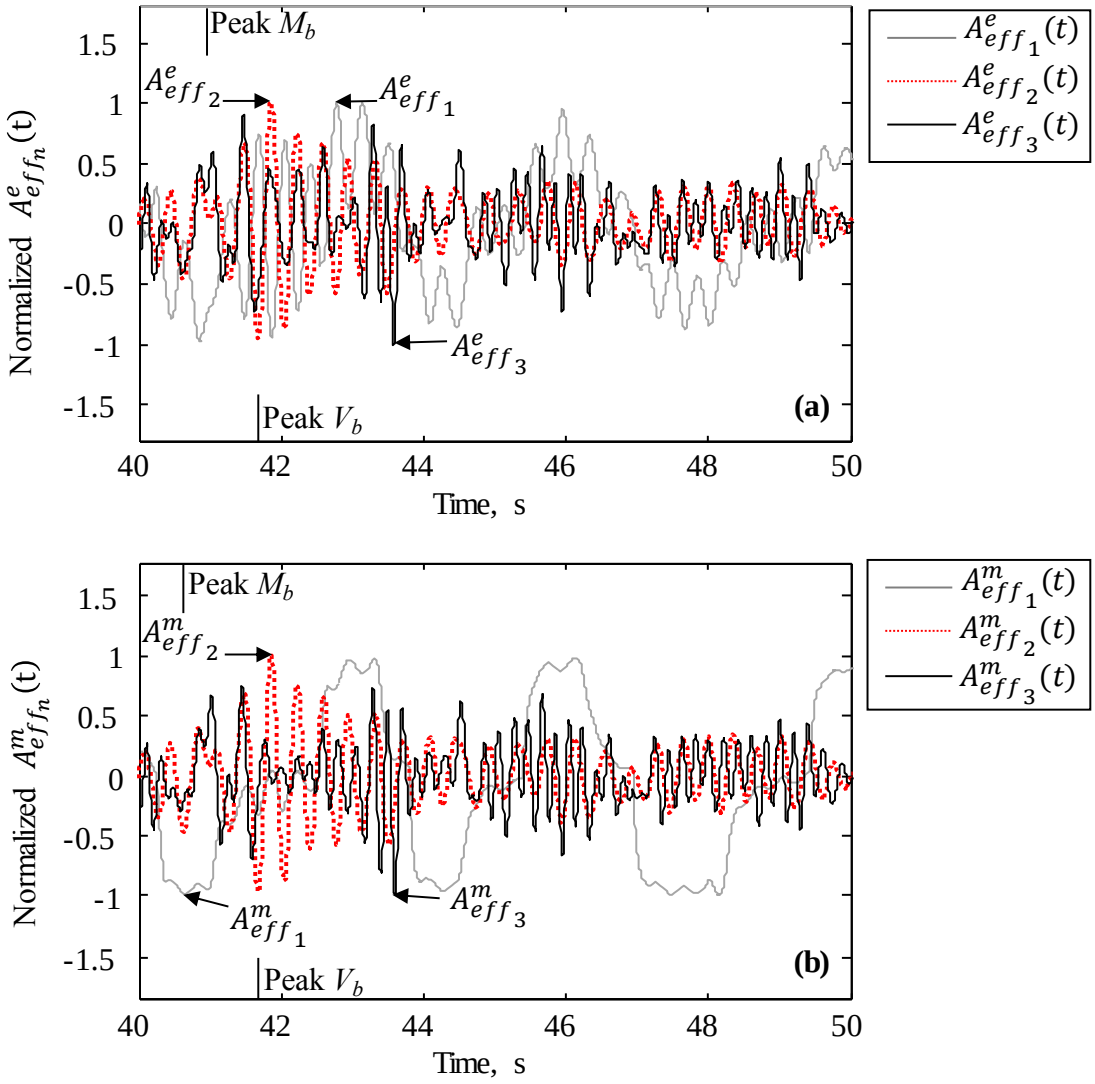

Figure 3.19 (a) $A^e_{eff_n}(t)$ normalized by $A^e_{eff_n}$; (b) $A^m_{eff_n}(t)$ normalized by $A^m_{eff_n}$ for first three modes of SC-CBF under HWA019N ground motion scaled to MCE

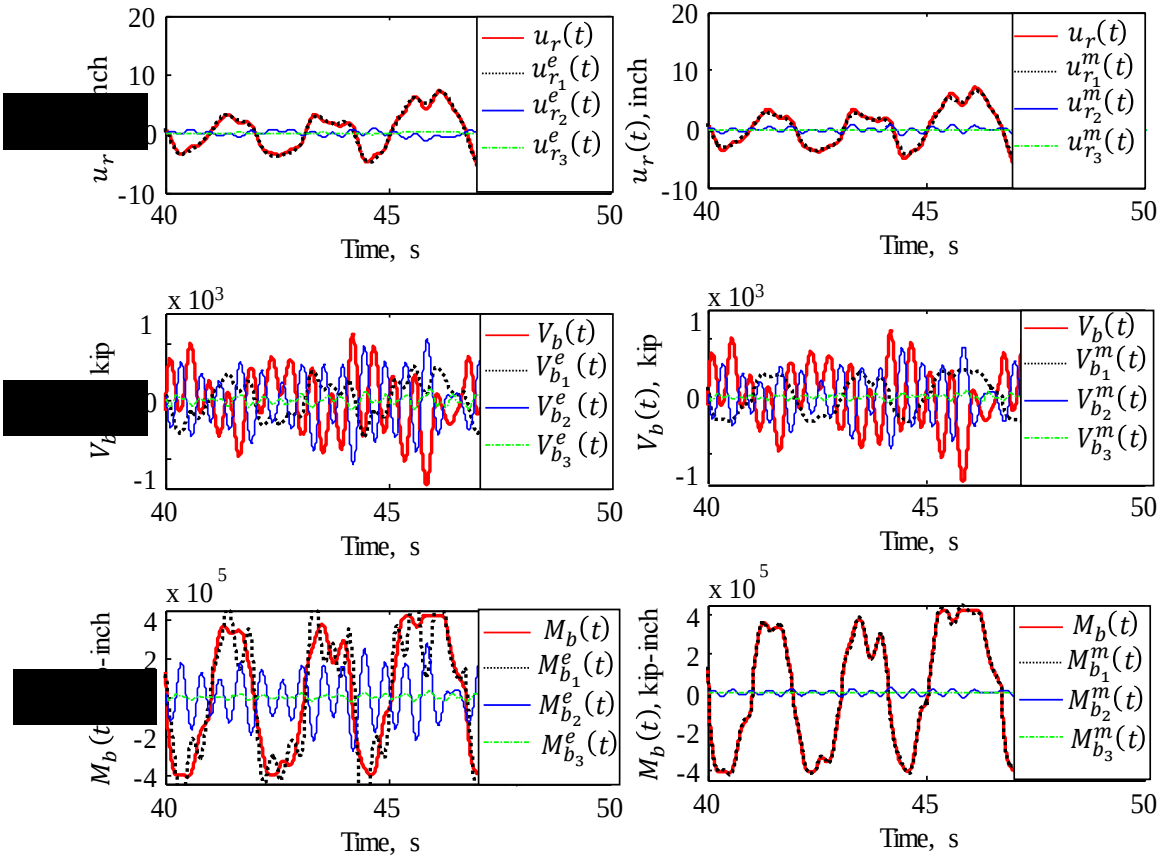

Figure 3.20 (a) $u_r(t)$ and $u_{rn}(t)$; (b) $V_b(t)$ and $V_{bn}(t)$; (c) $M_b(t)$ and $M_{bn}(t)$ for first three modes of SC-CBF under ILA013W ground motion scaled to MCE

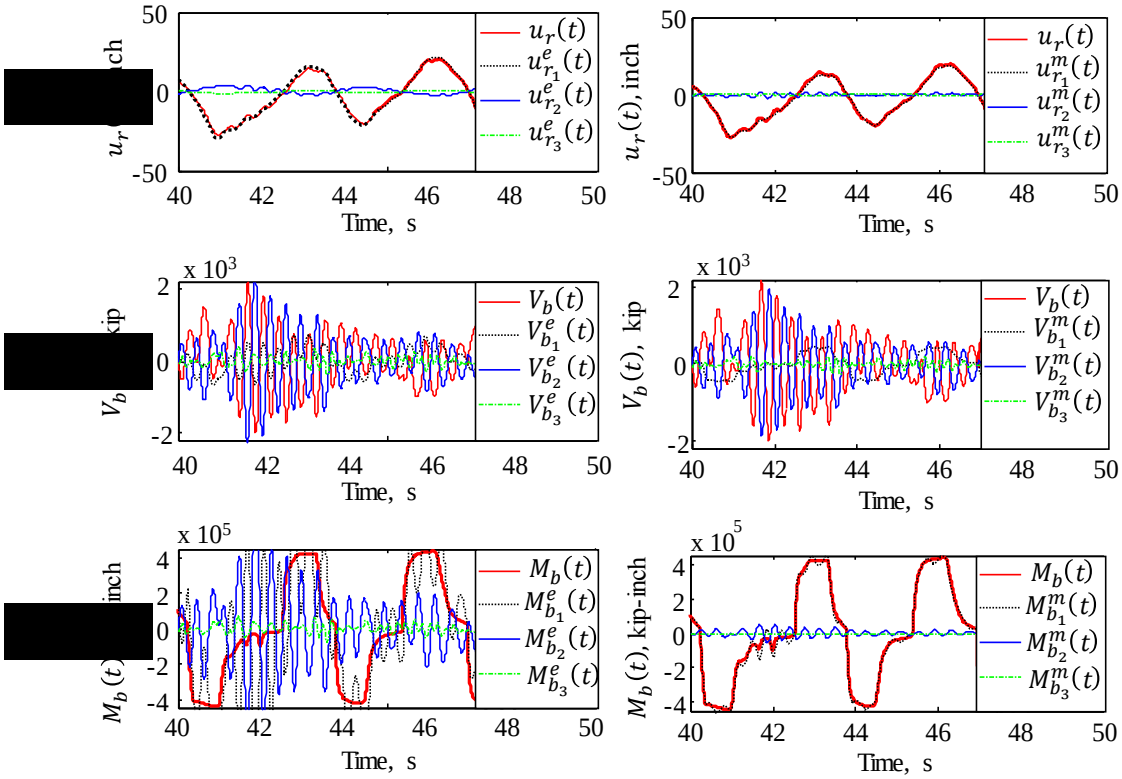

Figure 3.21 (a) $u_r(t)$ and $u_{rn}(t)$; (b) $V_b(t)$ and $V_{bn}(t)$; (c) $M_b(t)$ and $M_{bn}(t)$ for first three modes of SC-CBF under HWA019N ground motion scaled to MCE

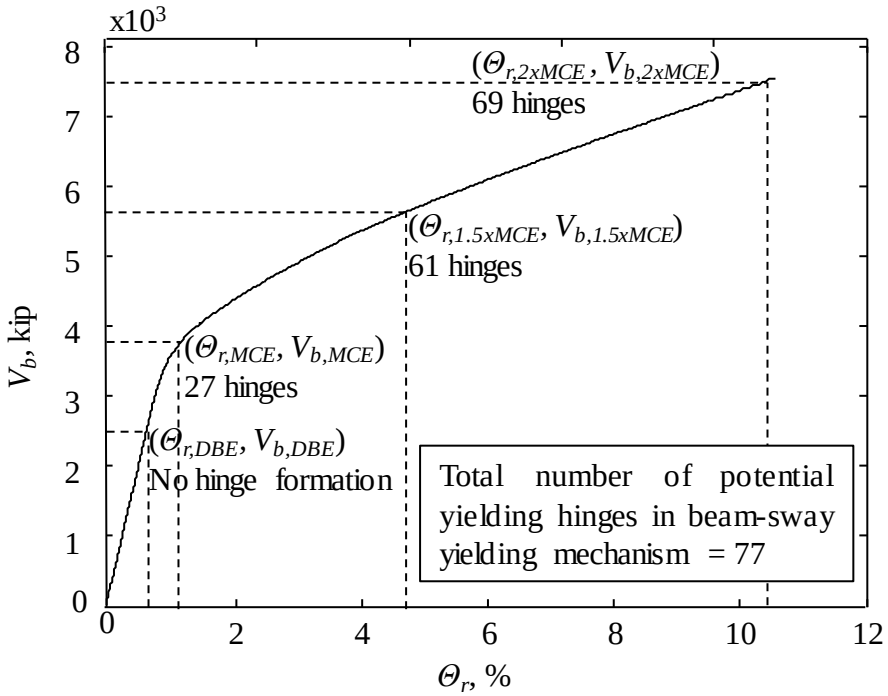

Figure 3.22 V_b vs. Θ_r response of SMRF from monotonic static pushover analysis

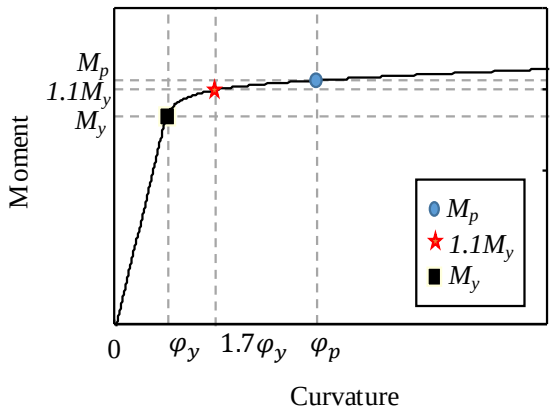

Figure 3.23 V_b vs. Θ_r response of SMRF from monotonic static pushover analysis

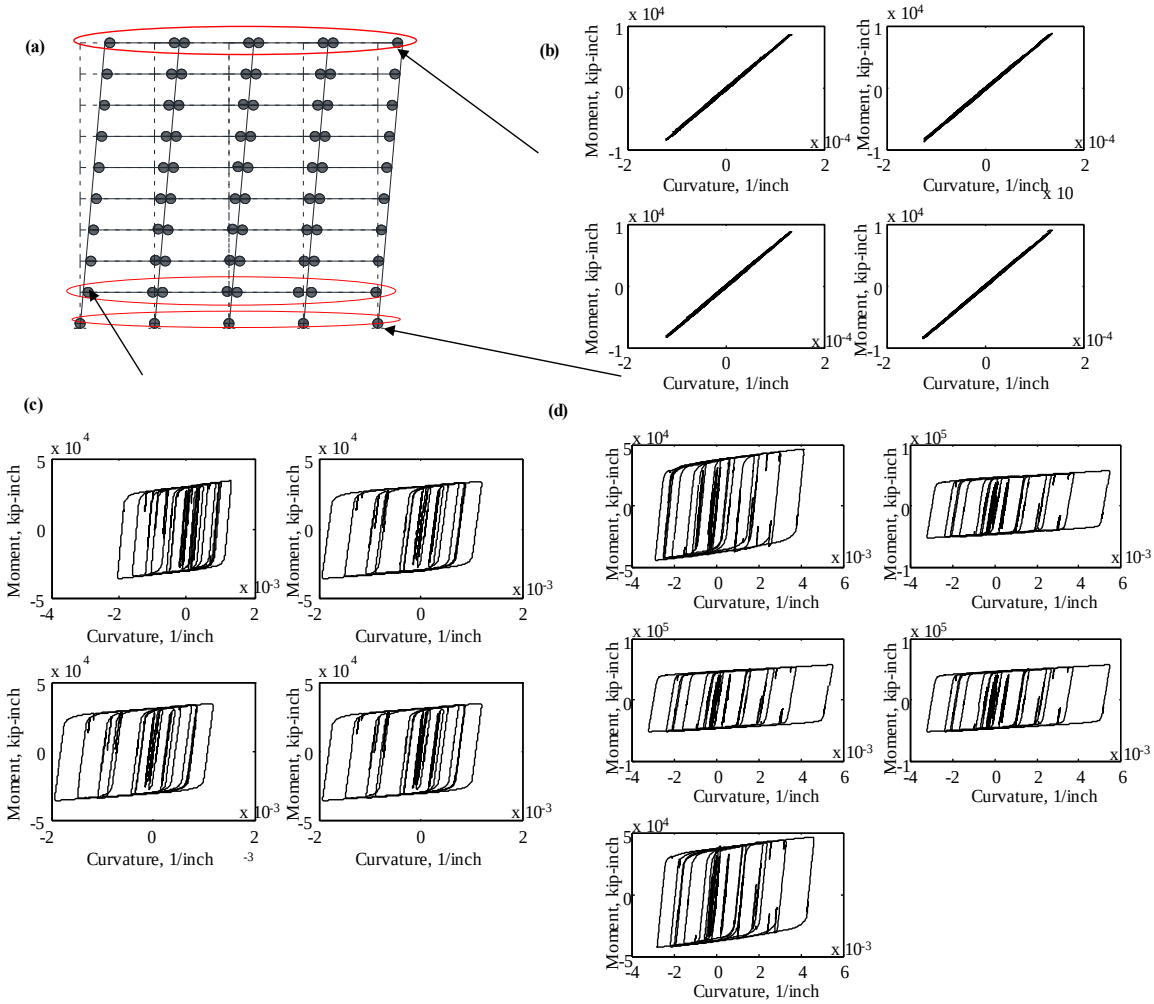

Figure 3.24 (a) Beam-sway yielding mechanism of SMRF; (b) moment vs. curvature hysteresis for hinges formed at left ends of 1st floor and (c) moment vs. curvature hysteresis for hinges formed at right ends of 9th floor beams; (d) moment vs. curvature hysteresis for hinges formed at the base of 1st story columns for SMRF subjected to HWA019N ground motion scaled to two times MCE

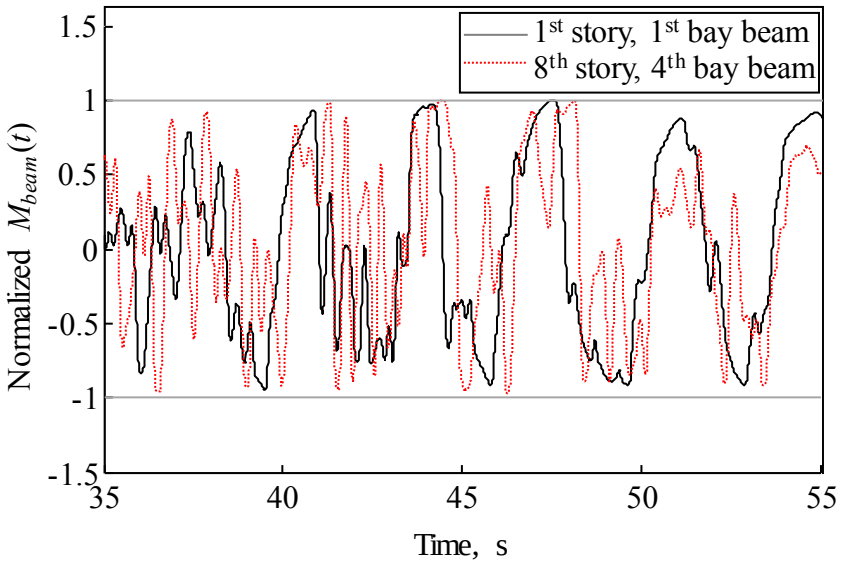

Figure 3.25 $M_{beam}(t)$ normalized by M_{beam} at right ends of 1st story, 1st bay and 8th story, 4th bay beams of SMRF subjected to HWA019N ground motion scaled to two times MCE

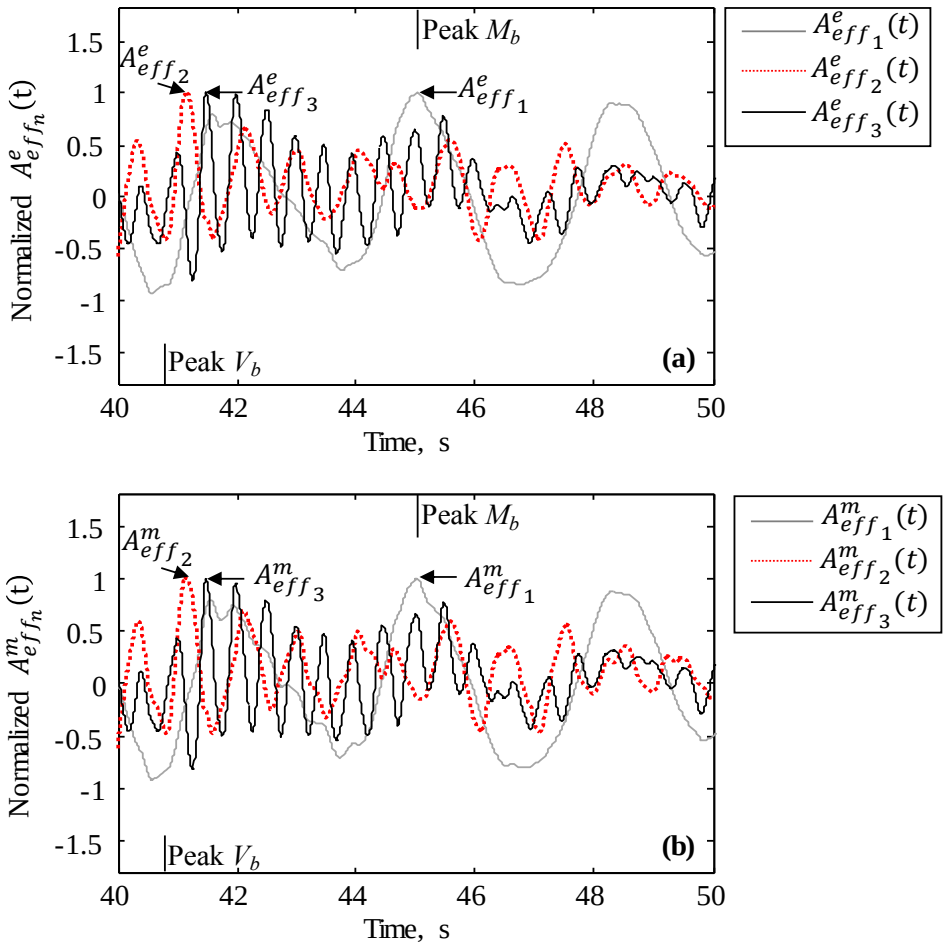

Figure 3.26 (a) $A^e_{eff_n}(t)$ normalized by $A^e_{eff_n}$; (b) $A^m_{eff_n}(t)$ normalized by $A^m_{eff_n}$ for first three modes of SMRF under HWA019N ground motion scaled to DBE

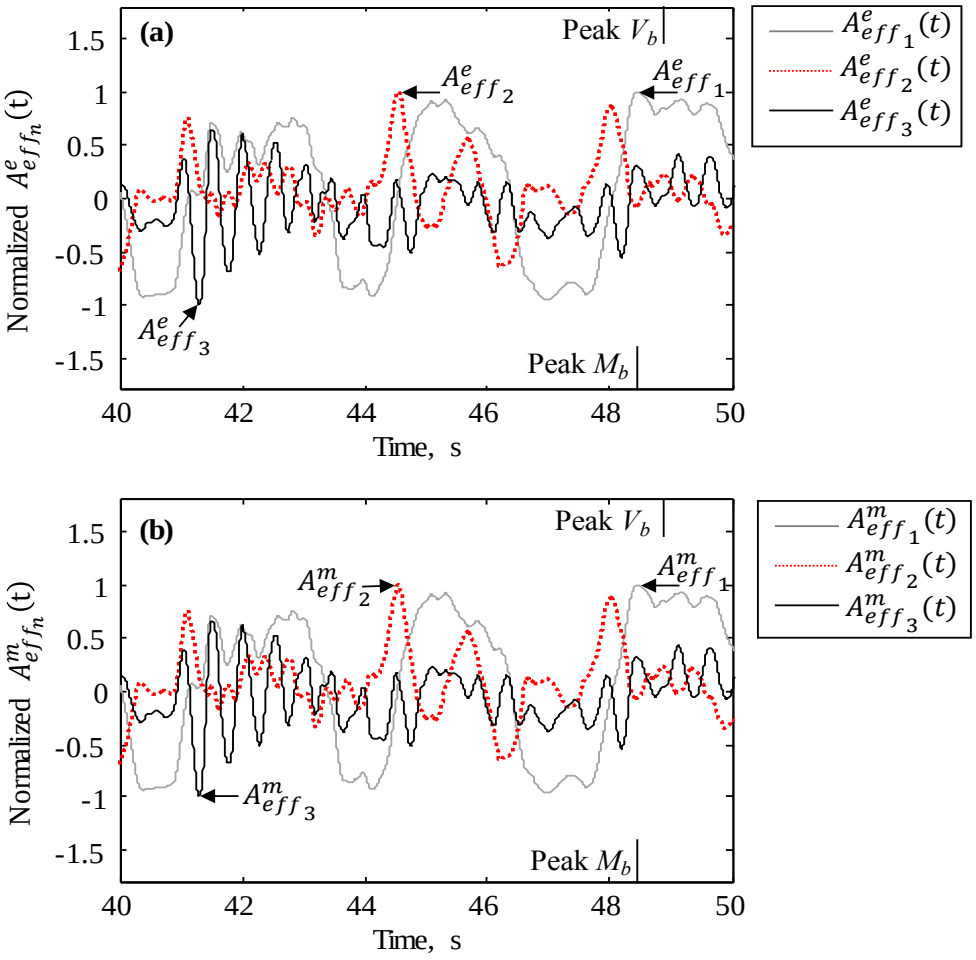

Figure 3.27 (a) $A^e_{eff_n}(t)$ normalized by $A^e_{eff_n}$; (b) $A^m_{eff_n}(t)$ normalized by $A^m_{eff_n}$ for first three modes of SMRF under HWA019N ground motion scaled to two times MCE

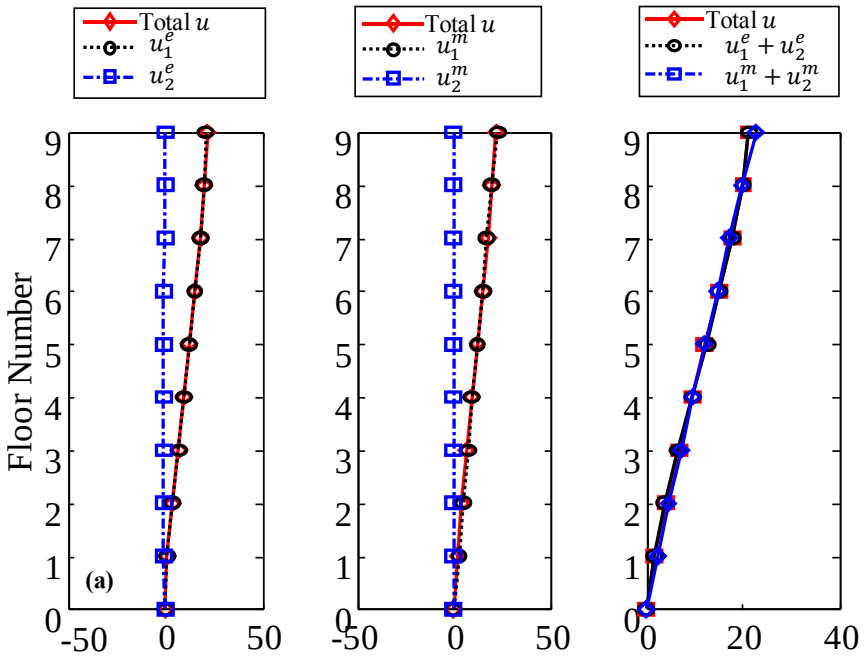

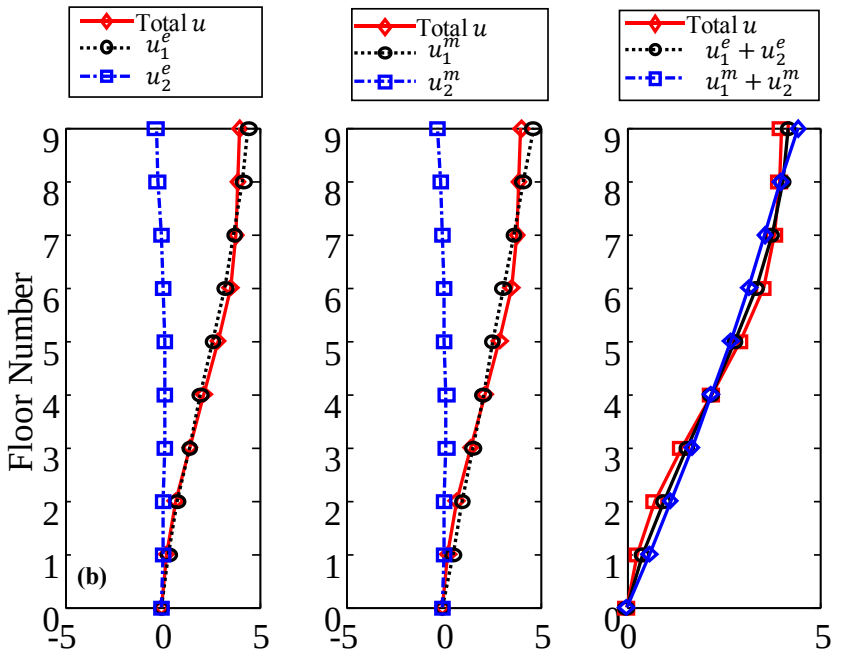

Figure 3.28 $\boldsymbol{u}(t)$ and $\boldsymbol{u}_n(t)$ response envelopes: (a) at the time of peak $M_b(t)$; (b) 10 s after peak $M_b(t)$ under HWA019N ground motion scaled to two times MCE

CHAPTER 4

DAMPING SUBSTRUCTURE CONCEPT FOR MODELING INHERENT DAMPING IN NONLINEAR STRUCTURES

Overview

The model for a nonlinear (NL) seismic response analysis of a building, should include the mass, the gravity force resisting system (GFRS), the lateral force resisting system (LRFS), and the energy dissipation mechanisms of the building. The energy dissipation mechanisms include the hysteretic energy and any other energy dissipated within the LFRS, as well as the inherent damping of the building. The hysteretic energy and other energy (for example, by viscous dampers) dissipated within the LFRS is modeled within the NL numerical model of the LFRS; this topic has been studied extensively for all commonly-used LFRS types. The *inherent damping* of the building is the energy dissipated within the building, which is independent from the hysteretic and other energy dissipated in the LFRS; significantly less research has focused on this inherent energy dissipation and how it can be modeled effectively for a NL seismic response analysis. Models of the inherent damping of the building are the subject of this chapter. The proposed models separate inherent damping from the NL lateral force resisting system (LFRS) through the introduction of a *damping substructure*. Applications of the *damping substructure* (DS) to conventional

structures are presented. The advantage of using a DS is the preservation of the expected static relationships among local forces in the LFRS during NL response analysis by removing the inherent damping model from the NL LFRS model. Important seismic design principles, such as capacity design, require preserving the static relationships among internal forces within the LFRS. The DS concept is extended to enable the modeling of inherent damping of a building using NL viscous damping.

4.1. Introduction

The model for a nonlinear (NL) seismic response analysis of a building (Figure 4.1(a)), should include the mass, the gravity force resisting system (GFRS), the lateral force resisting system (LRFS), and the energy dissipation mechanisms of the building. The energy dissipation mechanisms include (most importantly) the hysteretic energy and any other energy dissipated within the LFRS, as well as the inherent damping of the building. The hysteretic energy and other energy (for example, by viscous dampers) dissipated within the LFRS is modeled within the NL numerical model of the LFRS; this topic has been studied extensively for all commonly-used LFRS types. The *inherent damping* of the building is the energy dissipated within the building, which is independent from the hysteretic and other energy dissipated in the LFRS; significantly less research has focused on this inherent energy dissipation and how it can be modeled effectively for a NL seismic response analysis.

Figure 4.1(b) shows a schematic of a numerical model for a multi-story building, which includes a model for the mass and GFRS (shown as a lean-on column), and a model for the LFRS. The seismic mass is associated with the horizontal displacement degree-of-freedom (DOF) at each floor level. The horizontal displacements of the LFRS model and the GFRS model are constrained to each other with rigid links that model a rigid floor diaphragm at each floor level. We assume that the hysteretic energy and other energy dissipated within the LFRS is modeled within the NL model of the LFRS. Notably, Figure 4.1 shows no specific model for the inherent damping of the building. Such models are the subject of this chapter.

The equations of motion for the linear seismic response of the multi-story building in Figure 4.1 is as follows:

$$\boldsymbol{m}\,\ddot{\boldsymbol{u}} + \boldsymbol{c}\,\dot{\boldsymbol{u}} + \boldsymbol{k}\,\boldsymbol{u} = -\boldsymbol{m}\boldsymbol{i}\,\ddot{u}_g \tag{4.1a}$$

where $\boldsymbol{m}$ = total mass matrix for the building; $\boldsymbol{c}$ = total damping matrix for the building; $\boldsymbol{k}$ = total stiffness matrix for the building; $\ddot{\boldsymbol{u}}$ = acceleration vector; $\dot{\boldsymbol{u}}$ = velocity vector; $\boldsymbol{u}$ = deformation vector; $\ddot{u}_g$ = ground acceleration; $\boldsymbol{i}$ = ground motion influence vector. Note that for a NL seismic response analysis, Eq. (4.1a) is written more generally as follows:

$$\boldsymbol{m}\,\ddot{\boldsymbol{u}} + \boldsymbol{c}\,\dot{\boldsymbol{u}} + \boldsymbol{f}_{\boldsymbol{r}} = -\boldsymbol{m}\boldsymbol{i}\,\ddot{u}_g \tag{4.1b}$$

where $\boldsymbol{f}_{\boldsymbol{r}}$ = the restoring force vector = $\boldsymbol{k}\,\boldsymbol{u}$ when the response is linear.

The total damping matrix for the building, $\boldsymbol{c}$, in Eq. (4.1) is a representation of the inherent damping of the building. Evidence shows that the inherent damping of a building depends on the lateral deformation amplitude, and it may be best to model it with a hysteretic or frictional model (Charney, 2008). However, due to its simplicity, linear viscous damping is widely used to model the inherent damping of a building, as shown in Eq. (4.1) .

Assuming proportional linear viscous damping further simplifies the model for the inherent damping of a building. Proportional linear viscous damping expresses $\boldsymbol{c}$ in terms of $\boldsymbol{m}$ and $\boldsymbol{k}$. The most common form of proportional linear viscous damping is Rayleigh damping, with mass proportional ($\alpha\boldsymbol{m}$) and stiffness proportional ($\beta\boldsymbol{k}$) components, which is a special case of Caughey-series damping (Chopra, 2012). With Rayleigh damping, $\boldsymbol{c}$ is as follows:

$$\boldsymbol{c} = \alpha\boldsymbol{m} + \beta\boldsymbol{k} \tag{4.2}$$

where α, β = factors based on selected modal damping ratios and frequencies of the multi-DOF model for the building, and the modal damping ratios, ζ_n, are assumed based on typical engineering practice or empirical data for low-amplitude dynamic response of typical buildings.

Using Eq. (4.2), Eq. (4.1) is rewritten and re-arranged as follows:

$$\boldsymbol{m}\,\ddot{\boldsymbol{u}} + (\alpha\mathbf{m} + \beta\boldsymbol{k})\,\dot{\boldsymbol{u}} + \boldsymbol{f_r} = -\,\boldsymbol{m}i\,\ddot{u}_g \tag{4.3}$$

$$(\beta \boldsymbol{k})\dot{\boldsymbol{u}} + \boldsymbol{f_r} = -\boldsymbol{m}(\ddot{\boldsymbol{u}} + i\ddot{u}_g + \alpha \dot{\boldsymbol{u}}) \quad (4.4)$$

In the following discussion, the "global" DOF (Figure 4.1(b)) are the primary displacement DOF of a building, which are associated with the vast majority of the seismic mass of the building, and are usually the horizontal displacement DOF at the floor levels of the building. The "local" DOF (Figure 4.1(c)) are displacement DOF within the model of the LFRS, which are usually massless or associated with very small mass related to the total seismic mass of the building. The local DOF are important within the model for the LFRS as they enable accurate modeling of the NL force-deformation response of the LFRS. For the discussion presented in this paper, the local DOF are assumed to be massless.

Eq. (4.1) implies that for each DOF, there are damping forces (from $\boldsymbol{c}\,\dot{\boldsymbol{u}}$) and restoring forces (from $\boldsymbol{f_r}$). These forces for the global DOF are called "global damping forces", denoted f_d^{glo}, and "global restoring forces", denoted f_r^{glo}, and for the local DOF are called "local damping forces", denoted f_d^{local}, and "local restoring forces", denoted f_r^{local}.

When stiffness proportional ($\beta \boldsymbol{k}$) damping is used in the model for the building, f_d^{local} are generated within the LFRS model, which act in parallel with f_r^{local}. For example, Figures 4.1(c) and 4.1(d) show f_d^{local} and f_r^{local} from element 1 and element 2 acting on the horizontal displacement DOF of Node 1. When the local DOF is massless, equilibrium

requires that the sum of all f_d^{local} and f_r^{local} acting on a local DOF is zero, that is, $\sum(f_r^{local} + f_d^{local}) = 0$, as indicated by Eq. (4.4). This is true for both linear and NL models of the LFRS. It can be shown that for a linear model of the LFRS with $\beta\boldsymbol{k}$ damping, the local restoring forces and the local damping forces are in equilibrium independently, that is, $\sum f_r^{local} = 0$ and $\sum f_d^{local} = 0$. However, if non-stiffness proportional damping is used, or if a NL model of the LFRS is used, with a resulting loss of stiffness proportional damping after the LFRS becomes nonlinear, $\sum f_r^{local} \neq 0$ and $\sum f_d^{local} \neq 0$, although, $\sum(f_r^{local} + f_d^{local}) = 0$. One important consequence of $\sum f_r^{local} \neq 0$ at a local DOF, is that the expected static relationships among local forces in the LFRS from a NL response analysis are lost. For example, if one part of the LFRS yields, we expect to see the effects of that yielding on the internal forces of the adjacent parts of the LFRS. Important seismic design principles, such as capacity design, require such an understanding of the static relationships among internal forces within the LFRS, which depend on the assumption that $\sum f_r^{local} = 0$.

For NL seismic response analysis of buildings, three different "Rayleigh-like" damping models are commonly used, which assign "$\beta\boldsymbol{k}$-like" damping to the NL model of the LFRS:

(1) Initial stiffness proportional damping, ζ-k_i, where the damping is based on the factor β multiplied by the initial stiffness coefficients of all elements in the NL LFRS model, which is expressed as follows:

$$(\beta \boldsymbol{k_i})\dot{\boldsymbol{u}} + \boldsymbol{f_r} = -\boldsymbol{m}(\ddot{\boldsymbol{u}} + i\ddot{u}_g + \alpha\dot{\boldsymbol{u}}) \quad (4.5a)$$

Some previous research, for example Hall (2006) and Chang (2013), suggest using ζ-k_i and state that it is computationally efficient and enables an adequate approximation of the modal damping represented by ζ_n.

(b) Tangent stiffness proportional damping, ζ-k_t, where the damping is based on the factor β multiplied by the tangent stiffness coefficients of all elements in the NL LFRS, implying that the damping will change as the stiffness of the LFRS model changes, expressed as follows:

$$(\beta \boldsymbol{k_t})\dot{\boldsymbol{u}} + \boldsymbol{f_r} = -\boldsymbol{m}(\ddot{\boldsymbol{u}} + i\ddot{u}_g + \alpha\dot{\boldsymbol{u}}) \quad (4.5b)$$

Some previous research, for example, Charney (2008), Erduran (2012), and Jehel and Ibrahimbegovic (2014), suggests using ζ-k_t, since ζ-k_i does not capture local stiffness changes occurring in the NL LFRS. Hall (2006) argues that ζ-k_t, is not physically possible and causes discontinuous damping forces.

(c) Non-proportional stiffness based damping, ζ-k_{NP}, where the damping is based on the factor β multiplied by the tangent stiffness coefficients of *some* elements in the NL LFRS model:

$$(\bar{\beta} \boldsymbol{k_i})\dot{\boldsymbol{u}} + \boldsymbol{f_r} = -\boldsymbol{m}(\ddot{\boldsymbol{u}} + i\ddot{u}_g + \alpha\dot{\boldsymbol{u}}) \quad (4.5c)$$

Charney (2008) suggests using ζ-k_{NP} to model the inherent damping of buildings for NL seismic response analyses.

Past research has shown that when ζ-k_i is used, artificially large *local* damping forces are generated in the vicinity of local yielding mechanisms within the LFRS model. As the local yielding mechanism forms, large local relative velocities (deformation rates) are generated within elements in the LFRS model, and when these local relative velocities are multiplied by initial stiffness proportional damping coefficients, large local damping forces are generated. For example, if element 1 in Figure 4.1 yields, the deformation rates in element 1 will grow, generating large damping forces in element 1. Hall (2006) proposed a yielding mechanism to limit the damping forces of the structure, similar to the yielding mechanisms for restoring forces in a NL LFRS model. Similarly, Bernal (1994) proposed condensing massless "local" DOF from $\boldsymbol{k}_i$ of the NL LFRS model before forming the $\beta \boldsymbol{k}_i$ damping matrix (in Eq. (4.5a)), to avoid generating large local damping forces within the LFRS model. However, condensing DOF from only one of the terms in Eq. (4.5a) results in an inconsistent number and arrangement of DOF (and equations) in Eq. (4.5a), which can be addressed in an ad hoc manner in solving these equations, but this approach has not been introduced into commonly-used NL seismic response analysis software.

An important point to note about using ζ-k_i damping is that before yielding of element 1 in Figure 4.1, f_r^{local} from element 1 and element 2 are in equilibrium (since ζ-k_i is used), but after yielding, f_r^{local} from element 1 and element 2 are not in equilibrium from element 1

and element 2, although $\sum(f_r^{local} + f_d^{local})$ from element 1 and element 2 are in equilibrium before and after yielding, (assuming node 1 is massless).

Roke (2010) proposed using a *damping substructure* to model the inherent damping of buildings which use self-centering concentrically brace frames (SC-CBFs) as the LFRS. The *damping substructure* was comprised of linear viscous dashpots. The coefficients for the dashpots were determined from a total proportional damping matrix for the building. Bowland and Charney (2010) suggested eliminating the use of linear viscous damping and proposed two new concepts which incorporate a NL viscous damping model for the inherent damping of buildings. In the first approach, the inherent damping of the building is modeled using rotational damping elements with NL viscous response which are constrained to the main structural elements by rigid-link elements. In the second approach, which was called "instantaneous viscous damping", the inherent damping of the building is modeled using damping forces that are an exponential function of displacement.

This chapter presents two alternate methods to model the inherent damping of a building for NL seismic response analysis. The methods seek the modeling simplicity of proportional linear viscous damping but enable a more realistic representation of the inherent damping for the building. First, several problems encountered using Rayleigh-like proportional damping are illustrated using nonlinear time history analysis (NLTHA) results for a 2-story NL moment resisting frame (MRF) and 6-story NL special concentrically

braced frame (SCBF). To overcome these problems, an approach is introduced which separates the damping model from the NL LFRS model using a linear *damping substructure* (DS) to eliminate excessively large *local* damping forces. The damping substructure concept (DSC) is extended to model the inherent damping of buildings using NL viscous damping models, to avoid generating excessively large damping forces on the *global* DOF.

4.2. Problems Encountered with Rayleigh Proportional Damping Models

4.2.1. Case Study on a 2-story, 1-bay Moment Resisting Frame

To illustrate the problems arising in NL seismic response analysis of buildings with Rayleigh proportional damping models, the seismic response of a 2-story, 1-bay MRF is examined.

Description of MRF Structure

Schematics of the floor plan and elevation of the example MRF building are shown in Figure 4.2. A single MRF from the building, with the associated seismic mass and gravity loads (within the seismic tributary area), constitute the MRF structure.

The MRF building is assumed to be an office-type building on a site in Southern California with NEHRP Site Class D conditions. Dead and live gravity loads for the MRF building

are given in Table 4.1 and Table 4.2. Gravity and seismic loads were considered in the design of a typical MRF from the building. The MRF was designed in accordance with ASCE (2010) requirements. For design, the short period spectral acceleration (S_s) was taken as 1.5g and the 1 s period spectral acceleration (S_1) was taken as 0.6g. Conventional MRSA was used for seismic design of the MRF. The member sizes were governed by the drift control criteria of ASCE (2010). The strong column-weak beam design criterion of AISC (2010) was taken into account. All members of the MRF were ASTM A992 wide-flange shapes with a nominal steel yield strength of 50 ksi, meeting the seismic compactness requirements of AISC (2010).

A two dimensional concentrated plasticity model of the MRF was created in OpenSees (Mazzoni et al., 2009). Each beam and column of the frame was modeled by linear-elastic beam-column elements. The elements were connected to each other (i.e., element joints) using zero length elements (Mazzoni et al., 2009), with each element representing a rotational spring and where all the nonlinearity in the structure was concentrated. A bilinear hysteretic material behavior was assigned to each rotational spring. A lean-on-column with linear-elastic beam-column elements was used to model the second-order effects of the gravity loads within the seismic tributary area of the MRF. Seismic mass was assigned to the horizontal degree-of-freedom of the lean-on-column at each floor level. The horizontal displacements of the MRF and lean-on-column were constrained to each other with rigid links at each floor level. The vertical and horizontal displacements at the base of the lean-on-column were restrained. The corotational coordinate transformation was used for the elements. Figure 4.3 shows the schematic of the numerical model for the MRF. Newmark

constant average acceleration integration and the nonlinear Newton-Krylov solution algorithms were used in the NLTHA.

Three different Rayleigh proportional damping models are employed in the NL model for the MRF:

a. ζ-k_i with 2% damping ratio at the 1st and 2nd (i.e., with α = 0.2286, β= 0.0012) modes is assigned to all elements including the rotational springs;
b. ζ-k_t with 2% damping ratio at the 1st and 2nd modes (i.e., with α = 0.2286, β= 0.0012) is assigned to all elements including the rotational springs;
c. ζ-k_{NP} with 2% damping ratio at the 1st and 2nd modes (i.e., with α = 0.2286, β= 0.0012), in which ζ-k_i is assigned to every element except the rotational springs, as recommended by Charney (2008).

Ground Motion Set used in NLTHA

Several ground motion (GM) records were selected from the GM set developed by Chancellor (2014). These GM were selected in pairs from the NGA (PEER, 2011) database for the site of the MRF building, which has a short period spectral acceleration (S_s) of 1.5g and 1 s period spectral acceleration (S_1) of 0.6g based on ASCE (2010) definitions (ASCE, 2010).

The GM records scaled so that the geometric mean of the GM pair was scaled to matched the design basis earthquake spectrum (ASCE, 2010) over a period range of 0.1-7 s. The scale factor was calculated in accordance with the average scaling method described in Baker (2011). From the GM in Table 4.3, ILA013W GM record was used in the NLTHA of the MRF. The pseudo-acceleration response spectrum of the scaled ILA013W GM is shown in Figure 4.4.

Problems encountered in NLTHA

Previous studies (e.g., Hall, 2006) observed that when ζ-k_i is assigned to the rotational springs, artificially large f_d^{local} are generated when local yielding (i.e., yielding of the bilinear rotational springs) occurs. Figure 4.5 shows that the local viscous moments generated at the first-story, first column end springs is artificially large for ζ-k_i compared to ζ-k_t and ζ-k_{NP}. The nodal rotational velocities considerably increase with the formation of a local yielding mechanisms. This increase in nodal velocities result in large f_d^{local} when ζ-k_i damping is used. In ζ-k_t, the stiffness coefficients for the rotational DOFs at the plastic hinge locations are reduced when the local yielding mechanism (i.e., yielding of springs) occurs. Thus, the generation of artificially large f_d^{local} is avoided, since, in ζ-k_t the large nodal velocities are multiplied by tangent stiffness coefficients, which are much smaller than initial stiffness proportional damping coefficients. Similarly, in ζ-k_{NP}, since no damping coefficients are assigned to the elements (i.e., yielding bilinear rotational springs in this case) which will form yielding hinges, the increase in rotational velocities with the yielding of the rotational springs does not trigger the generation of artificially large f_d^{local}.

As stated earlier, for NL models of the LFRS, $\sum f_r^{local} \neq 0$ and $\sum f_d^{local} \neq 0$, although $\sum (f_r^{local} + f_d^{local}) = 0$, and the static relationships among internal forces within the LFRS with stiffness proportional damping, are very important for seismic design purposes, such as capacity design, which depends on $\sum f_r^{local} = 0$. Figure 4.6 illustrates how $\sum f_r^{local} \neq 0$ for all three types of stiffness proportional damping considered in this study. As shown in Figure 4.6, the internal member overturning moment response at the first-story, first-bay column end (M_m) is not in equilibrium with the spring force (M_s) so as the reaction force (M_r), unless the local viscous moment (M_d) is taken into account. The difference between M_m and M_r is largest for the model with ζ-k_i, since the generated local M_d is largest for this case (Figure 4.5). Figure 4.6 further shows the free body diagrams illustrating the contribution of local M_d to M_s, while $M_m + M_d = M_s$, $M_m \neq M_s$.

Figure 4.7 shows the V_{max}, M_{max}, and u_{max} response envelopes for each MRF with different Rayleigh proportional damping models. It can be seen from Figure 4.7 that for this particular structure, ζ-k_i leads to larger base shear (V_b) and base overturning moment (M_b) responses, but smaller deformation (u) responses along the height of the structure compared to ζ-k_t and ζ-k_{NP}.

These results show that stiffness proportional damping applied to a simple NL model of a simple 2-story MRF with only ζ_n = 2%, generates artificially large local damping forces. Using ζ-k_t and ζ-k_{NP} does not lead to static equilibrium between restoring (i.e., $\sum f_r^{local} \neq 0$).

4.2.2. Case Study of 6-Story Special Concentrically Braced Frame

To illustrate the problems arising in analysis of a NL model of a special concentrically braced frame (SCBF) with the use of stiffness proportional damping, the seismic response from NLTHA of a 6-story SCBF is examined. The effect of stiffness proportional damping on the critical buckling load capacity of proportionally damped NL braces is also investigated.

Description of SCBF Structure

A 6-story SCBF designed by Tahmasebi (2016) was used in this study. Figure 4.8 shows the floor plan and elevation view of the SCBF. The same dead and live loads tabulated for the MRF in Table 4.1 and Table 4.2 were also used in the design of this 6-story SCBF. The SCBF was designed in accordance with the ASCE (2010) requirements for a Site Class D. The seismic design category is Category D, the short period spectral acceleration (S_s) is 1.5g, and the 1 sec period spectral acceleration (S_1) is 0.6g (ASCE, 2010). The ELF procedure in ASCE (2010) was employed to design the SC-CBF.

A two dimensional numerical model of the SC-CBF was developed in OpenSees (Mazzoni et al., 2009). Each beam and column of the SCBF was modeled by five force-based beam-column elements with fiber sections. Five integration points were used along the length of each force-based beam-column elements. Gauss-Lobatto numerical integration was used.

Each brace of the SCBF was modeled using sixteen force-based beam-column elements with fiber sections. The brace connections were modeled as pin-ended connections, while the beam-column connections were modeled as rigid connections. The SCBF columns were fixed at the base. In AISC (2010), the maximum permitted out-of-straightness of a brace is 1/1000 of the length, L_{brace},(i.e., L_{brace}/1000) of the brace. Accordingly, to create initiate buckling, an initial imperfection of L_{brace}/1000 was assigned to each brace in the model. The effects of low-cycle fatigue and fracture of the braces (Powell, 2009) were also taken into account.

A lean-on-column with elastic beam-column elements was used to model the second-order effects of the gravity loads within the seismic tributary area of the SCBF. Seismic mass was assigned to the horizontal degree-of-freedom of the lean-on-column at each floor level. The horizontal displacements of the SCBF and lean-on-column were constrained to each other with rigid links at each floor level. The vertical and horizontal displacements at the base of the lean-on-column were restrained.

The corotational coordinate transformation was used for all elements. Newmark constant average acceleration integration and the nonlinear Newton-Krylov solution algorithms were used in the NLTHA. Two different types of stiffness proportional damping models are employed in NL model of the 6-story SCBF:

a. ζ-k_i with 3% damping ratio at 1st and 2nd modes (i.e., $\alpha = 0.4724$, $\beta = 0.001886$) is assigned to all elements including the braces;

b. ζ-k_t with 3% damping ratio at 1st and 2nd modes (i.e., $\alpha = 0.4724$, $\beta = 0.001886$) is assigned to all elements including the braces.

The SCBF is subjected to the ABN000 GM record (Table 4.3). The response of the SCBF under a linearly increasing portion of the ABN000 GM is examined (see Figure 4.9). Using the scaling method explained for the ILA013W GM record, the ABN000 GM record was scaled to the design spectrum from ASCE (2010). Figure 4.4 shows the scaled pseudo-acceleration response spectrum for the ABN000 GM record. To observe the brace buckling more easily, the ABN000 GM is further scaled up to the two times the maximum considered earthquake (MCE) level (FEMA 454, 2006) (i.e, 3 times the scale factor for the design spectrum).

Problems encountered in NLTHA

Figure 4.10 shows the brace axial force versus (vs.) brace axial deformation histories for the 1st -story, right-hand side (RHS) W12x120 brace of the SCBF from static pushover analysis and NLTHA with ζ-k_i and ζ-k_t. Based on static pushover analysis, the critical buckling load capacity of the brace is 1512 kip. However, as seen in Figure 4.10, the buckling load capacity of the brace for the SCBF model with ζ-k_i is 1860 kip. There is a 25% increase in the buckling load capacity due to the artificially large f_d^{local} generated in the direction of the chord of the brace when the brace buckles. As the brace buckles, large local relative velocities (deformation rates) are generated elements near the mid length of the brace and when these local relative velocities are multiplied by the initial stiffness

proportional damping coefficients of the brace elements, large f_d^{local} are generated which causes an overestimate of actual buckling load capacity of the brace.

On the other hand, when ζ-k_t is used, the buckling load capacity of the brace is calculated as 1581 kip. Although this result is not as large as for the model with ζ-k_i, some numerical convergence problems arise at the time of brace buckling. Figure 4.11 shows the axial viscous forces in the brace with ζ-k_i and ζ-k_t at the time of brace-buckling. For the model with ζ-k_i, the viscous forces are increasing in single direction and resisting the buckling of the brace. For the model with ζ-k_t, due to the rapid stiffness change in the brace, the viscous forces instantaneously increase and changes sign after the brace buckling. This suggests that for the model with ζ-k_t, f_d^{local} acts in the direction of the brace buckling and amplifies post-buckling deformation response of the brace. These results suggest that both ζ-k_i and ζ-k_t lead to the overestimation of the buckling load capacity of the brace.

4.3. Damping Substructure Concept and Modeling the Inherent Damping of a Building for NL Seismic Response Analysis

The examples in the previous section show the problems related to the use of proportional linear stiffness viscous damping applied to the NL model of the LFRS to model the inherent damping of a building. To summarize, the major problems encountered are the generation of artificially large f_d^{local} in the vicinity of local yielding mechanisms within the NL LFRS model and loss of expected static relationships among local forces in the LFRS.

This section investigates methods to model the inherent damping of a building which possess the simplicity of proportional linear viscous damping, but enable a more consistent representation of the inherent damping of a building. A *damping substructure concept* (DSC) is developed first. The DSC separates the inherent damping of the building from the NL LFRS model. Instead, the model of the inherent damping of the building is modeled through a *damping substructure* which is placed in parallel to the NL LFRS and is separate from the NL LFRS model. Advantage is that local DOF of damping substructure and NL LFRS model are separate.

The following section presents the DSC and proposes two different modeling approaches to model the inherent damping of NL buildings using a *damping substructure*.

4.4. DSC Formulation

When the DSC is used, the model for nonlinear (NL) seismic response analysis of a building is as a combination of three main substructures: inertial force (mass) substructure, damping substructure, and restoring force substructure. The substructuring concept is explained in Figure 4.12(a) for the example, 2-story. As seen in Figure 4.12(a), a 2-story MRF building can be expressed as a superposition of the three main substructures. While the (1) the inertial force substructure represents the floor masses of the structure without any contributions to stiffness and damping of the structure; (2) the damping substructure represents only the inherent damping of the building without any contributions to the mass and stiffness of the structure, and (3) the restoring force substructure represents only the

stiffness and strength of the building without any mass and damping assignments. Inertial forces, $\boldsymbol{f_I}$, which are a function of the mass matrix of the structure, $\boldsymbol{m}$, and acceleration, $\ddot{u}$, act on the inertial force substructure. Damping forces, $\boldsymbol{f_D}$, which are a function of the damping matrix, $\boldsymbol{c}$, and velocity, $\dot{u}$- act on the damping substructure. Restoring forces, $\boldsymbol{f_R}$,, which are a function of structural stiffness, $\boldsymbol{k}$, (for a linear structure) and displacement, u, act on the restoring force substructure. In presence of an externally applied load, $\boldsymbol{P}$, the sum of these three force components (i.e., $\boldsymbol{f_I}$, $\boldsymbol{f_D}$, and $\boldsymbol{f_R}$) equate to the externally applied load:

$$\boldsymbol{f_I} + \boldsymbol{f_D} + \boldsymbol{f_R} = -\boldsymbol{P} \tag{4.6}$$

$$\boldsymbol{m}\ddot{u} + \boldsymbol{c}\dot{u} + \boldsymbol{k}u = -\boldsymbol{P} \tag{4.7}$$

Under seismic excitation, the effects of the ground acceleration ($\ddot{u}_g$) also generate inertial forces which act on the inertial force substructure substructure. In such a case, the seismic excitation force and the three force components, $\boldsymbol{f_I}$, $\boldsymbol{f_D}$, and $\boldsymbol{f_R}$ are in equilibrium with each other (as shown in Figure 4.12 (b)), as follows:

$$\boldsymbol{m}\left(\ddot{u} + i\ddot{u}_g\right) + \boldsymbol{c}\dot{u} + \boldsymbol{k}u = 0 \tag{4.8a}$$

$$\boldsymbol{m}\ddot{u}^t + \boldsymbol{c}\dot{u} + \boldsymbol{k}u = 0 \tag{4.8b}$$

The restoring force substructure can be separated into two subcomponent structures: the restoring force substructure representing the gravity frame (including the P-delta effects)

and the restoring force substructure representing the LFRS of the building (as shown in Figure 4.12(c)). While the gravity frame is usually linear-elastic with geometric stiffness of the building, the LFRS model is usually NL. The restoring forces for the gravity frame substructure, $\boldsymbol{f_R^g}$, are a function of the stiffness of the gravity frame, $\boldsymbol{k^g}$, and u. The restoring forces for the LFRS substructure, $\boldsymbol{f_R^{lat}}$, are a function of the NL model of the LFRS, $\boldsymbol{k^{lat}}$, and u. Under seismic excitation, $\boldsymbol{f_R^g}$ and $\boldsymbol{f_R^{lat}}$ are in equilibrium with $\boldsymbol{f_I}$ and $\boldsymbol{f_D}$, as follows:

$$\boldsymbol{f_I} + \boldsymbol{f_D} + \boldsymbol{f_R^g} + \boldsymbol{f_R^{lat}} = 0 \tag{4.9}$$

$$\boldsymbol{m}(\ddot{u}^t) + \boldsymbol{c}\dot{u} + \boldsymbol{k^g}u + \boldsymbol{f_R^{lat}} = 0 \tag{4.10}$$

The inherent damping of the building modeled using linear viscous damping and the damping substructure could be understood to be comprised of linear dashpots (as shown in Figure 4.12(d)). For simplicity, proportional linear viscous damping (Eq. (4.3)) can be used to model the inherent damping. The damping matrix can be expressed as a function of $\boldsymbol{m}$ and $\boldsymbol{k}$, as follows:

$$\boldsymbol{m}(\ddot{u}^t) + (\alpha\boldsymbol{m} + \beta\boldsymbol{k})\dot{u} + \boldsymbol{k^g}u + \boldsymbol{f_R^{lat}} = 0 \tag{4.11}$$

The damping substructure can be separated into two component substructures: mass proportional and stiffness proportional damping substructures (as shown in Figure 4.12(e)). The damping forces for the mass proportional damping substructure, $\boldsymbol{f_D^m}$, are a function $\boldsymbol{m}$

and $\dot{u}$; while the damping forces for stiffness proportional damping substructure, $\boldsymbol{f_D^k}$, are a function of $\beta\boldsymbol{k}$ and $\dot{u}$. Under seismic loading, $\boldsymbol{f_D^m}$ and $\boldsymbol{f_D^k}$ are in equilibrium with $\boldsymbol{f_I}$, $\boldsymbol{f_R^g}$, and $\boldsymbol{f_R^{lat}}$, as follows:

$$\boldsymbol{f_I} + \boldsymbol{f_D^m} + \boldsymbol{f_D^k} + \boldsymbol{f_R^g} + \boldsymbol{f_R^{lat}} = \boldsymbol{0} \tag{4.12}$$

$$\boldsymbol{m}(\ddot{u}^t) + (\alpha\boldsymbol{m})\dot{u} + (\beta\boldsymbol{k})\dot{u} + \boldsymbol{k^g}u + \boldsymbol{f_R^{lat}} = 0 \tag{4.13}$$

The stiffness proportional damping substructure can be further separated into two component substructures: the damping substructure proportional to the stiffness of the gravity frame substructure and the damping substructure proportional to the initial stiffness of the LFRS. While the damping forces for the damping substructure proportional to the stiffness of the gravity frame are a function of $\boldsymbol{k^g}$ and $\dot{u}$, the damping forces for the damping substructure proportional to the initial stiffness of the NL LFRS are a function of $\boldsymbol{k^{lat}}$ and $\dot{u}$, as follows:

$$\boldsymbol{m}(\ddot{u}^t) + (\alpha\boldsymbol{m})\dot{u} + (\beta\boldsymbol{k^g})\dot{u} + (\beta\boldsymbol{k^{lat}})\dot{u} + \boldsymbol{k^g}u + \boldsymbol{f_R^{lat}} = 0 \tag{4.14}$$

While creating the numerical model of a building, the inertial force substructure and mass-proportional damping substructures can be combined. Similarly, the restoring force substructure for the gravity frame and the corresponding stiffness proportional damping substructure can be combined, and since both of them are linear (Figure 4.12(f)). Therefore, the equations of motion for seismic loading can be written as follows:

$$(\boldsymbol{f_I} + \boldsymbol{f_D^m}) + \left(\boldsymbol{f_D^k} + \boldsymbol{f_R^g}\right) + \boldsymbol{f_R^{lat}} = \boldsymbol{P} = -\boldsymbol{mi}\ddot{u}_g \quad (4.15)$$

$$[\boldsymbol{m}(\ddot{u}^t) + (\alpha\boldsymbol{m})\dot{u}] + [(\beta\boldsymbol{k^g})\dot{u} + \boldsymbol{k^g}u] + \left(\beta\boldsymbol{k^{lat}}\right)\dot{u} + \boldsymbol{f_R^{lat}} = 0 \quad (4.16)$$

4.5. Numerical Model for Damping Substructure

Exploiting the DSC, the inherent damping of a building for NL seismic response analysis can be separated from the NL LFRS as described above.

Based on Eq.(4.16) and shown in Figure 4.12(f), the two-dimensional numerical model of a building for NL seismic response analysis can be constructed using four substructures, which are placed in parallel to each other in the numerical model and connected to each other using rigid links. While global DOFs of the substructures are constrained to each other using rigid links, the local DOFs are not constrained, which prevents large local relative rotational velocities generated in the NL LFRS after yielding from influencing damping forces within the damping substructure.

In order not to overestimate the lateral stiffness capacity of the building, the stiffness of the stiffens proportional DS should be reduced by a factor (e.g., $F>10^5$) and to represent the inherent damping capacity of the building accurately the β coefficient should be scaled by the same factor, F. (i.e., this enables having the same amount of $\beta\boldsymbol{k}$ as the linear-elastic

LFRS). Since the stiffness proportional damping substructure is linear-elastic, it does not matter whether to model the Rayleigh proportional damping using ζ-k_i or ζ-k_t.

To indicate that the inherent damping capacity of a building is modeled using DSC, ζ-DS abbreviation is used in the rest of this chapter.

4.6. Modeling DS using Linear-Elastic Dashpots based on Roke et al. (2010)

Another way of modeling a DS in the numerical model of a building, is placing a series of linear-elastic dashpots in parallel to the numerical model of the NL LFRS and connecting it to the nodes of the lean-on-column, as proposed by Roke et al. (2010). For example, Figure 4.13 shows the DS for the SCBF, which is modeled using parallel dashpots. Each dashpot coefficient is determined from the proportional ***c*** matrix of the structure. While this approach requires a more complex finite element model and mathematical calculations to determine the dashpot coefficients, it enables not only the use of other proportional damping models in addition to Rayleigh proportional damping model such as Caughey damping and Superposition of Modal Damping Matrices method but also the extension of the concept to nonlinear viscous and non-proportional damping.

In this approach, for an N-story structure, N parallel damping substructures and in total [N*(N+1)/2] linear-elastic dashpots are required (Figure 4.13). To determine the damping coefficients of each dashpot for stiffness proportional linear viscous damping models, the

proportional damping matrix should be formed using either a Rayleigh-like proportional damping model, Caughey damping model or the method of Superposition of Modal Damping Matrices (Chopra, 2012):

$$\boldsymbol{c} = \alpha\boldsymbol{m} + \beta\boldsymbol{k} = \begin{bmatrix} c_{11} & \cdots & c_{1N} \\ \vdots & \ddots & \vdots \\ c_{N1} & \cdots & c_{NN} \end{bmatrix} \tag{4.17}$$

The coefficients of the damping matrix, c_{in} can be expressed in terms of dashpot coefficients, $\bar{c}_{in}$.

$$\boldsymbol{c} = \begin{bmatrix} \bar{c}_{11} + \bar{c}_{12} + \bar{c}_{13} + \cdots + \bar{c}_{1N} & \cdots & -\bar{c}_{1N} \\ \vdots & \ddots & \vdots \\ -\bar{c}_{N1} & \cdots & \bar{c}_{N1} + \bar{c}_{N2} + \bar{c}_{N3} + \cdots + \bar{c}_{NN} \end{bmatrix} \tag{4.18}$$

From Eq. (4.18), the dashpot coefficients of the off-diagonal elements are calculated as follows:

$$\bar{c}_{in} = -c_{in} \text{ , for i≠n} \tag{4.19}$$

Similarly, from Eq. (4.18), the dashpot coefficients of diagonal elements are calculated as follows:

$$\bar{c}_{ii} = c_{ii} - \sum_n \bar{c}_{in} \tag{4.20}$$

Then, the damping force provided by each dashpot is calculated, as follows:

$$f_D = \bar{c}_{ij}\,(\dot{u})^{\alpha_d} \tag{4.21}$$

where α_d = 1.0 for linear viscous damping and vary in between (0,1) for NL viscous damping.

To indicate that the inherent damping of a building for NL seismic response history analysis is modeled using a damping substructure with parallel linear dashpots, ζ-LDP abbreviation is used in the rest of this chapter.

4.7. Applying DSC to Case-Study Structures

To illustrate that the problems arising in NL seismic response analysis of buildings with Rayleigh proportional damping models are precluded with the use of DSC, the seismic responses of example structures with DS are examined.

4.7.1. Case Study on the 2-Story, 1-bay Moment Resisting Frame

Inherent damping of the MRF is modeled using ζ-DS and ζ-LDP and NLTHA are performed under ILA013W GM record. Figure 4.14 shows the schematics of the numerical models of the NL MRF with ζ-DS and ζ-LDP are shown, respectively. The dashpot coefficients, $\bar{c}_{in}$, for the ζ-LDP is determined from the damping matrix, $\boldsymbol{c}$, constructed using an initial stiffness proportional damping model (Eq. 4.18). Table 4.4 shows the

coefficients of the damping matrix, $\boldsymbol{c}$, and the linear dashpot coefficients calculated using Eq. (4.19) and Eq. (4.20).

Figure 4.15 shows the viscous moment and rotational velocity histories at the first-story, first-bay column bottom. As it is seen in Figure 4.15, the generation of artificially large local viscous moments is avoided in the model with ζ-DS as opposed to the model with ζ-k_i. Although the damping matrix is constructed based on the initial stiffness proportional damping for both cases (i.e., ζ-DS and ζ-k_i), the viscous moments generated in the model with ζ-k_i is significantly larger than the model with ζ-DS**.** These results suggest that by separating the inherent damping of the building from the NL LFRS model, the effect of the nonlinearity developed in the NL LFRS on damping forces is precluded.

Figure 4.16 compares the story moment response histories at the bottom of first-story column, i.e., M_m, with the spring moment hysteresis, i.e., M_s, for the models with ζ-DS and ζ-LDP. For both cases, the M_m are in equilibrium with the M_s without the contribution of M_d, unlike to the Rayleigh proportional damping models, i.e., ζ-k_i ,ζ-k_t, and ζ-k_{NP}, as it was shown in Figure 4.9. Therefore, by modeling the inherent damping capacity of a building using DSC, the static relationships among local forces in the NL LFRS are preserved.

Figure 4.17 shows the comparisons of the V_{max}, M_{max}, and u_{max} response envelopes for the MRF models with ζ-k_i, ζ-k_t, ζ-k_{NP}, ζ-DS, and ζ-LDP under ILA013W GM record. As seen

in Figure 4.17, for the models with ζ-DS, and ζ-LDP, neither the force response is overestimated nor the displacement response is underestimated like the model with ζ-k_i. V_{max}, M_{max}, and u_{max} responses are similar for the models with ζ -k_t, ζ-k_{NP}, ζ-DS, and ζ-LDP; however, as it was mentioned previously, all Rayleigh-like stiffness proportional damping models lead to the loss of static relationships among local forces in the LFRS.

4.7.2. Case Study of the 6-story Special Concentrically Braced Frame (SCBF)

The SCBF is modeled using ζ-DS and ζ-LDP, in which the damping matrix and corresponding dashpot coefficients are calculated based on the initial stiffness proportional damping model (Eq. 4.19). Table 4.5 shows the coefficients of the damping matrix, $\boldsymbol{c}$. Table 4.6 shows the linear dashpot coefficients, $\bar{c}_{ij}$, calculated using Eq. (4.19) and Eq. (4.20).

Figure 4.18 shows a schematic of the numerical models of SCBF with ζ-DS. Similar to the numerical models with ζ-k_i and ζ-k_t, NLTHA are performed on the numerical models with are ζ-DS and ζ-LDP under a linearly increasing portion of the ABN000 GM record scaled to the two times of the MCE level (Figure 4.9).

Figure 4.19 shows the brace axial force vs. brace axial deformation histories for the 1st story, RHS brace from the static pushover analysis and NLTHA of the structural models with ζ-DS and ζ-LDP. As seen in Figure 4.19, the brace axial force vs. brace axial

deformation histories almost match exactly with each other for all three cases. The buckling load capacity of the brace is found as 1512 kip, 1510 kip, and 1512 kip from static pushover analysis and the NLTHA with ζ-DS and ζ-LDP, respectively. These results imply that the contribution of viscous forces on the buckling load capacity of the NL braces is precluded in the models with ζ-DS and ζ-LDP.

4.8. Nonlinear Viscous Damping

In the previous sections, it was shown how the inherent damping of a building can be modeled separately from NL LFRS by using a DS. In these examples the inherent damping of structures was quantified using the linear viscous damping. However, although in the DSC the damping forces are isolated from the effects of local yielding mechanisms developed in the NL LFRS, since the total damping matrix of the system is constructed using linear viscous damping models, the damping forces that are generated during the seismic response of the building are still not bounded and tend to increase linearly with increasing velocity (see Eq. (4.21)). To bound the damping forces, NL viscous damping models need to be used. Therefore, the DSC is extended to enable the modeling of inherent damping of a building based on NL viscous damping so that the damping forces which develop during the seismic response of the building can be bounded and capped at a certain level.

4.8.1. Theory and Numerical Modeling of NL Viscous Damping based on DSC

To construct a DS based on NL viscous damping, the approach proposed by Roke et al. (2010) is modified and instead of linear dashpots, a series of NL dashpots are placed in parallel to the numerical model of NL LFRS and its nodes are constrained to the nodes of lean-on-column using rigid links. The dashpot coefficients are determined based on linear-elastic state of the structure using the initial stiffness proportional damping model as described in Section 3.3.

In this study, it is proposed that the linear dashpots should start behaving nonlinearly after the predefined maximum story drift limit is reached during NLTHA. This drift limit is set as 0.5%, in this study, which is the maximum expected story drift for a building subjected to a Frequently Occurring Earthquake (FOE; FEMA 454, 2006). Assuming harmonic excitation, the corresponding minimum velocity, $\dot{u}_{min}$, after which the viscous dashpot starts behaving nonlinearly is calculated by multiplying the maximum drift that each dashpot is experiencing based on their positions in the parallel DS, u_{cin}, with the first mode natural frequency, ω_1. So, for the dashpots representing the off-diagonal elements of $\bar{\boldsymbol{c}}$ in Eq. (4.18), the minimum velocity is set as follows:

$$\dot{u}_{in,min} = u_{cin}(\omega_1) \quad \text{, for i<n} \tag{4.22}$$

$$\dot{u}_{in,min} = (n-i)u_0(\omega_1) \quad \text{, for i<n} \tag{4.23}$$

where u_0 = maximum story displacement for 5% maximum story drift, i.e., $u_0 = (0.005)(H_{story})$; H_{story} = story height, in; ω_1 = first mode natural frequency; i = the dof and

the corresponding story which dashpots are constrained to; n = nth dof and nth story above the story of constraining dof i

For the dashpots representing the diagonal elements of $\bar{\boldsymbol{c}}$ and with dashpot coefficients c_{ii} (Eq. (4.20)), the minimum velocity for the transition from linear to NL viscous damping is calculated as follows:

$$\dot{u}_{ii,min} = (i)u_0(\omega_1) \tag{4.24}$$

Although the viscous damping models are widely used to model the inherent damping capacity of a building for seismic history analysis, the experimental studies have shown that the inherent damping capacity of a building is not a property of velocity or frequency but proportional to displacement amplitude (Clough and Penzien, 1975). It was stated that the hysteretic or frictions based damping models can represent the inherent damping of structures more accurately compared to viscous damping models (Charney, 2008). It is also known that as the α_d constant (Eq. (4.21)) approaches to zero, the viscous damping becomes velocity independent and approaches to the friction damping. Consequently, to have a more friction dominated response in the NL range of the viscous dashpots, the α_d constant is set to 0.2 when the predefined minimum velocity, $\dot{u}_{in,min}$ and $\dot{u}_{ii,min}$, is exceeded in each dashpot and the damping force at each dashpot is calculated accordingly:

$$f_{D_{in}} = \begin{Bmatrix} \bar{c}_{in}(\dot{u}_n)^{\alpha_d=1.0}, \text{for } \dot{u}_n < \dot{u}_{in,min} \\ \bar{c}_{in}(\dot{u}_n)^{\alpha_d=0.2}, \text{for } \dot{u}_n > \dot{u}_{in,min} \end{Bmatrix} \tag{4.25}$$

where $f_{D_{in}}$ = Damping force generated by the dashpot with a dashpot coefficient $\bar{c}_{in}$

To indicate that the inherent damping of a building is modeled using a damping substructure composed of a series of parallel NL dashpots, ζ-NLDP abbreviation is used in the rest of this chapter.

4.8.2. Applying ζ-NLDP on Example Structures

The inherent damping of example structures is modeled using ζ-NLDP. It is shown that damping forces developing in a building during seismic excitation can be bounded using NL viscous damping unlike to linear viscous damping.

4.8.2.1. Case Study on MRF

Inherent damping of the MRF is modeled using ζ-NLDP and NLTHA performed under ILA013W GM record. The $\dot{u}_{in,min}$ calculated for each dashpot using Eq.(4.22) and Eq.(4.23) for a 0.5% maximum drift limit is tabulated in Table 4.7. Figure 4.20(a) shows the viscous damping force generated by the first-story dashpot having a dashpot coefficient of $\bar{c}_{11}$, $f_{D_{11}}$, against the first-story translational velocity, $\dot{u}_{11}$, for the models with ζ-LDP and ζ-NLDP. As seen in Figure 4.20(a), for the model with ζ-NLDP, $f_{D_{11}}$is kept at maximum 3 kip, while for the model with ζ-LDP, $f_{D_{11}}$is almost tripled and reached to as large as 8.5 kip. Figure 4.20(b) shows the $f_{D_{11}}$ against the first-story translational

displacement, u_{11} for the models with both ζ-LDP and ζ-NLDP. As seen in Figure 4.20(b), despite the decrease in $f_{D_{11}}$, u_{11}has increased by 0.1 inch (i.e., ~2%) for the model with ζ-NLDP.

Figure 4.21 shows the V_{max}, M_{max}, and u_{max} response envelopes for the MRF with ζ-k_i, ζ-LDP, and ζ-NLDP models analyzed under ILA013W GM record. The base shear response is increased by 1% for the model with ζ-NLDP compared to the model with ζ-LDP, which is negligibly small. As it is also seen in Figure 4.22, the roof drift has increased by 2.5% for the model with ζ-NLDP compared to the model with ζ-LDP. It is once again observed in Figure 4.21 and Figure 4.22 that the ζ-k_i is causing considerably unconservative displacement response estimates compared to the both ζ-LDP and ζ-NLDP.

4.8.2.2. Case Study on SCBF

The inherent damping of the SCBF is modeled using ζ-NLDP and NLTHA performed under the full and a linearly increasing portion of ABN000 GM record scaled to the two times of the MCE level (Figure 4.9). Table 4.8 shows the NL dashpot coefficients, $\bar{c}_{ij}$, for the SCBF. The $\dot{u}_{in,min}$ calculated for each dashpot using Eq. (4.22) and Eq. (4.23) for a 0.5% maximum drift limit is tabulated in Table 4.9.

Figure 4.23 shows the brace axial force vs. brace axial deformation histories for the first-story, RHS W12X120 brace from the static pushover analyses and NLTHA of the models

with ζ-LDP and ζ-NLDP. As seen in Figure 4.23, the brace axial force vs. brace axial deformation histories almost exactly match with each other for all three cases. The buckling load capacity of the brace is found as 1512 kip for all models. Therefore, the contribution of viscous forces to the buckling load capacity of the NL braces is precluded in the models with ζ-LDP and ζ-NLDP.

4.9. Summary and Conclusions

Proportional linear viscous damping is widely used to model the inherent damping of a building for NL seismic response analysis. Research has shown that the proportional linear viscous damping models can cause the generation of artificially large local damping forces, f_d^{local} in the vicinity of local yielding mechanisms, loss of expected relationships among local forces in the LFRS from a NL response analysis as $\sum f_r^{local} \neq 0$ in NLTHA. Many researchers pointed out the problems encountered in NL seismic response analysis of buildings due to the use of Rayleigh-like proportional damping models. It is observed in this study based on the NLTHA performed on case study structures that ζ-k_i leads to the generation of artificially large local damping forces. It is further observed that all Rayleigh-like proportional damping models utilized in this study (i.e., ζ-k_i, ζ-k_t, and ζ-k_{NP}) leads to expected static relationships among internal restoring forces not being preserved. The NLTHA results for the SCBF show that the ζ-k_t promotes brace post-buckling deformation.

The inherent damping of a building for NL seismic response analysis is provided by the entire building and local yielding within the LFRS should not create large f_d^{local}. Therefore, a damping substructure concept (DSC) is proposed. To separate the model for the inherent damping of the building from the NL LFRS model is placed in parallel to the NL LFRS model. DSC preserves the modeling simplicity of Rayleigh proportional damping and also enables more realistic damping forces. Artificially large local damping forces are not generated as the inherent damping of the building is separated from the NL LFRS model. Using DSC, the expected static relationships among local forces in the LFRS are satisfied. The unexpected high brace buckling force or large post buckling forces deteriorating in the braces of a SCBF are enabled by using DSC.

DSC is extended to use NL viscous damping, which enables the more accurate representation of the inherent damping of a building for NL seismic response analysis by limiting the maximum damping forces in the numerical model of the building. It is shown in case study structures with ζ-NLDP that the peak value of damping forces can be controlled using DSC with NL viscous damping. Further research is required to investigate the limitations of the DSC and to improve the DSC with NL viscous damping. More varieties of buildings with different NL LFRSs need to be analyzed using DSC with linear or NL viscous damping.

4.10. References

AISC (2010). "Seismic Provisions for Structural Steel Buildings," *American Institute of Steel Construction*, Chicago, IL, USA.

ASCE (2010). "Minimum Design Loads for Buildings and Other Structures," *ASCE7-10*, Reston, VA, USA.

Baker, J.W. (2011). "Conditional Mean Spectrum: Tool for Ground-Motion Selection," *Journal of Structural Engrg.*, 137(3), pp 322-331.

Bernal, D. (1994). "Viscous Damping in Inelastic Structural Response," *Journal of Structural Engrg.*, 120(4), pp. 1240-1254.

Bowland, A. and Charney, F. (2010). "New Concepts in Modeling Damping in Structures," *Proc. of the Structures Congress 2010 at 19th Analysis and Computation Specialty Conference*, Orlando, FL, May 12-15.

Chang, S. Y. (2013). "Nonlinear Performance of Classical Damping." *Earthquake Engrg. and Engrg. Vibration*, 12(2), pp. 279-296.

Chancellor, N.B. (2014). "Seismic Design and Performance of Self-Centering Concentrically-Braced Frames", Ph.D. Dissertation, Dept. of Civil and Environmental Engrg., Lehigh Univ., Bethlehem, PA, USA.

Charney, F. A. (2008). "Unintended Consequences of Modeling Damping in Structures," *Journal of Structural Engrg.*, 134(4), pp. 581-592.

Chopra, A. K. (2012). *Dynamics of structures*. (4th ed.). Prentice Hall, New Jersey, NJ, USA.

Clough, R. W. and Penzien, J. (1975). *Dynamics of structures*. (No. Monograph).

Federal Emergency Management Agency (FEMA). (2009). "Quantification of Building Seismic Performance Factors," *FEMA-P695*, Washington, DC, USA.

FEMA (2006). "Designing for Earthquakes – a Manual for Architects," *FEMA-454*, Washington, DC, USA.

Erduran, E. (2012). "Evaluation of Rayleigh proportional damping and its Influence on Engineering Demand Parameter Estimates," *Earthquake Engrg. and Structural Dynamics*, 41(14), pp. 1905-1919.

Hall, J. F. (2006). "Problems Encountered from the Use (or Misuse) of Rayleigh proportional damping," *Earthquake Engrg. and Structural Dynamics*, 35(5), pp. 525-545.

Jehel, P., Léger, P., and Ibrahimbegovic, A. (2014). "Initial versus Tangent Stiffness-based Rayleigh proportional damping in Inelastic Time History Seismic Analyses." *Earthquake Engrg. and Structural Dynamics*, 43(3), pp. 467-484.

Karamanci, E., and Lignos, D. G. (2014). "Computational Approach for Collapse Assessment of Concentrically Braced Frames in Seismic Regions," *Journal of Structural Engrg.*, 140(8), pp. A4014019 1-15.

Mazzoni, S.; McKenna, F.; Scott, M.H.; Fenves, G.L.; et al. (2009). "Open System for Earthquake Engineering Simulation (OpenSEES) User Command-Language

Manual," *Pacific Earthquake Engrg. Research Center*, Univ. of California, Berkeley, CA, USA.

Pacific Earthquake Engrg. Research Center (PEER) (2011). "GM database flatfile," Retrieved from http://peer.berkeley.edu/nga/flatfile.html on December 12, 2013.

Powell, J.A. (2009). "Evaluation of Special Concentrically Braced Frames for Improved Seismic Performance and Constructability." M.S. Thesis, Dept. of Civil and Environmental Engrg., Univ. of Washington, Seattle, WA, USA.

Roke, D. A. (2010). "Damage-Free Seismic-Resistant Self-Centering Concentrically-Braced Frames," Ph.D. Dissertation, Dept. of Civil and Environmental Engrg., Lehigh Univ., Bethlehem, PA, USA.

Tahmasebi, E. (2016). "Damage Analysis of Steel Concentrically Braced Frame Systems Under Seismic Conditions," Ph.D. Dissertation, Dept. of Civil and Environmental Engrg., Lehigh Univ., Bethlehem, PA, USA.

Table 4.1 Summary of live loads used in design of MRF

Item	Dead Load for Floor 1 (psf)	Dead Load for Middle Floors (psf)	Dead Load for Roof (psf)
Floor/Roof Deck	3	3	3
Floor/Roof Slab	43	43	0
Roofing Material	0	0	10
Mechanical Weight	10	10	25
Ceiling Material	5	5	5
Floor Finish	2	2	0
Structural Steel	15	15	10
Steel Fireproofing	2	2	2
Building Envelope	8	7	5
Total	88	87	60

Table 4.2 Summary of live loads used in design of MRF

Item	Live Load for Floors (psf)	Live Load for Roof (psf)
Office	50	0
Partitions (included in seismic mass)	15	0
Roof	0	20
Total	65	20

Table 4.3 Ground motion records (Chancellor, 2014)

PEER-NGA Record Seq. #	Year	Event	Station	Component	*M*	*Dist.* (km)	Scale Factor
1100	1995	Kobe, Japan	Abeno (ABN)	000, 090	6.90	24.85	2.89
1317	1999	Chi-Chi, Taiwan	ILA013	N, W	7.62	81.71	2.17

Table 4.4 c_{ij} and $\bar{c}_{ij}$ for MRF

Damping matrix			Linear dashpot coefficients		
c_{11}	c_{12}	c_{22}	$\bar{c}_{11}$	$\bar{c}_{12}$	$\bar{c}_{22}$
0.97	-0.47	0.34	0.5	0.47	-0.13

Table 4.5 Damping matrix and c_{ij} for SCBF

	c_{ij}					
i/j	1	2	3	4	5	6
1	16.68	-9.25	1.50	-0.17	0.15	0.20
2		21.50	-8.45	-1.27	-0.14	0.29
3			14.10	-7.15	0.88	0.35
4	Diagonally symmetric			16.90	-6.61	-0.83
5					10.70	-3.97
6						4.57

Table 4.6 Linear-elastic dashpot coefficients, $\bar{c}_{ij}$ for SCBF

	$\bar{c}_{ij}$					
i/j	1	2	3	4	5	6
1	9.11	9.25	-1.50	0.17	-0.15	-0.20
2		2.66	8.45	1.27	0.14	-0.29
3			1.23	7.15	-0.88	-0.35
4	Diagonally symmetric			0.88	6.61	0.83
5					1.01	3.97
6						0.61

Table 4.7 $\bar{c}_{ij}$ and $\dot{u}_{in,min}$ for each NL dashpot of DS of MRF

$\bar{c}_{11}$	$\bar{c}_{12}$	$\bar{c}_{22}$	$\dot{u}_{11,min}$	$\dot{u}_{12,min}$	$\dot{u}_{22,min}$
0.5	0.47	-0.13	5.93	5.93	11.87

Table 4.8 NL dashpot coefficients for SCBF

	$\bar{c}_{ij}$					
i/j	1	2	3	4	5	6
1	9.11	9.25	-1.50	0.17	-0.15	-0.20
2		2.66	8.45	1.27	0.14	-0.29
3			1.23	7.15	-0.88	-0.35
4	Diagonally symmetric			0.88	6.61	0.83
5					1.01	3.97
6						0.61

Table 4.9 Minimum velocity set for each NL dashpot of DS of SCBF

	$\dot{u}_{in,min}$ inch/s^2					
i/j	1	2	3	4	5	6
1	7.51	7.51	15.02	22.53	30.04	37.55
2		7.51	7.51	15.02	22.53	30.04
3			7.51	7.51	15.02	22.53
4	Diagonally symmetric			7.51	7.51	15.02
5					7.51	7.51
6						7.51

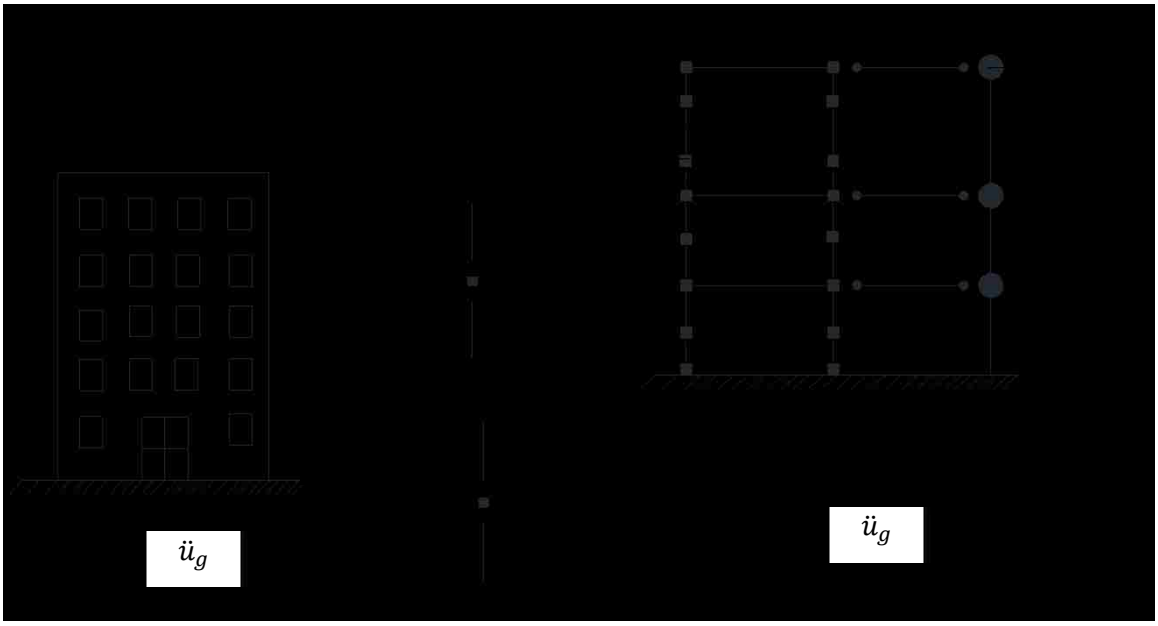

Figure 4.1 (a) Multi-story building; (b) numerical model; (c) local restoring forces from element 1 and element 2; (d) local damping forces from element 1 and element 2

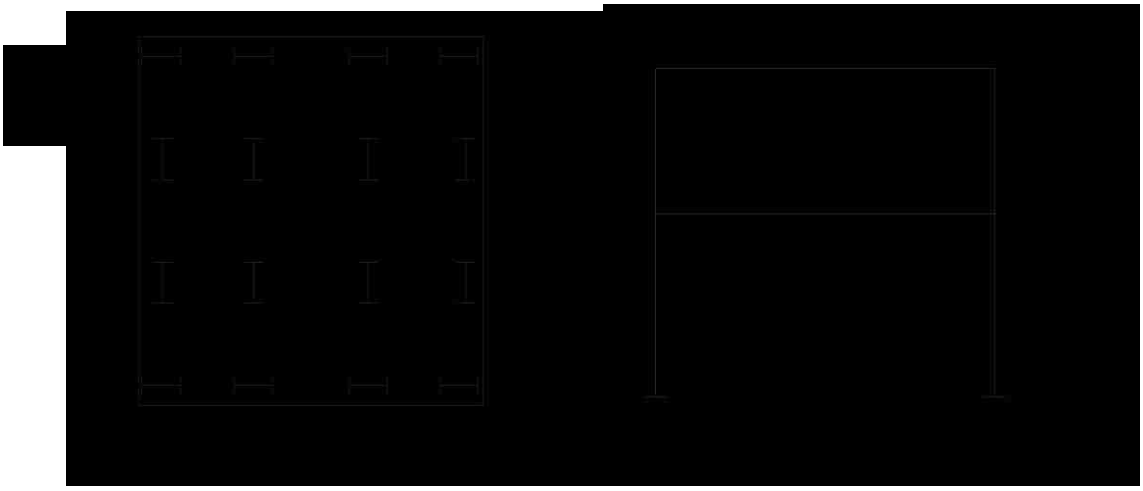

Figure 4.2 (a) Floor plan; (b) elevation view of MRF building

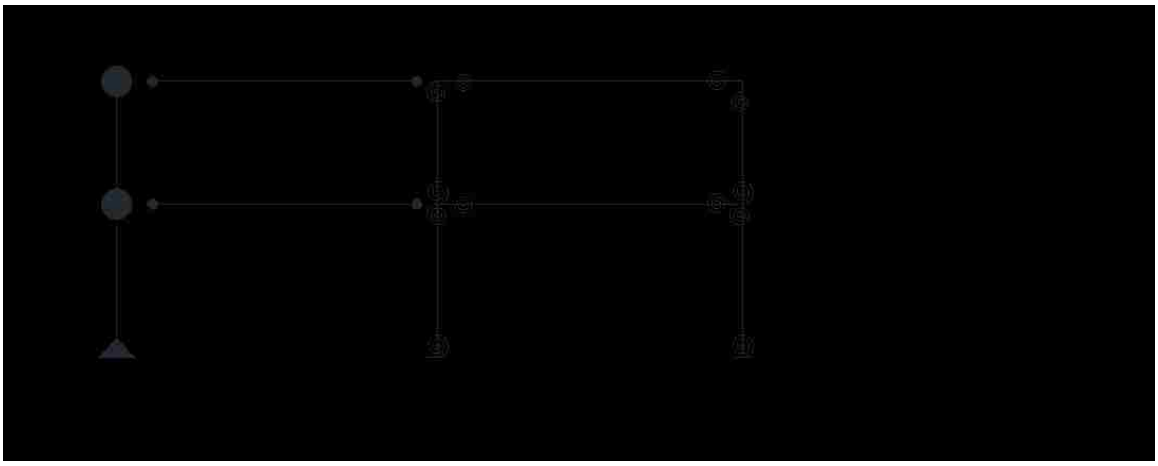

Figure 4.3 Two dimensional numerical model of MRF

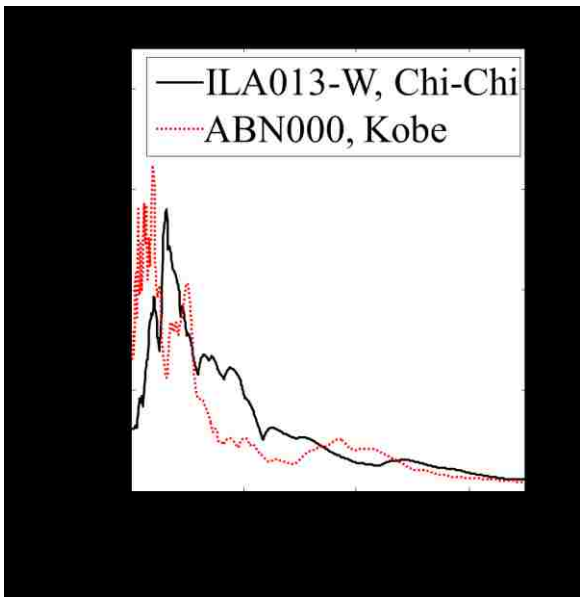

Figure 4.4 5% damped pseudo-acceleration response spectrum for ILA013W and ABN000 ground motion records

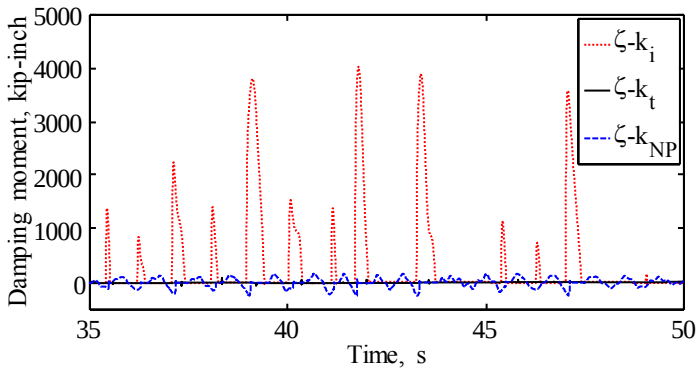

Figure 4.5 Comparison of viscous moment histories at first story, first bay column end springs of MRF with ζ-k_i, ζ-k_t, and ζ-k_{NP} damping under ILA013W ground motion record

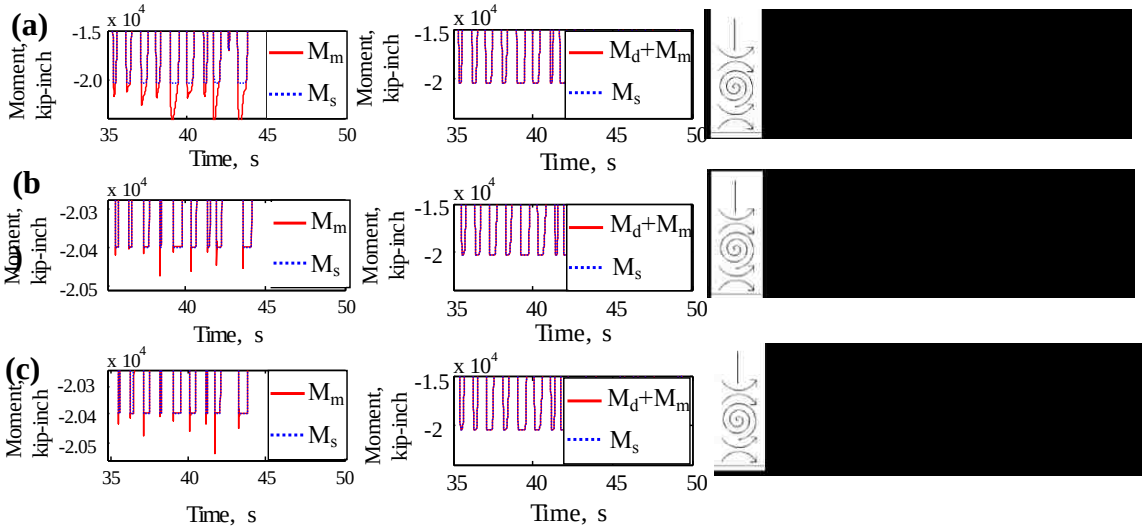

Figure 4.6 Local restoring forces and local damping forces from the bottom of first story column for models with: (a) ζ-k_i; (b) ζ-k_t; (c) ζ-k_{NP} damping under ILA013W ground motion record

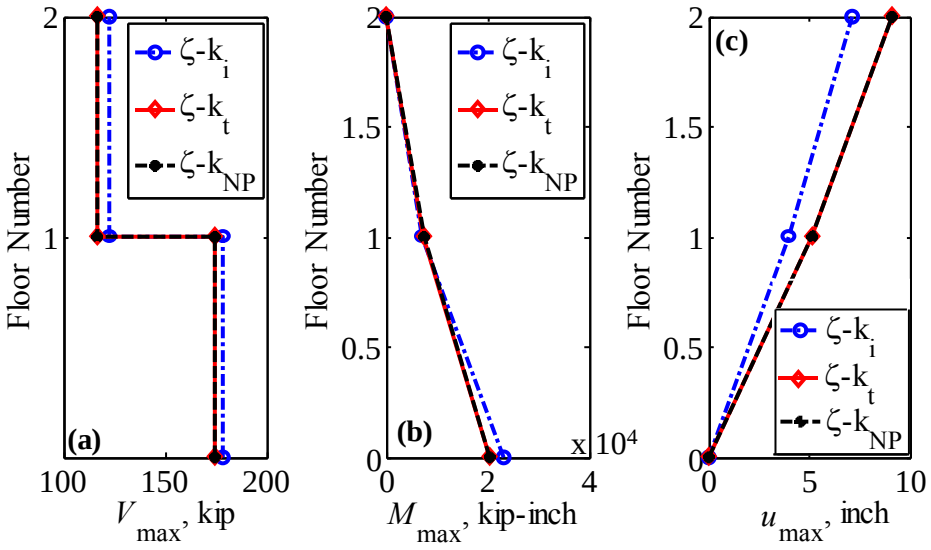

Figure 4.7 Comparison of: (a) V_{max}; (b) M_{max}; (c) u_{max} response envelopes for MRF analyzed under ILA013W ground motion record with ζ-k_i, ζ-k_t, and ζ-k_{NP} damping

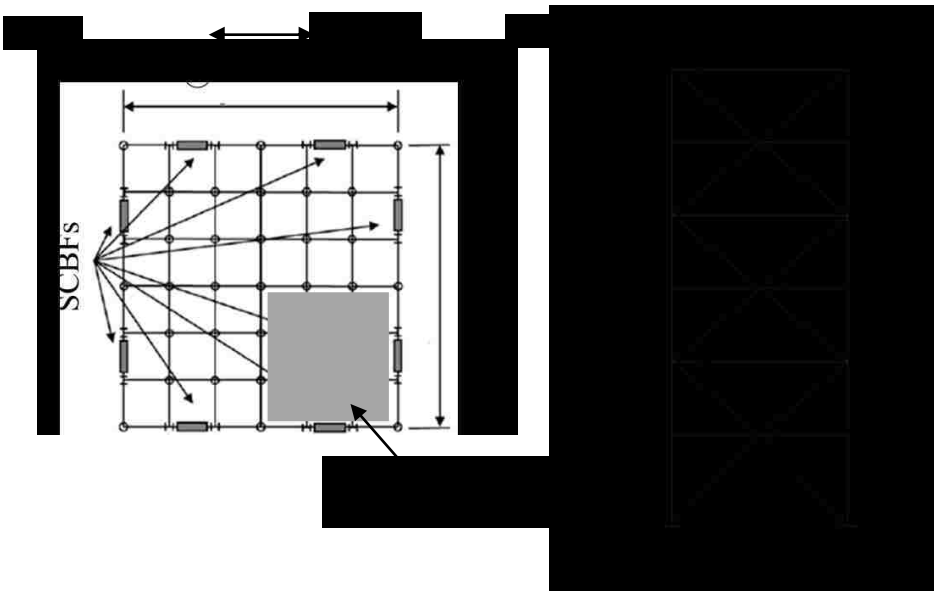

Figure 4.8 (a) Building floor plan; (b) elevation of SCBF (Tahmasebi, 2016)

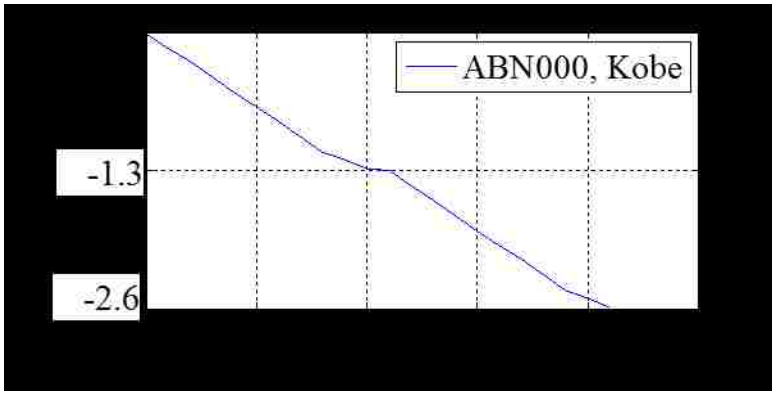

Figure 4.9 A linearly increasing from ABN000 ground motion record scaled to two times the MCE level

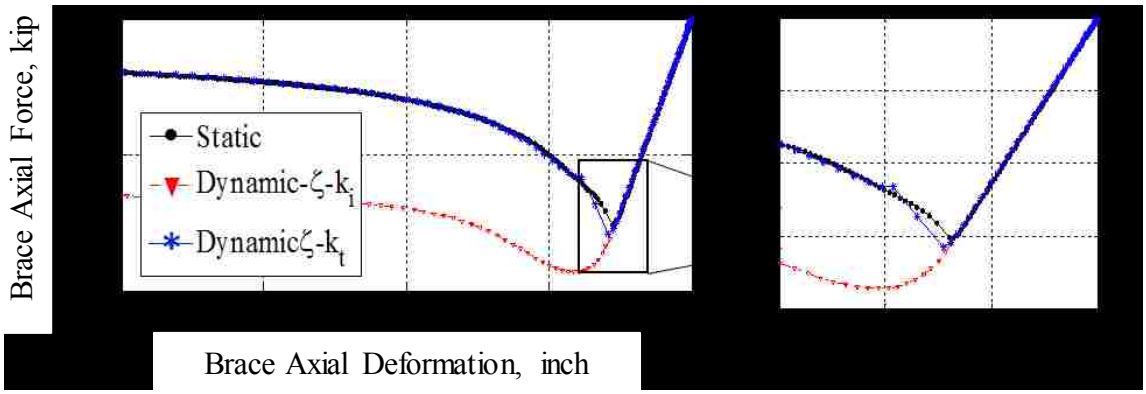

Figure 4.10 First story, right brace axial force vs. axial deformation plots for SCBF based on static pushover analysis and NLTHA with ζ-k_i and ζ-k_t damping

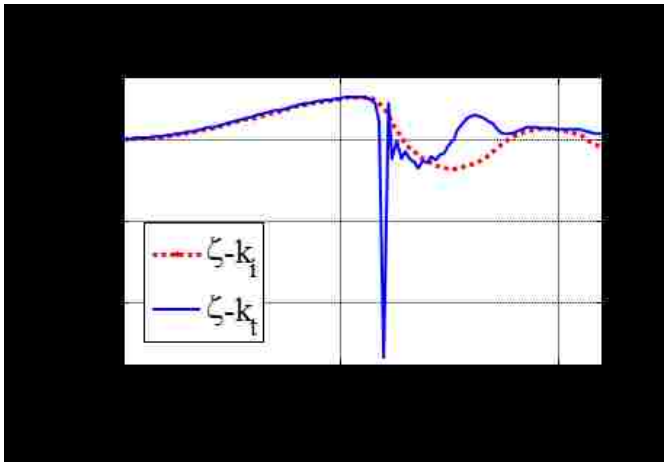

Figure 4.11 Viscous damping forces at the time of brace buckling for first story, right brace with ζ-ki and ζ-kt damping

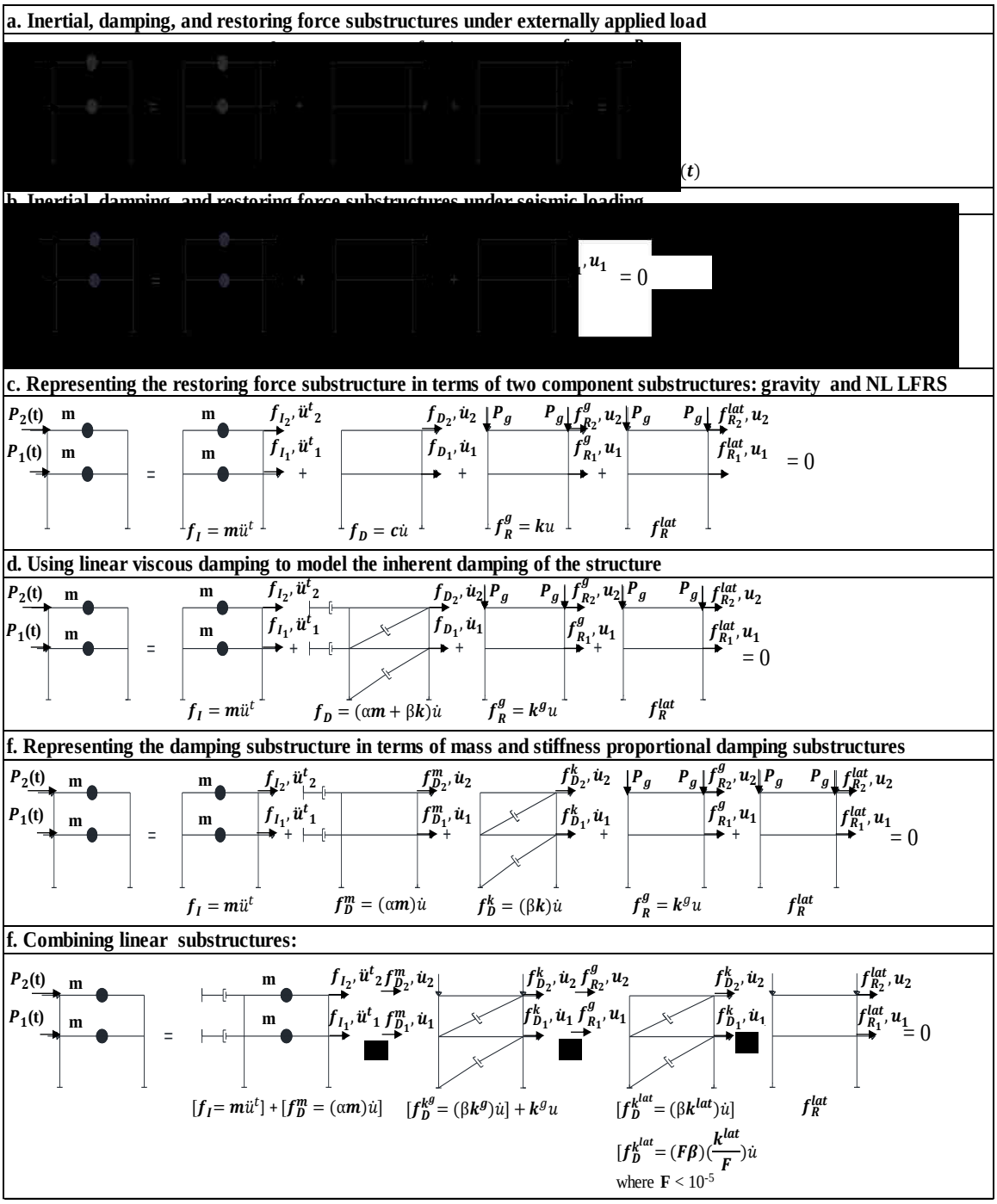

Figure 4.12 Substructuring for a 2-story MRF

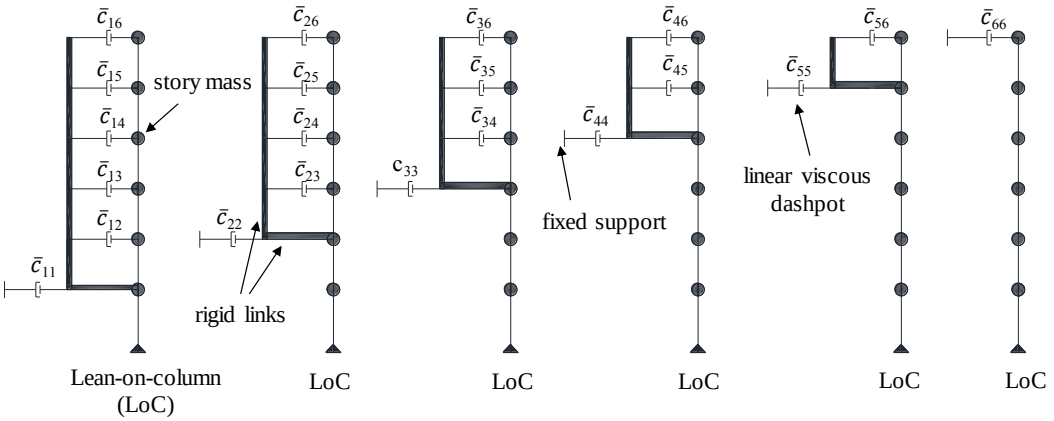

Figure 4.13 Schematic of six parallel substructures comprising DS of 6-story SCBF

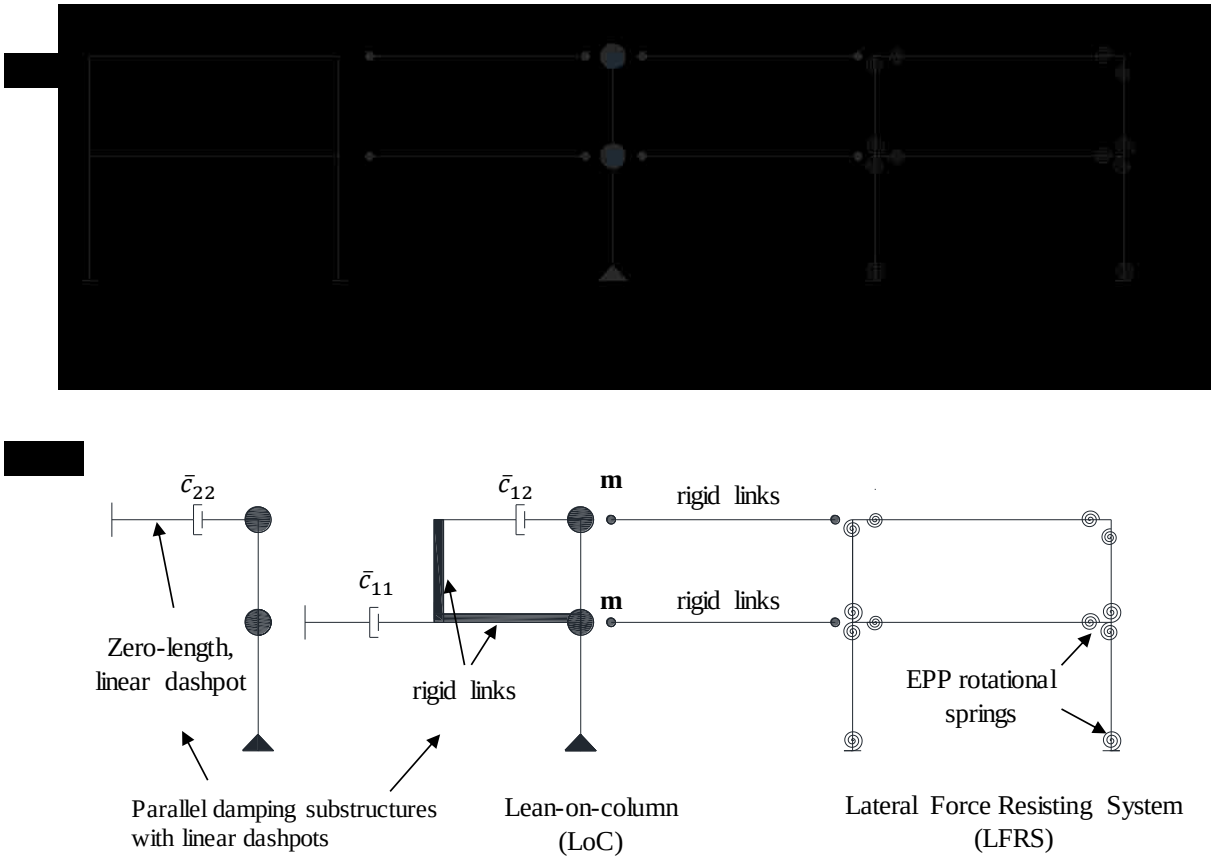

Figure 4.14 Numerical models of 2-story, 1-bay MRF with: (a) ζ-DS; (b) ζ-LDP damping

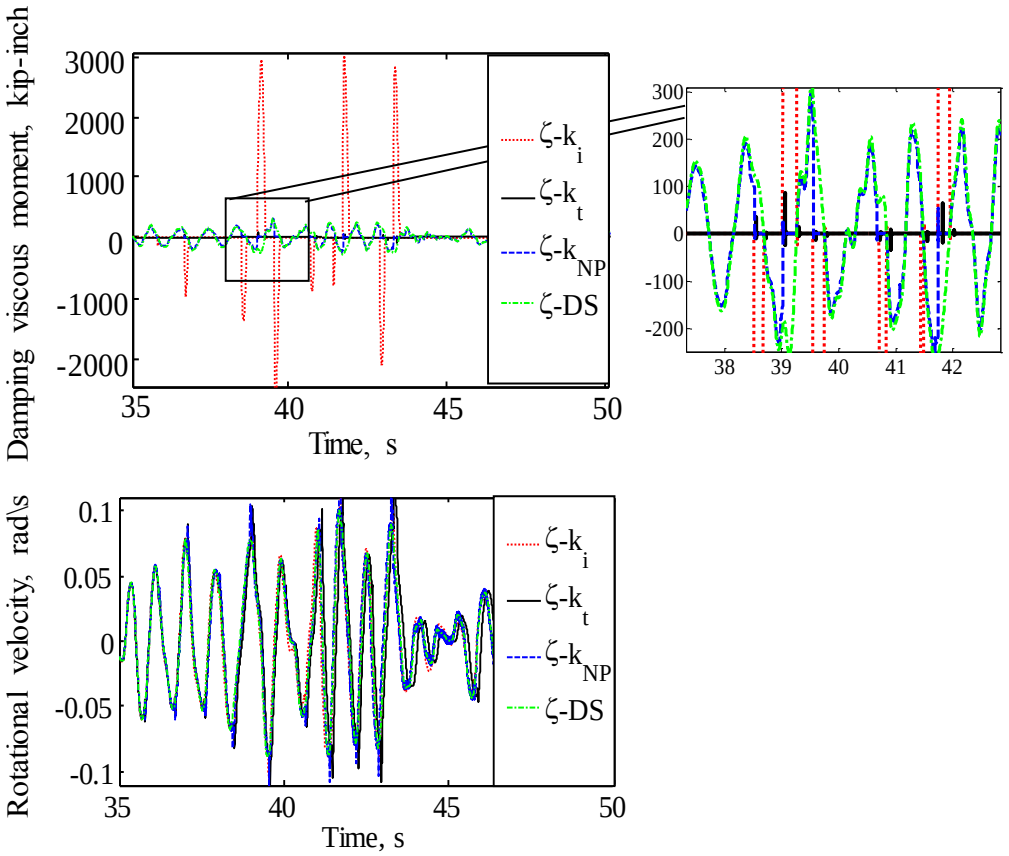

Figure 4.15 Comparison of viscous moment and rotational velocity histories at the end of first story, first bay column for MRF models with ζ-k_i, ζ-k_t, ζ-k_{NP}, and ζ-DS damping analyzed under ILA013W ground motion record

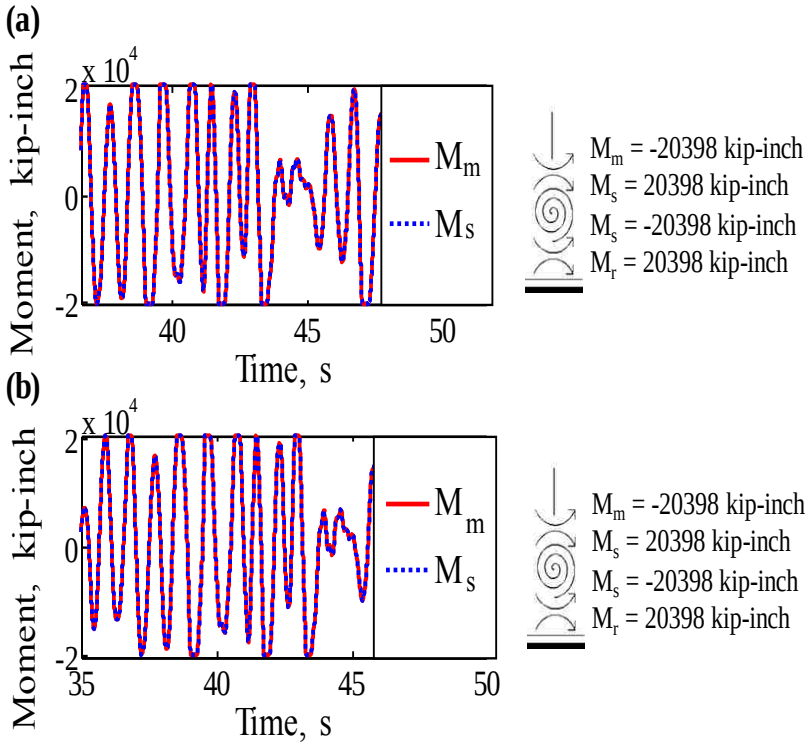

Figure 4.16 Comparison of internal member force (M_m), spring force (M_s), and viscous moment (M_d) histories at end of first story, first bay column (M_{c11}) for MRF model with ζ-DS and ζ-LDP damping analyzed under ILA013W ground motion record

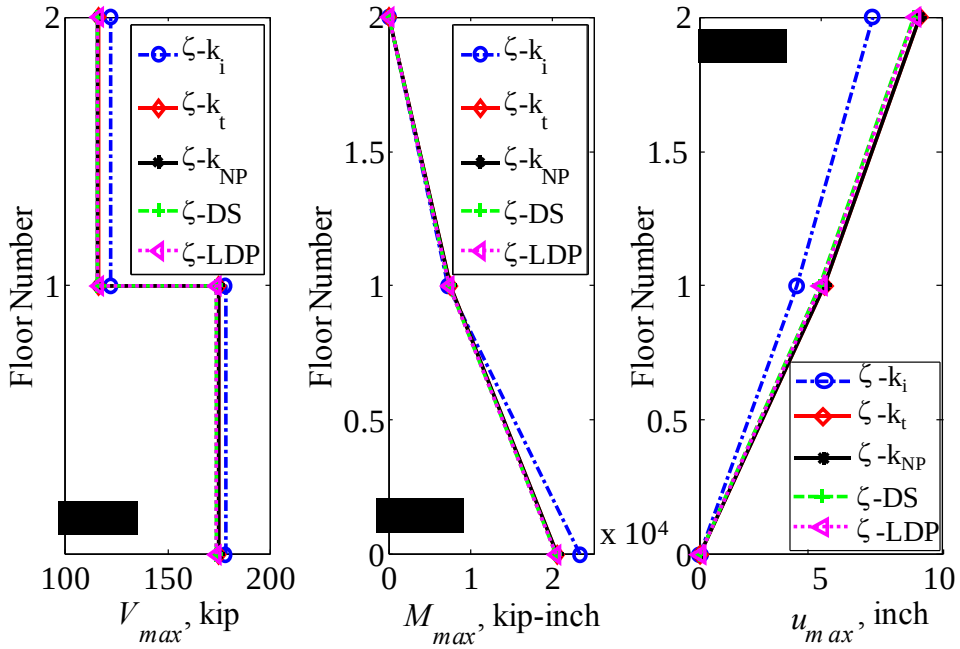

Figure 4.17 Comparison of: (a) V_{max}; (b) M_{max}; (c) u_{max} response envelopes for MRFs analyzed under ILA013W ground motion record with ζ-k_i, ζ-k_t, ζ-k_{NP}, ζ-DS, and ζ-LDP damping

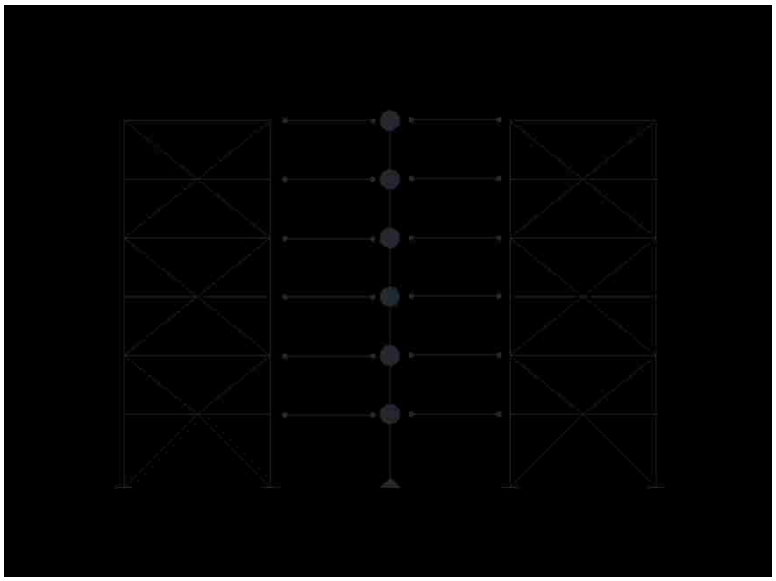

Figure 4.18 Numerical models of 6-story SCBF with ζ-DS

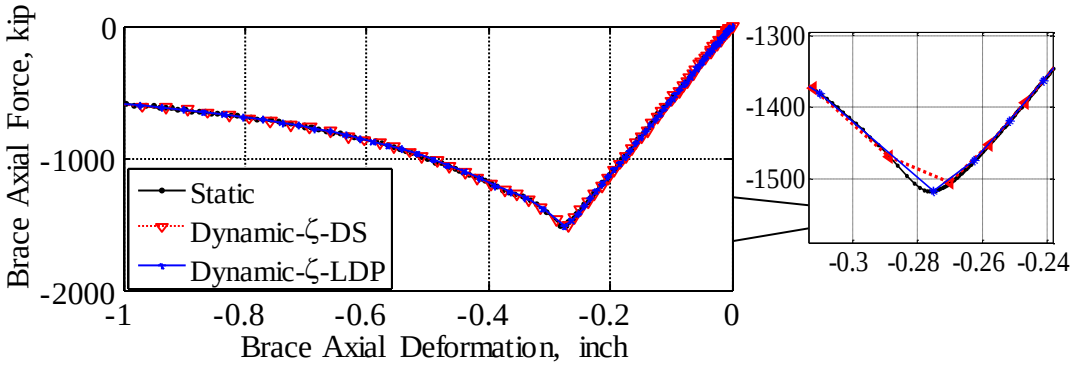

Figure 4.19 First story, right brace axial force vs. axial deformation plots for SCBF based on static pushover analysis and NLTHA with ζ-DS and ζ-LDP damping

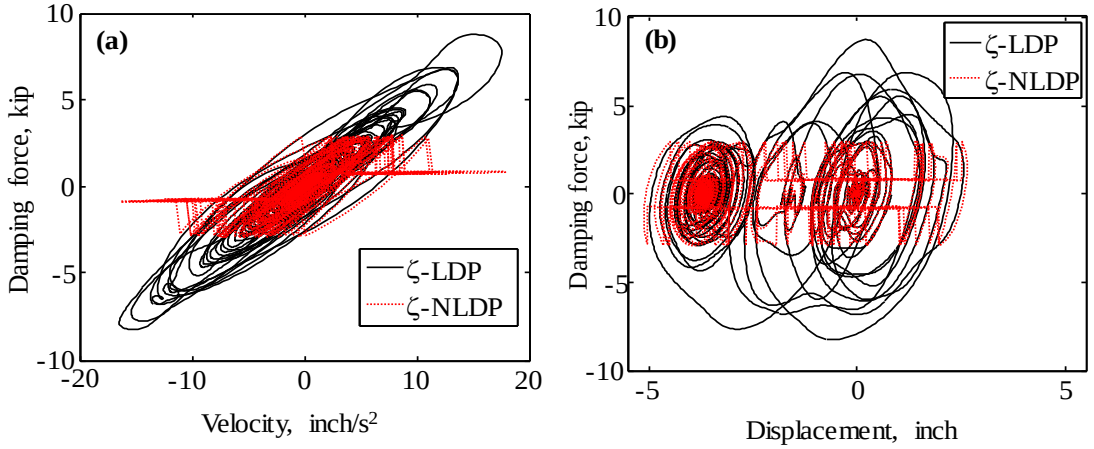

Figure 4.20 Comparison of: (a) linear and NL viscous damping force vs. velocity; (b) linear and NL viscous damping force vs. displacement histories for first story dashpot with coefficient c_{11}

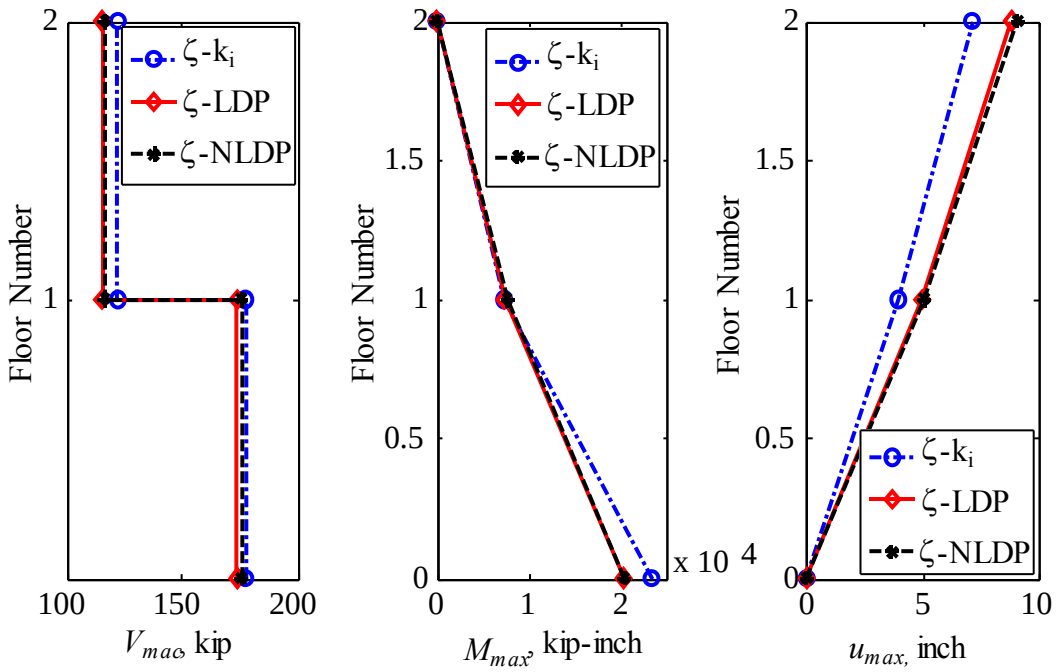

Figure 4.21 Comparison of: (a) V_{max}; (b) M_{max}; (c) u_{max} response envelopes MRF analyzed under ILA013W ground motion record with ζ-k_i, ζ-LDP, and ζ-NLD damping

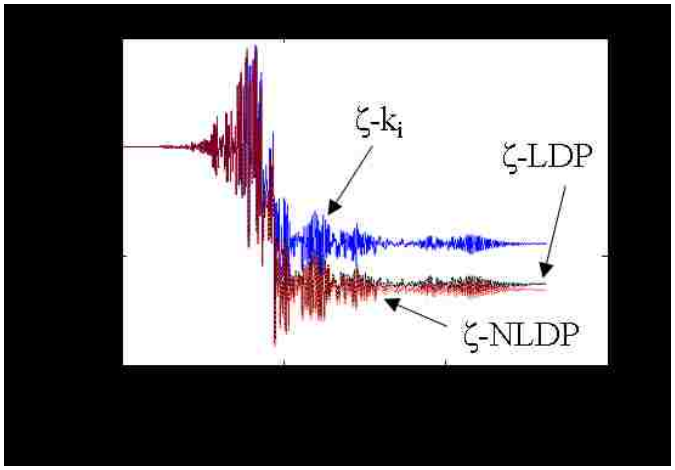

Figure 4.22 Roof displacement response histories for MRF models with ζ-k_i, ζ-LDP, and ζ-NLDP damping

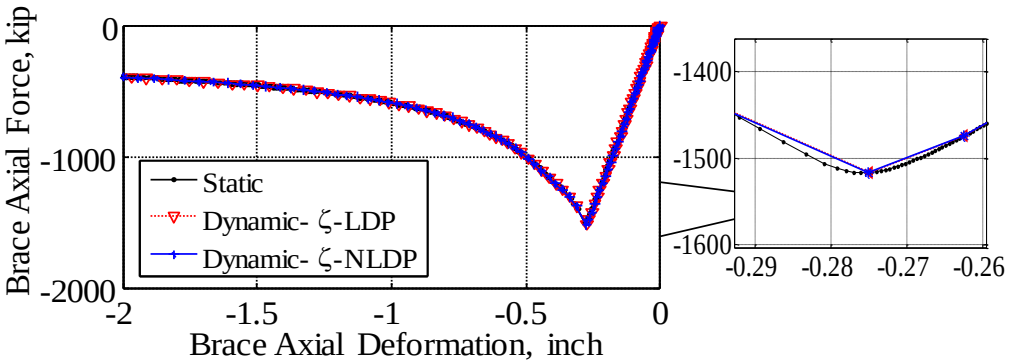

Figure 4.23 First story, right brace axial force vs. axial deformation plot for SCBF based on static pushover analysis and NLTHA with ζ-LDP and ζ-NL damping

CHAPTER 5

YIELDING MECHANISMS TO MITIGATE HIGHER MODE RESPONSE OF NONLINEAR STRUCTURES

Overview

Structures designed to resist earthquakes are usually given a distribution of internal member strength to promote the development of an intended yielding mechanism. The intended yielding mechanism is often assumed to reduce or limit the force demands on the structure. Research has shown that the formation of the intended yielding mechanism may not reduce the force response for all vibration modes, and the higher mode response may reach or exceed the linear-elastic level of response after the intended yielding mechanism has formed. Past research has investigated ways of reducing the higher mode response of a structure by designing the structure to have more than one yielding mechanisms. This paper investigates the n^{th} (first and higher) mode response of structures with one or two clearly-defined yielding mechanism. To mitigate the higher mode contribution to the total force response of a structure with one yielding mechanism, the addition of a second yielding mechanism is considered. The location and the strength of the second yielding mechanism are established based on modal properties. Nonlinear time-history analyses (NLTHA) of wall and frame structures designed with two yielding mechanisms are

conducted. Results are given to show the effectiveness of the second yielding mechanism on the higher mode force response.

5.1. Introduction

Earthquake-resistant structures are usually designed with a distribution of internal member strength to promote the development of an intended yielding mechanism. For example, slender reinforced concrete walls are designed to promote a flexural hinge near the base of the wall and to avoid a shear failure mechanism. The intended yielding mechanism is often assumed to limit the force demands on the structure. This assumption is evident from conventional modal response spectrum analysis (MRSA) procedures in seismic design code provisions where the linear-elastic design response spectrum is reduced uniformly by a response modification coefficient and the reduced spectrum is applied to all relevant modes of vibration (e.g., ASCE, 2010).

Research has shown that the formation of the intended yielding mechanism may not reduce the force response of all modes (e.g., Blakeley et al., 1975; Eibl and Keintzel, 1988; Paulay and Priestley, 1992). Often the force response of the higher modes (i.e., higher than the 1st mode) of a nonlinear (NL) structure will reach or exceed the linear-elastic design level of response after the intended yielding mechanism has formed. For example, Roke et al. (2010) and Chancellor et al. (2014) observed significant higher mode forces in the seismic response of self-centering concentrically braces frames (SC-CBFs) and proposed factoring

up the higher mode force response by modal load factors to estimate the total design member force demands.

A few researchers have studied ways of reducing the higher mode response of a NL structure by adding a second yielding mechanism to the structure. Panagiotou and Restrepo (2009) developed a dual-plastic hinge (DPH) design approach for reinforced concrete shear walls in which the shear wall is designed to form two yielding hinges, one at the base of the wall and one at the mid-height of the wall. In this work, instantaneous modal properties of the NL structure were calculated using the respective tangent stiffness at the yielding hinge locations to quantify the first and higher mode response of the NL wall with two yielding hinges. It was observed that the formation of the second yielding hinge at mid-height considerably decreases the story moment response at the upper floor levels compared to the wall with a single yielding hinge at the base of the wall.

Other researchers have investigated methods for controlling the higher mode force response in controlled rocking walls and rocking concentrically braced frames by introducing multiple rocking joints in the structure. A rocking joint is a joint which opens at one end of the wall or frame under base overturning moment (or story moment, if the joint is above the base). Uplift at the rocking joint opens a gap between the wall (or frame) and the foundation or the floor below, which permits rigid body rotation of the wall (or frame). Post-tensioning (PT) steel is generally included in controlled rocking walls and frames (e.g., see Kurama et al., 1999; Roke et al., 2006) to provide a restoring force to

self-center the wall or frame. Wiebe et al. (2009) proposed placing multiple rocking joints in a wall to mitigate the higher mode response. Based on parametric and analytical studies, it was concluded that introducing multiple rocking joints reduces the story moment response compared to a wall with a single, base rocking joint. Wiebe et al. (2013) proposed placing two rocking joints in a controlled rocking steel braced frame to mitigate the higher mode response. Based on test results and nonlinear time history analysis (NLTHA) results for an 8-story steel concentrically braced frame, it was observed that the story base moment and story shear responses were reduced considerably by using an upper rocking joint in addition to the base rocking joint.

This chapter investigates the n^{th} (1^{st} and higher) mode response of NL structures with one or two clearly-defined yielding mechanisms. The higher mode responses of example NL wall structures with yielding hinges or rocking joints and of a self-centering concentrically braced rocking frame (SC-CBF) structure are investigated. Each example structure is designed with one flexural yielding mechanism at the base of the structure (i.e., a yielding hinge or rocking joint for the wall, or a rocking joint for the SC-CBF). To control the higher mode force response, a second yielding mechanism (either a yielding hinge or a rocking joint) is added to the example structure. A method to determine the location and strength of the second yielding mechanism is described, which uses the modal properties of the structure. The example NL wall and SC-CBF structures, with a base flexural yielding mechanism, are then redesigned to form a second flexural yielding mechanism within the height of the structure. Parameters of the NL wall structures, such as the location, strength, hysteretic response of the first and second mechanisms are varied. The contributions of the

higher modes to various seismic response quantities are investigated. Nonlinear time-history analyses (NLTHA) are conducted on the example NL wall and SC frame structures. NLTHA results are used to understand the effectiveness of the second flexural yielding mechanism on reducing the higher mode force response of the example NL structures.

5.2. Theory

5.2.1. Elastic, Mechanism, and Two-Mechanism Mode Shapes

This study uses three sets of mode shapes determined for a NL structure which depend on the NL state of the NL structure, as follows (note that ***bold italic font*** is used to represent vector and matrix variables, and conventional *italic font* is used to represent scalar variables):

a. Elastic mode shapes, which are denoted as $\boldsymbol{\phi}_n^e$, are mode shapes based on the initial linear-elastic stiffness of a NL structure, $\boldsymbol{k}$. An eigen analysis of a linear-elastic model of the NL structure is carried out to determine $\boldsymbol{\phi}_n^e$.

b. Mechanism mode shapes, which are denoted as $\boldsymbol{\phi}_n^m$, are mode shapes based on the stiffness matrix of a NL structure after the first intended yielding mechanism has formed, $\boldsymbol{k_m}$. To derive $\boldsymbol{\phi}_n^m$, the initial linear-elastic numerical model of the NL structure is modified by adding hinges with negligible rotational stiffness at the expected yielding hinge (or rocking joint) locations of the intended yielding mechanism. An eigen analysis of the modified model (with the hinges) is carried out to determine $\boldsymbol{\phi}_n^m$.

c. Two-mechanism mode shapes, which are denoted as $\boldsymbol{\phi}_n^{sm}$, are mode shapes based on the stiffness matrix of a NL structure after both the first and second intended yielding mechanisms have formed, $\boldsymbol{k_{sm}}$. To derive $\boldsymbol{\phi}_n^{sm}$, the initial linear-elastic numerical model of the NL structure is modified by adding hinges with negligible rotational stiffness at the expected yielding hinge (or rocking joint) locations of the intended first and second yielding mechanisms. An eigen analysis of the modified model (with the hinges) is carried out to determine $\boldsymbol{\phi}_n^{sm}$.

$\boldsymbol{\phi}_n^e$, $\boldsymbol{\phi}_n^m$, $\boldsymbol{\phi}_n^{sm}$ are all orthogonal with respect to the mass matrix, $\boldsymbol{m}$:

$$(\boldsymbol{\phi}_i^e)^T \boldsymbol{m}\, \boldsymbol{\phi}_n^e = 0 \qquad (i \neq n) \tag{5.1a}$$

$$(\boldsymbol{\phi}_i^m)^T \boldsymbol{m}\, \boldsymbol{\phi}_n^m = 0 \qquad (i \neq n) \tag{5.1b}$$

$$(\boldsymbol{\phi}_i^{sm})^T \boldsymbol{m}\, \boldsymbol{\phi}_n^{sm} = 0 \qquad (i \neq n) \tag{5.1c}$$

where, $\boldsymbol{\phi}_n^T$= transpose of the nth mode shape

$\boldsymbol{\phi}_n^e$ are orthogonal with respect to $\boldsymbol{k}$, $\boldsymbol{\phi}_n^m$ are orthogonal with respect to $\boldsymbol{k_m}$, and $\boldsymbol{\phi}_n^{sm}$ are orthogonal with respect to $\boldsymbol{k_{sm}}$:

$$(\boldsymbol{\phi}_i^e)^T \boldsymbol{k}\, \boldsymbol{\phi}_n^e = 0 \qquad (i \neq n) \tag{5.2a}$$

$$(\boldsymbol{\phi}_i^m)^T \boldsymbol{k_m} \boldsymbol{\phi}_n^m = 0 \qquad (i \neq n) \tag{5.2b}$$

$$(\boldsymbol{\phi}_i^{sm})^T \boldsymbol{k_{sm}} \boldsymbol{\phi}_n^m = 0 \qquad (i \neq n) \tag{5.2c}$$

It is also important to note that $\boldsymbol{\phi}_n^m$ and $\boldsymbol{\phi}_n^{sm}$ are not orthogonal with respect to the initial linear-elastic stiffness matrix, $\boldsymbol{k}$:

$$(\boldsymbol{\phi}_n^m)^T \boldsymbol{k} \boldsymbol{\phi}_i^m \neq 0 \qquad (i \neq n) \tag{5.3a}$$

$$(\boldsymbol{\phi}_n^{sm})^T \boldsymbol{k} \boldsymbol{\phi}_i^{sm} \neq 0 \qquad (i \neq n) \tag{5.3b}$$

5.2.2. Elastic, Mechanism, and Two-Mechanism Modal Properties

nth mode static lateral force distributions and corresponding static story base moment profiles can be calculated using $\boldsymbol{\phi}_n^e$ or $\boldsymbol{\phi}_n^m$or $\boldsymbol{\phi}_n^{sm}$, respectively, as follows:

$$\boldsymbol{s}_n^e = \Gamma_n^e \, \boldsymbol{m} \, \boldsymbol{\phi}_n^e \quad \text{or} \quad \boldsymbol{s}_n^m = \Gamma_n^m \, \boldsymbol{m} \, \boldsymbol{\phi}_n^m \quad \text{or} \quad \boldsymbol{s}_n^{sm} = \Gamma_n^{sm} \, \boldsymbol{m} \, \boldsymbol{\phi}_n^{sm} \tag{5.4}$$

$$M_{in}^{st,e} = \sum_{j=i+1}^{N} (h_j - h_i) \boldsymbol{s}_{jn}^e \quad \text{or} \quad M_{in}^{st,m} = \sum_{j=i+1}^{N} (h_j - h_i) \boldsymbol{s}_{jn}^m \quad \text{or} \quad M_{in}^{st,sm} = \sum_{j=i+1}^{N} (h_j - h_i) \boldsymbol{s}_{jn}^{sm} \tag{5.5}$$

where $\boldsymbol{s}_n^e$ = nth elastic mode static lateral force distribution, $\boldsymbol{s}_n^m$ = nth mechanism mode static lateral force distribution, $\boldsymbol{s}_n^{sm}$ = nth two-mechanism mode static lateral forces distribution; Γ_n^e = nth elastic mode participation factor; Γ_n^m = nth mechanism mode participation factor; Γ_n^{sm} = nth two-mechanism mode participation factor; $M_{in}^{st,e}$ = nth elastic mode static story base moment response at floor level i, $M_{in}^{st,m}$ = nth mechanism mode static story base moment response at floor level i, $M_{in}^{st,sm}$ = nth two-mechanism mode static story base moment response at floor level i.

The contribution of the nth elastic, mechanism, and two-mechanism modes to the total static *base overturning* moment response (Chopra, 2012), M_b^{st}, are calculated as follows:

$$\overline{M}_{bn}^{\,e} = \frac{M_{bn}^{st,e}}{M_b^{st,e}} \quad \text{or} \quad \overline{M}_{bn}^{\,m} = \frac{M_{bn}^{st,m}}{M_b^{st,m}} \quad \text{or} \quad \overline{M}_{bn}^{\,sm} = \frac{M_{bn}^{st,sm}}{M_b^{st,sm}} \tag{5.6}$$

where $\overline{M}_{bn}^{e}$= nth elastic mode contribution to $M_b^{st,e}$; $\overline{M}_{bn}^{m}$= nth mechanism mode contribution to $M_{bn}^{st,m}$; $\overline{M}_{bn}^{sm}$= nth two-mechanism mode contribution to $M_b^{st,sm}$; $M_{bn}^{st,e} = M_{1n}^{st,e}$ = nth elastic mode static base overturning moment response; $M_{bn}^{st,m} = M_{0n}^{st,m}$ = nth mechanism mode static base overturning moment response; $M_{bn}^{st,sm} = M_{0n}^{st,sm}$ = nth two-mechanism mode static base overturning moment response; $M_b^{st} = \sum_{n=1}^{N} M_{bn}^{st,e} = \sum_{n=1}^{N} M_{bn}^{st,m} = \sum_{n=1}^{N} M_{bn}^{st,sm}$.

5.2.3. Quantification of nth Mode Contribution to Total Seismic Response

This study quantifies the nth mode contribution to the total seismic response of a structure using the conventional pseudo-acceleration response and the effective pseudo-acceleration (see Chapter 2 and Roke et al., 2010). This section briefly explains how the nth mode contribution is quantified.

5.2.3.1. Effective Modal Pseudo-Acceleration Concept

When the total NL restoring force vector, $\boldsymbol{f}_r^{NL}(t)$, is known from NLTHA of an MDF structure for a given ground motion (GM), the nth mode pseudo-acceleration response, $A_{eff_n}(t)$, is calculated from $\boldsymbol{f}_r^{NL}(t)$, as follows:

$$A_{eff_n}(t) = \frac{\boldsymbol{\phi}_n^T \boldsymbol{f}_r^{NL}(t)}{\Gamma_n M_n} \tag{5.7}$$

where $\boldsymbol{f}_r^{NL}(t)$ = total restoring force vector from NLTHA; $A_{eff_n}(t)$ = nth mode effective pseudo-acceleration; Γ_n = modal participation factor $= \frac{\boldsymbol{\phi}_n^T \boldsymbol{m}\{i\}}{M_n}$; $\boldsymbol{\phi}_n^T$ = transpose of the nth

mass-orthogonal mode shape; $M_n=\boldsymbol{\phi}_n^T \boldsymbol{m}\boldsymbol{\phi}_n$ = n[th] mode mass; $\{i\}$ = influence vector. $\boldsymbol{\phi}_n^e$ or $\boldsymbol{\phi}_n^m$ or $\boldsymbol{\phi}_n^{sm}$ can be used to calculate the n[th] mode effective pseudo-acceleration response, which are denoted as $A_{eff_n}^e(t)$ or $A_{eff_n}^m(t)$ or $A_{eff_n}^{sm}(t)$, respectively. The amplitude of $A_{eff_n}^e(t)$ or $A_{eff_n}^m(t)$ or $A_{eff_n}^{sm}(t)$ is denoted as $A_{eff_n}^e$ or $A_{eff_n}^m$ or $A_{eff_n}^{sm}$, respectively.

5.3. Introductory Example

To illustrate how the formation of an intended yielding mechanism changes the n[th] mode properties and the n[th] mode seismic response, the properties and response of a 9-story wall structure are examined.

5.3.1. Description of Example Wall Structure

The 9-story wall structure, which is denoted as MB1, has purely flexural response (i.e., is rigid in shear). The nonlinearity of the wall structure is concentrated in a flexural yielding spring at the base of the wall. The rest of the wall is assumed to be linear-elastic. The base flexural yielding spring has an assumed elastic-perfectly plastic (EPP) response. The initial stiffness of the base flexural yielding spring, k_{spg}, is set to 10 times the flexural stiffness of the first story. The yield strength of the base flexural yielding spring, M_1^h, is established uniquely for each GM record in the GM set (described later) as follows:

$$M_1^h = M_{b1}^{st} \frac{SA_{GM}(T_1^e)}{R} \tag{5.8}$$

where $SA_{GM}(T_1^e)$ = 1st elastic mode pseudo-acceleration for the GM; T_1^e = 1st elastic mode period; R = response modification factor assumed to be 6.

Figure 5.1 shows a schematic of the numerical model of the example wall structure (MB1) and the EPP response of the flexural yielding spring at the base. The details of the numerical model of the wall structure are described later.

5.3.2. nth Mode Response of Example Structure

The yielding mechanism of MB1 is yielding of base flexural yielding spring, which is controlled by the base overturning moment (M_b) response of the NL structure. To investigate the nth mode response of the example wall structure, results from static analysis, and from linear-elastic time history analysis (LETHA) and NLTHA of the wall structure under a set of GM records (Table 5.1) are presented. Figure 5.2 shows the 1st and 2nd mode story base moment responses for MB1 at each floor level from static analysis, LETHA, and NLTHA, which are denoted as $M_{i1}^{st,e}$ and $M_{i2}^{st,e}$, M_{i1}^{L} and M_{i2}^{L}, M_{i1}^{NL} and M_{i2}^{NL}, respectively. M_{in}^{L} is the product of $M_{in}^{st,e}$ and the peak $A_{eff_n}^{e}(t)$ from LETHA where the peak is denoted $A_{eff_n}^{e}$. M_{in}^{NL} is the product of $M_{in}^{st,e}$ and $A_{eff_n}^{e}$ from NLTHA. Figure 5.2 shows that $M_{i1}^{st,e}$ is considerably greater than $M_{i2}^{st,e}$ at all floor levels. For example, the first elastic mode static base overturning moment response (M_b), denoted $M_{b1}^{st,e}$, is 11 times greater than the second elastic mode static M_b, denoted $M_{b2}^{st,e}$. Figure 5.2(b) shows the first and second mode peak story base moment responses from LETHA for MB1 (i.e., M_{i1}^{L} and

M_{i2}^{L}). The results show that M_{i1}^{L} is greater than M_{i2}^{L} at all floor levels. The first mode linear-elastic M_b, denoted M_{b1}^{L}, is 2.5 times larger than the second mode linear-elastic M_b, denoted M_{b2}^{L}. Note that since $A_{eff\_2}^{e}$ is greater than $A_{eff\_1}^{e}$, M_{b1}^{L} is only 2.5 times M_{b2}^{L}, while $M_{b1}^{st,e}$ is 11 times $M_{b2}^{st,e}$. Figure 5.2(c) shows the distribution of first and second mode peak story base moment responses from NLTHA for MB1 (i.e., M_{i1}^{NL} and M_{i2}^{NL}), at a time after the base flexural yielding mechanism has formed. The results show that because $A_{eff\_1}^{e}$ is significantly influenced (i.e., "controlled") by the yielding mechanism, M_{i1}^{NL} are *generally smaller* than M_{i2}^{NL}. For example, M_{b2}^{NL} is 2 times larger than M_{b1}^{NL}. As discussed in Chapter 2 and Chapter 3, and consistent with previous studies (e.g., Priestley, 2003), the 1st mode force response of a NL structure can be effectively controlled by the formation of the base flexural yielding mechanism, but the higher mode responses are not strongly affected by this yielding mechanism. Therefore, as shown in Figure 5.2(c), the 2nd mode force response can exceed the first mode response.

These results show that the formation of the intended base flexural yielding mechanism does not control the higher mode force responses of a NL structure. This study investigates a method to control the second mode response of NL structures by including a second yielding mechanism in the structure.

5.4. Properties of Second Yielding Mechanism for Example Structure

As mentioned earlier, the intended, first yielding mechanism for the example wall structure, MB1, is a base yielding hinge implemented as a base flexural yielding spring. To control the higher mode response, a second yielding mechanism, which is another yielding hinge, is added to MB1. The first and second flexural yielding mechanisms are called the "base" and "upper" flexural yielding mechanisms (which are either yielding hinges or rocking joints). This section presents a method based on modal analysis to determine the location and strength of the upper yielding hinge.

5.4.1. Location of Upper Yielding Hinge

To determine the location of the upper yielding hinge, the first and second mode moment responses and the relative contributions of the first and second mode story base moment responses to the total story base moment response for MB1 are examined.

Figure 5.3 shows the distributions of $M_{i1}^{st,e}$ and $M_{i2}^{st,e}$ and $M_{i1}^{st,m}$ and $M_{i2}^{st,m}$ for MB1. Table 5.2 shows the values of $M_{i1}^{st,e}$ and $M_{i2}^{st,e}$ and $M_{i1}^{st,m}$ and $M_{i2}^{st,m}$ at each floor level. Table 5.2 and Figure 5.3 shows that $M_{i2}^{st,e}$ is largest at the 5th floor. $M_{i2}^{st,e}$ also changes sign in the 3rd story (between 2nd and 3rd floors) and decreases in magnitude above the 5th floor. On the contrary, Table 5.2 shows that $M_2^{st,m}$ is largest in magnitude at the 4th floor. These results suggest that the upper yielding hinge can be placed at 4th or 5th floor, where $M_{i2}^{st,m}$ or $M_{i2}^{st,e}$ is largest in magnitude, respectively.

Based on the observations from Figure 5.3, two modified versions of MB1 were designed. One version forms an upper yielding hinge in the 5th story at 4th floor level (denoted MBU1 as shown in Table 5.3), and other version forms an upper yielding hinge in the 6th story at 5th floor level (denoted MBU2 as shown in Table 5.3). Figure 5.4 shows $\boldsymbol{\phi}_1^{sm}$ and $\boldsymbol{\phi}_2^{sm}$, and $M_1^{st,sm}$ and $M_2^{st,sm}$ for MBU1 and MBU2.

Table 5.4 shows $\overline{M}_{bn}^{sm}$, $\overline{M}_{4n}^{sm}$, and $\overline{M}_{5n}^{sm}$ for the first three modes of MBU1 and MBU2. As shown in Table 5.4, since $\boldsymbol{\phi}_n^{sm}$ are derived after the base and upper flexural yielding mechanisms have formed, only the first two-mechanism mode contributes to the M_b response. Thus, while $\overline{M}_{b1}^{sm}$ is non-zero, the higher mode $\overline{M}_{bn}^{sm}$ are zero. Similarly, only first and second two-mechanism modes contribute to the story base moment response at floor level 4 (where the upper yielding hinge forms) for MBU1, and only first and second two-mechanism modes contribute to the story base moment response at floor level 5 (where the upper yielding mechanism forms) for MBU2. Thus, only $\overline{M}_{41}^{sm}$ and $\overline{M}_{42}^{sm}$ are non-zero for MBU1, and only $\overline{M}_{51}^{sm}$ and $\overline{M}_{52}^{sm}$ are non-zero for MBU2.

5.4.2. Strength of Upper Yielding Hinge

The strength of the upper (i.e., second) yielding hinge is related to the strength of the base (i.e., first) yielding hinge, M_1^h, which is established for each GM as follows:

$$M_1^h = M_{b1}^{st,sm}\left(\frac{SA_{GM}(T_1^e)}{R}\right) \tag{5.9}$$

where $M_{b1}^{st,sm} = M_{01}^{st,sm}$ = 1st two-mechanism mode static base overturning moment response; R = 6; T_1^e = linear-elastic 1st mode period of the structure.

The yielding strength of the upper yielding hinge, M_2^h, is expressed as a fraction of M_1^h, as follows:

$$M_2^h = f_h\, M_1^h \tag{5.10}$$

where f_h = factor applied to M_1^h

To preclude forming the upper flexural yielding mechanism prematurely, relative to when the base flexural yielding mechanism forms, which may cause a concentration of inelastic deformation in the upper yielding hinge, the expected 1st mode story base moment response at the location of the upper yielding hinge should be considered in selecting the strength of the yielding hinge:

$$M_{2,1}^h = M_{i1}^{st,sm}\left(\frac{SA_{GM}(T_1^e)}{R}\right) \tag{5.11}$$

where i =u; u indicates the location of the upper hinge and u = 4 for MBU1 and u = 5 for MBU2.

From Eq. (5.9), Eq. (5.10), and Eq. (5.11), the value of f_h corresponding to $M_{2,1}^h$ denoted f_{h1}, is as follows:

$$f_{h1} = \frac{M_{u1}^{st,sm}}{M_{b1}^{st,sm}} \tag{5.12}$$

Using f_{h1} in Eq. (5.10) gives the required yielding strength for the upper yielding hinge if only 1st mode response is considered, and the base hinge and upper hinge yield simultaneously (i.e., at the same lateral load level).

When f_h exceeds f_{h1}, the overstrength of M_2^h compared to $M_{2,1}^h$, denoted f_{os}, is as follows:

$$f_{os} = \frac{f_h}{f_{h1}} \tag{5.13}$$

If the strength of the upper yielding hinge is selected without overstrength, f_{os} = 1. Alternatively, f_{os} could be less than 1.0, indicating the upper yielding hinge would form first under only 1st mode response.

5.4.3. Expected Second Mode Response, $A_{eff_2}^{sm}$

In general for an N degree-of-freedom structure, with N modes, the story base moment at floor level i is:

$$M_i(t) = M_{i1}^{st,sm} A_{eff_1}^{sm}(t) + M_{i2}^{st,sm} A_{eff_2}^{sm}(t) + \ldots + M_{i\mathrm{N}}^{st,sm} A_{eff_N}^{sm}(t) \tag{5.14}$$

At the location of the upper yielding hinge (i.e., at floor level i = u, where and u = 4 for MBU1 and u = 5 for MBU2), due to the properties of $\boldsymbol{\phi}_n^{sm}$, $M_{u\mathrm{n}}^{sm} = 0$ for n > 2 (i.e, only the 1st and 2nd modes contribute to the moment at the location of the upper yielding hinge as shown in Table 5.4). Since the moment at the location of the upper yielding is constrained by the hinge strength (i.e., $|M_u(t) \le M_2^h|$), then the sum of $M_{u1}^{sm}(t)$ and $M_{u2}^{sm}(t)$ are constrained by the strength of the upper yielding hinge as follows:

$$|M_{u1}^{sm}(t)+M_{u2}^{sm}(t)| \le M_2^h \tag{5.15a}$$

$$\left|M_{u1}^{st,sm}A_{eff_1}^{sm}(t)+M_{u2}^{st,sm}A_{eff_2}^{sm}(t)\right| \le M_2^h \tag{5.15b}$$

where Eq. (5.15b) shows the constraint from M_2^h results in a constraint $A_{eff_2}^{sm}(t)$. Note that $M_{u1}^{st,sm} > 0$ and $M_{u2}^{st,sm} < 0$, as shown in Figure 5.3. Dividing both sides of Eq. (5.15b) by $\left|M_{u2}^{st,sm}\right|$ results in:

$$\left|\frac{M_{u1}^{st,sm}}{\left|M_{u2}^{st,sm}\right|}A_{eff_1}^{sm}(t)-A_{eff_2}^{sm}(t)\right| \le \frac{M_2^h}{\left|M_{u2}^{st,sm}\right|} \tag{5.16}$$

Defining $r_u = M_{u1}^{st,sm} / |M_{u2}^{st,sm}|$ and $A_{2SL} = M_2^h / |M_{u2}^{st,sm}|$, Eq. (5.16) is rewritten as follows:

$$\left|r_u A_{eff_1}^{sm}(t)-A_{eff_2}^{sm}(t)\right| \le A_{2SL} \tag{5.17}$$

where A_{2SL}= a simple limit on $A_{eff_2}^{sm}$which can be derived based on a simple (and incorrect) assumption that only $|M_{u2}^{st,sm}A_{eff_2}^{sm}(t)|$ contributes to $M_u(t)$, (which is limited by M_2^h).

In general,

$$M_b(t) = M_{b1}^{st,sm}A_{eff_1}^{sm}(t)+M_{b2}^{st,sm}A_{eff_2}^{sm}(t)+\ldots+M_{bN}^{st,sm}A_{eff_N}^{sm}(t) \tag{5.18}$$

At the base of the wall, however, $M_{bn}^{st,sm} = 0$ for n > 1 due to the properties of $\boldsymbol{\phi}_n^{sm}$ (see Table 5.4). Since $|M_b(t)| \le M_1^h$ and only $M_{b1}^{st,sm} \neq 0$, $M_{b1}(t)$ is constrained as follows:

$$|M_{b1}(t)| \le M_1^h \tag{5.19a}$$

$$\left|M_{b1}^{st,sm}A_{eff_1}^{sm}(t)\right| \le M_1^h \tag{5.19b}$$

where Eq. (5.19b) shows that the constraint from M_1^h results in a constraint on $A_{eff_1}^{sm}(t)$.

Dividing both sides of Eq. (5.19b) by $M_{b1}^{st,sm}$ (which is positive), results in:

$$\left|A_{eff_1}^{sm}(t)\right| \leq \frac{M_1^h}{M_{b1}^{st,sm}} \tag{5.20a}$$

where Eq. (5.20a) shows that the 1st two-mechanism mode effective pseudo-acceleration ($A_{eff_1}^{sm}(t)$) is constrained by the yield strength of the base hinge.

Using Eq. (5.12) and Eq. (5.13), Eq. (5.20a) is rewritten as follows:

$$\left|A_{eff_1}^{sm}(t)\right| \leq \frac{1}{f_{os}} \frac{M_2^h}{M_{u1}^{st,sm}} \tag{5.20b}$$

where Eq. (5.20b) shows that the 2nd two-mechanism mode effective pseudo-acceleration ($A_{eff_2}^{sm}(t)$) is constrained by the yield strength of the upper hinge.

Multiplying both sides of Eq. (5.20b) by r_u and replacing $M_2^h / |M_{u2}^{st,sm}|$ with A_{2SL}, the constraint on $A_{eff_1}^{sm}(t)$ is expressed as follows:

$$\left|r_u A_{eff_1}^{sm}(t)\right| \leq \frac{1}{f_{os}} A_{2SL} \tag{5.21}$$

Figure 5.5(a) shows the possible range of $\left(r_u A_{eff_1}^{sm}(t)\right)$ and $\left(r_u A_{eff_1}^{sm}(t) \text{-} A_{eff_2}^{sm}(t)\right)$, which are $\left[-\frac{A_{2SL}}{f_{os}}, \frac{A_{2SL}}{f_{os}}\right]$ and $[-A_{2SL}, A_{2SL}]$, respectively. The figure shows $\left|r_u A_{eff_1}^{sm}(t) \text{-} A_{eff_2}^{sm}(t)\right|$ is

constrained by the simple limit on $A_{eff_2}^{sm}$, denoted A_{2SL}. The figure also shows the constraint on $A_{eff_1}^{sm}(t)$ expressed in terms of A_{2SL}. As seen in Figure 5.5(a), at any point in time, t, of the NL response of the wall structure, when $A_{eff_1}^{sm}(t)$ is positive, A_{2SL} is reached (and yielding of the second yielding hinge initiates) at a larger absolute value of $A_{eff_2}^{sm}(t)$ when $A_{eff_2}^{sm}(t)$ is also positive, and A_{2SL} is reached at a smaller absolute value of $A_{eff_2}^{sm}(t)$ when $A_{eff_2}^{sm}(t)$ is negative. In fact, when $A_{eff_1}^{sm}(t)$ is positive and $A_{eff_2}^{sm}(t)$ is positive, the absolute value of $A_{eff_2}^{sm}(t)$ can exceed A_{2SL}. When $A_{eff_1}^{sm}(t)$ is negative, the results are reversed.

Based on Eq. (5.17) and Eq. (5.21), the largest possible absolute value of $A_{eff_2}^{sm}(t)$, that is, the largest possible $A_{eff_2}^{sm}$, denoted $A_{2,max}$, is reached when $|r_u A_{eff_1}^{sm}(t)| = A_{2SL}/f_{os}$ and $A_{eff_1}^{sm}(t)$ and $A_{eff_2}^{sm}(t)$ have the same sign, as follows:

$$A_{2,max} = A_{2SL} + \frac{A_{2SL}}{f_{os}} \tag{5. 22}$$

Replacing A_{2SL} in Eq. (5.22) with $M_2^h/|M_{u2}^{st,sm}|$ results in:

$$A_{2,max} = \frac{M_2^h}{\left|M_{u2}^{st,sm}\right|}\left(1+\frac{1}{f_{os}}\right) \tag{5. 23}$$

which shows how the response of the 2nd mode (i.e., the largest possible $A_{eff_2}^{sm}$, $A_{2,max}$) can be controlled by selecting the strength of the upper yielding hinge, M_2^h. Using Eq. (5.13), $A_{2,max}$ is expressed as follows:

$$A_{2,max} = \frac{M_1^h}{\left|M_{u2}^{st,sm}\right|}(f_h + f_{h1}) \tag{5. 24}$$

which shows that the largest possible $A_{eff_2}^{sm}$ is determined by the strength of the base yielding hinge, M_1^h, and the factors f_h and f_{h1}, which relate M_2^h to M_1^h.

5.4.4. Expected Peak Story Force Response, r_x

In general, a total story force response (i.e., story base moment or story shear of a NL structure), $r_x(t)$, can be expressed as a sum of the modal force responses $r_{xn}(t)$, which equal the modal static responses, $r_{xn}^{st,sm}$, under the modal lateral forces, $\boldsymbol{s}_n^{st,sm}$, multiplied by the modal effective pseudo-accelerations, $A_{eff_n}^{sm}(t)$, as follows (see Chapter 2 and Chopra, 2012):

$$r_x(t) = r_{x1}^{st,sm} A_{eff_1}^{sm}(t) + r_{x2}^{st,sm} A_{eff_2}^{sm}(t) + \cdots + r_{x\mathrm{N}}^{st,sm} A_{eff_N}^{sm}(t) \tag{5.25a}$$

Considering the contributions of only the first two-mechanism modes and assuming r_{xn} = 0 for n > 2, r_x is expressed as follows:

$$r_x(t) = r_{x1}^{st,sm} A_{eff_1}^{sm}(t) + r_{x2}^{st,sm} A_{eff_2}^{sm}(t) \tag{5.25b}$$

Note that when $r_x(t)$ represents the story base moment or story shear, $r_{x1}^{st,sm}$ is always positive, while $r_{x2}^{st,sm}$ can be either positive or negative based on the type of force response $r_x(t)$ and the story x.

The largest possible absolute value of $r_x(t)$ is estimated using Eq. (5.25b) and considering three different cases for $A_{eff_1}^{sm}(t)$ and $A_{eff_2}^{sm}(t)$, as follows:

Case I: The primary assumption for this case are, that $A_{eff_1}^{sm}(t)$ and $A_{eff_2}^{sm}(t)$ are positively correlated and that $A_{eff_1}^{sm}(t)$ is at its largest possible absolute value, which is $A_{eff_1}^{sm} = \frac{1}{f_{os}} \frac{M_2^h}{M_{u1}^{st,sm}}$ from Eq. (5.20b) and denoted $A_{1,maxb}$ in Eq. (5.26a). Then $A_{eff_2}^{sm} = A_{2,max}$ from Eq. (5.24), which is the largest possible absolute value of $A_{eff_2}^{sm}(t)$. The largest absolute value of $r_x(t)$ for this case with $A_{eff_1}^{sm}(t) = A_{1,maxb}$ and $A_{eff_2}^{sm}(t) = A_{2,max}$, denoted r_x^I, is expressed as follows:

$$r_x^I = | r_{x1}^{st,sm} A_{1,maxb} + r_{x2}^{st,sm} A_{2,max} | \tag{5.26a}$$

Case II: The primary assumption for this case is that $A_{eff_1}^{sm}(t)$ and $A_{eff_2}^{sm}(t)$ are negatively correlated. Two possible conditions for f_{os} are considered, namely $f_{os} \geq 1$ or $f_{os} < 1$.

If $f_{os} \geq 1$, and $A_{eff_1}^{sm}(t)$ is at its largest possible positive value, that is, $A_{eff_1}^{sm} = A_{1,maxb}$, then the minimum negative value for $A_{eff_2}^{sm}(t)$ is $A_{eff_2}^{sm}(t) = -A_{2SL}\left(1 - \frac{1}{f_{os}}\right)$ from Eq. (5.17) and Eq. (5.21). The largest absolute value of $r_x(t)$ for this case with $A_{eff_1}^{sm}(t) = A_{1,maxb}$ and $A_{eff_2}^{sm}(t) = -A_{2SL}\left(1 - \frac{1}{f_{os}}\right)$, denoted r_x^{II} is expressed as follows:

$$r_x^{II} = \left| r_{x1}^{st,sm} A_{1,maxb} + r_{x2}^{st,sm} \left(-A_{2SL}\left(1 - \frac{1}{f_{os}}\right)\right)\right| \qquad f_{os} \geq 1 \tag{5.26b}$$

If $f_{os} < 1$, that is, when the upper hinge forms before the base hinge forms under only 1st mode response, the $A_{eff_1}^{sm}(t) = M_2^h / M_{u1}^{st,sm}$, denoted $A_{1,maxu}$ in Eq. (5.26c), which results in $A_{eff_2}^{sm}(t) = 0$. Then, the largest absolute value of r_x^{II} for $A_{eff_1}^{sm}(t) = A_{1,maxu}$ and $A_{eff_2}^{sm}(t) = 0$ is expressed as follows:

$$r_x^{II} = \left| r_{x1}^{st,sm} A_{1,maxu} \right| \qquad f_{os} < 1 \tag{5.26c}$$

Case III: The primary assumption for this case is that $A_{eff_1}^{sm}(t) = 0$. Then the largest absolute value of $A_{eff_2}^{sm}(t)$ is A_{2SL}. The value of $r_x(t)$ for this case, denoted r_x^{III} is expressed, as follows:

$$r_x^{III} = \left| r_{x2}^{st,sm} A_{2SL} \right| \tag{5.26d}$$

Results presented later show the need to consider the third mode contribution to $r_x(t)$ in addition to the 1st and 2nd mode contributions in Eq. (5.25b) and Eq. (5.26). The challenge of including the 3rd mode (and higher modes) is that the 3rd and higher mode responses are not controlled by a yielding mechanism. For simplicity, it is assumed that $A_{eff_3}^{sm}(t)$ equals the median peak value of $A_{eff_3}^{sm}(t)$ (i.e., the median value of $A_{eff_3}^{sm}$) from NLTHA of the NL structure under the selected GM set, denoted $A_{eff_3,m}^{sm}$. In addition the absolute value of $r_{x3}^{st,sm}$ from Eq. (5.25a) is used.

The equations for Case I and Case II are then modified to include the 3rd mode response. The largest possible absolute values of $r_x(t)$ for Case I and Case II including the median 3rd mode response, denoted $r_x^{I,3}$ and $r_x^{II,3}$, are as follows:

$$r_x^{I,3} = r_{x1}^{st,sm} A_{1,maxb} + r_{x2}^{st,sm} A_{2,max} + \left| r_{x3}^{st,sm} \right| A_{eff_3,m}^{sm} \quad (5.26e)$$

$$r_x^{II,3} = r_{x1}^{st,sm} A_{1,maxb} + r_{x2}^{st,sm} \left(-A_{2SL} \left(1 - \frac{1}{f_{os}} \right) \right) + \left| r_{x3}^{st,sm} \right| A_{eff_3,m}^{sm} \qquad f_{os} \geq 1 \quad (5.26f)$$

$$r_x^{II,3} = r_{x1}^{st,sm} A_{1,maxu} + \left| r_{x3}^{st,sm} \right| A_{eff_3,m}^{sm} \qquad f_{os} < 1 \quad (5.26g)$$

(Note that Case III was not modified to include the 3rd mode response because it was found that Case III does not control the peak story force response).

For an arbitrary response quantity, Case I, Case II, or Case III may control, so the envelope maximum absolute (i.e., peak) value of $r_x(t)$ from r_x^I, r_x^{II}, and r_x^{III} is denoted as r_x^{en},. The envelope peak value of $r_x(t)$ among $r_x^{I,3}$ and $r_x^{II,3}$ is also determined and denoted as $r_x^{en,3}$. The results from Eq. (5.26a through g), and the envelope values r_x^{en} and $r_x^{en,3}$ are compared with the NLTHA results for the example structures, later in the chapter. The *absolute* maximum peak value and the *median* peak value of r_x from the NLTHA results for each example structure for the GM set, are denoted $r_{x,a}$ and $r_{x,m}$, respectively. Assuming r_x from the NLTHA results of each example structure for the GM set is log-normally distributed, the median + 2 standard deviation value for the peak r_x, denoted as $r_{x,2\sigma}$, is calculated as follows:

$$r_{x,2\sigma} = exp^{mean(ln(r_x))+2(\sigma(ln(r_x)))} \quad (5.27)$$

where σ = standard deviation of the natural log of r_x over the ground motion set.

In addition, NLTHA results for $r_x(t)$ including only the contributions of the first two-mechanism modes are calculated as follows:

$$r_{x(1+2)}(t) = r_{x1}(t) + r_{x2}(t) \tag{5.28a}$$

$$r_{x(1+2)}(t) = r_{x1}^{st,sm} A_{eff_1}^{sm}(t) + r_{x2}^{st,sm} A_{eff_2}^{sm}(t) \tag{5.28b}$$

The peak value of $r_{x(1+2)}(t)$ was found from the NLTHA results and the maximum peak value of $r_{x(1+2)}(t)$ over the GM set, denoted $r_{x(1+2),a}$ was determined and compared with the other results.

5.5. Description of NL Wall Structures

Ten example cantilever wall structures with purely flexural response (MB1 and MBU1 to MBU9) are studied. Each wall structure has a constant story height of 13 ft., and is idealized as a lumped-mass system with a unit mass at each floor level. Each story has the same stiffness, and this stiffness is selected so that the first mode period of the linear-elastic model is 1.5 s. While MB1 has a single, base flexural yielding mechanism (which is a base yielding hinge), MBU1 to MBU9 have two yielding mechanisms, implemented as inelastic (yielding or SC) hinges. The strength of the base flexural yielding spring, M_1^h, is based on Eq. (5.9) and the strength of the upper flexural yielding spring, M_2^h, is established using Eq. (5.10). The properties of the wall structures are summarized in Table 5.3.

To investigate the effect of the location of the upper yielding hinge, the study includes two 9-story wall structures with purely flexural response having an upper yielding hinge at the 4th and 5th story levels, respectively (denoted MBU1 and MBU2 as shown in Table 5.3).

The base and upper flexural yielding springs of MBU1 and MBU2 are assumed to have an elastic-perfectly plastic (EPP) response.

To investigate the effect of the strength of the upper yielding hinge, the study includes three 9-story wall structures with M_2^h based on f_{os} values of 0.80, 1.10, and 1.20, respectively (denoted MBU3, MBU4, and MBU5 as shown in Table 5.3). The base and upper flexural yielding springs for MBU3, MBU4, and MBU5 are assumed to have an EPP response.

To investigate the effect of a post-yielding stiffness of the base and upper flexural yielding springs, the study includes a 9-story wall structure with base and upper flexural yielding springs that provide the wall structure with a 2% global post-yielding slope, α_g (denoted MBU6 as shown in Table 5.3). The post-yielding slope for the flexural yielding springs, α_s, is based on α_g as well as the initial flexural stiffness of the spring, k_{spg}, and the linear-elastic flexural stiffness of the first story of the wall structure , denoted k_e. The global post-yield stiffness, denoted $\alpha_g k_e$, is a combination of the post-yield stiffness of the yielding rotational spring, denoted $\alpha_s k_{spg}$, and k_e, since the yielding rotational spring and the element are springs in series:

$$\frac{1}{\alpha_g k_e} = \frac{1}{\alpha_s k_{spg}} + \frac{1}{k_e} \tag{5.29}$$

where $k_e = 3\ (E\ I\ /L)$; E = modulus of elasticity of the wall; I = moment of inertia of the wall; L = first story height.

By rearranging the terms in Eq. (5.29), α_s is calculated as follows:

$$\alpha_s = \frac{\alpha_g}{(1-\alpha_g)} \frac{k_e}{k_{spg}} \tag{5.30}$$

To investigate the effect of using rocking joints in place of yielding hinges, the study includes three 9-story wall structures with base and upper SC inelastic rotational springs to represent rocking joints (denoted MBU7, MBU8, and MBU9 as shown in Table 5.3). MBU7 and MBU8 have f_{os} = 1.1, while MBU9 has f_{os} = 1.0. The parameter used to describe the energy dissipation of the rocking joints, β_e, is defined as the ratio of the hysteresis loop area of an SC system over the hysteresis loop area of a bilinear elastoplastic system with similar strength (Seo and Sause, 2005). To investigate the effect of the energy dissipation ratio (β_e) of the SC rotational springs, the base and upper SC rotational springs of MBU8 have unequal β_e values, as shown in Table 5.3. MBU7 and MBU9 have β_e values of 0.30 for the base and upper rocking joints. MBU7 and MBU8 have α_g = 0, but α_g = 2% is assigned to the SC rotational springs of MBU9.

Two dimensional numerical models of the wall structures were created in OpenSees (Mazzoni et al., 2009). Schematics of the wall structure models are shown in Figure 5.6. Force-based beam-column elements with linear-elastic material definitions were used to model the walls. The base and upper yielding hinges or rocking joints with SC response were modeled by using a zero length rotational element (Mazzoni et al., 2009). A bi-linear material model (using the Steel02 material definition in OpenSees (Mazzoni et al., 2009)) was used for the rotational spring used to model the yielding hinges. A self-centering material model (using the SelfCentering material definition in OpenSees (Mazzoni et al.,

2009)) was used for the rotational spring used to model the rocking joints. A lean-on-column with linear-elastic beam-column members was included to model the second-order effects of vertical loads. A unit seismic mass was assigned to the horizontal degree-of-freedom of each node of the lean-on-column at each floor level. The horizontal displacements of the wall and lean-on-column were constrained to each other with rigid links at each floor level. The corotational coordinate transformation was used for the elements. Caughey damping with a 5% damping ratio for each mode was used. Newmark constant average acceleration integration and the nonlinear Newton-Krylov solution algorithms were used in the NLTHA.

5.6. Ground Motion Set Used in NLTHA

A ground motion (GM) set composed of 18 GM pairs listed in Table 5.1 was used in the NLTHA of the example structures. The GM records were selected from the NGA (PEER, 2011) database for a site located in Orange County, California (Chancellor, 2014). The site has a short period spectral acceleration (S_s) of 1.5g and 1 s period spectral acceleration (S_1) of 0.6g based on ASCE (2010) definitions (ASCE, 2010).

Each GM pair was scaled so that the geometric mean of the pseudo-acceleration response for the GM pair matches the design basis earthquake (DBE) spectrum (ASCE, 2010) over a period range of 0.1-7.0 s. The DBE has a 10% probability of exceedance (POE) in 50 years corresponding to a return period of 475 years (BSSC, 2003). The scale factors were calculated in accordance with the average scaling method described in Baker (2011). The

pseudo-acceleration response spectra of GMs scaled to the DBE and the median spectrum for the GM set are shown in Figure 5.7.

5.7.Response of NL Wall Structures

5.7.1. nth Mode Contribution to Dynamic Response

The effectiveness of upper flexural yielding mechanism (i.e., upper yielding hinge or upper rocking joint with SC response) on controlling the second mode response for each NL wall structure is examined based on NLTHA results for the GM set. The 5% damped *median* linear-elastic and *median* reduced (by R = 6) pseudo-acceleration response spectra were constructed for the GM set. The nth two-mechanism mode peak effective pseudo spectral accelerations, $A_{eff_n}^{sm}$, were calculated from the NLTHA results for each wall structure for each GM in the GM set, and the median value of $A_{eff_n}^{sm}$ for the GM set, $A_{eff_n,m}^{sm}$, was calculated. $A_{eff_n,m}^{sm}$ is compared with the nth mode pseudo-accelerations (i.e, at T_n^e) from the median linear-elastic and median reduced pseudo-acceleration response spectra which are denoted $SA_{GM,m}(T)$ and $SA_{GM,m}(T)/R$, respectively.

Effect of Location of Second Flexural Yielding Mechanism on $A_{eff_2}^{sm}$

Figure 5.8 shows the 5% damped median linear-elastic and median reduced (by R = 6) pseudo-acceleration response spectra for the GM set. The peak median effective pseudo-accelerations $A_{eff_n,m}$ for the first three modes of MB1, MBU1, and MBU2 are also shown.

For MB1, which does not have an upper yielding mechanism, the mechanism mode $A_{eff_n,m}$, denoted $A^{m}_{eff_n,m}$ is shown. For MBU1 and MBU2, the two-mechanism mode $A_{eff_n,m}$, denoted $A^{sm}_{eff_n,m}$ are shown. Table 5.5 shows $SA_{GM,m}(T^e_n)$ for MB1, MBU1, and MBU2. Table 5.6 shows $A^{m}_{eff_n,m}$ for MB1, and $A^{sm}_{eff_n,m}$ for MBU1 and MBU2. Table 5.7 shows the ratio of $SA_{GM,m}(T^e_n)$ to $A^{m}_{eff_n,m}$ and the ratio of $SA_{GM,m}(T^e_n)$ to $A^{sm}_{eff_n,m}$, which are denoted as $R^{m}_{act_n}$ and $R^{sm}_{act_n}$, respectively. As seen in Figure 5.8, the first mode response is controlled by the formation of base yielding mechanism for MB1, MBU1, and MBU2. $R^{m}_{act_1}$ for MB1, and $R^{sm}_{act_1}$ for MBU1 and MBU2, are 6.0, 6.0, and 6.0, respectively (Table 5.7). The higher modes are not strongly affected by the formation of the base yielding mechanism for MB1, and $R^{m}_{act_2}$ and $R^{m}_{act_3}$ are 1.0 and 0.57, respectively (Table 5.7). Figure 5.8 shows that the formation of the upper yielding mechanism at the 5th floor level (i.e., MBU2) has more effect on the 2nd mode response than the formation of the upper yielding mechanism located at the 4th floor level (i.e., MBU1). $R^{sm}_{act_2}$ is 1.18 for MBU1, but is 1.38 for MBU2. The formation of the upper yielding mechanism at the 4th floor level for MBU1, slightly increased the 3rd mode response relative to MB1. While $R^{m}_{act_3}$ is 0.57 for MB1, $R^{sm}_{act_3}$ is 0.46 and 0.63 for MBU1 and MBU2, respectively.

Figure 5.9 shows the *median* peak story base moment response at floor level i ($M_{i,m}$), peak story shear response of story i ($V_{i,m}$), and peak story drift response of story i ($\Theta_{si,m}$) envelopes for MB1, MBU1, and MBU2 under the selected GM set. The reduction in $M_{i,m}$ for both MBU1 and MBU2 compared to MB1, is apparent in Figure 5.9. The median peak story base moment response at the 4th floor level, $M_{4,m}$ in MBU1, is reduced by a factor of

2.5 by the upper flexural yielding hinge, while the peak story base moment response at the 5th floor level, $M_{5,m}$ in MBU2 is reduced by a factor of 3.3 by the upper yielding mechanism. Unlike $M_{i,m}$, the peak $V_{i,m}$ is not strongly affected by the formation of the upper yielding mechanism in the structure. Figure 5.9 shows that in the upper stories, the peak $\Theta_{si,m}$ for MBU2 is about 1.12 larger than the $\Theta_{si,m}$ for MBU1. The increase in $\Theta_{si,m}$ for MBU2 may be due to the formation of upper yielding mechanism prior to the base yielding mechanism. Based on NLTHA results for MBU2 under the ABN000 GM record, the upper yielding mechanism forms prior to the base yielding mechanism. For this GM, the time of when the upper yielding mechanism forms, t_{upper}, is much earlier than the time when the base yielding mechanism forms, t_{base}, where (t_{upper} /t_{base}) = 0.80. Methods to avoid forming upper yielding mechanism before the base yielding mechanism forms are discussed later in this chapter.

Figure 5.8 and Figure 5.9 show that $A^{sm}_{eff_2,m}$ and $A^{sm}_{eff_3,m}$ and M_i are better controlled for MBU2 compared to MBU1. These results suggest that the upper yielding hinge located at the 5th floor level is more effective than the upper yielding hinge located at the 4th floor level, which suggests that the location of upper yielding hinge should be determined based on $M^{st,e}_{i2}$ rather than $M^{st,m}_{i2}$(referring to the discussion in Section 5.4.1).

Estimating M_i and V_i Response Envelopes

Peak values of $M_i(t)$ and $V_i(t)$ for the NL wall structures under the selected GM set are estimated using Eq. (5.26a) through Eq. (5.26g) and are denoted as M_i^I and V_i^I, M_i^{II} and V_i^{II}, and M_i^{III} and V_i^{III}, respectively. The envelopes for M_i^I, M_i^{II}, M_i^{III}, and V_i^I, V_i^{II}, V_i^{III} are denoted as M_i^{en} and V_i^{en}, respectively. The envelopes of $M_i^{I,3}$and $M_i^{II,3}$and $V_i^{I,3}$and $V_i^{II,3}$ are denoted as $M_i^{en,3}$ and $V_i^{en,3}$, respectively. The *absolute* peak value and the *median* peak value of $M_i(t)$ and $V_i(t)$ from the NLTHA results for the NL wall structures for the GM set, are denoted $M_{i,a}$ and $V_{i,a}$ and $M_{i,m}$ and $V_{i,m}$, respectively. The median + 2 standard deviation values of the $M_i(t)$ and $V_i(t)$ from the NLTHA results for the NL wall structures for the GM set are denoted as $M_{i,2\sigma}$ and $V_{i,2\sigma}$, respectively. The values for $M_i(t)$ and $V_i(t)$ including only the 1st and 2nd mode contributions, from (Eq. (5.28b)), (i.e., ($M_{i1}(t) + M_{i2}(t)$) and ($V_{i1}(t) + V_{i2}(t)$)) from NLTHA results for the NL wall structures for the GM set and the absolute mean peak values are denoted as $M_{i(1+2),a}$ and $V_{i(1+2),a}$, respectively.

Figure 5.10(a) shows the results for M_i^I, M_i^{II}, M_i^{III}, and M_i^{en} normalized by M_1^h for MBU2. Since f_{os} is 1.0 for MBU2, M_i^{II} includes only the 1st mode response (see Eq. (5.26b)). As shown in Figure 5.10(a), M_i^I, M_i^{II}, and M_i^{III} are different from each other. While M_i^{II} controls M_i^{en} up to the 5th floor, M_i^I controls M_i^{en} above the 5th floor. M_i^{III} never controls M_i^{en}. These results suggest that M_i^{en} is dominated by the 1st mode response up to the 5th floor, and by the 1st and 2nd modes (with positive correlation) above the 5th floor.

Figure 5.10(b) shows V_i^I, V_i^{II}, V_i^{III}, and V_i^{en} normalized by V_b^h for MBU2. V_b^h is M_1^h divided by the effective height of the first two-mechanism mode (see Chopra, 2012 for the definition of the effective height of a mode). Since f_{os} is 1.0 for MBU2, V_i^{II} includes only the 1st mode response (see Eq. (5.26b)). Figure 5.10(b) shows that V_i^I controls V_i^{en} up to the 4th floor level and above the 6th floor level. V_i^{II} controls V_i^{en} in the 5th and 6th stories (i.e., between the 4th and 6th floor levels). V_i^I, V_i^{II}, and V_i^{III} equal V_i^{en} in the 7th story. These results suggest that V_i^{en} is mostly dominated by V_i^I, which includes the 1st and 2nd mode contributions to V_i with positive correlation of $A_{eff_1}^{sm}(t)$ and $A_{eff_2}^{sm}(t)$.

Figure 5.11(a) compares M_i^{en} with $M_{i,a}$, $M_{i,m}$, $M_{i,2\sigma}$, and $M_{i(1+2),a}$ normalized by M_1^h for MBU2. Figure 5.11(a) shows that M_b^{en} and M_5^{en} exactly match $M_{b,a}$ and $M_{5,a}$ showing that (for EPP yielding hinges) the yielding mechanisms fully control the story base moment at the yielding hinge locations. In addition, M_i^{en} exactly matches $M_{i(1+2),a}$ indicating that M_i^{en} accurately predicts the absolute maximum of the 1st and 2nd mode response from NLTHA. Therefore, differences between M_i^{en} and the other results are due to the 3rd mode response, which is not controlled by either yielding mechanism. The difference between M_i^{en} and $M_{i,m}$ is less than 15% at all floor levels indicating that the median 3rd mode response provides a modest, but important increase in the moment away from the locations of the yielding hinges. The difference between M_i^{en} and $M_{i,a}$ is less than 27% up to 5th floor level and up to 35% at the 6th floor level. The difference between M_i^{en} and $M_{i,2\sigma}$ is less than 23% up to the 5th floor level and up to 35% at the 6th floor level.

Figure 5.11(b) compares V_i^{en} with $V_{i,a}$, $V_{i,m}$, $V_{i,2\sigma}$, and $V_{i(1+2),a}$ normalized by V_b^h for MBU2. Figure 5.11(b) shows that V_i^{en} is about 5% larger than $V_{i(1+2),a}$ at all floor levels indicating that V_i^{en} is a good envelope for the absolute maximum 1st and 2nd mode response from NLTHA. The difference between V_b^{en} and $V_{b,a}$ is about 50%. This difference increases to 67% at the 4th floor level. The difference between V_i^{en} and $V_{i,m}$ is smaller compared to $V_{i,a}$, and is 24% at the base level and up to 50% at the 6th floor level. These results show that the differences between V_i^{en} and $V_{i,a}$ and V_i^{en} and $V_{i,m}$ are larger compared the moment response, which shows that the higher mode (i.e., n > 2) contribution to V_i is more important than to M_i. Therefore, neglecting the higher mode (i.e., n > 2) contribution to V_i based on Eq. (5.25b) will lead to unconservative and/or inaccurate design force estimates for MBU2.

Figure 5.11(c) compares M_i^{en} and $M_i^{en,3}$ with $M_{i(1+2),a}$ and $M_{i,2\sigma}$ normalized by M_1^h for MBU2. Figure 5.12(a) shows that the difference between $M_i^{en,3}$ and $M_{i,2\sigma}$ is less than 5% below 5th floor level and is about 15% above the 5th floor level. These results show the importance of the 3rd mode contribution to M_i, and suggest that including the median 3rd mode response, in combination (by using an absolute sum) with the envelope response for the 1st and 2nd mode, which are controlled by yielding mechanisms, provides a good upper bound to the total response.

Figure 5.11(d) compares V_i^{en} and $V_i^{en,3}$ with $V_{i(1+2),a}$ and $V_{i,2\sigma}$ normalized by V_b^h for MBU2. Figure 5.11(d) shows that $V_i^{en,3}$ is much closer to $V_{i,2\sigma}$ than V_i^{en}. $V_i^{en,3}$ is almost three times

larger than V_i^{en} in the 5th story. The difference between $V_i^{en,3}$ and $V_{i,2\sigma}$ is less than 35% for all stories and as small as 2% in the 5th story. These results show the importance of the 3rd mode contribution to V_i, and suggest that including the median 3rd mode response, in combination with the envelope response for the 1st and 2nd mode, which are controlled by the yielding mechanisms, provide a reasonable upper bound to the total response.

Effect of GM on $A_{eff_2}^{sm}$

To investigate the sensitivity of the higher mode response to the GM, the NLTHA results for MBU2 subjected to the ABN000, ILA013W, and HDA165 GM records (see Table 5.1) are examined.

Figure 5.12 shows the pseudo-acceleration response spectra for the ABN000, ILA013W, and HDA165 GM records. Table 5.8 shows $SA_{GM}(T_n^e)$ and $A_{eff_n}^{sm}$ for MBU2 subjected to ABN000, ILA013W, and HDA165 GM records. The ratio of $SA_{GM}(T_2^e)$ to $SA_{GM}(T_1^e)$ is calculated for each GM to examine whether the GM is strong enough to generate a second mode response which is greater than the first mode response. Based on Table 5.8, the ratio of $SA_{GM}(T_2^e)$ to $SA_{GM}(T_1^e)$ is 4.5, 0.80, and 2.13 for the ABN000, ILA013W, and HDA165 GM records, respectively. $R_{act_2}^{sm}$ is 2.83, 0.61, and 1.33 for MBU2 subjected to the ABN000, ILA013W, and HDA165 GM records, respectively. These ratios suggest that the formation of upper yielding mechanism is most effective in controlling the second mode response for MBU2 subjected to ABN000 GM record and least effective for MBU2 subjected to

ILA013W GM record. These results show that as the ratio of $SA_{GM}(T_2^e)$ to $SA_{GM}(T_1^e)$ increases, the second mode response is more strongly affected by the formation of the upper (i.e., second) yielding mechanism.

Table 5.8 shows $A_{1,max}$ from Eq. (5.20) and $A_{2,max}$ from Eq. (5.23), as well as $SA_{GM}(T_n^e)$, and $A_{eff_n}^{sm}$ from the NLTHA results for MBU2 under the ABN000, ILA013W and HDA165 GM records. Note that $A_{1,max}$ and $A_{2,max}$ are different for each GM since M_1^h is a function of $SA_{GM}(T_1^e)$ (see Eq. (5.10)). Table 5.8 shows $A_{1,max}$ equals $A_{eff_1}^{sm}$, and the ratio of $A_{2,max}$ to $A_{eff_2}^{sm}$ is 1.0, 1.24, and 1.0 for MBU2 subjected to ABN000, ILA013W, HDA165, respectively. These results show that the predicted $A_{2,max}$ is less than the actual $A_{eff_2}^{sm}$ from the NLTHA results for MBU2 under ILA013W, since the ILA013W GM record is not strong enough to generate a second mode response with an $A_{eff_2}^{sm}$ as a large as $A_{2,max}$.

Figure 5.13 shows $M_5(t)$ normalized by M_2^h and $A_{eff_n}^{sm}(t)$ normalized by $A_{eff_n}^{sm}$ for the first two modes of MBU2 subjected to the ABN000 GM record. Note that $A_{eff_1}^{sm}(t)$ normalized by $A_{eff_1}^{sm}$ is same as the $M_1^h(t)$ normalized by M_1^h, since $M_{in}^{sm} = 0$ for n > 1 and the base yielding mechanism forms. Therefore, the plotted response history for $A_{eff_1}^{sm}(t)$ normalized by $A_{eff_1}^{sm}$ can also be used to understand $M_b(t)$ normalized by M_1^h. As shown in Table 5.8, $A_{eff_2}^{sm} = A_{2,max}$ for MBU2 subjected to the ABN00 GM record (see Table 5.8). Figure 5.12 shows that $A_{eff_1}^{sm}(t)$ and $A_{eff_2}^{sm}(t)$ both have flat-topped response, which illustrate that the 1st

and 2nd mode responses are controlled by the formation of the base and upper yielding mechanisms. Figure 5.13 shows that there are times in the NL response of the wall when both base and upper yielding mechanisms form (e.g. at 19.8 s of the response), while $A_{eff_1}^{sm}(t)$ and $A_{eff_2}^{sm}(t)$ are at their peak values and responding with the same sign. These results suggest that 1st and 2nd mode responses are fully positively correlated and both of them contribute to the formation of upper yielding mechanism. There are also times (e.g., at 20 s of the response) when the upper yielding mechanisms forms with the contribution of only $A_{eff_1}^{sm}(t)$, i.e., $A_{eff_2}^{sm}(t) = 0$. There are also times (e.g., at 18.88 s of the response) when the upper yielding mechanism forms without the formation of the base yielding mechanism with the contribution of only $A_{eff_2}^{sm}(t)$, i.e., $A_{eff_1}^{sm}(t) = 0$. There are also times (e.g., at 18.92 s of the response) when the upper yielding mechanism forms without the formation of the base yielding mechanism but with the contribution of both $A_{eff_1}^{sm}(t)$ and $A_{eff_2}^{sm}(t)$. for example, at 18.92 s of the response, $A_{eff_1}^{sm}(t)$ and $A_{eff_2}^{sm}(t)$ are positively correlated but responding at 50% and 75 % of their peak response amplitudes, $A_{eff_1}^{sm}$ and $A_{eff_2}^{sm}$, respectively.

Figure 5.14 shows $A_{eff_n}^{sm}(t)$ normalized by $A_{eff_n}^{sm}$ for the first three modes of MBU2 subjected to the ABN00 GM record. At the time of the peak $M_b(t)$, the $A_{eff_1}^{sm}(t)$ is at its peak value, while the amplitudes of $A_{eff_2}^{sm}(t)$ and $A_{eff_3}^{sm}(t)$ are 60% of $A_{eff_2}^{sm}$ and 20% $A_{eff_3}^{sm}$, respectively, with the same sign as $A_{eff_1}^{sm}(t)$. At the time of the peak $V_b(t)$, $A_{eff_1}^{sm}(t)$ and $A_{eff_2}^{sm}(t)$ are at their peak values and $M_5(t) = M_2^h$ implying that both base and upper yielding mechanisms form, while the amplitude of $A_{eff_3}^{sm}(t)$ is 70% of $A_{eff_3}^{sm}$, with the same sign as $A_{eff_1}^{sm}(t)$ and $A_{eff_2}^{sm}(t)$.

At the time of peak V_b (t), $A_{eff_1}^{sm}(t)$ and $A_{eff_2}^{sm}(t)$ are at their peak values and fully positively correlated. Therefore, the largest absolute possible of V_b is estimated using Eq. (5.26a) and Eq. (5.26e). V_b^I from Eq. (5.26a) and $V_b^{I,3}$ from Eq. (5.26e) are 309 kip and 542 kip, respectively. The actual peak $V_b(t)$ from NLTHA is 585 kip. The difference between V_b^I and the V_b from NLTHA is 52%, while the difference between $V_b^{I,3}$ and the V_b from NLTHA is less than 8%. Table 5.9 shows the $V_{bn}^{st,sm}$ for the first three modes of MBU2. Table 5.10 shows $A_{eff_n}^{sm}$ for the first three modes of MBU2 subjected to ABN000 GM records. As shown in Table 5.10, the ratio of $A_{eff_3}^{sm}$ to $A_{eff_2}^{sm}$ is 2.9 and ratio of $A_{eff_3}^{sm}$ to $A_{eff_1}^{sm}$ is 27.6. Using Eq. (25a), $V_{b1}(t)$, $V_{b2}(t)$, and $V_{b3}(t)$ are calculated, which are 138.6 kip, 171.4 kip, and 276.8 kip, respectively. These results suggest that the third mode contribution to peak $V_b(t)$ is not negligible for MBU2 subjected to ABN000 GM record and should be taken into account while estimating the peak V_b.

Figure 5.15(a) shows $M_5(t)$ normalized by M_2^h and $A_{eff_n}^{sm}(t)$ normalized by $A_{eff_n}^{sm}$ for the first two modes of MBU2 subjected to the ILA013W GM record. Figure 5.14(b) shows $M_5(t)$ normalized by M_2^h, $A_{eff_1}^{sm}(t)$ normalized by $A_{eff_1}^{sm}$, and $A_{eff_2}^{sm}(t)$ normalized by $A_{2,max}$ for MBU2 subjected to the ILA013W GM record. Note that $A_{eff_1}^{sm}(t)$ normalized by $A_{eff_1}^{sm}$ is same as the $M_1^h(t)$ normalized by M_1^h, since $M_{in}^{sm} = 0$ for n > 1 and the base yielding mechanism forms. Figure 5.15(a) shows there are times (e.g. 50.8 s) in the response of the wall when $A_{eff_2}^{sm}(t) = 0$ and both base and upper yielding mechanisms form with the contribution of only $A_{eff_1}^{sm}(t)$ and the amplitude of $A_{eff_1}^{sm}(t)$ is at 100% of $A_{eff_1}^{sm}$ (also 100% of $A_{1,max}$). There are also times

(e.g., at 48.9 s of the response) when the upper yielding mechanism forms without the formation of the base yielding mechanism but with the contribution of both $A_{eff_1}^{sm}(t)$ and $A_{eff_2}^{sm}(t)$, which are positively correlated but responding at 80% and 60 % of $A_{eff_1}^{sm}$ and $A_{eff_2}^{sm}$, respectively. Figure 15(b) also shows that $A_{eff_2}^{sm}$ is 98% of $A_{2,max}$ for MBU2 under the ILA013W ground motion, indicating that ILA013W ground motion is not strong enough to generate a second mode response which has an $A_{eff_2}^{sm}$ as large as $A_{2,max}$.

Effect of Yield Strength of Second Flexural Yielding Mechanism on $A_{eff_2}^{sm}$

Table 5.10 shows $SA_{GM}(T_n^e)$ and $A_{eff_n}^{sm}$ for MBU2 to MBU9 subjected to the ABN000 GM record. Table 5.11 shows $R_{act_n}^{sm}$ together with the ratio of the time when the upper yielding mechanism forms, t_{upper}, to the time when the base yielding mechanism forms, t_{base}, for MBU2 to MBU9. The ratio of $R_{act_2}^{sm}$ is 3.15, 2.70, and 2.57 for MBU3, MBU4, and MBU5, respectively. These results suggest that as M_2^h increases, $A_{eff_2}^{sm}$ also increases, which is in agreement with Eq. (5.23). Table 5.10 shows that the ratio of t_{upper} to t_{base}, is 0.78, 0.80, 1.01, and 1.01 for MBU2, MBU3, MBU4, and MBU5, respectively. These results suggest that to avoid the formation of upper yielding mechanism prior to the formation of base flexural yielding mechanism, f_{os} should be at least 1.1.

Figure 5.16(a) shows the results for M_i^I, M_i^{II}, M_i^{III}, and M_i^{en} normalized by M_1^h for MBU3. Since f_{os} is 0.80 for MBU3, M_i^{II} includes only the 1st mode response (see Eq. (5.26c)). As

shown in Figure 5.10(a), M_i^I, M_i^{II}, and M_i^{III} are different from each other. While M_i^{II} controls M_i^{en} between the 1st and 5th floors, M_i^I controls M_i^{en} between the base and 1st floor, and above the 5th floor. M_i^{III} never controls M_i^{en}. These results suggest that M_i^{en} is dominated by the 1st mode response between the 1st and 5th floors, and by the 1st and 2nd modes (with positive correlation) below first 1st and above the 5th floor.

Figure 5.16(b) shows V_i^I, V_i^{II}, V_i^{III}, and V_i^{en} normalized by V_b^h for MBU3. Similarly, since f_{os} is 0.80 for MBU3, V_i^{II} includes only the 1st mode response (see Eq. (5.26c)). Figure 5.16(b) shows that V_i^I controls V_i^{en} up to the 4th floor level and above the 6th floor level. V_i^{II} controls V_i^{en} at 5th and 6th stories (i.e., between the 4th and 6th floor levels). V_i^I, V_i^{II}, and V_i^{III} equal V_i^{en} in the 7th story. These results suggest that V_i^{en} is mostly dominated by V_i^I, which includes the 1st and 2nd mode contributions to V_i with positive correlation of $A_{eff_1}^{sm}(t)$ and $A_{eff_2}^{sm}(t)$.

Figure 5.16(c) compares M_i^{en} and $M_i^{en,3}$ with $M_{i(1+2),a}$ and $M_{i,2\sigma}$ normalized by M_1^h for MBU3. Figure 5.16(c) shows that M_b^{en} and M_5^{en} exactly match with the $M_{b(1+2),a}$ and $M_{5(1+2),a}$ (i.e., the EPP yielding hinges control the moment at hinge lcoations). M_i^{en} is less than $M_{i(1+2),a}$ up to 5th floor indicating that M_i^{en} does not accurately predict $M_{i(1+2),a}$ up to the 5th floor. Since $f_{os} = 0.80 < 1.0$, M_i^{en}, which is controlled by M_1^h between the 1st and 5th floor, includes only the 1st mode response between the 1st and 5th floors and does not include any 2nd mode contribution, as shown in Figure 5.16 (a). These results in Figure

5.16(c) show the importance of the 2nd mode contribution to M_i which is not taken into account in M_i^{II} for $f_{os} < 1.0$, and suggest that M_i^{en} may not provide a good upper bound to $M_{i(1+2),a}$ for $f_{os} < 1.0$. Figure 5.16(c) shows that the difference between $M_i^{en,3}$ and $M_{i,2\sigma}$ is less than 5% at all floors except for the 1st floor where $M_1^{en,3}$ is 10% smaller than $M_{1,2\sigma}$. $M_i^{en,3}$ is more than 1.5 times larger than M_i^{en}. These results show the importance of the 3rd mode contribution to M_i, but since it is combined with the M_i^{en} which does not provide a good estimate of $M_{i(1+2),a}$, $M_i^{en,3}$ also does not provide a good estimate of $M_{i,2\sigma}$ for MBU3 with $f_{os} < 1.0$.

Figure 5.16(d) compares V_i^{en} and $V_i^{en,3}$ with $V_{i(1+2),a}$ and $V_{i,2\sigma}$ normalized by V_b^h for MBU3. Figure 5.16(d) shows that V_i^{en} is 5% greater than $V_{i(1+2),a}$ in all stories. These results suggest that V_i^{en} provides an accurate envelope to $V_{i(1+2),a}$. The difference between $V_i^{en,3}$ and $V_{i,2\sigma}$ is less than 10% for all stories. These results show the importance of the 3rd mode contribution to V_i, and suggest that including the median 3rd mode response, in combination with the envelope response for the 1st and 2nd mode, which are controlled by the yielding mechanisms, provide a reasonable upper bound to the total response.

Figure 5.17(a) compares M_i^{en} and $M_i^{en,3}$ with $M_{i(1+2),a}$ and $M_{i,2\sigma}$ normalized by M_1^h for MBU5, with $f_{os} = 1.2$. Figure 5.17(a) shows that M_i^{en} matches $M_{i(1+2),a}$ indicating that M_i^{en} accurately predicts the absolute maximum of the 1st and 2nd mode response from NLTHA. Therefore, the differences between M_i^{en} and $M_{i,2\sigma}$ are due to the 3rd mode response, which

is not controlled by a yielding mechanism. Figure 5.17(a) shows that M_b^{en} and M_5^{en} exactly match $M_{b,2\sigma}$ and $M_{5,2\sigma}$. The difference between $M_i^{en,3}$ and $M_{i,2\sigma}$ is less than 10% at all floors, while $M_i^{en,3}$ is greater than $M_{i,2\sigma}$ below the 5th floor, it is less than $M_{i,2\sigma}$ above the 5th floor. These results show the importance of the 3rd mode contribution to M_i, and suggest that including the median 3rd mode response, in combination with the envelope response for the 1st and 2nd mode, which are controlled by the yielding mechanisms, provide a good upper bound to the total response.

Figure 5.17(b) compares V_i^{en} and $V_i^{en,3}$ with $V_{i(1+2),a}$ and $V_{i,2\sigma}$ normalized by V_b^h for MBU5. Figure 5.17(b) shows that V_i^{en} matches $V_{i(1+2),a}$ indicating that V_i^{en} accurately predicts the absolute maximum of the 1st and 2nd mode response from NLTHA. Therefore, the differences between V_i^{en} and $V_{i,2\sigma}$ are due to the 3rd mode response, which is not controlled by a yielding mechanism. Figure 5.17(b) shows that the difference between V_b^{en} and $V_{b,a}$ is less than 20%. This difference increases to 25% at the 4th floor level. The difference between V_i^{en} and $V_{i,m}$ is smaller for MBU5 compared to MBU3. These results suggest that including the median 3rd mode response, in combination with the envelope response for the 1st and 2nd mode, which are controlled by the yielding mechanisms, provide a good estimate of the total response.

Effect of the Hysteretic Response of Second Flexural Yielding Mechanism on $A_{eff_2}^{sm}$

Figure 5.18 shows $M_5(t)$ normalized by M_2^h and $A_{eff_n}^{sm}(t)$ normalized by $A_{eff_n}^{sm}$ for the first two modes of MBU2 and MBU6 under the ABN000 GM record. As shown in Figure 5.18, while $M_2^h(t)$ has flat-topped response for MBU2, $M_5(t)$ for MBU6 instantaneously reaches its peak value due to the 2% global post-yield stiffness, α_g, of the flexural yielding springs, which is α_g = 2%. For both MBU2 and MBU6, there are times when the base and upper yielding mechanisms form at the same time while $A_{eff_1}^{sm}(t)$ and $A_{eff_2}^{sm}(t)$ are at their peak values and are responding with the same sign (i.e., fully positively correlated).

Table 5.11 shows that $R_{act_2}^{sm}$ is 2.8 and 2.7 for MBU2 and MBU6, respectively. The difference between the two $R_{act_2}^{sm}$ values is less than 4%. These results suggest that having a non-zero α_g for the base and upper yielding hinges of MBU6 does not preclude the second mode response from being controlled by the formation of upper yielding mechanism.

Figure 5.19 shows $A_{eff_n}^{sm}(t)$ normalized with $A_{eff_n}^{sm}$ for the first two modes of MBU7 and MBU8 under the ABN000 GM record. The base and upper SC rotational springs of MBU8 have unequal β_e values, as shown in Table 5.3. MBU7, on the contrary, has β_e values of 0.30 for the base and upper rocking joints. Figure 5.19 shows that the 2nd mode response for MBU7 is smaller compared to MBU8. There are times for both MBU7 and MBU8, when the base and upper yielding mechanisms (i.e., SC inelastic rotational springs) form at the same time, while $A_{eff_1}^{sm}(t)$ and $A_{eff_2}^{sm}(t)$ are at their peak values and fully positively

correlated. Figure 5.19 shows that there also times when the base and upper yielding mechanisms form at different times for MBU7 and MBU8. For example, at 20.6 s, while the base hinge is forming, the upper hinge is unloading for MBU7, and at 17.3 s, while the base hinge is forming, the upper hinge is unloading for MBU8.

Table 5.11 shows that $R_{act_2}^{sm}$ is 2.7 for both MBU7 and MBU8, respectively. These results suggest that having a larger β_e for the upper rocking joint does not significantly alter the effect of the upper rocking joint on the 2nd mode response. Table 5.11 further shows that $R_{act_2}^{sm}$ is 2.6 for MBU9, which has α_g = 2%. The reduction of the peak 2nd mode response with the formation of the upper yielding mechanism is 4% smaller for MBU9 compared to MBU7, which suggests that having a non-zero α_g assigned to the SC rotational springs, slightly decreases the effect of the upper rocking joint over the 2nd mode response.

Figure 5.20 shows the distributions of the peak M_i, V_i, and Θ_{s_i} responses based on NLTHA results for MB1, MBU4, and MBU6 under the ABN000 GM record. The addition of an upper yielding hinge for MBU4 and MBU6 considerably reduces the story base moment response at the upper floor levels compared to MBU1. For example, the peak M_5 is reduced by a factor of 3.3 for MBU4 and MBU6 compared to MBU1. The peak V_i is not strongly affected by the formation of upper yielding mechanism for MBU4 and MBU6. The peak V_i for MBU4 and MBU6 are similar to the peak V_i for MB1**.** Figure 5.20 shows that the presence of a non-zero α_g for MBU6, decreased the peak Θ_{s_i}, especially at the stories above

the 5th floor where the upper yielding hinge is located, compared to MBU4. Figure 5. 20 shows that the peak Θ_{s_i} for MBU6 is very similar to that for MB1.

Figure 5.21(a) compares M_i^{en} and $M_i^{en,3}$ with $M_{i(1+2),a}$ and $M_{i,2\sigma}$ normalized by M_1^h for MBU7. Figure 5.21(a) shows that M_i^{en} matches $M_{i(1+2),a}$ indicating that M_i^{en} accurately predicts the absolute maximum of the 1st and 2nd mode response from NLTHA. Figure 5.21(a) shows that M_b^{en} and M_5^{en} exactly match with the $M_{b,2\sigma}$ and $M_{5,2\sigma}$. As shown in Figure 5.21(a), while $M_i^{en,3}$ is greater than $M_{i,2\sigma}$ below the 5th floor, $M_{i,2\sigma}$ is greater than $M_i^{en,3}$ above the 5th floor. The difference between $M_i^{en,3}$ and $M_{i,2\sigma}$ is as much as 20% at the 2nd floor. These results show the importance of the 3rd mode contribution to M_i. These results suggest that M_i^{en} is less accurate for a NL wall structure with base and upper rocking joints with SC response compared to a NL wall structure with base and upper hinges with EPP response.

Figure 5.21(b) compares V_i^{en} and $V_i^{en,3}$ with $V_{i(1+2),a}$ and $V_{i,2\sigma}$ normalized by V_b^h for MBU7. Figure 5.21(b) shows that V_i^{en} matches $V_{i(1+2),a}$ in all stories indicating that V_i^{en} accurately predicts the absolute maximum of the 1st and 2nd mode response from NLTHA. Figure 5.21(b) shows that $V_i^{en,3}$ is smaller than $V_{i,2\sigma}$ in all stories. These results show the importance of the higher mode (n > 3) contribution to V_i, and suggest that including the median 3rd mode response, in combination with the envelope response for the 1st and 2nd mode, does not provide a good upper bound to the total response of MBU7.

Figure 5.22(a) compares M_i^{en} and $M_i^{en,3}$ with $M_{i(1+2),a}$ and $M_{i,2\sigma}$ normalized by M_1^h for MBU9. Figure 5.22(a) shows that contrary to the M_i^{en} and $M_i^{en,3}$ envelopes for MBU2 and other wall structures presented previously, the differences between M_i^{en} and $M_{i(1+2),a}$ and between $M_i^{en,3}$ and $M_{i,2\sigma}$ are considerable for MBU9. Since α_g = 2% for MBU9, M_5^{en} is considerably less than $M_{5,a}$, since the hardening of the SC rotational springs is not included in calculating M_i^{en} and $M_i^{en,3}$. The difference between M_5^{en} and $M_{5(1+2),a}$ is as large as 50%. These results suggest that M_i^{en} will not provide a good upper bound for $M_{i(1+2),a}$ and $M_{i,2\sigma}$, unless hardening of the yielding (or rocking) mechanism is considered.

Figure 5.22(b) compares V_i^{en} and $V_i^{en,3}$ with $V_{i(1+2),a}$ and $V_{i,2\sigma}$ normalized by V_b^h for MBU9. Figure 5.22(b) shows that V_i^{en} macthes $V_{i(1+2),a}$ in all stories indicating that V_i^{en} accurately predicts the absolute maximum of the 1st and 2nd mode response from NLTHA. Figure 5.22(b) shows that $V_i^{en,3}$ is smaller than $V_{i,2\sigma}$ in all stories. These results show the importance of the higher mode (n > 3) contribution to V_i.

5.8. Case Study of a 9-story SC-CBF with Base and Upper Yielding Mechanisms

A self-centering concentrically braced frame (SC-CBF) (Sause et al., 2006; Roke, 2009; Chancellor, 2014) is a concentrically braced frame (CBF) with special column base details. Unlike a conventional CBF, the columns of an SC-CBF are not fully attached to the

foundation and the special column details permit the CBF to "rock" on the foundation. During the controlled rocking response of the SC-CBF, the column under incremental tension from overturning moment uplifts from the foundation. As a result, the lateral drift capacity of the system prior to the initiation of structural damage is increased considerably. The resistance to rocking is provided by vertically-oriented post tensioning (PT) bars located within the CBF, which enable the system to self-center during the earthquake. Under the DBE, yielding of the CBF members is precluded by a performance-based design procedure for SC-CBFs; however, a 50% probability of PT bar yielding is considered acceptable (Chancellor, 2014). Figure 5.23 shows the configuration of a typical SC-CBF with energy dissipaters (EDPs) and the base overturning moment, M_b, versus lateral roof drift response, Θ_r, for an SC-CBF under monotonic lateral loading together with the respective identified structural limit states.

The tests and analytical studies conducted by Roke et al. (2010) on 6-story SC-CBFs showed that while the first mode response is controlled by the yielding of PT bars, the higher mode responses of SC-CBFs remain "uncontrolled" and may be amplified by the rocking. The decrease of the lateral stiffness of SC-CBFs during the rocking response of the SC-CBF, and consequent period elongation promotes higher mode effects, while limiting the first mode response. Roke (2010) and Chancellor (2014) proposed using modal load factors to factor the elastic higher mode response while estimating the design member force demands.

The design philosophy for SC-CBFs is based on the assumption that the M_b response is a first mode dominant response and the rocking response of the SC-CBF with consequent PT bar yielding limits the forces that can develop in the structure. Even though this assumption is true for pure static response (similar to MB1, as shown in Figure 5.2), studies by Chancellor et al. (2014) on a wider range of SC-CBFs with different aspect ratios (4-, 6-, 9-, 12-, 15-, and 18-stories) reveal that as the aspect ratio of the structure increases, the base yielding mechanism does not control the higher mode response. Consequently, the contribution of higher, especially the second, mode response to M_b considerably increases and becomes comparable to the contribution of the first mode response. Figure 5.24 shows that the second mode contribution to M_b increases with the increasing aspect ratio of the SC-CBF. As seen in Figure 5.24, the second mode contribution to M_b becomes comparable to the first mode contribution as the SC-CBF reaches 9 stories in height.

Using the method presented for the NL wall structures with base and upper yielding hinges, this section discusses adding an upper rocking joint with SC response to the 9-story SC-CBF to control the higher mode response, rather than designing the SC-CBF for the amplified higher mode response, as done in prior studies (i.e. Roke, 2010; Chancellor, 2014).

5.8.1. Description of Self-Centering Concentrically Braced Frame Structure

A 9-story SC-CBF structure designed by Chancellor (2014) denoted as 9EO-GL, is used in this study. Figure 5.25 shows the floor plan and elevation of the SC-CBF. The braces of

the example SC-CBF are arranged in an X configuration. To transfer the base shear from the uplifted column to the column in contact with foundation, a horizontal brace strut is located at the bottom of the SC-CBF. The structure is assumed to be an office-type structure. Dead and live loads used in design are given in Table 5.12 and Table 5.13. All members of the SC-CBF are ASTM A992 wide-flange shapes with a nominal steel yield strength of 50 ksi, meeting the seismic compactness requirements of AISC (2010). Table 5.14 summarizes the design parameters of the example 9-story SC-CBF (denoted SCCBF1 in Table 5.14), based on the studies of Chancellor (2014). The total area of the PT bars, A_{PT}, located at the center of the SC-CBF is 3.4 in^2. The design yield strength for the PT steel, f_{py}, is 120 ksi. An initial prestressing force of $0.50f_{py}$ is assigned to the PT bars. A vertically-oriented energy dissipation device (EDP), which is assumed to be a constant-force energy dissipation device (e.g., a friction device), is attached to the foundation and to the base of each SC-CBF column. The force developed in each EDP, denoted V_{ED}, is 50 kip. The EDP dissipates energy when the SC-CBF column uplifts from the foundation.

A two dimensional numerical model of the SC-CBF was developed in OpenSees (Mazzoni et al., 2009). Each beam and column of the SC-CBF was modeled by five force-based beam-column elements with fiber sections. Five integration points were used along the length of each force-based beam-column element. Gauss-Lobatto numerical integration was used. A bi-linear material model (using the Steel02 material definition in OpenSees (Mazzoni et al., 2009)) was used for the steel material of the SC-CBF. A force-based beam-column element is used to the design the steel-posttensioning (PT) bars. The steel of PT bars was modeled with bilinear-elastic-plastic material model with 2% post-yield slope.

The potential for slack in the PT bar, i.e., a gap occurring between the PT anchorage nut and the anchorage block after significant yielding and permanent deformation of the PT bar, was modeled using a zero-length element (Mazzoni et al., 2009) with a compressive stiffness equal to the 30000 kips/inch. Two zero-length elements are used to model the vertical and horizontal gap conditions at the end of each SC-CBF column. Similarly, two zero-length elements are used to model the vertical and horizontal gap conditions at the upper rocking joint level. EDP elements having vertical orientation are modeled using a corotational truss. A bi-linear material model (using the Steel02 material definition in OpenSees (Mazzoni et al., 2009)) was used for the steel material of the EDP elements. Each EDP element at the base floor level is attached to the corresponding SC-CBF column at the first floor column node and to a fixed node at the foundation level. Each EDP element at the upper rocking joint level us attached to the SC-CBF column at the sixth floor column node and the fifth floor column node.

A lean-on-column with elastic beam-column elements was used to model the second-order effects of the gravity loads within the seismic tributary area of the SC-CBF. Seismic mass was assigned to the horizontal degree-of-freedom of the lean-on-column at each floor level. The horizontal displacements of the SC-CBF and lean-on-column were constrained to each other with rigid links at each floor level. The vertical and horizontal displacements at the base of the lean-on-column were restrained. The corotational coordinate transformation was used for the elements. Rayleigh damping with a 2.6% damping ratio for the first mode and 6.1% damping ratio for the third mode was assigned using a damping substructure (see

Chapter 4 and Roke, 2010). Newmark constant average acceleration integration and the nonlinear Newton-Krylov solution algorithms were used in the NLTHA.

5.8.2. Location of Upper Rocking Joint

Similar to the NL wall structures, the location of the upper rocking joint with SC response is determined based on the $M_{i1}^{st,e}$ and $M_{i2}^{st,e}$ for the SC-CBF. Table 5.15 shows $M_{i1}^{st,e}$ and $M_{i2}^{st,e}$, $M_{i1}^{st,m}$ and $M_{i2}^{st,m}$. As seen in Table 5.15, $M_{i2}^{st,e}$ changes sign between the 2nd and 3rd floor levels and reaches its peak negative value at the 5th floor level. On the contrary, Table 5.15 shows that $M_{i2}^{st,m}$ reaches its peak negative value at 4th floor level. Based on the NLTHA results for MBU1 and MBU2, it was concluded that to effectively control the second mode response, the upper rocking joint should be located based on $M_{i2}^{st,e}$ rather than $M_{i2}^{st,m}$. Therefore, the upper rocking joint of the SC-CBF is located at the 5th floor level, where $M_{i2}^{st,e}$ reaches its peak negative value.

5.8.3. Strength of Upper Rocking Joint

In SC-CBF design, the base flexural yielding mechanism forms (i.e., base rocking joint) with the rocking response of the SC-CBF followed by the yielding of the PT bars. Based on Figure 5.26, the weight of the SC-CBF ($W_{SC\text{-}CBF}$), yielding force of the PT bars (PT_y), the gravity loads on the left and right columns (F_{col}), and the force provided by the EDPs (V_{ED}) contribute to the M_b resistance against the driving M_b due to applied lateral forces. The overturning moment resistance capacity of the SC-CBF at the yielding of PT bars, is

assumed to be equal to M_1^h and is calculated by considering the M_b resistance provided by the forces acting on the SC-CBF as follows (Chancellor, 2014):

$$M_1^h = \left(PT_y + W_{SC\text{-}CBF}\right)\frac{b_{SC\text{-}CBF}}{2} + \left(V_{ED} + F_{col}\right)\left(b_{SC\text{-}CBF}\right) \tag{5.31}$$

where $PT_y = F_y A_{PT}$; F_y = yield stress of PT steel; A_{PT} = area of PT bars; $b_{SC\text{-}CBF}$ = width of SC-CBF. Table 5.15 shows the value of the M_1^h together with the values of the contributing forces.

The strength of the upper rocking hinge located at the 5th floor level, M_2^h, is determined using Eq. (5.10). An overstrength factor, f_{os}, of 1.1 is selected based on the parametric study carried out for the NL wall structures. Based on Eq. (5.11), the factor, f_{h1}, used to calculate M_2^h is calculated as the ratio of $M_{51}^{st,sm}$ to $M_{b1}^{st,sm}$. Then plugging Eq. (5.12) and Eq. (5.13) into Eq. (5.10), M_2^h is calculated in terms of M_1^h, as follows:

$$M_2^h = 1.1\, f_{h1}\, M_1^h \approx 0.3 M_1^h \tag{5.32}$$

The design of the SC-CBF is modified to have a story base moment capacity at the 5th floor level, equal to M_2^h. Having the same area of PT bars along the entire height of the structure would result in a story base moment capacity much greater than M_2^h at the 5th floor level. Therefore, the PT bars are discontinued below the upper rocking joint at the 5th floor level and a different area of PT bars is used through the upper rocking joint upto the roof. While the area of PT bars at the base rocking joint, denoted A_{PT}, is determined using Eq. (5.31),

the area of PT bars at the upper rocking joint, denoted A_{pt}^{u}, is determined from M_2^h as follows:

$$M_2^h = \left(PT_y^u + W_{SC\text{-}CBF}^u\right)\frac{b_{SC\text{-}CBF}}{2} + (F_{col}^u)\left(b_{SC\text{-}CBF}\right) \tag{5.33a}$$

$$M_2^h = \left(f_{py}A_{pt}^u + W_{SC\text{-}CBF}^u\right)\frac{b_{SC\text{-}CBF}}{2} + (F_{col}^u)\left(b_{SC\text{-}CBF}\right) \tag{5.33b}$$

$$A_{pt}^u = \frac{M_2^h - (V_{ED}^u + F_{col}^u)\left(b_{SC\text{-}CBF}\right) - W_{SC\text{-}CBF}^u\frac{b_{SC\text{-}CBF}}{2}}{f_{py}\left(\frac{b_{SC\text{-}CBF}}{2}\right)} \tag{5.34}$$

where V_{ED}^u = force provided by the EDPs located between the 5th and 6th floor levels; $W_{SC\text{-}CBF}^u$ = self-weight of SC-CBF above the 5th floor; F_{col}^u = gravity load on top of columns above the 5th floor; f_{py} = yielding stress of PT bars.

Although having EDPs at the upper rocking joint location is not mandatory, the EDPs at the upper rocking joint level (in between the 5th and 6th floor levels) help to control the lateral story drifts at the stories above the upper rocking joint level and also decreases the required A_{pt}^u, as the EDPs contribute to story base moment resistance at 5th floor level (see Eq. (5.34)).

Two new SCCBFs with base and upper rocking joints were designed based on SCCBF1, with the only base rocking joint. SCCBF2 has an upper rocking joint at the 5th floor level without EDPs between 5th and 6th floor levels (Table 5.16). SCCBF3 has an upper rocking joint at the 5th floor level with EDPs between 5th and 6th floor levels (Table 5.16). Figure

5.27 shows the configuration of these SC-CBFs with base and upper rocking joints. Table 5.16 summarizes the design parameters for SCCBF2 and SCCBF3.

5.8.4. Response of SC-CBFs with Base and Upper Rocking Joints

n^{th} Mode Contribution to Static Response

Figure 5.28 shows the $\boldsymbol{\phi}_1^m$ and $\boldsymbol{\phi}_2^m$and $M_1^{st,m}$ and $M_2^{st,m}$ for SCCBF1 as well as $\boldsymbol{\phi}_1^{sm}$ and $\boldsymbol{\phi}_2^{sm}$and $M_1^{st,sm}$ and $M_2^{st,sm}$ for SCCBF2. The effect of the formation of base rocking joint is apparent in $\boldsymbol{\phi}_1^m$ and $\boldsymbol{\phi}_1^{sm}$. Similarly, the effect of the base and upper rocking joints is apparent in $\boldsymbol{\phi}_2^{sm}$. As shown in Figure 5.28, while $M_{b1}^{st,m}$ and $M_{b1}^{st,sm}$ are non-zero, $M_{b2}^{st,m}$ and $M_{b2}^{st,sm}$ are zero, showing that $\boldsymbol{\phi}_1^m$ for SCCBF1 and $\boldsymbol{\phi}_1^{sm}$ for SCCBF2 are both uncoupled from the higher mode responses through the base rocking joint.

Table 5.17 shows $M_{in}^{st,sm}$ and $\overline{M}_{in}^{sm}$ calculated for the first three modes of SCCBF3. As seen in Table 5.17, $\overline{M}_{b1}^{sm}$ is 100% and the higher mode $\overline{M}_{bn}^{sm}$ is zero. These results show that the higher mode (n > 1) response is uncoupled from the base overturning moment response using $\boldsymbol{\phi}_n^{sm}$. Table 5.17 shows that the cumulative $\overline{M}_{51}^{sm}$ and $\overline{M}_{52}^{sm}$ is 100%, while $\overline{M}_{53}^{sm}$ is zero. These results indicate that the higher mode (n > 2) response is uncoupled from the story base moment at 5th floor using $\boldsymbol{\phi}_n^{sm}$, and only the 1st and 2nd two-mechanism modes contribute to M_5.

n^{th} Mode Contribution to Dynamic Response

Figure 5.29 shows the 5% damped median elastic and median reduced (by *R*) pseudo-acceleration spectra for the GM set together with the design spectrum based on ASCE (2011). The median peak effective pseudo-accelerations, $A^{m}_{eff_{n},m}$ for SCCBF1, $A^{sm}_{eff_{n},m}$ for SCCBF2, $A^{sm}_{eff_{n},m}$ for SCCBF3 are shown. Table 5.18 shows the $SA_{GM}(T^{e}_{n})$ and $SA_{DS}(T^{e}_{n})$, for the first three modes of SCCBF1, SCCBF2, and SCCBF3. Table 5.19 shows $A^{m}_{eff_{n},m}$ and $A^{sm}_{eff_{n},m}$ for the first three modes of SCCBF2 and SCCBF3. Table 5.20 shows $R^{m}_{act_{n}}$ and $R^{sm}_{act_{n}}$ for the first three modes of SCCBF1, SCCBF2, and SCCBF3. Figure 5.29 shows that the first mode response is effectively controlled for all these SC-CBF designs. $R^{m}_{act_{1}}$ is 7.37 for SCCBF1, while $R^{sm}_{act_{1}}$ is 7.47 for SCCBF2 and 7.54 for SCCBF3. Figure 5.29 shows that the second mode response is controlled by adding the upper rocking joint at the 5th floor. $R^{m}_{act_{2}}$ is 0.87 for SCCBF1, $R^{sm}_{act_{2}}$ is 1.34 for both SCCBF2 and SCCBF3. Based on Figure 5.24, the third mode response is amplified with the addition of upper rocking joint. $R^{m}_{act_{3}}$ is 0.88 for SCCBF1, $R^{sm}_{act_{3}}$ is 0.60 for SCCBF2 and 0.61 for SCCBF3.

Figure 5.30(a) shows $A^{m}_{eff_{n}}(t)$ normalized by $A^{m}_{eff_{n}}$ for the first three modes of SCCBF1 subjected to ABN000 GM record. The times of $A^{m}_{eff_{n}}$, the peak M_b (*t*), the V_b(*t*), and the peak 5th floor overturning moment response (M_5(*t*)) are also indicated on the plot. The $A^{m}_{eff_{1}}(t)$ has a relatively flat-topped response compared to the $A^{m}_{eff_{2}}(t)$ and $A^{m}_{eff_{3}}(t)$, which suggest that the first mode response is effectively "controlled" for the SCCBF1, but the second and third mode responses are not controlled by the base rocking joint. At the time of peak $M_b(t)$,

$A^m_{eff_1}(t)$ is at its peak value, while the amplitudes of $A^m_{eff_2}(t)$ and $A^m_{eff_3}(t)$ are close to zero. At the time of peak $V_b(t)$, $A^m_{eff_1}(t)$ and $A^m_{eff_2}(t)$ are at their peak values and the amplitude of $A^m_{eff_3}(t)$ is at 65% of $A^m_{eff_3}$, with the same sign as $A^m_{eff_1}(t)$ and $A^m_{eff_2}(t)$.

Figure 5.30(b) shows the $A^{sm}_{eff_n}(t)$ normalized by $A^{sm}_{eff_n}$ for the first three modes of SCCBF2 under the ABN000 GM record. The times of $A^{sm}_{eff_n}$, peak $M_b(t)$, peak $V_b(t)$, and peak $M_5(t)$ are also indicated on the plot. Unlike Figure 5.25 (a), both $A^{sm}_{eff_1}(t)$ and $A^{sm}_{eff_2}(t)$ have relatively flat-topped response. These results suggest that both first and second mode responses are effectively "controlled" by the formation of the base and upper yielding mechanism. At the time of peak $M_b(t)$, while $A^{sm}_{eff_1}(t)$ and $A^{sm}_{eff_2}(t)$ are at their peak values, the amplitude of $A^{sm}_{eff_3}(t)$ is close to zero. At the time of peak $V_b(t)$, the amplitudes of $A^{sm}_{eff_3}(t)$ is 100% of $A^{sm}_{eff_3}$, while the amplitudes of $A^{sm}_{eff_1}(t)$ and $A^{sm}_{eff_2}(t)$ are both at 80% of $A^{sm}_{eff_1}$ and $A^{sm}_{eff_2}$, respectively. At the time of peak $M_5(t)$, $A^{sm}_{eff_1}(t)$ and $A^{sm}_{eff_2}(t)$ are nearly at their peak values, while the amplitude of $A^{sm}_{eff_3}(t)$ is 50% of $A^{sm}_{eff_3}$, with the same sign as $A^{sm}_{eff_1}(t)$ and $A^{sm}_{eff_2}(t)$.

Using Eq. (5.23), the expected maximum possible value of $A^{sm}_{eff_2}$, that is, $A_{2,max}$, is calculated. $A_{2,max}$ is 0.815 for both SCCBF2 and SCCBF3. The ratio of $A_{2,max}$ to $A^{sm}_{eff_2,m}$ is 1.125 for both SCCBF2 and SCCBF3. These results suggest that $A_{2,max}$ overestimates the

actual $A_{eff_2,m}^{sm}$ by 12.5%. However, for a design force response calculation, having a conservative estimate for $A_{eff_2,m}^{sm}$ is more favorable than having an unconservative estimate.

Peak Median Response Envelopes for SC-CBFs with Single Base and Base and Upper Rocking Joints

Figure 5.31 compares the distribution of median peak story base moment response at floor level i ($M_{i,m}$), peak story shear response ($V_{i,m}$), and peak story drift response ($\Theta_{si,m}$) for SCCBF1, SCCBF2, and SCBF3. Figure 5.26 shows that adding an upper rocking joint in the SC-CBF considerably reduced the $M_{i,\mathrm{m}}$ response. $M_{5,m}$ is reduced by a factor of 3.4 for SCCBF2 and SCCBF3 compared to SCCBF1. Similar to the NL wall structures, the reduction of $V_{i,m}$ is not as pronounced as the reduction of $M_{i,\mathrm{m}}$. $V_{i,m}$ for SCCBF2 and SCCBF3 are similar to SCCBF1. $\Theta_{si,m}$ is not amplified much by adding the upper rocking joint. $\Theta_{si,m}$ for SCCBF2 and SCCBF3 are similar to SCCBF1. However, $\Theta_{s9,m}$ is smaller for SCCBF3 compared to SCCBF2, due to the presence of EDPs between the 5$^{\mathrm{th}}$ and 6$^{\mathrm{th}}$ floor levels for SCCBF3. These results suggest that having EDPs in the upper rocking joint reduces $\Theta_{si,m}$ at the upper stories compared to the SC-CBF design without EDPs in the upper rocking joint.

Figure 5.32(a) compares M_i^{en} with $M_{i,m}$ and $M_{i(1+2),a}$ normalized by M_1^h for SCCBF3. Figure 5.32(a) shows that M_b^{en} and $M_{b(1+2),a}$ are not equal, unlike for the NL wall structures with base and upper yielding hinges with EPP response. This result is due to the mechanism

of the SC-CBF, which starts by rocking that is limited by PT bar yielding. Yielding of the PT is used to defined the base rocking strength, and although the SC-CBF rocks at the base under each GM, the PT bars do not yield under some GMs. Therefore, the maximum base overturning moment response for some GM is not strong enough to reach the base moment capacity, so M_b^{en} is greater than $M_{b(1+2),a}$. The difference between M_i^{en} and $M_{i,m}$ is 15% at the base and less than 10% at the upper floor levels. M_i^{en} is as much as 10% greater than $M_{i(1+2),a}$. These results show that M_i^{en} provide a good envelope for the median peak total story base moment and cumulative 1st and 2nd mode story base moment responses from NLTHA.

Figure 5.32(b) compares V_i^{en} with $V_{i,m}$ and $V_{i,2\sigma}$ normalized by V_b^h for SCCBF3. Figure 5.32(b) shows that the difference between V_i^{en} and $V_{i,m}$ is less than 10%., and the difference between V_i^{en} and $V_{i(1+2),a}$ is 5%. These results suggest that V_i^{en} provide a reasonable envelope for the cumulative first and second mode story base moment response from NLTHA.

Figure 5.32(c) compares M_i^{en} and $M_i^{en,3}$ with $M_{i,2\sigma}$ normalized by M_1^h for SCCBF3. M_i^{en} and $M_i^{en,3}$ are less than $M_{i,2\sigma}$ except at the base. $M_i^{en,3}$ is less than $M_{i,2\sigma}$. These results suggest that M_i^{en} and $M_i^{en,3}$ do not provide a good envelope for $M_{i,2\sigma}$ from NLTHA.

Figure 5.32(d) compares V_i^{en} and $V_i^{en,3}$ with $V_{i,2\sigma}$, normalized by V_b^h for SCCBF3. Figure 5.32(b) shows that the difference between $V_i^{en,3}$ and $V_{i,2\sigma}$ is as much as 40%. These results suggest that the higher mode contributiond (i.e., n > 3) to $V_{i,2\sigma}$ are significant as including the median 3rd mode response in combination with the envelope response for the 1st and 2nd mode, which are controlled by the yielding mechanism, does not provide a good estimate of the total response.

Comparison of Utility Ratios for the Three SC-CBF Designs

Figure 5.33 compares the 5th story normalized brace axial force utilization ratios for SCCBF1 and SCCBF2. These utilization ratios are defined by Chancellor (2014). The median peak utilization ratio in all stories is less than 1.0 for both SCCBF1 and SCCBF2. Except for the 4th and 5th story braces the normalized median brae axial force utilization ratios are decreased for SCCBF2 compared to SCCBF1. The normalized median brae axial force utilization ratios for 4th and 5th story braces are 0.44 and 0.58 for SCCBF1 and 0.58 and 0.71 for SCCBF2, respectively. These results correspond to a 32% and a 22% increase in 4th and 5th story brace axial force utilization ratios for SCCBF2 compared to SCCBF1, respectively. These results show that effects off the increased 3rd mode response from adding the upper rocking joint, shown in Figure 5.29.

5.9.Summary and Conclusions

This chapter investigated the n^{th} mode response of NL structures with one or two clearly-defined yielding mechanisms. The higher mode responses of example NL wall structures with yielding hinges or rocking joints and a self-centering concentrically braced rocking frame (SC-CBF) structure are investigated. To control the second mode contribution to the total force response of NL structures with one yielding mechanism, it is proposed to introduce a second yielding mechanism in the structure. A method is described to determine the location and strength of the second yielding mechanism using the modal properties of the structure. Example structures are designed with clearly defined base and upper flexural yielding mechanisms (i.e., a yielding hinge or rocking joint for the wall and rocking joint for the SC-CBF). Parameters of the NL wall structures, such as the location, strength, hysteretic response of the first and second mechanisms are varied. The contributions of the higher modes to various seismic response quantities are investigated. Nonlinear time-history analyses (NLTHA) are performed on the example NL wall and SC frame structures to understand the effectiveness of the second flexural yielding mechanism on controlling the second mode force response.

The main findings of this study are:

- The NLTHA results of NL wall structures showed that the optimum location and strength of the upper yielding mechanism can be estimated using the modal properties of the structure. The upper yielding mechanism is observed to be more effective in controlling the second mode response, if its location is determined based on the elastic mode shapes, $\boldsymbol{\phi}_n^e$, rather than the mechanism mode shapes, $\boldsymbol{\phi}_n^m$.

- It is shown that using two-mechanism mode shapes, ϕ_n^{sm}, higher mode response (i.e., n > 2) can be uncoupled from the base and upper yielding mechanisms. Therefore, using ϕ_n^{sm}, $M_i(t)$ at upper hinge location can be expressed in terms of 1st and 2nd mode response.
- It is shown that using ϕ_n^{sm}, the expected range of the peak 1st mode response, $A_{eff_1}^{sm}$, and the peak 2nd mode response, $A_{eff_2}^{sm}$, as well as the upper bound limit for $A_{eff_1}^{sm}$ and $A_{eff_2}^{sm}$, denoted $A_{1,maxb}$ and $A_{2,max}$ can be estimated.
- It is shown that the peak cumulative 1st and 2nd mode response from NLTHA (i.e., peak value of $r_{x1}(t) + r_{x2}(t)$) is accurately estimated using $A_{1,maxb}$ and $A_{2,max}$.
- It is shown that to accurately estimate the upper bound response quantities from NLTHA, the third mode response should be taken into account, in addition to the estimated cumulative peak 1st and 2nd mode response.
- To preclude the formation of upper yielding mechanism prior to the base yielding mechanism, the M_2^h should have an overstrength (f_{os}) relative to the 1st mode contribution to the story base moment at the location of the upper yielding mechanism. Based on NLTHA results for wall structures. f_{os} should be about 1.1.
- It is observed that the frequency content of the GM used in NLTHA influences the effectiveness of the upper yielding mechanism on the 2nd mode response. The upper yielding mechanism is more effective in reduces the 2nd mode response, if the GM has a larger high frequency (short period) content.
- For the particular SC-CBFs analyzed in this study, it is observed that the 2nd mode response of SC-CBFs is reduced by adding an upper rocking joint to the structure without increasing the story drift demands. It is also observed that the 3rd mode

response of SC-CBFs is slightly amplified with the addition of an upper rocking joint.

- To make general conclusions regarding the effectiveness of the upper rocking joint on the higher mode response of SC-CBFs, a more detailed investigation should be performed on SC-CBFs with different configurations and aspect ratios.

In conclusion, the results of this study show that a second flexural yielding mechanism added to a NL wall structure and/or an SC-CBF is effective in controlling the 2nd mode response of these structures.

5.10.References

ASCE (2010). "Minimum Design Loads for Buildings and Other Structures," ASCE7-10, Reston, VA, USA.

Baker, J.W. (2011). "Conditional Mean Spectrum: Tool for Ground-Motion Selection," *Journal of Structural Engrg.*, 137(3), pp. 322-331.

Blakeley, R. W. G., Cooney, R. C., and Megget, L. M. (1975). "Seismic Shear Loading at Flexural Capacity in Cantilever Wall Structures," *Bulletin of the New Zealand National Society for Earthquake Engrg.*, 8 (4), pp. 278-290.

BSSC (2003). NEHRP Recommended Provisions for Seismic Regulations for New Buildings and Other Structures. FEMA 450. Building Seismic Safety Council, National Institute of Building Sciences, Washington, D.C., USA.

Chancellor, N.B., Sause, R., Ricles, J.M., Tahmasebi, E., and Akbas, T. (2013). “Seismic Response of Post-Tensioned Steel Rocking Concentrically Braced Frames with Various Aspect Ratios,” COMPDYN 2013, Proc. of the 4th ECCOMAS Thematic Conference on Computational Methods in Structural Dynamics and Earthquake Engrg., Kos Island, Greece. June 12-14.

Chancellor, N.B. (2014). "Seismic Design and Performance of Self-Centering Concentrically-Braced Frames,” Ph.D. Dissertation, Dept. of Civil and Environmental Engrg., Lehigh Univ., Bethlehem, PA, USA.

Chopra, A. K. (2012). *Dynamics of Structures*. (4th ed.). Prentice Hall, New Jersey, NJ, USA.

Eatherton, M.R.; Hajjar, J.F. (2010). “Residual Drifts of Self-Centering Systems Including Effects of Ambient Building Resistance,” *Earthquake Spectra*, 27(3), pp. 719-744.

Eibl, J. and Keintzel E. (1988). “Seismic shear forces in RC cantilever shear walls,” *Proc. of the 9th World Conference on Earthquake Engrg*. (vol. VI), Tokyo-Kyoto, Japan, August 2-9.

Kurama, Y., Pessiki, S., Sause, R., and Lu, L.-W. (1999). “Seismic Behavior and Design of Unbonded Post-Tensioned Precast Concrete Walls,” *PCI Journal*, 44 (3), pp 72-89.

Ma, X.; Eatherton, M.; Hajjar, J.; Krawinkler, H.; and Deierlein, G. (2010). “Seismic Design and Behavior of Steel Frames with Controlled Rocking – Part II: Large

Scale Shake Table Testing and System Collapse Analysis," *Proc. of the ASCE/SEI Structures Congress 2010*, Orlando, FL, May 12-15.

Mazzoni, S., McKenna, F., Scott, M.H., Fenves, G.L., et al. (2009). "Open System for Earthquake Engrg. Simulation (OpenSEES) User Command-Language Manual*," Pacific Earthquake Engrg. Research Center*, Univ. of California, Berkeley, CA, USA.

Pacific Earthquake Engrg. Research Center (PEER) (2011). "GM Database Flatfile," http://peer.berkeley.edu/nga/flatfile.html on December 12, 2013.

Panagiotou, M., & Restrepo, J. I. (2009). "Dual-plastic Hinge Design Concept for Reducing Higher-Mode effects on High-Rise Cantilever Wall Buildings," *Earthquake Engrg. and Structural Dynamics*, 38(12), 1359.

Paulay, T. and Priestley, M.J.N. (1992). *Seismic design of reinforced concrete and masonry buildings*. Wiley, New York, NY, USA.

Priestley, M.J.N. (2003). "Does Capacity Design Do The Job? An Investigation of Higher Modes Effects in Cantilever Walls," *Bulletin New Zealand Society for Earthquake Engrg.*, 36(4), pp. 276-292.

Roke, D., Sause, R., Ricles, J.M., Seo, C.-Y., and Lee, K.-S. (2006). "Self-Centering Seismic-Resistant Steel Concentrically-Braced Frames," *Proc. of the 8th U.S. National Conference on Earthquake Engrg., EERI*, San Francisco, April 18-22.

Roke, D., Sause, R., Ricles, J.M., and Chancellor, N.B. (2010). "Damage-Free Seismic-Resistant Self-Centering Concentrically-Braced Frames," ATLSS Report 10-09, ATLSS Engrg. Research Center, Lehigh Univ., Bethlehem, PA, USA.

Seo, C.-Y., and Sause, R. (2005). "Ductility Demands on Self-Centering Systems under Earthquake Loading," *ACI Structural Journal*, 102(2), pp. 275-285.

Wiebe, L. and Christopoulos, C. (2009). "Mitigation of Higher Mode Effects in Base-rocking Systems by Using Multiple Rocking Sections," *Journal of Earthquake Engrg.*, 13(S1), pp. 83-108.

Wiebe, L., Christopoulos, C., Tremblay, R., & Leclerc, M. (2013). "Mechanisms to Limit Higher Mode Effects in a Controlled Rocking Steel Frame. 1: Concept, Modelling, and Low-Amplitude Shake Table Testing," *Earthquake Engrg. and Structural Dynamics*, 42(7), pp. 1053-1068.

Table 5.1 Ground motion set (Chancellor, 2014)

PEER-NGA Record Seq. #	Year	Event	Station	Component	Scale Factor (DBE)
165	1979	Imperial Valley-06	Chihuahua	012, 282	2.17
169	1979	Imperial Valley-06	Delta	262, 352	1.63
728	1987	Superst. Hills-02	Westmorland	090, 180	2.01
778	1989	Loma Prieta	Hollister (HDA)	165, 255	1.61
949	1994	Northridge-01	Arleta	090, 360	1.92
1100	1995	Kobe, Japan	Abeno (ABN)	000, 090	2.89
1101	1995	Kobe, Japan	Amagasaki	000, 090	1.20
1110	1995	Kobe, Japan	Morigawachi	000, 090	2.23
1187	1999	Chi-Chi, Taiwan	CHY015	N, W	2.31
1203	1999	Chi-Chi, Taiwan	CHY036	E, N	1.41
1204	1999	Chi-Chi, Taiwan	CHY039	E, N	2.62
1209	1999	Chi-Chi, Taiwan	CHY047	N, W	2.37
1236	1999	Chi-Chi, Taiwan	CHY088	E, N	2.56
1269	1999	Chi-Chi, Taiwan	HWA019	E, N	2.85
1294	1999	Chi-Chi, Taiwan	HWA048	N, W	2.84
1317	1999	Chi-Chi, Taiwan	ILA013	N, W	2.17
1484	1999	Chi-Chi, Taiwan	TCU042	E, N	1.75

Table 5.2 $M_{in}^{st,e}$ and $M_{in}^{st,m}$ for first two modes of MB1

Floor (i)	$M_{i1}^{st,e}$	$M_{i2}^{st,e}$	$M_{i1}^{st,m}$	$M_{i2}^{st,m}$
Base	6269.4	551.9	7020.0	0.0
1	5358.8	273.1	5911.6	-197.6
2	4452.9	8.3	4827.8	-363.6
3	3564.2	-212.1	3793.3	-471.9
4	2712.3	-356.2	2832.6	-507.2
5	1922.1	-404.7	1970.5	-467.5
6	1222.9	-358.7	1231.6	-365.7
7	646.7	-243.0	640.4	-228.1
8	227.4	-103.3	221.7	-91.6

Table 5.3 Basic structural and modal properties of cantilever wall structures

Id	Upper Yielding Hinge Location	f_{os}	Material behavior	α_g, %	β_e, %
MB1	-	-	EPP	0	1.00, 1.00
MBU1	4th floor	1.00	EPP	0	1.00, 1.00
MBU2	5th floor	1.00	EPP	0	1.00, 1.00
MBU3	5th floor	0.80	EPP	0	1.00, 1.00
MBU4	5th floor	1.10	EPP	0	1.00, 1.00
MBU5	5th floor	1.20	EPP	0	1.00, 1.00
MBU6	5th floor	1.00	EPP	2	1.00, 1.00
MBU7	5th floor	1.10	SC	0	0.30, 0.30
MBU8	5th floor	1.10	SC	0	0.30, 0.40
MBU9	5th floor	1.00	SC	2	0.30, 0.30

Table 5.4 $\overline{M}_{bn}^{sm}$, $\overline{M}_{4n}^{sm}$, and $\overline{M}_{5n}^{sm}$ for first three modes of MB1

Id	$\overline{M}_{b1}^{sm}$	$\overline{M}_{b2}^{sm}$	$\overline{M}_{b3}^{sm}$	$\overline{M}_{41}^{sm}$	$\overline{M}_{42}^{sm}$	$\overline{M}_{43}^{sm}$	$\overline{M}_{51}^{sm}$	$\overline{M}_{52}^{sm}$	$\overline{M}_{53}^{sm}$
MBU1	1.000	0.000	0.000	1.211	-0.211	0.000	1.263	-0.284	0.031
MBU2	1.000	0.000	0.000	1.211	-0.183	-0.039	1.263	-0.263	0.000

Table 5.5 $SA_{GM,m}(T_n^e)$ for first three modes of MB1, MBU1, and MBU2

Id	$SA_{GM,m}(T_1^e)$	$SA_{GM,m}(T_2^e)$	$SA_{GM,m}(T_3^e)$
MB1	0.419	0.896	0.524
MBU1	0.419	0.896	0.524
MBU2	0.419	0.896	0.524

Table 5.6 $A_{eff_n,m}^m$ and $A_{eff_n,m}^{sm}$ for first three modes of MB1, MBU1, and MBU2

Id	$A_{eff_1,m}^m$	$A_{eff_1,m}^{sm}$	$A_{eff_2,m}^m$	$A_{eff_2,m}^{sm}$	$A_{eff_3,m}^m$	$A_{eff_3,m}^{sm}$
MB1	0.071	-	0.911	-	0.927	-
MBU1	-	0.071	-	0.759	-	1.149
MBU2	-	0.071	-	0.645	-	0.839

Table 5.7 $R_{act_n}^m$ and $R_{act_n}^{sm}$ for first three modes of MB1, MBU1, and MBU2

Id	$R_{act_1}^m$	$R_{act_1}^{sm}$	$R_{act_2}^m$	$R_{act_2}^{sm}$	$R_{act_3}^m$	$R_{act_3}^{sm}$
MB1	6.0	-	1.0	-	0.57	-
MBU1	-	6.0	-	1.2	-	0.46
MBU2	-	6.0	-	1.4	-	0.63

Table 5.8 $SA_{GM}(T_n^e)$ and $A_{eff_n}^{sm}$ for MBU2 under ABN000, ILA013W, and HDA165 GM records

GM record	$SA_{GM}(T_1^e)$	$A_{eff_1}^{sm}$	$A_{1,max}$	$SA_{GM}(T_2^e)$	$A_{eff_2}^{sm}$	$A_{2,max}$
ABN000	0.303	0.051	0.051	1.372	0.484	0.484
ILA013W	0.636	0.106	0.106	0.509	0.822	0.836
HDA165	0.491	0.082	0.082	1.044	0.785	0.785

Table 5.9 $V_{bn}^{st,sm}$ for first three modes of MBU2

Id	$V_{b1}^{st,sm}$	$V_{b2}^{st,sm}$	$V_{b3}^{st,sm}$
MBU2	0.419	0.896	0.524

Table 5.10 $SA_{GM}(T_n^e)$ and $A_{eff_n}^{sm}$ MBU2 to MBU9 under ABN000 ground motion

Id	$SA_{GM}(T_1^e)$	$A_{eff_1}^{sm}$	$SA_{GM}(T_2^e)$	$A_{eff_2}^{sm}$	$SA_{GM}(T_3^e)$	$A_{eff_3}^{sm}$
MBU2	0.303	0.051	1.372	0.485	1.208	1.409
MBU3	0.303	0.051	1.372	0.436	1.208	1.297
MBU4	0.303	0.051	1.372	0.509	1.208	1.356
MBU5	0.303	0.051	1.372	0.533	1.208	1.208
MBU6	0.303	0.051	1.372	0.516	1.208	1.398
MBU7	0.303	0.051	1.372	0.509	1.208	1.150
MBU8	0.303	0.051	1.372	0.509	1.208	1.503
MBU9	0.303	0.051	1.372	0.531	1.208	1.252

Table 5.11 $R_{act_n}^{sm}$ for MBU2 to MBU9 under ABN000 ground motion

Id	$R_{act_1}^{sm}$	$R_{act_2}^{sm}$	$R_{act_3}^{sm}$	t_{upper} / t_{base}
MBU2	6.0	2.8	0.9	0.788
MBU3	6.0	3.1	0.9	0.794
MBU4	6.0	2.7	0.9	1.008
MBU5	6.0	2.6	1.0	1.008
MBU6	5.9	2.7	0.9	1.009
MBU7	6.0	2.7	1.1	1.008
MBU8	6.0	2.7	0.8	1.008
MBU9	5.9	2.6	1.0	1.122

Table 5.12 Summary of dead loads for SCCBF1

Item	Dead Load for Floor 1 (psf)	Dead Load for Middle Floors (psf)	Dead Load for Roof (psf)
Floor/Roof Deck	3	3	3
Floor/Roof Slab	43	43	0
Roofing Material	0	0	10
Mechanical Weight	10	10	25
Ceiling Material	5	5	5
Floor Finish	2	2	0
Structural Steel	15	15	10
Steel Fireproofing	2	2	2
Building Envelope	8	7	5
Total	88	87	60

Table 5.13 Summary of live loads for SCCBF1

Item	Live Load for Floors (psf)	Live Load for Roof (psf)
Office	50	0
Partitions (included in seismic mass)	15	0
Roof	0	20
Total	65	20

Table 5.14 Summary of design parameters for SCCBF1

	A_{pt}	f_{py}	f_{pi}	PT_y	V_{ED}	β_e	M_1^h
Id	in^2	ksi	-	kip	kip	%	kip-inch
SCCBF1	3.4	120	0.5	408	50	0.48	446,306

Table 5.15 $M_{in}^{st,e}$ and $M_{in}^{st,m}$ for first and second modes of SCCBF1

Floor (i)	$M_{i1}^{st,e}$	$M_{i2}^{st,e}$	$M_{i1}^{st,m}$	$M_{i2}^{st,m}$
Base	13243.6	975.6	14642.3	-70.5
1	10954.6	299.4	11905.0	-508.7
2	8986.2	-230.0	9601.7	-811.1
3	7071.9	-634.8	7422.1	-999.5
4	5254.8	-869.1	5421.2	-1032.8
5	3601.0	-888.7	3653.7	-920.6
6	2175.4	-724.4	2174.3	-682.8
7	1053.3	-441.5	1036.8	-393.7
8	302.6	-148.7	294.7	-132.9

Table 5.16 Summary of design parameters for SCCBF1, SCCBF2, and SCCBF3

Id	A_{pt} in^2	A_{pt}^u in^2	PT_y kip	f_{pi} ksi	V_{ED} kip	V_{ED}^u kip	M_1^h kip-inch	M_2^h kip-inch	α_{kT} %
SCCBF1	3.40	-	408	0.5	550	-	446,306	-	0.46
SCCBF2	3.40	2.55	408	0.5	550	-	446,306	127,230	0.92
SCCBF3	3.40	1.70	408	0.5	500	50	446,306	126,870	0.92

Table 5.17 $M_{in}^{st,sm}$ and $\overline{M}_{in}^{sm}$ for first three modes of SCCBF3

Floor (i)	$M_{i1}^{st,sm}$	$M_{i2}^{st,sm}$	$M_{i3}^{st,sm}$	$\overline{M}_{i1}^{sm}$	$\overline{M}_{i2}^{sm}$	$\overline{M}_{i3}^{sm}$
Base	14559.52	0.00	0.00	1.0000	0.0000	0.0000
1	11853.49	-327.26	-167.00	1.0624	-0.0331	-0.0121
2	9572.09	-575.40	-246.70	1.1223	-0.0714	-0.0314
3	7409.16	-758.10	-247.50	1.1725	-0.1222	-0.0426
4	5419.71	-845.28	-149.98	1.2221	-0.1935	-0.0331
5	3658.76	-806.58	0.00	1.2842	-0.2842	0.0000
6	2181.30	-614.77	119.72	1.3437	-0.3813	0.0737
7	1042.35	-355.89	134.04	1.4031	-0.4828	0.1841
8	296.92	-120.82	61.80	1.4716	-0.6043	0.3112

Table 5.18 $SA_{DS}(T_n)$ and $SA_{GM,m}(T_n^e)$ for first three modes of SCCBF1

Id	$SA_{DS}(T_1)$	$SA_{DS}(T_2)$	$SA_{DS}(T_3)$	$SA_{GM,m}(T_1^e)$	$SA_{GM,m}(T_2^e)$	$SA_{GM,m}(T_3^e)$
SCCBF1	0.532	1.00	1.000	0.544	0.972	0.731

Table 5.19 $A_{eff_{n,m}}^{m}$ and $A_{eff_{n,m}}^{sm}$ for first three modes of SCCBF1, SCCBF2, and SCCBF3

Id	$A_{eff_1,m}^{m}$	$A_{eff_1,m}^{sm}$	$A_{eff_2,m}^{m}$	$A_{eff_2,m}^{sm}$	$A_{eff_3,m}^{m}$	$A_{eff_3,m}^{sm}$
SCCBF1	0.073	-	1.120	-	0.831	-
SCCBF2	-	0.072	-	0.725	-	1.225
SCCBF3	-	0.072	-	0.723	-	1.190

Table 5.20 $R_{act_n}^{m}$ and $R_{act_n}^{sm}$ for first three modes of SCCBF1, SCCBF2, and SCCBF3

Id	$R_{act_1}^{m}$	$R_{act_1}^{sm}$	$R_{act_2}^{m}$	$R_{act_2}^{sm}$	$R_{act_3}^{m}$	$R_{act_3}^{sm}$
SCCBF1	7.37	-	0.87	-	0.88	-
SCCBF2	-	7.47	-	1.34	-	0.60
SCCBF3	-	7.54	-	1.34	-	0.61

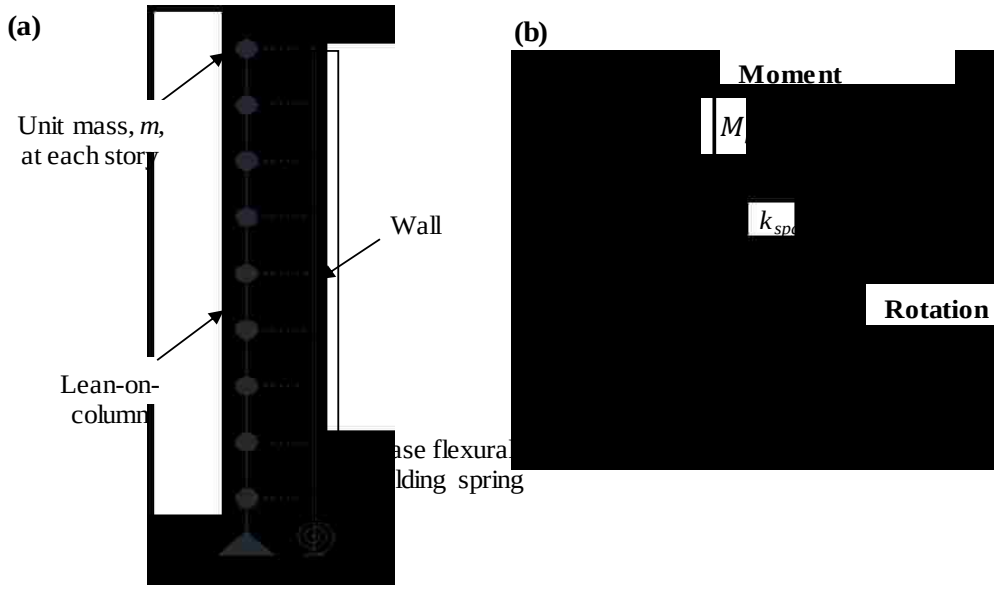

Figure 5.1 (a) 9-story cantilever wall structure model; (b) elastic-perfectly plastic hysteresis of base flexural yielding spring

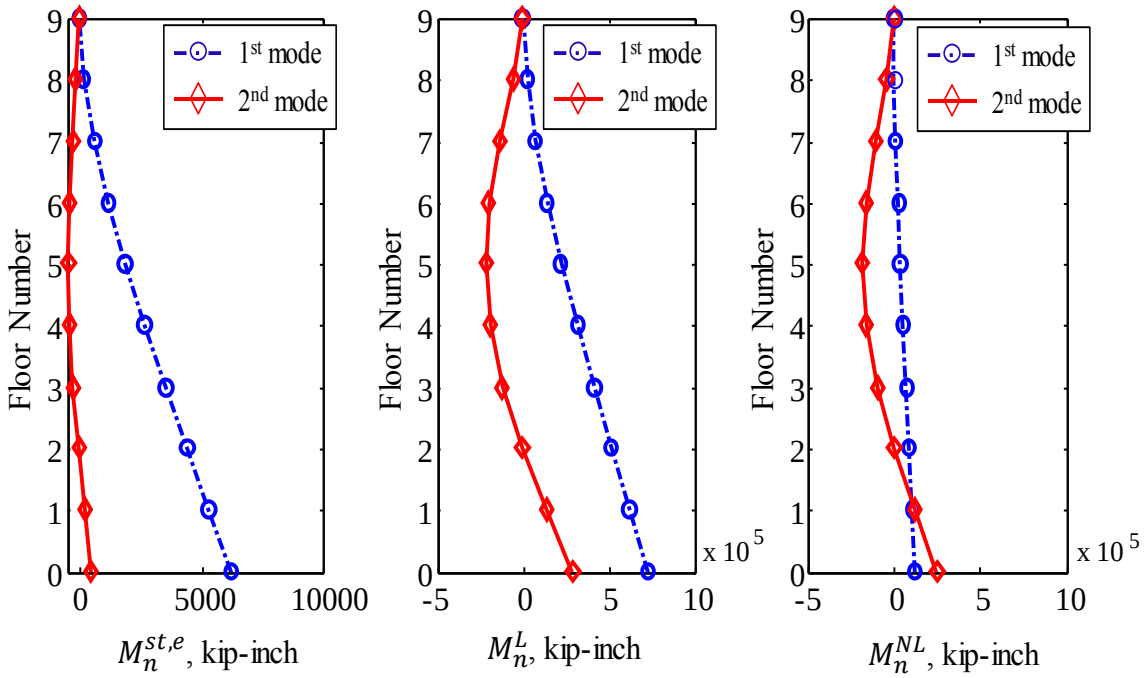

Figure 5.2 First and second mode story base moment profiles for MB1 based on: (a) static; (b) linear-elastic dynamic; (c) NL dynamic analyses

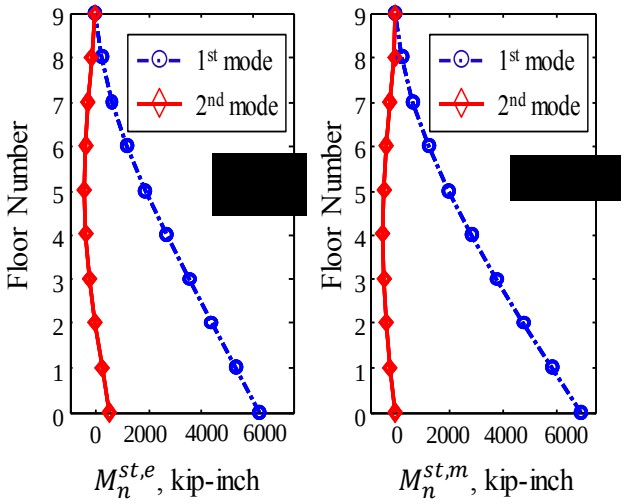

Figure 5.3 Static story base moment at floor i: (a) $M_1^{st,e}$and $M_2^{st,e}$; (b) $M_1^{st,m}$ and $M_2^{st,m}$

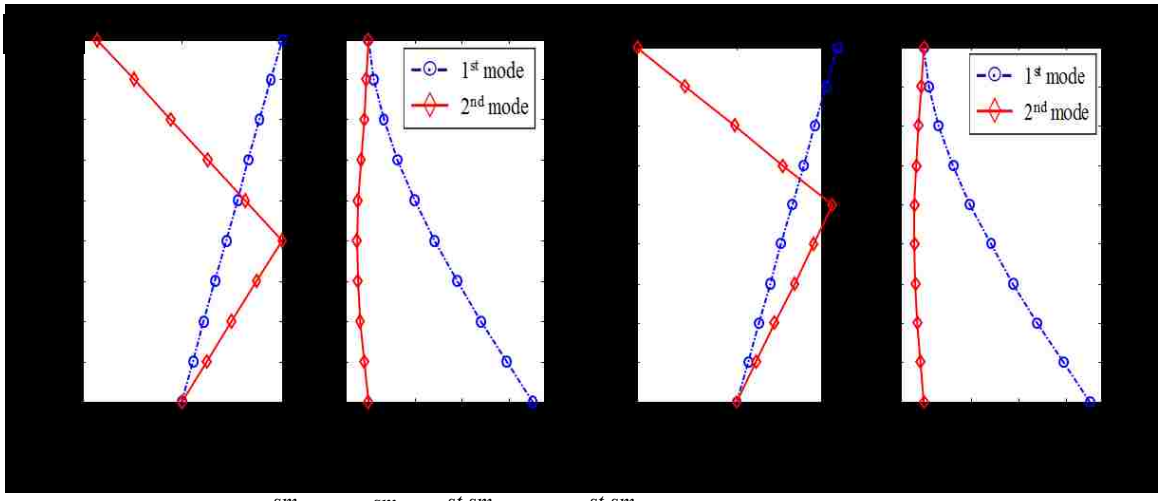

Figure 5.4 $\phi_1^{sm}$and ϕ_2^{sm}, $M_1^{st,sm}$ and $M_2^{st,sm}$for: (a) MBU1; (b) MBU2

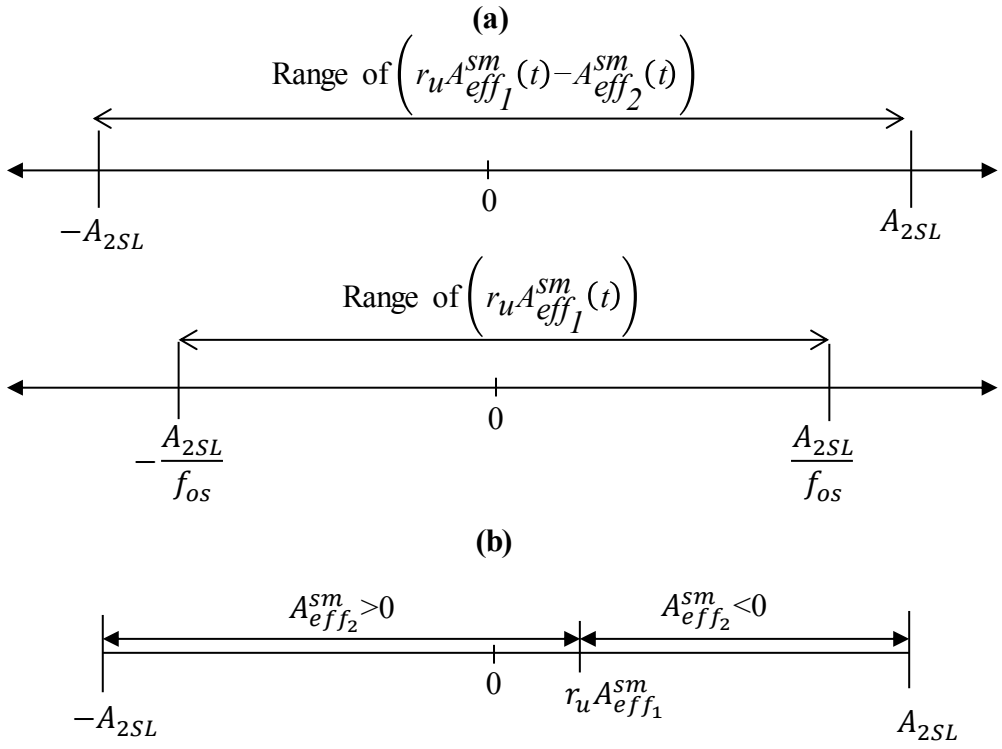

Figure 5.5 (a) Range of $\left(r_u A^{sm}_{eff_1}(t)\right)$ and $\left(r_u A^{sm}_{eff_1}(t) - A^{sm}_{eff_2}(t)\right)$; (b) range of $A^{sm}_{eff_2}$ for a given positive value of $r_u A^{sm}_{eff_1}$

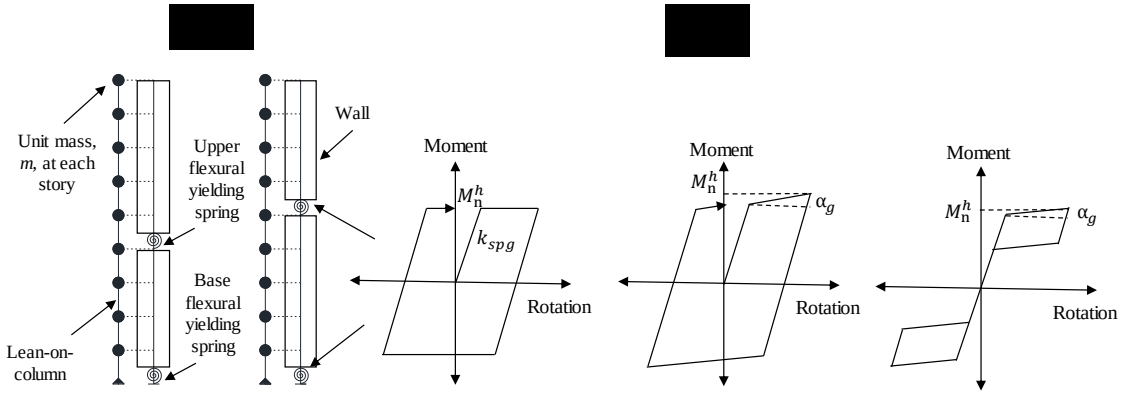

Figure 5.6 (a) Schematic of numerical models of 9-story wall structure with first yielding mechanism at base and second yielding mechanism at 4th or 5th floor; (b) elastic-perfectly plastic (EPP), bilinear elasto-plastic (BP), and self-centering (SC) hysteresis of inelastic hinges

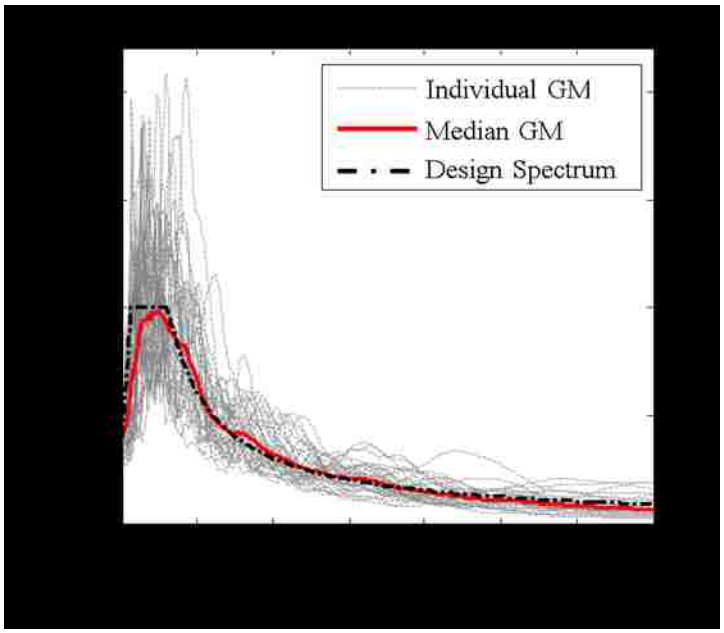

Figure 5.7 Pseudo-acceleration response spectra for ground motion set

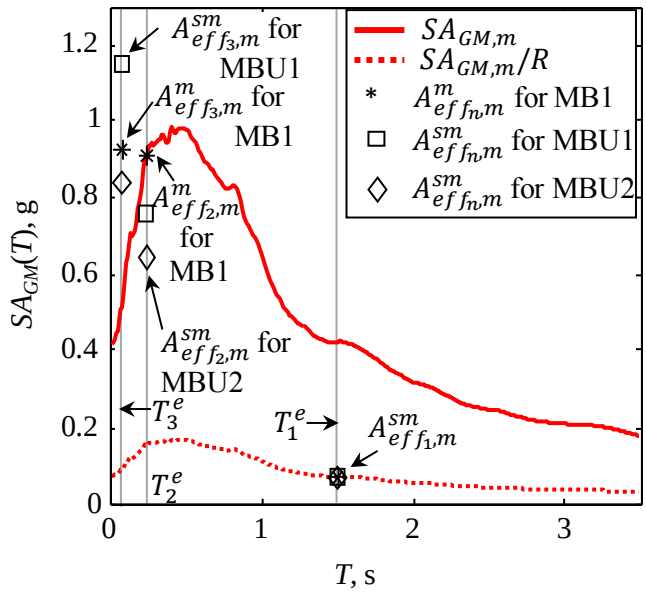

Figure 5.8 5% damped median elastic and reduced pseudo-acceleration spectrum with median peak modal effective pseudo accelerations for first three mechanism modes of MB1 and first three mechanism two-mechanism modes MBU2 from NLTHA

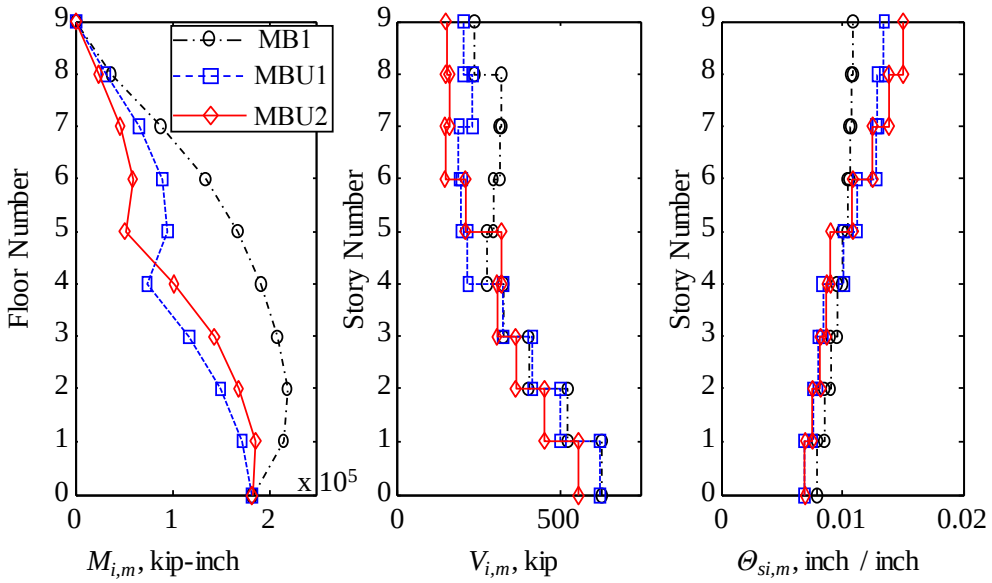

Figure 5.9 Comparison of median peak response envelopes of MB1, MBU1, and MBU2 based on the NLTHA under GM set

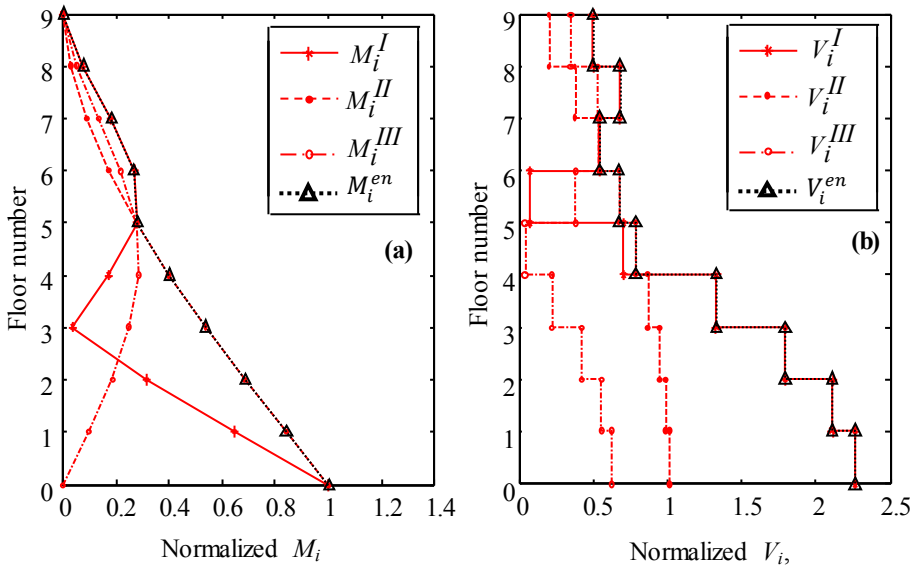

Figure 5.10 Comparison of: (a) M_i^I, M_i^{II}, M_i^{III} with M_i^{en} normalized by M_1^h; (b) V_i^I, V_i^{II}, V_i^{III} with V_i^{en} normalized by V_b^h from NLTHA results for MBU2 under GM set

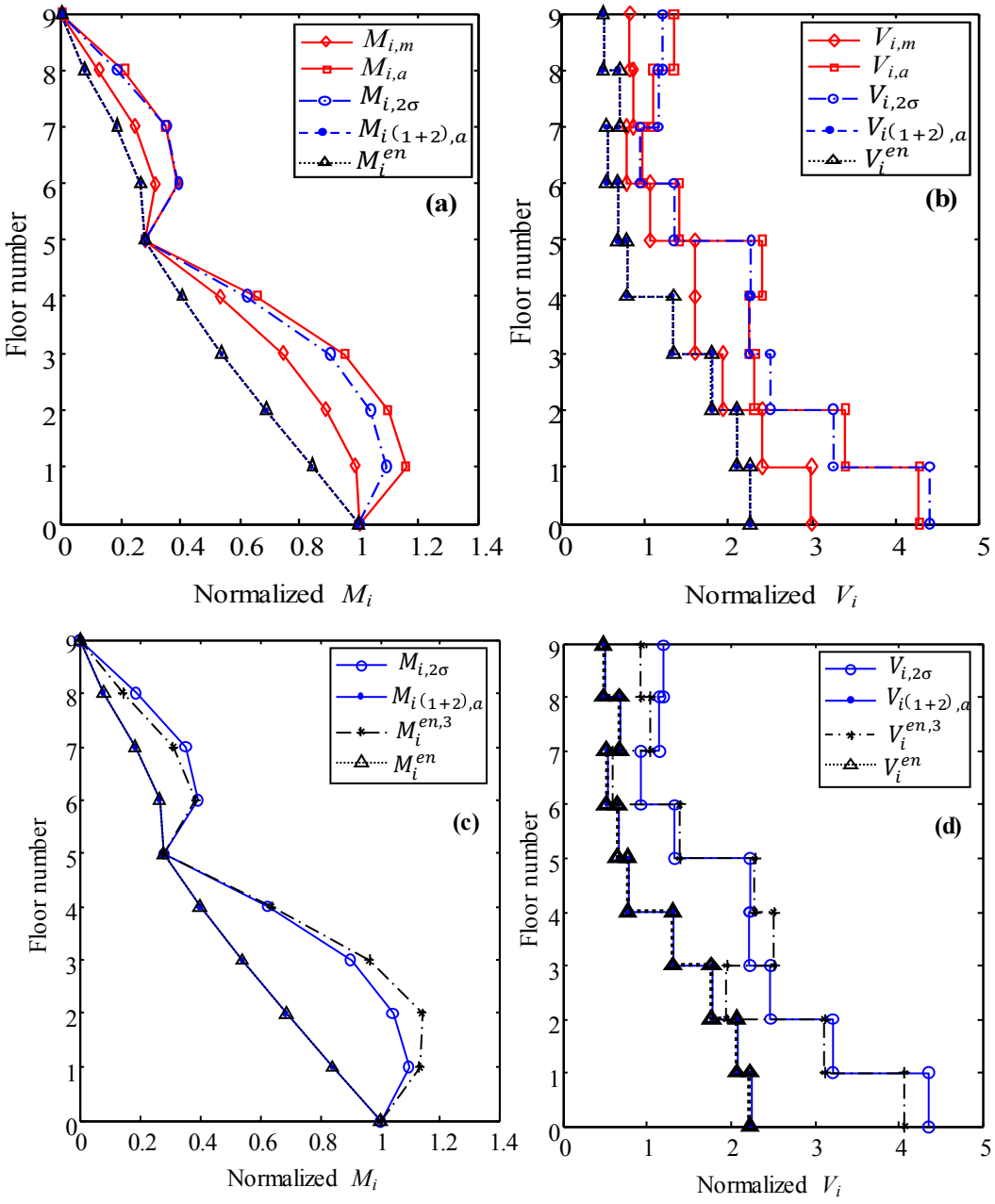

Figure 5.11 Comparison of: (a) M_i^{en} with $M_{i,a}$, $M_{i,m}$, $M_{i,2\sigma}$, and $M_{i(1+2),a}$ normalized by M_1^h; (b) V_i^{en} with $V_{i,a}$, $V_{i,m}$, $V_{i,2\sigma}$, and $V_{i(1+2),a}$ normalized by V_b^h; (c) M_i^{en} and $M_i^{en,3}$ with $M_{i(1+2),a}$ and $M_{i,2\sigma}$ normalized by M_1^h; (d) V_i^{en} and $V_i^{en,3}$ with $V_{i(1+2),a}$ and $V_{i,2\sigma}$ normalized by V_b^h from NLTHA results for MBU2 under GM set

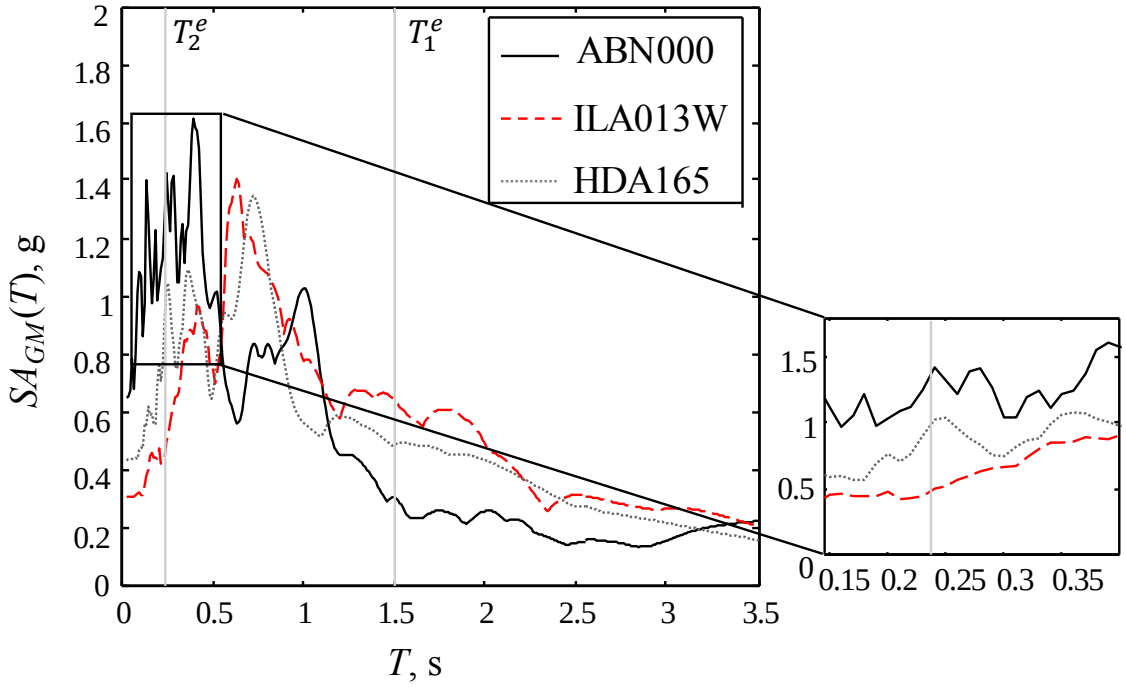

Figure 5.12 Ground motion spectrum of ABN000, ILA013W, and HDA165 ground motions

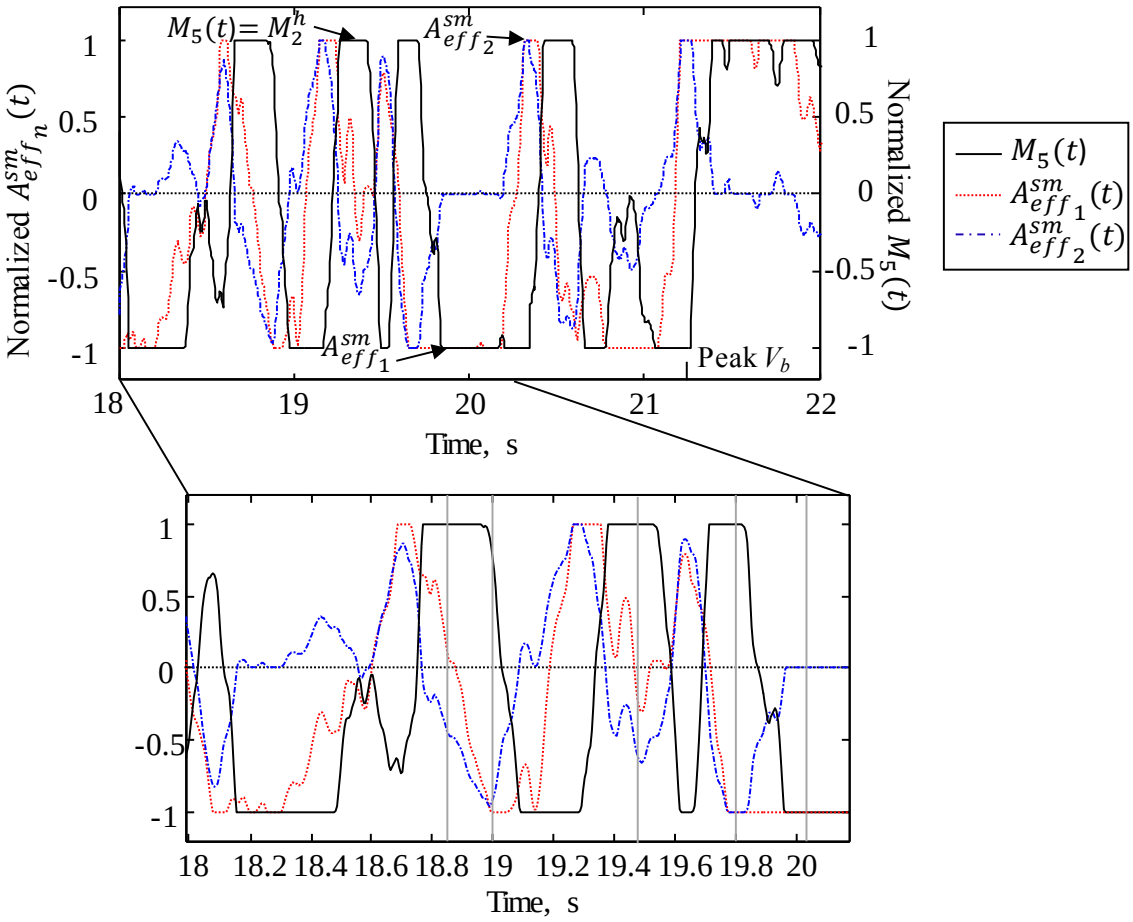

Figure 5.13 $A_{eff_n}^{sm}(t)$ normalized by $A_{eff_n}^{sm}$ together with $M_5(t)$ normalized by M_2^h for first two modes of MBU2 under ABN000 ground motion

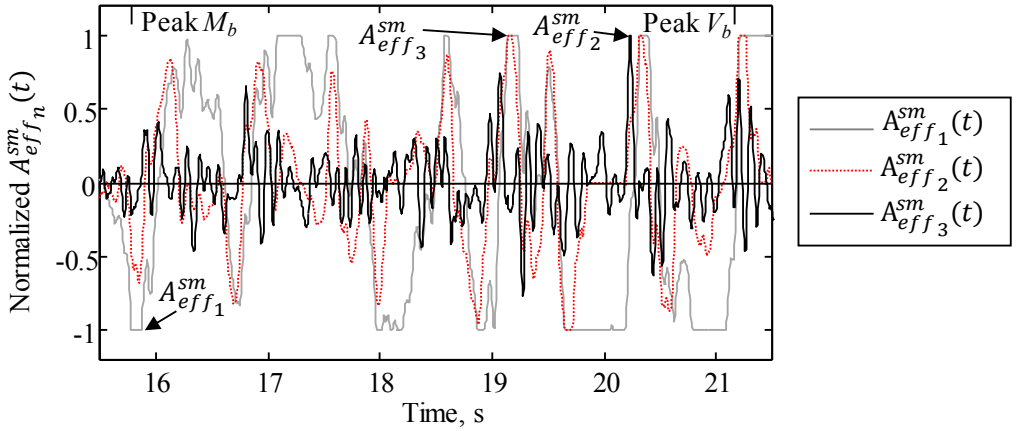

Figure 5.14 $A_{eff_n}^{sm}(t)$ normalized by $A_{eff_n}^{sm}$ for first three modes of MBU2 under ABN000 ground motion

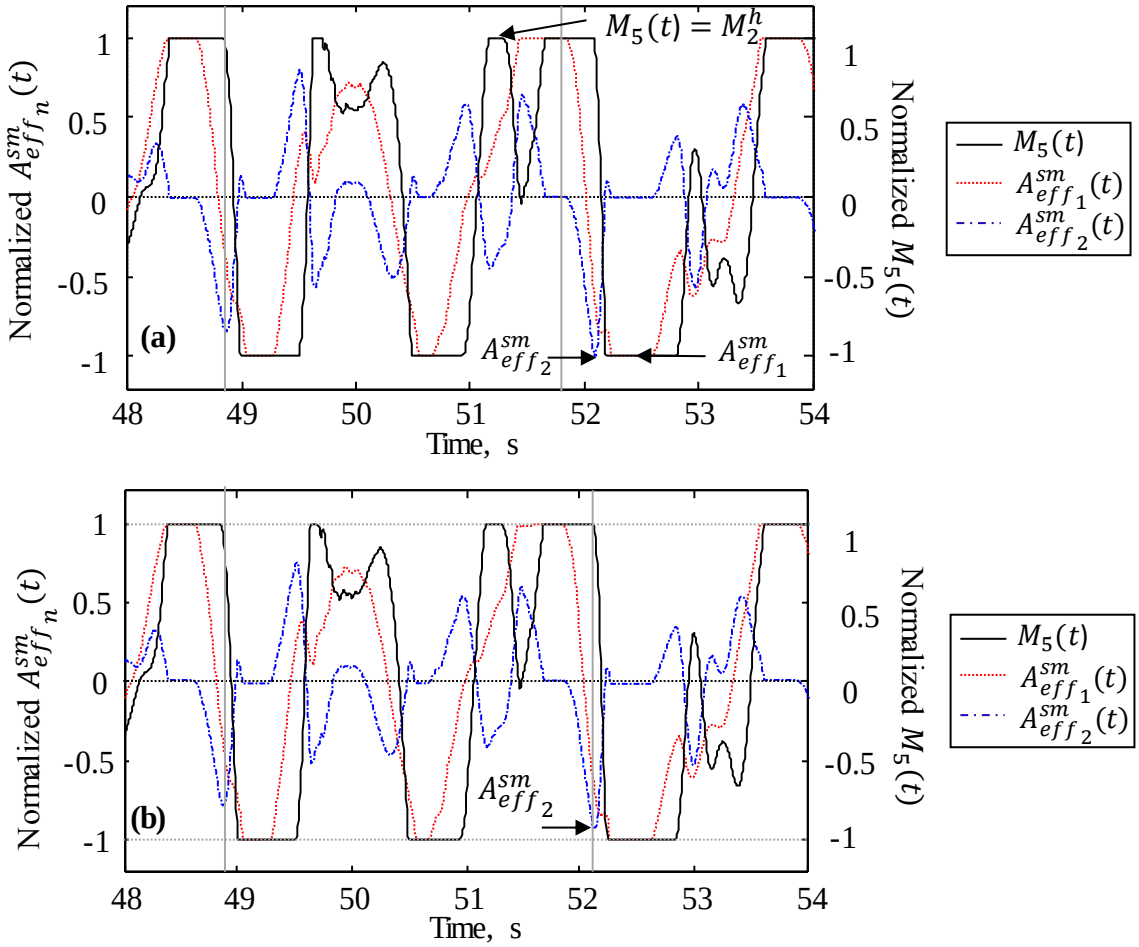

Figure 5.15 (a) $A_{eff_n}^{sm}(t)$ normalized by $A_{eff_n}^{sm}$ together with $M_5(t)$ normalized by M_2^h for first two modes of MBU2 under ILA013W ground motion; (b) $A_{eff_1}^{sm}(t)$ normalized by $A_{eff_1}^{sm}$ and $A_{eff_2}^{sm}(t)$ normalized by A_{2max} together with $M_5(t)$ normalized by M_2^h for MBU2 under ILA013W ground motion

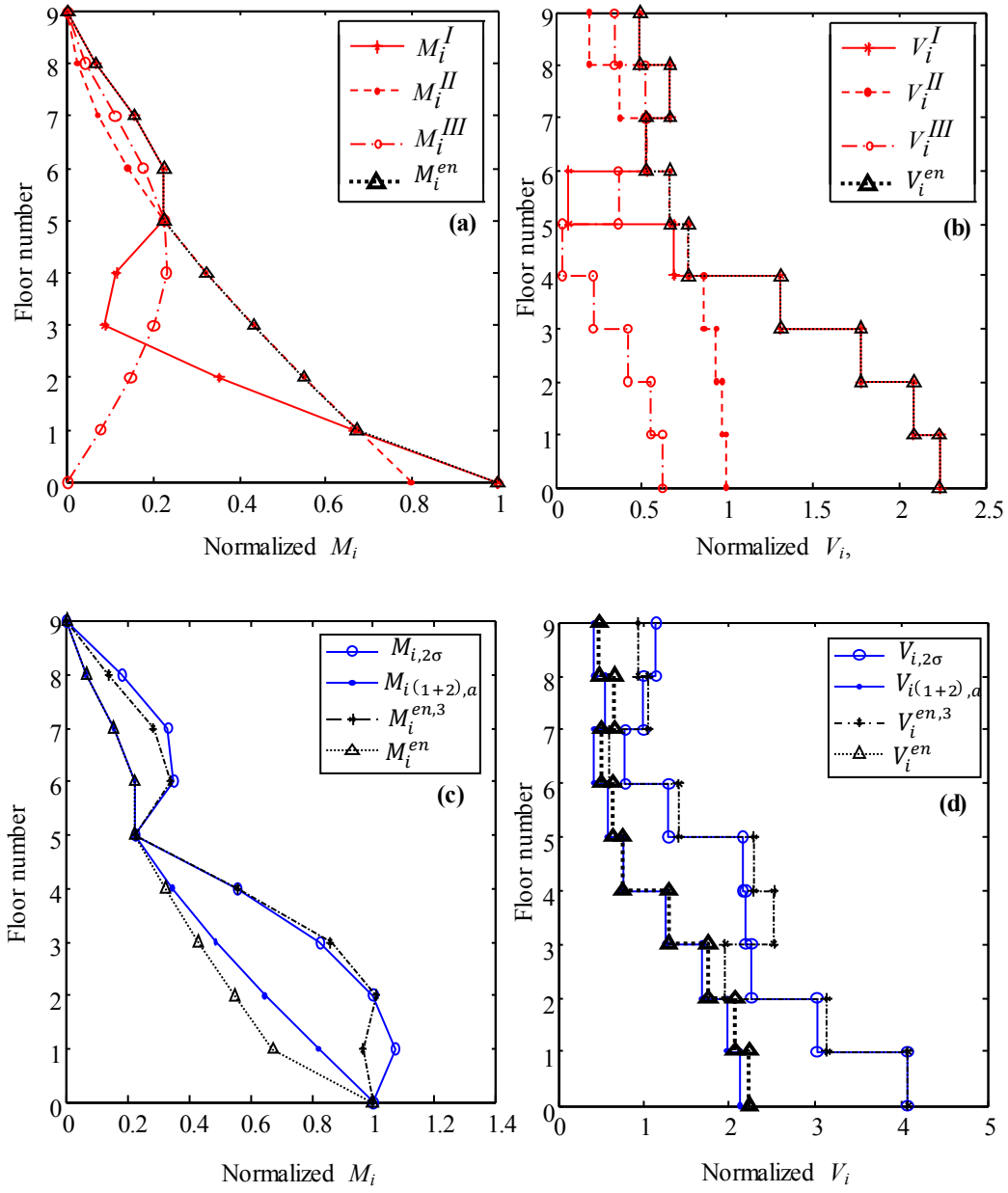

Figure 5.16 Comparison of: (a) M_i^I, M_i^{II}, M_i^{III} with M_i^{en} normalized by M_1^h; (b) V_i^I, V_i^{II}, V_i^{III} with V_i^{en} normalized by V_b^h; (c) M_i^{en} and $M_i^{en,3}$ with $M_{i(1+2),a}$ and $M_{i,2\sigma}$ normalized by M_1^h; (c) V_i^{en} and $V_i^{en,3}$ with $V_{i(1+2),a}$ and $V_{i,2\sigma}$ normalized by V_b^h from NLTHA results for MBU3 under GM set

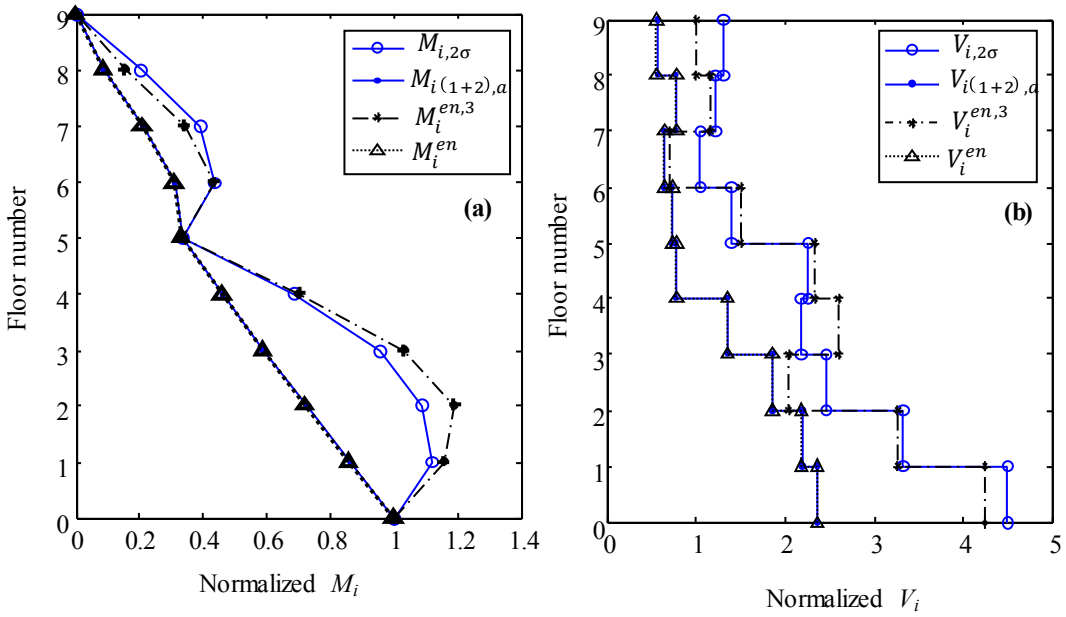

Figure 5.17 Comparison of: (a) M_i^{en} and $M_i^{en,3}$ with $M_{i(1+2),a}$ and $M_{i,2\sigma}$ normalized by M_1^h; (b) V_i^{en} and $V_i^{en,3}$ with $V_{i(1+2),a}$ and $V_{i,2\sigma}$ normalized by V_b^h from NLTHA results for MBU5 under GM set

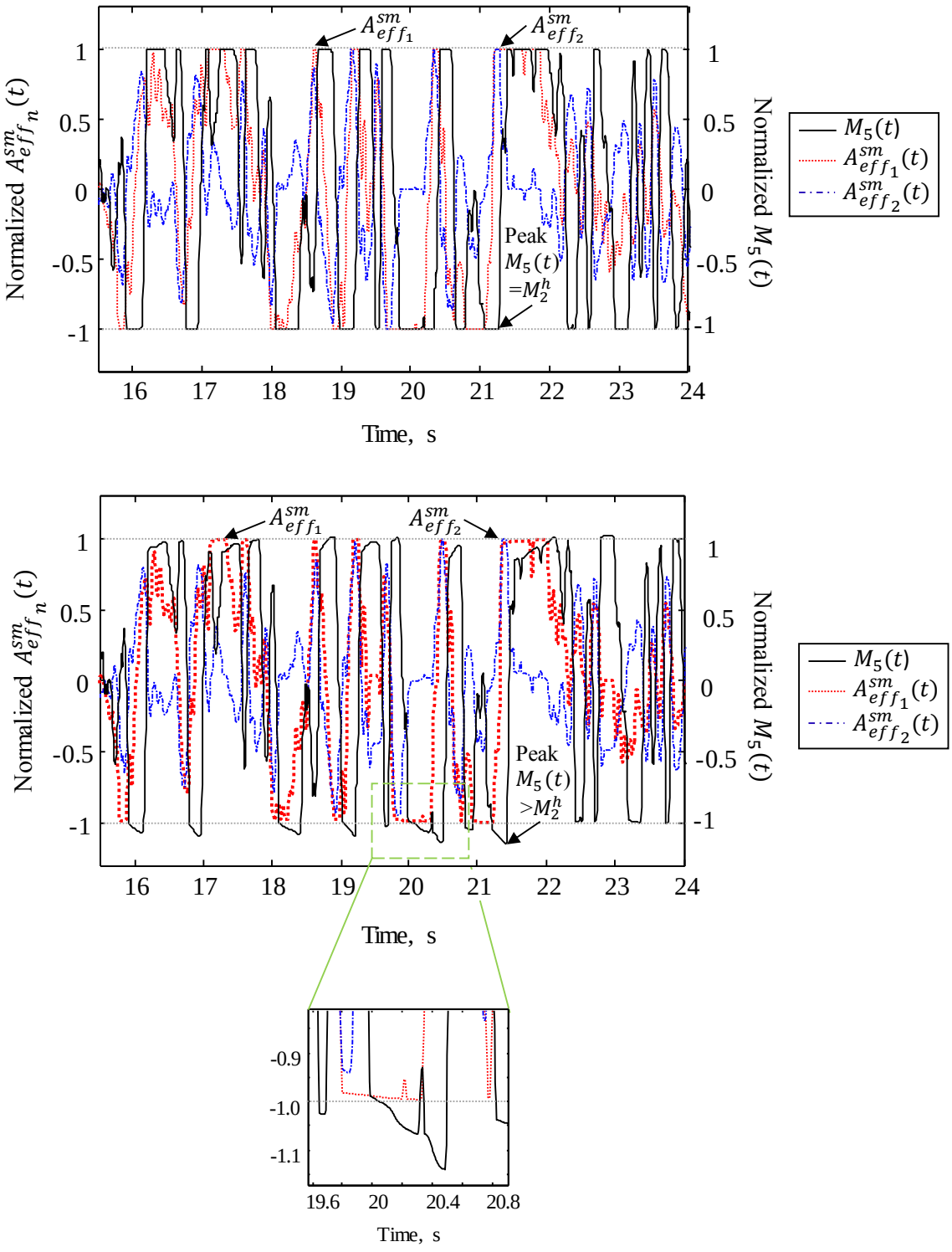

Figure 5.18 $A^{sm}_{eff_n}(t)$ normalized by $A^{sm}_{eff_n}$ together with $M_5(t)$ normalized by M_2^h for first two modes of: (a) MBU2; (b) MBU6 under ABN000 ground motion

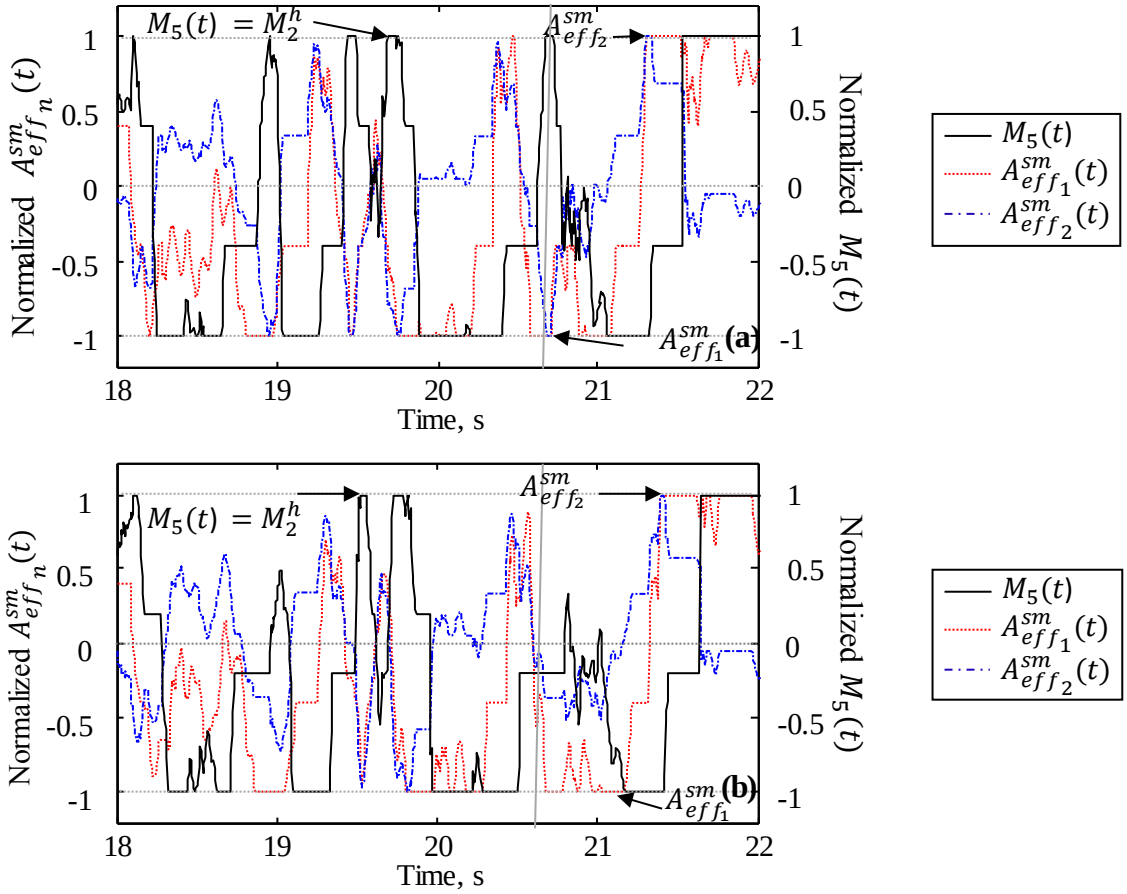

Figure 5.19 $A_{eff_n}^{sm}(t)$ normalized by $A_{eff_n}^{sm}$ together with $M_5(t)$ normalized by M_2^h for first two modes of: (a) MBU7; (b) MBU8 under ABN000 ground motion

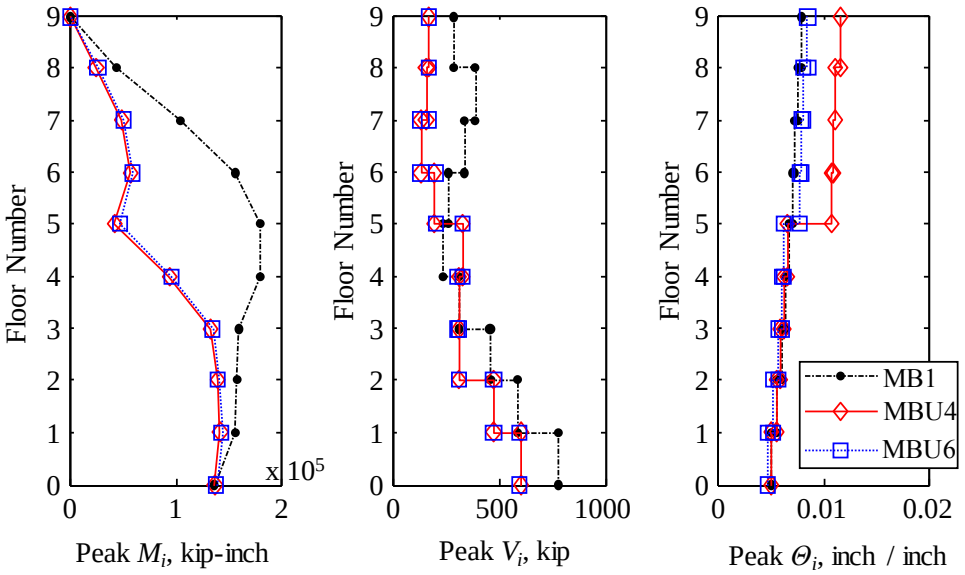

Figure 5.20 Peak M_i, V_i, and Θ_i responses for MB1, MBU4, and MBU6 under ABN000 GM record

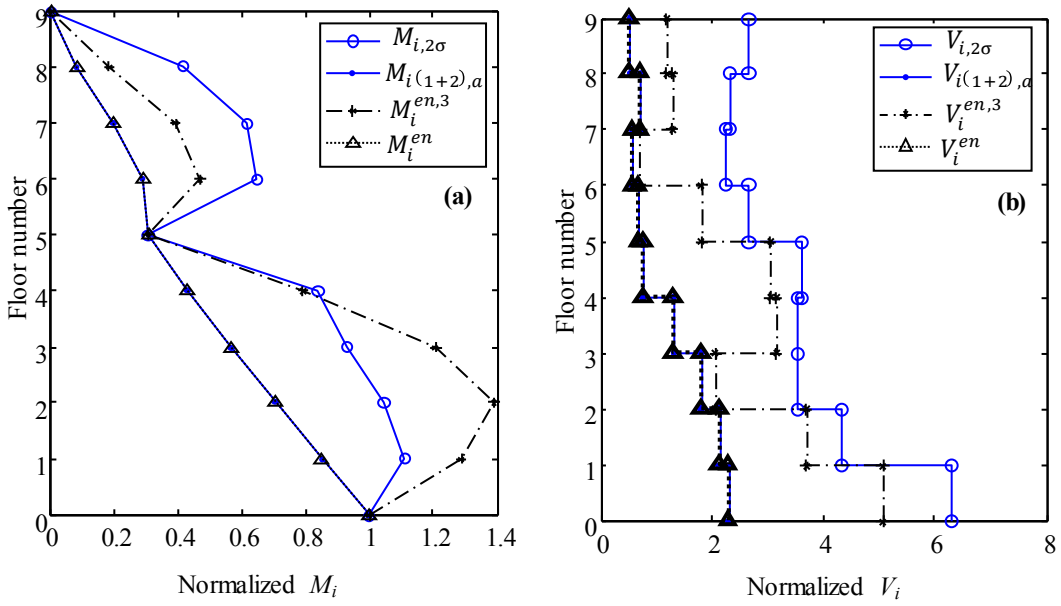

Figure 5.21 Comparison of: (a) M_i^{en} and $M_i^{en,3}$ with $M_{i(1+2),a}$ and $M_{i,2\sigma}$ normalized by M_1^h; (b) V_i^{en} and $V_i^{en,3}$ with $V_{i(1+2),a}$ and $V_{i,2\sigma}$ normalized by V_b^h from NLTHA results for MBU7 under GM set

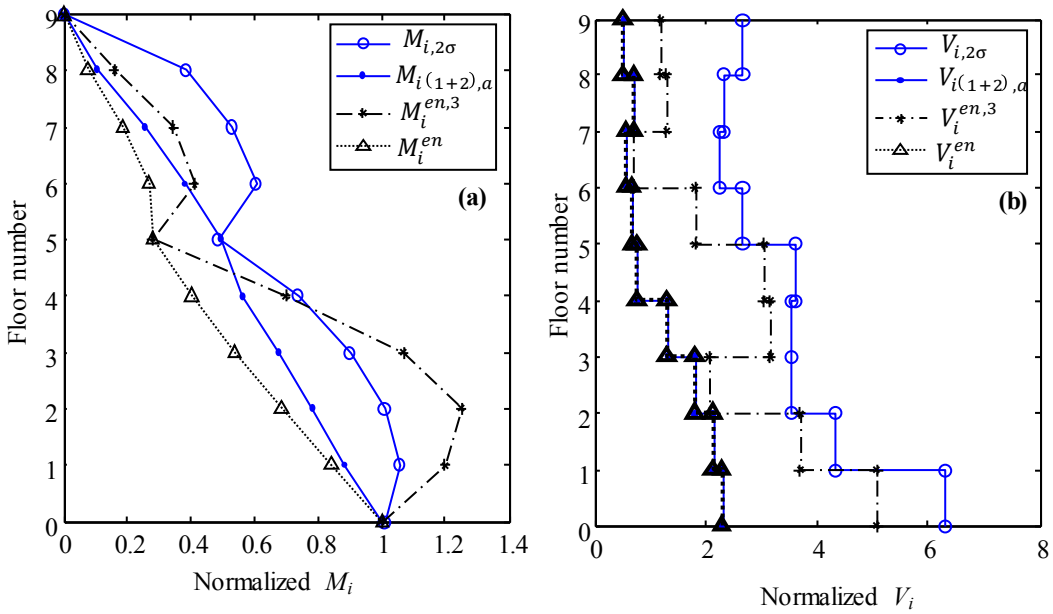

Figure 5.22 Comparison of: (a) M_i^{en} and $M_i^{en,3}$ with $M_{i(1+2),a}$ and $M_{i,2\sigma}$ normalized by M_1^h; (b) V_i^{en} and $V_i^{en,3}$ with $V_{i(1+2),a}$ and $V_{i,2\sigma}$ normalized by V_b^h from NLTHA results for MBU9 under selected GM set

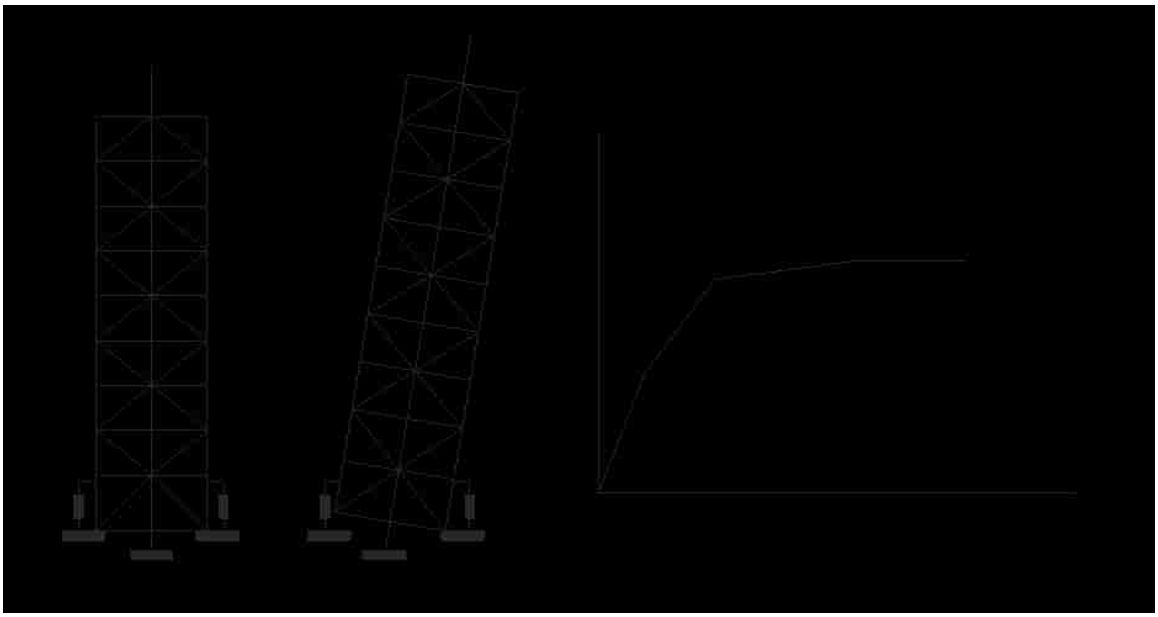

Figure 5.23 (a) Configuration of an SC-CBF with energy dissipaters; (b) limit states during the lateral load response of an SC-CBF

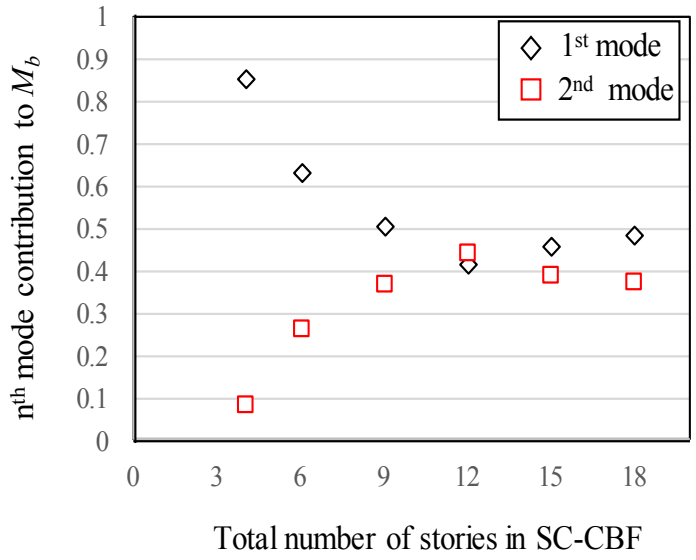

Figure 5.24 Plot of first and second mode contributions to base overturning moment response for the 4, 6, 9, 12, 15, and 18-story SC-CBFs (Chancellor, 2014)

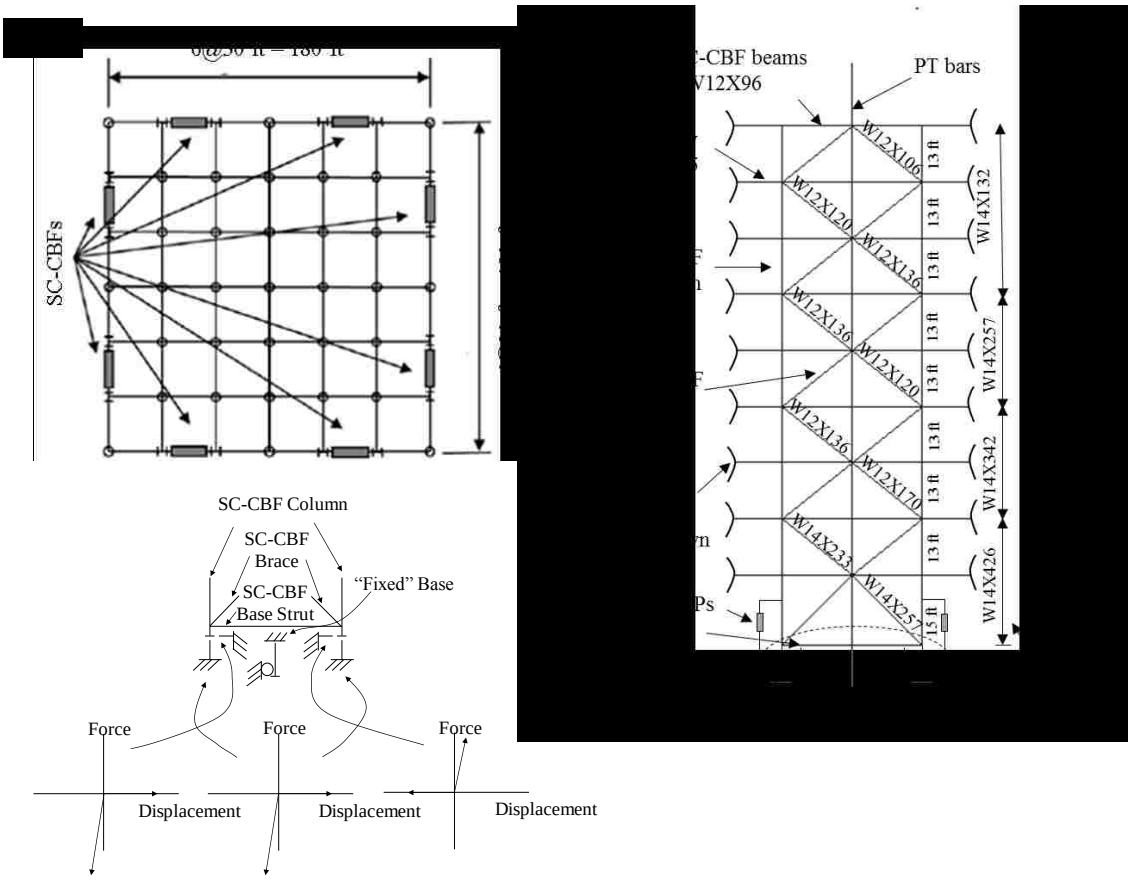

Figure 5.25 (a) Example SC-CBF building floor plan; (b) elevation of 9-story SC-CBF; (c) column base detail for numerical modeling (Chancellor, 2014)

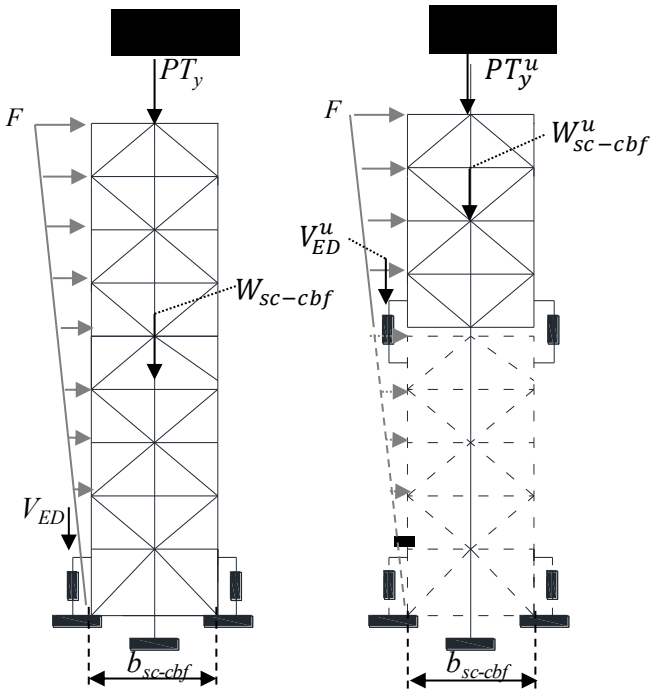

Figure 5.26 Forces acting on SC-CBF: (a) base flexural yield mechanism; (b) upper flexural yield mechanisms

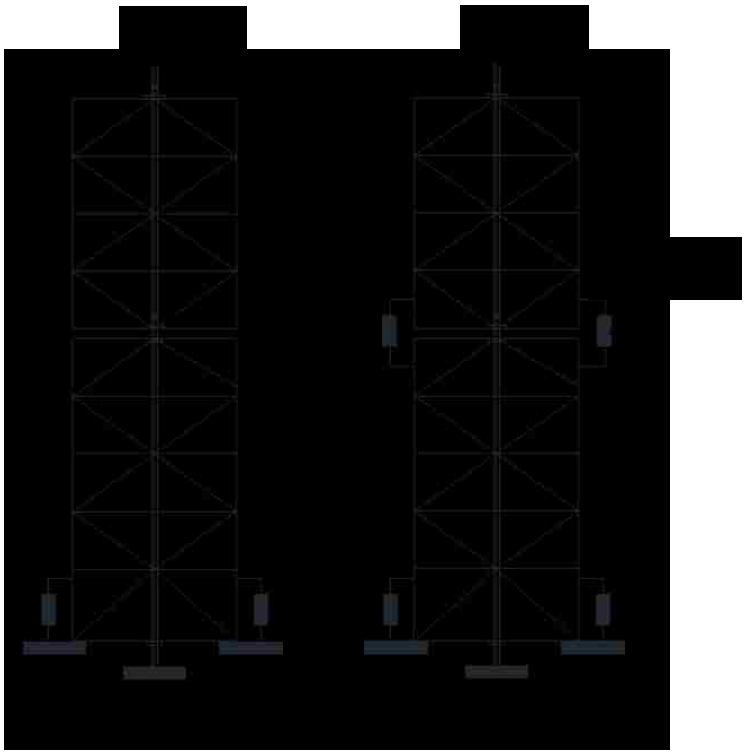

Figure 5.27 Model buildings, SC-CBFs with upper flexural yield mechanism: (a) SCCBF1; (b) SCCBF2

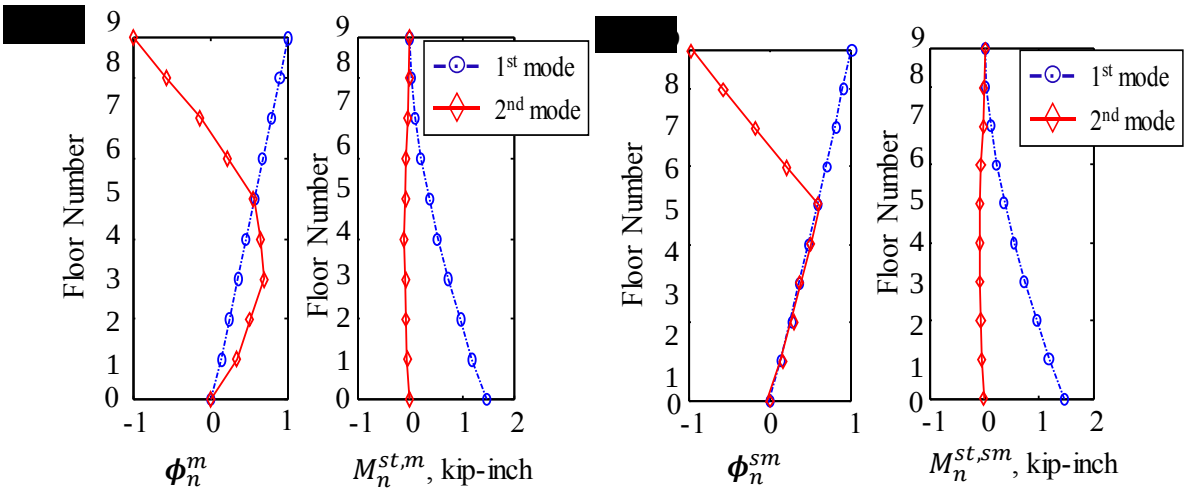

Figure 5.28 (a) ϕ_1^m and ϕ_2^m and $M_1^{st,m}$ and $M_2^{st,m}$ for SCCBF1; (b) ϕ_1^{sm} and ϕ_2^{sm} and $M_1^{st,sm}$ and $M_2^{st,sm}$ for SCCBF2

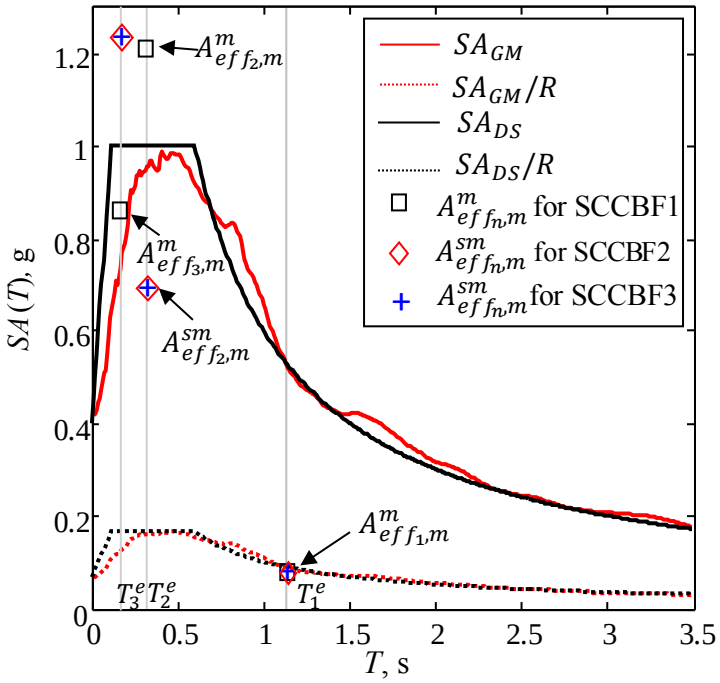

Figure 5.29 Design, median linear-elastic and median reduced 5% damped pseudo-acceleration spectra and $A_{eff_{n,m}}^m$ and $A_{eff_{n,m}}^{sm}$ for first three modes of SCCBF1, SCCBF2, and SCCBF3

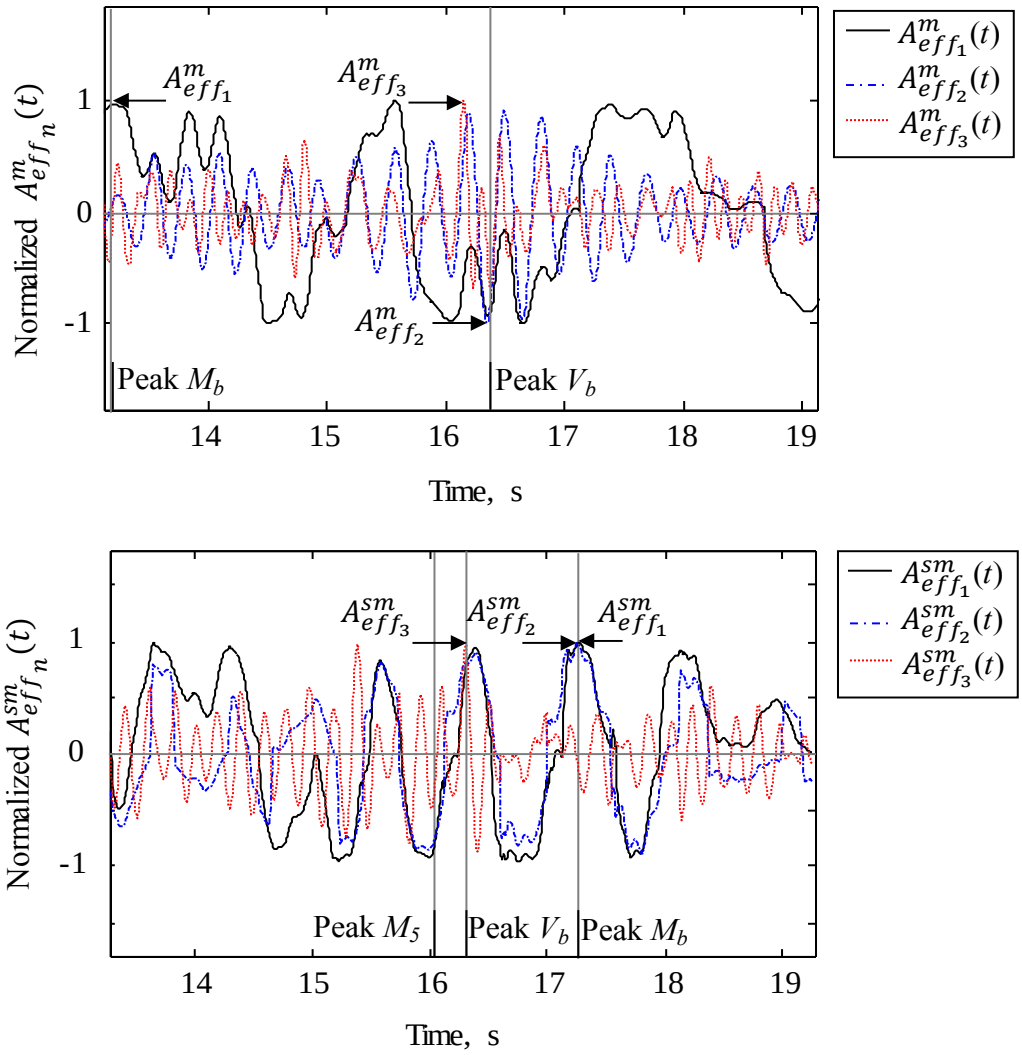

Figure 5.30 (a) $A^m_{eff_n}(t)$ normalized by $A^m_{eff_n}$ for first three modes of SCCBF1; (b) $A^{sm}_{eff_n}(t)$ normalized by $A^{sm}_{eff_n}$ for first three modes of SCCBF2 under ILA013W ground motion

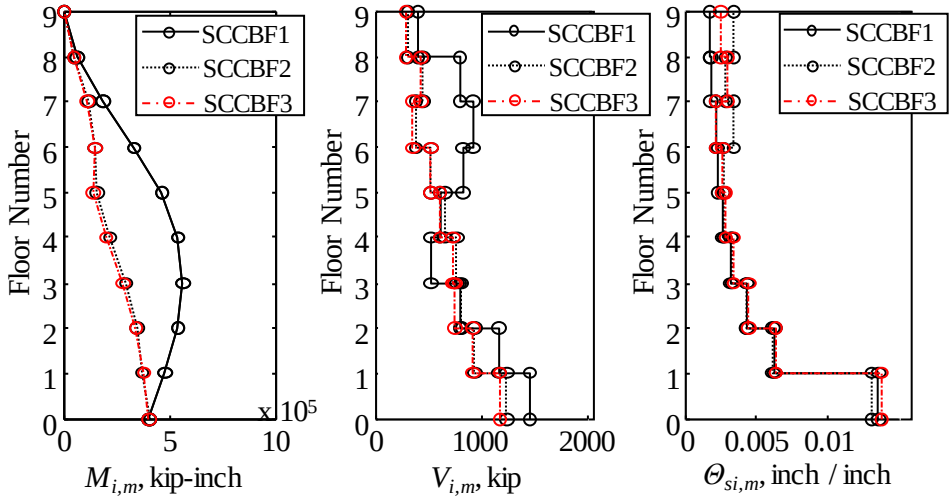

Figure 5.31 Peak $M_{i,m}$, $V_{i,m}$, and $\Theta_{i,m}$ response envelopes for SCCBF1, SCCBF2, and SCCBF3

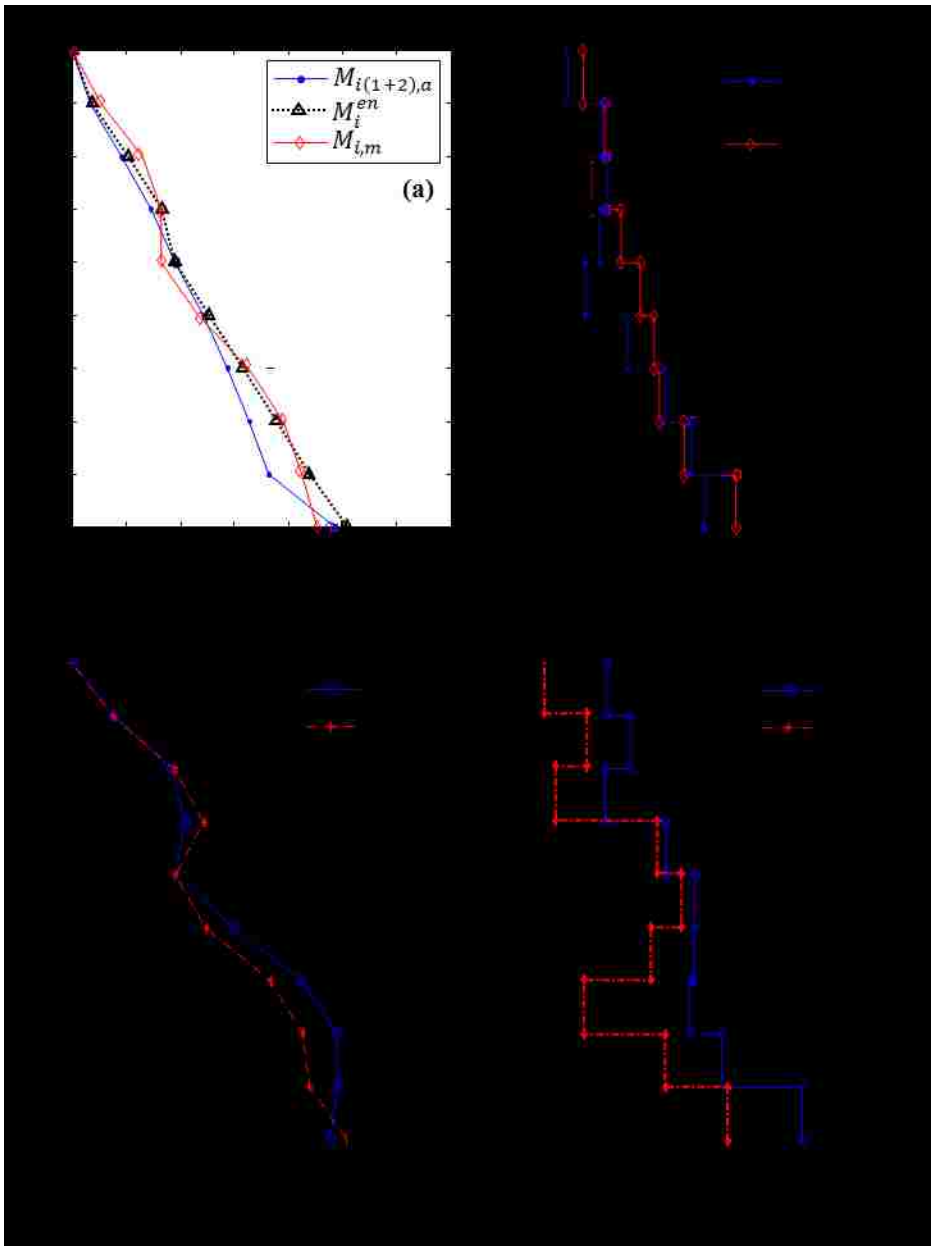

Figure 5.32 Comparison of: (a) M_i^{en} with $M_{i,m}$ and $M_{i(1+2),a}$ normalized by M_1^h; (b) V_i^{en} $V_{i,m}$ and $V_{i(1+2),a}$ normalized by V_b^h; (c) M_i^{en} and $M_i^{en,3}$ with $M_{i,2\sigma}$ normalized by M_1^h; (d) V_i^{en} and $V_i^{en,3}$ with $V_{i,2\sigma}$ normalized by V_b^h from NLTHA results for SCCBF3 under GM set

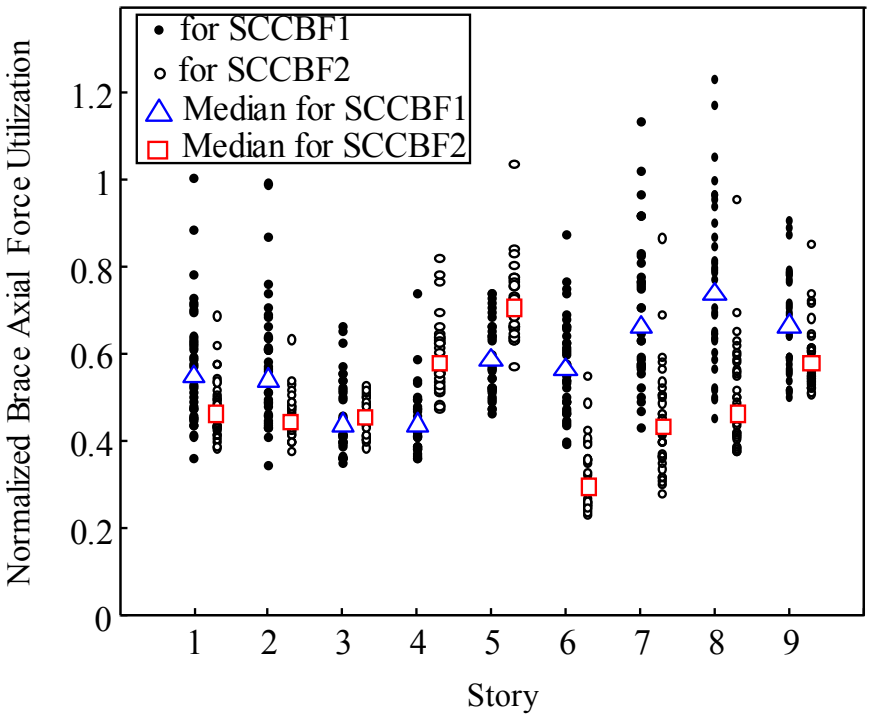

Figure 5.33 Utility ratios for SCCBF1 and SCCBF2

CHAPTER 6

ANALYTICAL AND EXPERIMENTAL LATERAL LOAD RESPONSE OF SELF-CENTERING CROSS-LAMINATED TIMBER WALLS

Overivew

A cross laminated timber (CLT) panel is a heavy timber structural component fabricated by laminating layers of timber boards in an orthogonal pattern. This paper presents a study of the lateral load response of self-centering (SC) CLT structural walls (i.e., SC-CLT walls), which are constructed by post-tensioning CLT wall panels to the foundation with vertical post-tensioning steel bars. The bars pass through the CLT panels and are anchored to the CLT panels at the top of the wall and to the foundation at the bottom of the wall. Cyclic loading tests were conducted on a series of SC-CLT wall specimens with different configurations. Structural limit states of SC-CLT walls under lateral load are identified. Two types of analytical models are proposed to predict SC-CLT wall response, namely, a design-oriented analytical model based on simple mathematical expressions, and a fiber-element-based numerical model. Comparisons between the analytical and experimental results are made, which indicate that the simple mathematical equations and the fiber-element-based numerical model provide accurate estimates of the lateral load response of SC-CLT walls under cyclic loading.

6.1. Introduction

A cross laminated timber (CLT) panel is a heavy timber structural component fabricated by laminating layers of timber boards in an orthogonal pattern. This paper presents a study of the lateral load response of self-centering (SC) CLT structural walls (i.e., SC-CLT walls), which are constructed by post-tensioning CLT wall panels to the foundation with vertical post-tensioning steel bars. The bars pass through the CLT panels and are anchored to the CLT panels at the top of the wall and to the foundation at the bottom of the wall. Past research on CLT walls focused mainly on conventional shear walls made from CLT panels connected by mechanical connectors to the floor diaphragms at each story (e.g., Dujic et al. 2008). The preliminary studies of Pei et al. (2012) on the seismic response of a 6-story CLT building show the necessity of further research on CLT buildings. Lateral load tests of conventional mechanically-connected CLT walls show that these walls have good deformation capacity, when the height-to-width ratio is reasonable, and have self-centering tendencies (Popovski et al., 2011). Earthquake simulations (Ceccotti, 2006) show that CLT buildings with conventional CLT walls are capable of resisting severe earthquake ground motions but will sustain structural damage. Extensive research on prestressed laminated veneer lumber (LVL) structural systems (e.g., Pampanin et al., 2006; Newcombe et al., 2008) has been conducted. Single-panel and multi-panel post-tensioned heavy timber walls have been tested in New Zealand (Dunbar et al., 2014). However, the lateral load response of post-tensioned SC-CLT rocking walls has not been studied extensively. Application of this type of CLT wall system in multi-story buildings requires a clear understanding of their lateral load response characteristics and structural limit states, and validated numerical models for simulation and design.

This chapter presents the experimental and analytical response of SC-CLT walls under cyclic lateral loading. Structural limit states of SC-CLT walls under lateral load are identified. Two types of analytical models are proposed to predict SC-CLT wall response, namely, a design-oriented analytical model based on simple mathematical expressions, and a fiber-element-based numerical model. Comparisons between analytical and experimental results are made, which indicate that the simple mathematical equations and fiber-element-based numerical model provide accurate estimates of the lateral load response of SC-CLT walls.

6.2. Expected Response of SC-CLT Walls under Lateral Load

Two types of SC-CLT walls are discussed in this paper, namely "single-panel" SC-CLT walls with vertical post-tensioning (PT) bars (see Figure 6.1) and "multi-panel" SC-CLT walls constructed from side-by-side single-panel SC-CLT walls attached along vertical joints with ductile connectors (i.e., ductile "vertical joint connectors" as in Perez et al., 1999). The ductile vertical joint connectors transfer shear force between two side-by-side CLT wall panels and provide energy dissipation under seismic loading. As shown in Figure 6.1, U-shaped flexural plates (UFPs) are used as the vertical joint connectors (as in Dunbar et al., 2014; Priestley et al., 1999). Figure 6.1 shows the configurations of typical single-panel and multi-panel SC-CLT walls. The walls shown in Figure 6.1 have only a single panel over the height of the wall, but walls taller than the height of available panels can be constructed by stacking panels vertically. The base CLT panel of an SC-CLT wall is precompressed against, but not otherwise attached directly to, the foundation (although

shear keys to prevent sliding are necessary). As a result, when the overturning moment due to lateral load is large enough to overcome the precompression, a gap opens between the base panel and the foundation, and the SC-CLT wall rocks on the foundation. The vertical PT bars provide a restoring moment to return the wall to its initial vertical position.

The lateral load response of an SC-CLT wall is governed by flexural behavior, including flexural deformation of the CLT panels and rocking of the wall on the foundation (Figure 6.2 (a)). To characterize the lateral load response of an SC-CLT wall, the structural limit states are identified, based on strains, stresses, and level of damage in the CLT material and PT bars. Figure 6.2 (b) shows the structural limit states on an idealized base shear versus (vs.) roof drift curve for an SC-CLT wall, which are: (1) decompression of the base of the wall (DEC); (2) effective limit of the linear-elastic response of the wall (effective linear limit, ELL); (3) yielding of the composite CLT section material (YCLT) at the compression edge of the wall (right edge of the wall in Figure 6.2 (a)); (4) splitting of the composite CLT section material (SCLT) at the compression edge of the wall; (5) crushing of the composite CLT section material (CCLT) at the compression edge of the wall; and (6) yielding of the PT bars (LLP). These limit states are similar to those identified for unbonded post-tensioned precast concrete walls (e.g., Kurama et al., 1998; Perez, 2004). If energy dissipating vertical joint connectors (e.g., UFPs) are included in the SC-CLT wall, yielding of these energy dissipating connectors (EDP) is also treated as a structural limit state. The roof drift ratio, Θ_r, used in Figure 6.2 is the lateral relative displacement at the roof level, Δ_r, divided by the height of the wall, H_w (see Figure 6.2 (a)). The base rotation, θ_b, due to gap opening between the base CLT panel and foundation (i.e., "rocking" of the

wall) is also shown in Figure 6.2 (a). Throughout the paper, Θ_r and θ_b are given in percent (%) radians.

Decompression (DEC) is the limit state when the overturning moment resistance at the base of the wall (between the base panel and foundation), provided by the initial force in the PT bars and gravity loads acting on the wall, is overcome by the applied overturning moment from the lateral forces. The base shear (V_b), base overturning moment (M_b), and roof drift ratio (Θ_r) at the DEC limit state (see Figure 6.2 (b)) are denoted as $V_{b,dec}$, $M_{b,dec}$, and $\Theta_{r,dec}$, respectively. After DEC, a gap opens (i.e., gap opening initiates) at the base of the wall at the edge subjected to tension under the applied overturning moment (the left edge in Figure 6.2 (a)). However, the lateral load response is essentially linear-elastic until this gap opening spreads over a certain length of the wall under increasing lateral load.

The effective linear limit (ELL) is the limit state at which the geometric nonlinearity from the increasing length of the gap opening along the base of the wall and/or nonlinear (NL) behavior of the composite CLT material in compression near the base of the wall reduce the lateral stiffness of the wall to an extent that significant NL behavior can be observed in the V_b (or M_b) vs. Θ_r response. The observation of NL behavior in the experimental results will be discussed later. V_b, M_b, and Θ_r at the ELL limit state (see Figure 6.2 (b)) are denoted as $V_{b,ell}$, $M_{b,ell}$, and $\Theta_{r,ell}$, respectively.

Yielding of the composite CLT material (YCLT) is the limit state at which the composite CLT material at the compression edge of the wall at the base of the wall "yields" in compression. This limit state is defined analytically as the point when the CLT panel fiber at the compression edge reaches the yield strain of the composite CLT material, ε_{c0} (see Figure 6.3 (a)). V_b, M_b, and Θ_r at the YCLT limit state (see Figure 6.2(b)) are denoted as $V_{b,yclt}$, $M_{b,yclt}$, and $\Theta_{r,yclt}$, respectively. The YCLT limit state may occur simultaneously with ELL when "yielding" of the CLT is the cause of the reduced lateral stiffness of the wall, or it may occur after ELL (as shown in Figure 6.2 (b)), when ELL is a result of geometric nonlinearity (i.e., gap opening along the base of the wall) rather than material nonlinearity.

Splitting of the composite CLT material (SCLT) is the limit state at which the composite CLT material at the compression edge near the base of the wall experiences considerable splitting. This limit state is defined analytically as the point when the CLT panel fiber at the compression edge reaches the splitting strain of the composite CLT material, ε_{cs} (see Figure 6.3(a)). V_b, M_b, and Θ_r at the SCLT limit state (see Figure 6.2 (b)) are denoted as $V_{b,sclt}$, $M_{b,sclt}$, and $\Theta_{r,sclt}$, respectively.

Crushing of the composite CLT material (CCLT) is the limit state at which the composite CLT material at the compression edge near the base of the wall fails in compression. This limit state is defined analytically as the point when the CLT panel fiber at the compression edge reaches the crushing strain of the composite CLT material, ε_{cu} (see Figure 6.3 (a)). V_b,

M_b, and Θ_r at the CCLT limit state (see Figure 6.2 (b)) are denoted as $V_{b,cclt}$, $M_{b,cclt}$, and $\Theta_{r,cclt}$, respectively.

The linear limit of the post-tensioning steel (LLP) is the limit state at which the first PT bar reaches its yield strain in tension, ε_{py} (see Figure 6.3 (b)). The strains in the PT bars increase above the initial strain from post-tensioning as a result of elongation due to gap opening and rocking of the SC-CLT wall on the foundation. If the roof drift ratio and corresponding rocking are large enough, the PT bars will yield. V_b, M_b, and Θ_r at the LLP limit state (see Figure 6.2 (b)) are denoted as $V_{b,llp}$, $M_{b,llp}$, and $\Theta_{r,llp}$, respectively. Depending on the level of initial prestress in the PT bars and the level of initial prestress in the CLT panel, LLP may occur prior to the SCLT or CCLT limit state.

In this study, the stress vs. strain behavior of the CLT material is idealized as elastic-perfectly-plastic (EPP), as shown in Figure 6.3 (a). The idealized stress-strain behavior of the CLT wall is defined by the modulus of elasticity (E_c), yield stress (f_{c0}), yield strain (ε_{c0}), splitting strain (ε_{cs}), and crushing strain (ε_{cu}) of the composite CLT material. Tests on composite CLT specimens (e.g., Ganey, 2015) show that the compressive strength of the CLT material may degrade after reaching ε_{cs} (see Figure 6.3 (a)). The EPP model for the CLT material used in the present study does not include strength degradation after ε_{cs} is reached or after ε_{cu} is reached, so the V_b vs. Θ_r response of the SC-CLT wall in Figure 6.2(b) does not show any loss in stiffness after the SCLT and CCLT limit states. However,

the SCLT and CCLT limit states are identified in the analysis results based on these strain values.

6.3. Summary of Experimental Program

To investigate the lateral load response of SC-CLT walls, quasi-static cyclic-loading tests on six SC-CLT walls (Table 6.1) were conducted at the Composite Materials & Engineering Center at Washington State University (WSU). Each test specimen (TS) was designed to represent part of a 40 ft. long 4-story tall SC-CLT wall at 0.40 scale. Figure 6.4 shows a full scale prototype SC-CLT wall panel and a corresponding floor plan. The prototype 40 ft. long shear wall shown in the plan is divided by vertical joints into four 10 ft. long wall panels. Three options for the vertical joints were considered: (1) a single, monolithic, 40 ft. long SC-CLT wall with rigid vertical joints made by field gluing and/or mechanical fasteners; (2) a 40 ft. long wall made with wall panels unattached along the vertical joints, resulting in four individual 10 ft. long SC-CLT walls (as shown in Figure 6.4 (a)); and (3) a 40 ft. long wall made from panels attached along the vertical joints with ductile connectors (i.e., UFPs), resulting in a multi-panel SC-CLT wall. Among these three options, only option (2) and option (3) were studied experimentally. Each 0.4 scale TS was 4 ft. long, approximately 6½ inch thick, and approximately 16 ft. tall. The panels were either 5-layer CLT panels or structural composite lumber (SCL) core CLT panels constructed at WSU. The 5-layer CLT panels were constructed by laminating 1.3 inch thick Grade 1 Douglas Fir boards with the outer two layers and center layer oriented with the grain parallel to the vertical (8 ft.) direction of the panel, and the two intermediate layers

oriented with the grain parallel to the transverse (4 ft.) direction of the panel (Figure 6.1 (b)). The SCL core CLT panels were constructed with a 3.6 inch thick SCL panel (APA, 2011) replacing the 3 inner layers of the 5-layer CLT; the SCL panel was glued to the outer two CLT layers, which are oriented with the grain parallel to the vertical direction of the panel (Figure 6.1 (b)). Table 6.2 lists material properties for the CLT panels.

Table 6.1 shows that six TS were tested. TS1, TS2, TS3, and TS4 had 5-layer CLT panels and TS5 had SCL-core CLT panels. Each of these TS had a single PT bar. The PT bar area (A_{pt}), initial pre-stressing ratio (f_{pi}/f_{pu} where f_{pi} is the initial pre-stress and f_{pu} is the ultimate stress of the PT bars (Figure 6.3 (b)), and initial pre-stressing force ($F_{pi} = A_{pt} f_{pi}$) on the CLT panels were varied among the TS. Note that the f_{pi} and F_{pi} values in Table 6.1 are based on the measured PT bar force at the beginning of the test. The first TS (TS1) was constructed by post-tensioning a 5-layer CLT panel using a 1.25 in^2 PT bar with an initial prestress ratio of 0.30. TS2 was constructed by post-tensioning a 5-layer CLT panel using a 1.58 in^2 PT bar with an initial prestressing ratio of 0.10. TS3 was constructed by post-tensioning a 5-layer CLT panel using a 1.25 in^2 PT bar with an initial prestressing ratio of 0.40. TS4 was constructed by post-tensioning a 5-layer CLT panel using 1.25 in^2 PT bars with an initial prestressing ratio of 0.38. TS5 was constructed by post-tensioning an SCL core CLT panel using a 1.58 in^2 PT bar with an initial prestressing ratio of 0.30. TS6 was a multi-panel SC-CLT wall constructed with two UFPs between two 5-layer CLT wall panels; each CLT wall panel had a single 1.25 in^2 PT bar.

The strength of the UFPs in TS6 was selected to provide an energy dissipation ratio of at least 10%, as defined by Seo and Sause (2005). In addition, to avoid having one wall panel permanently uplifted by a residual vertical joint force, the total plastic strength of the two UFPs in the joint, i.e., $2F_{ufp,p}$, was designed to be smaller than F_{pi}. Finally, the UFPs were intended to fully yield prior to the ELL, so the deformation of each UFP when the plastic strength, $F_{ufp,p}$, is reached, denoted as $\Delta_{ufp,p}$, was designed to be smaller than the estimated vertical joint deformation at the ELL limit state. The vertical joint deformation at the ELL limit state was estimated as the uplift at the (tension) edge at the base of the CLT wall panel at ELL. The thickness (t_{ufp}), width (b_{ufp}), and diameter (D_{ufp}) of each UFP (as shown in Figure 6.1(a)) in TS6 are ⅜ inch, 4, and $4^{1}/_{16}$ inch inch, respectively. $F_{ufp,p}$ = 1.5 times the initial UFP yield strength, $F_{ufp,y}$, the UFP stiffness, k_{0ufp}, and $\Delta_{ufp,p} = F_{ufp,y} / k_{0ufp}$, were estimated from t_{ufp}, b_{ufp}, and D_{ufp} using the equations presented by Kelly et al. (1972) (see Appendix B).

Except for TS4, each TS was tested on a W12x72 steel beam simulating the foundation. TS4 was tested with a horizontally-oriented CLT panel section under the SC-CLT wall to simulate a platform-framed CLT system with single-story CLT wall panels supported on bare wood CLT floor panels (Ganey, 2015). The bearing of the CLT wall panel on the horizontally-oriented CLT "floor" panel resulted in significant, local, perpendicular-to-grain crushing of the horizontally-oriented CLT panel, which added substantial inelastic flexibility to the system (Ganey, 2015). The lateral load response of TS4 is not discussed in the present paper.

Figure 6.5 (a) shows the test set-up for TS1, TS2, TS3, and TS5. The height of the lateral load actuator, H_{act}, was equal to 162 inch, which corresponds approximately to the height of the resultant force for a triangular lateral force pattern (Figure 6.4 (a)). H_w is the height of the 2 panels (Figure 6.5), and was planned to be 16 ft., constructed from two 8 ft. tall CLT panels. However, TS3 was tested first and the tests were carried out in three stages, referred to as Tests *3a*, *3b*, and *3c* in Ganey (2015). Prior to conducting Test *3c* the lowest 1.5 ft. of the bottom CLT panel of TS3 was cut off to remove damage from the first two stages of testing. To keep H_w constant for the remaining TS, the upper CLT panel of TS1, TS2, TS5, and TS6 were shortened by 1.5 ft. Table 1 lists H_w for each TS. The length of the PT bars between the anchor points, H_{pt}, for each TS is approximately 10 inch longer than H_w (Figure 6.5). In addition to the PT bar force acting downward on the CLT panels of the TS, the PT bar prestressing apparatus and steel PT force distribution beam placed on top of each TS (Figure 6.5 (a)) provided about 1.0 kip of additional vertical (gravity) force. Figure 6.5(b) shows an example of the cyclic lateral drift history imposed on the TS (i.e., for TS2).

6.3.1. Instrumentation

Figure 6.5 (c) shows the instrumentation placed on the wall to measure the displacements and the applied forces during the tests of TS1, TS2, TS3, and TS5. Two sets (denoted as the upper region and lower region in Figure 6.5 (c)) of linear variable differential transformers (LVDTs) were used to measure shear and flexural deformations. The lower region was expected to be subjected to significant NL shear deformation (e.g., shear slip)

and significant NL flexural deformation (e.g., NL deformation of the CLT panel material). The upper region was expected to be linear elastic during the early stages of the tests and was used to estimate the "linear-elastic" properties of the CLT panels. In each set of LVDTs, two LVDTs were placed in an X configuration to measure the shear deformation and two LVDTs were placed vertically to measure the axial and flexural deformations. Two rotation meters (RM) were placed 9⅝ inch and 35⅝ inch above the base of the wall (Figure 6.5 (c)) to measure the in-plane rotation. Five linear potentiometers were placed at the base of the wall to measure vertical "deformation" (gap opening) at the base of the wall. The two vertical LVDTs at the outer edges of the CLT wall panel were used to identify the initiation of gap opening at the base of the wall. Lateral displacements at the level of the lateral force actuator (at height H_{act}) were measured using an LVDT attached to the actuator and a string potentiometer attached between the wall and a fixed reference. The data from this potentiometer, divided by $H_{act,}$ is treated as the roof drift ratio, Θ_r, for the TS. An additional vertical string potentiometer was attached between the lab floor and the actuator to measure the vertical displacement of the actuator, where it is attached to the wall (Figure 6.5). Any slip of the steel beam at the base of the wall (simulating the foundation) relative to the lab floor was measured using a string potentiometer. One load cell measured the force in the PT bar and another load cell measured the lateral force applied by the actuator.

For TS6, a string potentiometer was positioned along the vertical joint to measure the relative vertical displacement between the two CLT wall panels at each UFP location, and this relative vertical displacement of the CLT panels at the UFP location was taken as the UFP deformation.

6.3.2. Estimated Material Properties

CLT material properties for the TS are estimated in three ways: (1) from results of CLT material tests; (2) using data from the lateral load tests; and (3) using empirical formulas from the literature.

Material Tests

Material tests were performed on CLT samples made from materials similar to the TS panels; including: (i) 3-layer CLT specimens, (ii) 5-layer CLT specimens, and (iii) SCL core CLT specimens (Ganey, 2015). For each type of specimen, the boards of the exterior layers are arranged so the grain is parallel to the vertical direction (Figure 6.1). Figure 6.3 (a) shows a simplified EPP constitutive relationship for the CLT material defined by the composite modulus of elasticity (E_c), yield stress (f_{c0}), yield strain (ε_{c0}), splitting strain (ε_{cs}), and crushing strain (ε_{cu}). Table 6.2 shows the average E_c, f_{c0}, $\varepsilon_{c0,}$ for the 5-layer and SCL core CLT specimens based on compression test results performed in the vertical direction (see Figure 6.1 (b)). Note that E_c and f_{c0} refer to the composite material property including all layers of the CLT together. The material tests for 5-layer CLT specimens and SCL core CLT specimens were terminated right after yielding of the specimens was observed (i.e., after reaching ε_{c0}). Therefore ε_{cs} is not available for the 5-layer CLT specimens and SCL core CLT specimens from the material tests, and the value of ε_{cs} is estimated as 0.02 inch/inch based on material tests performed on 3-layer CLT specimens. In addition, ε_{cu} was not measured in the material tests. The value of ε_{cu} is estimated to be about 0.05 inch/inch from the lateral load test results, as explained later.

Flexural Stiffness

The composite modulus of elasticity, E_c, for each TS was estimated from lateral load test data in the "linear-elastic" response range of each TS. To make this estimate, the flexural stiffness was estimated from the moment vs. curvature response in the "linear-elastic" response range. Figure 6.6 shows the moment and assumed curvature profile under the lateral force, *F*. Assuming a linear curvature distribution between the upper RM and lower RM (i.e., over h_2), the curvature, φ_{h_2}, and the average moment, M_{h_2}, within h_2 were calculated from the test data. The relation between M_{h_2} and φ_{h_2} is:

$$(EI)_c \varphi_{h_2} = M_{h_2} \tag{6.1}$$

where $(EI)_c$= the composite flexural rigidity = $E_c I_c$; I_c= the calculated moment of inertia of the composite section based on the measured dimensions $= \frac{1}{12}(t_w)(L_w)^3$; t_w= the measured thickness of the wall; and L_w= the measured length of the wall.

Figure 6.6 shows a linear regression of the M_{h_2} vs. φ_{h_2} data for the "linear-elastic" response range of TS2, which includes the first seven full cycles of the Θ_r history (see Figure 6.5 (b)). (i.e., up to Θ_r = 0.30%). The slope of the linear regression of the M_{h_2} vs. φ_{h_2} data, assumed equal to $(EI)_c$, was used to estimate E_c for each TS. Table 6.3 shows the estimated E_c values for TS1, TS2, TS3, and TS5, which are relatively close to E_c from the material test results.

Additionally, the modulus of elasticity in the parallel-to-grain direction, E_0, was estimated from the E_c results, as follows. Based on results in the CLT Handbook (Karacbeyli and Douglas, 2013), the modulus of elasticity in the perpendicular-to-grain direction, E_{90}, for each board was assumed to be one-thirtieth (1/30) of E_0. For a 5-layer CLT panel comprised of boards with equal thickness E_0 can be estimated from E_c, as follows:

$$E_0 = \frac{5(E_c)}{\left(3+2\left(\frac{1}{30}\right)\right)} \tag{6.2}$$

Similarly, the shear modulus of the timber boards, G_0, can be approximated as 1/12 to 1/20 of E_0 (Karacabeyli and Douglas, 2013). Table 6.3 shows the estimated E_0 and G_0, for TS1, TS2, and TS3, which are made of 5-layer CLT wall panels.

Shear Stiffness

The adjacent boards of the CLT panels of the TS were not glued together along their edges (Figure 6.1), and small gaps were present between the edges of the boards. The shear stiffness of a composite CLT panel with the boards not edge-glued together is smaller than the shear stiffness of a fully composite panel (with the boards in each layer edge-glued together). Therefore, formulas from the literature were used to estimate the composite shear modulus, G_c, from the shear modulus of the timber boards, G_0.

Flaig and Blass (2013) and Bogensperger et al. (2010) developed empirical formulas to estimate the in-plane shear stiffness of CLT panels made with boards that are not edge-glued together. These expressions were used to estimate G_c from the G_0 values given in Table 6.3, and the results are given in Table 6.4.

The lateral force vs. shear deformation response in the "linear-elastic" response range was used to estimate the composite shear stiffness, $(GA)_c$, for each TS (Figure 6.7). The method given by Massone and Wallace (2004) was adapted to calculate the average shear deformation, $\overline{U_s}$, within the upper region using data from the upper LVDT set. The F vs. $\overline{U_s}$ data was used to estimate $(GA)_c$ as follows:

$$F = (GA)_c \frac{\overline{U_s}}{h_2} \tag{6.3}$$

where $(GA)_c = G_c A_c$; A_c= the effective shear area of the composite section $= L_w t_w$.

Figure 6.7 (b) shows a linear regression of the F vs. $\frac{\overline{U_s}}{h_2}$ data for the "linear-elastic" response range (i.e., up to Θ_r = 0.30%) of TS2. Table 6.4 shows the estimated G_c for TS1, TS2, TS3, and TS5. The estimated G_c values for TS1 and TS2 are in good agreement with the G_c values from the empirical formulas by Flaig and Blass (2013) and Bogensperger et al. (2010). The estimated G_c value for TS3 is much larger than the values for TS1 and TS2 and the values from the empirical formulas. Since the empirical formulas were derived for CLT sections comprised of conventional timber boards, G_c for the SCL core CLT panel was not estimated using these formulas. Other estimates of G_c were made as 1/12 to 1/20

times E_c (Karacabeyli and Douglas, 2013). Table 6.3 shows that the estimated upper bound G_c (i.e., (1/12)E_c) and lower bound G_c (i.e., (1/20)E_c) are consistent with the G_c values for TS1 and TS2 estimated from the test data.

6.4. Analytical Models

Two types of analytical models for the lateral load response of SC-CLT walls are presented: (1) closed-from expressions (CFE), which are adapted for SC-CLT walls from expressions derived for unbonded post-tensioned precast concrete walls (Kurama et al. 1997; Perez et al. 1999); and (2) fiber-element-based numerical models.

Several assumptions were made in developing in these analytical models. It is assumed that plane horizontal sections within the CLT panel remain plane. The wall is assumed to be braced against out-of-plane deformations, so out-of-plane deformations are not considered, and it is assumed that the wall is subjected to only in-plane axial, flexural, and shear deformations. The foundation is assumed to be rigid. Based on the material tests performed at WSU (Ganey, 2015), where the CLT material specimens showed nearly elastic-perfectly plastic (EPP) behavior under compression, the compressive behavior of the composite CLT section is idealized as EPP (as shown in Figure 6.3 (a)).

6.4.1. Closed Form Expressions

The closed-form expressions (CFE) adapted for SC-CLT walls from expressions derived for unbonded post-tensioned precast concrete walls (Kurama et al. 1997; Perez et al. 1999) are presented in Appendix B. The application of the CFE to the TS and the corresponding results are presented here. Figure 6.8 shows diagrams of the forces (stress resultants), stresses, and strains at the base of the wall at DEC, ELL, YCLT, SCLT, CCLT, and LLP.

The M_b capacity at each limit state is estimated by adding the elastic deformation (denoted as Δ_r^{el}) to the lateral deformation, Δ_{rb}, due to base rotation θ_b. The base shear, V_b, is equal to the resultant of the lateral forces applied to the wall, F (see Figure 6.4 (a)). V_b is estimated by dividing M_b by the height of the lateral force resultant. For each TS, V_b is calculated as M_b divided by H_{act}. The total roof level lateral deformation, Δ_r, is estimated by adding the roof level elastic deformation (denoted as Δ_r^{el}) to the lateral deformation due to the base rotation θ_b (denoted as Δ_{rb}). Δ_r^{el} includes the flexural deformation (Δ_{rf}) and the shear deformation (Δ_{rs}). For the TS, Δ_{rf} is calculated using the estimated $(EI)_c$ from Table 6.3, and Δ_{rs} is calculated using the estimated $(GA)_c$ from Table 6.4. The base rotation, θ_b, (see Figure 6.2 (a)) is a function of the strain at the compression edge of the CLT panel (ε_c), the contact length (c), and the height along the compression edge of the CLT panel over which the NL material behavior is assumed to spread, H_{cr}. Here, H_{cr} is assumed to be two times the thickness of the CLT panel (i.e., $2t_w$). Δ_{rp} is an additional component of Δ_r^{el} from P-Δ effects. P is the gravity load acting on the wall (for the TS) or braced by the wall (in the

prototype building). Δ includes all components of Δ_r (i.e., Δ_r^{el} and Δ_{rb}). The roof drift ratio, Θ_r, equals Δ_r divided by H_{act}.

At DEC (Figure 6.8 (a)), it is assumed that the CLT panel is in full contact with the foundation at the base, the PT bar force equals the initial pre-stressing force, $T_{p,i}$, and the CLT panel material is linear-elastic. $M_{b,dec}$ (and $V_{b,dec}$) is calculated from the stress resultants in Figure 6.8 (a). ELL occurs after DEC and subsequent gap opening, when only part of the base CLT panel is in contact with the foundation (Figure 7(b)). Assuming that 3/8 of the base CLT panel is in contact with the foundation (consistent with observations by Ganey (2015)), and that the CLT panel material is linear-elastic, $V_{b,ell}$ is estimated as 2.25 times $V_{b,dec}$. At YCLT, SCLT, or CCLT, a linear distribution of compressive strain across the length of the base CLT panel in contact with the foundation ($c_{yclt,}$ c_{sclt}, and c_{cclt}) is assumed, , and the strain at the compression edge of the base CLT panel is assumed to equal ε_{c0}, ε_{cs}, or ε_{cu} (Figures 6.8 (c), 6.8 (d), and 6.8 (e)), respectively. ε_{c0} is given in Table 6.2 . ε_{cs} is estimated to be approximately 0.02 inch/inch as mentioned earlier. ε_{cu} is estimated to be approximately 0.05 inch/inch, as follows.

The experimental results show that the TS start to fail in compression (i.e., crushing of the CLT material) at a roof drift, $\Theta_{r,cclt}$, of about 7.5% for all TS. Assuming that the contact length at the CCLT limit state is c_{cclt}, and crushing of the CLT material at the compression edge extends over H_{cr}, the corresponding crushing strain, ε_{cu}, near the compression edge of

the base of each CLT panel is estimated from the base rotation at the CCLT limit state, $\theta_{b,cclt}$, as follows (see Figure 6. 8 (e) for the CLT strain profile at the CCLT limit state):

$$\varepsilon_{cu} = c_{cclt} \frac{\theta_{b,cclt}}{Hcr} \tag{6.4}$$

$\theta_{b,cclt}$ is estimated by subtracting the elastic deformation of the CLT panels (based on Δ_{rf} and Δ_{rs}) from $\Theta_{r,cclt}$ = 7.5%. H_{cr}, is assumed to be $2t_w$. Table 6.5 shows c_{cclt} for each TS from the experimental results, and the corresponding ε_{cu}.

6.4.2. Fiber-element-based Numerical Model

A two dimensional fiber-element-based numerical model of the each TS was developed using OpenSees (Mazzoni et al, 2009). Figure 6.9 shows schematics of the FM. Force-based beam-column elements with fiber sections are used to model the CLT wall panel. The fiber element theory assumes that plane sections remain plane. Each fiber element is comprised of vertically oriented fibers distributed across the length of the wall. The lateral load test results show that NL deformations of the CLT wall panel concentrate near the base of the wall, so a finer distribution of fibers is used within c_{ell} near the base of the wall, as shown in Figure 6.9. The height of the element with the finer distribution of fibers is equal to $2H_{cr}$. The compressive stress-strain behavior of the CLT wall panel material is idealized as elastic-perfectly plastic (EPP), as shown in Figure 6.3 (a), with E_c from Table 6.3 and f_{c0} from Table 6.2.

To model the gap opening behavior along the base of the wall, the tensile strength of the CLT wall panel fiber elements is set to zero for the first element at the base of the wall, (i.e., over a height of $2H_{cr}$). 2-point Gauss-Legendre numerical integration, with a weight of 0.5 for the integration points located at $0.21(2H_{cr})$ and $0.78(2H_{cr})$, is used for the first element at the base of the wall. For the elements above the first element (i.e., above $2H_{cr}$), the CLT panel is assumed to have a linear-elastic response in tension. Gauss-Lobatto integration with five integration points is used for these elements. The response of the CLT panel in shear is assumed to be linear-elastic with a shear stiffness of $(GA)_c$ from Table 6.4.

The single PT bar of the TS is modeled using a single force-based beam-column element. The steel of the PT bar is modeled with the Steel02 material model (Mazzoni et al., 2009) calibrated using material test results performed for each bar size. The nominal bar areas are 0.85 in^2, 1.0 in^2, and 1.58 in^2, respectively. Table 6.6 gives the average modulus of elasticity, E_p, yield stress, f_{py}, and ultimate stress, f_{pu}, for each PT bar size calculated from the material test results using the nominal bar areas. At the top of the wall, the horizontal, vertical, and rotational degrees-of-freedom of the top node of the PT bar element are constrained to the horizontal, vertical, and rotational degrees-of-freedom of the element modeling the CLT panel using a rigid link. The bottom node of the PT bar element is located 10 inch below the bottom node of the bottom CLT panel element, since the PT bar length between the anchor points, H_{pt}, for each TS is approximately 10 inch longer than H_w. The bottom CLT panel node is fixed. The potential for slack in the PT bar, i.e., a gap occurring between the PT anchorage nut and the anchorage block after significant yielding

and permanent deformation of the PT bar, is modeled using a zero-length contact element (Mazzoni et al., 2009), with a compressive stiffness equal to the 30000 kips/inch, which is between the bottom node of the PT bar element and the CLT panel node.

Each UFP used in TS6 is modeled using a zero-length element oriented in the vertical direction. The nodes at each end of the UFP element are constrained to the corresponding nodes of the fiber beam-column element modeling the CLT panels by rigid links as shown in Figure 6.9. The Giuffre-Menegotto-Pinto material model (Mazzoni et al., 2009) was used for the UFP elements. This material model was calibrated using UFP test results from Ganey (2015). Figure 6.10 (a) and Figure 6.10 (b) compare the UFP force vs. deformation response from the experiment and the FM up to 0.5 inch and 3 inch, respectively. Formulas from Kelly et al. (1972) (see Appendix B) were used to estimate the UFP model properties. Good agreement between the UFP force vs. deformation response from the test results and the FM was obtained when the "yield" strength of the UFP model is set equal to the plastic strength, $F_{ufp,p}$ (Ganey, 2015). The UFP stiffness from the test is less than $k_{0,ufp}$ calculated based on Kelly et al. (1972), so the stiffness of the UFP model stiffness is set equal to $0.85k_{0,ufp}$ (see Figure 6.10 (a)). Table 6.7 summarizes the UFP model.

6.5. Discussion of Analytical and Experimental Results

6.5.1. Comparison of Base-Shear-Lateral-Drift Response under Cyclic Loading

Cyclic loading analyses were performed using the fiber-element-based numerical model (FM) for each TS. Figure 6.11 and Figure 6.12 compare the experimental V_b vs. Θ_r response for TS2, TS3, TS5, and TS6 under cyclic loading with the results from the FM under the same cyclic loading lateral displacement history (see Figure 6.5 (b)). The comparisons are shown up to Θ_r of 5.0% and 9.5%, in Figure 6.10 and Figure 6.11 respectively. The experimental and the FM results include three cycles at each level of maximum drift. To obtain the FM results for each TS, the lateral displacement history recorded by the string potentiometer during the cyclic-loading test was imposed on the FM, and the V_b vs. Θ_r response was obtained. Due to flexibility of the reaction frame that supported the lateral load actuator, the lateral displacement history applied in the experiments was unsymmetric (as shown in Figure 6.5 (b)), so the V_b vs. Θ_r responses shown in Figure 6.11 and Figure 6.12 are unsymmetric. Also as shown in Figure 6.11, TS2 and TS5 were loaded with the first half cycle of each full drift cycle in the southward (negative) direction, while TS3 and TS6 were loaded with the first half cycle in the northward (positive) direction.

Figure 6.11 shows that the V_b vs. Θ_r responses from the experiments and FM for each TS are overall in good agreement. The identified ELL limit state from the experiments is marked in Figure 6.11. Figure 6.11 shows that after the ELL limit state, the V_b vs. Θ_r responses for TS3 and TS6 from the FM are softer (smaller V_b) than the V_b vs. Θ_r responses from the experiments. For TS2 and TS5, the V_b vs. Θ_r responses from the FM and

experiments are in good agreement up to Θ_r = 5.0%. Figure 6.11 shows that due to the presence of the UFPs, TS6 has additional energy dissipation capacity (other than energy dissipation provided by yielding of the PT bars and the CLT material at the base) compared to TS2, TS3, and TS5.

Figure 6.12 shows that for each TS the differences between the V_b vs. Θ_r responses from the experiments and FM increase with increasing roof drift. Figure 6.12 identifies the SCLT, CCLT, and LLP limit states from the experiments. The EPP model for the CLT material used in the FM, which does not fail in compression at CCLT, is one reason for these increasing differences.

The DEC limit state in the experiments is identified as the state when the vertical LVDT at the tension edge of the base of the wall (Figure 6.5 (c)) measures zero deformation, indicating that the compressive deformation from the post-tensioning has been overcome. To check the accuracy of the vertical LVDT measurements, the linear potentiometer measurements along the base of the wall were used to estimate the vertical deformation profile along the base of the wall, which is expected to be linear at the DEC limit state. The ELL limit state in the experiments is identified visually as the state where the experimental V_b vs. Θ_r response, softens significantly. The SCLT and CCLT limit states in the experiments are identified from the visual observations (Ganey, 2015). The SCLT limit state in the experiments is the state when splitting at the compression edge at the base of the wall was first observed. The CCLT limit state in the experiments is identified as the

drift level when crushing at the compression edge at the base of the wall was first observed. The LLP limit state in the experiments is identified as the state when the measured force in the PT bar (from the PT bar load cell) reached the yield force based on the material tests. The EDP limit state in the TS6 experiment is the state when yielding of the UFPs was observed by Ganey (2015).

Table 6.8 compares the $M_{b,dec}$, $V_{b,dec}$, and $\Theta_{r,dec}$ results from the experiments and the CFE. As shown in Table 6.8, $M_{b,dec}$ estimated from the LVDT and linear potentiometer measurements is always much greater than $M_{b,dec}$ from the CFE. These results suggest that the experimental deformation measurements are not representative of the actual contact stress condition at the base of the wall. That is, the zero contact stress condition that occurs at decompression is reached before the deformation measurements from the LVDTs and linear potentiometers reach zero. This discrepancy is likely due to non-uniform contact flexibility between the CLT panel and the steel beam simulating the foundation (which is assumed to be rigid in the CFE and FM). The non-uniform flexibility is a result of downward bending of the beam flanges under contact stresses, which is larger at locations away from the web compared to locations near the beam web. The contact flexibility is smallest (i.e., the contact stiffness is largest) near the beam web at the mid-thickness of the CLT panel, and largest near the surface of the CLT panel away from the web, where the LVDTs and linear potentiometers are located. As a result, the experimental deformation measurements do not accurately indicate the region of the CLT panel base cross section that has significant contact stresses. Table 6.8 shows that as F_{pi} increases, the differences between $M_{b,dec}$ from the experiments and from the CFE tends to decrease, which indicates

the importance of the contact flexibility in determining $M_{b,dec}$ from the experiments. For example, as shown in Table 6.8, the ratio of $M_{b,dec}$ from the experiment to $M_{b,dec}$ from the CFE is 2.60 for TS2, with F_{pi} of 22.5 kips, while it is 1.80 for TS5 with F_{pi} of 75 kips.

Tables 6.9, 6.10, 6.11, and 6.12, for TS2, TS3, TS5, and TS6, respectively, show V_b and Θ_r values at the ELL, SCLT, CCLT, and LLP limit states from the experiments and from the CFE and FM. The analytical results are in general in good agreement with the experimental results. The values of $V_{b,ell}$ and $\Theta_{r,ell}$ from the analytical models are relatively close to the experimental results for each TS. The YCLT limit state was not identified during the experiments because yielding of the CLT material could not be measured or observed visually. Thus, experimental results for $V_{b,yclt}$ and $\Theta_{r,yclt}$ are not included in the tables. However, $V_{b,yclt}$ and $\Theta_{r,yclt}$ from the CFE and FM are always greater than $V_{b,ell}$ and $\Theta_{r,ell}$, which implies that softening of the V_b vs. Θ_r response of each TS is due to geometric nonlinearity, and not due to material nonlinearity. The $\Theta_{r,sclt}$ values from the analytical models are within 10% of the experimental results. Except for TS5 (SCL core CLT), the $\Theta_{r,cclt}$ values from the analytical models are within 6% of the experimental results. Except for TS3, the $\Theta_{r,llp}$ values from the analytical models are within 10% of the experimental results.

The CFE results for $\Theta_{r,llp}$ are smaller than the FM results for TS2 and TS5. A detailed study of the analytical results showed that the contact length at LLP (c_{llp}) is smaller for the CFE than for the FM. The smaller contact length results in a smaller rigid body rotation of the

CLT panel when yielding of the PT bar is reached. Therefore, the PT bar yields at a smaller Θ_r.

The assumptions made in developing the FM and CFE, as well as the use of estimated material properties in these analytical models, are possible reasons for the differences between the experimental and analytical results. For example, the constitutive relationship of the CLT material in compression is assumed to be elastic-perfectly plastic and the shear force-deformation response of the CLT panel is assumed to be linear-elastic. The analytical models are based on the assumption that plane sections remain plane in the CLT panel and the CLT section has a linear strain distribution at the base of the CLT panel. The experimental results also have significant variability suggesting that the CLT panel material properties in the inelastic range of response also have significant variability. For example, Figure 6.13 shows the V_b vs. Θ_r response for TS1, which had relatively little deformation capacity compared to TS3, which has the same A_{pt} and nearly the same f_{pi}.

6.5.2. Effect of SC-CLT Wall Parameters

Figure 6.14 compares envelope V_b vs. Θ_r responses for TS1, TS3, and TS5 which are constructed using the V_b and Θ_r values at ELL, SCLT, CCLT, and LLP from the experiments. The response for TS1 is plotted up to the failure point (see Figure 6.13). Figure 6.14 (a) compares the V_b vs. Θ_r responses for TS1 and TS5. Table 6.1 shows that TS1 and TS5 have the same $f_{pi,}$ but TS5 has larger A_{pt} and F_{pi}. As seen in Figure 6.14 (a), TS5 has a larger $V_{b,ell}$ than TS1, since $V_{b,ell}$ increases with F_{pi}. Figure 6.14 (b) compares

the V_b vs. Θ_r responses for TS1 and TS3. TS1 and TS3 have the same A_{pt}, but TS3 has larger f_{pi} and F_{pi}. As shown in Figure 6.14 (b), TS3 has a larger $V_{b,ell}$ than TS1 since $V_{b,ell}$ increases with F_{pi}. Figure 6.14 (c) compares the V_b vs. Θ_r responses for TS3 and TS5. TS3 and TS5 have nearly the same F_{pi}, but TS3 has a larger f_{pi} and a smaller A_{pt}. As shown in Figure 6.14 (c), the $V_{b,ell}$ values for TS3 and TS5 are nearly equal. TS5 has slightly smaller $\Theta_{r,sclt}$ than TS3, because TS5 has a larger A_{pt}. TS3 has a smaller $\Theta_{r,llp}$ than TS5, because TS3 has a larger f_{pi}. However, since TS5 has a larger A_{pt} than TS3, $V_{b,llp}$ for TS5 is 1.2 times larger than $V_{b,llp}$ for TS3.

Using the CFE, more general results showing the effect of f_{pi} and A_{pt} on the response of SC-CLT walls were generated, and are shown in Figure 6.15. Figure 6.15 (a) shows the effect of increasing f_{pi} with constant A_{pt} on the V_b vs. Θ_r response of a single-panel SC-CLT wall based on the CFE. With constant A_{pt}, increasing f_{pi} increases $V_{b,ell}$ and decreases $\Theta_{r,yclt}$, due to the increased F_{pi}, and decreases $\Theta_{r,llp}$, due to the increased f_{pi}. Since $V_{b,llp}$ is controlled by the PT bar yield force, $V_{b,llp}$ is not affected by increasing $f_{pi.}$ Figure 6.15 (b) shows the effect of increasing A_{pt} with constant f_{pi} on the V_b vs. Θ_r response based on the CFE. With constant f_{pi}, increasing A_{pt} increases V_b at all limit states. $\Theta_{r,ell}$ and $\Theta_{r,llp}$ also increase with increasing A_{pt}, but $\Theta_{r,yclt}$, $\Theta_{r,sclt}$, and $\Theta_{r,cclt}$ (not shown) decrease as A_{pt} increases since increased F_{pi} initiates NL response of the CLT material at smaller values of Θ_r.

6.5.3. Comparison of Contact Length at Wall Base

Figure 6.16 shows the experimental and analytical contact length along the base of the wall for TS2 and TS3. The contact length from the experiments is plotted for the entire drift history of TS2 and TS3. The vertical LVDT measurements at the edge of the wall and the linear potentiometer measurements along the base of the wall were used to estimate the contact length along the base of the wall. The contact length from the FM is estimated from the first fiber element at the base of the wall. The contact length estimates at ELL, YCLT, and SCLT limit states from the CFE are also marked in Figure 6.16.

Figure 6.16 (a) shows that at Θ_r values less than approximately 3%, the contact length for TS2 from the experiment is larger than the analytical results (i.e., CFE and FM). The experimental and analytical results are closer to each other at around 9 inch when the roof drift is greater than approximately3%. The contact length estimates from CFE and FM are similar to each other. The contact length for TS2 from the experiments is larger under northward loading than under southward loading. Ganey (2015) reports that the damage at the north end of the wall was more severe than the damage at the south end of the wall, which suggests that under northward loading, a greater contact length is required to provide the same amount of compression force resistance in the contact zone.

Similar to TS2, Figure 6.16 (b) shows that at Θ_r values less than approximately 3%, the contact length for TS3 from the experiments is larger than the analytical results. For TS3, the contact length from the CFE is slightly smaller than from the FM. The contact length

for TS3 from the experiments under northward and southward loading are more similar to each other than for TS2.

Figure 6.16 shows that at Θ_r values less than approximately 3%, the contact lengths from the experiments are smaller than the analytical results for both TS2 and TS3. As mentioned earlier in the comparison of the experimental and analytical $M_{b,dec}$ values, this discrepancy is likely due to non-uniform contact flexibility between the CLT panel and the steel beam simulating the foundation (which is assumed to be rigid in the CFE and FM). The non-uniform flexibility is a result of downward bending of the beam flanges under contact stresses, which is larger at locations away from the web compared to locations near the beam web. The contact flexibility is smallest (i.e., the contact stiffness is largest) near the beam web at the mid-thickness of the CLT panel, and largest near the surface of the CLT panel away from the web, where the LVDTs and linear potentiometers are located. As a result, the experimental deformation measurements do not accurately indicate the region of the CLT panel base cross section that has significant contact stresses. Figure 6.17 shows schematically the apparent (based on the deformation measurements) area with significant contact stresses and the likely area with significant contact stresses at the base of the CLT panel. Although, a uniform stress distribution through the thickness of the CLT panel is assumed in the analytical models (Figure 6.17 (a)), the likely stress distribution is non-uniform due to the non-uniform contact flexibility (as shown in Figure 6.17 (b)). As a result, the effective contact length (denoted as $c_{effective}$ in Figure 6.17 (b)) is much smaller than the apparent contact length (denoted as $c_{apparent}$ in Figure 6.17 (a)) based on experimental deformation measurements.

6.5.4. Comparison of PT Bar Forces

Figure 6.18 and Figure 6.19 compare the experimental and analytical (FM) results for the PT bar force vs. Θ_r response for TS2 and TS3, which are shown up to 5% roof drift in Figure 6.18 and 8.6% roof drift in Figure 6.19. The experimental and analytical results are in good agreement with each other for most of the drift history. For TS2, the PT bar did not yield up to Θ_r = 8.6%. As a result, the difference between the experimental and FM results are small. For TS3, after yielding of the PT bar and as the lateral drift increases, the differences between the FM and experimental PT bar force vs. Θ_r response increase.

6.6. Summary and Conclusions

The lateral load response of self-centering (SC) CLT structural walls has been presented in this paper. The limit states for single-panel and multi-panel SC-CLT walls were identified. An experimental program of cyclic lateral load tests on SC-CLT walls was summarized. Material properties for 5-layer CLT panels and SCL core CLT panels were estimated from material test results and data from the lateral load tests. A design-oriented analytical model for the lateral load response of SC-CLT walls based on closed-form equations (CFE) was presented, and the base shear (V_b), base overturning moment (M_b), and roof drift ratio (Θ_r) capacities of the test specimens at the identified structural limit states were estimated and compared to the experimental results. A fiber-element-based numerical model (FM) was presented and applied to the test specimens, and the analytical results from the FM were compared with the experimental results.

The experimental results show that the lateral load response of SC-CLT walls is highly ductile and that SC-CLT walls have adequate Θ_r deformation capacity to be used as a primary lateral load resisting system in regions of high seismicity. It is shown that by attaching two CLT wall panels along vertical joints with ductile connectors to form a multi-panel SC-CLT wall, the V_b capacity of the SC-CLT walls can be increased without reducing the ductile Θ_r capacity. Considering the assumptions made for the CFE and FM analytical models and the potential variability of the CLT material properties, the experimental V_b vs. Θ_r response for each TS was observed to be in good agreement with the results from the analytical models. The use of UFPs in a multi-panel SC-CLT wall provided additional energy dissipation to the SC-CLT wall system.

Further research is needed to study and potentially improve the CLT material model used in the analytical studies presented herein. Advances over the elastic-perfectly plastic model for the CLT material in compression and the linear-elastic shear force-deformation response of the CLT panel are needed. Analytical studies of the seismic response of SC-CLT wall building systems are needed. Finally, experimental studies of the seismic performance of complete SC-CLT wall building systems, including floor systems are needed.

6.7. Acknowledgements

This paper is based upon work supported by grants from National Science Foundation, Awards No. CMMI-1344617, CMMI-1344621, CMMI-1344590, CMMI-1344646, and

CMMI-1344798 within the George E. Brown, Jr. Network for Earthquake Engineering Simulation Research (NEESR) program. The first author was also supported by a Lehigh University Fellowship. The experiments were performed at Washington State University (WSU). Dr. Shiling Pei was the PI of this collaborative project. Dr. James D. Dolan, Dr. John W. van de Lindt, Dr. Jeffrey W. Berman, Dr. James M. Ricles, and Dr. Richard Sause were co-PIs of the project. The opinions expressed in this paper are those of the authors and do not necessarily reflect the views of the sponsors.

6.8. References

APA-The Engineered Wood Association (2011). Engineered Wood Construction Guide Excerpt: Structural Composite Lumber. Form E30.

Bogensperger, T., Moosbrugger, T., Silly, G. (2010). "Verification of CLT-plates under Loads in Plane," *Proc. of the 11th World Conf. on Timber Engrg*, Riva del Garda, Italy, June 20-24.

Ceccotti, A., Lauriola, M., Pinna, M., Sandhaas, C. (2006). "SOFIE Project Cyclic Tests on Cross-laminated Wooden Panels," *Proc. of the 9th World Conf. on Timber Engrg.*, Portland, Oregon, USA, June 20-24.

Dujic B., Klobcar S., Zarnic, R. (2008). "Shear Capacity of Cross-Laminated Wooden Walls," *Proc. of the 10th World Conf. on Timber Engrg.*, Myazaki, Japan, June 2-5.

Dunbar, A., Moroder, D., Pampanin, S., Buchanan, A. (2014). "Timber Core-Walls for Lateral Load Resistance of Multi-Storey Timber Buildings," *Proc. of the 13th World Conf. on Timber Engrg.*. Quebec, Canada, Aug. 10-14.

Flaig M., Blass H. J. (2013). "Shear Strength and Shear Stiffness of CLT-beams Loaded in Plane," *Proc. of the CIB-W18 Meeting 46*, Vancouver, Canada, Aug. 26-29.

Ganey, R. (2015). "Seismic Design and Testing of Rocking Cross Laminated Timber Walls," M.Sc. Thesis, Department of Civil and Environmental Engrg., Univ. of Washington, Seattle, USA.

Karacabeyli, E., Douglas, B. (Eds.). (2013). CLT Handbook: Cross-laminated Timber- US Edition. FPInnovations.

Kelly, J. M., Skinner, R. I., Heine, A. J. (1972). "Mechanism of Energy Absorption in Special Devices for Use in Earthquake Resistant Structures," *Bulletin New Zealand Society of Earthquake Engrg.*, (5)3, pp. 63-88.

Kurama, Y. C., Pessiki, S., Sause, R., Lu, L. W., El-Sheikh, M. (1996). "Analytical Modeling and Lateral Load Behavior of Unbonded Post-Tensioned Precast Concrete Walls," ATLSS Research Report No. EQ-96-02, ATLSS Engrg. Research Center, Lehigh Univ., Bethlehem, PA, USA.

Kurama, Y. C. (1997). "Seismic Analysis, Behavior, and Design of Unbonded Post-Tensioned Precast Concrete Walls," Ph.D Dissertation, Dept. of Civil and Environmental Engrg., Lehigh Univ., Bethlehem, PA, USA.

Newcombe, M. P., Pampanin, S., Buchanan, A., Palermo, A. (2008). "Section Analysis and Cyclic Behavior of Post-tensioned Jointed Ductile Connections for Multi-story Timber Buildings," *Journal of Earthquake Engrg.,* 12(1), pp.83-110.

Pampanin, S., Palermo, A., Buchanan, A. H., Fragiacomo, M., Deam, B. L. (2006). "Code Provisions for Seismic Design of Multi-Storey Post-tensioned Timber Buildings," *Proc. of the International Council for Research and Innovation in Building and Construction--Working Commission W18--Timber Structures*, Florence, Italy, Aug. 22-26.

Pei, S., Popovski, M., van de Lindt, J. W. (2012). "Seismic design of a multi-story cross laminated timber building based on component level testing," *Proc. of the 12th World Conf. on Timber Engrg.*, Auckland, New Zealand, July 15-19.

Perez, F. J., Pessiki, S., Sause, R. (1999). "Lateral Load Behavior and Design of Unbonded Post-tensioned Precast Concrete Walls with Ductile Vertical Joints Connectors," ATLSS Research Report No. EQ-99-01, ATLSS Engrg. Research Center, Lehigh Univ., Bethlehem, PA, USA.

Perez, F. J., Sause, R., Pessiki, S. (2007). "Analytical and Experimental Lateral Load Behavior of Unbonded Post-Tensioned Precast Concrete Walls," *Journal of Structural Engrg., American Society of Civil Engineers*, 133(11), pp. 1531-1540.

Popovski, M., Karacabeyli, E., Ceccotti, A. (2011). "Seismic performance of cross-laminated timber buildings," Chapter 4 in CLT handbook: Cross-laminated timber - Canadian Edition, Quebec, Canada.

Priestley, M. J. N., Sritharan, S., Conley, J., R., Pampanin, S., 1999. "Preliminary results and conclusions from the PRESSS five-story precast concrete test building," *PCI Journal*, 44(6), pp. 42-67.

Seo, C.-Y., Sause, R., (2005). "Ductility demands on self-centering systems under earthquake loading," *ACI Structural Journal*, 102 (2), pp. 275-285.

Table 6.1 Test Matrix

Test Specimen	A_{pt} (in^2)	f_{pi} (ksi)	F_{pi} (kips)	H_w (inch)	Base	Description
TS1	1.25	0.30f_{pu}	59	175	Steel	Low decompression force and low post-decompression stiffness
TS2	1.58	0.10f_{pu}	25.5	174	Steel	Low decompression force and high post-decompression stiffness
TS3	1.25	0.40f_{pu}	80	174	Steel	High decompression force and low post-decompression stiffness
TS4	1.25	0.38f_{pu}	75	174	CLT	Rocking on CLT floor panel
TS5	1.58	0.30f_{pu}	75	174	Steel	SCL core CLT
TS6	1.25	0.38f_{pu}	75x2	192	Steel	Multi-panel CLT wall

Table 6.2 Material test results for 5-layer and SCL core CLT specimens (Ganey et al., 2015)

	E_c (ksi)	f_{c0} (ksi)	ε_{c0} (inch/inch)
5-layer CLT	441	3.60	0.0082
SCL core CLT	842	6.20	0.0074

Table 6.3 Flexural properties and modulus of elasticity for each TS

Test Specimen	$(EI)_c$ (kip.in^2)	L_w (inch)	t_w (inch)	I_c (in^4)	E_c (ksi)	E_0 (ksi)	$G_0 = E_0/12$ (ksi)	$G_0 = E_0/20$ (ksi)
TS1	3.12E+07	48	6.3	58500	530	868	72.3	43.4
TS2	3.46E+07	48	6.6	61700	561	914	76.1	45.7
TS3	3.42E+07	48	6.6	61700	550	902	75.2	45.1
TS5	7.16E+07	48	6.7	61900	1160	-	-	-

Table 6.4 Shear properties and shear modulus for each TS

Information	Experimental			Empirical Formulas					
				Bogensperger et al. (2010)		Flaig and Blass (2013)		E_c /12	E_c /20
Test Specimen	$(GA)_c$ (ksi)	A_c (in^2)	G_c (ksi)	G_c^* (ksi)	G_c^{**} (ksi)	G_c^* (ksi)	G_c^{**} (ksi)	G_c (ksi)	G_c (ksi)
TS1	1.20E+04	312	38.5	48.3	29.0	33.8	25.8	44.4	26.0
TS2	1.17E+04	323	36.2	53.6	32.1	34.7	26.6	46.7	28.9
TS3	2.20E+04	323	68.1	52.8	31.7	34.5	26.4	46.1	28.5
TS5	4.30E+04	317	135.7	-	-	-	-	-	-

***** using $G_0 = E_0/12$; ****** using $G_0 = E_0/20$

Table 6.5 Estimated ε_{cu} for each TS

	c_{cclt} (inch)	H_{cr} (inch)	ε_{cu} (inch/inch)
TS2	8.6	13.0	0.044
TS3	9.4	13.0	0.048
TS5	8.3	13.0	0.043

Table 6.6 PT bar material test results

Diameter (inch)	Nominal A_{pt} (in^2)	E_{pt} (ksi)	f_{py} (ksi)	ε_{pt} (inch/inch)	f_{pu} (ksi)	ε_{pu} (inch/inch)
1	0.85	31200	132.5	0.0063	158.1	0.82
1¼	1.25	32000	132.5	0.0062	157.6	0.55
1⅜	1.58	31800	129.5	0.0060	159.0	0.58

Table 6.7 UFP dimensions and test results

t_{UFP}	b_{UFP}	D_{UFP}	$F_{ufp,y}$	$F_{ufp,p}$	$k_{0,ufp}$	0.85 $k_{0,ufp}$
(inch)	(inch)	(inch)	(kip)	(kip)	(kip/inch)	(kip/inch)
3/8	4	4-1/16	2.77	4.15	17.2	14.6

Table 6.8 Experimental and CFE results for $M_{b,dec}$, $V_{b,dec}$, and $\Theta_{r,dec}$

		Experimental			CFE			$\frac{(M_{b,dec})_{Exp}}{(M_{b,dec})_{CFE}}$
	Loading direction	$M_{b,dec}$ (kip-inch)	$V_{b,dec}$ (kips)	$\Theta_{r,dec}$ (%)	$M_{b,dec}$ (kip-inch)	$V_{b,dec}$ (kips)	$\Theta_{r,dec}$ (%)	
TS1	N	912	5.63	0.27	480	2.3	0.13	2.01
	S	1015	6.27	0.40				
TS2	N	582	3.59	0.24	212	1.3	0.05	2.62
	S	531	3.28	0.22				
TS3	N	1528	9.43	0.37	608	3.8	0.14	2.33
	S	1299	8.02	0.43				
TS5	N	1192	7.36	0.29	645	3.9	0.09	1.80
	S	1129	6.97	0.33				

Table 6.9 Experimental and Analytical Limit State Results for TS2

	ELL		YCLT		SCLT		CCLT		LLP	
Result Type	$V_{b,ell}$ (kips)	$\Theta_{r,ell}$ (%)	$V_{b,yclt}$ (kips)	$\Theta_{r,yclt}$ (%)	$V_{b,sclt}$ (kips)	$\Theta_{r,sclt}$ (%)	$V_{b,cclt}$ (kips)	$\Theta_{r,cclt}$ (%)	$V_{b,llp}$ (kips)	$\Theta_{r,llp}$ (%)
Exp.	3.8	0.3	-	-	19.2	4.9	25.1	7.4	23.8	8.6
FM	3.05	0.26	10.4	1.90	17.50	4.69	20.62	7.67	20.76	9.51
CFE	3.05	0.22	10.8	1.92	19.36	4.07	24.74	7.85	24.13	9.12

Table 6.10 Experimental and Analytical Limit State Results for TS3

	ELL		YCLT		SCLT		CCLT		LLP	
Result Type	$V_{b,ell}$ (kips)	$\Theta_{r,ell}$ (%)	$V_{b,yclt}$ (kips)	$\Theta_{r,yclt}$ (%)	$V_{b,sclt}$ (kips)	$\Theta_{r,sclt}$ (%)	$V_{b,cclt}$ (kips)	$\Theta_{r,cclt}$ (%)	$V_{b,llp}$ (kips)	$\Theta_{r,llp}$ (%)
Exp.	10.5	0.5	-	-	21.83	3.8	22.6	7.4	22.6	4.7
FM	9.61	0.59	15.68	2.03	20.86	3.65	19.3	7.41	20.75	4.24
CFE	9.26	0.55	14.84	1.96	20.36	3.80	20.87	7.47	20.40	5.36

Table 6.11 Experimental and Analytical Limit State Results for TS5

	ELL		YCLT		SCLT		CCLT		LLP	
Result Type	$V_{b,ell}$ (kips)	$\Theta_{r,ell}$ (%)	$V_{b,yclt}$ (kips)	$\Theta_{r,yclt}$ (%)	$V_{b,sclt}$ (kips)	$\Theta_{r,sclt}$ (%)	$V_{b,cclt}$ (kips)	$\Theta_{r,cclt}$ (%)	$V_{b,llp}$ (kips)	$\Theta_{r,llp}$ (%)
Exp.	10.3	0.5	-	-	22.50	3.5	25.2	7.3	27.4	6.5
FM	9.60	0.40	18.38	1.95	22.50	3.57	24.91	8.90	24.70	5.21
CFE	10.64	0.52	17.51	1.86	21.70	3.62	27.56	9.13	27.30	5.02

Table 6.12 Experimental and Analytical Limit State Results for TS6

	ELL		YCLT		SCLT		CCLT		LLP	
Result Type	$V_{b,ell}$ (kips)	$\Theta_{r,ell}$ (%)	$V_{b,yclt}$ (kips)	$\Theta_{r,yclt}$ (%)	$V_{b,sclt}$ (kips)	$\Theta_{r,sclt}$ (%)	$V_{b,cclt}$ (kips)	$\Theta_{r,cclt}$ (%)	$V_{b,llp}$ (kips)	$\Theta_{r,llp}$ (%)
Exp.	20.9	0.4	-	-	46.5	3.6	45.3	7.3	47.6	4.2
FM	20.41	0.51	30.14	1.68	43.21	4.62	36.54	7.58	42.83	3.88
CFE	18.90	0.60	30.88	1.78	46.68	4.43	37.23	7.62	43.65	3.94

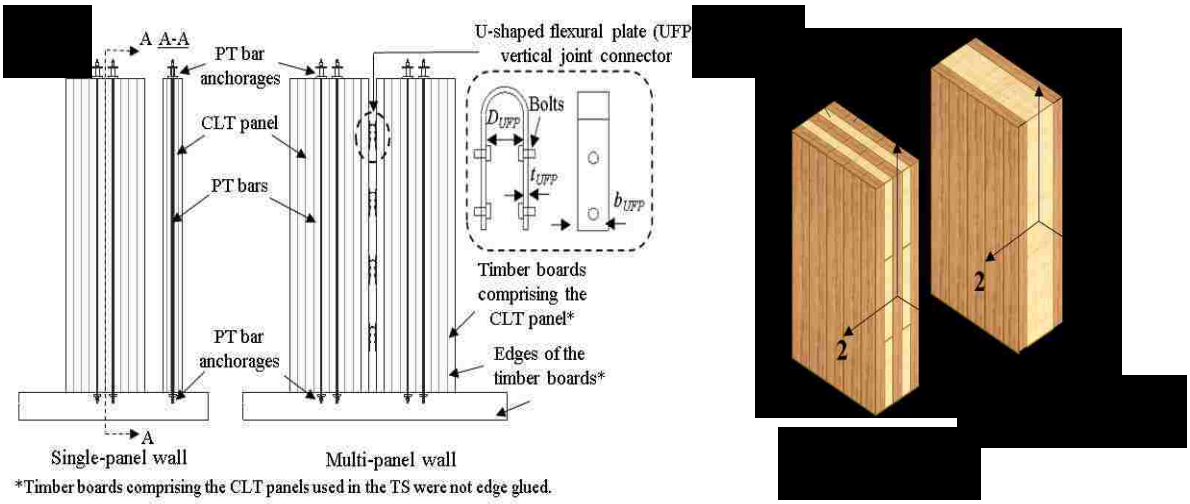

Figure 6.1 (a) Typical single-panel and multi-panel SC-CLT walls; (b) CLT material within CLT panels

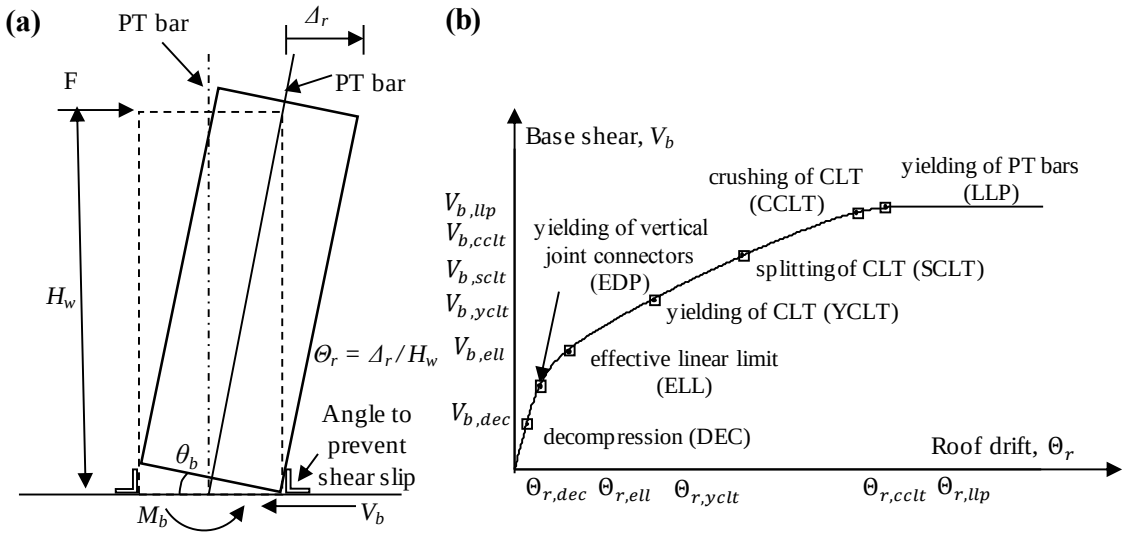

Figure 6.2 (a) Rocking behavior of SC-CLT wall under lateral load; (b) base shear-roof drift response of SC-CLT walls under lateral load with limit states

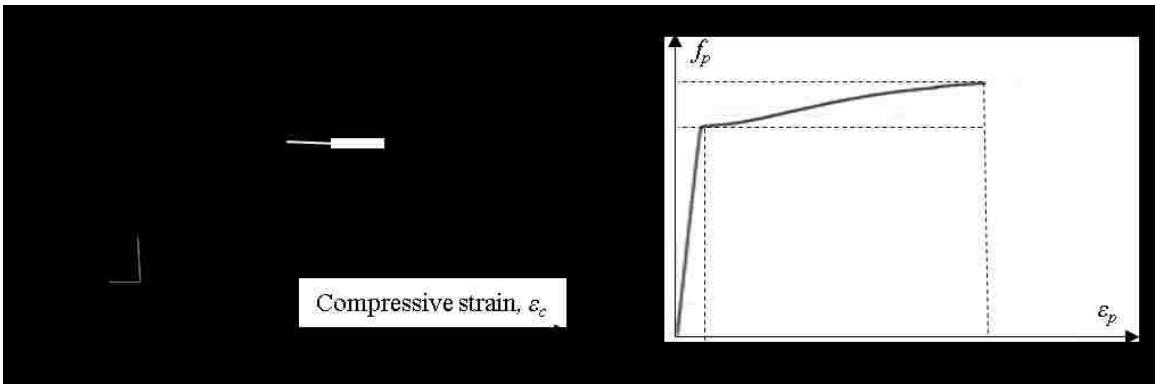

Figure 6.3 (a) Stress-strain relationship for CLT material idealized as elastic perfectly plastic; (b) idealized stress-strain relationship for PT bar

Figure 6.4 (a) Elevation view of prototype SC-CLT wall; (b) prototype floor plan

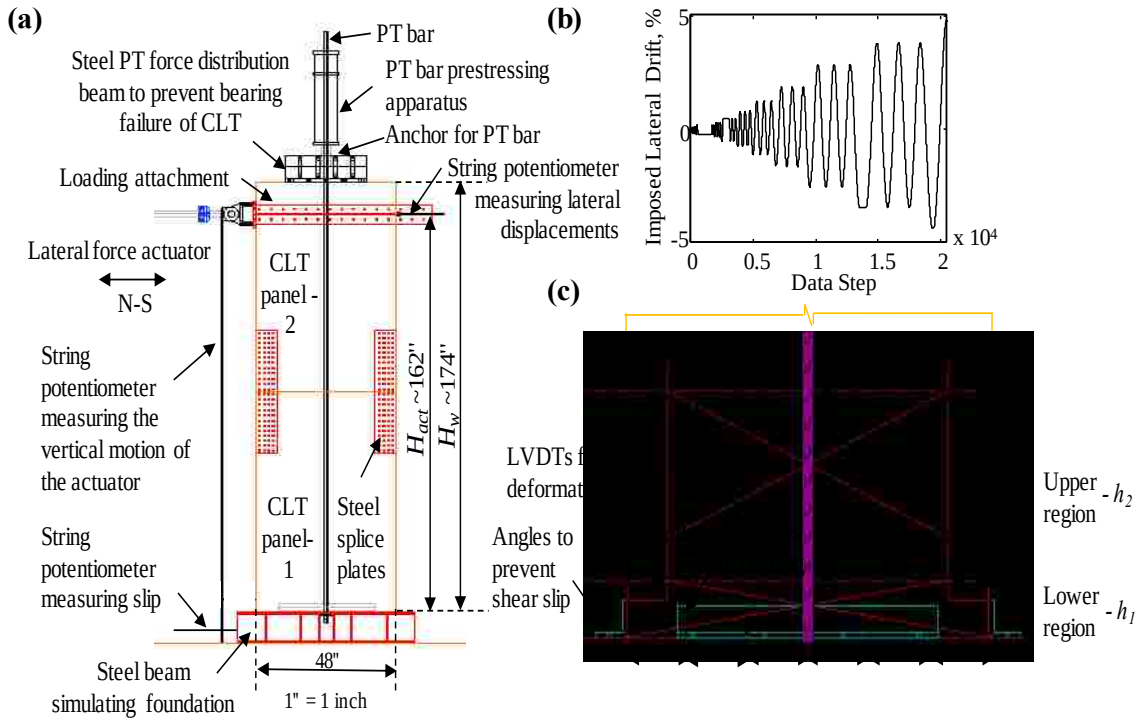

Figure 6.5 (a) Elevation view of test set-up; (b) lateral drift history imposed on TS2; (c) layout of instrumentation to measure shear and flexural deformation

Figure 6.6 (a) Moment and curvature profiles for TS under imposed lateral force F; (b) estimated flexural stiffness from test data for TS2

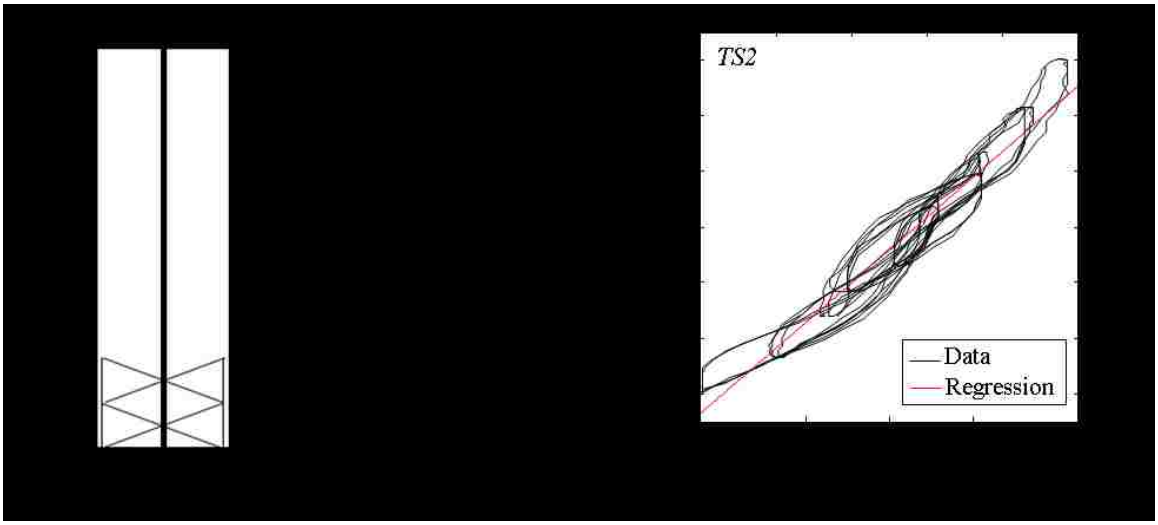

Figure 6.7 (a) Shear and shear deformation profiles for TS under imposed F; (b) estimated shear stiffness from test data for TS2

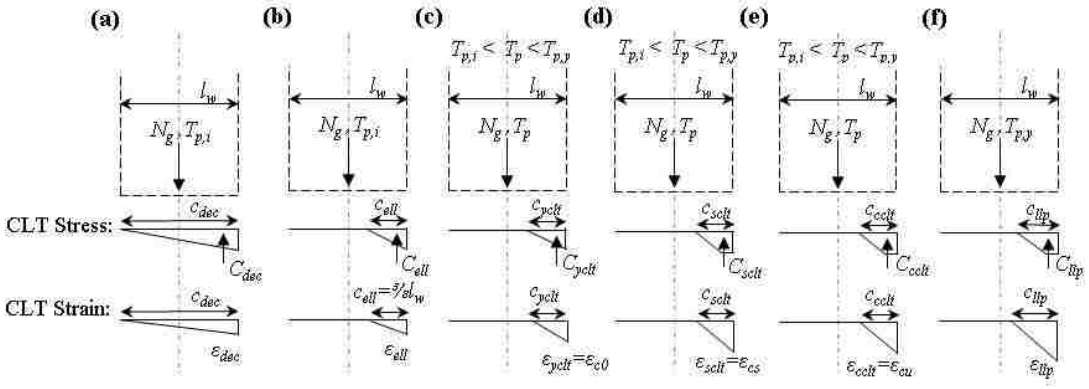

Figure 6.8 Stresses and strains at the base of a single-panel SC-CLT wall at: (a) DEC; (b) ELL; (c) YCLT; (d) SCLT; (e) CCLT; (f) LLP limit states

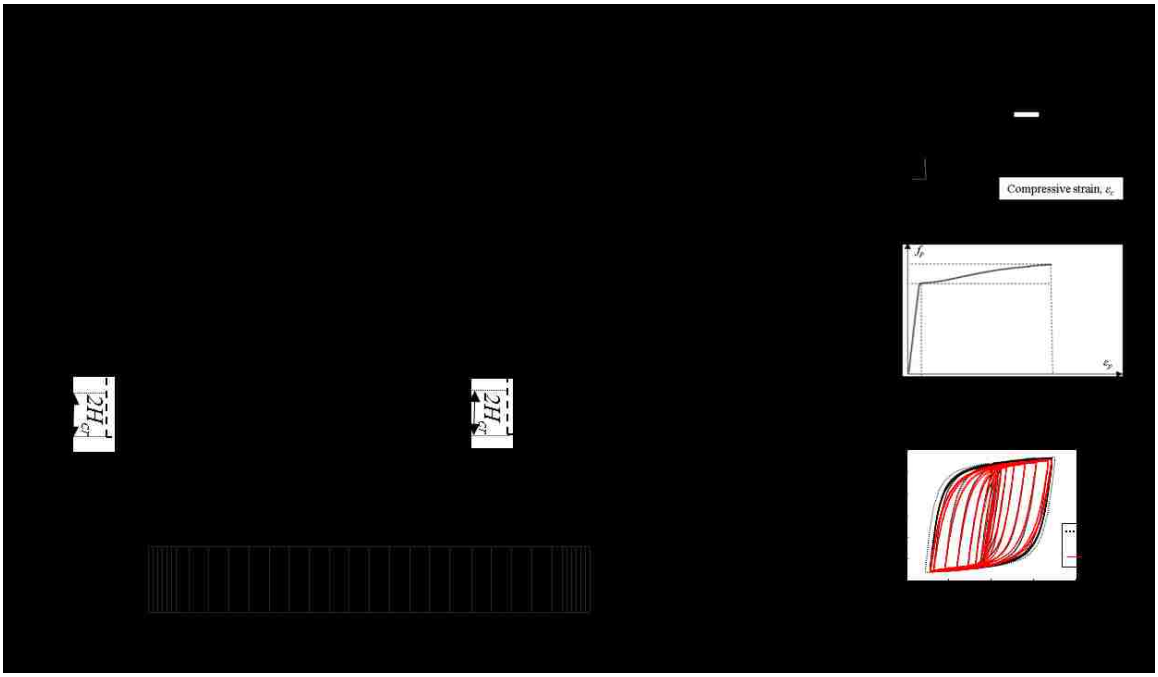

Figure 6.9 Fiber-element models of single-panel and multi-panel SC-CLT walls

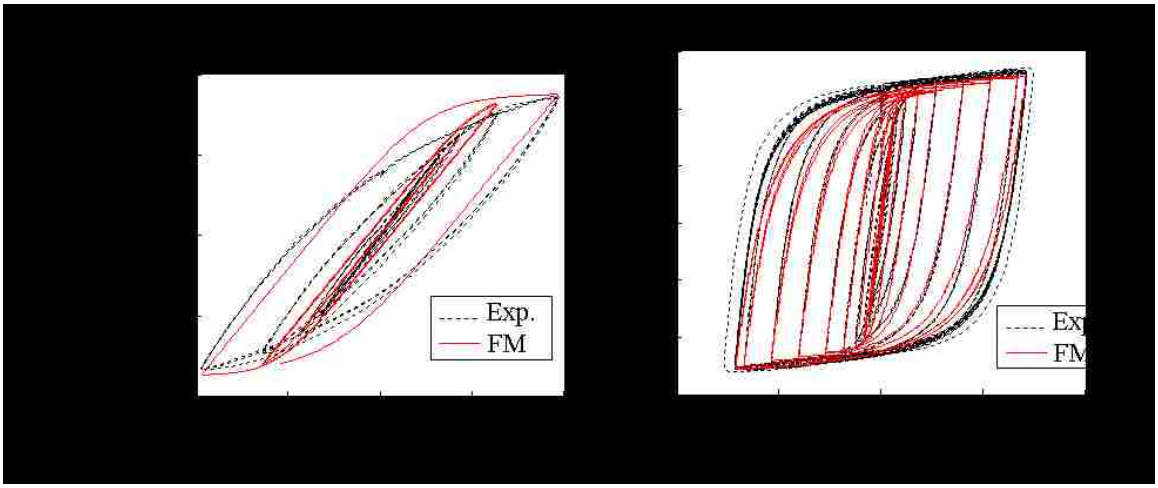

Figure 6.10 Comparison of experimental and analytical results for the UFP response up to: (a) Δ_{ufp} = 0.5 inch; (b) Δ_{ufp} = 3 inches

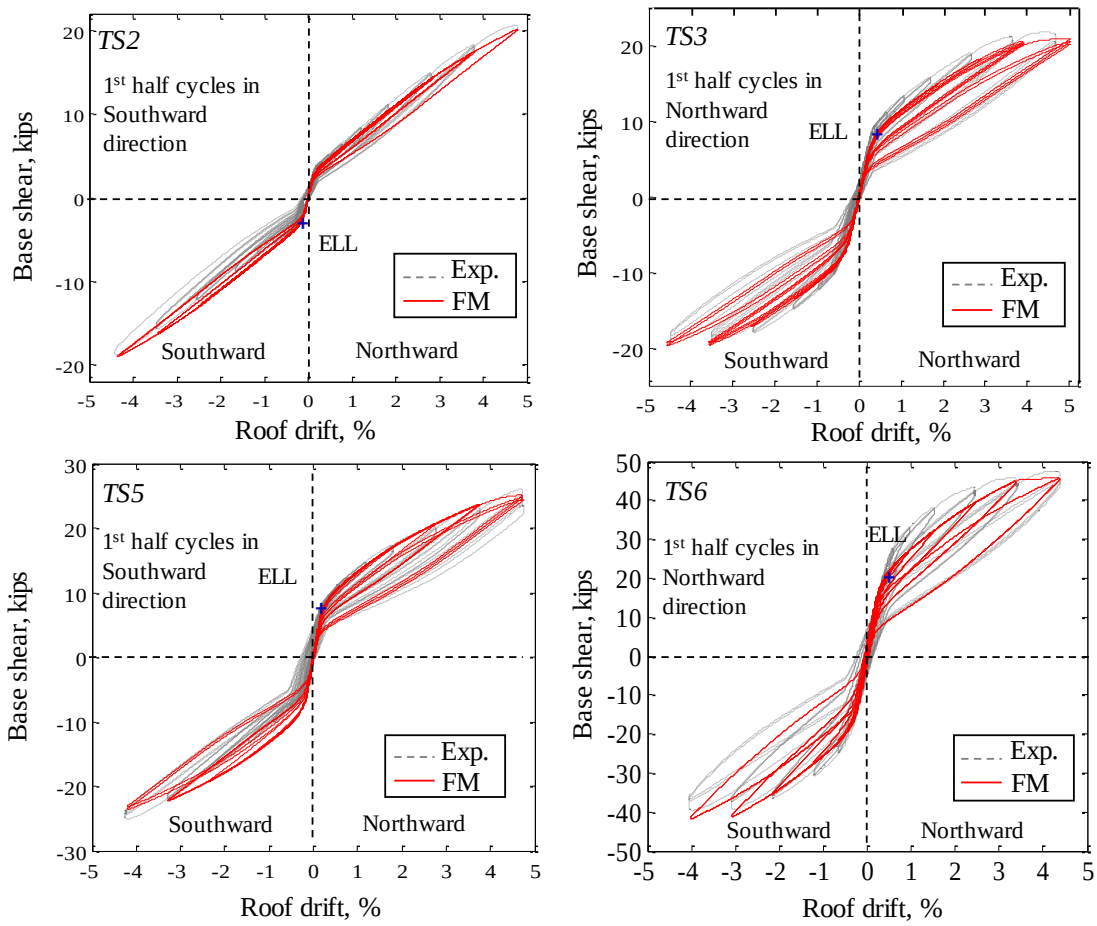

Figure 6.11 Comparison of experimental and analytical results under cyclic loading for TS2, TS3, TS5, and TS6 up to Θ_r = 5%

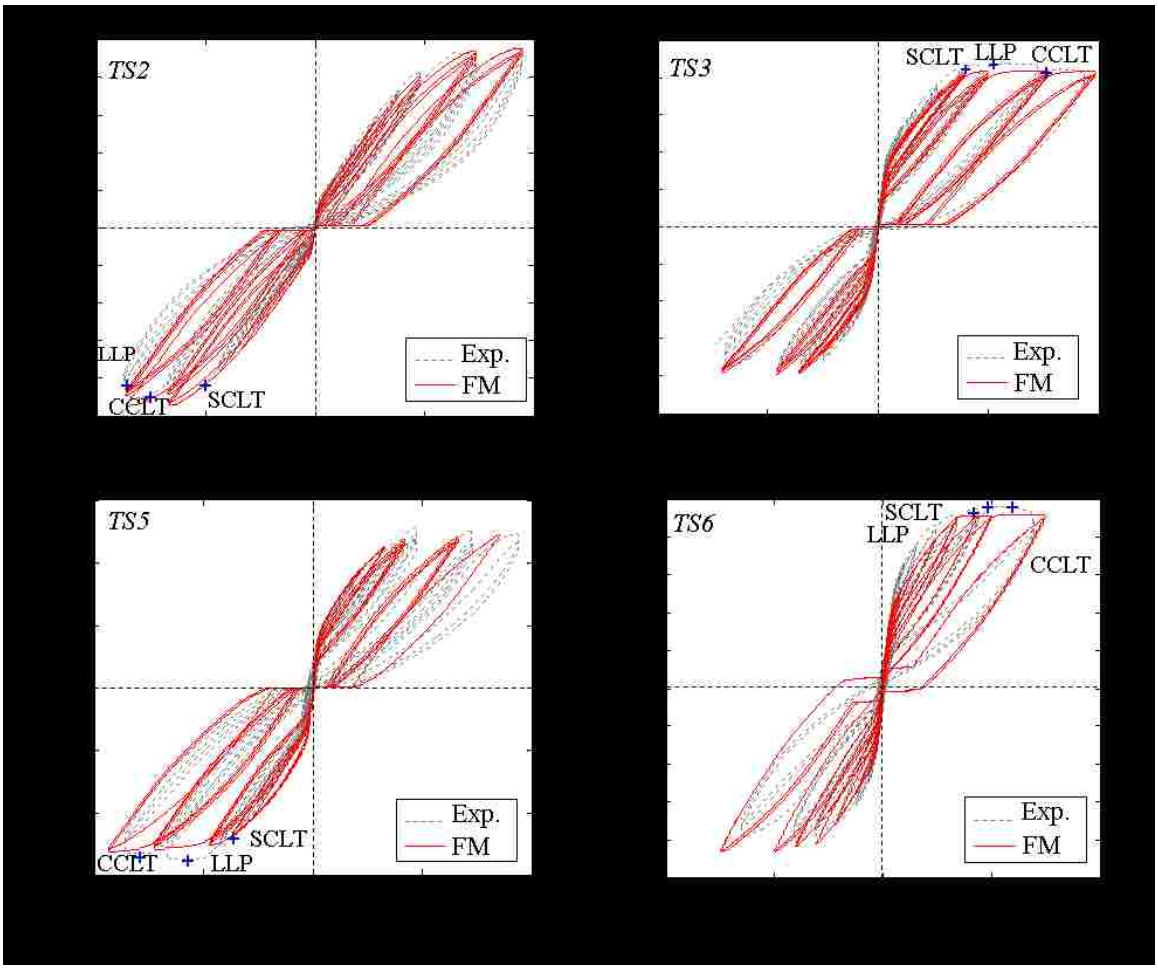

Figure 6.12 Comparison of experimental and analytical results under cyclic loading for TS2, TS3, TS5, and TS6 up to Θ_r = 9.5%

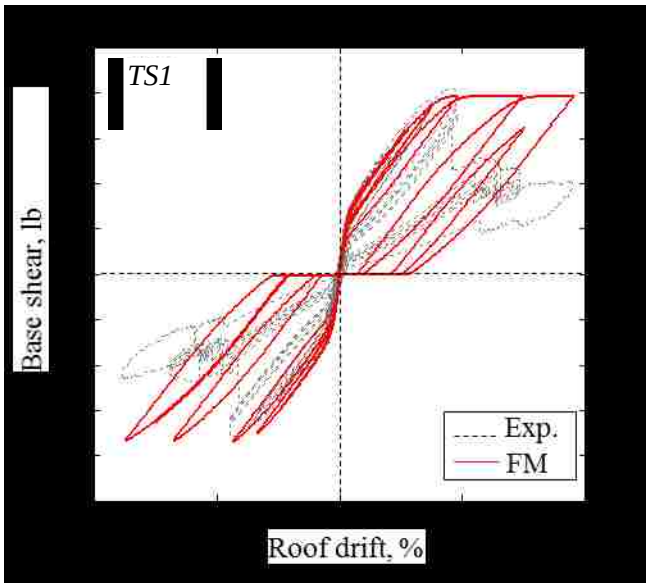

Figure 6.13 Comparison of experimental and analytical results under cyclic loading for TS1

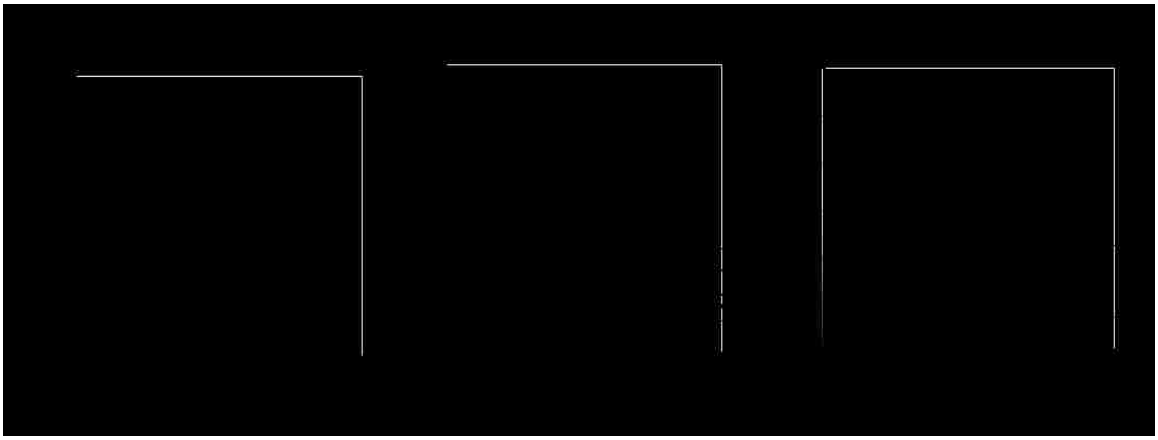

Figure 6.14 Effect of initial design parameters on the envelope V_b vs. Θ_r response of: (a) TS1 and TS5; (b) TS1 and TS3; (c) TS3 and TS5

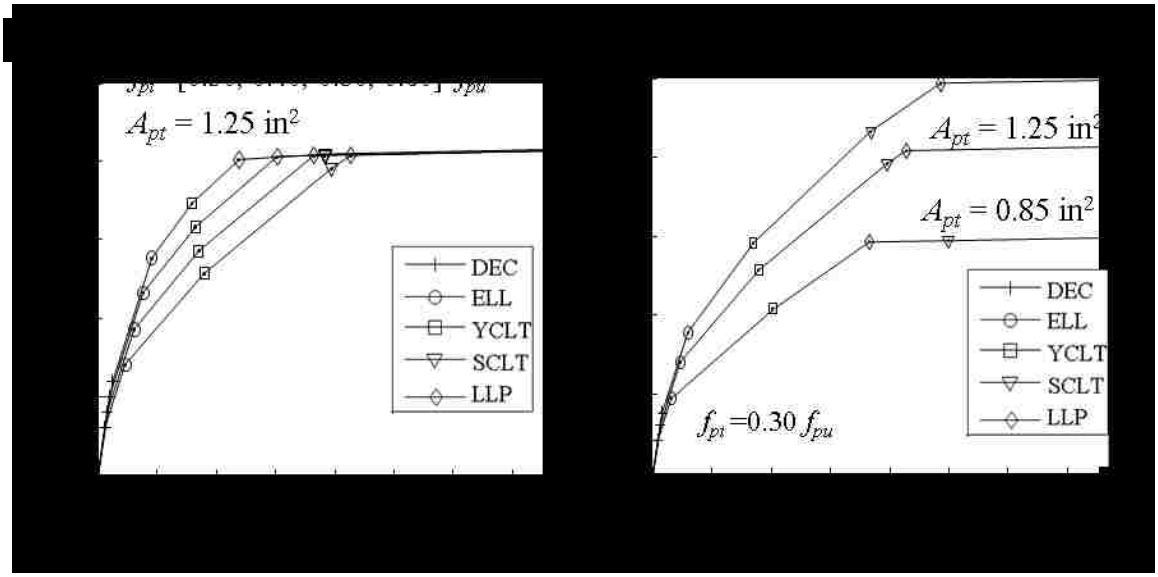

Figure 6.15 (a) Effect of initial prestress in post-tensioning steel, i.e, f_{pi} , with constant A_{pt} on wall V_b vs. Θ_r response; (b) effect of A_{pt} with constant f_{pi} on wall V_b vs. Θ_r response

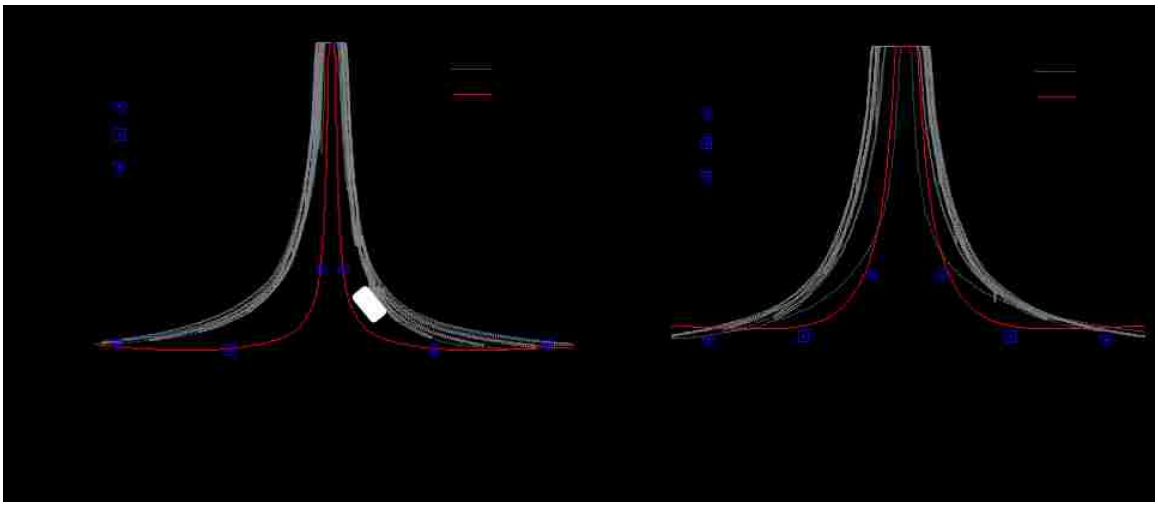

Figure 6.16 Comparison of contact length (measured from compression edge of wall)

Figure 6.17 Discussion of contact length and contact stress

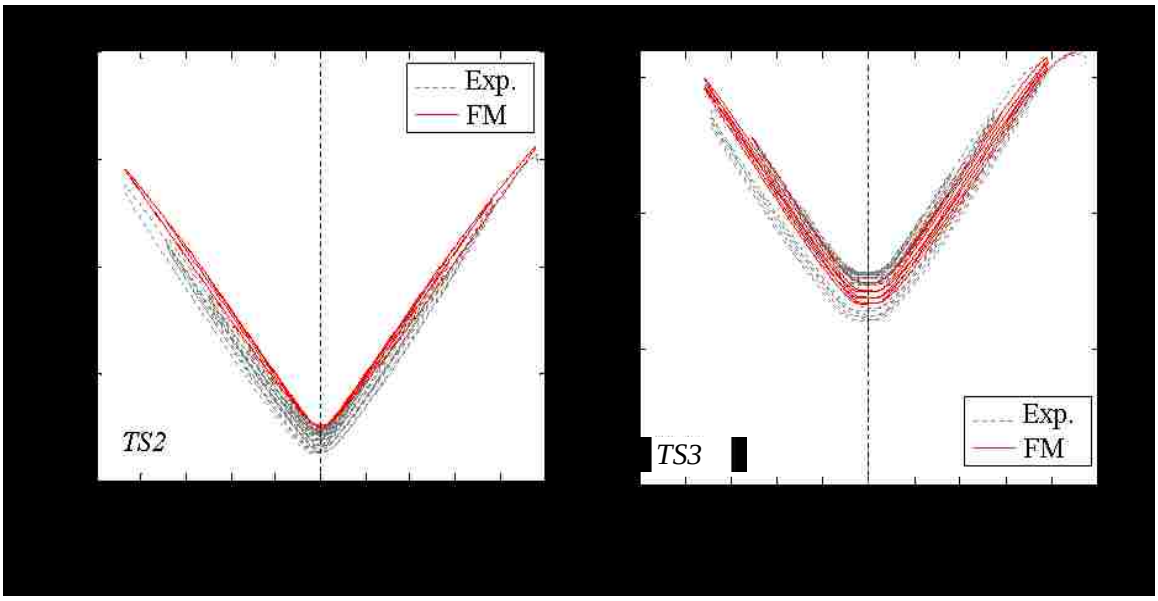

Figure 6.18 Comparison of experimental and analytical results for PT bar force for TS2 and TS3 up to Θ_r = 5%

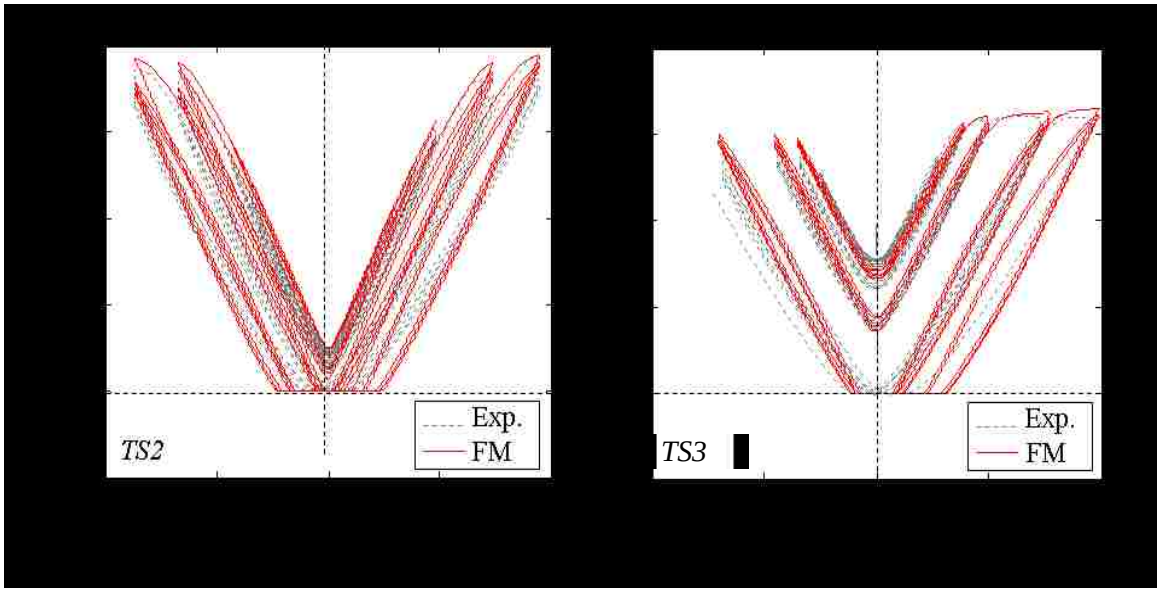

Figure 6.19 Comparison of experimental and analytical results for PT bar force for TS2 and TS3 up to Θ_r = 9.5%

CHAPTER 7

SEISMIC DESIGN AND RESPONSE OF SELF-CENTERING CROSS-LAMINATED TIMBER WALLS

Overview

A cross laminated timber (CLT) panel is a heavy timber structural component fabricated by laminating layers of timber boards in an orthogonal pattern. This chapter presents research on the seismic response of self-centering (SC) CLT structural walls (i.e., SC-CLT walls), which are constructed by post-tensioning CLT wall panels to the foundation with vertical post-tensioning steel bars. The post-tensioning bars pass through the CLT panels and are anchored to the CLT panels at the top of the wall and to the foundation at the bottom of the wall. This research focuses on multi-panel SC-CLT walls with ductile connectors in vertical joint between the panels. A seismic design approach is proposed for these SC-CLT walls, with the objectives of minimal damage under the design basis earthquake (DBE) and life safety performance under the maximum considered earthquake (MCE). The design approach is evaluated using nonlinear time history analysis (NLTHA) results for 6- and 11-story prototype SC-CLT wall buildings for ground motions at the DBE and MCE intensity levels. The NLTHA results show that SC-CLT walls designed using the proposed approach satisfy the design objectives.

7.1. Introduction

A cross laminated timber (CLT) panel is a heavy timber structural component fabricated by laminating layers of timber boards in an orthogonal pattern. This chapter presents research on the seismic response of self-centering (SC) CLT structural walls (i.e., SC-CLT walls), which are constructed by post-tensioning CLT wall panels vertically to the foundation. The vertical post-tensioning steel bars pass through the CLT panels anchored to the CLT panels at the top of the wall and to the foundation at the bottom of the wall. This research focuses on multi-panel SC-CLT walls with adjacent panels attached to each other along vertical joints with ductile connectors (referred as "vertical joint connectors" in Perez et al. (2004)) as shown in Figure 7.1. In a multi-panel SC-CLT wall, the vertical joint connectors transfer shear force between the two adjacent CLT wall panels and provide energy dissipation under seismic loading.

Recent experimental and analytical studies on the lateral load response of SC-CLT walls under cyclic loading (Ganey, 2015 and Chapter 6) show that SC-CLT walls have large lateral deformation capacity, which suggest that SC-CLT walls can be used as the primary lateral-load resisting system for buildings located in regions of high seismicity.

This paper investigates the seismic response and performance of multi-panel SC-CLT walls with ductile vertical joint ductile connectors. First, the configuration and the lateral load response of these SC-CLT walls are discussed. Seismic design criteria are proposed and used to design 6- and 11-story prototype SC-CLT walls. A parametric study is conducted

to investigate the effect of the SC-CLT wall structural properties on their lateral load design capacities. Nonlinear time history analysis (NLTHA) is used to determine the seismic response of the prototype SC-CLT wall buildings. The NLTHA results for the prototype walls are discussed and evaluated with respect to the seismic design criteria.

7.2. Response of SC-CLT Wall under Lateral Load

Figure 7.1 shows an SC-CLT wall comprised of two CLT panels attached by ductile vertical joint connectors. U-shaped flexural plates (UFPs, described by Kelly et al., 1972) are used as the vertical joint connectors. Figure 7.1 shows a schematic of a typical UFP. Each CLT wall panel is post-tensioned vertically, using PT bars anchored to the CLT panels at the top of the wall and to the foundation. Unlike a conventional CLT wall, which has CLT wall panels attached to the foundation with mechanical connectors, the base CLT panel of an SC-CLT wall is precompressed against, but not otherwise attached directly to, the foundation (although shear keys to prevent sliding are necessary). As a result, when the overturning moment due to lateral load is large enough to overcome the precompression, a gap opens between the base panel and the foundation, and the SC-CLT wall rocks on the foundation (see Figure 7.2(a)). The vertical PT bars provide a restoring moment to return the wall to its initial vertical position.

Under lateral loading, the SC-CLT wall initially deforms elastically. After the base overturning moment (M_b) resistance provided by the PT bars and the gravity loads is overcome by the applied overturning moment, the SC-CLT wall begins to rock on the

foundation. Rocking initiates when the edges of the CLT panels subjected to tension from the applied base overturning moment (i.e., the left edges of the CLT panels in Figure 7.2(a)) decompress and a gap opens at the wall-foundation interface. When the applied lateral load decreases, the SC-CLT wall returns back to its initial plumb position due to the restoring moment provided by the PT bars. The corresponding roof drift ratio, Θ_r, is determined by dividing the roof level lateral deformation, Δ_r, (see Figure 7.2(a)) by the height of the wall, H_w. The base rotation, θ_b, due to rocking (gap opening between the base panel and the foundation) is also shown in Figure 7.2(a). Throughout the paper, Θ_r and θ_b are given in % radians.

7.3. Structural Limit States of Lateral Load Response

Figure 7.2(b) shows the structural limit states for an SC-CLT wall on an idealized base overturning moment resistance (M_b) versus (vs.) roof drift ratio (Θ_r) response for the wall under monotonic lateral loading. The structural limit states for an SC-CLT wall are: (1) decompression of the base of the wall (DEC); (2) yielding of energy dissipating ductile vertical joint connectors (EDP); (3) effective linear limit of the linear-elastic response of the wall (ELL, at $M_{b,ell}$ and $\Theta_{r,ell}$ in Figure 7.2(b)); (4) yielding of the composite CLT section material (YCLT) at the compression edge of the wall; (5) splitting of the composite CLT section material at the compression edge of the wall (SCLT); (6) crushing of the composite CLT section material at the compression edge of the wall (CCLT, at $M_{b,cclt}$ and $\Theta_{r,cclt}$ in Figure 7.2(b)); (7) yielding of the PT bars (LLP, at $M_{b,llp}$ and $\Theta_{r,llp}$ in Figure 7.2(b)). More detailed descriptions of these limit states are in Chapter 6 and Appendix B.

The closed-form expressions (CFE) derived for unbonded post-tensioned precast concrete walls (Kurama et al. 1997; Perez et al. 1999) were adapted to SC-CLT walls, to estimate the M_b and Θ_r capacities of an SC-CLT wall as discussed in Chapter 6. Derivations of the CFE for an SC-CLT wall are in Appendix B. Figure 7.3 shows the forces on an SC-CLT wall at the DEC, ELL, and LLP limit states. As shown in Figure 7.3, the PT bars are assumed to be in 2 groups, one group with an eccentricity of e_{pt} to the left and one group with an eccentricity of e_{pt} to right of the centerline of the wall. The post-tensioning forces for each group of PT bars is assumed to be at the initial prestress levels, $T_{p1,i}$ and $T_{p2,i}$, for the DEC and ELL limit state, and at the yield strengths, $T_{p1,y}$ and $T_{p2,y}$, for the LLP limit state. The gravity load resultant on each panel, $\sum_{i=1}^{N} N_{g,i}^{panel}$, which is the sum of the gravity load acting on each wall panel at floor level i from vertical load combination (VLC1), described later, is assumed to act at the center of the wall. The resultant compression force of each CLT panel, C_{dec}, C_{ell} or C_{llp}, is distributed at the base of the wall over a contact length of c_{dec}, c_{ell} or c_{llp}, respectively. The total shear force transferred by the number (N_{con}) of vertical joint connectors, assumed to be UFPs, ($N_{con}F_{ufp}$), is shown in Figure 7.3.

For design purposes, $M_{b,ell}$ can be expressed as multiple of $M_{b,dec}$, assuming that $c_{ell} = 3l_w/8$ based on results from tests on SC-CLT walls and neglecting the M_b resistance provided by the UFPs (see Chapter 6 and Ganey, 2015), as follows:

$$M_{b,ell}=2.25M_{b,dec} \tag{7.1}$$

where $M_{b,dec}=2\left(\left(2T_{p1,i}+\left(\sum_{i=1}^{N}N_{g,i}^{panel}\right)_1\right)(l_w/3)\right)$ for $T_{p1,i}=T_{p2,i}$ and $N_{g,1}^{panel}=N_{g,2}^{panel}$. Appendix B provides derivations of these expressions.

7.4. Other considerations for seismic design

For seismic design of an SC-CLT wall, the energy dissipation provided by the ductile vertical joint connectors, is estimated using the hysteretic energy dissipation ratio, β_e, defined by Seo and Sause (2005). β_e, is the ratio of the hysteresis loop area of an SC system over the hysteresis loop area of a bilinear elastoplastic system with similar strength. β_e for an SC-CLT wall is estimated as the ratio of the M_b resistance contributed by the UFPs, $M_{b,ufp}$, over the M_b capacity at ELL, $M_{b,ell}$:

$$\beta_e=\frac{M_{b,ufp}}{M_{b,ell}} \tag{7.2}$$

where $M_{b,ufp}=N_{con}F_{ufp,p}L_w$; N_{con} = number of UFP connectors; $F_{ufp,p}$ = nominal plastic strength of the UFP $=f_{y,ufp}b_{ufp}t_{ufp}^2/2D_{ufp}$ (based on Kelly et al. (1972); see Appendix B); t_{ufp} = thickness of the UFP; b_{ufp} = width of the UFP; D_{ufp} = diameter of the UFP (as shown in Figure 7.1); $f_{y,ufp}$ = expected yield stress of the UFP steel (including material overstrength); and L_w = length of the wall. Note that to have SC behavior, β_e should be less than 0.50. Also, note that in the design calculations presented in this paper, the material overstrength is included in $f_{y,ufp}$ to produce accurate estimates of response since the UFPs were observed to experience considerable strain hardening in previous studies (e.g., Ganey, 2015 and Chapter 6).

The post-decompression stiffness ratio, α_{kT} of an SC-CLT wall considering second order effects, is also needed for seismic design. α_{kT} can be estimated using Eq. (7.3) developed by Chancellor (2014):

$$\alpha_{kT} = \frac{k_{pdT}}{k_{elastic}} \tag{7.3}$$

where k_{pdT} = total post-decompression stiffness of the SC-CLT wall; $k_{elastic}$ = fixed-base elastic stiffness (M_b vs. Θ_r) of the SC-CLT wall $= M_{b,dec}/\Theta_{r,dec}$.

k_{pdT} is estimated from $k_{elastic}$ and the stiffness of the PT bars, but also including the global second order effects, as follows (Chancellor, 2014):

$$k_{pdT} = \frac{k_{pd2}\, k_{elastic}}{k_{pd2} + k_{elastic}} \tag{7.4}$$

where k_{pd2} = post-decompression stiffness of the SC-CLT wall including 2nd order effects $= \left((A_{pt}^{total} E_{pt}) \left(\frac{L_w}{3}\right)^2 / L_{pt} - OM_{pd} \right)$; A_{pt} = total area of the PT bars; E_{PT} = modulus of elasticity of the PT bars; L_{PT} = length of the PT bars; OM_{pd} = second-order overturning moment due to P-delta effects resulting from the applied gravity load = $\sum_{i=1}^{N} (N_{g,i}^{total} h_{s,i})$; $N_{g,i}^{total}$= total gravity load within the seismic tributary area for the SC-CLT wall at floor i = $N_{g,i}^{LOC} + N_{g,i}^{wall}$; $N_{g,i}^{LOC}$= gravity load in the seismic tributary area the SC-CLT wall at floor i except for the gravity load acting on the SC-CLT wall; $N_{g,i}^{wall}$ = gravity load acting on the SC-CLT wall at floor i = $2N_{g,i}^{panel}$; $N_{g,i}^{panel}$= gravity load acting on each panel of the two-

panel SC-CLT wall at floor i; $h_{s,i}$ = height of the wall up to floor i. Note that in calculating k_{pd2}, the elongation of the PT bars is calculated from the base rotation θ_b assuming the center of rotation is $L_w/6$ from the compression edge of each base CLT panel.

7.5. Proposed Seismic Design Criteria

The seismic design criteria used in this study for SC-CLT walls are similar to criteria given by Kurama et al. (1996, 1997, 1999a, 1999b) and Perez et al. (2004, 2007) for unbonded post-tensioned precast concrete walls. Seismic performance levels, structural limit states and corresponding capacities of an SC-CLT wall (Figure 7.2(b)), as well as the seismic intensity (hazard) levels, and corresponding seismic force and deformation response demands are defined. Each seismic performance level has corresponding structural limit states and an associated level of structural damage to the SC-CLT wall. Each design objective associates a seismic performance level with a seismic intensity (hazard) level.

7.5.1. Seismic Design Performance Objectives

The seismic design performance objectives for SC-CLT walls consider two seismic intensity levels: (1) the design basis earthquake (DBE) level, with approximately 10% probability of exceedance in 50 years; and (2) the maximum considered earthquake (MCE) level, with 2% probability of exceedance in 50 years. The design objectives for an SC-CLT wall are: (1) to enable immediate occupancy (IO) under the DBE by minimizing damage to the SC-CLT wall; and (2) to provide life safety (LS) under the MCE.

7.5.2. Seismic Design Demands under DBE and MCE

Figure 7.4 shows the expected M_b vs. Θ_r behavior of an SC-CLT wall together with the seismic performance levels and structural limit states. For the DBE, the M_b, Θ_r, and story drift, Θ_s, demands are $M_{b,d}$, $\Theta_{r,De}$, and $\Theta_{s,De}$, respectively. For the MCE level GM, the Θ_r demand is $\Theta_{r,Me}$. The linear-elastic base overturning moment demands for a fixed-based SC-CLT wall under the DBE and MCE are denoted as $M_{b,ed}$ and $M_{b,em}$ in Figure 7.4, respectively.

The linear-elastic (R=1) M_b demand, $M_{b,ed}$, of a fixed-base linear-elastic SC-CLT wall model under the DBE level ground motion is the basis for the strength of an SC-CLT wall. $M_{b,ed}$ is determined from the equivalent lateral force procedure in ASCE (2010) for walls shorter than 65 ft. and modal response spectrum analysis (MRSA) in ASCE (2010) for walls taller than 65 ft.. $M_{b,ed}$ is divided by the response modification factor, R, which is taken to be 6 in this study, to obtain $M_{b,d}$. $M_{b,d}$ does not include the base moment demand from 2nd order effects (i.e., P-Δ effects) from the gravity loads braced by the SC-CLT wall, but P-Δ effects are included in numerical models used to estimate the drift demands $\Theta_{r,De}$, $\Theta_{s,De}$, and $\Theta_{r,Me}$. The linear-elastic roof drift ratio corresponding to $M_{b,d}$ and $M_{b,ed}$ are $\Theta_{r,d}$ and $\Theta_{r,e}$, respectively, where $\Theta_{r,e}$ is $R\Theta_{r,d}$. Similarly, the linear-elastic story drift ratio corresponding to $M_{b,d}$ and $M_{b,ed}$ are $\Theta_{s,d}$ and $\Theta_{s,e}$, respectively, where $\Theta_{s,e}$ is $R\Theta_{s,d}$.

To estimate $\Theta_{r,d}$ and $\Theta_{s,d}$, a fixed-base linear-elastic numerical model (LEM) of the SC-CLT wall is created, which includes P-Δ effects from gravity loads within the seismic

tributary area of the SC-CLT wall and the stiffness of the UFPs. $\Theta_{r,d}$ and $\Theta_{s,d}$ are estimated from linear static analysis of the LEM under lateral forces from the ELF (for walls shorter than 65 ft.) or MRSA procedure (for walls taller than 65 ft.) in ASCE (2010) with $R = 6$. Figure 7.4 shows that $\Theta_{r,De}$, $\Theta_{s,De}$, and $\Theta_{r,Me}$ are estimated using an "equal displacement" assumption (i.e., $\Theta_{r,e} = R\,\Theta_{r,d}$ and $\Theta_{s,e} = R\,\Theta_{s,d}$), where the peak deformation for a nonlinear (NL) structure is assumed to be equal to that of a linear-elastic structure with the same initial period. $\Theta_{r,De}$ is estimated as $1.15\Theta_{r,e}$ and $\Theta_{s,De}$ is estimated as $1.15\Theta_{s,e}$. The 1.15 factor is included because $\Theta_{r,e} = R\Theta_{r,d}$ was found to underestimate the DBE-level drift results from NLTHA. As shown in Figure 7.4, the drift demand under the MCE is assumed to be 1.5 times the drift demand under the DBE, based on ASCE (2010), so $\Theta_{r,Me}$ is estimated as $1.5\Theta_{r,De}$.

The peak M_b under the DBE, $M_{b,DBE}$, is estimated from the M_b vs. Θ_r response in Figure 7.4 as follows:

$$M_{b,DBE} = M_{b,ell}\left(1 + \alpha_{kT}\left(\frac{\Theta_{r,De}}{\Theta_{r,ell}} - 1\right)\right) \tag{7.5}$$

7.5.3. Structural Limit States and Damage under DBE and MCE

For IO performance, minor structural damage to an SC-CLT wall is permitted to occur. Accordingly, for IO performance, the DEC, EDP, ELL, and YCLT limit states are permitted to occur, and the SCLT, CCLT and LLP limit states are not permitted to occur.

The expected response under the DBE is as follows: (1) NL behavior of the wall is primarily due to gap opening and rocking of the base panels of the SC-CLT wall rather than significant damage of the CLT panels; (2) the wall maintains its original strength and stiffness under applied gravity and lateral loads; (3) the UFPs yield; (4) the PT bars remain linear-elastic.

For LS performance, the structure is expected to "retain significant margin against collapse" despite a substantial decrease in lateral stiffness (FEMA 450). Accordingly, for LS performance of an SC-CLT wall, the CCLT and LLP limit states are not permitted to occur. The expected response under the MCE is as follows: (1) NL behavior of the CLT material occurs at the bottom corners of the base CLT panels, including yielding and splitting in compression; (2) crushing of the CLT material does not occur; (3) the PT bars remain linear-elastic and the wall maintains its SC capability.

7.5.4. Seismic Design Criteria

To achieve the seismic design objectives described above, seismic design criteria are established to relate the SC-CLT wall capacities at the identified limit states to the seismic design demands. Figure 7.4 shows the first four criteria, which are as follows:

$$M_{b,ell} \geq M_{b,d} = \frac{M_{b,ed}}{R} \tag{7.6}$$

$$\Theta_{r,sclt} \geq \Theta_{r,De} \tag{7.7}$$

$$\Theta_{r,cclt} \geq \Theta_{r,Me} \tag{7.8a}$$

$$\Theta_{r,llp} \geq \Theta_{r,Me} \tag{7.8b}$$

In addition to these design criteria, a story drift limit, $\Theta_{s,all}$, is imposed to control damage within the building associated with the SC-CLT wall. $\Theta_{s,all}$ is taken to be 1.5% in this study, but other values could be used.

$$\Theta_{s,all} \geq \Theta_{s,se} \tag{7.9}$$

Finally, a criterion is used to balance the M_b resistance contributed by the vertical joint connectors (i.e., UFPs) and the total M_b resistance. To provide sufficient energy dissipation so that the equal displacement assumption can be used (Seo and Sause, 2005), a minimum hysteretic energy dissipation ratio, β_e, of 25% is specified, as follows:

$$\beta_e = \frac{M_{b,ufp}}{M_{b,ell}} \geq \beta_{e,min} = 25\% \tag{7.10a}$$

Therefore, the nominal plastic strength of one UFP, $F_{ufp,p}$ should meet the following criteria:

$$F_{ufp,p} \geq \frac{\beta_{e,min} M_{b,ell}}{1.3 N_{con} L_w} \tag{7.10b}$$

In previous studies, UFPs were observed to strain harden significantly, so that the force in the UFP, F_{ufp}, reached 1.3 times $F_{ufp,p}$ (Ganey, 2015; Kelly et al., 1972). Therefore, the overstrength of the UFP due to strain hardening is taken into account in calculating β_e, as shown in Eq. (7.10b).

To avoid having one wall panel permanently uplifted by a residual vertical joint force, the total maximum expected plastic strength of the connectors (i.e., the UFPs) in a vertical joint, taken as 1.3 times the nominal plastic strength (i.e., $1.3N_{con}F_{ufp,p}$) should be less than the sum of the dead load (DL) acting on each wall-panel and the total initial prestressing force acting on each panel, denoted F_{pi}, as follows:

$$\left(\sum_{i=1}^{N}\left(N_{g,i}^{panel}\right) + F_{pi}\right) \geq 1.3\, N_{con}\, F_{ufp,p} \tag{7.11}$$

where $\sum_{i=1}^{N}(N_{g,i}^{panel})$ = sum of dead load on each panel at each floor level i from vertical load combination (VCL2) described later; $F_{pi} = T_{p1,i} + T_{p2,i}$ (see Figure 7.3).

The UFPs are intended to fully yield prior to the ELL limit state, so the deformation of each UFP when the plastic strength, $F_{ufp,p}$, is reached, denoted as $\Delta_{ufp,p}$, is designed to be smaller than the estimated vertical joint deformation at the ELL limit state:

$$\Delta_{r,ell} \geq \Delta_{ufp,p} \tag{7.12}$$

7.6. Prototype Buildings and Walls

Figure 7.5 shows the floor plan of the prototype buildings, which includes 40 ft. long SC-CLT walls in the E-W and N-S directions. Two prototype buildings are considered, one with 6 stories and another with 11 stories. The first story height is 15 ft. and the height of the stories above the first story is 10 ft. Each prototype building is assumed to be a residential building located in Seattle, WA. Table 7.1 and Table 7.2 show the assumed dead and live loads (denoted as DL and LL, respectively). The walls in the E-W direction and the N-S direction have different seismic tributary areas and different levels of gravity load acting on the wall, as follows. It is assumed that the floor diaphragm is rigid. At each floor, the E-W walls each have a seismic tributary area equal to 1/4 of the floor plan area, while the N-S walls each have a seismic tributary area equal to 1/6 of the floor plan area. The E-W walls each have a gravity load tributary area equal to 2.5% of the floor plan area, while the central N-S walls (which are treated as the N-S prototype wall) have a gravity load tributary area to equal 12% of the floor plan area. Four SC-CLT walls, denoted as 6CEW, 6CNS, 11CEW, and 11CNS, are designed for the floor plan in Figure 7.5. Figure 7.6 shows the elevation of these 6- and 11-story SC-CLT walls

For the 6-story prototype building, the SC-CLT walls are made from 5-layer CLT panels. For the 11-story prototype wall, the SC-CLT walls are made from CLT panels which have a structural composite lumber (SCL) panel (APA, 2011) at the core. The 5-layer CLT panels are constructed from 1.3 inch thick Grade 1 Douglas Fir boards boards with the boards in the two outer layers and the center layer oriented with the grain parallel to the

vertical direction, and the two intermediate layer boards oriented with grain parallel to the horizontal direction (Table 7. 3). The SCL-core CLT panels are constructed with a 3.6 inch thick SCL panel glued to two outer layers of Douglas fir boards oriented with the grain parallel to the vertical direction (Table 7.3). Table 7.3 shows the material properties for the 5-layer and SCL-core CLT panels based on material tests by Ganey (2015). As shown in Table 7.3, the composite modulus of elasticity, E_c, and composite compressive yield strength, f_{c0}, of the SCL-core panels are almost twice as large as those of the 5-layer CLT panels.

Figure 7.6 shows the 6-story SC-CLT walls are made of two 20 ft. long 5-layer CLT panels with one vertical joint with UFP connectors between the CLT panels. To achieve a total height of 65 ft., one 35 ft. tall panel and one 30 ft. tall panel are rigidly connected. The 11-story SC-CLT walls are made of two 20 ft. long SCL-core CLT panels with one vertical joint with UFP connectors between the CLT panels. To achieve total height of 115 ft., one 35 ft. panel and two 40 ft. tall panels are rigidly connected.

In each prototype wall, two groups of PT bars are placed with an eccentricity of 18.0 in. from the centerline of each CLT wall panel as shown in Figure 7.6. Table 7.4 summarizes the material properties of the PT bars. Table 7.5 shows the diameter and the total area of PT bars (i.e., both groups) in the prototype walls where it is noted that for 6CNS, 6CEW, and 11CNS each group of PT bars in each wall panel has a single bar, while for 11CEW each group has two PT bars.

The panels of the 6- and 11-story SC-CLT walls are connected along the vertical joints using 4 UFPs and 6 UFPs, respectively. The UFPs are placed at the third points along the height of each individual panel as shown in Figure 7.6. Table 7.6 shows the material properties of the UFPs. The $f_{y,UFP}$ value used to design the UFPs includes the expected overstrength of the steel. Material test results (Ganey, 2015), show that considerable strain hardening of the UFP material can be expected, so the ultimate force capacity of the UFP can be as much as 1.5 times $F_{ufp,p}$.

Vertical (gravity) load combinations used in design and analysis of the prototype walls are summarized in Table 7.7 which shows that three load combination are used. VLC1 is used for calculating the $M_{b,ell}$ strength of the wall, based on the (0.9 - 0.2S_{DS})DL load combination from FEMA P695 (2009), where S_{DS} is the 5% damped, spectral response acceleration parameter at short periods (ASCE, 2010). VLC2 is used for checking the uplift criteria (see Eq. (7.11)) for the wall based on the 1.0DL load combination. VLC3 is used for estimating the lateral drifts and period of the prototype buildings, and in the NLHTA (described later) of the prototype structure. VLC3 is based on the 1.05DL + 0.25 LL load combination from FEMA P695 (2009).

Table 7.5 summarizes the properties for each prototype wall. Table 7.8 shows for each vertical load combination the relevant gravity load acting on each prototype wall panel at each floor, $N_{g,i}^{panel}$, as well as the gravity load within the seismic tributary area of each floor (except for the gravity load acting on the prototype wall) $N_{g,i}^{LOC}$.

7.6.1. Seismic Design of Prototype Walls

Each prototype wall is designed using the seismic design criteria given previously. For the 6-story prototype walls, the ELF procedure (ASCE, 2010) with R = 6 was used to establish $M_{b,d}$. For the 11-story prototype walls, the modal response spectrum analysis (MRSA) procedure with R = 6 was used to establish $M_{b,d}$. The SC-CLT wall buildings are assumed to be located on a site in Seattle with NEHRP Site Class D conditions. Each prototype wall was designed in accordance with ASCE (2010) requirements. For design, the short period spectral acceleration (S_s) was taken as 1.343g and the 1 s period spectral acceleration (S_1) was taken as 0.520g. The upper period limit in ASCE (2010) was not used in determining $M_{b,d}$, instead, the actual periods of the prototype buildings were estimated from the LEM of each prototype structure.

To account for the P-Δ effects, a fixed-base numerical model of the SC-CLT wall with $N_{g,i}^{LOC}$ (from VLC3) acting on a lean-on-column was created in OpenSees (Mazzoni et al., 2009). $\Theta_{r,d}$ and $\Theta_{s,d}$ are estimated using this model including the P-Δ effects. Table 7.9 shows the seismic properties and selected seismic design demands for the prototype walls. Note that the lateral drift design demands are discussed later. Table 7.10 and Table 7.11 summarizes the estimated M_b and Θ_r capacities of each prototype wall at the identified structural limit states using CFE.

In calculating the seismic demands, $M_{b,d}$, $\Theta_{r,d}$, and $\Theta_{s,d}$, R = 6 was used with C_d = 6 based on the equal displacement assumption. In previous studies of CLT walls, different response

modification factors, R, and deflection amplification factors, C_d, were used. For example, Pei et al. (2012) and Amini et al. (2014) used R and C_d equal to 4.5 for mid-rise CLT walls with mechanical fasteners. R and C_d values for CLT walls are not specified in ASCE (2010), but R = 6.5 and C_d = 4.0 are recommended for light-frame (wood) walls. The use of R = 6.0 and C_d = R = 6.0 is evaluated later using NLTHA results.

7.6.2. Analytical Model for Prototype Walls

A two dimensional fiber-element-based numerical model of the each prototype wall was developed in OpenSees (Mazzoni et al., 2009). Figure 7.7 shows a schematic of the numerical model together with constitutive relationships assumed for the CLT panels, the PT bars, and the UFPs. The stress-strain behavior of the CLT wall panel material was idealized as elastic-perfectly plastic (EPP), as shown in Figure 7.7, with E_c and f_{c0} from Table 7.3. In some specific analysis cases, as discussed later, the stress-strain behavior of the CLT wall panel was made linear-elastic. The steel of the PT bar was modeled with the Steel02 material model (Mazzoni et al., 2009) calibrated using material test results for each bar size (see Chapter 6). The Giuffre-Menegotto-Pinto material model (Mazzoni et al., 2009), calibrated using test results by Ganey (2015), was used to model the UFPs. A detailed explanation of the fiber-element-based numerical model is provided in Chapter 6.

The capacities estimated using the CFE for the prototype walls are given in Table 7.10 and Table 7.11. Figure 7.8 compares the estimated M_b versus Θ_r behavior of the 6CEW from NL pushover analysis of the FM with the results from the CFE.

7.6.3. Study of $\Theta_{r,d}$ Response for Prototype Walls

Table 7.12 compares the $\Theta_{r,d}$ estimates based on static analyses results from four different numerical models of each prototype wall. These four numerical models are: (1) fixed base (non-rocking) linear-elastic model (LEM) considering the P-Δ effects and the stiffness of the UFPs, (2) LEM neglecting the stiffness of the UFPs, (3) fixed-base (non-rocking) linear-elastic FM with a NL UFP model (see Figure 7.7 for the NL material model for the UFPs), (4) full NL FM (with rocking) in which NL material models are used for the CLT wall panels and the UFPs (see Figure 7.7).

Table 7.12 shows that the $\Theta_{r,d}$ responses from the LEM of each prototype wall with the UFP stiffness are the smallest among all four models and establish a lower bound for $\Theta_{r,d}$. The $\Theta_{r,d}$ response from the LEM without UFP stiffness shows that neglecting the UFP stiffness increases the $\Theta_{r,d}$ response by an average of 16% and as much as 28% compared to the LEM with UFP stiffness. Table 7.12 shows that including the NL material response of the UFP increases the $\Theta_{r,d}$ responses by an average of 35% and as much as 45% compared to the LEM with UFP stiffness. Including the NL material response of the CLT panels and rocking of the SC-CLT wall panels increases $\Theta_{r,d}$ by an average of 11% and as much as 22% compared to the non-rocking LEM with NL UFP material response.

As it is stated in the discussion of the seismic design criteria, $\Theta_{r,De}$, $\Theta_{s,De}$, and $\Theta_{r,Me}$ are estimated using an equal displacement assumption. In this study, $\Theta_{r,e}$ is estimated by scaling $\Theta_{r,d}$ from the LEM with the UFP stiffness by R and then factoring $\Theta_{r,e}$ by 1.15 to

estimate $\Theta_{r,De}$ for each prototype wall. Similarly, $\Theta_{s,e}$ by is estimated by scaling $\Theta_{s,d}$ by R and then factoring $\Theta_{s,e}$ by 1.15 to estimate $\Theta_{s,De}$.

7.7. Parametric Study on the Lateral Load Response of SC-CLT walls

A parametric study of the prototype SC-CLT walls was made using the CFE, to observe the effect on the lateral load response of SC-CLT walls of the initial pre-stressing ratio (f_{pi}), total area of post-tensioning in each panel (A_{pt}), total gravity load acting on each panel ($N_{g,i}^{panel}$), and compressive yield strength of CLT ($f_{c,y}$).

Figure 7.9 shows the M_b normalized by $M_{b,d}$ vs. Θ_r responses for 6- and 11-story SC-CLT walls with various parameter variations for these prototype walls. The structural limit states of each SC-CLT wall are identified and indicated on each plot. Note that $\sum_{i=1}^{N} N_{g,i}^{panel}$ is denoted as N_g on each plot in Figure 7.9.

Figure 7.9(a) shows the M_b normalized by $M_{b,d}$ vs. Θ_r responses for four parametric variations of a 6-story SC-CLT wall. The effect of varying f_{pi} with constant A_{pt} and $N_{g,i}^{panel}$, on the lateral load response is shown. The design parameters (i.e., $N_{g,i}^{panel}$, f_{pi}, A_{pt}) used for 6CEW (in Table 7.5) are the basis for the wall and f_{pi} is varied while the other parameters are those of 6CEW. Figure 7.9(a) shows that as f_{pi} increases, $M_{b,dec}$ and $M_{b,ell}$, and the respective $\Theta_{r,dec}$ and $\Theta_{r,ell}$, increase. Although increasing f_{pi} increases $M_{b,yclt}$, $M_{b,sclt}$, and

$M_{b,llp}$, it decreases $\Theta_{r,yclt}$, $\Theta_{r,sclt}$, and $\Theta_{r,llp}$. As f_{pi} increases, a smaller base rotation (i.e., rocking) is required to yield the PT bars, which results in a decreased $\Theta_{r,llp}$.

Figure 7.9(b) shows the M_b normalized by $M_{b,d}$ vs. Θ_r responses for five parametric variation of a 6-story SC-CLT wall. The effect of varying A_{pt} on the lateral load response is shown. The design parameters used for 6CEW (in Table 7.5) are the basis for the wall and A_{pt} is varied while the other parameters are those of 6CEW. Figure 7.9(b) shows that as A_{pt} increases, $M_{b,llp}$ and $\Theta_{r,llp}$ increase. On the other hand, since the total vertical force acting on each panel increases as A_{pt} increases, $\Theta_{r,yclt}$, $\Theta_{r,sclt}$, and $\Theta_{r,cclt}$ decrease with increasing A_{pt}.

Figure 7.9(c) shows the M_b normalized by $M_{b,d}$ vs. Θ_r responses for five parametric variations of a 6-story SC-CLT wall. The effect of varying $N_{g,i}^{panel}$ on the lateral load response is shown. For the floor plan considered in this study (Figure 7.5), the gravity load acting on the 6CNS wall is much larger than on the 6CEW wall (see $N_{g.i}^{panel}$ in Table 7.5). Therefore, the design parameters used for 6CNS are the basis for the wall and $N_{g.i}^{panel}$ is varied while the other parameters are those of 6CNS. A larger $N_{g,i}^{panel}$ increases the M_b capacity of the wall without increasing A_{pt} or increasing f_{pi}. The results in Figure 7.9(c) show that $M_{b,dec}$ and $M_{b,ell}$ can be increased by increasing $N_{g.i}^{panel}$, but $\Theta_{r,yclt}$, $\Theta_{r,sclt}$, and $\Theta_{r,cclt}$ decrease with increasing $N_{g,i}^{panel}$.

Figure 7.9(d) shows the M_b normalized by $M_{b,d}$ vs. Θ_r responses for two 11-story SC-CLT walls. The effect of the type of CLT panel (i.e., 5-layer CLT panel or SCL-core CLT panel) is shown. As the CLT type is varied, $f_{c,y}$ and $(EI)_c$ of the CLT material varies. The design parameters used for 11CNS (in Table 7.7) are the basis for the study. Table 7.5 shows that 11CNS has SCL core CLT panels, however, the parameter variation includes one wall with SCL-core CLT panels, and one wall with 5-layer CLT panels. $f_{c,y}$ and $(EI)_c$ for the SCL-core and 5-layer CLT panels are shown in Table 7.3. Figure 7.9(d) shows that the M_b capacity of the wall with SCL-core CLT panels is greater than the M_b capacity of the wall with 5-layer CLT panel. Since the compressive yield stress capacity (i.e., $f_{c,y}$) of the SCL-core CLT panel is almost twice as much as $f_{c,y}$ of the 5-layer CLT panel (as shown in Table 7.3), a difference in the M_b capacities of the two walls is expected. Figure 7.9(d) shows that, $\Theta_{r,dec}$ and $\Theta_{r,ell}$ for the wall with SCL-core CLT panels are about half of $\Theta_{r,dec}$ and $\Theta_{r,ell}$ for the wall with 5-layer CLT panels. Since $(EI)_c$, of the SCL-core CLT panels are almost twice $(EI)_c$ of the 5-layer CLT panels (as shown in Table 7.3), this result is expected. Despite increasing M_b, Figure 7.9(d) shows that the wall with the SCL-core panels is less ductile than the wall with the 5-layer CLT panels.

As the number of stories increases, $\sum_{i=1}^{N} N_{g,i}^{panel}$ carried by each CLT wall panel also increases. Accordingly, to carry these vertical forces without premature yielding of the CLT section, an increased compressive strength of the CLT panel is needed, either by increasing the thickness of the panel or increasing $f_{c,y}$. Therefore, the 11-story SC-CLT walls are made of SCL-core CLT panels which have $f_{c,y}$ and $(EI)_c$ that are about twice those of the 5-layer CLT panels.

7.8. Ground Motion Set used in Nonlinear Time History Analysis

A ground motion (GM) set composed of 18 GM pairs listed in Table 7.13 was used in the NLTHA of the prototype structures. The GM records were selected from the NGA (PEER 2011) database for a site in Seattle, WA. The site has a short period spectral acceleration (S_s) of 1.343g and 1 s period spectral acceleration (S_1) of 0.520g based on ASCE (2010) definitions (ASCE, 2010).

Each GM pair was initially scaled so that the geometric mean of the pseudo-acceleration response for the GM pair matched the design basis earthquake (DBE) spectrum (ASCE, 2010) over a period range of 0.1-7.0 s. The DBE has a 10% probability of exceedance (POE) in 50 years corresponding to a return period of 475 years (BSSC 2003). In addition, each GM was scaled to the maximum considered earthquake (MCE) spectrum. The MCE has a 2% POE in 50 years (BSSC 2003). The scale factors were calculated using the average scaling method described in Baker (2011). The pseudo-acceleration response spectra of GMs scaled to the DBE and the median spectrum for the GM set are shown in Figure 7.10.

7.9. Seismic Response of Prototype Walls

The seismic response of the prototype walls is investigated in this section. NLTHA are conducted using the fiber-element-based numerical model of each prototype wall under the selected set of ground motions (GMs) scaled to the DBE and MCE levels.

7.9.1. M_b vs. Θ_r Response for Prototype Walls

Figure 7.11 to Figure 7.14 show the hysteretic M_b vs. Θ_r responses for the 6CNS, 6CEW, 11CNS, and 11CEW prototype wall subjected to HWA019E ground motion record scaled to the DBE and MCE levels. For the DBE-level responses of the prototype wall structures, except for 11CEW, only the DEC, EDP, and ELL limit states are reached. YCLT is also reached for the DBE level response of the 11CEW prototype wall structure. For the MCE level responses of the prototype walls, the CCLT and LLP limit states are not reached in any prototype wall. These result suggest that the design of the prototype walls are adequate according to the design criteria (see Section 7.4 and Figure 7.4).

7.9.2. M_b Demands for Prototype Walls

Table 7.14 shows the design M_b demands (i.e., $M_{b,ed}$, $M_{b,d}$, $M_{b,ell}$, and $M_{b,DBE}$) and the median peak M_b responses of each prototype wall from NLTHA of the prototype structures under the GM set scaled to the DBE level (denoted as $M_{b,DmNL}$ in Table 7.14). Table 7.15 shows the different response modification factor, R, calculated as a ratio of $M_{b,ed}$ divided by different M_b demands from Table 7.14. The ratio of $M_{b,ed}$ to $M_{b,d}$ (denoted R_{des} in Table

7.15) is 6 for all prototype walls based on the design criteria. The ratio of $M_{b,ed}$ to $M_{b,ell}$ (denoted $R_{ell,des}$ in Table 7.15) is 5.87, 5.72, 5.53, and 5.80. These results suggest that the design capacities of the prototype walls are fairly close to but greater than the design demands, $M_{b,d}$. The ratio of $M_{b,DBE}$ to $M_{b,d}$ (denoted as $R_{D,des}$ in Table 7.15) is 5.23, 5.09, 5.76, and 5.80, which reflects the increased base moment that develops after $M_{b,ell}$ as the wall is deformed up to $\Theta_{r,De}$ as shown in Figure 7.4. The ratio of $M_{b,DmNL}$ to $M_{b,d}$ (denoted as $R_{D,NL}$ in Table 7.16) is 4.59, 4.57, 3.49, and 3.96, which suggest that although $R_{ell,des}$ and $R_{D,des}$ are very close to R_{des} for all prototype walls, 11CNS and 11CEW have considerable overstrength in the NLTHA since $R_{D,NL}$ is smaller than both $R_{ell,des}$ and $R_{D,des}$.

7.9.3. Θ_r Demands for Prototype Walls

NLTHA were performed on prototype walls using fiber-element-based numerical models shown schematically in Figure 7.7. A lean-on-column with elastic beam-column elements was used to model the P-Δ effects of the gravity loads within the seismic tributary area of the SC-CLT wall. Seismic mass was assigned to the horizontal degree-of-freedom of the lean-on-column at each floor level. The horizontal displacements of the SC-CLT and lean-on-column were constrained to each other with rigid links at each floor level. The vertical and horizontal displacements at the base of the lean-on-column were restrained. For NLTHA, the inherent damping of the prototype buildings was modeled using a damping substructure (Chapter 4 and Roke et al., 2010). Caughey damping with 5% damping ratio for first and second modes was used. Newmark constant average acceleration integration and the nonlinear Newton-Krylov solution algorithms were used in the NLTHA.

Figure 7.15 compares $\Theta_{r,De}$ and $\Theta_{r,Me}$ (indicated by the ○ marker in Figure 7.15 and shown in Table 7.16) with the median peak Θ_r demands from the NLTHA of each prototype wall under the GM set scaled to the DBE level and MCE level, $\Theta_{r,DmNL}$ and $\Theta_{r,MmNL}$ (indicated by a □ marker in Figure 7.15 and shown in Table 7.16). The peak Θ_r demands from the NLTHA results under each GM scaled to the DBE and MCE, $\Theta_{r,DNL}$ and $\Theta_{r,MNL}$, are also shown and indicated by • markers in Figure 7.15.

In addition to the design demands $\Theta_{r,d}$, $\Theta_{r,e}$, and $\Theta_{r,De}$ described previously, Table 7.16 includes the median roof drift demand under the DBE estimated from the median deformation response spectrum shown in Figure 7.10 at the first mode period of each prototype wall, $Sd_{1,m}$. $Sd_{1,m}$ values for each prototype wall structure are given in Table 7.17. $\Theta_{r,Sdm}$ (shown in Table 7.16) is calculated from $Sd_{1,m}$ as follows:

$$\Theta_{r,Sdm} = \frac{\Gamma_1 \phi_{r1} S_{d1,m}}{H_w} \tag{7.13}$$

where $\Gamma_1 = \frac{\Phi_1^T \mathbf{m} i}{M_1}$ (see Chopra, 2012); $\boldsymbol{\phi}_1$ = first mode shape; $M_1 = \boldsymbol{\phi}_1^T \mathbf{m} \boldsymbol{\phi}_1$; **m** = mass matrix for the N degree of freedom structure; i = influence vector for the structure; $\boldsymbol{\phi}_{r1}$ = value of $\boldsymbol{\phi}_1$ at the roof level; H_w = height of the wall.

$\Theta_{r,Sdm}$ should be similar to $\Theta_{r,e}$ since they are based on linear-elastic analysis of the same structure, but differences are expected since $\Theta_{r,e}$ is based on the design spectrum (ASCE,

2010) and the use of the ELF or MRSA procedure, while $\Theta_{r,Sdm}$ is based on the median single degree-of-freedom response to the scaled (to the DBE) GM set. The similarity of $\Theta_{r,Sdm}$ and $\Theta_{r,e}$ shows the scaled GM set represents the DBE at the first mode period of the prototype wall structures.

Figure 7.15 and Table 7.16 show that for 6CNS, $\Theta_{r,DmNL}$ is 0.89% and $\Theta_{r,De}$ is 0.97%. The ratio of $\Theta_{r,DmNL}$ to $\Theta_{r,De}$ is 0.91. In addition $\Theta_{r,MmNL}$ is 1.40% and $\Theta_{r,Me}$ is 1.46 %. The ratio of $\Theta_{r,MmNL}$ to $\Theta_{r,Me}$ is 0.96. These results suggest that $\Theta_{r,DmNL}$ and $\Theta_{r,MmNL}$ are well predicted by $\Theta_{rD,e}$ and $\Theta_{r,Me}$ for 6CNS.

Figure 7.15 and Table 7.16 show that for 6CEW, $\Theta_{r,DmNL}$ is 1.07% and $\Theta_{r,MmNL}$ is 1.71%. The ratio of $\Theta_{r,DmNL}$ to $\Theta_{r,De}$ is 0.80. In addition $\Theta_{r,MmNL}$ is 1.71% and $\Theta_{r,Me}$ is 2.0%. The ratio of $\Theta_{r,MmNL}$ to $\Theta_{r,Me}$ is 0.86. These results suggest that $\Theta_{r,DmNL}$ and $\Theta_{r,MmNL}$ are conservatively estimated by $\Theta_{rD,e}$ and $\Theta_{r,Me}$ for 6CEW.

Figure 7. 15 and Table 7.16 show that for 11CNS, $\Theta_{r,DmNL}$ is 0.97% and $\Theta_{r,De}$ is 1.33%. The ratio of $\Theta_{r,DmNL}$ to $\Theta_{r,De}$ is 0.98. In addition $\Theta_{r,MmNL}$ is 1.57% and $\Theta_{r,Me}$ is 1.47%. The ratio of $\Theta_{r,MCEmNL}$ to $\Theta_{r,Me}$ is 1.07. These results suggest that $\Theta_{r,DmNL}$ and $\Theta_{r,MmNL}$ are accurately estimated by $\Theta_{rD,e}$ and $\Theta_{r,Me}$ for 11CNS.

Figure 7. 15 and Table 7.17 show that for 11CEW, $\Theta_{r,DmNL}$ is 1.26% and $\Theta_{r,MmNL}$ is 1.93%. The ratios of $\Theta_{r,DmNL}$ to $\Theta_{r,De}$ is 1.05. In addition $\Theta_{r,MmNL}$ is 1.93% and $\Theta_{r,Me}$ is 1.81%. The ratio of $\Theta_{r,MmNL}$ to $\Theta_{r,Me}$ is 1.06. The ratio of $\Theta_{r,MmNL}$ to $\Theta_{r,Me}$ is 1.07. These results suggest that $\Theta_{r,DmNL}$ and $\Theta_{r,MmNL}$ are accurately estimated by $\Theta_{rD,e}$ and $\Theta_{r,Me}$ for 11CEW.

The results in Figure 7.15 and Table 7.17 suggest that the $\Theta_{r,De}$ estimates for the prototype wall structures are slightly conservative compared to $\Theta_{r,DmNL.}$ However, the differences between $\Theta_{r,De}$ and $\Theta_{r,DmNL}$ for each prototype wall are less than 20%. As stated earlier, different vertical load combinations were used in design and analysis of the walls (see Table 7.7). The $N_{g,i}^{panel}$ value used to determine the SC-CLT wall strength is less than the $N_{g,i}^{panel}$ value used in the numerical analysis model for the NLTHA (see Table 7.7 and Table 7.8). Therefore, having conservative $\Theta_{r,De}$ estimates compared to the actual $\Theta_{r,DmNL}$ responses might be expected.

The ductility demand, μ, as defined by Seo and Sause (2005), is the ratio of the maximum absolute NL displacement from NLTHA results to the yield displacement. Accordingly, the median ductility demands of the prototype wall structures based on the NLTHA results from the DBE- and MCE-level GMs, $\mu_{D,NL}$ and $\mu_{M,NL}$, are calculated as follows:

$$\mu_{D,NL} = \frac{\Theta_{r,DmNL}}{\Theta_{r,d}} \tag{7.14a}$$

$$\mu_{M,NL} = \frac{\Theta_{r,MmNL}}{\Theta_{r,d}} \quad (7.14b)$$

Table 7.18 shows the energy dissipation ratio for each prototype wall structure based on NLTHA results under the GM set scaled to the DBE (denoted as $\beta_{e,NL}$ in Table 7.15). $\beta_{e,NL}$ is almost same as the $\beta_{e,des}$ (Table 7.6) for all prototype walls, showing that differences between NLTHA Θ_r results and Θ_r design demands are not from differences in energy dissipation.

Table 7.17 shows that $\mu_{D,NL}$ is 6.31, 5.53, 6.80, and 7.25 for 6CNS, 6CEW, 11CNS, and 11CEW, respectively. $\mu_{M,NL}$ is 9.96, 8.86, 11.07, and 11.11 for 6CNS, 6CEW, 11CNS, and 11CEW, respectively. The $\mu_{D,NL}$ values are greater than the $R_{ell,des}$ values shown in Table 7.15 for all prototype walls. This result is consistent with prior studies of SC systems. For example, Chancellor (2014) showed that the $\mu_{DBE,NL}$ of a set of SC concentrically braced frames (i.e., SC-CBFs) with different configurations is greater than $R_{ell,des}$.

To further investigate the ductility demand for each wall, NLTHA were performed on SC single degree-of-freedom (SC-SDF) systems which are designed using the first mode period (T_1, obtained from the fixed-base linear-elastic FM with the UFP stiffness), $\beta_{e,NL}$, and α_{kT} for each prototype wall, respectively. $R_{ell,des}$, shown in Table 7.15, was used to determine the yield strength of each SDOF system. The median μ from NLTHA of each SC-SDF system for the DBE-level GM set, $\mu_{SDF,NL}$, was estimated. Table 7.18 shows that

$\mu_{SDF,NL}$ are 7.42, 8.18, 8.71, and 7.39 for each prototype wall, respectively. These results are consistent with the studies of Seo and Sause (2005) on SC-SDOF systems showing that μ is greater than the corresponding R value, for SC systems with β_e around 25% and small α values.

7.9.4. Median Peak M_i, V_i, and $\Theta_{s,i}$ Envelopes for Prototype Walls

Figure 7.16 and Figure 7.17 show the median peak story base moment ($M_{i,m}$), story shear ($V_{i,m}$), and story drift ($\Theta_{si,m}$) response envelopes for each prototype wall based on the NLTHA results under the GM record set scaled to the DBE level and the MCE level. For each prototype wall, $\Theta_{si,m}$ was less than $\Theta_{s,all}$, which was set as 1.5 % in the seismic design criteria. Figure 7.17 shows that the $M_{i,m}$ has slight local minima at the 5th and 9th floor levels for 11CNS. UFPs are located right below and right above 5th floor level and similarly, UFPs are located right below and right above the 9th floor level. The moment contribution and energy dissipation provided by the UFPs may the reason for the local minima in $M_{i,m}$ at the 5th and 9th floor levels for 11CNS.

7.10. SC-CLT Wall with Base and Upper Rocking Joints

7.10.1. Seismic Design of SC-CLT Wall with Base and Upper Rocking Joints

To better control the second mode response of prototype wall 11CEW, this wall was redesigned by adding a second rocking joint to the wall such that rocking within the height of the wall is allowed in addition to rocking between the base panel and the foundation,

which is the first (i.e., the base) rocking joint for 11CEW. The version of 11CEW wall with a base (first) and a upper (second) rocking joint, is denoted as 11CEWU.

Location of Upper Rocking Joint

11CEW is designed based on the approach given in Chapter 5. Accordingly, the location of the upper rocking joint in 11CEWU is determined by examining the first and second elastic mode static story base moment profiles, $M_{i1}^{st,e}$ and $M_{i2}^{st,e}$, for 11CEW. Elastic mode shapes, which are denoted as $\boldsymbol{\phi}_n^e$, are mode shapes based on the initial linear-elastic stiffness of the NL structure (see Chapter 5). Table 7.19 shows $M_{i1}^{st,e}$ and $M_{i2}^{st,e}$ (as defined in Chapter 5). As seen in Table 7.19, $M_{i2}^{st,e}$ is largest in magnitude at the 5th floor level. Therefore, the upper rocking joint of 11CEWU is located at the 5th floor level, where the $M_{i2}^{st,e}$ reaches its peak negative value.

Strength of Upper Rocking Joint

Using the design approach given in Chapter 5 for structures with base and upper rocking joints, the required story base moment capacity of the wall at upper rocking joint location at ELL limit state, $M_{u,ell}$, is expressed as fraction of $M_{b,ell}$, as follows:

$$M_{u,ell} = f_h M_{b,ell} \tag{7.15}$$

where f_h = factor applied to $M_{b,ell}$

f_h is selected as 0.3 in this study. Therefore, using Eq. (7.1) and (7.15):

$$M_{u,ell}=(0.3)M_{b,ell}=(0.3)(2.25)M_{b,dec} \quad (7.16)$$

where $M_{u,ell}$ is the moment at the upper rocking joint at the effective linear limit state of this joint.

The upper rocking joint at the 5th floor level of 11CEWU was designed to provide $M_{u,ell}$. Having constant PT bar properties constant over the entire height of the wall would result in a story base moment capacity at the 5th floor level much greater than $M_{u,ell}$ from Eq. (7.16). Therefore, the PT bars which provide the base overturning moment capacity (e.g., $M_{b,ell}$) are discontinued at the 5th floor level and PT bars with different properties are used at the upper rocking joint. The decompression moment at upper rocking joint location, $M_{u,dec}$, is calculated, as follows:

$$M_{u,dec}=2\left(2T^{u}_{p1,i}+\sum_{i=6}^{N}N^{panel}_{g,i}\right)l_w/3 \quad (7.17)$$

where $T^{u}_{p1,i}$ = intial post-tensioning force for PT bars passing through the upper rocking joint at the 5th floor level; $T^{u}_{p2,i} = T^{u}_{p1,i}$ (i.e., the initial post-tensioning force for the right group is assumed to equal the force for the left group); $\sum_{i=6}^{N}N^{panel}_{g,i}$ = total gravity load on each panel at the upper rocking joint at the 5th floor level.

For design purposes, $M_{u,ell}$ is expressed in terms of $M_{u,dec}$, assuming $M_{u,ell}$ is also reached when 3/8 of the CLT panel above the upper rocking joint is in contact with the CLT panel

below (similar to the assumption for calculating $M_{b,ell}$) and neglecting the contributions of the UFPs located above the upper rocking joint, as follows:

$$M_{u,ell}=2.25M_{u,dec}= (2.25)(0.3)M_{b,dec} \quad (7.18)$$

Based on Eq. (7.18), one of the two PT bars in in each group of PT bars passing through the rocking joint at the base of each wall panel of 11CEWU are terminated and anchored within the 5th story and does not pass through the upper rocking joint. Table 7.21 shows the seismic properties and selected seismic design demands and capacities for 11CEWU. Figure 7.18(a) shows the elevation view of 11CEWU.

7.10.2. Seismic Response of SC-CLT Wall with Base and Upper Rocking Joint

The seismic responses of 11CEW and 11CEWU are compared in this section. A fiber-based numerical model of 11CEWU was developed and NLTHA were conducted for the set of ground motions scaled to the DBE and MCE levels.

The roof level floor pseudo-acceleration spectrum is employed to quantify the modal dynamic responses of 11CEW and 11CEWU. Floor pseudo-acceleration spectrum were generated from the absolute acceleration response of the roof level of the 11CEW and 11CEWU structures from NLTHA. Figure 7.18(b) shows the median roof pseudo-acceleration spectra from the NLTHA results for 11CEW for the GM set compared with

the median roof pseudo-acceleration spectra from the NLTHA results for 11CEWU for the GM set. With the addition of the upper rocking joint, while the second mode roof pseudo-acceleration is reduced by a factor of 1.2, the third mode roof pseudo-acceleration is amplified by a factor of 1.36.

In addition to the floor pseudo-acceleration spectrum, the effective modal pseudo-acceleration, $A_{eff_n}(t)$, presented in Chapter 2, is used to quantify the NL modal responses of 11CEW and 11CEWU. The nth mode peak effective pseudo-accelerations, A_{eff_n}, were calculated from the NLTHA results for 11CEW and 11CEWU for each GM in the GM set, and the median value of A_{eff_n} for the GM set, $A_{eff_n,m}$ was calculated. Table 7.22 shows $A_{eff_n,m}$ for the first three modes of 11CEW and 11CEWU, expressed in terms of gravitational acceleration (g). $A_{eff_n,m}$ for the first three modes of 11CEW are 0.0786, 1.075, and 0.871, respectively. $A_{eff_n,m}$ for the first three modes of 11CEWU are 0.0726, 0.801, and 1.21, respectively. As shown in Table 7.22, with the addition of the upper rocking joint, while $A_{eff_1,m}$ is not affected much, $A_{eff_2,m}$ is reduced by a factor of 1.34, and $A_{eff_3,m}$ is amplified by a factor of 1.40. The amplification of the third mode $A_{eff_3,m}$ is less significant compared to the reduction of the second mode $A_{eff_2,m}$. For example, while the second mode effective modal mass is 19.6% of the total effective modal mass, the third mode effective modal mass is 4.6% of the total.

Figure 7.19 compares the $M_{i,m}$, $V_{i,m}$, and $\Theta_{si,m}$ response envelopes for 11CEW and 11CEWU based on the NLTHA results under the GM records scaled to DBE and MCE levels. $M_{i,m}$, especially at upper floor levels, is reduced by the addition of the upper rocking joint. $M_{i,m}$ is reduced by a factor of 1.33 at the 5th and 6th floor levels. $V_{i,m}$ is less influenced by the addition of the upper rocking joint. The addition of the upper rocking joint did not increase $\Theta_{si,m}$ under either DBE or MCE level ground motions. The multi-panel configuration of the SC-CLT wall and the presence of the UFPs above the upper rocking joint location may help prevent an increase in $\Theta_{si,m}$.

7.11. Summary and Conclusions

A seismic design procedure and related design criteria for SC-CLT walls are presented. 6- and 11-story, SC-CLT prototype buildings and corresponding walls are designed in accordance with the design procedure. The effect of several structural parameters on the lateral load behavior of the SC-CLT prototype walls was shown. A fiber-based analytical model of each prototype wall was developed and the responses of each wall under ground motions scaled to the DBE and MCE levels were examined using NLTHA. The NLTHA results show that the SC-CLT walls perform well under earthquake loading and are a viable alternative to existing types of lateral load resisting systems. The primary source of nonlinear drift is observed to be rocking and gap opening along the base of each wall panel. Even under MCE-level ground motions, the results show that little damage is expected to occur in the walls as the SCLT limit state was not reached under MCE-level ground motions, which implies limited post-earthquake repair is needed.

To reduce the response of the second mode, a second (upper) rocking joint was introduced into one of the 11-story prototype SC-CLT walls. A design criterion was established to enable the formation of the upper rocking joint. NLTHA results for the 11-story SC-CLT wall with base and upper rocking joints showed that the story base moment and story shear responses were reduced by the addition of an upper rocking joint. The roof level floor accelerations were decreased by the addition of the upper rocking joint.

The seismic design approach presented here should be validated for buildings with different floor plans and seismic conditions to develop general conclusions regarding the seismic behavior of SC-CLT walls and the validity of the design approach presented here.

7.12. Acknowledgements

This paper is based upon work supported by grants from National Science Foundation, Awards No. CMMI-1344617, CMMI-1344621, CMMI-1344590, CMMI-1344646, and CMMI-1344798 within the George E. Brown, Jr. Network for Earthquake Engineering Simulation Research (NEESR) program. The research was done as part of a collaborative project; Dr. Shiling Pei was the PI of this collaborative project. Dr. James D. Dolan, Dr. John W. van de Lindt, Dr. Jeffrey W. Berman, Dr. James M. Ricles, and Dr. Richard Sause were co-PIs of the project.

7.13. References

Amini, M. O., van de Lindt, J. W., Pei, S., Rammer, D., Line, P., and Popovski, M. (2014). "Overview of a project to quantify seismic performance factors for cross laminated timber structures in the United States," *Materials and Joints in Timber Structur*es. Springer, Netherlands, pp. 531-541.

APA-The Engineered Wood Association (2011). Engineered Wood Construction Guide Excerpt: Structural Composite Lumber. Form E30.

ASCE (2010). "Minimum design loads for buildings and other structures," *ASCE7-10*, Reston, VA, USA.

Baker, J.W. (2011). "Conditional Mean Spectrum: Tool for Ground-Motion Selection," *Journal of Structural Engrg.*, 137(3), pp. 322-331.

BSSC (2003). "NEHRP Recommended Provisions for Seismic Regulations for New Buildings and Other Structures," *FEMA 450. Building Seismic Safety Council, National Institute of Building Sciences*, Washington, D.C., USA.

Chancellor, N.B. (2014). "Seismic Design and Performance of Self-Centering Concentrically-Braced Frames," Ph.D. Dissertation, Department of Civil and Environmental Engrg., Lehigh Univ., Bethlehem, PA, USA.

Chopra, A. K. (2012). *Dynamics of Structures*. (4th ed.). Prentice Hall, New Jersey, NJ, USA.

Dunbar, A., Moroder, D., Pampanin, S., and Buchanan, A. (2014). "Timber Core-Walls for Lateral Load Resistance of Multi-Storey Timber Buildings," *Proc. of the World Conf. on Timber Engrg. (WCTE)*. Quebec, Canada, August 10-14.

Federal Emergency Management Agency (FEMA). (2009). "Quantification of building seismic performance factors." Report No. FEMA P695, *Federal Emergency Management Agency*, Washington, DC, USA.

Ganey, R. (2015). "Seismic Design and Testing of Rocking Cross Laminated Timber Walls," M.Sc. Thesis, Department of Civil and Environmental Engrg., *Univ. of Washington, Seattle, USA.*

Kelly, J. M., Skinner, R. I., and Heine, A. J. (1972). "Mechanism of Energy Absorption in Special Devices for Use in Earthquake Resistant Structures," *Bulletin New Zealand Society of Earthquake Engrg.*, 5(3), pp. 63-88.

Kurama, Y. C., Pessiki, S., Sause, R., Lu, L. W., El-Sheikh, M. (1996). "Analytical Modeling and Lateral Load Behavior of Unbonded Post-Tensioned Precast Concrete Walls," Research Report, No. EQ-96-02, Department of Civil and Environmental Engrg., Lehigh Univ., Bethlehem, PA, USA.

Kurama, Y. C. (1997). "Seismic Analysis, Behavior, and Design of Unbonded Post-Tensioned Precast Concrete Walls," Ph.D. Dissertation, Department of Civil and Environmental Engrg., Lehigh Univ., Bethlehem, PA, USA.

Kurama, Y.; Pessiki, S.; Sause, R.; and Lu, L.-W. (1999a). "Seismic Behavior and Design of Unbonded Post-Tensioned Precast Concrete Walls," *PCI Journal*, 44(3), pp 72-89.

Kurama, Y.; Pessiki, S.; Sause, R.; and Lu, L.-W. (1999b). "Lateral Load Behavior and Seismic Design of Unbonded Post-Tensioned Precast Concrete Walls," *ACI Structural Journal*, 96(4), pp 622-632.

Mazzoni, S.; McKenna, F.; Scott, M.H.; Fenves, G.L.; et al. (2009). "Open System for Earthquake Engineering Simulation (OpenSEES) User Command-Language Manual*"*. *Pacific Earthquake Engineering Research Center,* University of California, Berkeley, CA, USA.

Pacific Earthquake Engineering Research Center (PEER) (2011). "Ground motion database flatfile". Retrieved from http://peer.berkeley.edu/nga/flatfile.html on December 12, 2013.

Pei, S., van de Lindt, J. W., and Popovski, M. (2012). "Approximate R-factor for cross-laminated timber walls in multistory buildings," *Journal of Architectural Engrg.*, 19(4), pp. 245-255.

Perez, F. J. (2004). "Experimental and Analytical Lateral Load Response of Unbonded Post-Tensioned Precast Concrete Walls," Ph.D. Dissertation, Department of Civil and Environmental Engrg., Lehigh Univ., Bethlehem, PA, USA.

Perez, F. J., Sause, R., and Pessiki, S. (2007). "Analytical and Experimental Lateral Load Behavior of Unbonded Post-Tensioned Precast Concrete Walls," *Journal of*

Structural Engrg., American Society of Civil Engineers, 133(11), pp. 1531-1540.

Roke, D.; Sause, R.; Ricles, J.M.; and Chancellor, N.B. (2010). "Damage-Free Seismic-Resistant Self-Centering Concentrically-Braced Frames," *ATLSS Report 10-09*, Lehigh Univ., Bethlehem, PA, USA.

Seo, C.-Y., and Sause, R. (2005). "Ductility Demands on Self-Centering Systems Under Earthquake Loading," *ACI Structural Journal*, 102(2), pp. 275-285.

Table 7.1 Summary of dead loads for prototype structures

Item	Floor Dead Load (DL) (psf)
CLT Panel floor (depth: 6-7/8 inch)	20
Concrete Overlay (depth: 2.5 inch)	31
Ceiling	7
Mechanical Equipment	3
Self-weight of CLT wall panel (thickness: 6.5 inch)	14
Total	75

Table 7.2 Summary of live loads for prototype structures

Item	Floor Live Load (LL) (psf)
Residential	40
Partitions	10
Total	50
Live Load Included in Seismic Mass	10

Table 7.3 Material test results for 5-layer and SCL-core CLT specimens (Ganey, 2015)

	E_c (ksi)	f_{c0} (ksi)	ε_{c0} (inch/inch)
5-layer CLT	441	3.60	0.0082
SCL-core CLT	842	6.20	0.0074

Table 7.4 PT bar properties

f_{py} (ksi)	f_{pu} (ksi)	E_p (ksi)
131	160	29000

Table 7.5 Nominal properties of each CLT wall panel of prototype walls

Id	L_w (kips)	H_w (inch)	PT bar dia. (inch)	A_{pt} (in^2)	e_{pt} (inch)	$\frac{f_{pi}}{f_{pu}}$	F_{pi} (kips)	α_{kT} %
6CNS	240	780	1	2x0.85	18	0.25	68	2.57
6CEW	240	780	1¼	2x1.25	18	0.40	160	3.34
11CNS	240	1380	1	2x0.85	18	0.25	68	0.0*
11CEW	240	1380	1	4x0.85	18	0.30	163	0.0*

* When α_{kT} <0, it is taken equal to 0.0%.

Table 7.6 U-shaped flexural plates (UFPs) properties

Id	Number of UFPs	t_{UFP} (inch)	b_{UFP} (inch)	D_{UFP} (inch)	$f_{y,UFP}$ (ksi)	$F_{ufp,p}$ (kips)	$\Delta_{ufp,p}$ (inch)	β_e (%)
6CNS	4	4/8	4+3/8	4	60	8.20	0.18	24
6CEW	4	5/8	4	4+1/2	60	10.42	0.18	26
11CNS	6	4/8	4	4	60	7.50	0.18	24
11CEW	6	5/8	4	4+5/8	60	10.14	0.19	26

Table 7.7. Vertical load combinations used in design and analysis of prototype walls

Id	Analysis Type	Vertical Load Combination
VLC1	Vertical load on wall for strength design	(0.9 - 0.2 S_{DS}) DL
VLC2	Vertical load on wall for uplift criteria	1.0 DL
VLC3	Vertical load on wall for calculating lateral drifts and periods, and for NLTHA	1.05 DL + 0.25 LL

Table 7.8 Vertical forces used in design and analysis of prototype walls

Id	VLC1		VLC2		VCL3	
	N_g^{LOC} (kips)	$N_{g,i}^{panel}$ (kips)	N_g^{LOC} (kips)	$N_{g,i}^{panel}$ (kips)	N_g^{LOC} (kips)	$N_{g,i}^{panel}$ (kips)
6CNS	117	-	163	-	280	188
6CEW	86	-	119	-	734	134
11CNS	215	-	299	-	519	348
11CEW	158	-	219	-	1359	248

Table 7.9 Estimated seismic properties and design demands for prototype walls

Id	W per wall (kips)	T (s)	C_s	V_b from ELF (kips)	V_b from MRSA (kips)	$M_{b,d}$ (kip-inch)
6CNS	650.3	0.80	0.1081	70.30	-	4.01E+04
6CEW	975.5	1.03	0.0856	83.50	-	4.85E+04
11CNS	1203.3	1.44	0.060	72.46	66.65	5.55E+04
11CEW	1806.0	1.74	0.050	90.00	90.50	7.00E+04

Table 7.10 Estimated base overturning moment capacities for prototype walls at identified limit states based on CFE

Id	$M_{b,dec}$ (kip-inch)	$M_{b,ell}$ (kip-inch)	$M_{b,yclt}$ (kip-inch)	$M_{b,sclt}$ (kip-inch)	$M_{b,cclt}$ (kip-inch)	$M_{b,llp}$ (kip-inch)
6CNS	2.03E+04	4.10E+04	5.63E+04	7.22E+04	7.51E+04	7.92E+04
6CEW	2.00E+04	5.09E+04	7.28E+04	9.14E+04	1.02E+05	1.08E+05
11CNS	2.25E+04	6.02E+04	7.51E+05	8.05E+04	8.10E+04	6.72E+04
11CEW	2.53E+04	7.24E+04	9.19E+05	1.11E+05	1.25E+05	1.29E+05

Table 7.11 Estimated lateral roof drift ratio capacities for prototype walls at identified limit states based on CFE

Id	$\Theta_{r,dec}$ (%)	$\Theta_{r,ell}$ (%)	$\Theta_{r,yclt}$ (%)	$\Theta_{r,sclt}$ (%)	$\Theta_{r,cclt}$ (%)	$\Theta_{r,llp}$ (%)
6CNS	0.107	0.251	0.814	1.894	3.816	3.426
6CEW	0.123	0.273	0.818	1.756	2.574	3.723
11CNS	0.139	0.321	0.924	2.367	4.908	5.692
11CEW	0.135	0.293	0.926	2.219	4.288	5.412

Table 7.12 Comparison of $\Theta_{r,d}$ from different models of prototype walls

Id	Fixed-Base with UFP stiffness			Fixed-Base without UFP stiffness			Fixed-Base, Linear-Elastic FM with NL UFP		Full NL FM with UFP	
	T_1 (s)	$\Delta_{r,d}$ (inch)	$\Theta_{r,d}$ (%)	T_1 (s)	$\Delta_{r,d}$ (inch)	$\Theta_{r,d}$ (%)	$\Delta_{r,d}$ (inch)	$\Theta_{r,d}$ (%)	$\Delta_{r,d}$ (inch)	$\Theta_{r,d}$ (%)
6CNS	0.80	1.07	0.137	0.88	1.35	0.173	1.37	0.176	1.41	0.181
6CEW	1.03	1.45	0.186	1.09	1.91	0.245	1.65	0.212	1.69	0.217
11CNS	1.44	1.94	0.141	1.68	2.71	0.196	2.15	0.156	2.48	0.180
11CEW	1.74	2.38	0.172	2.08	3.47	0.251	2.69	0.195	3.28	0.238

Table 7.13 Ground motion set (Chancellor, 2014)

PEER-NGA Record Seq. #	Year	Event	Station	Component	Scale Factor	
					DBE	MCE
165	1979	Imperial Valley-06	Chihuahua	012, 282	2.51	3.77
169	1979	Imperial Valley-06	Delta	262, 352	1.05	1.58
728	1987	Superst. Hills-02	Westmorland	090, 180	1.97	2.95
778	1989	Loma Prieta	Hollister	165, 255	2.04	3.07
949	1994	Northridge-01	Arleta	090, 360	1.25	1.88
1100	1995	Kobe, Japan	Abeno	000, 090	2.33	3.5
1101	1995	Kobe, Japan	Amagasaki	000, 090	2.09	3.13
1110	1995	Kobe, Japan	Morigawachi	000, 090	2.26	3.38
1187	1999	Chi-Chi, Taiwan	CHY015	N, W	2.52	3.79
1203	1999	Chi-Chi, Taiwan	CHY036	E, N	2.5	3.76
1204	1999	Chi-Chi, Taiwan	CHY039	E, N	1.92	2.88
1209	1999	Chi-Chi, Taiwan	CHY047	N, W	1.54	2.32
1236	1999	Chi-Chi, Taiwan	CHY088	E, N	1.57	2.36
1269	1999	Chi-Chi, Taiwan	HWA019	E, N	1.9	2.84
1294	1999	Chi-Chi, Taiwan	HWA048	N, W	1.42	2.13
1317	1999	Chi-Chi, Taiwan	ILA013	N, W	1.77	2.65
1484	1999	Chi-Chi, Taiwan	TCU042	E, N	1.42	2.12

Table 7.14 Base overturning moments calculated in design and from NLTHA for prototype wall structures

Id	$M_{b,ed}$ (kip-inch)	$M_{b,d}$ (kip-inch)	$M_{b,ell}$ (kip-inch)	$M_{b,DBE}$ (kip-inch)	$M_{b,DmNL}$ (kip-inch)
6CNS	2.47E+05	4.12E+04	4.10E+04	4.72E+04	5.38E+04
6CEW	2.99E+05	4.99E+04	5.09E+04	5.87E+04	6.54E+04
11CNS	3.33E+05	5.55E+04	6.02E+04	5.78E+04	9.54E+04
11CEW	4.20E+05	7.00E+04	7.24E+04	7.24E+04	1.06E+05

Table 7.15 Response modification factor estimates for prototype wall structures

Id	R_{des} (-)	$R_{ell,des}$ (-)	$R_{D,des}$ (-)	$R_{D,NL}$ (-)
6CNS	6	5.87	5.23	4.59
6CEW	6	5.72	5.09	4.57
11CNS	6	5.53	5.76	3.49
11CEW	6	5.80	5.80	3.96

Table 7.16 Comparison of peak roof drift ratio demands for prototype wall structures

Id	$\Theta_{r,d}$ (%)	$\Theta_{rSd,m}$ (%)	$\Theta_{r,e}$ (%)	$\Theta_{r,De}$ (%)	$\Theta_{r,Me}$ (%)	$\Theta_{r,DmNL}$ (%)	$\Theta_{r,MmNL}$ (%)	$\mu_{D,NL}$ (-)	$\mu_{M,NL}$ (-)
6CNS	0.141	0.141	0.846	0.973	1.460	0.890	1.404	6.31	9.96
6CEW	0.193	0.192	1.158	1.332	1.998	1.067	1.710	5.53	8.86
11CNS	0.142	0.140	0.852	0.980	1.470	0.965	1.572	6.80	11.07
11CEW	0.174	0.174	1.044	1.201	1.802	1.261	1.933	7.25	11.11

Table 7.17 First mode median GM pseudo acceleration and deformation for prototype wall structures

Id	$SA_{GM,m}(T_1)$ (g)	$S_{d1,m}$ (inch)
6CNS	0.73	4.47
6CEW	0.56	5.65
11CNS	0.37	7.43
11CEW	0.34	9.89

Table 7.18 Estimated median from NLTHA for prototype wall structures

Id	T_1 (s)	$\beta_{e,mNL}$ (%)	α_{kT} (%)	$R_{ell,des}$ -	$\mu_{SDF,NL}$ -
6CNS	0.80	23.0	2.57	5.87	7.42
6CEW	1.03	26.0	3.34	5.72	8.18
11CNS	1.44	24.0	0.0	5.53	8.71
11CEW	1.74	25.0	0.0	5.80	7.39

Table 7.19 $M_{i1}^{st,e}$ and $M_{i2}^{st,e}$ for 11CEW

Floor/ Moment	$M_{i1}^{st,e}$ (kip-inch)	$M_{i2}^{st,e}$ (kip-inch)
Base	3483.71	208.90
1	2861.44	30.20
2	2450.66	-76.49
3	2048.67	-161.78
4	1661.40	-218.49
5	1295.76	-242.68
6	959.30	-234.61
7	660.01	-199.09
8	406.18	-144.97
9	206.14	-84.34
10	68.08	-31.19

Table 7.20 Properties of 11CEWU

Id	*PT bar dia.* (inch)	A_{pt} at base joint (in^2)	A_{pt} at upper joint (in^2)	e_{pt} (inch)	f_{pi}/f_{pu} for PT bars running from		α_{kT} (%)
					base to top*	base to 5th floor**	
11CEWU	1	4x0.85	2x0.85	18	0.25	0.35	0

*passing through base and upper rocking joints
** passing through only base rocking joint

Table 7.21 Estimated seismic properties, and design demands and capacities for 11CEWU

Id	W per wall (kips)	T (s)	C_s	$M_{b,d}$ (kip-inch)	$M_{u,d}$ (kip-inch)	$M_{b,ell}$ (kip-inch)	$M_{u,ell}$ (kip-inch)
11CEWU	1806.0	1.74	0.050	7.00E+04	2.45E+04	7.24E+04	2.52E+04

Table 7.22 $A_{eff_n,m}$ for first three modes of 11CEW and 11CEWU

Id	$A_{eff_1,m}$	$A_{eff_2,m}$	$A_{eff_3,m}$
11CEW	0.0786	1.075	0.871
11CEWU	0.0726	0.801	1.210

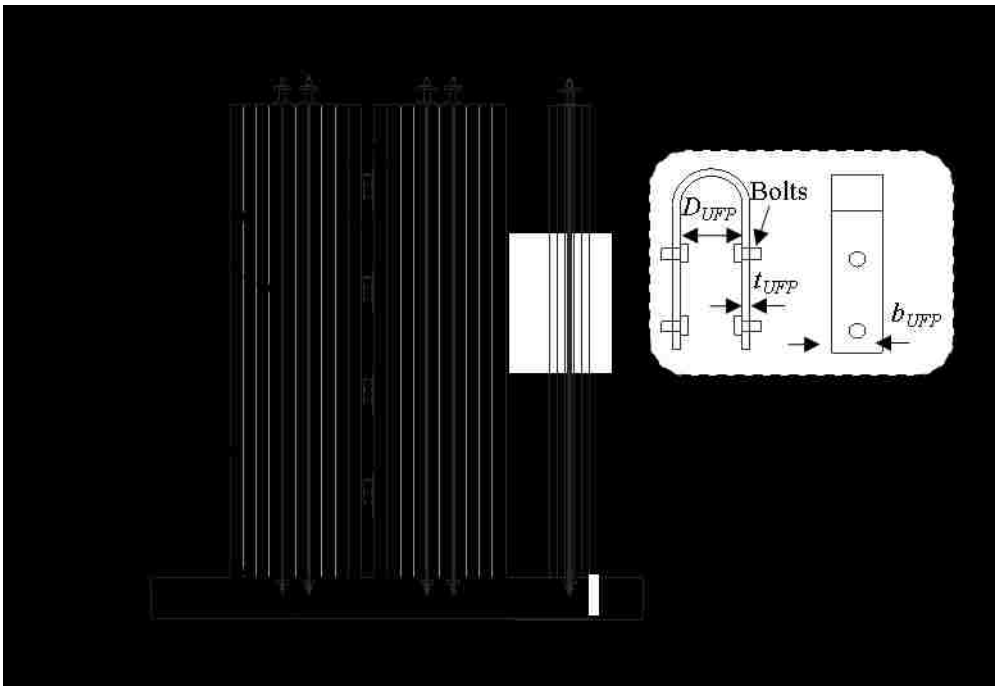

Figure 7.1 Configuration of a multi-panel SC-CLT wall with UFP connectors

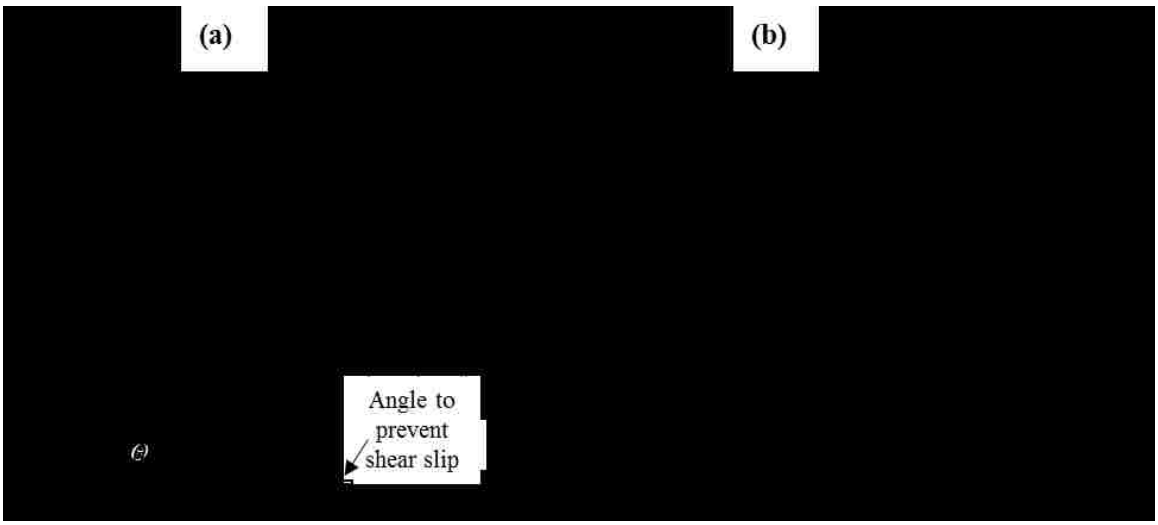

Figure 7.2 (a) Rocking behavior of multi-panel SC-CLT wall under lateral load; (b) base-overturning moment-roof-drift-relationship of SC-CLT walls

Figure 7.3 Forces on the SC-CLT wall at: (a) DEC; (b) ELL; and (c) LLP limit states

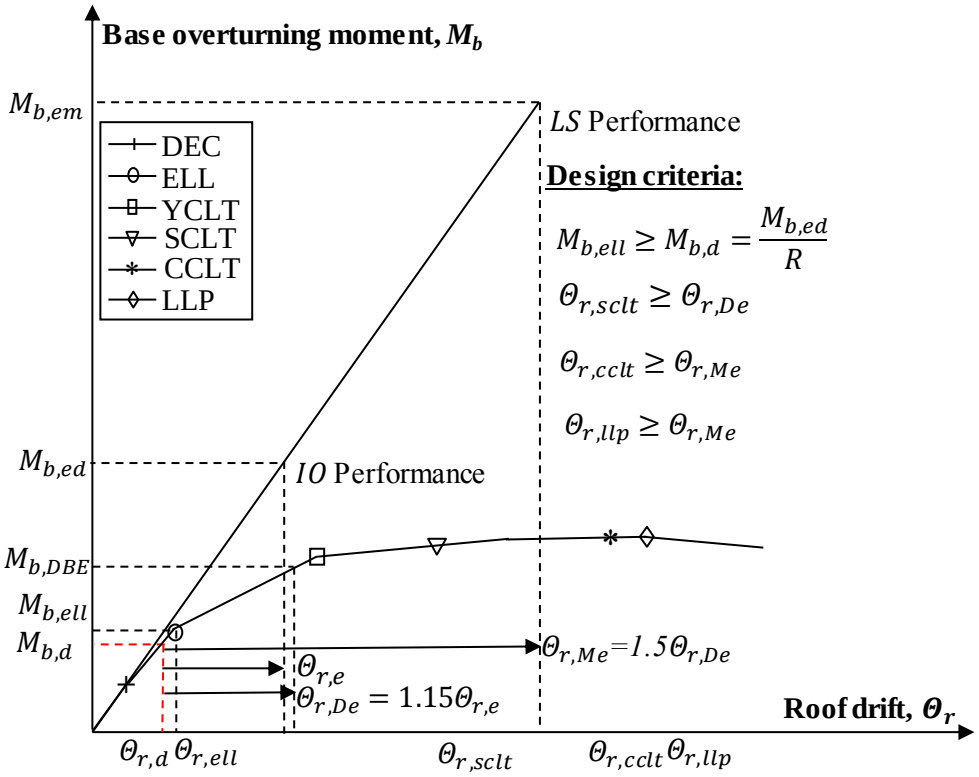

Figure 7.4 Proposed seismic design approach graphical representation of structural limit states, design performance conditions, response for DBE and MCE intensity levels, and design criteria

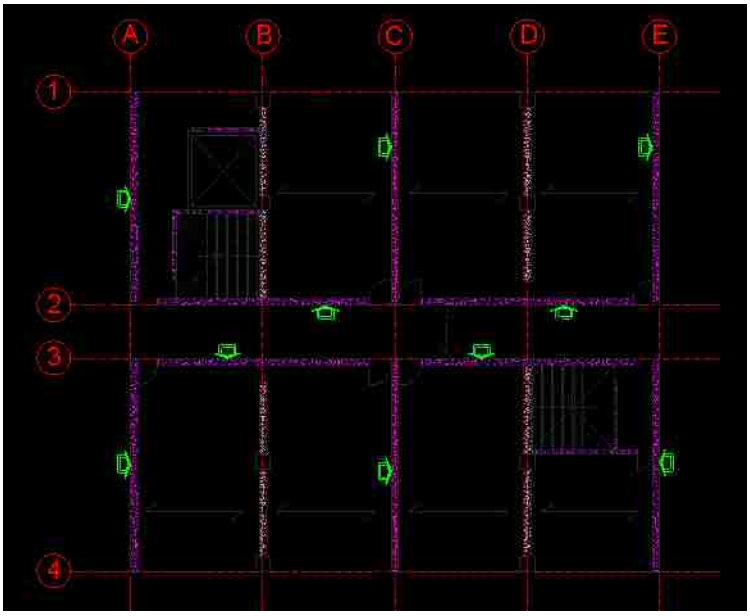

Figure 7.5 Floor plan of prototype buildings

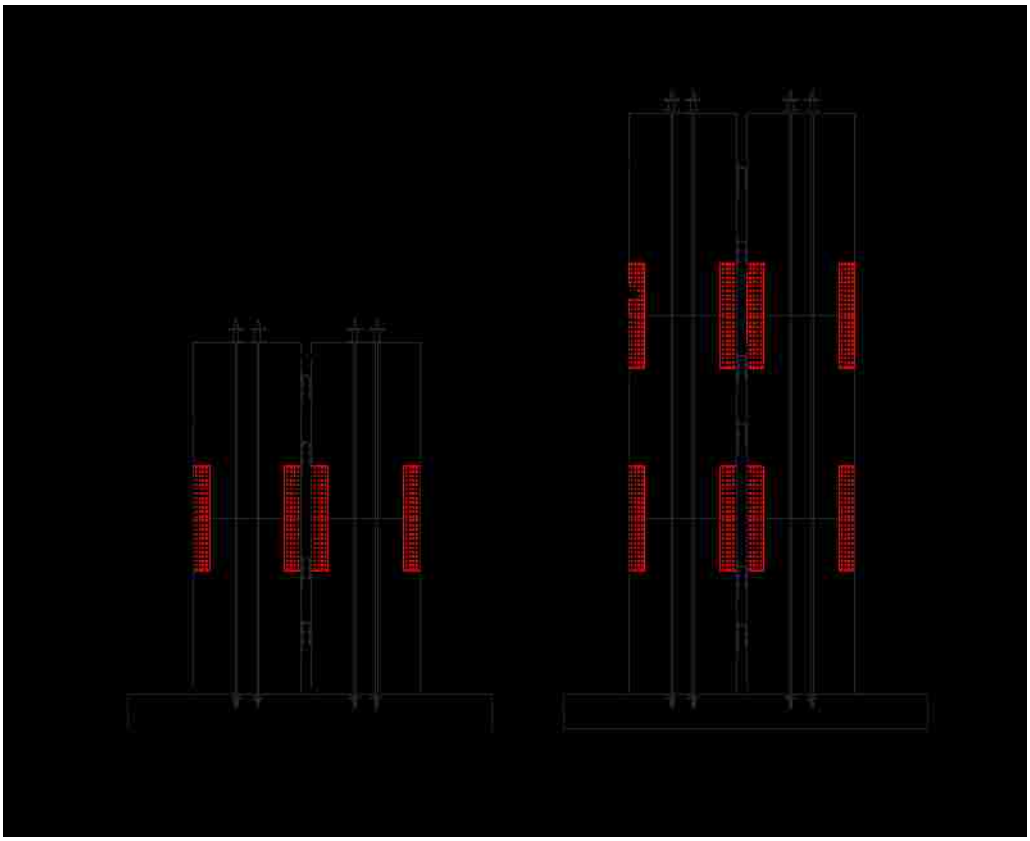

Figure 7.6 Prototype: (a) 6-story; (b) 11-story SC-CLT walls

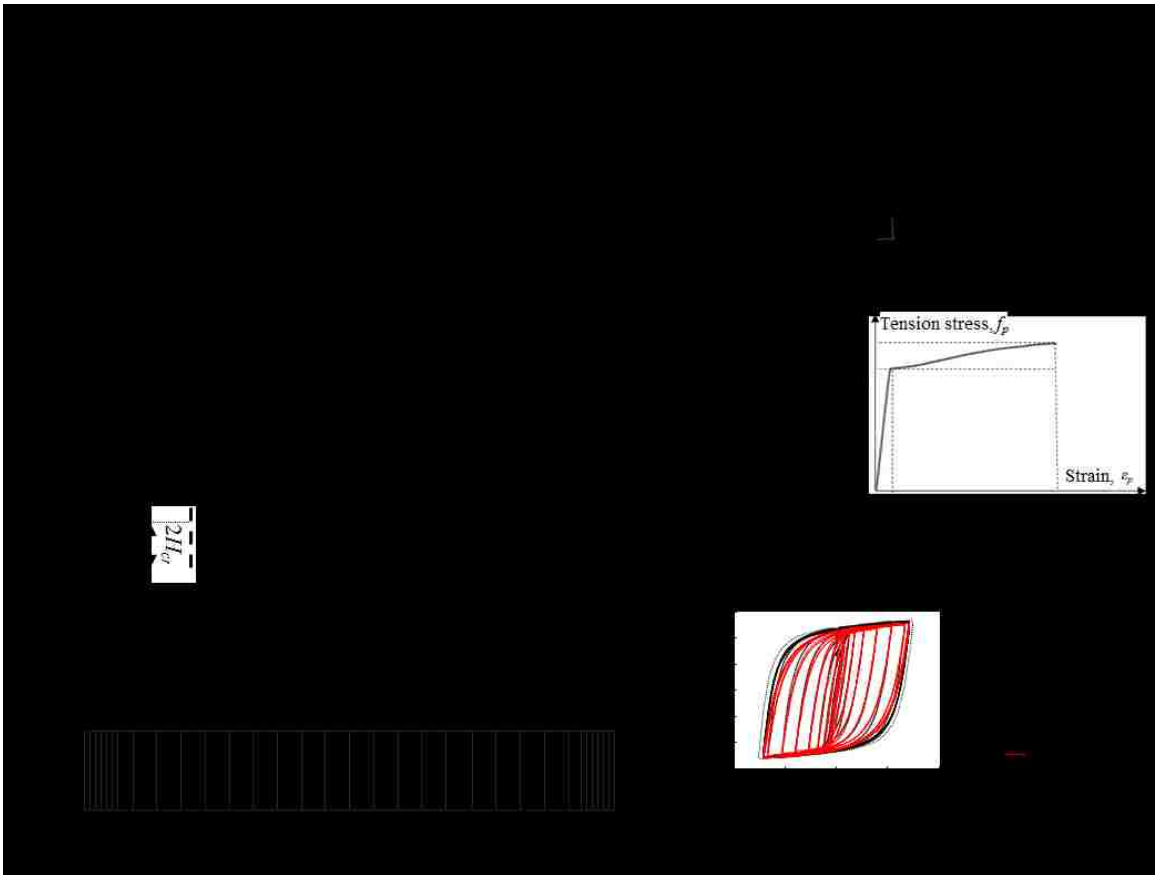

Figure 7.7 Fiber element numerical model for 6-story prototype SC-CLT walls

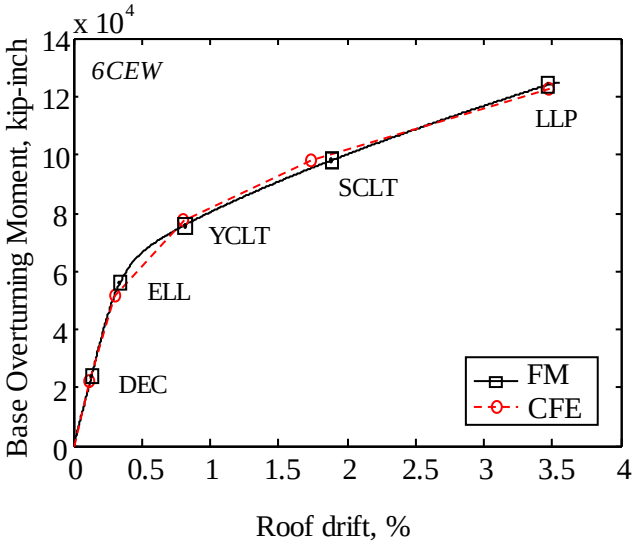

Figure 7.8 Comparison of lateral load response of 6CEW wall from FM and CFE

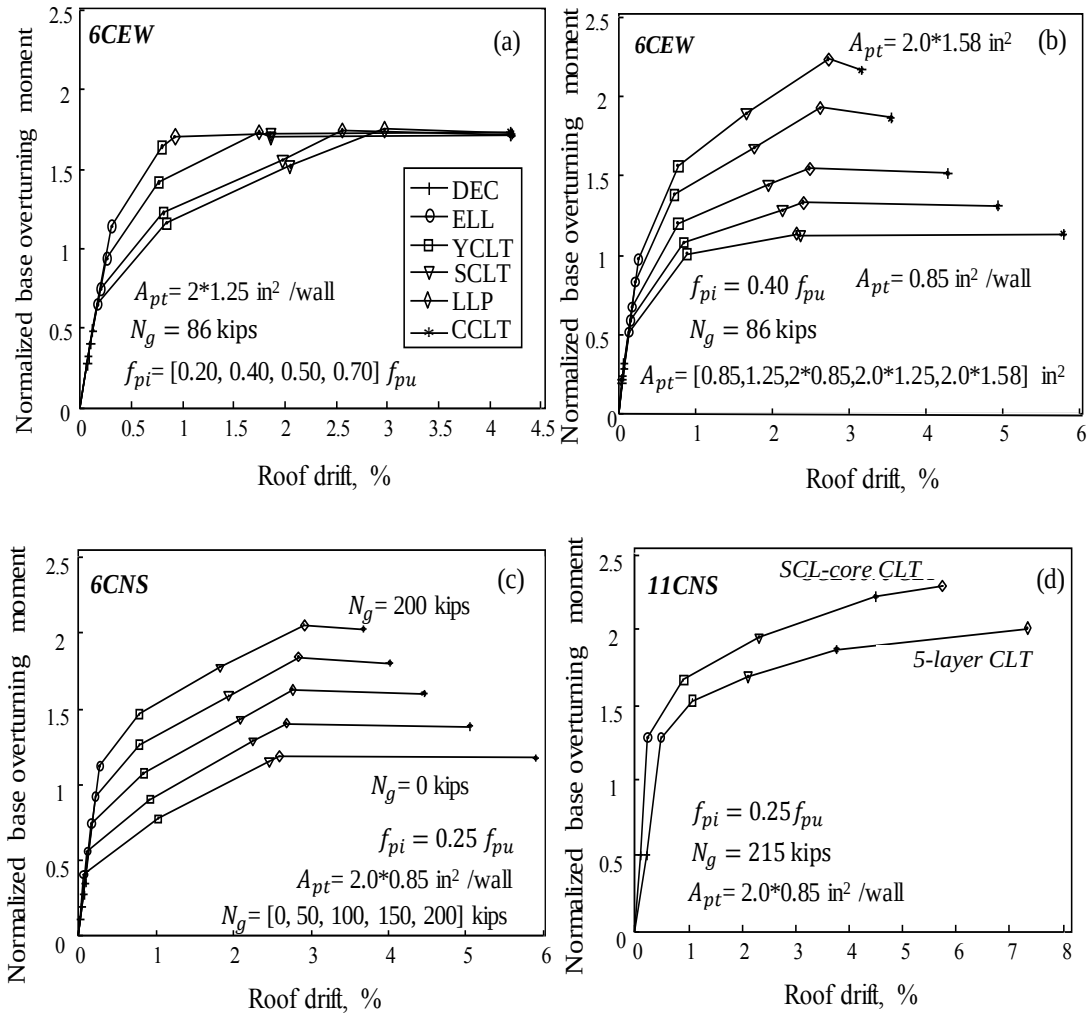

Figure 7.9 Effect of parameters on M_b vs. Θ_r response of 6- and 11-story SC-CLT walls

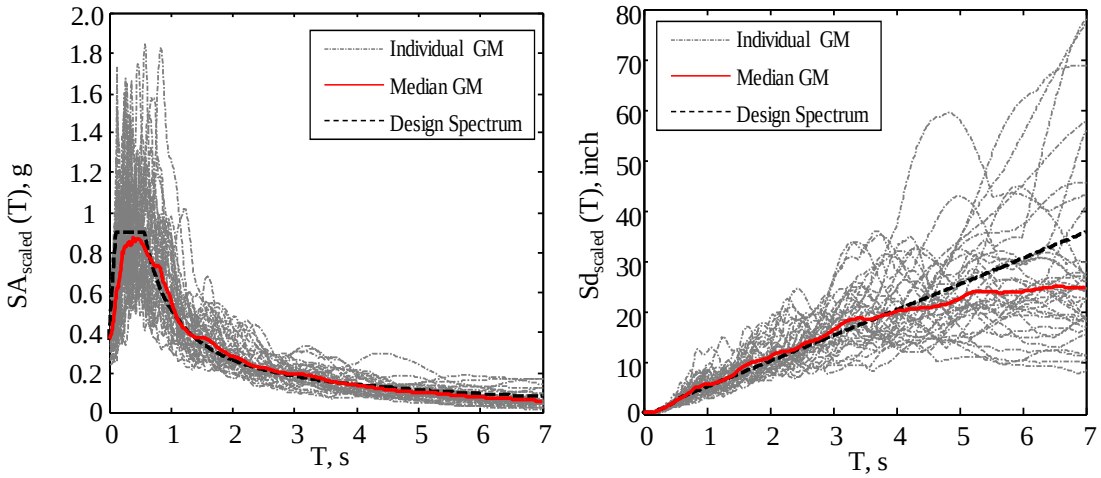

Figure 7.10 Pseudo-acceleration and deformation response spectra for ground motions scaled to DBE

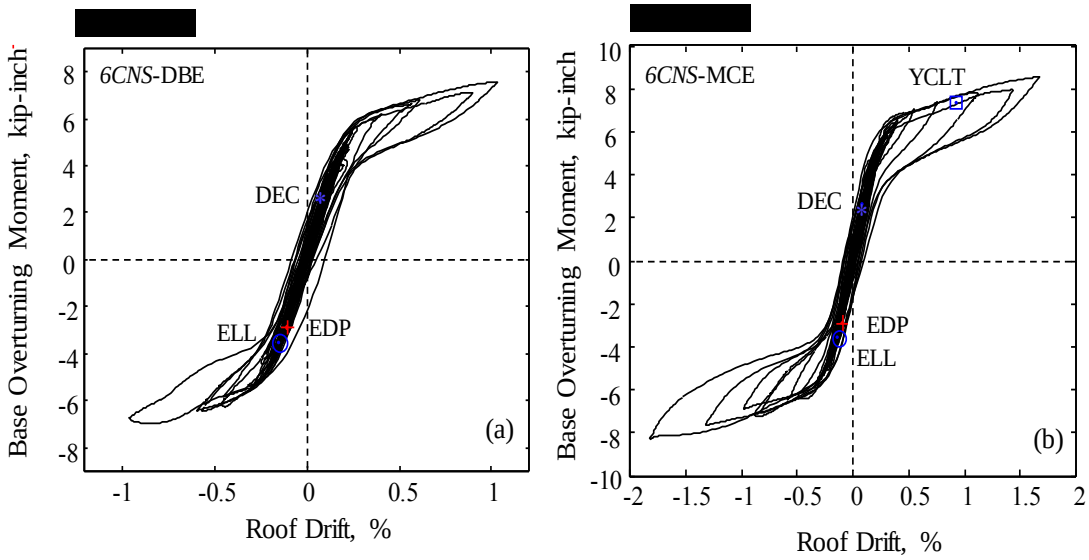

Figure 7.11 M_b vs. Θ_r response of 6CNS under HWA019E scaled to (a) DBE, (b) MCE

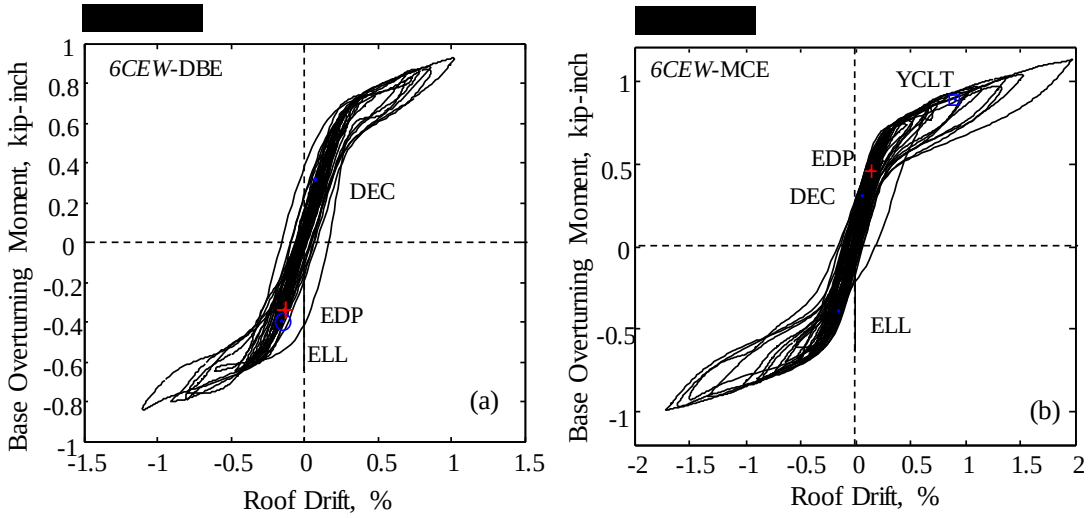

Figure 7.12 M_b vs. Θ_r response of 6CEW under HWA019E scaled to (a) DBE, (b) MCE

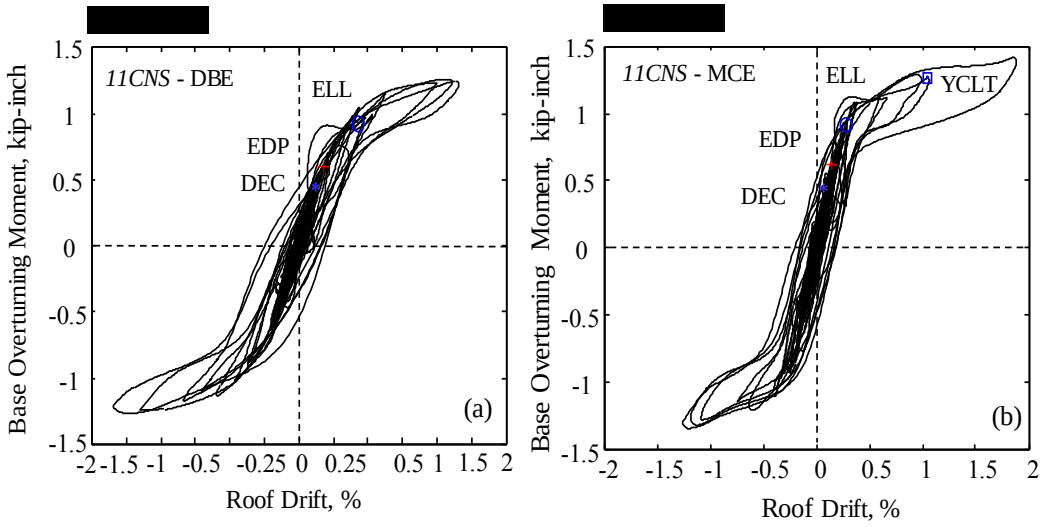

Figure 7.13 M_b vs. Θ_r response of 11CNS under HWA019E scaled to (a) DBE, (b) MCE

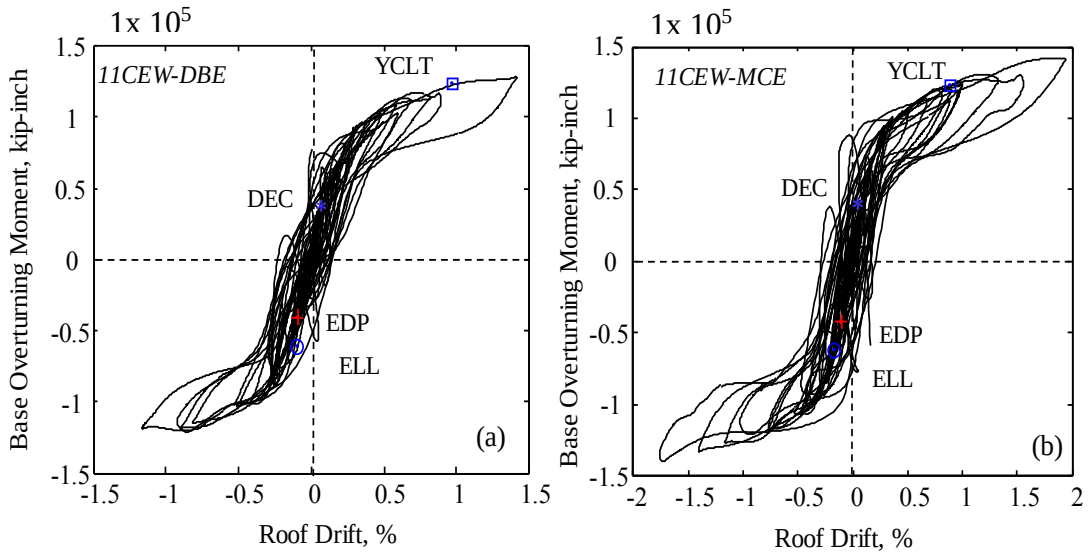

Figure 7.14 M_b vs. Θ_r response of 11CEW under HWA019E scaled to (a) DBE, (b) MCE

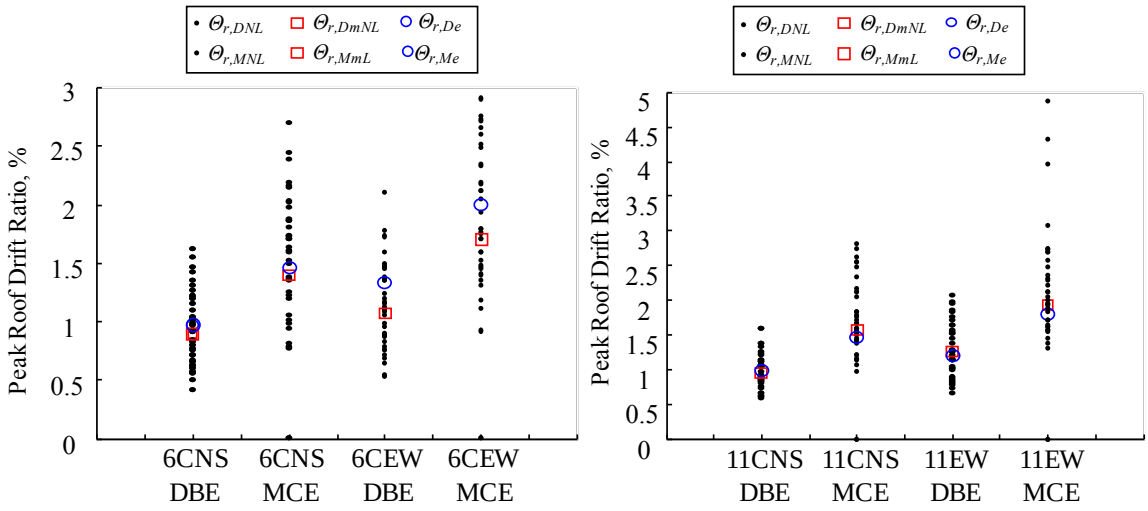

Figure 7.15 Comparison of roof drift demands with NLTHA peak roof drift ratio results

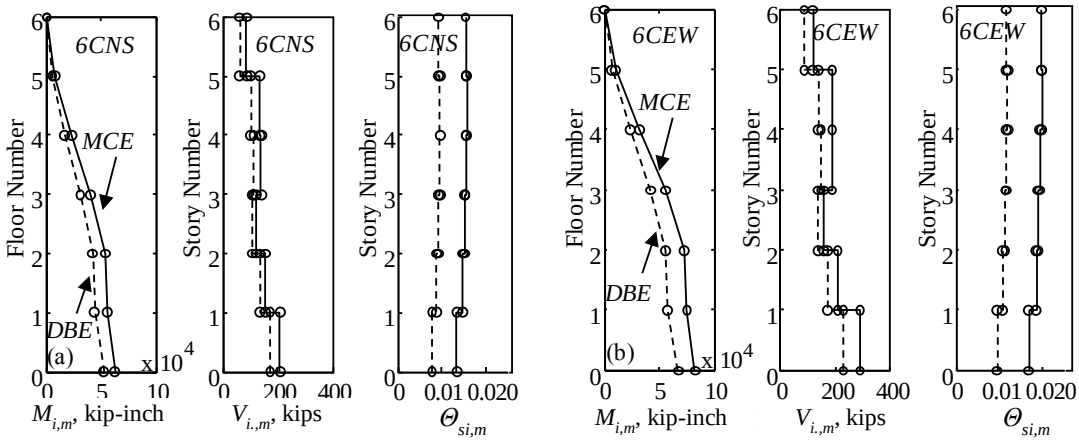

Figure 7.16 Median peak story base moment, story shear, and story drift ratio response envelopes from NLTHA for (a) 6CNS; (b) 6CEW

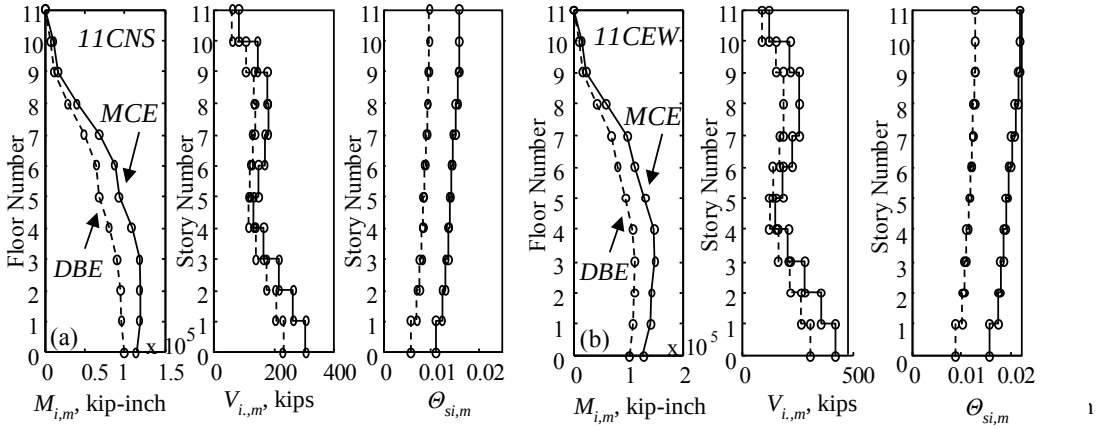

Figure 7.17 Median peak story base moment, story shear, and story drift ratio response envelopes from NLTHA for (a) 11CNS; (b) 11CEW

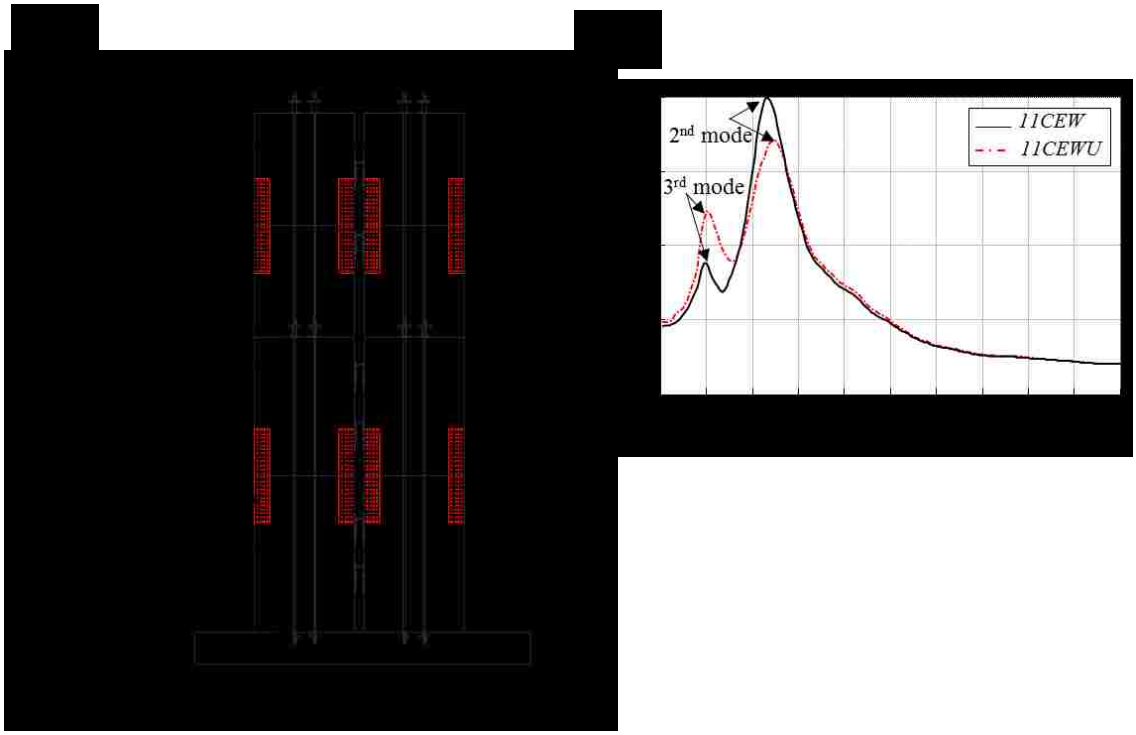

Figure 7.18 (a) Elevation view of 11CEWU; (b) comparison of median peak floor acceleration spectra for 11CEW and 11CEWU

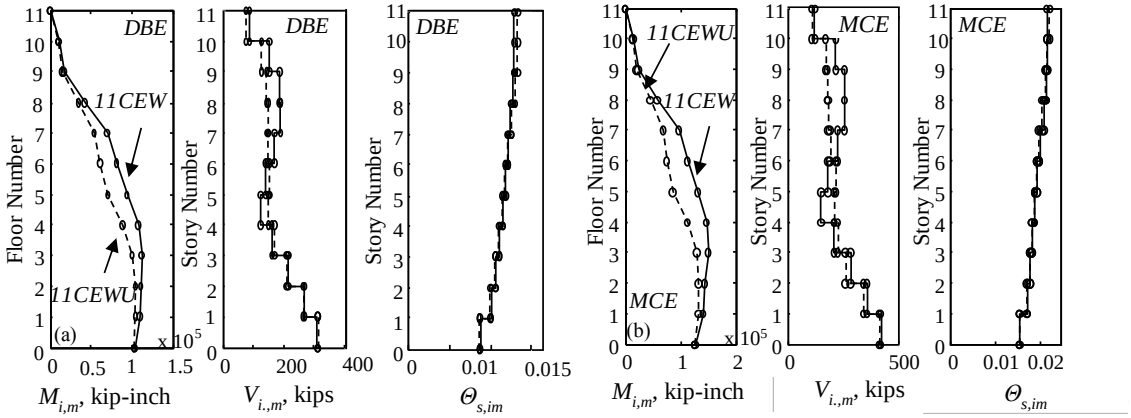

Figure 7.19 Comparison of peak M_m, V_m, and Θ_m response envelopes from NLTHA for 11CEW and 11CEWU under the selected set of ground motions scaled to (a) DBE; (b) MCE level

CHAPTER 8

SUMMARY, CONCLUSIONS, AND FUTURE WORK

This chapter presents a brief summary of the research presented in this dissertation and conclusions drawn from this research. The related research areas needing further investigation are also identified.

8.1. Summary

Chapter 2 presents a study of methods to accurately quantify the 1st and higher (i.e., the nth) mode responses of nonlinear (NL) wall and frame structures. The seismic NL responses of 4-, 9-, and 12-story wall structures and a 9-story, 4-bay SMRF structure to a set of ground motions were studied. Two time-varying response variables, the nth mode effective pseudo-acceleration, $A_{eff_n}(t)$ and the nth mode effective deformation, $D_{eff_n}(t)$, were introduced to quantify the nth mode response of NL multi-degree-of-freedom (MDF) structures. $A_{eff_n}(t)$ and $D_{eff_n}(t)$ are derived from total NL response from nonlinear time history analysis (NLTHA) using a set of mass-orthogonal deformation shapes. A parametric study was implemented to observe the sensitivity of the nth mode seismic response to structural and modal properties of NL cantilever wall structures. Wall structure parameters, such as the

shear stiffness, number of stories, fundamental period, and ductility demand were varied. The contributions of higher mode responses quantified using $A_{eff_n}(t)$ and $D_{eff_n}(t)$, were compared with results from existing methods to estimate the NL modal response including modal response spectrum analysis (MRSA) and uncoupled modal response history analysis (UMRHA).

Chapter 3 presents a study of a consistent approach to quantify the nth mode response of NL structures with clearly defined yielding mechanisms. The seismic responses of NL wall and frame structure were studied. A new approach for quantifying the nth mode seismic response of NL structures with clearly defined yielding mechanisms was presented. In this approach, a set of mode shapes, which are called as *mechanism mode shapes*, $\boldsymbol{\phi}_n^m$, determined after the yielding mechanism forms are used to quantify the nth mode NL seismic response of the structure. The *mechanism mode shapes* were presented as an alternate to the set of linear-elastic mode shapes, $\boldsymbol{\phi}_n^e$. The nth mode response quantified using $\boldsymbol{\phi}_n^e$ which are often used to quantify the model response and $\boldsymbol{\phi}_n^m$ of example structures were compared with each other. The advantages and limitations of $\boldsymbol{\phi}_n^m$ were shown using the nonlinear time history analysis (NLTHA) results.

Chapter 4 presents a study on the modeling of the inherent damping of a building for NL seismic response analysis. The problems from using conventional stiffness proportional linear viscous damping models were presented using NLTHA for a 2-story NL moment

resisting frame (MRF) and a 6-story NL special concentrically braced frame (SCBF). It was proposed to separate the inherent damping model from the model of NL lateral force resisting system (LFRS) by introducing a *damping substructure* to eliminate the generation of artificially large local damping forces due to nonlinearity in the LFRS. Applications of the *damping substructure concept* (DSC) to conventional structures were presented. The DSC was extended to enable the modeling of inherent damping of a building for NL seismic response analysis using NL viscous damping.

Chapter 5 presents a study of methods for controlling the 2nd mode response of NL structures with clearly-defined yielding mechanisms. A rational method for locating and determining the strength of the second flexural yielding mechanisms was established based on the modal properties of NL wall structures. The method developed for NL wall structures was used to design a 9-story self-centering concentrically braced frame (SC-CBF) with base and upper flexural yielding mechanisms. The effect of the upper yielding mechanism on controlling the higher mode response of the SC-CBF was demonstrated using NLTHA results.

Chapter 6 presents a study of the lateral load response of self-centering cross-laminated timber (SC-CLT) walls under quasi-static cyclic loading. A cross laminated timber (CLT) panel is constructed by laminating multiple layers of timber boards, with the boards in adjacent layers oriented in orthogonal directions. SC-CLT walls are constructed by post-tensioning CLT wall panels to the foundation with vertical post-tensioning steel bars. The

seismic lateral load response of SC-CLT walls is dominated by the rocking of the wall on its foundation. Structural limit states of SC-CLT walls under lateral load were identified. The experimental and analytical response of single and multi-panel SC-CLT walls under cyclic lateral loading were investigated and compared to test results. Two types of analytical models were proposed to predict SC-CLT wall response, namely, a design-oriented analytical model based on simple mathematical expressions and a fiber-element-based numerical model. Comparisons between analytical and experimental results for the lateral load response of SC-CLT walls were made.

Chapter 7 presents a study of the seismic response of SC-CLT wall buildings. A seismic design approach and design criteria were proposed for SC-CLT wall buildings. 6- and 11-story SC-CLT prototype walls were presented that were designed in accordance with the design criteria. The effect of wall parameters on the lateral load response of the prototype walls was investigated. A fiber-based analytical model of each prototype wall was developed. The response of each wall under a ground motion set scaled to design basis earthquake (DBE) and maximum considered earthquake (MCE) levels was examined through NLTHA. For an 11-story SC-CLT wall, an upper rocking joint in addition to the base rocking of the wall on the foundation was introduced and designed. Design criteria for the upper rocking joint, were discussed.

8.2. Findings and Conclusions

Findings associated from the work presented in Chapter 2 are as follows:

- For the wall structures, when a mode has a large nth mode contribution to the static base overturning moment response (i.e., $\overline{M}_{bn}$), the corresponding nth mode response is more effectively "controlled" by a base flexural yielding mechanism. In particular, the 1st mode has a large $\overline{M}_{b1}$, and is effectively "controlled" by the base flexural yielding mechanism.
- The higher mode responses of the wall structures, which are not strongly affected by the base flexural yielding mechanism, are sensitive to the characteristics of the ground motion (GM) record.
- The higher mode responses of a special moment frame (SMRF) is not highly sensitive to the GM intensity due to the formation of additional plastic hinges within the height of the structure, in addition to intended beam-sway yielding mechanism of the SMRF.
- The assumption of a conventional MRSA, that the higher mode responses and 1st mode response are equally reduced by the yielding mechanism, which results in the use of a single response modification (R) factor in conventional design practice, is not valid for the wall structures. This finding was also noted in some prior studies (e.g., Eibl and Keintzel, 1988; Rodriguez et al., 2002).
- The results for the wall structures and the SMRF show that the 1st mode response, $A_{eff_1}(t)$, is not accurately "controlled" by the yielding mechanism when the linear-elastic mode shapes, $\boldsymbol{\phi}_n^e$, are used to calculate $A_{eff_1}(t)$. The linear-elastic mode shapes

are orthogonal with respect to the mass and linear elastic stiffness matrices, but they are coupled through the base flexural yielding mechanism.

- To uncouple the modes from the base flexural yielding mechanism, an alternate set of mode shapes, $\boldsymbol{\phi}_n^m$, can be developed by making the 1st mode deformation mode shape equal to the shape of the structure after the yielding mechanism forms.

Findings associated from the work presented in Chapter 3 are as follows:

- When $\boldsymbol{\phi}_n^e$ are used to quantify the nth mode responses, the 1st elastic mode effective pseudo-acceleration response, $A_{eff_1}^e(t)$, has fluctuations during its entire response history, even during times when the yielding mechanism forms. The fluctuations in $A_{eff_1}^e(t)$ indicate that the 1st mode response and the response of the higher modes (i.e., $A_{eff_n}^e(t)$ for n > 1) are coupled through the yielding mechanism.
- The higher mode responses can be decoupled from the 1st mode response using mechanism mode shapes, $\boldsymbol{\phi}_n^m$. When $\boldsymbol{\phi}_n^m$ are used to quantify the nth mode responses, the time of the peak 1st mechanism mode effective pseudo-acceleration response (i.e., the peak $A_{eff_1}^m(t)$) is coincident with the time of the peak base overturning moment response $M_b(t)$, and the times when the yielding mechanism forms can be clearly identified by a flat-topped $A_{eff_1}^m(t)$ history.
- $A_{eff_n}^m$ can be used to *accurately* quantify the 1st mode and higher mode response of a NL structure.
- The 2nd and 3rd mode responses, $A_{eff_2}^e(t)$ and $A_{eff_2}^m(t)$ and $A_{eff_3}^e(t)$ and $A_{eff_3}^m(t)$, were similar to each other (i.e., regardless of whether $\boldsymbol{\phi}_n^m$ or $\boldsymbol{\phi}_n^e$ are used) indicating that

the higher modes are not strongly affected by the formation of the yielding mechanism in the structure.

- When multiple GMs are considered, there is no scatter in the peak value of $A^m_{eff_1}(t)$, denoted as $A^m_{eff_1}$. $A^m_{eff_1}$ precisely equals to $SA_{GM}(T^e_n)/R$. On the other hand, there is significant scatter $A^e_{eff_1}$ (from using $\boldsymbol{\phi}^e_n$).
- For the SC-CBF example structure, differences between $A^e_{eff_n}(t)$ and $A^m_{eff_n}(t)$ are significant due to the base rocking response of the SC-CBF. However, due to variations in the PT bar force as the SC-CBF rocks, $A^m_{eff_1}(t)$ does not have a smooth flat-topped response. When various GM are considered, there is much less scatter in the $A^m_{eff_1}$ values compared to the $A^e_{eff_1}$ values showing that the 1st mode response is observed to be accurately controlled by the yielding mechanism of the SC-CBF (i.e., base rocking motion followed by PT bar yielding), when $\boldsymbol{\phi}^m_n$ are used to quantify the response.
- The NLTHA results for the SMRF example structure show that, even under intense seismic response, an SMRF with numerous stories and bays is unlikely to fully form the intended beam-sway mechanism. Therefore, the SMRF example structure is categorized as a structure which may not develop a clearly defined yielding mechanism for a significant duration of the NLTHA, although significant yielding occurs, and the use of $\boldsymbol{\phi}^m_1$ appears to be less useful for quantifying the NL response.

Findings associated from the work presented in Chapter 4 are as follows:

- Based on the result from NLTHA implemented on 2-story MRF and 6-story SCBF:
    - Initial stiffness proportional Rayleigh damping models, denoted as ζ-k_i, lead to the generation of artificially large local damping forces.
    - All Rayleigh-like stiffness proportional damping models utilized in this study, which are initial-stiffness proportional (ζ-k_i), tangent-stiffness proportional (ζ-k_t), and non-proportional (ζ-k_{NP}) Rayleigh damping models, leads to the loss of static relationships among local forces in the LFRS.
- NLTHA results of the 6-story SCBF show that ζ-k_t promotes brace buckling.
- It is shown that the generation of artificially large local damping forces due to the formation of local yielding mechanisms in the NL LRFS is precluded by separating the inherent damping of the building from the NL LFRS model.
- Using DSC, the static relationships among local forces in the LFRS are preserved.
- DSC is extended to NL viscous damping, which enables the more accurate representation of the inherent damping of a building by limiting the maximum damping forces that can generate in the building. It is shown on case study structures with NL viscous damping models that the peak value of damping forces can be controlled using DSC with NL viscous damping.

Findings associated from the work presented in Chapter 5 are as follows:

- The NL response of wall structures shows that an appropriate location and strength for the upper yielding mechanism can be estimated using the modal properties of the structure. The upper yielding mechanism is observed to be more effective in controlling the 2nd mode response, if its location is determined based on the distribution of elastic story base moment response (from using $\boldsymbol{\phi}_n^e$), rather than mechanism story base moment response (from using $\boldsymbol{\phi}_n^m$).
- It is shown that using an alternate set of mode shapes, determined after both base and upper yielding mechanism have formed and called two-mechanism mode shapes, $\boldsymbol{\phi}_n^{sm}$, the higher mode response (i.e., n > 2) can be uncoupled from the base and upper yielding mechanisms. Therefore, using $\boldsymbol{\phi}_n^{sm}$, the story base moment at the upper hinge location can be expressed in terms of 1st and 2nd mode response.
- It is shown that using $\boldsymbol{\phi}_n^{sm}$, the range of 1st two-mechanism mode effective pseudo acceleration, $A_{eff_1}^{sm}$(from using $\boldsymbol{\phi}_1^{sm}$), and that of the 2nd two-mechanism mode, $A_{eff_2}^{sm}$(from using $\boldsymbol{\phi}_2^{sm}$), can be estimated.
- It is shown that the cumulative 1st and 2nd mode response from NLTHA can be accurately estimated from the estimated range of $A_{eff_1}^{sm}$ and $A_{eff_2}^{sm}$.
- To accurately estimate the median absolute maximum response quantities observed from NLTHA, the 3rd mode response should be taken into account in addition to the cumulative 1st and 2nd mode response.
- To preclude the formation of upper yielding mechanism prior to the base yielding mechanism, the strength of the upper hinge, M_2^h, should have an embedded

overstrength (f_{os}) compared to the pure first mode contribution to the story base moment response at the floor level where the upper yielding mechanism is located. Based on NLTHA results of NL wall structures, M_2^h should 1.1 times greater than the pure first mode contribution (i.e., $f_{os} \geq 1.1$).

- It is observed that the higher mode frequency content of the GM that the NL structure is subjected to also affects how well the second mode response is controlled with the formation of upper yielding mechanism. The upper yielding mechanism is more effective in controlling the second mode response, if the GM that is subjected to has a larger higher mode frequency content.
- For the particular SC-CBFs analyzed in this study, it is observed that the upper the second mode response of SC-CBFs is controlled with the addition of an upper rocking joint in the structure without increasing the story drift demands. It is also observed that despite the reduction on second mode response, third mode response of SC-CBFs is slightly amplified with the addition of an upper rocking joint.

Findings associated from the work presented in Chapter 6 are as follows:

- The base shear (V_b), base overturning moment (M_b), and roof drift ratio (Θ_r) estimates from results closed-form equations (CFE) and the fiber-based numerical model of single- and multi-panel SC-CLTs show a good agreement with the experimental results. These results suggest that the analytical models can be used to estimate the actual lateral load response of single- and multi-panel SC-CLT walls.

- The experimental results showed that the lateral load response of SC- CLT walls is sufficiently ductile to be used as a primary lateral load resisting system in regions of high seismicity.
- Using a structural composite limber (SCL) core CLT panel rather than 5-layer CLT panel is observed to increase the ultimate lateral load capacity of SC- CLT walls, while leading the wall to soften at a smaller drift.
- It is shown that by attaching two CLT wall panels along vertical joints with ductile connectors to form a multi-panel SC-CLT wall, the V_b capacity of the SC-CLT walls can be increased without reducing the ductile Θ_r capacity.
- The use of U-shaped flexural plates (i.e., UFPs) as energy dissipating devices in a multi-panel SC-CLT wall provided additional energy dissipation to the SC-CLT wall system.

Findings associated from the work presented in Chapter 7 are as follows:

- It is observed from the NLTHA results of 6- and 11-story prototype SC-CLT wall buildings that SC-CLT walls perform well under earthquake loading and are a viable alternative to the conventional lateral force resisting systems.
- The primary source of nonlinear drift is observed to be the gap opening along the base of each wall. Even under MCE-level ground motions, the results show that little damage is expected to occur in the SC-CLT walls, which implies a limited post-earthquake repair need.
- It is observed from the NLTHA results for the 11-story SC-CLT wall with base and upper rocking joints that the story base moment and story shear responses decrease

with the addition of an upper rocking joint. It is also observed that the roof level floor accelerations decreases for the SC-CLT wall with base and upper rocking joints compared to the SC-CLT wall with single base rocking joint.

8.3. Original Contributions to the Literature

Chapter 2. The contributions to the literature of the work presented in Chapter 2 are as follows:

- It is demonstrated that the nth mode responses of NL structures are accurately quantified using $A_{eff_n}(t)$ and $D_{eff_n}(t)$.
- It is demonstrated that important force and deformation response quantities can be rigorously expressed (and clearly understood) as individual modal contributions using $A_{eff_n}(t)$ and $D_{eff_n}(t)$, respectively.
- Two time varying modal parameters, $A_{eff_n}(t)$ and $D_{eff_n}(t)$, were introduced to accurately quantify the nth mode response of a NL structure. It is shown that $A_{eff_n}(t)$ and $D_{eff_n}(t)$ are useful for understanding and comparing the nth mode response.
- Numerous comparisons of $A_{eff_n}(t)$ and $D_{eff_n}(t)$ results for the example structures enabled the accuracy of the assumptions made in conventional MRSA and UMRHA to be evaluated.
- A parametric study showed the effects of wall structure deformation type (shear-dominated, flexural-dominated), number of stories in the wall structure, and level of ductility demand on $A_{eff_n}(t)$ and $D_{eff_n}(t)$.

Chapter 3. The contributions to the literature of the work presented in Chapter 3 are as follows:

- It is demonstrated that for structures which form clearly-defined yielding mechanisms, higher mode responses can be decoupled from the yielding mechanism using mechanism mode shapes. Results show that the 1st mode response becomes precisely dependent on yielding mechanism.
- The advantages and disadvantages of mechanism mode shapes compared to elastic mode shapes are critically examined by comparing the accuracy of the nth mode response quantifications for NL wall and frame structures.

Chapter 4. The contributions to the literature of the work presented in Chapter 4 are as follows:

- It is shown that by using a *damping substructure* to model the inherent damping of a building for NL seismic response history analysis the static relationships among local forces in the LFRS are preserved during the NLTHA.
- It is shown that damping substructure concept can be used to model the inherent damping of a building for NL seismic response history analysis using NL viscous damping, which enables a more realistic representation of the inherent damping of a building compared to linear viscous damping.

Chapter 5. The contributions to the literature of the work presented in Chapter 5 are as follows:

- It is demonstrated that the location and strength of a second flexural yielding mechanisms can be determined using the modal properties of the structure.
- It is demonstrated that the strength of the base and upper hinges bound the 1st and 2nd mode response amplitudes and using the bounds on 1st and 2nd mode response amplitudes, the maximum absolute values of important force response quantities can be estimated.

Chapter 6. The contributions to the literature of the work pres ented in Chapter 6 are as follows:

- A design-oriented analytical model based on simple mathematical expressions and a fiber-element-based numerical model which provide accurate estimates of the lateral load response of SC-CLT walls under cyclic loading are developed.
- The limit states for single- and multi-panel SC-CLT walls are identified.

Chapter 7. The contributions to the literature of the work presented in Chapter 7 are as follows:

- Seismic design criteria have been developed for SC-CLT wall buildings with vertical joints and ductile connectors and NLTHA results demonstrate the effectiveness of the criteria for the prototype structures.

- An upper rocking joint is introduced to 11-story SC-CLT wall, in addition to the base rocking joint. The effect of upper rocking joint in controlling the higher mode response and median peak structural response envelopes is examined.

8.4. Future Work

Chapter 2. The future work associated with the study presented Chapter 2 is as follows:

- To evaluate the broad applicability of $A_{eff_n}(t)$ and $D_{eff_n}(t)$, the nth mode response of a wider range of NL MDF structures should be quantified using $A_{eff_n}(t)$ and $D_{eff_n}(t)$.
- The quantifications made by using $A_{eff_n}(t)$ and $D_{eff_n}(t)$ should be compared with existing methods in addition to the conventional MRSA; for example, with those of based on multi-modal and adaptive pushover analyses (e.g., Gupta and Kunnath, 2000; Antoniou and Pinho, 2004).

Chapter 3. The future work associated with the study presented Chapter 2 is as follows:

- For structures do not form a clear yielding mechanism, so that we can define a unique set of ϕ_n^m (e.g. SMRFs), the use of ϕ_n^m should be critically evaluated and the existence of some other alternate mode shapes to quantify and understand the nth mode response of NL structure should be investigated.

Chapter 4. The future work associated with the study presented Chapter 4 is as follows:

- Further research is needed to study the limitations of the damping substructure concept and potentially to improve the damping substructure concept with NL viscous damping.
- Damping substructure concept presented here should be validated for buildings with different configurations, types, floor plans, and seismic conditions need to be analyzed using a *damping substructure* to develop general conclusions regarding the usefulness of damping substructure concept.

Chapter 5. The future work associated with the study presented Chapter 5 is as follows:

- The design approach presented here for the SC-CBFs with base and upper rocking joints should be validated for buildings with different floor plans and seismic conditions to develop general conclusions regarding the seismic behavior of SC-CBFs with base and upper rocking joints and the validity of the design approach presented here.

Chapter 6. The future work associated with the study presented Chapter 6 is as follows:

- Further research is needed to study and potentially improve the CLT material model used in the analytical studies presented herein. Advances over the elastic-perfectly plastic model for the CLT material in compression and the linear-elastic shear force-deformation response of the CLT panel are needed.

- The TS of this study was 0.40 scale of the prototype wall. TS with a larger scale factor can be constructed and tested to better simulate the lateral load response of the SC-CLT walls.

Chapter 7. The future work associated with the study presented Chapter 7 is as follows:

- Seismic design approach presented here should be validated for buildings with different floor plans and seismic conditions to develop general conclusions regarding the seismic behavior of SC-CLT walls and the validity of the design approach presented here.
- Further research is needed to further investigate the seismic response of SC-CLT walls with base and upper yielding mechanism. The effect of second yielding mechanism/ rocking joint on controlling the higher mode response should be further studied.

REFERENCES

AISC (2010). "Seismic Provisions for Structural Steel Buildings," *American Institute of Steel Construction*, Chicago, IL, USA.

Amini, M. O., van de Lindt, J. W., Pei, S., Rammer, D., Line, P., and Popovski, M. (2014). "Overview of a project to quantify seismic performance factors for cross laminated timber structures in the United States," *Materials and Joints in Timber Structure*s. Springer, Netherlands, pp. 531-541.

Antoniou, S. and Pinho, R. (2004) "Advantages and limitations of adaptive and non-adaptive force-based pushover procedures*," Journal of Earthquake Engrg.*, 8(4), pp. 497–522.

APA-The Engineered Wood Association (2011). Engineered Wood Construction Guide Excerpt: Structural Composite Lumber. Form E30.

ASCE (2010). "Minimum Design Loads for Buildings and Other Structures," *ASCE7-10*, Reston, VA, USA.

Baker, J.W. (2011). "Conditional Mean Spectrum: Tool for Ground-Motion Selection," *Journal of Structural Engrg.*, 137(3), pp 322-331.

Bernal, D. (1994). "Viscous Damping in Inelastic Structural Response," *Journal of Structural Engrg.*, 120(4), pp. 1240-1254.

Blakeley, R. W. G., Cooney, R. C., and Megget, L. M. (1975). "Seismic shear loading at flexural capacity in cantilever wall structures," *Bulletin of the New Zealand National Society for Earthquake Engrg.*, 8(4), pp. 278-290.

Bracci, J. M., Kunnath, S. K. and Reinhorn, A. M. (1997). "Seismic Performance and Retrofit Evaluation for Reinforced Concrete Structures," *Journal of Structural Engrg.*, 123(1), pp. 3-10.

Bogensperger, T., Moosbrugger, T., Silly, G. (2010). "Verification of CLT-plates under Loads in Plane," *Proc. of the 11th World Conf. on Timber Engrg*, Riva del Garda, Italy, June 20-24.

Bowland, A. and Charney, F. (2010). "New Concepts in Modeling Damping in Structures," *Proc. of the Structures Congress 2010 at 19th Analysis and Computation Specialty Conference*, Orlando, FL, May 12-15.

BSSC (2003). "NEHRP Recommended Provisions for Seismic Regulations for New Buildings and Other Structures," *Building Seismic Safety Council, National Institute of Building Sciences, FEMA-450*, Washington, DC, USA.

Calugaru, V. and Panagiotou, M. (2010). "Seismic Isolation Using Single and Dual Shear Hinging of Tall Cantilever Wall Buildings Subjected to Near Fault Ground Motions," *Proc. of the 9th US National and 10th Canadian Conference on Earthquake Engrg.*, Toronto, Canada. July 25-29.

Ceccotti, A., Lauriola, M., Pinna, M., Sandhaas, C. (2006). "SOFIE Project Cyclic Tests on Cross-laminated Wooden Panels," *Proc. of the 9th World Conf. on Timber Engrg.*, Portland, Oregon, USA, June 20-24.

Chang, S. Y. (2013). "Nonlinear Performance of Classical Damping." *Earthquake Engrg. and Engrg. Vibration*, 12(2), pp. 279-296.

Chancellor, N.B. (2014). "Seismic Design and Performance of Self-Centering Concentrically-Braced Frames", Ph.D. Dissertation, Dept. of Civil and Env. Engrg., Lehigh Univ., Bethlehem, PA, USA.

Chancellor, N.B., Sause, R., Ricles, J.M., Tahmasebi, E., and Akbas, T. (2013). "Seismic Response of Post-Tensioned Steel Rocking Concentrically Braced Frames with Various Aspect Ratios," COMPDYN 2013, Proc. of the 4th ECCOMAS Thematic Conference on Computational Methods in Structural Dynamics and Earthquake Engrg., Kos Island, Greece. June 12-14.

Charney, F. A. (2008). "Unintended Consequences of Modeling Damping in Structures," *Journal of Structural Engrg.*, 134(4), pp. 581-592.

Chao, S. H., Goel, S. C., and Lee, S. S. (2007). "A seismic design lateral force distribution based on inelastic state of structures," *Earthquake Spectra*, 23(3), pp. 547-569.

Chopra, A. K. (2012). *Dynamics of structures*. (4th ed.). Prentice Hall, New Jersey, NJ.

Chopra, A. K. and Goel, R. K. (2002). "A modal pushover analysis procedure for estimating seismic demands for buildings," *Earthquake Engrg. and Structural Dynamics*, 31(3), pp. 561-582.

Chopra, A. K., Goel, R. K., and Chintanapakdee, C. (2004). "Evaluation of a modified MPA procedure assuming higher modes as elastic to estimate seismic demands," *Earthquake Spectra*, 20(3), pp. 757-778.

Clough, Ray W. "On the importance of higher modes of vibration in the earthquake response of a tall building." *Bulletin of the Seismological Society of America* 45 (1955), pp. 289-301.

Derecho, A. T., Ghosh, S. K., Iqbal, M., Freskakis, G. N., and Fintel, M. (1978). "Structural walls in earthquake-resistant buildings–analytical investigations, dynamic analysis of isolated structural walls–parametric studies," Final Report to the National Science Foundation, Portland Cement Association, Skokie, IL, USA.

Dujic B., Klobcar S., Zarnic, R. (2008). "Shear Capacity of Cross-Laminated Wooden Walls," *Proc. of the 10th World Conf. on Timber Engrg.*, Myazaki, Japan, June 2-5.

Dunbar, A., Moroder, D., Pampanin, S., Buchanan, A. (2014). "Timber Core-Walls for Lateral Load Resistance of Multi-Storey Timber Buildings," *Proc. of the 13th World Conf. on Timber Engrg.*. Quebec, Canada, Aug. 10-14.

Eatherton, M.R.; Hajjar, J.F. (2010). "Residual Drifts of Self-Centering Systems Including Effects of Ambient Building Resistance," *Earthquake Spectra*, 27(3), pp. 719-744.

Eberhard, M. O. and Sozen, M. A. (1993). "Behavior-based method to determine design shear in earthquake-resistant walls," *Journal of Structural Engrg.*, 119(2), pp. 619-640.

Eibl, J. and Keintzel, E. (1988). "Seismic shear forces in RC cantilever shear walls," *Proc. of the 9th World Conference on Earthquake Engrg. (vol. VI)*, Tokyo-Kyoto, Japan, August 2-9.

Elnashai, A. S. (2000). "Advanced Static Inelastic (pushover) Analysis for Seismic Design and Assessment," *Proc. of the George Penelis Symposium on Concrete and Masonry Structures*, Aristotle Univ. of Thessaloniki, Thessaloniki, Greece, October, pp. 23-34.

Erduran, E. (2012). "Evaluation of Rayleigh proportional damping and its Influence on Engineering Demand Parameter Estimates," *Earthquake Engrg. and Structural Dynamics*, 41(14), pp. 1905-1919.

Federal Emergency Management Agency (2000). "Recommended Seismic Design Criteria for New Steel Moment Frame Buildings," *Prepared for the Federal Emergency Management Agency for FEMA, FEMA-350*, Washington, DC, USA.

FEMA (2009). "Quantification of building seismic performance factors." Report No. FEMA P695, *Federal Emergency Management Agency*, Washington, DC, USA.

Flaig M., Blass H. J. (2013). "Shear Strength and Shear Stiffness of CLT-beams Loaded in Plane," *Proc. of the CIB-W18 Meeting 46*, Vancouver, Canada, Aug. 26-29.

Ganey, R. (2015). "Seismic Design and Testing of Rocking Cross Laminated Timber Walls," M.Sc. Thesis, Department of Civil and Environmental Engrg., *Univ. of Washington, Seattle, USA.*

Gupta, B. and Kunnath, S. K. (2000). "Adaptive spectra-based pushover procedure for seismic evaluation of structures," *Earthquake Spectra*, 16(2), pp. 367-392.

Hall, J. F. (2006). "Problems Encountered from the Use (or Misuse) of Rayleigh proportional damping," *Earthquake Engrg. and Structural Dynamics*, 35(5), pp. 525-545.

Jehel, P., Léger, P., and Ibrahimbegovic, A. (2014). "Initial versus Tangent Stiffness-based Rayleigh proportional damping in Inelastic Time History Seismic Analyses." *Earthquake Engrg. and Structural Dynamics*, 43(3), pp. 467-484.

Kabeyasawa, T. and Ogata, K. (1984). "Ultimate-state design of RC wall-frame structures," *Transaction of the Japan Concrete Institute*, 6, pp. 629- 636.

Kalkan, E. and Kunnath, S.K. (2006). "Adaptive Modal Combination Procedure for Nonlinear Static Analysis of Building Structures," *Journal of Structural Engrg.*, 132(11), pp. 1721-1732.

Karacabeyli, E., Douglas, B. (Eds.). (2013). CLT Handbook: Cross-laminated Timber- US Edition. FPInnovations.

Karamanci, E., and Lignos, D. G. (2014). "Computational Approach for Collapse Assessment of Concentrically Braced Frames in Seismic Regions," *Journal of Structural Engrg.*, 140(8), pp. A4014019 1-15.

Kelly, J. M., Skinner, R. I., and Heine, A. J. (1972). "Mechanism of Energy Absorption in Special Devices for Use in Earthquake Resistant Structures," *Bulletin New Zealand Society of Earthquake Engrg.*, 5(3), pp. 63-88.

Kurama, Y. C., Pessiki, S., Sause, R., Lu, L. W., El-Sheikh, M. (1996). "Analytical Modeling and Lateral Load Behavior of Unbonded Post-Tensioned Precast Concrete Walls," Research Report, No. EQ-96-02, Department of Civil and Environmental Engrg., Lehigh Univ., Bethlehem, PA, USA.

Kurama, Y. C. (1997). "Seismic Analysis, Behavior, and Design of Unbonded Post-Tensioned Precast Concrete Walls," Ph.D. Dissertation, Department of Civil and Environmental Engrg., Lehigh Univ., Bethlehem, PA, USA.

Kurama, Y.; Pessiki, S.; Sause, R.; and Lu, L.-W. (1999a). "Seismic Behavior and Design of Unbonded Post-Tensioned Precast Concrete Walls," *PCI Journal*, 44(3), pp 72-89.

Kurama, Y.; Pessiki, S.; Sause, R.; and Lu, L.-W. (1999b). "Lateral Load Behavior and Seismic Design of Unbonded Post-Tensioned Precast Concrete Walls," *ACI Structural Journal*, 96(4), pp 622-632.

Ma, X.; Eatherton, M.; Hajjar, J.; Krawinkler, H.; and Deierlein, G. (2010). "Seismic Design and Behavior of Steel Frames with Controlled Rocking – Part II: Large Scale Shake Table Testing and System Collapse Analysis," *Proc. of the ASCE/SEI Structures Congress 2010*, Orlando, FL, May 12-15.

Mazzoni, S., McKenna, F., Scott, M.H., Fenves, G.L., et al. (2009). "Open System for Earthquake Engrg. Simulation (OpenSEES) User Command-Language Manual*,"*

Pacific Earthquake Engrg. Research Center, Univ. of California, Berkeley, CA, USA.

Pacific Earthquake Engrg. Research Center (PEER) (2011). "Ground motion database flatfile," Retrieved from http://peer.berkeley.edu/nga/flatfile.html on December 12, 2013.

Pampanin, S., Palermo, A., Buchanan, A. H., Fragiacomo, M., Deam, B. L. (2006). "Code Provisions for Seismic Design of Multi-Storey Post-tensioned Timber Buildings," *Proc. of the International Council for Research and Innovation in Building and Construction--Working Commission W18--Timber Structures*, Florence, Italy, Aug. 22-26.

Panagiotou, M., & Restrepo, J. I. (2009). "Dual-plastic Hinge Design Concept for Reducing Higher-Mode effects on High-Rise Cantilever Wall Buildings," Earthquake Engrg. and Structural Dynamics, 38(12), 1359.

Paulay, T. and Priestley, M.J.N. (1992). *Seismic design of reinforced concrete and masonry buildings*. Wiley, New York, NY, USA.

Pei, S., van de Lindt, J. W., and Popovski, M. (2012). "Approximate R-factor for cross-laminated timber walls in multistory buildings," *Journal of Architectural Engrg.*, 19(4), pp. 245-255.

Perez, F. J. (2004). "Experimental and Analytical Lateral Load Response of Unbonded Post-Tensioned Precast Concrete Walls," Ph.D. Dissertation, Department of Civil and Environmental Engrg., Lehigh Univ., Bethlehem, PA, USA.

Perez, F. J., Sause, R., and Pessiki, S. (2007). "Analytical and Experimental Lateral Load Behavior of Unbonded Post-Tensioned Precast Concrete Walls," *Journal of Structural Engrg., American Society of Civil Engineers*, 133(11), pp. 1531-1540.

Priestley, M.J.N. (2003). "Does capacity design do the job? An investigation of higher modes effects in cantilever walls," *Bulletin of the New Zealand Society for Earthquake Engrg.*, 36(4), pp. 276-292.

Priestley, M.J.N. and Amaris, A. (2003). "Dynamic amplification of seismic moments and shear forces in cantilever walls," *Proc. of the fib symposium on concrete structures in seismic regions*, Athens, Greece, May 6-8.

Popovski, M., Karacabeyli, E., Ceccotti, A. (2011). "Seismic performance of cross-laminated timber buildings," Chapter 4 in CLT handbook: Cross-laminated timber - Canadian Edition, Quebec, Canada.

Powell, J.A. (2009). "Evaluation of Special Concentrically Braced Frames for Improved Seismic Performance and Constructability." M.S. Thesis, Dept. of Civil and Environmental Engrg., Univ. of Washington, Seattle, WA, USA.

Rodriguez, M. E., Restrepo, J. I., and Carr, A. J. (2002). "Earthquake-induced floor horizontal accelerations in buildings," *Earthquake Engrg. and Structural Dynamics*, 31(3), pp. 693-718.

Roke, D., Sause, R., Ricles, J. M., and Chancellor, N.B. (2010). "Damage- Free Seismic-Resistant Self-Centering Concentrically-Braced Frames." ATLSS Report 10-09, ATLSS Engrg. Research Center, Lehigh Univ., Bethlehem, PA, USA..

Roke, D. A. (2010). "Damage-Free Seismic-Resistant Self-Centering Concentrically-Braced Frames," Ph.D. Dissertation, Dept. of Civil and Environmental Engrg., Lehigh Univ., Bethlehem, PA, USA.

Seo, C.-Y., Lin, Y.C., Sause, R., and Ricles, J.M., (2012), "Development of Analytical Models and Performance Evaluation for 0.6 Scale Self-Centering MRF with 355 Web Friction Devices," ATLSS Engrg. Research Center, Lehigh Univ., Bethlehem, PA, USA.

Sullivan, T. J., Priestley, M. J. N., and Calvi, G. M. (2008). "Estimating the higher-mode response of ductile structures," *Journal of Earthquake Engrg., ASCE*, 12(3), pp. 456-472.

Tahmasebi, E. (2016). "Damage Analysis of Steel Concentrically Braced Frame Systems Under Seismic Conditions," Ph.D. Dissertation, Dept. of Civil and Environmental Engrg., Lehigh Univ., Bethlehem, PA, USA.

Villaverde, R. (1991). "Explanation for the Numerous Upper Floor Collapses During the 1985 Mexico City Earthquake," *Earthquake Engrg. and Structural Dyn*amics, 20, pp. 223–241.

Wiebe, L. and Christopoulos, C. (2009). "Mitigation of Higher Mode Effects in Base-rocking Systems by Using Multiple Rocking Sections," *Journal of Earthquake Engrg.*, 13(S1), pp. 83-108.

Wiebe, L., Christopoulos, C., Tremblay, R., & Leclerc, M. (2013). "Mechanisms to Limit Higher Mode Effects in a Controlled Rocking Steel Frame. 1: Concept, Modelling,

and Low-Amplitude Shake Table Testing," *Earthquake Engrg. and Structural Dynamics*, 42(7), pp. 1053-1068.

Wilson, E. L. (1998). *Three dimensional static and dynamic analysis of structures: a physical approach with emphasis on earthquake engineering*. Computers and Structures Inc., Berkeley, CA, USA.

APPENDIX A

DERIVATION OF MECHANISM MODE SHAPES

A.1. Derivation of Mechanism Mode Shapes for NL MDF Structure from Elastic Structural Stiffness Matrix

This section presents a method to derive the mechanism mode shapes, $\boldsymbol{\phi}_n^m$, and mechanism stiffness matrix of the structure, $\boldsymbol{k}_m$ from the initial elastic structural stiffness matrix, $\boldsymbol{k}$, and the pre-defined first mechanism mode shape, $\boldsymbol{\phi}_1^m$.

A simple cantilever wall structure with a single base flexural yielding hinge at the base is used as an example.

To derive $\boldsymbol{\phi}_n^m$ and $\boldsymbol{k}_m$ from $\boldsymbol{k}$ and the assumed $\boldsymbol{\phi}_1^m$, the following conditions should be satisfied:

Condition 1: After the yielding mechanism has formed, the structure has no restoring force when it is displaced by the mechanism shape, that is $\boldsymbol{\phi}_1^m$, since $\boldsymbol{\phi}_1^m$ should provide rigid body motion:

$$\boldsymbol{k}_m \boldsymbol{\phi}_1^m = 0 \tag{A.1}$$

Condition 2: $\boldsymbol{k}_m$ should be symmetric.

$$\boldsymbol{k}_m = \boldsymbol{k}_m^T \tag{A.2}$$

Condition 3: $\boldsymbol{k}_m$ is non-zero.

$$\boldsymbol{k}_m \neq \mathbf{0} \tag{A.3}$$

The derivation is as follows:

The change in stiffness with the formation of mechanism is denoted as $\Delta\boldsymbol{k}$. $\boldsymbol{k}_m$ is obtained by subtracting $\Delta\boldsymbol{k}$ from the initial linear-elastic stiffness matrix ($\boldsymbol{k}$).

$$\boldsymbol{k}_m = \boldsymbol{k} - \Delta\boldsymbol{k} \tag{A.4}$$

Substituting Eq. (A.4) into Eq. (A.5):

$$(\boldsymbol{k} - \Delta\boldsymbol{k})\boldsymbol{\phi}_1^m = 0 \tag{A.5}$$

Moving $(\Delta\boldsymbol{k})\,\boldsymbol{\phi}_1^m$ to the right side:

$$\boldsymbol{k}\,\boldsymbol{\phi}_1^m = (\Delta\boldsymbol{k})\boldsymbol{\phi}_1^m \tag{A.6}$$

The first mechanism mode stiffness, $\widetilde{K_1}$, is as follows:

$$\widetilde{K_1} = (\boldsymbol{\phi}_1^m)^T \boldsymbol{k}\,\boldsymbol{\phi}_1^m \tag{A.7}$$

Multiplying and dividing the left-hand side of Eq. (A.6) by $\widetilde{K_1}$, result is:

$$\boldsymbol{k}\,\boldsymbol{\phi}_1^m \frac{\widetilde{K_1}}{\widetilde{K_1}} = (\Delta \boldsymbol{k})\boldsymbol{\phi}_1^m \tag{A.8}$$

$$\frac{1}{\widetilde{K_1}}\boldsymbol{k}\,\boldsymbol{\phi}_1^m((\boldsymbol{\phi}_1^m)^T\boldsymbol{k}\,\boldsymbol{\phi}_1^m) = (\Delta \boldsymbol{k})\,\boldsymbol{\phi}_1^m$$

$$\left(\frac{1}{\widetilde{K_1}}\boldsymbol{k}\,\boldsymbol{\phi}_1^m(\boldsymbol{\phi}_1^m)^T\boldsymbol{k}\right)\boldsymbol{\phi}_1^m = (\Delta \boldsymbol{k})\,\boldsymbol{\phi}_1^m$$

Now, $\Delta\boldsymbol{k}$ can be expressed in terms of $\widetilde{K_1}$, $\boldsymbol{k}$, and $\boldsymbol{\phi}_1^m$:

$$\Delta\boldsymbol{k} = \frac{1}{\widetilde{K_1}}\boldsymbol{k}\,\boldsymbol{\phi}_1^m(\boldsymbol{\phi}_1^m)^T\boldsymbol{k} \tag{A.9}$$

The force corresponding to mechanism, $\boldsymbol{F}_1^m$ can be written as follows:

$$\boldsymbol{F}_1^m = \boldsymbol{k}\,\boldsymbol{\phi}_1^m \tag{A.10}$$

By replacing $\boldsymbol{k}\boldsymbol{\phi}_1^m$ in Eq. (A.9) with $\boldsymbol{F}_1^m$, $\Delta\boldsymbol{k}$ can be rewritten as

$$\Delta\boldsymbol{k} = \frac{1}{\widetilde{K_1}}\boldsymbol{F}_1^m\boldsymbol{F}_1^{mT} \tag{A.11}$$

Substituting into Eq. (A.4), $\boldsymbol{k}_m$ can be expressed in terms of $\boldsymbol{k}$, $\boldsymbol{\phi}_1^m$, and $\widetilde{K_1}$:

$$\boldsymbol{k}_m = \boldsymbol{k} - \frac{1}{\widetilde{K_1}}\boldsymbol{k}\,\boldsymbol{\phi}_1^m(\boldsymbol{\phi}_1^m)^T\boldsymbol{k} \tag{A.12}$$

or, in terms of $\boldsymbol{F}_{m_1}$ and $\widetilde{K_1}$:

$$\boldsymbol{k}_m = \boldsymbol{k} - \frac{1}{\widetilde{K_1}}\boldsymbol{F}_1^m\boldsymbol{F}_1^{mT} \tag{A.13}$$

A.2. Checking that Conditions Are Satisfied

Checking Condition 1

$$\boldsymbol{k}_m\,\boldsymbol{\phi}_1^m = (\boldsymbol{k} - \Delta\boldsymbol{k})\boldsymbol{\phi}_1^m$$

$$= \boldsymbol{k}\,\boldsymbol{\phi}_1^m - \frac{1}{\widetilde{K_1}}\boldsymbol{k}\,\boldsymbol{\phi}_1^m((\boldsymbol{\phi}_1^m)^T\boldsymbol{k}\,\boldsymbol{\phi}_1^m)$$

$$= \boldsymbol{k}\,\boldsymbol{\phi}_1^m - \frac{1}{\widetilde{K_1}}\boldsymbol{k}\,\boldsymbol{\phi}_1^m\widetilde{K_1}$$

$$= \boldsymbol{k}\,\boldsymbol{\phi}_1^m - \boldsymbol{k}\,\boldsymbol{\phi}_1^m$$

$$\boldsymbol{k}\,\boldsymbol{\phi}_1^m = \mathbf{0}$$

Checking Condition 2

Since $\Delta\boldsymbol{k}$ and $\boldsymbol{k}$ are symmetric, $\boldsymbol{k}_m$ is also symmetric.

$$\boldsymbol{k}_m = \boldsymbol{k} - \Delta\boldsymbol{k}$$

Checking Condition 3

Since $\Delta\boldsymbol{k} \neq \boldsymbol{k}$, $\boldsymbol{k}_m \neq \mathbf{0}$

APPENDIX B

CLOSED-FORM EXPRESSIONS TO ESTIMATE THE BASE SHEAR, BASE OVERTURNING MOMENT, AND ROOF DRIFT CAPACITIES OF SINGLE-PANEL AND MULTI-PANEL SC-CLT WALLS

B.1. Introduction

The closed-form expressions (CFE) derived for unbonded post-tensioned concrete walls (Kurama et al. 1997; Perez et al. 1999) using simple section analyses, are adapted for single and multi-panel SC-CLT walls to estimate the base overturning moment (M_b), base shear (V_b), and roof drift (Θ_r) capacities at the identified structural limit states, which are DEC, EDP, ELL, YCLT, SCLT, CCLT, and LLP.

Figure B.1 shows the forces acting on a multi-panel SC-CLT wall: (1) the external lateral loads, $F_{k,n}$, are assumed to act at each floor level- where k refers to the panel number for the coupled configuration and n refers to the floor number; (2) the resisting base shear force for each wall panel, $V_{b,k}$; (3) the resisting base overturning moment for each wall panel, $M_{b,k}$; (4) The gravity load resultant on each panel, $N_{g,k} = \sum_{i=1}^{N} N_{g,i}^{panel}$, which is the sum of the gravity load acting on each wall panel at floor level i, is assumed to act at the center of the wall; (5) the post-tensioning forces, T_{p1} and T_{p2}, from the PT bars located at an

eccentricity of e_{pt} to the left and right hand side of the centerline of the wall; (6) the resultant compression force of each CLT panel, C_k, for a contact length of c; (7) the shear force provided by each vertical joint connector (e.g. U-shaped flexural plates (UFP), if any exists), F_{ufp}. In Figure B.1, the length of the wall is denoted as l_w and the height of the building is denoted as H_w. It is assumed that each panel comprising the multi-panel SC-CLT wall are identical.

The lateral load on each wall panel at floor level i can be expressed in terms of the total base shear of the wall, V_b:

$$F_{1,i} = r_{F_i} V_{b,1} \text{ for panel 1 in Figure B.1} \quad \text{(B.1a)}$$

$$F_{2,i} = r_{F_i} V_{b,2} \text{ for panel 2 in Figure B.1} \quad \text{(B.1b)}$$

The height of the wall up to floor level i, H_i, can be expressed in terms of the total height of the wall, H_w:

$$H_i = r_{Hi} H_w \quad \text{(B.2)}$$

Several assumptions were made in CFE. It is assumed that plane horizontal sections within the CLT panel remain plane. The out-of-plane deformations are not considered, and it is assumed that the wall is subjected to only in-plane axial, flexural, and shear deformations. The wall is assumed to be braced against out-of-plane deformations. The foundation is assumed to be rigid. Based on the material tests performed at WSU (Ganey et al., 2015),

where the CLT material specimens showed nearly elastic-perfectly plastic (EPP) behavior under compression up to a measured average strain value 0.02 in/in, the compressive behavior of the composite CLT section is idealized as EPP. The height of the failure zone of the CLT panel, H_{cr}, which is needed to determine Θ_r (Kurama et al., 1999) is also assumed to be two times the thickness of the CLT panel, t_w.

In CFE, the yield deformation ($\Delta_{ufp,y}$), stiffness ($k_{0,ufp}$), yield foce ($F_{ufp,y}$), plastic force ($F_{ufp,p}$), and plastic deformation ($\Delta_{ufp,p}$) for each UFP are estimated from the thickness (t_{ufp}), width(b_{ufp}), and diameter (D_{ufp}) of the UFP (as shown in Figure 7.1) made of a steel with a yield stress of $f_{y,ufp}$ and a modulus of elasticity of E_{ufp}, using the equations derived by Kelly et al. (1975) as follows:

$$\Delta_{ufp,y} = \frac{27\pi F_{ufp,y} D_{ufp}}{16 E_{ufp} b_{ufp} t_{ufp}^3} \tag{B.3}$$

$$k_{0,ufp} = \frac{16 E b_{ufp}}{27\pi} \left(\frac{t_{ufp}}{D_{ufp}}\right)^3 \tag{B.4}$$

$$F_{ufp,p} = \frac{f_{y,ufp} b_{ufp} t_{ufp}^2}{2 D_{ufp}} \tag{B.5}$$

$$F_{ufp,y} = \frac{2}{3} F_{ufp,p} \tag{B.6}$$

$$\Delta_{ufp,p} = \frac{F_{ufp,p}}{k_{0,ufp}} \tag{B.7}$$

In CFE, the tensile behavior of the PT steel and the UFPs are idealized as bilinear elastic perfectly plastic. The post-yield slope for the PT steel is assumed as 2%. It is assumed that

the UFP starts yielding at $F_{ufp,p}$ (Eq.(B.5)) and gravity load resultant for each panel is equal (i.e., $N_{g,1} = N_{g,2} = N_g$).

B.2. Closed-Form Expressions for Multi-Panel SC-CLT walls

This section derives the CFE to estimate the V_b, M_b, and Θ_r for DEC, ELL, YCLT, SCLT, CCLT, and LLP limit states.

Decompression (DEC)

Figure B.2 shows the strain, stress profiles, and free body diagram of the forces acting at the base of each wall panel at DEC. Since the applied lateral load is fairly small at DEC, it is assumed that the wall is still in full contact with the base and hence strain compatibility between the CLT section and PT bars exist, the PT bars preserve their initial pre-stressing force, $T_{p1,i}$ and $T_{p,2i}$, the CLT section has linear-elastic response, and UFPs has not activated yet and not contributing to the resisting moment. The base shear, base overturning moment and roof drift at DEC limit state are denoted as $V_{b,dec}$, $M_{b,dec}$, and $\Theta_{r,dec}$, respectively.

The $M_{b,ec}$ is estimated by summing the moments of left and right CLT panels $M_{b,dec1}$ and $M_{b,dec2}$ with respect to the base of the left CLT panel:

$$M_{b,dec} = M_{b,dec1} + M_{b,dec2} \quad \text{(B.8a)}$$

where

$$M_{b,dec1} = T_{p1,i}\left(\frac{l_w}{2} - e_{pt}\right) + T_{p2,i}\left(\frac{l_w}{2} + e_{pt}\right) + N_g\left(\frac{l_w}{2}\right) - C_{dec}\frac{2l_w}{3} \quad \text{(B.8b)}$$

$$M_{b,dec2} = T_{p1,i}\left(l_w + \frac{l_w}{2} - e_{pt}\right) + T_{p2,i}\left(l_w + \frac{l_w}{2} + e_{pt}\right) + N_g\left(l_w + \frac{l_w}{2}\right) - C_{dec}\left(l_w + \frac{2l_w}{3}\right) \quad \text{(B.8c)}$$

from vertical force equilibrium for each panel

$$C_{dec} = T_{p1,i} + T_{p2,i} + N_g \quad \text{(B.9)}$$

$$C_{dec} = \frac{1}{2} f_{c,dec} l_w t_w \quad \text{(B.10)}$$

C_{dec} and $f_{c,dec}$ are the respective resultant compression force and stress in each CLT panel.

Assuming the external lateral load acts at an effective height, H_{eff}, the V_{dec} is:

$$V_{b,dec} = \frac{M_{b,dec}}{H_{eff}} \quad \text{(B.11)}$$

The total lateral roof deformation at DEC, $\Delta_{r,dec}$, is estimated by summing the elastic flexural ($\Delta_{rf,dec}$), elastic shear ($\Delta_{rs,dec}$), and second-order ($\Delta_{rp,dec}$ due to N_g) lateral roof deformations due to lateral forces applied at each floor level i. Each CLT panel comprising the coupled SC-CLT wall is assumed to have a composite flexural rigidity of $(EI)_c$ and

composite shear rigidity of $(GA)_c$. (It is important to note that since the two SC-CLT wall is connected to each other using vertical connectors, UFPs, it can be assumed that they act as springs in parallel.) The $\Theta_{r,dec}$ is obtained by dividing $\Delta_{r,dec}$with H_w:

$$\Theta_{r,dec} = \frac{\Delta_{r,dec}}{H_w} \tag{B.12}$$

where

$$\Delta_{r,dec} = \Delta_{rf,dec} + \Delta_{rs,dec} + \Delta_{rp,dec} \tag{B.13a}$$

where each component of Δ_{dec} is calculated from statics as:

$$\Delta_{rf,dec} = \sum_{i=1,r} \frac{1}{2(EI)_c}\left(r_{F_i} V_{b,dec}\right)\left(r_{H_i}.H_w\right)^2 \left[H_w\left(1 - \frac{1}{3} r_{H_i}\right)\right] \tag{B.13b}$$

$$\Delta_{rs,dec} = \sum_{i=1,r} \frac{1}{(GA)_c}\left(r_{F_i} V_{b,dec}.r_{H_i}.H_w\right) \tag{B.13c}$$

$$\Delta_{rp,dec} = \sum_{i=1,r} \frac{1}{2(EI)_c}\left(r_{p_i} F_{P-\Delta}^{total}\right)\left(r_{H_i}.H_w\right)^2 \left[H_w\left(1 - \frac{1}{3} r_{H_i}\right)\right] + \sum_{i=1,r} \frac{1}{(GA)_c}\left(r_{p_i} F_{P-\Delta}^{total}.r_{H_i}.H_w\right) \tag{B.13d}$$

where $r_{H_i} = \frac{h_i}{\sum_1^N h_i}$; $r_{F_i} = \frac{F_i}{\sum_1^N F_i}$; $r_{p_i} = \frac{F_{P-\Delta i}}{F_{P-\Delta}^{total}} = \frac{N_{g_{i+1}}}{\sum_2^N N_{g_i}}$ for $h_1 = h_2$ and $h_i = h_{i+1;}$ N_{g_i} = the total gravity load braced by the SC-CLT wall at floor level i; $F_{P-\Delta i}$ = the equivalent lateral load at floor level i for the moment due to P-Δ effects; $F_{P-\Delta}^{total}$= the total lateral load due to P-Δ effects; h_i = story height at level i; $(EI)_c = E_c I_c$; $(GA)_c = G_c A_c$; E_c = Modulus of elasticity of the composite CLT section; I_c= Moment of inertia of the composite CLT section; $I_c = \frac{1}{12}(t_w)(L_w)^3$; t_w= Thickness of the wall; G_c = Modulus of rigidity of the composite CLT section; A_c= Effective area of the composite CLT section; $A_c = L_w t_w$;

Calculation of deformation due to P-Δ effects is an iterative procedure for all limit states including the DEC limit state (i.e., $\Delta_{rp,dec}$). The initial trial starts with the $F_{P-\Delta_i}$ due to a lateral drift equals to ($\Delta_{rf,dec}$+$\Delta_{rs,dec}$). Please see the end of this section for the derivation of Eq. (12c).

Effective Linear Limit (ELL)

Figure B.3 shows the strain, stress profiles, and free body diagram of the forces acting at the base of each wall panel at ELL. ELL is the limit state at which a noticeable softening is observed on M_b versus Θ_r response of the wall. Based on experimental test results, it is assumed that at ELL the three eighth of the wall is in compression. It is also assumed that the UFPs are at their plastic strength (i.e., at $F_{ufp,p}$) and the PT bars are at their initial prestressing force (i.e., at $T_{p1,i}$ and $T_{p2,i}$) since the elongation of PT bars is expected to be small relative to the unbonded length of the PT bars (Perez et al., 1999). The base shear, base overturning moment, and roof drift at ELL limit state are denoted as $V_{b,ell}$, $M_{b,ell}$, and $\Theta_{r,ell}$, respectively.

The $M_{b,ell}$ is estimated by summing the moments of left and right CLT panels, $M_{b,ell1}$ and $M_{b,ell2}$ with respect to the base of the left CLT panel. Each wall is assumed to have a contact length, c_{ell}, of $3l_w/8$.

$$M_{b,ell} = M_{b,ell1} + M_{b,ell2} \tag{B.14a}$$

where

$$M_{b,ell1} = T_{p1,i}\left(\frac{l_w}{2} - e_{pt}\right) + T_{p2,i}\left(\frac{l_w}{2} + e_{pt}\right) + N_g\left(\frac{l_w}{2}\right) - F_{ufp,p}(l_w) - C_{ell,1}\left(l_w - \frac{c_{ell}}{3}\right) \tag{B.14b}$$

$$M_{b,ell2} = T_{p1,i}\left(l_w + \frac{l_w}{2} - e_{pt}\right) + T_{p2,i}\left(l_w + \frac{l_w}{2} + e_{pt}\right) + N_g\left(l_w + \frac{l_w}{2}\right) - F_{ufp,p}(l_w) - C_{ell,2}\left(l_w + l_w - \frac{c_{ell}}{3}\right) \tag{B.14c}$$

From vertical force equilibrium for the first and second CLT wall panel:

$$C_{ell,1} = T_{p1,i} + T_{p2,i} + N_g - F_{ufp,p} \tag{B.15a}$$

$$C_{ell,2} = T_{p1,i} + T_{p2,i} + N_g + F_{ufp,p} \tag{B.15b}$$

And for the "linear-elastic" response of the CLT wall panels:

$$C_{ell,1} = \frac{1}{2} f_{c,ell,1} c_{ell} t_w \tag{B.16a}$$

$$C_{ell,2} = \frac{1}{2} f_{c,ell,2} c_{ell} t_w \tag{B.16b}$$

$C_{ell,1}$ and $f_{c,ell,1}$, $C_{ell,2}$ and $f_{c,ell,2}$ are the respective resultant compression force and stress for the first and second CLT wall panel, respectively.

Assuming the external lateral load acts at an effective height, H_{eff}, the V_{ell} is:

$$V_{ell} = \frac{M_{b,ell}}{H_{eff}} \tag{B.17}$$

The total lateral roof deformation at ELL, $\Delta_{r,ell}$, is estimated by summing the elastic flexural ($\Delta_{rf,ell}$), elastic shear ($\Delta_{rs,ell}$), second-order ($\Delta_{rp,ell}$) lateral roof deformations due to lateral forces applied at each floor level *i*, together with the deformation due to gap opening ($\Delta_{rg,ell}$). The $\Theta_{r,ell}$is obtained by dividing $\Delta_{r,ell}$ with H_w:

$$\Theta_{r,ell} = \frac{\Delta_{r,ell}}{H_w} \tag{B.18}$$

where,

$$\Delta_{r,ell} = \Delta_{rf,ell} + \Delta_{rs,ell} + \Delta_{rp,ell} + \Delta_{rg,ell} \tag{B.19a}$$

where each elastic components of $\Delta_{r,ell}$ is calculated from statics as:

$$\Delta_{rf,ell} = \sum_{i=1,r} \frac{1}{2(EI)_c} \left(r_{F_i} V_{b,ell}\right)\left(r_{H_i}.H_w\right)^2 \left[H_w\left(1 - \frac{1}{3} r_{H_i}\right)\right] \tag{B.19b}$$

$$\Delta_{rs,ell} = \sum_{i=1,r} \frac{1}{(GA)_c} \left(r_{F_i} V_{b,ell}.r_{H_i}.H_w\right) \tag{B.19c}$$

$$\Delta_{rp,ell} = \sum_{i=1,r} \frac{1}{2(EI)_c} \left(r_{p_i} F_{P-\Delta}^{total}\right)\left(r_{H_i}.H_w\right)^2 \left[H_w\left(1 - \frac{1}{3} r_{H_i}\right)\right] + \sum_{i=1,r} \frac{1}{(GA)_c} \left(r_{p_i} F_{P-\Delta}^{total}.r_{H_i}.H_w\right) \tag{B.19d}$$

and the lateral roof deformation due to rigid body rotation, θ_{ell}, is

$$\Delta_{rg,ell} = \theta_{ell} H_w \tag{B.20}$$

where θ_{ell} caused by the deformation in CLT section, $\Delta_{c,ell}$, is estimated with respect to the assumed H_{cr} for the assumed c_{ell}:

$$\theta_{ell} = \frac{\Delta_{c,ell}}{c_{ell}} \tag{B.21}$$

and the strain in CLT section at ELL, $\varepsilon_{c,ell}$, assuming that it is still responding in linear-elastic range is

$$\varepsilon_{c,ell} = \frac{f_{c,ell}}{E_c} \tag{B.22}$$

It is important to note that if the contribution of UFPs to $M_{b,ell}$ is neglected and assuming $c_{ell} = 3l_w/8$, $M_{b,ell}$ can be conservatively estimated as 2.25 times of the $M_{b,dec}$:

$$M_{b,ell} = 2.25M_{b,dec} \tag{B.23}$$

Yielding of the composite CLT section (YCLT)

Figure B.4 shows the strain, stress profiles, and free body diagram of the forces acting at the base of each wall panel at YCLT. YCLT is the limit state at which the composite CLT material near the compression edge at the base of the wall "yields" in compression. This limit state is defined analytically by the CLT panel fiber at this edge (i.e., the edge subjected to compression) reaching the yield strain of the composite CLT material, ε_{cy}. The base shear, base overturning moment, and roof drift at YCLT limit state are denoted as $V_{b,yclt}$, $M_{b,yclt}$, and $\Theta_{r,yclt}$, respectively.

The $M_{b,yclt}$ is estimated by summing the moments of left and right CLT panels, $M_{b,yclt1}$ and $M_{b,yclt2}$, with respect to the base of the left CLT panel:

$$M_{b,yclt} = M_{b,yclt1} + M_{b,yclt2} \tag{B.24a}$$

where

$$M_{b,yclt1} = T_{p1}\left(\frac{l_w}{2} - e_{pt}\right) + T_{p2}\left(\frac{l_w}{2} + e_{pt}\right) + N_g\left(\frac{l_w}{2}\right) - F_{ufp}(l_w) - C_{yclt}\left(l_w - \frac{c_{yclt}}{3}\right) \tag{B.24b}$$

$$M_{b,yclt2} = T_{p1}\left(l_w + \frac{l_w}{2} - e_{pt}\right) + T_{p2}\left(l_w + \frac{l_w}{2} + e_{pt}\right) + N_g\left(l_w + \frac{l_w}{2}\right) + F_{ufp}(l_w) - C_{yclt}\left(l_w + l_w - \frac{c_{yclt}}{3}\right) \tag{B.24c}$$

The stress and strain near the compression edge at the base of each CLT panel equals to the "yield" stress and strain of the CLT material recorded during material tests, f_{c0} and ε_{c0}, respectively. For a contact length of c_{yclt}, the resultant compression force at the base of each CLT panel, C_{yclt} is:

$$C_{yclt} = \frac{1}{2} f_{c0} c_{yclt} t_w \tag{B.25}$$

Finding the c_{yclt} needs an iterative procedure. For an assumed value of c_{yclt},

- the deformation (Δ_{v1} and Δ_{v2}), strain (ε_{pt1} and ε_{pt2}), stress(f_{p1} and f_{p2}), and forces(F_{p1} and F_{p2}) in the PT bar groups, assuming the unbonded length of PT bars is H_{punb}, are:

$$\Delta_{v1} = \frac{\varepsilon_{c0}}{H_{cr}} \frac{(l_{p1} - c_{yclt})}{(c_{yclt})} \tag{B.26a}$$

$$\Delta_{v2} = \frac{\varepsilon_{c0}}{H_{cr}} \frac{(l_{p2} - c_{yclt})}{(c_{yclt})} \tag{B.26b}$$

$$\varepsilon_{p1} = \frac{f_{p1,i}}{E_p} \frac{\Delta_{v1}}{H_{punb}} \tag{B.27a}$$

$$\varepsilon_{p2} = \frac{f_{p2,i}}{E_p} \frac{\Delta_{v2}}{H_{punb}} \tag{B.27b}$$

$$f_{p1} = f_{p1,i} + (\varepsilon_{p1} - \varepsilon_{p1,i}) E_p \tag{B.28a}$$

$$f_{p2} = f_{p2,i} + (\varepsilon_{p2} - \varepsilon_{p2,i}) E_p \tag{B.28b}$$

$$T_{p1} = f_{p1} A_{pt} \tag{B.29a}$$

$$T_{p2} = f_{p2} A_{pt} \tag{B.29b}$$

- the deformation (Δ_{ufp}) and force (F_{ufp}) in each UFP, for a UFP having a stiffness of k_{ufp} are:

$$\Delta_{ufp} = \Delta_{v1} \frac{(l_{p1} - c_{yclt})}{(l_w - c_{yclt})} \tag{B.30}$$

$$F_{ufpi} = \begin{cases} k_{ufp} \Delta_{ufp} & if \ \Delta_{ufp} \leq \Delta_{ufp,p} \\ k_{ufp} \Delta_{ufp} + (\Delta_{ufp} - \Delta_{ufp,p}) \left(\frac{F_{ufp,p} - F_{ufp,p}}{\Delta_{ufp,p} - \Delta_{ufp,p}} \right) & if \ \Delta_{ufp} > \Delta_{ufp,p} \end{cases} \tag{B.31}$$

- The total force provided by N_{con} number of UFPs is:

$$F_{ufp} = N_{con}F_{ufpi} \quad \text{(B.32)}$$

- The resultant downward force at YCLT limit state is:

$$T_{yclt} = T_{p1} + T_{p2} + N_g - F_{ufp} \text{ for the left panel} \quad \text{(B.33a)}$$

$$T_{yclt} = T_{p1} + T_{p2} + N_g + F_{ufp} \text{ for the right panel} \quad \text{(B.33b)}$$

- The iterative process for c_{yclt} continues till the vertical force equilibrium is satisfied:

$$T_{yclt} - C_{yclt} = 0 \quad \text{(B.34)}$$

Assuming the external lateral load acts at an effective height, H_{eff}, the $V_{b,yclt}$ is:

$$V_{b,yclt} = \frac{M_{b,yclt}}{H_{eff}} \quad \text{(B.35)}$$

The total lateral roof deformation at YCLT, $\Delta_{r,yclt}$, is estimated by summing the elastic flexural ($\Delta_{rf,yclt}$), elastic shear ($\Delta_{rf,yclt}$), second-order ($\Delta_{rp,yclt}$) lateral roof deformations due to lateral forces applied at each floor level i, together with the deformation due to gap opening ($\Delta_{rg,yclt}$). The $\Theta_{r,yclt}$ is obtained by dividing $\Delta_{r,yclt}$ with H_w:

$$\Theta_{r,yclt} = \frac{\Delta_{r,yclt}}{H_w} \quad \text{(B.36)}$$

where,

$$\Delta_{r,yclt} = \Delta_{rf,yclt} + \Delta_{rs,yclt} + \Delta_{rp,yclt} + \Delta_{rg,yclt} \quad \text{(B.37a)}$$

where each elastic components of $\Delta_{r,yclt}$ is calculated from statics as:

$$\Delta_{rf,yclt} = \sum_{i=1,r} \frac{1}{2(EI)_c}\left(r_{F_i} V_{b,yclt}\right)\left(r_{H_i}.H_w\right)^2 \left[H_w\left(1-\frac{1}{3}r_{H_i}\right)\right] \quad \text{(B.37b)}$$

$$\Delta_{rs,yclt} = \sum_{i=1,r} \frac{1}{(GA)_c}\left(r_{F_i} V_{b,yclt}.r_{H_i}.H_w\right) \quad \text{(B.37c)}$$

$$\Delta_{rp,yclt} = \sum_{i=1,r} \frac{1}{2(EI)_c}\left(r_{p_i} F_{P-\Delta}^{total}\right)\left(r_{H_i}.H_w\right)^2 \left[H_w\left(1-\frac{1}{3}r_{H_i}\right)\right] + \sum_{i=1,r} \frac{1}{(GA)_c}\left(r_{p_i} F_{P-\Delta}^{total}.r_{H_i}.H_w\right) \quad \text{(B.37d)}$$

and the roof deformation due to rigid body rotation, θ_{yclt}, is

$$\Delta_{rg,yclt} = \theta_{yclt} H_w \quad \text{(B.38)}$$

where θ_{yclt} caused by the deformation in CLT section, $\Delta_{c,yclt}$, is estimated with respect to the assumed H_{cr} for the estimated c_{yclt}:

$$\theta_{yclt} = \frac{\Delta_{c,yclt}}{c_{yclt}} \quad \text{(B.39)}$$

$$\Delta_{c,yclt} = \varepsilon_{c,yclt}\, H_{cr} \quad \text{(B.40)}$$

Splitting of the composite CLT section (SCLT)

Figure B.5 shows the strain, stress profiles, and free body diagram of the forces acting at the base of each wall panel at SCLT. SCLT is the limit state at which the composite CLT material at the compression edge of the wall near the base of the wall experiences considerable splitting. This limit state is defined analytically by the CLT panel fiber at this edge (i.e., the edge subjected to compression) reaching the maximum strain value, ε_{cs},

recorded during material tests. The base shear, base overturning moment, and roof drift at SCLT limits state are denoted as $V_{b,sclt}$, $M_{b,sclt}$, and $\Theta_{r,cclt}$, respectively.

The $M_{b,sclt}$ is estimated by summing the moments of left and right CLT panels, $M_{b,sclt1}$ and $M_{b,sclt2}$, with respect to the base of the left CLT panel:

$$M_{b,sclt} = M_{b,sclt1} + M_{b,sclt2} \tag{B.41a}$$

where

$$M_{b,sclt1} = T_{p1}\left(\frac{l_w}{2} - e_{pt}\right) + T_{p2}\left(\frac{l_w}{2} + e_{pt}\right) + N_g\left(\frac{l_w}{2}\right) - F_{ufp}(l_w) - C_{sclt}\left(l_w - \frac{c_{sclt}}{3}\right) \tag{B.41b}$$

$$M_{b,sclt2} = T_{p1}\left(l_w + \frac{l_w}{2} - e_{pt}\right) + T_{p2}\left(l_w + \frac{l_w}{2} + e_{pt}\right) + N_g\left(l_w + \frac{l_w}{2}\right) + F_{ufp}(l_w) - C_{sclt}\left(l_w + l_w - \frac{c_{sclt}}{3}\right) \tag{B.41c}$$

The strain near the compression edge at the base of each CLT panel is assumed to be equal to the maximum strain observed during the material tests, i.e. ε_{cs}. For a total contact length of c_{sclt}, the portion of the contact length, $c_{sclt,y}$, where the CLT material starts behaves linear is estimated from similar triangles (see Figure B.5):

$$c_{sclt,y} = c_{sclt}\frac{\varepsilon_{c0}}{\varepsilon_{cs}} \tag{B.42}$$

Then, the resultant compression force at the base of each CLT panel, C_{sclt}, assuming EPP response, is:

$$C_{sclt} = \frac{1}{2} f_{c0} c_{sclt,y} t_w + f_{c0}(c_{sclt} - c_{sclt,y}) t_w \quad \text{(B.43)}$$

Finding the exact value for the c_{sclt} needs an iterative procedure. For an assumed value of c_{sclt},

- the deformation (Δ_{v1} and Δ_{v2}), strain (ε_{pt1} and ε_{pt2}), stress(f_{p1} and f_{p2}), and forces(F_{p1} and F_{p2}) in the PT bar groups are:

$$\Delta_{v1} = \varepsilon_{cs} H_{cr} \frac{(l_{p1} - c_{sclt})}{(c_{sclt})} \quad \text{(B.44a)}$$

$$\Delta_{v2} = \frac{\varepsilon_{cs}}{H_{cr}} \frac{(l_{p2} - c_{sclt})}{(c_{sclt})} \quad \text{(B.44b)}$$

$$\varepsilon_{p1} = \frac{f_{p1,i}}{E_p} \frac{\Delta_{v1}}{H_{punb}} \quad \text{(B.45a)}$$

$$\varepsilon_{p2} = \frac{f_{p2,i}}{E_p} \frac{\Delta_{v2}}{H_{punb}} \quad \text{(B.45b)}$$

$$f_{p1} = f_{p1,i} + (\varepsilon_{p1} - \varepsilon_{p1,i}) E_p \quad \text{(B.46a)}$$

$$f_{p2} = f_{p2,i} + (\varepsilon_{p2} - \varepsilon_{p2,i}) E_p \quad \text{(B.46b)}$$

$$T_{p1} = f_{p1} A_{pt} \quad \text{(B.47a)}$$

$$T_{p2} = f_{p2} A_{pt} \quad \text{(B.47b)}$$

- the deformation (Δ_{ufp}) and force (F_{ufp}) in each UFP, for a UFP having a stiffness of k_{ufp} are:

$$\Delta_{ufp} = \Delta_{v1}\frac{(l_{p1}-c_{sclt})}{(l_w-c_{sclt})} \tag{B.48}$$

$$F_{ufpi} = \begin{cases} k_{ufp}\Delta_{ufp} & if\ \ \Delta_{ufp} \le \Delta_{ufp,p} \\ k_{ufp}\Delta_{ufp} + (\Delta_{ufp} - \Delta_{ufp,p})\left(\frac{F_{ufp,p}-F_{ufp,p}}{\Delta_{ufp,p}-\Delta_{ufp,p}}\right) & if\ \ \Delta_{ufp} > \Delta_{ufp,p} \end{cases} \tag{B.49}$$

- The total force provided by N_{con} number of UFPs is:

$$F_{ufp} = N_{con}F_{ufpi} \tag{B.50}$$

- The resultant downward force at SCLT limit state is:

$$T_{sclt} = T_{p1} + T_{p2} + N_g - F_{ufp} \text{ for the left panel} \tag{B.51}$$

$$T_{sclt} = T_{p1} + T_{p2} + N_g + F_{ufp} \text{ for the right panel}$$

- The iterative process for c_{sclt} continues till the vertical force equilibrium is satisfied:

$$T_{sclt} - C_{sclt} = 0 \tag{B.52}$$

Assuming the external lateral load acts at an effective height, H_{eff}, the $V_{b,sclt}$ is:

$$V_{b,sclt} = \frac{M_{b,sclt}}{H_{eff}} \tag{B.53}$$

The total lateral roof deformation at SCLT, $\Delta_{r,sclt}$, is estimated by summing the elastic flexural ($\Delta_{rf,sclt}$), elastic shear ($\Delta_{rf,sclt}$), second-order ($\Delta_{rp,sclt}$) lateral roof deformations due

to lateral forces applied at each floor level *i*, together with the deformation due to gap opening ($\Delta_{rg,sclt}$). The $\Theta_{r,sclt}$ is obtained by dividing $\Delta_{r,sclt}$ with H_w:

$$\Theta_{r,sclt} = \frac{\Delta_{r,sclt}}{H_w} \tag{B.54}$$

where,

$$\Delta_{r,sclt} = \Delta_{rf,sclt} + \Delta_{rs,sclt} + \Delta_{rp,sclt} + \Delta_{rg,sclt} \tag{B.55a}$$

where each elastic components of $\Delta_{r,sclt}$ is calculated from statics as:

$$\Delta_{rf,sclt} = \sum_{i=1,r} \frac{1}{2(EI)_c} \left(r_{F_i} V_{b,sclt}\right)\left(r_{H_i}.H_w\right)^2 \left[H_w\left(1 - \frac{1}{3} r_{H_i}\right)\right] \tag{B.55b}$$

$$\Delta_{rs,sclt} = \sum_{i=1,r} \frac{1}{(GA)_c} \left(r_{F_i} V_{b,sclt}.r_{H_i}.H_w\right) \tag{B.55c}$$

$$\Delta_{rp,sclt} = \sum_{i=1,r} \frac{1}{2(EI)_c} \left(r_{p_i} F_{P-\Delta}^{total}\right)\left(r_{H_i}.H_w\right)^2 \left[H_w\left(1 - \frac{1}{3} r_{H_i}\right)\right] + \sum_{i=1,r} \frac{1}{(GA)_c} \left(r_{p_i} F_{P-\Delta}^{total}.r_{H_i}.H_w\right) \tag{B.55d}$$

and the roof deformation due to rigid body rotation, θ_{sclt}, is

$$\Delta_{rg,sclt} = \theta_{sclt} H_w \tag{B.56}$$

where θ_{sclt} caused by the deformation in CLT section, $\Delta_{c,sclt}$, is estimated with respect to the assumed H_{cr} for the estimated c_{sclt}:

$$\theta_{sclt} = \frac{\Delta_{c,sclt}}{c_{sclt}} \tag{B.57}$$

$$\Delta_{c,sclt} = \varepsilon_{c,sclt}\, H_{cr} \tag{B.58}$$

Crushing of the composite CLT section (CCLT)

Figure B.5 shows the strain, stress profiles, and free body diagram of the forces acting at the base of each wall panel at CCLT. CCLT is the limit state at which the composite CLT material at the compression edge of the wall near the base of the wall experiences considerable splitting. This limit state is defined analytically by the CLT panel fiber at this edge (i.e., the edge subjected to compression) reaching the maximum strain value, ε_{cu}, recorded during material tests. The base shear, base overturning moment, and roof drift at CCLT limits state are denoted as $V_{b,cclt}$, $M_{b,cclt}$, and $\Theta_{r,cclt}$, respectively.

The $M_{b,cclt}$ is estimated by summing the moments of left and right CLT panels, $M_{b,cclt1}$ and $M_{b,sclt2}$, with respect to the base of the left CLT panel:

$$M_{b,cclt} = M_{b,cclt1} + M_{b,cclt2} \tag{B.59a}$$

where

$$M_{b,cclt1} = T_{p1}\left(\frac{l_w}{2} - e_{pt}\right) + T_{p2}\left(\frac{l_w}{2} + e_{pt}\right) + N_g\left(\frac{l_w}{2}\right) - F_{ufp}(l_w) - C_{cclt}\left(l_w - \frac{c_{cclt}}{3}\right) \tag{B.59b}$$

$$M_{b,cclt2} = T_{p1}\left(l_w + \frac{l_w}{2} - e_{pt}\right) + T_{p2}\left(l_w + \frac{l_w}{2} + e_{pt}\right) + N_g\left(l_w + \frac{l_w}{2}\right) + F_{ufp}(l_w) - C_{cclt}\left(l_w + l_w - \frac{c_{cclt}}{3}\right) \tag{B.59c}$$

The strain near the compression edge at the base of each CLT panel is assumed to be equal to the maximum strain observed during the material tests, i.e. ε_{cu}. For a total contact length

of c_{cclt}, the portion of the contact length, $c_{cclt,y}$, where the CLT material starts behaves linear is estimated from similar triangles (see Figure B.5):

$$c_{cclt,y} = c_{cclt}\frac{\varepsilon_{c0}}{\varepsilon_{cu}} \tag{B.60}$$

Then, the resultant compression force at the base of each CLT panel, C_{cclt}, assuming EPP response, is:

$$C_{cclt} = \frac{1}{2}f_{c0}c_{cclt,y}t_w + f_{c0}(c_{cclt} - c_{cclt,y})t_w \tag{B.61}$$

Finding the exact value for the c_{cclt} needs an iterative procedure. For an assumed value of c_{cclt},

- the deformation (Δ_{v1} and Δ_{v2}), strain (ε_{pt1} and ε_{pt2}), stress(f_{p1} and f_{p2}), and forces(F_{p1} and F_{p2}) in the PT bar groups are:

$$\Delta_{v1} = \varepsilon_{cu}H_{cr}\frac{(l_{p1}-c_{cclt})}{(c_{cclt})} \tag{B.62a}$$

$$\Delta_{v2} = \frac{\varepsilon_{cu}}{H_{cr}}\frac{(l_{p2}-c_{cclt})}{(c_{cclt})} \tag{B.62b}$$

$$\varepsilon_{p1} = \frac{f_{p1,i}}{E_p}\frac{\Delta_{v1}}{H_{punb}} \tag{B.63a}$$

$$\varepsilon_{p2} = \frac{f_{p2,i}}{E_p} \frac{\Delta_{v2}}{H_{punb}} \quad \text{(B.63b)}$$

$$f_{p1} = f_{p1,i} + (\varepsilon_{p1} - \varepsilon_{p1,i}) E_p \quad \text{(B.64a)}$$

$$f_{p2} = f_{p2,i} + (\varepsilon_{p2} - \varepsilon_{p2,i}) E_p \quad \text{(B.64b)}$$

$$T_{p1} = f_{p1} A_{pt} \quad \text{(B.65a)}$$

$$T_{p2} = f_{p2} A_{pt} \quad \text{(B.65b)}$$

- the deformation (Δ_{ufp}) and force (F_{ufp}) in each UFP, for a UFP having a stiffness of k_{ufp} are:

$$\Delta_{ufp} = \Delta_{v1} \frac{(l_{p1} - c_{cclt})}{(l_w - c_{cclt})} \quad \text{(B.66)}$$

$$F_{ufpi} = \begin{cases} k_{ufp} \Delta_{ufp} & if \ \Delta_{ufp} \le \Delta_{ufp,p} \\ k_{ufp} \Delta_{ufp} + (\Delta_{ufp} - \Delta_{ufp,p}) \left(\frac{F_{ufp,p} - F_{ufp,p}}{\Delta_{ufp,p} - \Delta_{ufp,p}} \right) & if \ \Delta_{ufp} > \Delta_{ufp,p} \end{cases} \quad \text{(B.67)}$$

- The total force provided by N_{con} number of UFPs is:

$$F_{ufp} = N_{con} F_{ufpi} \quad \text{(B.68)}$$

- The resultant downward force at CCLT limit state is:

$T_{cclt} = T_{p1} + T_{p2} + N_g - F_{ufp}$ for the left panel (B.69a)

$T_{cclt} = T_{p1} + T_{p2} + N_g + F_{ufp}$ for the right panel (B.69b)

- The iterative process for c_{cclt} continues till the vertical force equilibrium is satisfied:

$$T_{cclt} - C_{cclt} = 0 \quad \text{(B.70)}$$

Assuming the external lateral load acts at an effective height, H_{eff}, the $V_{b,cclt}$ is:

$$V_{b,cclt} = \frac{M_{b,cclt}}{H_{eff}} \quad \text{(B.71)}$$

The total lateral roof deformation at CCLT, $\Delta_{r,cclt}$, is estimated by summing the elastic flexural ($\Delta_{rf,cclt}$), elastic shear ($\Delta_{rf,cclt}$), second-order ($\Delta_{rp,cclt}$) lateral roof deformations due to lateral forces applied at each floor level i, together with the deformation due to gap opening ($\Delta_{rg,cclt}$). The $\Theta_{r,cclt}$ is obtained by dividing $\Delta_{r,cclt}$ with H_w:

$$\Theta_{r,cclt} = \frac{\Delta_{r,cclt}}{H_w} \quad \text{(B.72)}$$

where,

$$\Delta_{r,cclt} = \Delta_{rf,cclt} + \Delta_{rs,cclt} + \Delta_{rp,cclt} + \Delta_{rg,cclt} \quad \text{(B.73a)}$$

where each elastic components of $\Delta_{r,cclt}$ is calculated from statics as:

$$\Delta_{rf,cclt} = \sum_{i=1,r} \frac{1}{2(EI)_c} \left(r_{F_i} V_{b,cclt}\right)\left(r_{H_i}.H_w\right)^2 \left[H_w \left(1 - \frac{1}{3} r_{H_i}\right)\right] \quad \text{(B.73b)}$$

$$\Delta_{rs,cclt} = \sum_{i=1,r} \frac{1}{(GA)_c} \left(r_{F_i} V_{b,cclt}.r_{H_i}.H_w\right) \quad \text{(B.73c)}$$

$$\Delta_{rp,cclt} = \sum_{i=1,r} \frac{1}{2(EI)_c}\left(r_{p_i} F_{P-\Delta}^{total}\right)\left(r_{H_i}.H_w\right)^2\left[H_w\left(1-\frac{1}{3}r_{H_i}\right)\right] + \sum_{i=1,r} \frac{1}{(GA)_c}\left(r_{p_i} F_{P-\Delta}^{total}.r_{H_i}.H_w\right) \quad \text{(B.73d)}$$

and the roof deformation due to rigid body rotation, θ_{cclt}, is

$$\Delta_{rg,cclt} = \theta_{cclt} H_w \quad \text{(B.74)}$$

where θ_{cclt} caused by the deformation in CLT section, $\Delta_{c,cclt}$, is estimated with respect to the assumed H_{cr} for the estimated c_{cclt}:

$$\theta_{cclt} = \frac{\Delta_{c,cclt}}{c_{cclt}} \quad \text{(B.75)}$$

$$\Delta_{c,cclt} = \varepsilon_{c,cclt}\, H_{cr} \quad \text{(B.76)}$$

Linear limit of Post-tensioning Steel (LLP)

Figure B.6 shows the strain, stress profiles, and free body diagram of the forces acting at the base of each wall panel at LLP. LLP is the limit state at which the first PT bar reaches its yield strain in tension. The strain in the PT bars increases above the initial strain from ost tensioning as a result of elongation due to gap opening and rocking of the SC-CLT wall on the foundation. The base shear, base overturning moment, and roof drift at LLP limits state are denoted as $V_{b,llp}$, $M_{b,llp}$, and $\Theta_{r,llp}$, respectively.

The $M_{b,llp}$ is estimated by summing the moments of left and right CLT panels, $M_{b,llp1}$ and $M_{b,llp2}$, with respect to the base of the left CLT panel:

$$M_{b,llp} = M_{b,llp1} + M_{b,llp2} \quad \text{(B.77a)}$$

where

$$M_{b,llp1} = T_{p1,y}\left(\frac{l_w}{2} - e_{pt}\right) + T_{p2}\left(\frac{l_w}{2} + e_{pt}\right) + N_g\left(\frac{l_w}{2}\right) - F_{ufp}(l_w) - C_{llp}\left(l_w - \frac{c_{llp}}{3}\right) \quad \text{(B.77b)}$$

$$M_{b,llp2} = T_{p1,y}\left(l_w + \frac{l_w}{2} - e_{pt}\right) + T_{p2}\left(l_w + \frac{l_w}{2} + e_{pt}\right) + N_g\left(l_w + \frac{l_w}{2}\right) + F_{ufp}(l_w) - C_{llp}\left(l_w + l_w - \frac{c_{llp}}{3}\right) \quad \text{(B.77c)}$$

Finding the exact value for the c_{llp} needs an iterative procedure. For an assumed value of c_{llp},

- knowing that the strain at the yielded first PT bar, $\varepsilon_{p1,}$ equals to ε_{py}, the deformation (Δ_{v1}), stress(f_{p1})and force(F_{p1}) in the first PT bar group are:

$$\Delta_{v1} = H_{punb}\left(\varepsilon_{py} - \frac{f_{pi}}{E_p}\right) \quad \text{(B.78)}$$

$$f_{p1} = f_{py} \quad \text{(B.79)}$$

$$T_{p1,y} = f_{py}A_{pt} \quad \text{(B.80)}$$

- the deformation (Δ_{v2}), strain (ε_{p2}), stress(f_{p2})and force(F_{p2}) in the second PT bar group are:

$$\Delta_{v2} = \Delta_{v1}\left(\frac{l_{p2} - c_{llp}}{l_{p1} - c_{llp}}\right) \quad \text{(B.81)}$$

$$\varepsilon_{p2} = \frac{f_{pi}}{E_p} + \frac{\Delta_{v2}}{H_{punb}} \quad \text{(B.82)}$$

$$f_{p2} = f_{p2,i} + (\varepsilon_{p2} - \varepsilon_{p2,i})E_p \quad \text{(B.83)}$$

$$T_{p2,y} = f_{p2}A_{pt} \quad \text{(B.84)}$$

- the deformation (Δ_{ufp}) and force (F_{ufp}) in each UFP, for a UFP having a stiffness of k_{ufp} are:

$$\Delta_{ufp} = \Delta_{v1}\frac{(l_{p1} - c_{llp})}{(l_w - c_{llp})} \quad \text{(B.85)}$$

$$F_{ufpi} = \begin{cases} k_{ufp}\Delta_{ufp} & if\ \Delta_{ufp} \le \Delta_{ufp,p} \\ k_{ufp}\Delta_{ufp} + (\Delta_{ufp} - \Delta_{ufp,p})\left(\frac{F_{ufp,p} - F_{ufp,p}}{\Delta_{ufp,p} - \Delta_{ufp,p}}\right) & if\ \Delta_{ufp} > \Delta_{ufp,p} \end{cases} \quad \text{(B.86)}$$

- The total force provided by N_{con} number of UFPs is:

$$F_{ufp} = N_{con}F_{ufpi} \quad \text{(B.87)}$$

- The resultant downward force at SCLT limit state is:

$T_{llp} = T_{p1,y} + T_{p2} + N_g - F_{ufp}$ for the left panel (B.88a)

$T_{llp} = T_{p1,y} + T_{p2} + N_g + F_{ufp}$ for the right panel (B.88b)

- The strain near the compression edge at the base of each CLT panel at this limit state, ε_{cllp}, is obtained by assuming deformation compatibility between of PT bar on tension side with respect to H_{cr} of concrete in compression (see Figure B.6):

$$\varepsilon_{cllp} = \frac{c_{llp}}{(l_{p1} - c_{llp})} \frac{\Delta_{v1}}{H_{ph}} \tag{B.89}$$

- For a total contact length of c_{llp}, the portion of the contact length, $c_{llp,y}$, where the CLT material starts behaves linear is estimated from similar triangles (see Figure B.6):

$$c_{llp,y} = c_{llp} \frac{\varepsilon_{c0}}{\varepsilon_{cllp}} \tag{B.90}$$

- Then, the resultant compression force at the base of each CLT panel, C_{llp}, assuming EPP response, is:

$$C_{llp} = \frac{1}{2} f_{c0} c_{llp,y} t_w + f_{c0} (c_{llp} - c_{llp,y}) t_w \tag{B.91}$$

- The iterative process for c_{llp} continues till the vertical force equilibrium is satisfied:

$$T_{llp} - C_{llp} = 0 \tag{B.92}$$

Assuming the external lateral load acts at an effective height, H_{eff}, the $V_{b,llp}$ is:

$$V_{b,llp} = \frac{M_{b,llp}}{H_{eff}} \tag{B.93}$$

The total lateral roof deformation at LLP, $\Delta_{r,llp}$, is estimated by summing the elastic flexural ($\Delta_{rf,llp}$), elastic shear ($\Delta_{rf,llp}$), second-order ($\Delta_{rp,llp}$) lateral roof deformations due to lateral forces applied at each floor level i, together with the deformation due to gap opening ($\Delta_{rg,llp}$). The $\Theta_{r,llp}$ is obtained by dividing $\Delta_{r,llp}$ with H_w:

$$\Theta_{r,llp} = \frac{\Delta_{r,llp}}{H_w} \tag{B.94}$$

where,

$$\Delta_{r,llp} = \Delta_{rf,llp} + \Delta_{rs,llp} + \Delta_{rp,llp} + \Delta_{rg,llp} \tag{B.95a}$$

where each elastic components of $\Delta_{r,llp}$ is calculated from statics as:

$$\Delta_{rf,llp} = \sum_{i=1,r} \frac{1}{2(EI)_c} \left(r_{F_i} V_{b,llp}\right)\left(r_{H_i}.H_w\right)^2 \left[H_w\left(1 - \frac{1}{3} r_{H_i}\right)\right] \tag{B.95b}$$

$$\Delta_{rs,llp} = \sum_{i=1,r} \frac{1}{(GA)_c} \left(r_{F_i} V_{b,llp}.r_{H_i}.H_w\right) \tag{B.95c}$$

$$\Delta_{rp,llp} = \sum_{i=1,r} \frac{1}{2(EI)_c} \left(r_{p_i} F_{P-\Delta}^{total}\right)\left(r_{H_i}.H_w\right)^2 \left[H_w\left(1 - \frac{1}{3} r_{H_i}\right)\right] + \sum_{i=1,r} \frac{1}{(GA)_c} \left(r_{p_i} F_{P-\Delta}^{total}.r_{H_i}.H_w\right) \tag{B.95d}$$

and the roof deformation due to rigid body rotation, θ_{llp}, is

$$\Delta_{rg,llp} = \theta_{llp} H_w \tag{B.96}$$

where θ_{llp} caused by the deformation in CLT section, $\Delta_{c,llp}$, is estimated with respect to the assumed H_{cr} for the estimated c_{llp}:

$$\theta_{llp} = \frac{\Delta_{c,llp}}{c_{llp}} \tag{B.97}$$

$$\Delta_{c,llp} = \varepsilon_{c,llp} H_{cr} \quad \text{(B.98)}$$

***Derivation of $\Delta_{rp,dec}$**

Figure B.8 (a) shows the displaced position of an N-story fixed-base cantilever wall under story weights, $N_{g,}$. Figure B.8 (b) shows the overturning moment due to story weight at i^{th}, $N_{g,i}$, and Figure B.8 (c) shows the statically equivalent force couple, $F_{P\text{-}\Delta,i}$, as previously illustrated by Wilson and Habibullah (1987).

The total overturning moment at level i due to applied gravity loading is:

$$M_i = N_{g,r} (\Delta_r - \Delta_{N-1}) + N_{g,N-1} (\Delta_{N-1} - \Delta_{N-2}) + \ldots + N_{g,i+1} (\Delta_{i+1} - \Delta_i) \quad \text{(B.100)}$$

The total overturning moment at level i+1 due to applied gravity loading is:

$$M_{i+1} = N_{g,r} (\Delta_r - \Delta_{N-1}) + N_{g,N-1} (\Delta_{N-1} - \Delta_{N-2}) + \ldots + N_{g,i+2} (\Delta_{i+2} - \Delta_{i+1}) \quad \text{(B.101)}$$

The overturning moment difference, ΔM_i, between levels i and i+1 is:

$$\Delta M_i = (\sum_{i=i+1}^{N} N_{g,i})(\Delta_{i+1} - \Delta_i) \quad \text{(B.102)}$$

The total force couple at level i , $F_{P\text{-}\Delta,i}$, can be written in terms of ΔM_i and ΔM_{i+1},as shown in Figure B.9:

$$F_{P\text{-}\Delta,i} = \frac{\Delta M_i}{h_i} - \frac{\Delta M_{i+1}}{h_{i+1}} \quad \text{(B.103a)}$$

$$F_{P\text{-}\Delta,i} = \frac{(\sum_{i=i+1}^{N} N_{g,i})(H_{i+1} - H_i)\Theta_r}{h_i} - \frac{(\sum_{i=i+2}^{N} N_{g,i})(H_{i+2} - H_{i+1})\Theta_r}{h_{i+1}} \quad \text{(B.103b)}$$

where H_i = the total height of the wall up to floor level i; h_i = the story height at level i; Θ_r = the total roof drift ratio

For $h_i = h_{i+1}$, $F_{P\text{-}\Delta,i}$ can be simplified as follows::

$$F_{P\text{-}\Delta,i} = N_{g,i+1}\,\Theta_r \quad \text{(B.104)}$$

and the total equivalent lateral forces due to P- Δ effects along the height of the structure, $F_{P-\Delta}^{total}$, can be expressed as a summation of $F_{P\text{-}\Delta,i}$:

$$F_{P-\Delta}^{total} = \sum_{i=1}^{N-1} F_{P-\Delta,i} = (\sum_{i=2}^{N} N_{g,i})\,\Theta_r \quad \text{(B.105)}$$

The total force couple at level i , $F_{P\text{-}\Delta,i}$,can be expressed as a fraction of the $F_{P-\Delta}^{total}$:

$$F_{P-\Delta,i} = r_{Pi} F_{P-\Delta}^{total} \quad \text{(B.106)}$$

Then, the total roof level lateral deformation due to $F_{P-\Delta,i}$, can be obtained using Eq. (12b) and Eq.(12c):

$$\Delta_{rp} = \sum_{i=1,r} \frac{1}{2(EI)_c}\left(r_{p_i} F_{P-\Delta}^{total}\right)\left(r_{H_i}.H_w\right)^2 \left[H_w\left(1 - \frac{1}{3} r_{H_i}\right)\right] + \sum_{i=1,r} \frac{1}{(GA)_c}\left(r_{p_i} F_{P-\Delta}^{total}.r_{H_i}.H_w\right) \quad \text{(B.107)}$$

Finding Δ_{rp} from Eq. (B.115) is an iterative procedure. Θ_r in Eq.(B.113) is assumed to be equal to the roof level flexural and shear deformations due to inertial force for the initial trial.

B.3. References

E. L. Wilson and A. Habibullah (1987). "Static and Dynamic Analysis of Multi-Story Buildings Including P-Delta Effects," *Earthquake Spectra*, Earthquake Engineering Research Institute, 3 (3), pp. 289-298.

Kelly, J. M., Skinner, R. I., and Heine, A. J. (1972). "Mechanism of Energy Absorption in Special Devices for Use in Earthquake Resistant Structures." *Bulletin New Zealand Society of Earthquake Engineering*, (5) 3, pp. 63-88.

Kurama, Y. C., Pessiki, S., Sause, R., Lu, L. W., El-Sheikh, M. (1996). "Analytical Modeling and Lateral Load Behavior of Unbonded Post-Tensioned Precast Concrete Walls". Research Report No. EQ-96-02, Department of Civil and Environmental Engineering, Lehigh University, Bethlehem, PA.

Kurama, Y. C. (1997). "Seismic Analysis, Behavior, and Design of Unbonded Post-Tensioned Precast Concrete Walls," Ph.D Dissertation, Department of Civil and Environmental Engineering, Lehigh University, Bethlehem, PA.

Perez, F. J., Pessiki, S., and Sause, R. (1999). "Lateral Load Behavior and Design of Unbonded Post-tensioned Precast Concrete Walls with Ductile Vertical Joints Connectors". Research Report No. EQ-99-01, Department of Civil and Environmental Engineering, Lehigh University, Bethlehem, PA.

Perez, F. J. (2004). "Experimental and Analytical Lateral Load Response of Unbonded Post-Tensioned Precast Concrete Walls", Ph.D. Dissertation, Department of Civil and Environmental Engineering, Lehigh University, Bethlehem, PA.

Perez, F. J., Sause, R., and Pessiki, S. (2007). "Analytical and Experimental Lateral Load Behavior of Unbonded Post-Tensioned Precast Concrete Walls," *Journal of Structural Engineering, American Society of Civil Engineers*, 133 (11), pp. 1531-1540.

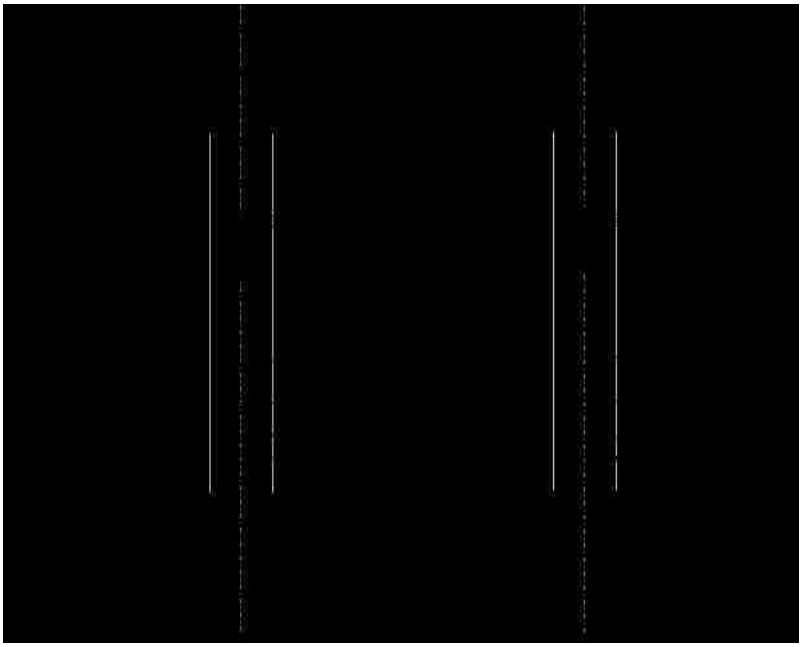

Figure B.1 Forces acting on a multi-panel SC-CLT wall

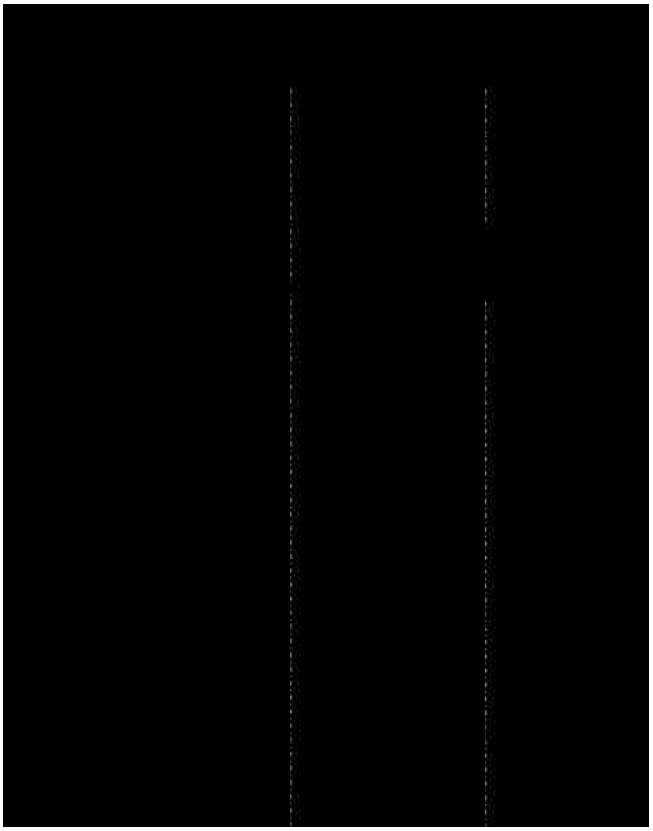

Figure B.2 Free-body diagram of the forces, stress, and strain profiles at the base of each wall panel at DEC

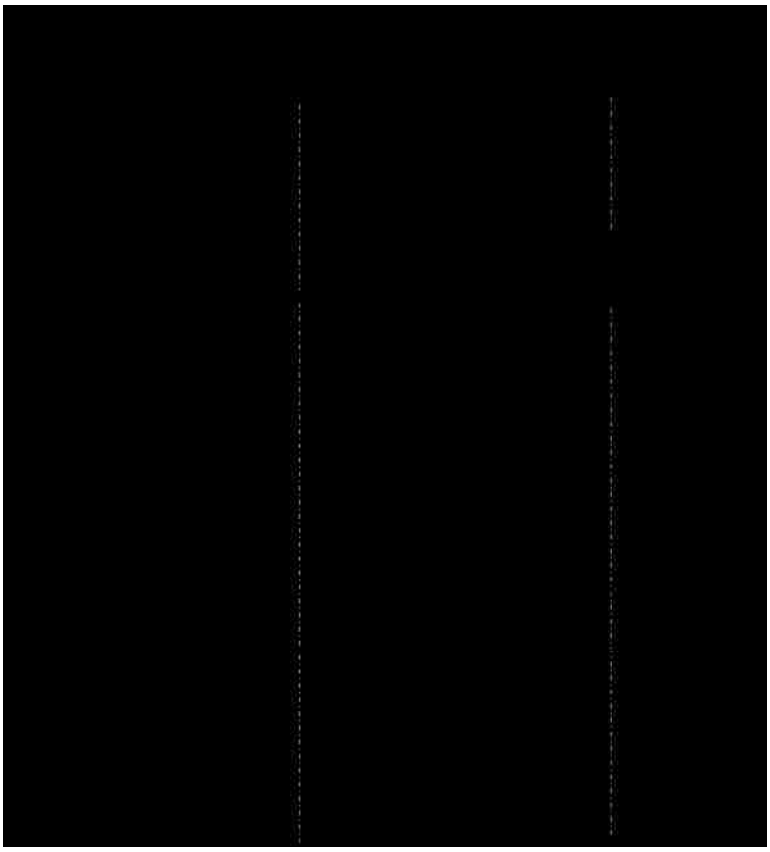

Figure B.3 Free-body diagram of the forces, stress, and strain profiles at the base of each wall panel at ELL

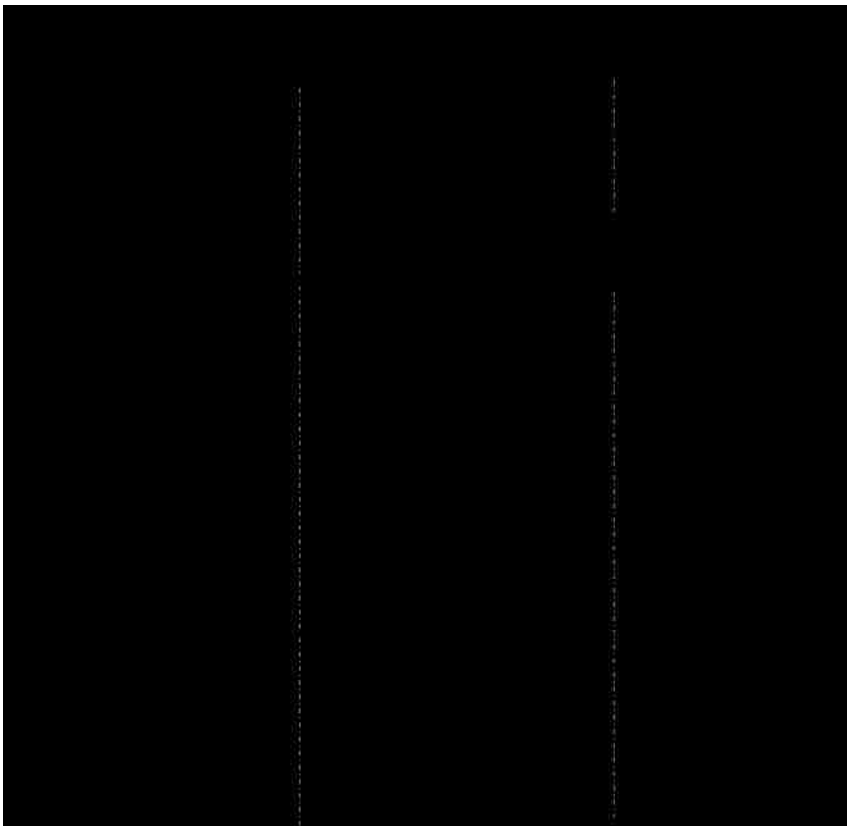

Figure B.4 Free-body diagram of the forces, stress, and strain profiles at the base of each wall panel at YCLT

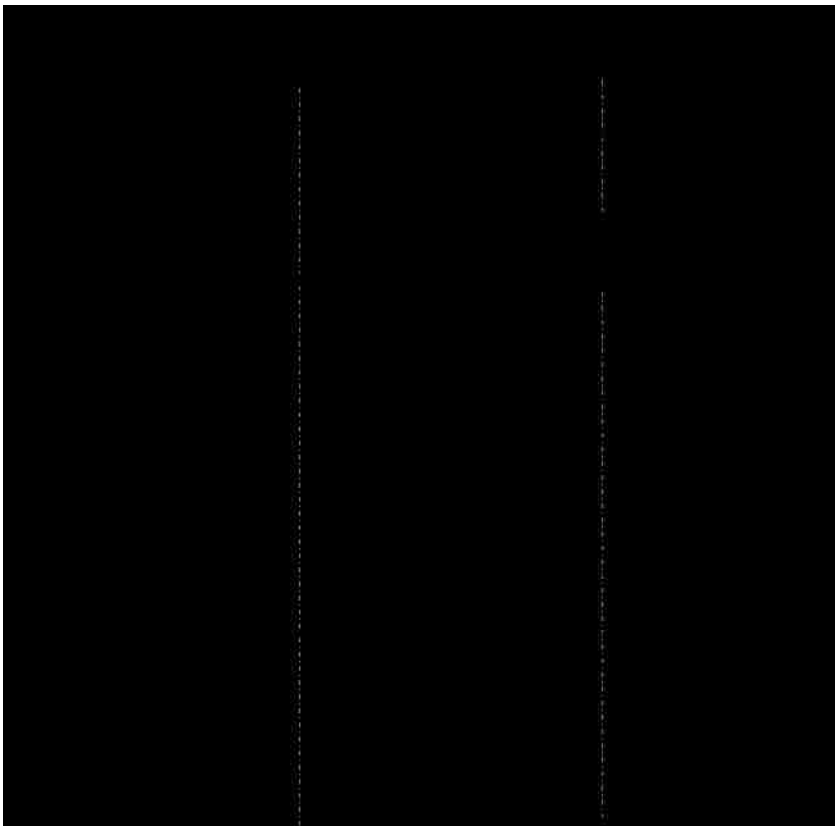

Figure B.5 Free-body diagram of the forces, stress, and strain profiles at the base of each wall panel at SCLT

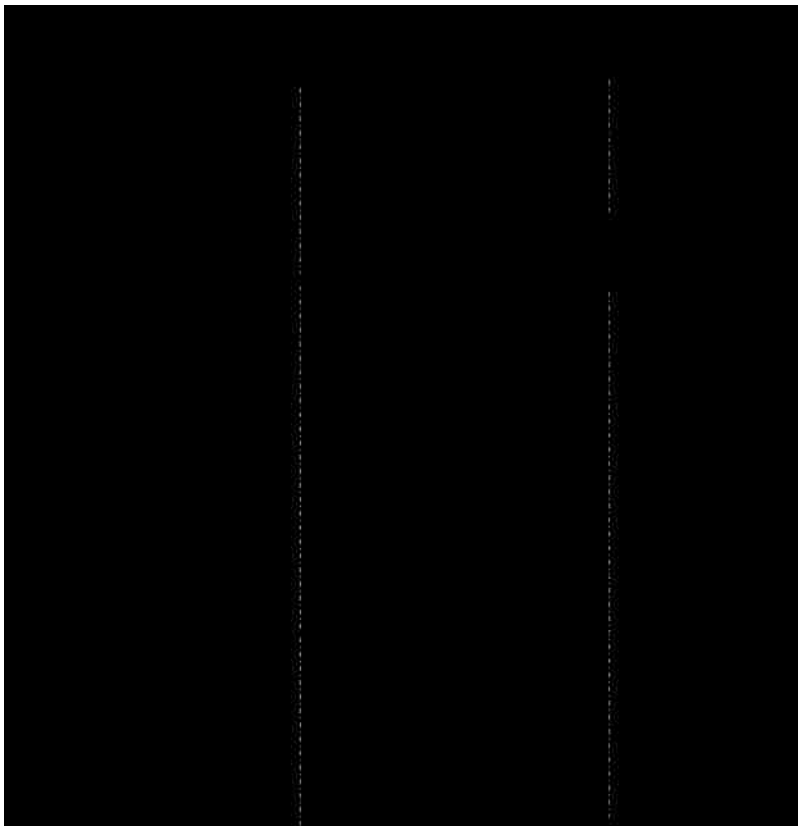

Figure B.6 Free-body diagram of the forces, stress, and strain profiles at the base of each wall panel at CCLT

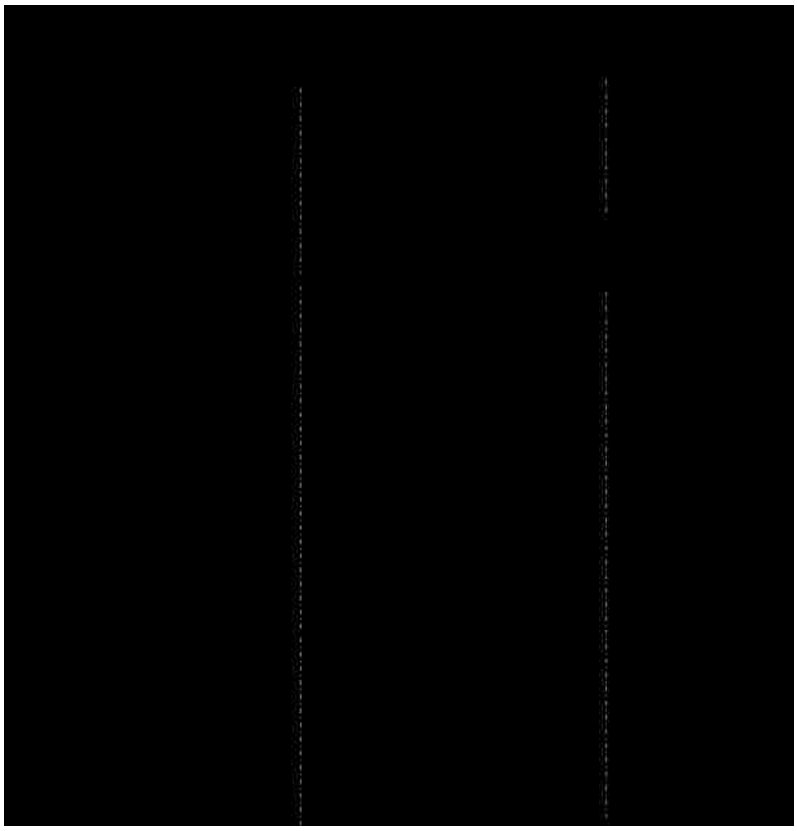

Figure B.7 Free-body diagram of the forces, stress, and strain profiles at the base of each wall panel at LLP

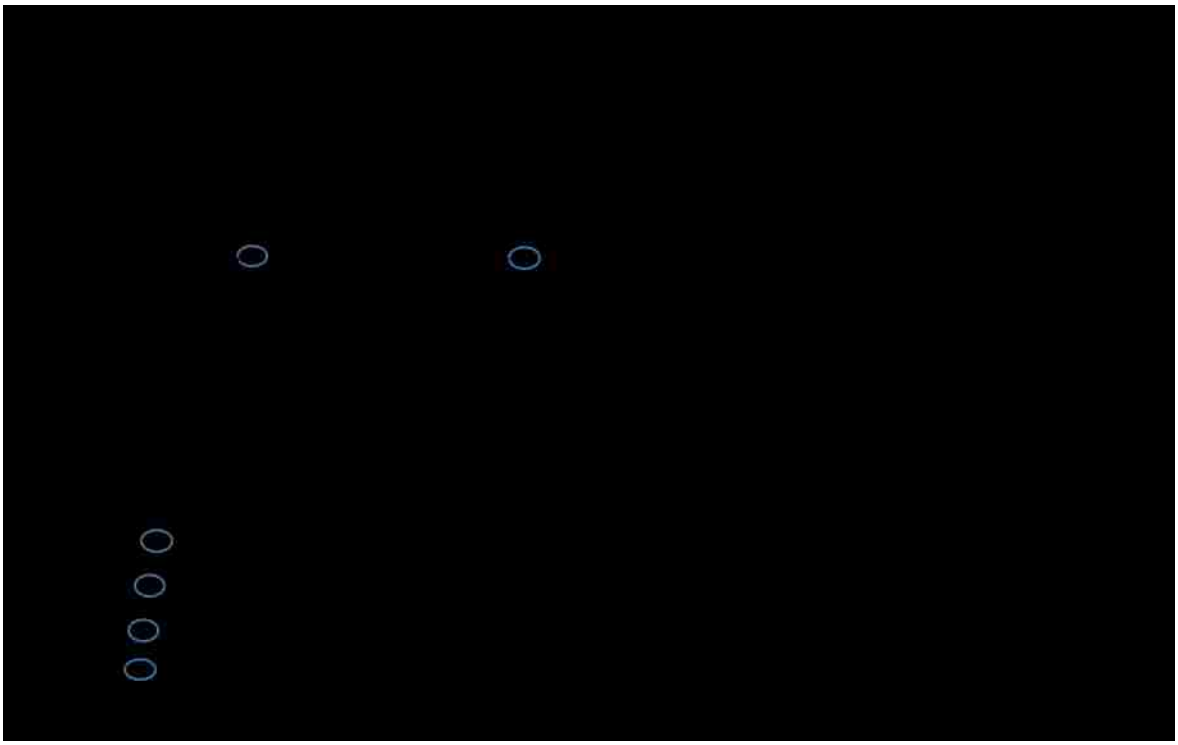

Figure B.8 (a) Deformed position of the wall; (b) overturning moment due to P-Δ effects and the equivalent lateral forces

Figure B.9 Equivalent lateral forces representing the overturning moment due to P-Δ effects at each floor level *i*

APPENDIX C

ESTIMATION OF SHEAR STIFFNESS FROM LATERAL LOAD TEST RESULTS

This appendix presents the estimation of the composite shear stiffness, $(GA)_c$, of test specimens (TS), TS1, TS2, and TS3, as briefly described in Chapter 6 and Ganey (2015) from the applied lateral force, F, versus average shear deformation, $\overline{U_s}$, response.

C.1. Introduction

During the linear-elastic response of the wall, the total elastic deformation response has three components: flexural deformation, Δ_f, shear deformation, Δ_s, and the deformation due to second order effects, Δ_p. Since the gravity loading, N_g, on top of each test specimen (TS) was negligibly small compare to the applied lateral force, F, at H_{act} (see Figure C.1(a)), Δ_p is neglected for all TSs.

To measure the Δ_f and Δ_s, instrumentation was attached to each TS. Figure C.1(b) shows the configuration of the LVDTs and rotation-meters (RMs) placed on the wall to measure the shear and flexural deformations. The lower region was assumed to be subjected to

significant nonlinear (NL) shear deformation (e.g. shear slip) and significant NL flexural deformation (e.g., NL deformation of the CLT panel material). The upper region was assumed to be linear elastic during the first seven full cycles of the applied lateral deformation history (see Figure C.1(c)) and was used to estimate the elastic properties of the CLT panels. In each set of LVDTs, two LVDTs were placed in an X configuration to measure the shear deformation and two LVDTs were placed vertically to measure the axial and flexural deformations. Two rotation meters (RM) were placed 9⅝ inch and 35⅝ inch above the base of the wall (Figure C.1 (b)) to measure the in-plane rotation.

Figure C.2 shows the moment, curvature, rotation, and flexural deformation profiles for each TS under imposed *F* and Figure C.3 shows the shear force and shear deformation profiles for each TS under imposed *F*.

C.2. Estimation of Shear Deformation

The method proposed by Massone and Wallace (2004) was adapted to calculate the average shear deformation, $\overline{U_s}$, within the upper region using the data from the upper LVDT set during the "linear-elastic" response of each TS. The lower LVDT set was not used as the nonlinear (NL) response of the wall initiates earlier in the lower part of the wall compared to the upper region and to avoid the effects of slipping on the deformation estimates.

C.2.1. Estimation of Shear Deformation from One-Story LVDT configuration

Figure C.4(a) shows an *h* tall element from TS deformed by pure shear. The displacement of the two LVDTs positioned in X configuration due to pure shear forces are indicated as D_1^{shear} and D_2^{shear} in Figure C.4. The horizontal displacements of the left and right edges of the wall at the top of *h* are indicated as U_{s1} and U_{s2}, respectively. The average shear deformation for the element in Figure C.4(a) is estimated using the D_1^{shear} and D_2^{shear} as follows:

$$\overline{Us} = \frac{Us_1 + Us_2}{2} = \frac{L_1 - L_2}{2} \quad \text{(C.1)}$$

where $L_1 = \sqrt{D_1^{shear^2} - h^2}$ and $L_2 = \sqrt{D_2^{shear^2} - h^2}$, as shown in Figure C.4(a)

Then,

$$\overline{Us} = \frac{\sqrt{D_1^{shear^2} - h^2} - \sqrt{D_2^{shear^2} - h^2}}{2} \quad \text{(C.2)}$$

Figure C.4(b) shows an *h* tall element from TS deformed by combined shear and flexure. The displacement of the two LVDTs positioned in X configuration by shear are indicated as D_1^{shear} and D_2^{shear} in Figure C.4(b). The horizontal displacements of the left and right edges at the top of the *h* tall element are indicated as U_{s1} and U_{s2}, respectively. The vertical and flexural displacements of the left and right edges at the top of the *h* tall element are shown as V_1, V_2, U_{f1}, and U_{f2}, respectively. The average shear deformation for the element

in Figure C.4(b) is estimated from Eq. (C.1) for $L_1 = \sqrt{D_1^{meas^2} - (h + V_2)^2} - U_{f2}$ and $L_2 = \sqrt{D_2^{meas^2} - (h + V_1)^2} + Uf_1$ as follows:

$$\overline{Us} = \frac{\sqrt{D_1^{meas^2} - (h + V_2)^2} - \sqrt{D_2^{meas^2} - (h + V_1)^2}}{2} - Uf \quad \text{(C.3)}$$

where U_f = the total flexural deformation = $U_{f1} + U_{f2}$

As proposed by Massoni and Wallace (2004), U_f can be estimated from the centroid rotation, θ, for an assumed curvature distribution, which is defined by the relative distance from h to the center of the curvature, α, as follows:

$$U_f = \alpha\theta h \quad \text{(C.4)}$$

where $0.5 \leq \alpha \leq 0.67$ which is bounded by the values for linear and constant distribution curvature; θ can either be estimated from the data recorded by the RM or LVDTs. θ from LVDT data can be approximated as = $(V_1 - V_2)/ 2$

C.2.2. Estimation of Shear Deformation from Two-Story LVDT configuration

In two-story LVDT configuration, the shear deformation from the lower LVDT set is estimated as explained in part C.2.1. The shear deformation form the upper LVDT set is estimated by considering the effect of the deformation of the lower region on the readings of the upper LVDTs. The estimation of shear deformation of the upper LVDT set is explained step by step in this section.

Figure C.5(a) shows the configuration of the vertical and diagonal lower and upper LVDTs which are labeled from 1 to 8, respectively. The lower vertical LVDTs, 7 and 8, and the upper vertical LVDTs, 6 and 6, are assumed to be spaced L_o apart from each other.

Figure C.5(b) and Figure C.6 show the deformed configuration of the wall within lower and upper LVDT regions. In Figure C.5(b), the initial length, deformation, horizontal and vertical displacement of each LVDT are denoted as L_n, ΔL_n, Δh_n and Δv_n, respectively, where n is the respective number label of the LVDT.

The vertical and horizontal displacements of LVDTs 7 and 8 at the top of the lower LVDT region, Δv_7 and Δh_7 and Δv_8 and Δh_8 are estimated from the recorded deformations of the lower LVDT set, ΔL_3, ΔL_4, ΔL_7 and ΔL_8, as follows:

$$\Delta v_7 = (L_7 + \Delta L_7)\, cos(\theta_{\Delta 3} - 90) - L_7 \quad \text{(C.5a)}$$

$$\Delta h_7 = (L_7 + \Delta L_7)\sin(\theta_{\Delta 3} - 90) \quad \text{(C.5b)}$$

$$\Delta v_8 = (L_8 + \Delta L_8)\cos(90 - \theta_{\Delta 4}) - L_8 \quad \text{(C.6a)}$$

$$\Delta h_8 = (L_8 + \Delta L_8)\sin(90 - \theta_{\Delta 4}) \quad \text{(C.6b)}$$

where $\cos\theta_{\Delta 3} = \frac{{L_0}^2 + (L_7+\Delta L_7)^2 - (L_3+\Delta L_3)^2}{2L_0(L_7+\Delta L_7)}$ and $\cos\theta_{\Delta 4} = \frac{{L_0}^2 + (L_8+\Delta L_8)^2 - (L_4+\Delta L_4)^2}{2L_0(L_8+\Delta L_8)}$

The vertical and horizontal displacements of LVDTs 5 and 6 at the top of the upper LVDT region, Δv_5 and Δh_5 and Δv_6 and Δh_6 are estimated from the recorded deformations of the upper LVDT set, $\Delta L_3, \Delta L_4$, ΔL_7 and ΔL_8, and $\Delta v_7, \Delta h_7$, Δv_8, and Δh_8 as follows:

$$\Delta v_5 = (L_5 + \Delta L_5)\, cos(\theta_{\Delta 1} + \theta_{78} - 90) - L_5 \quad \text{(C.7a)}$$

$$\Delta h_5 = (L_5 + \Delta L_5)\, \sin(\theta_{\Delta 1} + \theta_{78} - 90) \quad \text{(C.7b)}$$

$$\Delta v_6 = (L_6 + \Delta L_6)\, \cos(90 + \theta_{78} - \theta_{\Delta 2}) - L_6 \quad \text{(C.8a)}$$

$$\Delta h_6 = (L_6 + \Delta L_6)\, \sin(90 + \theta_{78} - \theta_{\Delta 2}) \quad \text{(C.8b)}$$

where θ_{78} = the rigid body rotation at the bottom of the upper LVDT set due to flexural deformation at the top of the lower LVDT set $= \tan^{-1}\left(\frac{\Delta v_8 - \Delta v_7}{L_0 + \Delta h_7 - \Delta h_8}\right)$; $L_{78} = \frac{\Delta v_8 - \Delta v_7}{\sin \theta_{78}}$; $\cos \theta_{\Delta 1} = \frac{{L_{78}}^2 + (L_5 + \Delta L_5)^2 - (L_1 + \Delta L_1)^2}{2 L_{78} (L_5 + \Delta L_5)}$; $\cos \theta_{\Delta 2} = \frac{{L_{78}}^2 + (L_6 + \Delta L_6)^2 - (L_2 + \Delta L_2)^2}{2 L_{78} (L_6 + \Delta L_6)}$

Then, the average shear deformation at the top of the upper LVDT is:

$$\overline{Us} = \frac{\sqrt{(L_1 + \Delta L_1)^2 - (h + \Delta v_5)^2} - \sqrt{(L_6 + \Delta L_6)^2 - (h + \Delta v_6)^2}}{2} - Uf \quad \text{(C.9)}$$

where $Uf = \theta_2 \alpha L_5$; θ_2 =the flexural rotation at the top of the upper LVDT set.

C.2.3. Corrections Imposed

C.2.3.1. Correction Applied to the Readings from Lower Diagonal LVDTs

Except for TS3c, the bottom end of the upper diagonal LVDTs (i.e. LVDTs 3 and 4) were attached to a point 2.75 inch higher than the point where the upper end of the lower diagonal LVDTs were attached (Figure C.6(a) and Figure C.6(b). Therefore, the Δh_7 and Δh_8 are

corrected to take in to account the contribution of the rigid boy rotation, θ_{78}, on the horizontal displacements at the bottom attachment points of the upper LVDTs, $\Delta h'_7$ and $\Delta h'_8$ (see Figure C. 7(b)).

$$\Delta h'_8 = \Delta h_8 + \theta_{78} h' \qquad \text{(C.10a)}$$

$$\Delta h'_7 = \Delta h_7 + \theta_{78} h' \qquad \text{(C.10b)}$$

where h' = the vertical distance between the top attachment of the lower LVDT set and the bottom attachment point of the lower LVDT set.

C.2.3.2. Correction Applied to the Readings from Lower Vertical LVDTs

The lower vertical LVDTs (i.e., LVDTs 7 and 8) were attached right at the South and North edge of the wall, while the upper vertical LVDTs were attached ~3.75 inch away from the South and North edges of the wall (see Figure C.8(a)). As a result, they are measuring a larger vertical displacement than the vertical displacements used in shear deformation calculations presented in part C.2.2, which are derived assuming the lower and upper vertical LVDTs were aligned.

Therefore, to accurately estimate the shear deformation of the wall using the equations presented in part C3.2, a correction is applied to the readings from lower vertical LVDTs, 7 and 8. Figure C.8(b) shows that the lower vertical LVDTs were displaced by the same rotation regardless of where they are attached. Accordingly, the vertical displacement recordings from the LVDTs 7 and 8, Δv_7 and Δv_8, are corrected for an attachment position ~3.75 inch away from the edge:

$$\Delta v'_7 = \Delta v_7 \left(\frac{\frac{L_0}{2}}{\frac{L_{wall}}{2}} \right) \quad \text{(C.11a)}$$

$$\Delta v'_8 = \Delta v_8 \left(\frac{\frac{L_0}{2}}{\frac{L_{wall}}{2}} \right) \quad \text{(C.11b)}$$

where $\Delta v'_7$ = the vertical displacement of LVDT 7, if it was located 3.75 inch away from the edge; $\Delta v'_8$ = the vertical displacement of LVDT 8, if it was located 3.75 inch away from the edge.

C.2.4. Estimation of $(GA)_c$ for TS1 and TS2

The $\overline{U_s}$ was estimated for each TS from the upper LVDT data using Eq. (C.9). Figure C.9(a) and Figure C.9(b) show the estimated average shear deformation history for TS1 and TS2, respectively.

The lateral force, F, vs. $\overline{U_s}$ response in the linear-elastic response range was used to estimate the composite shear stiffness, $(GA)_c$, for each TS (Figure C.3). The F vs. $\overline{U_s}$ data was used to estimate $(GA)_c$ as follows:

$$F = (GA)_c \frac{\overline{U_s}}{h_2} \quad \text{(C.12)}$$

where $(GA)_c = G_c A_c$; A_c= the effective shear area of the composite section $= L_w t_w$

Figure C.10(a) and Figure C.10(b) show a linear regression of the F vs. $\frac{\overline{U_s}}{h_2}$ data for the linear-elastic response range (i.e., up to Θ_r = 0.30%) of TS1 and TS2, respectively.

C.3. References

Ganey, R. (2015). “Seismic Design and Testing of Rocking Cross Laminated Timber Walls,” M.Sc. Thesis, Department of Civil and Environmental Engrg., Univ. of Washington, Seattle, USA.

Massone, L. M. and Wallace, J. W. (2004). “Load-deformation Responses of Slender Reinforced Concrete Walls." ACI Structural Journal, 101(1), pp. 103-113.

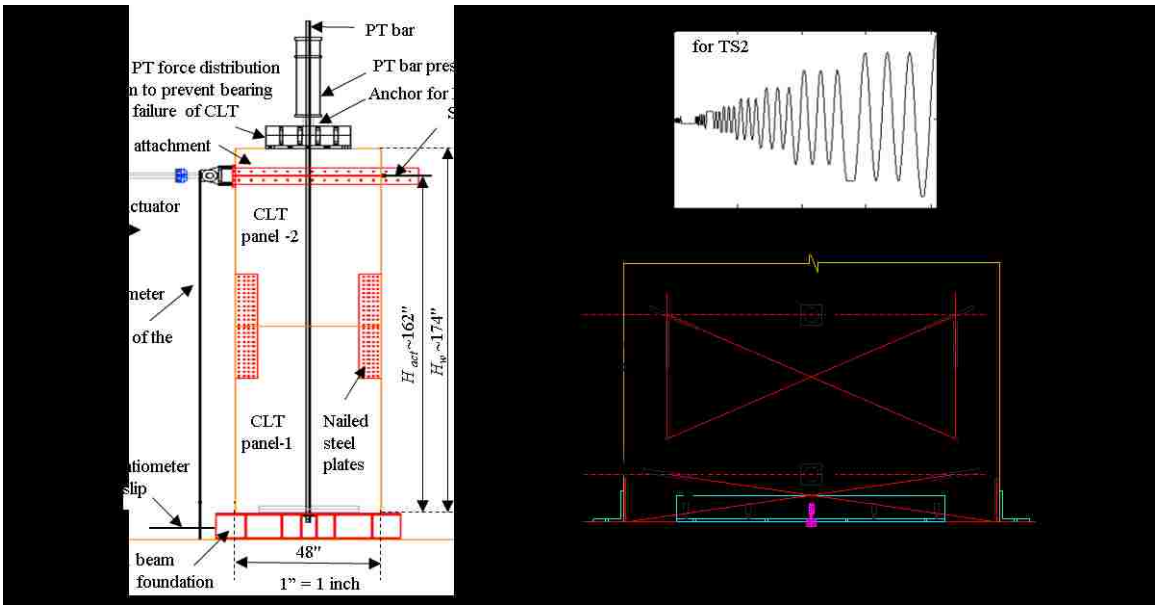

Figure C.1 (a) Elevation view of test set-up; (b) lateral drift history imposed on TS2; (c) layout of instrumentation to measure shear and flexural deformation

Figure C.2 Moment, curvature, rotation, and flexural deformation profiles for TS under imposed *F*

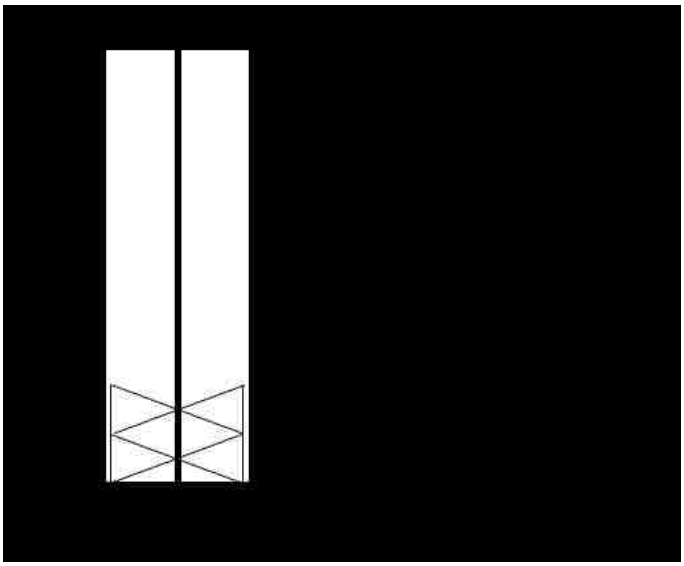

Figure C.3 Shear force and shear deformation profiles for TS under imposed *F*

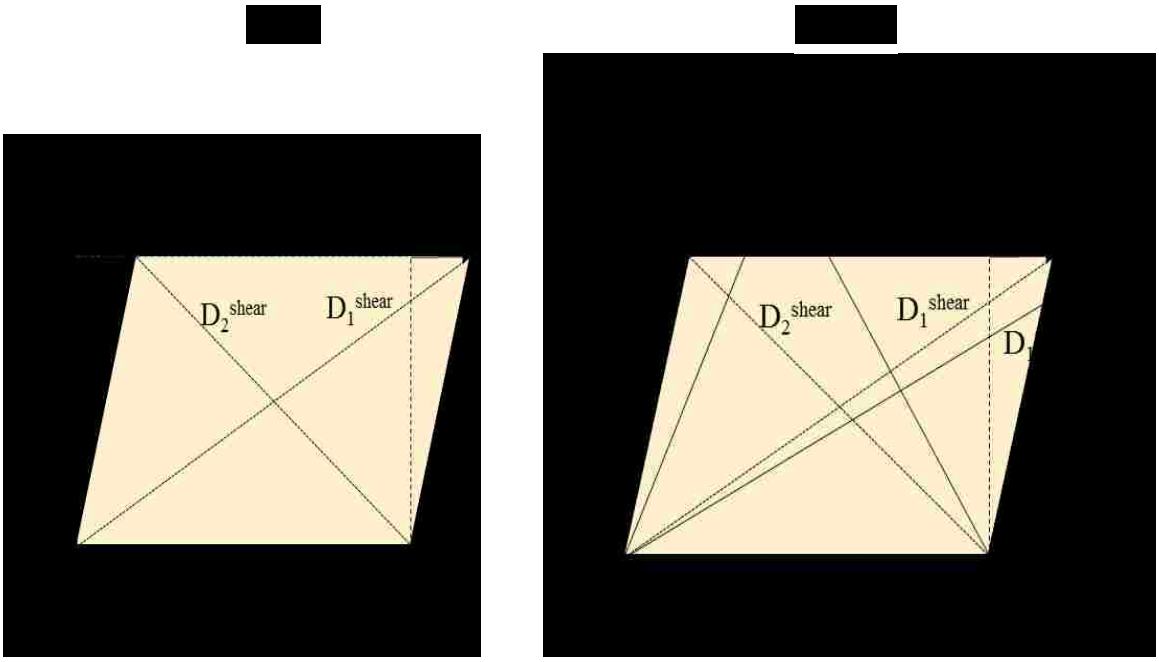

Figure C.4 An *h* tall element from TS deformed: (a) by pure shear; (b) by combined shear and flexure

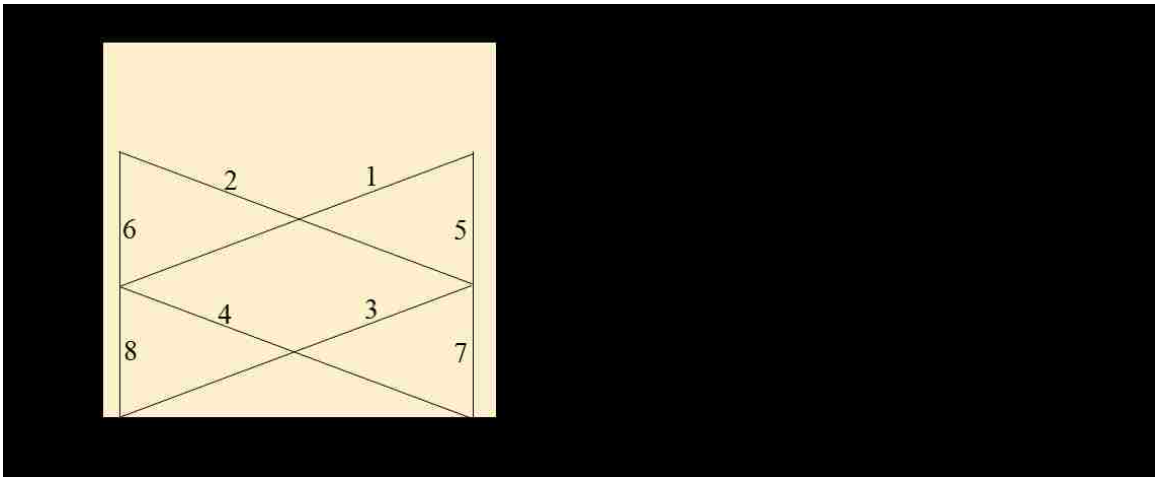

Figure C.5 (a) Standard configuration of vertical and diagonal lower and upper LVDTs; (b) Deformed configuration of a one-story wall element within lower LVDT region


Figure C.6 Deformed configuration of a two-story wall element within upper LVDT region

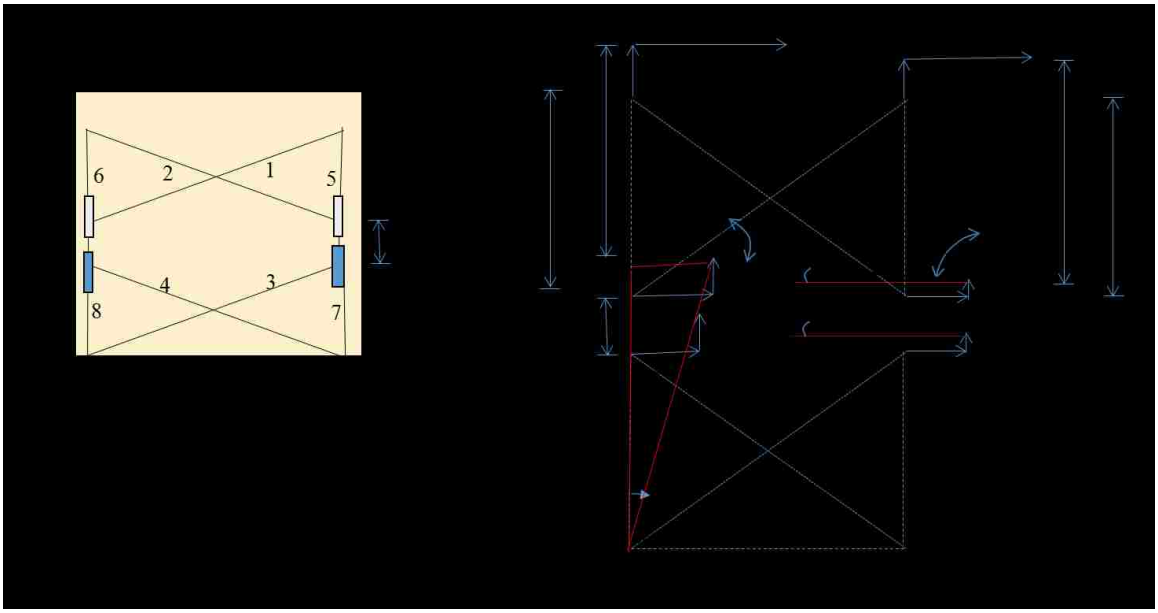

Figure C.7 (a) Actual configuration of vertical and diagonal lower and upper LVDTs for each TS; (b) deformed configuration of each TS within lower and upper LVDT regions

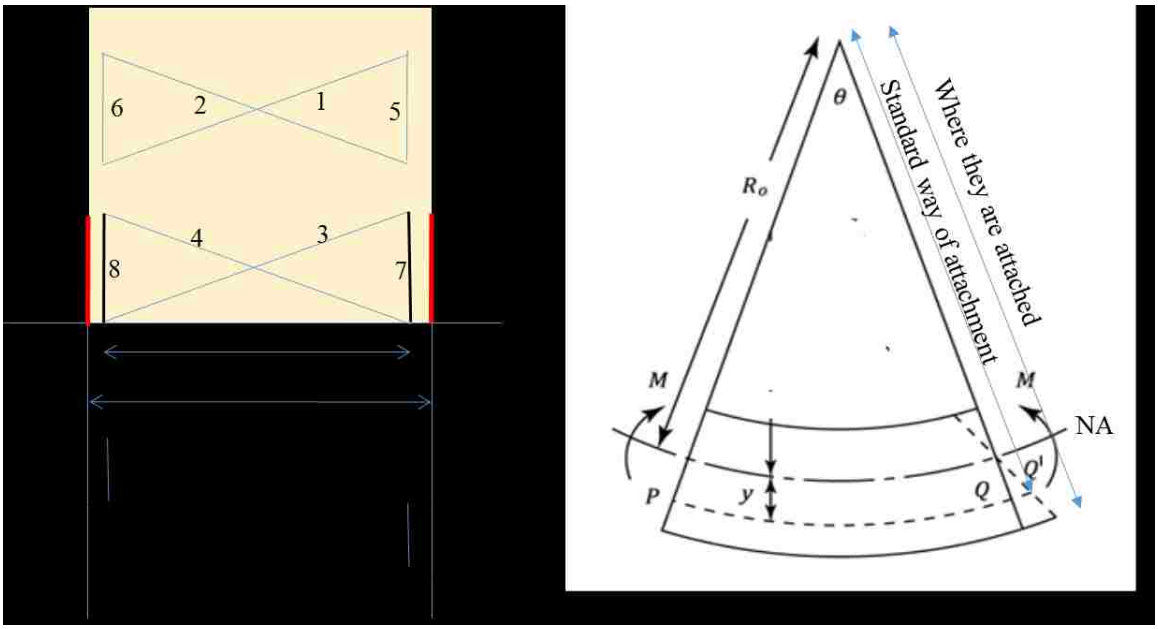

Figure C.8 (a) Comparison of the standard and actual configuration of the vertical lower LVDTs for each TS; (b) curvature distribution for both LVDT attachment positions

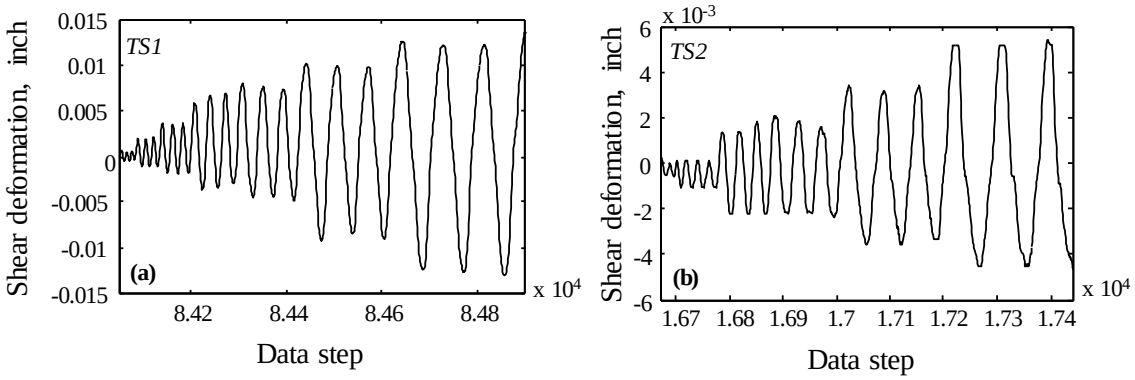

Figure C.9 Average shear deformation history from Eq.(C.9) for: (a) TS1; (b) TS2

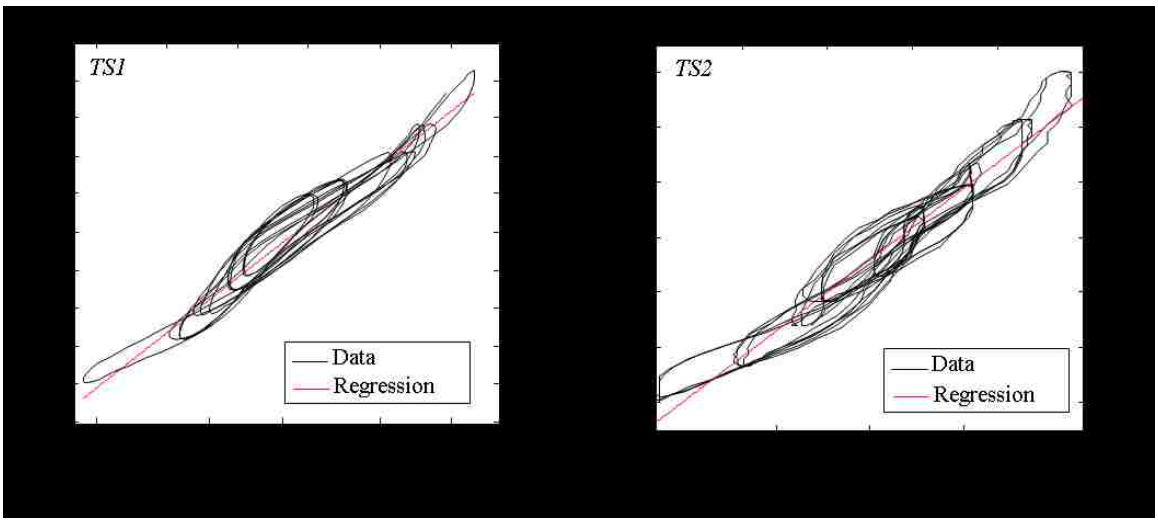

Figure C.10 Estimated shear modulus from test data for: (a) TS1; (b) TS2

VITA

Tugce Akbas was born on August 24, 1990 in Ankara, Turkey. She is the younger of the two daughters of Mrs. Gulsun Akbas and Mr. Halit Levent Akbas. Tugce completed her high school education from Ankara Ari Science High School in 2007. Tugce graduated with the first rank from the Department of Civil Engineering at Middle East Technical University in June 2011 by receiving her Bachelors of Science degree in Civil Engineering. She started her graduate studies in the Department of Civil and Environmental Engineering at Lehigh University in August 2011. Tugce received her Master of Science degree in Structural Engineering in May 2013 and expects to complete her PhD education in the same field in April 2016.